

Small Molecule Effects on Amyloidogenic, Intrinsically Disordered Peptides

by

Lucy Claire Elizabeth Barber

Astbury Centre for Structural Molecular Biology
University of Leeds

Submitted in accordance with the requirements for the degree of
Doctor of Philosophy

July 2019

Declaration of Authorship

The candidate confirms that the work submitted is her own and that appropriate credit has been given where reference has been made to the work of others.

This copy has been supplied on the understanding that it is copyright material and that no quotation from the thesis may be published without proper acknowledgement.

The right of Lucy Claire Elizabeth Barber to be identified as Author of this work has been asserted by her in accordance with the Copyright, Designs and Patents Act 1988.

Acknowledgements

It is with great pleasure that I thank all the people who have helped me throughout my time in Leeds. Firstly, my supervisors Prof. Sheena Radford and Dr Anastasia Zhuravleva. This work would have been impossible without your support and advice. I am very glad to have been mentored by two strong and successful women in science and I am incredibly grateful for the time and hard work that has gone into all aspects of the project and in preparing this thesis. Thanks to my funders: BBRSC White Rose and the University of Leeds.

I would like to thank the members of the Radford and Zhuravleva groups who have provided endless advice, support, and baking opportunities during this project. Special thanks go to Dr Patrick Knight and Dr Yong Xu for conducting the mass spectrometry included in this project, Dr Arnout Kalverda and Dr Roberto Maya for their help and NMR advice, and Dr Hugh Smith for helping with command line and LaTeX. Thanks go to Dr Katie Stewart, Dr Lorna Kelly, and The French Guy for their friendship and advice. Particular thanks go to Mike Davies for his friendship and ever present desire to have tea, and Patrick, again, for being an excellent housemate and helping me overcome so much (also for encouraging my unhealthy relationship with Tesco). I would like to express my gratitude to Nasir Khan who has been extremely helpful and caring throughout my PhD.

Thanks to my incredible support teams. Joanna Hargreaves and Katie Nicoll Baines, who have been truly wonderful friends throughout this PhD, ever feisty and always there for me. My amazing Worcester family (and Cookie) who rallied around when things got really tough. Jean-Claude who has been patient, caring, and ever ready to offer encouragement. The White Rosettes, an incredible group of women, singing with whom has been the highlight of my time in Leeds and a welcome focus when science was being mean. Thanks should not be forgotten to good friends from the early years, Julia, Anna, and the BRFC.

Finally my deepest gratitude goes to my family. A sturdy anchor in the storm. I am so grateful for all that you have done to support me, I really could not have done this without you. Special thanks goes to my amazing sister for the work dates, pep talks, and a more than healthy splash of humour.

I have been incredibly lucky to have had all the support and care from so many people who have helped me to complete this PhD.

Abstract

In recent years there has been an explosion of interest in the physiological functions of intrinsically disordered peptides (IDPs) and how they are involved in diseases, specifically amyloid diseases. A fascinating aspect of amyloid is that rigid, ordered fibrils can be formed from highly flexible IDPs such as, Amyloid- β ($A\beta$) and human Islet Amyloid Polypeptide (hIAPP). These two peptides aggregate to form amyloid in two, currently incurable diseases: Alzheimer's disease and Type II Diabetes Mellitus (TIIDM) respectively.

The early steps of how $A\beta$ and hIAPP transition from disordered monomers to conformers compatible with amyloid formation is an enigma which remains a challenge to understand in molecular detail. The combination of IDP structural fluidity and the complexities of amyloid formation makes structural analysis and study of this area challenging to investigate but has the potential to reveal invaluable information. The strategy for such investigation presented here focuses on searching for small molecules able to stabilise monomeric conformers of these peptides and hence to potentially disfavour amyloid formation.

This work presents a methodological strategy to assess small molecule effects on recombinantly expressed and purified $A\beta_{40}$ amyloid aggregation. The strategy is then implemented on a carefully selected set of lead molecules; a library of 67 compounds were selected from *in silico* rapid overlay of chemical structures (ROCS) analysis based on structural similarity to either 1,2-naphthoquinone, adapalene, bexarotene, MM3003, or UV11352. These were screened for $A\beta_{40}$ amyloid perturbation effects using a Thioflavin-T fluorescence assay and lead compounds were identified. Lead compounds which could modulate amyloid formation were then assessed by a carefully selected toolbox of methods including Electrospray ionisation ion mobility mass spectrometry, and electron microscopy. Finally a set of complementary NMR methods are presented which enable residue specific structural propensity (residual dipolar couplings, temperature coefficients and $\delta C\alpha$ measurements) and flexibility (transverse relaxation rates, heteronuclear nuclear Overhauser effects) of small molecule-induced conformers to be monitored and compared with the same proteins in the absence of bound ligand.

The framework laid out in this work has great impact potential due to its applicability to the amyloid and IDP fields. The ability to study early species in the amyloid process will reveal insights on important structures and potential folding routes in the amyloid aggregation process.

Contents

Declaration of Authorship	iii
Acknowledgements	v
Abstract	vii
List of Figures	xv
List of Tables	xix
Abbreviations	xxi
1 Introduction	1
1.1 The Impact of Amyloid	2
1.1.1 Introducing Amyloid	2
1.1.2 The Major Architecture for Amyloid Aggregates	4
1.1.3 Current Understanding of the Mechanism of Amyloid Formation	7
1.1.4 Amyloid Diseases have an Immense Impact Globally	10
1.1.5 Amyloid Toxicity in Disease	14
1.1.6 Functional Roles of Amyloid	16
1.2 Intrinsically Disordered Peptides	18
1.2.1 Defining Intrinsic Disorder	18
1.2.1.1 Contrasting Disordered, Misfolded, and Unfolded Peptides	19
1.2.2 Functional Disorder	22
1.3 Intrinsic Disorder in Amyloid	25
1.3.1 Introducing $A\beta_{40}$: an important IDP in Alzheimer’s Disease	25
1.3.2 Introducing hIAPP: an important IDP in Type II Diabetes Mellitus	28
1.3.3 Links between Alzheimer’s Disease and Type II diabetes Mellitus	29
1.3.4 $A\beta_{40}$ and hIAPP interactions	30
1.3.5 Current understanding of the $A\beta_{40}$ and hIAPP monomer roles in the amyloid pathway	31
1.4 Strategies for Studying IDPs in Amyloid Formation: Approaches for Trap- ping Amyloid Species for Structural Analysis	34
1.4.1 ThT Fluorescence as a Reporter for Amyloid Aggregation <i>in vitro</i>	39

1.4.2	Testing Small Molecule effects on Amyloid Aggregation in a Physiological Environment	41
1.4.3	The Value of Electron Microscopy in Amyloid Fibril Observation	44
1.4.4	Use of Electrospray Ionisation Ion Mobility Spectrometry Mass Spectrometry (ESI-IMS-MS) to Observe Monomer and Small Oligomers in IDP ensembles	44
1.4.5	Residue Specific Effects of Small Molecules Can be Monitored by Complementary NMR Methods	47
1.5	Thesis Aims	49
2	Materials and Methods	51
2.1	Materials	51
2.1.1	Technical Equipment	51
2.1.2	Chemicals	54
2.2	Methods	57
2.2.1	Molecular Biology	57
2.2.1.1	<i>E. coli</i> Bacterial strains and plasmids	57
2.2.1.2	Preparation of competent <i>E. coli</i> cells	57
2.2.1.3	LB medium and Agar Plate Preparation	58
2.2.1.4	Transformation of <i>E. coli</i> cells	58
2.2.1.5	Plasmid Amplification	59
2.2.1.6	Agarose Gel Electrophoresis to Indicate DNA Size and DNA sequencing	59
2.2.2	Protein Expression and Purification	60
2.2.2.1	Expression of unlabelled A β_{40}	60
2.2.2.2	Expression of ¹⁵ N/ ¹³ C-labelled A β_{40}	60
2.2.2.3	Multistep Purification of A β_{40}	61
2.2.2.4	Expression of the hIAPP-containing Quadripartite Construct	64
2.2.2.5	Multistep purification of hIAPP	65
2.2.3	SDS-PAGE	69
2.2.4	Computational ROCS	71
2.2.5	Biophysical Techniques	71
2.2.5.1	ThT fluorometry	71
2.2.5.2	Transmission Electron Microscopy Techniques	72
2.2.5.3	Measuring Fibril Yield	72
2.2.5.4	ESI-IMS-MS	73
2.2.5.5	Nuclear Magnetic Resonance techniques	73
2.2.6	<i>In vivo</i> β -lactamase assay	77
3	Creating a Toolbox of Methods to Study Small Molecule Effects on Amyloidogenic Peptides	81
3.1	Objectives	81
3.2	Recombinant Expression and Purification of A β_{40} from Insoluble Inclusion Bodies	82
3.2.1	Optimisation of Expression Conditions of A β_{40} to Maximise Yield	84
3.2.2	Optimisation of Ion Exchange Chromatography in A β_{40} Purification	85
3.2.3	Completion of A β_{40} purification	88

3.2.4	Summary of A β_{40} Production	89
3.3	Production of IAPP for <i>in vitro</i> Aggregation Studies	89
3.3.1	Recombinant Expression of hIAPP as a Soluble Quadripartite Construct	93
3.3.1.1	Variation of Cell strain to Increase Peptide Expression Yield	93
3.3.1.2	Optimisation of Growth Conditions for Efficient Peptide Production	96
3.3.2	Multi-step Purification of IAPP from the Soluble Quadripartite Construct	98
3.3.2.1	Optimising Flows for Chitin Affinity Purification	98
3.3.2.2	Solubilisation of Buffer Salts in the Intein Cleavage Solution Solubilisation for C-terminal Amidation.	101
3.3.2.3	Optimisation of the Glu-C Endoprotease Cleavage for IAPP Release	102
3.3.2.4	Separation of 4 kDa and 2 kDa Peptides using RP-HPLC	105
3.3.3	Methods to Measure hIAPP Concentration	108
3.3.4	Summary of IAPP Production	109
3.4	Compilation of Methods to Study IDP Amyloid Formation	110
3.4.1	Summary and Outline of the Toolbox	113
3.5	Method Optimisation for Monitoring Small Molecule Effects on Amyloid Aggregation of Intrinsically Disordered Peptides	114
3.5.1	ThT Fluorometry to Screen for Small Molecule Effects on A β_{40} Aggregation	114
3.5.1.1	Validation of Fluorescence Detection Strategy	114
3.5.1.2	Assessment of the Effect of DMSO on A β_{40} Aggregation	115
3.5.1.3	Assessment of Varying Preparations of A β_{40}	116
3.5.1.4	Assurance of Sample Consistency through Testing of A β_{40} Solubilisation Methods	117
3.5.1.5	The Influences of Buffer Choice on Aggregation Kinetics	118
3.5.1.6	Compatibility of ThT Fluorometry as an Indicator of Compound Effects on A β_{40} Aggregation	121
3.5.2	Development of Quantification Strategies to Extract Objective Measures of Aggregation Kinetics from ThT fluorometry	122
3.5.3	Development of an SDS-PAGE-based Method to Measure the Yield of A β_{40} Aggregation	124
3.5.4	Transmission Electron Microscopy to Qualitatively Observe Aggregate Forms	126
3.5.4.1	Investigation of the Diversity of Fibril Morphology in Different Preparations using TEM	127
3.5.4.2	Investigation of Effect of DMSO on A β_{40} Aggregate Morphology	130
3.5.4.3	Comparison of Small Molecule Effects on A β_{40} Aggregates	132
3.5.5	ESI-IMS-MS Analysis of the Interactions Between Small Compounds and A β_{40}	134
3.5.6	Tripartite A β -lactamase Assay to Provide <i>in vivo</i> Information on A β_{40}	135
3.6	Discussion	139

4	Screening for Novel Modulators of Aβ₄₀ Aggregation	143
4.1	Objectives	143
4.2	Introducing Focused Screening and Compound Library Selection using ROCS.	144
4.2.1	Selection of Known Modulators of A β ₄₀ Aggregation as a Basis for Library Production	146
4.2.2	Compound Library Creation using ROCS	149
4.3	Screening for Compounds which Modulate A β ₄₀ Aggregation using Thioflavin-T Fluorescence	156
4.3.1	Initial screening of 67 compounds for A β ₄₀ modulatory behaviour	156
4.3.2	Quantitative Analysis of Compound Effects on A β ₄₀ Aggregation Profiles	166
4.3.2.1	Confirmation of Compound Identity by Mass Spectrometry	176
4.4	Verification of Compound-mediated effects on Amyloid Aggregation using a Multi-method Approach	189
4.4.1	Assessment of the Reproducibility of Compound-Induced Modulation of A β ₄₀ Aggregation using Titration Effects	189
4.4.2	Quantification of the Extent of Aggregation of A β ₄₀ in the Presence of Each Compound	194
4.4.3	A β ₄₀ forms Fibrillar Aggregates in the Presence and Absence of Compounds	196
4.5	Probing the Interaction between Small Molecules and A β ₄₀ Species	199
4.5.1	Probing the Molecular Interaction between Compounds and A β ₄₀ by ESI-IMS-MS to Indicate Binding Mode	199
4.6	Probing for Potential Molecular Interactions between Compounds and A β ₄₀ by NMR	203
4.6.1	Analysis of Promising Compound A12a in Modulating A β ₄₀ Aggregation and Discovery of Compound Stability	210
4.7	Discussion	214
5	Residue Specific Investigation into the Intrinsically Disordered Aβ₄₀ Peptide	219
5.1	Prerequisites to the study of A β ₄₀ by NMR	221
5.1.1	Optimisation of Sample Conditions for NMR Investigation	221
5.1.1.1	Comparing Ammonium Acetate and Sodium Phosphate as Buffers for NMR Samples	222
5.1.1.2	Effect of Temperature on the ¹ H ¹⁵ N-HSQC A β ₄₀ Spectrum	222
5.1.1.3	Effect of pH on the ¹ H ¹⁵ N-HSQC A β ₄₀ Spectrum	224
5.1.2	Ensuring Stability of the A β ₄₀ Peptide for the Time Period Required for NMR Data Acquisition	226
5.1.3	The Effect of DMSO on A β ₄₀ Conformation	227
5.1.4	Backbone Amide Assignment of A β ₄₀	230
5.2	Characterisation of residue-specific structural propensity in IDPs	236
5.2.1	Predicting Secondary Structure using $\delta^{13}\text{C}\alpha$ Chemical Shifts	236
5.2.2	Hydrogen-bonding and Secondary Structure Indications from Temperature Coefficients	238
5.2.3	Characterisation of Residual Secondary Structure Elements in A β ₄₀ using RDCs	241

5.3	Characterisation of residue-specific dynamics in IDPs	246
5.3.1	T ₂ Measurements to probe ps-ns and μ s-ms Conformational Dynamics of A β ₄₀	247
5.3.2	Heteronuclear NOEs to probe ps-ns Dynamics	250
5.4	Discussion	252
6	Concluding Remarks	257
6.1	Summary of Findings	257
6.2	Future Work	260
A	Appendix A	263
A.1	Absolute ThT fluorescence measured for A β ₄₀ aggregation in the presence of each compound screened	263
A.2	T-test values for quantitative analysis of the ThT screen	269
B	Appendix B: NMR parameters	273
B.1	Data for calculating temperature coefficients	273
B.2	Data for calculating R _{2s}	278
	Bibliography	283

List of Figures

1.1	The progression of amyloid structure research over nearly four centuries	3
1.2	Common indicators of amyloid.	4
1.3	Great heterogeneity is observed in fine fibril structures.	6
1.4	The amyloid formation pathway is complex.	7
1.5	A generic ThT fluorescence profile of amyloid aggregation.	9
1.6	A schematic showing energy barriers between conformational states for folded peptides and IDPs.	19
1.7	A summary of roles of IDPs.	24
1.8	Prevalence of disorder in proteomes across different domains of life.	25
1.9	The proteolytic processing of APP.	27
1.10	Sequences of $A\beta$ cleavage products.	27
1.11	The hIAPP peptide sequence.	28
1.12	Physiological links between Alzheimer’s disease and TIIDM.	30
1.13	Alignment of $A\beta_{42}$ and hIAPP peptide sequences.	31
1.14	Structural predictions for $A\beta_{40}$ and hIAPP.	32
1.15	Sequence comparison of hIAPP and rIAPP.	33
1.16	Free energy landscape predicted for $A\beta_{40}$	34
1.17	Sequence comparison of hIAPP, pramlintide and rIAPP.	36
1.18	ThT ring orientation is restricted when bound to β -sheets.	40
1.19	The Gly-Ser linker sequence between the two domains of β -lactamase	43
1.20	The tripartite β -lactamase assay can identify aggregation-prone sequences.	43
1.21	A schematic of the ESI-IMS-MS set up.	46
2.1	A map of the pMB1 plasmid encoding the β -lactamase construct.	78
3.1	Expression and purification protocol for $A\beta_{40}$	83
3.2	Expression of $A\beta_{40}$ in various cultures.	84
3.3	$A\beta_{40}$ can be expressed in labelled M9 medium.	85
3.4	SDS-PAGE gel to show the protein profile at each stage in the $A\beta_{40}$ purification procedure.	86
3.5	SDS-PAGE gel to show the protein profile at each stage in the optimised $A\beta_{40}$ purification procedure.	87
3.6	Confirmation of $A\beta_{40}$ purification.	88
3.7	Anatomy of the quadripartite construct for the expression of hIAPP.	90
3.8	Workflow of the expression and purification of hIAPP.	92
3.9	The pTXB1 plasmid encoding the hIAPP-containing quadripartite construct.	94
3.10	Expression of the quadripartite construct in different <i>E. coli</i> strains.	95

3.11	SDS-PAGE showing the effect of culture conditions on the expression of the quadripartite construct.	97
3.12	Time course of the expression of the quadripartite construct.	98
3.13	SDS-PAGE showing the protein contents of each wash step during chitin affinity purification.	101
3.14	SDS-PAGE showing efficient production of the leader-hIAPP construct by intein cleavage.	102
3.15	Site directed mutagenesis of the leader sequence.	103
3.16	Variations on the N-terminal leader sequence to improve V8 cleavage.	104
3.17	Optimisation of the V8 cleavage reaction to release hIAPP from the leader sequence.	105
3.18	Separation of Leader and IAPP by RP-HPLC	107
3.19	Compilation of methods for investigating small molecule effect on amyloid aggregation.	111
3.20	3D representation of amyloid distribution in sample wells.	115
3.21	DMSO titration effects on $A\beta_{40}$ aggregation measured by ThT fluorescence.	116
3.22	Effect of preparation methods of $A\beta_{40}$ on aggregation.	117
3.23	Effects of different solubilisation techniques on the reproducibility of amyloid aggregation kinetics.	119
3.24	Effect of buffer on $A\beta_{40}$ aggregation.	120
3.25	Effect of temperature on $A\beta_{40}$ aggregation in different buffers.	121
3.26	Monitoring effect of EGCG or aspirin on $A\beta_{40}$ aggregation by ThT fluorescence.	122
3.27	Schematic for lag time measurement	124
3.28	Demonstration of the Optimised Fibril Yield Sedimentation Assay.	125
3.29	Gross morphology of $A\beta_{40}$ fibrils visualised by TEM	126
3.30	$A\beta_{40}$ aggregate morphology for different scales of ThT fluorescence.	127
3.31	The effect of buffer on $A\beta_{40}$ aggregate morphology by TEM.	129
3.32	$A\beta_{40}$ aggregates formed in varying DMSO concentrations visualised by TEM.	131
3.33	$A\beta_{40}$ aggregate morphology formed in the presence of EGCG or aspirin observed by TEM.	133
3.34	Mass spectrum and drift scope of $A\beta_{40}$	134
3.35	ESI-MS of $A\beta_{40}$ in the presence of EGCG or Aspirin.	135
3.36	Demonstration of the tripartite β -lactamase assay with hIAPP and curcumin.	136
3.37	A comparison of the Tripartite β -lactamase assay with a hIAPP or $A\beta_{40}$ insert.	137
3.38	Optimised tripartite β -lactamase assay for use with an $A\beta_{40}$ insert	138
3.39	A titration of EGCG in the $A\beta_{40}$ tripartite β -lactamase assay	138
3.40	Cell survival monitored using the tripartite β -lactamase assay in the presence of aspirin	139
4.1	The multi-method approach to find and verify compounds which robustly modulate amyloid aggregation.	145
4.2	Structures of the five query compounds used as a root for the screening library.	148
4.3	Examples of structural comparison using ROCS.	149

4.4	The 96-well plate layout used in the ThT screen.	157
4.5	Compound screening by ThT fluorescence.	158
4.6	Screening by ThT fluorescence of compounds A01-A15.	160
4.7	Further screening by ThT fluorescence of compounds A16-A22.	161
4.8	Screening by ThT fluorescence of compounds B01-B14.	162
4.9	Screening by ThT fluorescence of compounds Q01-Q15.	163
4.10	Further screening by ThT fluorescence of compounds Q16-Q28.	164
4.11	Screening by ThT fluorescence of compounds M01, M02, and U01.	165
4.12	A plot of the relative lag times for $A\beta_{40}$ aggregation in the presence of each compound.	168
4.13	A plot of the relative T_{50} for $A\beta_{40}$ aggregation in the presence of each compound.	170
4.14	A plot of the relative final fluorescence intensities for $A\beta_{40}$ aggregation in the presence of each compound.	172
4.15	A heat map to represent extent of evidence of aggregation for each compound to perturb $A\beta_{40}$ aggregation.	174
4.16	Summary of the eight compounds selected for further investigation.	175
4.17	The chemical structures of each of the eight compounds selected for further investigation.	176
4.18	LC chromatogram and MS spectra of library compound A12 and commercial compound A12a.	178
4.19	LC chromatogram and MS spectra of library compound A13 and commercial compound A13a.	179
4.20	LC chromatogram and MS spectra of library compound A14 and commercial compound A14a.	180
4.21	LC chromatogram and MS spectra of library compound A18 and commercial compound A18a.	181
4.22	LC chromatogram and MS spectra of library compound A21 and commercial compound A21a.	182
4.23	LC chromatogram and MS spectra of library compound Q06 and commercial compound Q06a.	183
4.24	LC chromatogram and MS spectra of library compound B08 and commercial compound B08a.	184
4.25	ThT fluorometry screen of the new commercial compounds.	188
4.26	Titration analysis of 1,2-naphthoquinone on $A\beta_{40}$ aggregation.	191
4.27	Titration analysis of the commercial compounds on $A\beta_{40}$ aggregation.	193
4.28	Application of the SDS-PAGE fibril yield assay.	195
4.29	Transmission electron micrographs of $A\beta_{40}$ aggregates in the absence or presence of compounds.	197
4.30	Transmission electron micrographs of $A\beta_{40}$ aggregates in the absence or presence of compounds (continued).	198
4.31	Observation by TEM of circular species formed by $A\beta_{40}$ in the presence of 1,2-naphthoquinone.	199
4.32	Mass spectra of $A\beta_{40}$ in the presence of query compounds.	200
4.33	ESI-Mass spectra of $A\beta_{40}$ in the presence of lead compounds.	201
4.34	ESI-Mass spectra of $A\beta_{40}$ in the presence of different compounds.	202
4.35	Effect of EGCG on $^1\text{H}^{15}\text{N}$ -HSQC spectra of $A\beta_{40}$	203
4.36	Assigned HSQC spectrum for $A\beta_{40}$	204

4.37	HSQC to detect chemical shift perturbations of $A\beta_{40}$ in the presence of A12a.	206
4.38	$^1\text{H}^{15}\text{N}$ -HSQC to detect chemical shift perturbations of $A\beta_{40}$ in the presence of A13a.	208
4.39	$^1\text{H}^{15}\text{N}$ -HSQC to detect chemical shift perturbations of $A\beta_{40}$ in the presence of other lead compounds.	209
4.40	ESI-mass spectra of the hydrolysis of A12a.	211
4.41	Predicted hydrolysed product of A12a.	212
4.42	$^1\text{H}^{15}\text{N}$ -HSQC and ThT fluorescence investigation of the effect of compound A12a on $A\beta_{40}$ aggregation as it undergoes hydrolysis.	213
4.43	The improved toolbox strategy for finding robust modulators of amyloid aggregation.	215
5.1	Preliminary $^1\text{H}^{15}\text{N}$ -HSQC spectra of $A\beta_{40}$ in different salt solutions . . .	223
5.2	Comparison of $^1\text{H}^{15}\text{N}$ -HSQC spectra of $A\beta_{40}$ at high and low temperatures.	224
5.3	$A\beta_{40}$ $^1\text{H}^{15}\text{N}$ -HSQC spectra dependence on pH.	225
5.4	Stability of $A\beta_{40}$ in optimised buffer conditions.	227
5.5	Monitoring the effect of DMSO percentage on the $^1\text{H}^{15}\text{N}$ -HSQC spectrum of $A\beta_{40}$	229
5.6	Assigned $^1\text{H}^{15}\text{N}$ -HSQC spectrum of $A\beta_{40}$	231
5.7	Examples of how $A\beta_{40}$ spectral assignment was conducted.	234
5.8	Evidence for the tentative assignment of Asp1.	235
5.9	Backbone conformation indication from $^{13}\text{C}\alpha$ chemical shifts.	237
5.10	Amide temperature coefficients in $A\beta_{40}$	239
5.11	Representation of how RDCs are measured from protein samples.	242
5.12	RDC probes of $A\beta_{40}$ structural propensity.	244
5.13	Correlation of experimental and published RDCs.	245
5.14	Diverse NMR methods to collect data on different dynamic timescales.	246
5.15	Schematic of transverse relaxation which gives rise to R_2 rates.	247
5.16	R_2 rates for backbone amides in $A\beta_{40}$ to indicate ps-ns dynamics.	249
5.17	Heteronuclear NOEs for $A\beta_{40}$	251
5.18	Schematic of investigation into how small molecules may influence conformation distribution of $A\beta_{40}$	253

List of Tables

1.1	Amyloid diseases and their associated proteins. Reproduced and adapted from [1].	10
1.2	Functional amyloid in various organisms. Reproduced and adapted from [2].	16
1.3	Biophysical methods for monitoring IDP behaviour at various stages of amyloid formation. Adapted from [3–6] and references therein.	37
2.1	The programme used to purify $A\beta_{40}$ by SEC.	63
3.1	Example small molecules used.	81
3.2	hIAPP expression conditions and final OD_{600}	96
4.1	Selected compounds based on the structure of adapalene.	150
4.2	Selected compounds based on the structure of bexarotene.	152
4.3	Selected compounds based on the structure of 1,2-naphthoquinone.	153
4.4	Selected compounds based on the structure of MM11253 and UVI3003.	155
4.5	Mass spectrometry analysis of compound molecular weight.	184
5.1	Table of ^1H , ^{15}N , and ^{13}C values for each residue in $A\beta_{40}$. Resonances are given in ppm and those preceded by a ‘t’ indicate that these assignments are tentative.	232
A.1	Table of t-test values	269

Abbreviations

Aβ	Amyloid-beta peptide
AD	Alzheimer's disease
AFM	Atomic force microscopy
ANS	1-Anilinonaphthalene-8-sulfonic acid
APP	Amyloid precursor protein
AU	Arbitrary units
BACE	Beta-secretase 1
CBD	Chitin binding domain
CCPN	Collaborative computational project for NMR
CD	Circular dichroism
CHC	Central hydrophobic core
CSP	chemical shift perturbation
CSTC	Chemical shift temperature coefficient
CTF	C-terminal fragment
DMSO	Dimethyl sulfoxide
DNA	Deoxyribonucleic acid
DTT	Dithiothreitol
EDTA	Ethylenediaminetetraacetic acid
EGCG	Epigallocatechin-3-gallate
EM	Electron microscopy
ER	Endoplasmic reticulum
ESI	Electrospray ionisation
FDA	U.S. Food and Drug Administration
FRET	Förster resonance energy transfer
FTIR	Fourier-transform infrared spectroscopy

HEPES	4-(2-hydroxyethyl)-1-piperazineethanesulfonic acid
hetNOEs	Heteronuclear nuclear Overhauser effect
hIAPP	Human islet amyloid peptide (or amylin)
HSQC	Heteronuclear single-quantum coherence
HSR	Heat shock response
HTP	High throughput
IDE	Insulin degrading Enzyme
IDP	Intrinsically disordered peptide
IDR	intrinsically disordered region
IMS	Ion mobility spectrometry
IPAP	Inphase antiphase
IPTG	Isopropyl β -D-1-thiogalactopyranoside
LB	Lysogeny broth
LC	Liquid chromatography
LDS	Lithium dodecyl sulfate
mAU	Milli absorbance units
MD	Molecular dynamics
MS	Mass spectrometry
MW	Molecular weight
MWCO	Molecular weight cut off
NEB	New England Biolabs
NMR	Nuclear magnetic resonance
ns	Nanosecond
OD	Optical density
PAINS	Pan assay interference
PCR	Polymerase chain reaction
PDB	Protein data bank
PMSF	Phenylmethylsulfonyl fluoride
ppb	Parts per billion
ppm	Parts per million
ps	Picosecond
QSBDD	Quasi structure based drug design
R₁	Longitudinal relaxation rate

R₂	Transverse relaxation rate
RAR	Retinoid A receptor
RDC	Residual dipolar coupling
RNA	Ribonucleic acid
ROCS	Rapid Overlay of Chemical Structures
RP-HPLC	Reversed-phase high-performance liquid chromatography
RXR	Retinoid X receptor
SDS-PAGE	Sodium dodecyl sulphate-polyacrylamide gel electrophoresis
SEC	Size exclusion chromatography
T₁	Longitudinal relaxation time
T₂	Transverse relaxation time
T7	Bacteriophage T7
TAE	Tris-acetate-EDTA
TB	Terrific broth
TBP	TATA-box binding protein
TFA	Trifluoroacetic acid
TIIDM	Type II Diabetes Mellitus
TEM	Transmission electron microscopy
ThT	Thioflavin-T
Tris	Tris(hydroxymethyl)aminomethane
v/v	Volume to volume ratio
w/v	Weight to volume ratio

Chapter 1

Introduction

The purpose of this thesis is to create a methods approach to study structural conformations in the intrinsically disordered Amyloid-beta₄₀ ($A\beta_{1-40}$) and human Islet Amyloid Polypeptide (hIAPP) monomers which are important in either encouraging or delaying amyloid formation. The aim was to achieve this using small molecules to stabilise various monomer conformations.

To provide context for this work, this chapter introduces key concepts required for understanding amyloid formation, intrinsically disordered peptides (IDPs) and how they can be entwined. Some major amyloidogenic peptides are intrinsically disordered and understanding of the disorder to amyloid transition remains imprecisely defined. The heterogeneous conformer landscapes of intrinsically disordered peptides (IDPs) add complexity to the already elaborate amyloid system. Methods which have contributed to the challenging study of such transitions in these fields are also introduced

Firstly, amyloid will be introduced and a summary of the current understanding of how it is formed will be presented. Additionally, the association of amyloid with disease will be highlighted to demonstrate why amyloid formation needs to be better understood. A key area where more research is needed is the identification of precursor states, in amyloid formation especially for intrinsically disordered peptides since they are responsible for approximately 30 human amyloid diseases [1].

Next intrinsically disordered peptides (IDPs) will be discussed, challenging the common misconception that structure is required for function. Contrasts between IDPs and misfolded proteins will be highlighted. To relate specifically to the topic of this

work, two amyloidogenic IDPs, $A\beta_{40}$ and hIAPP, will be discussed focusing on current understanding of the monomer behaviour.

Finally, a selection of methods will be discussed which have been used to investigate various stages of amyloid aggregation, and IDP conformations. This section will highlight why a multi-method approach is required for studying such heterogeneous systems and will note strategies which have been implemented to battle some of the major challenges which still afflict the field today.

This chapter concludes with clarification of the thesis aims and the approaches which will be taken to accomplish them.

1.1 The Impact of Amyloid

1.1.1 Introducing Amyloid

The aggregation of proteins into amyloid fibrils, a process known as amyloidosis, and their subsequent deposition into extracellular plaques or intracellular inclusion bodies is the key marker of amyloid diseases [1]. Amyloid structures can form both intracellularly and extracellularly [7]. Intracellularly, amyloid can perturb protein and RNA transport [8] as well as cause physiological disruption by sequestering cellular proteins impairing their functionality [9] and perturbing chaperones [10] and homeostasis. Approximately 50 different proteins are associated with amyloid formation in human diseases [1, 11], including Alzheimer's disease, Type II Diabetes Mellitus, and Parkinson's disease, thus elucidation of how amyloid formation occurs is of paramount importance.

Owing to this there has been great advancement in methodology to study amyloid, as reviewed by Iadanza *et al.*, [1]. Figure 1.1 shows the journey of Amyloid understanding from its discovery in the 16th century until recently.

Amyloid fibrils are the most thermally stable, low energy protein aggregates known [7, 12]. It is currently thought that amyloid is a structure which is accessible to most small, simple polypeptides showing little or no sequence homology [13–16] (although there is contradiction and not all studies agree [17]), but cellular control and tight protein homeostatic regulation prevent most proteins from aggregating. This section

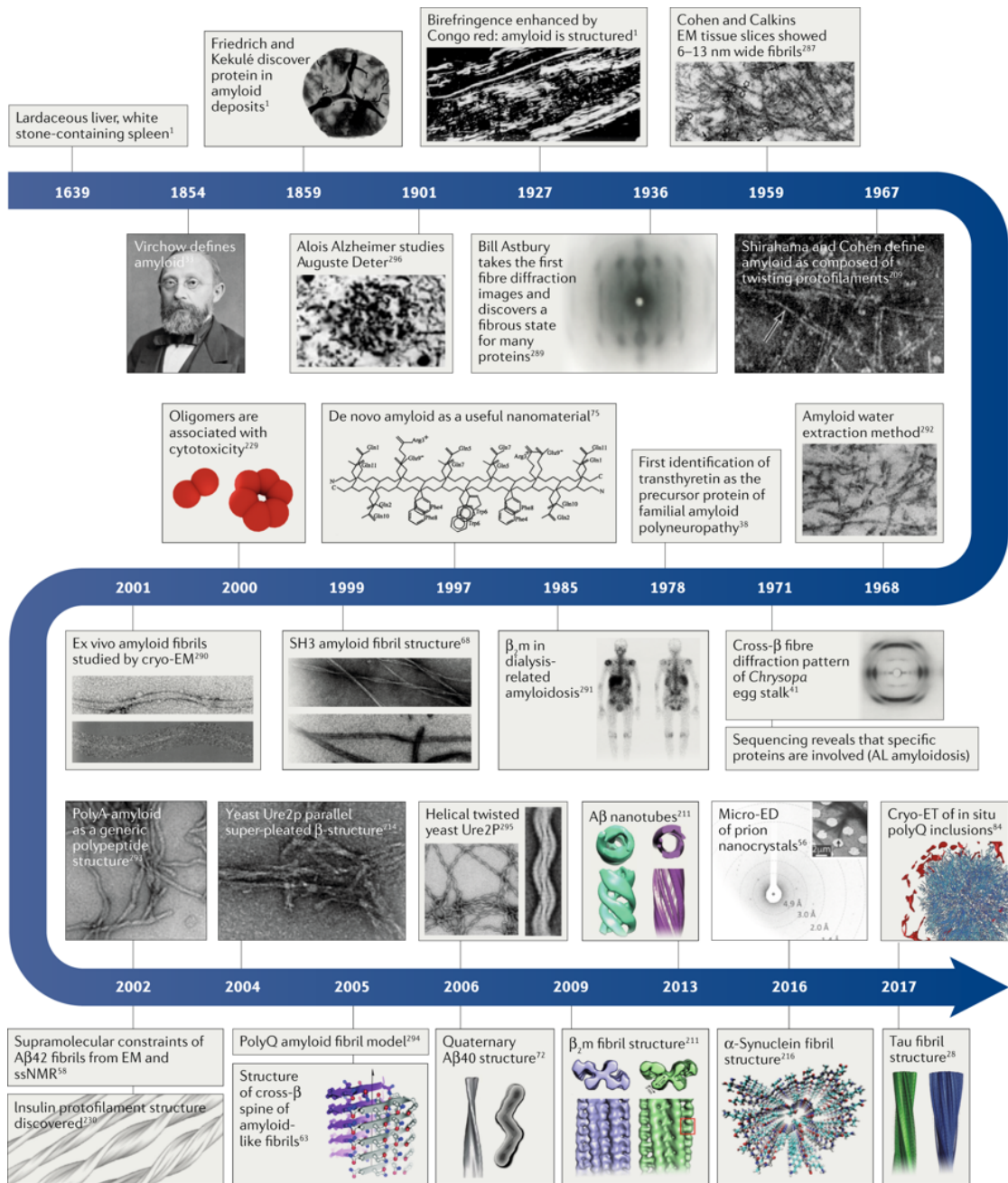


Figure 1.1: The progression of amyloid structure research over nearly four centuries. The timeline displays the history of key discoveries across the amyloid field showing the path to finding atomic level structures of amyloid fibrils. Taken from [1].

summarises the current understanding and remaining key questions and challenges in the field.

1.1.2 The Major Architecture for Amyloid Aggregates

Amyloid can be defined as a stable non-covalent, fibrillar protein aggregate with a dominating cross- β core where the β -sheets lie perpendicular to the fibril axis [1, 7, 12, 18–21] arranged either in parallel or anti-parallel orientations. The fibrillar structures can be observed using electron microscopy (EM), Figure 1.2(a), [7, 12] and the repetitive cross- β structure gives rise to a distinctive X-ray diffraction pattern, Figure 1.2(b), exhibiting 9.7 Å (caused by the packing of β -sheets perpendicular to the fibril axis [21–25]) and 4.7 Å reflections (caused by the packing of adjacent β -strands along the fibril axis [21–25]), Figure 1.2(e). A further typical characteristic of amyloid is red green biofringence under polarised light, Figure 1.2(c and d) [7, 26, 27]. Figure 1.2(f) shows a model fibril reconstructed from cryo-EM data.

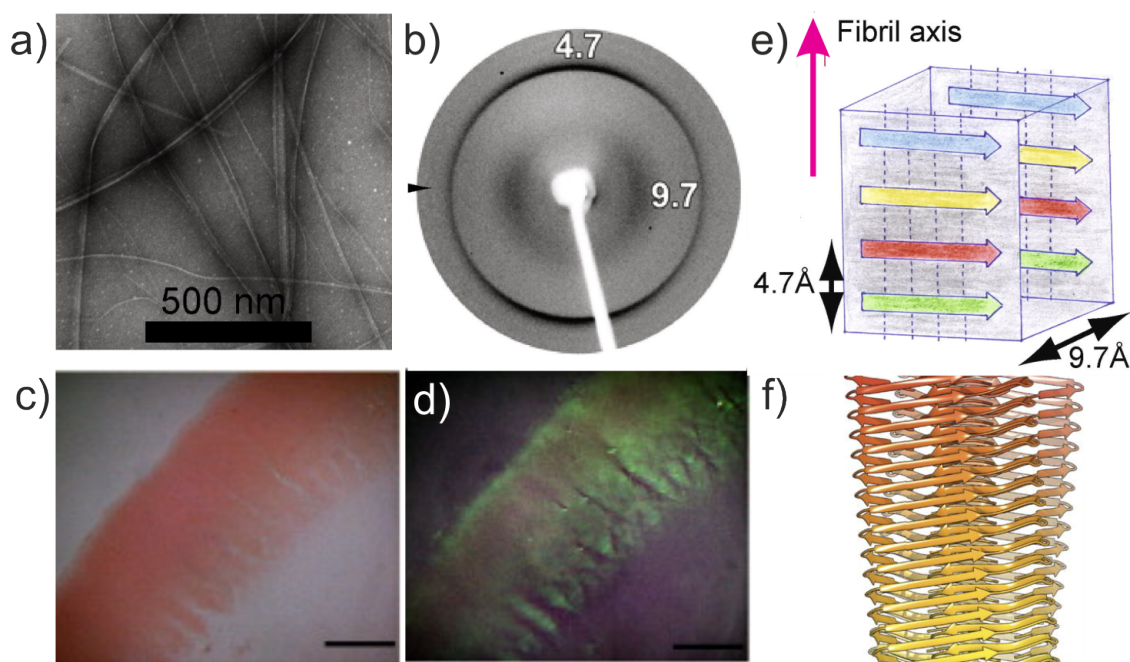


Figure 1.2: Common indicators of amyloid.

- a) A negative stain EM image of $A\beta_{40}$ aggregates which shows long fibrillar species. b) X-ray fibre diffraction pattern showing ~ 10 Å and 4.7 Å reflections of the cross- β fibril architecture. c) $A\beta$ stained with congo red under bright light and d) under polarised light pictures showing congo red-green birefringence, indicative for the β -sheet content. Scale bars: 100 μm . e) Schematic of how the reflections observed in the X-ray diffraction pattern map onto a fibril with parallel β -sheet packing, perpendicular to the fibril axis (pink arrow). f) Atomic model of $A\beta_{42}$ fibril based on cryo-EM. Adapted from [28, 29].

When observed at a macroscopic scale, amyloid fibrils formed from different peptides, regardless of whether they are natively folded (such as β_2 -microglobulin or insulin) or

intrinsically disordered (such as Amyloid- β ($A\beta$), hIAPP, or α -synuclein) are morphologically similar when visualised using techniques such as negative stain transmission electron microscopy (TEM) or atomic force microscopy (AFM) [21, 22]. The fibrils present as unbranched, linear structures with twisted patterning. The length of the fibrils can vary greatly up to the micron scale [12, 21, 22, 30]. In contrast, the fibril diameters observed are much smaller, typically 50 - 100 Å [25, 31] which vary depending on the number of protofilaments which are twisted together. Within samples there is variation in protofibril stoichiometry of fibril composition [32, 33] and the protofilaments can be observed in different arrangements; wrapped around one another, or lined up side-by-side forming ribbons [32, 34–37].

Due to the repetitive backbone structure, a ‘dry steric zipper’ interface is formed (from which water is excluded) as subsequent backbone groups interdigitate [38, 39] resulting in the highly ordered, and densely packed amyloid structures. The β -strands in the cross- β core are extended so the approximate dihedral angles around the C_α are $\phi = -120^\circ$ and $\psi = +120^\circ$ and the hydrogen bonds between each β -strand are essentially planar [40]. The cross- β structure dependence on backbone interactions for stability [23] could partially explain why so many peptides are able to form amyloid [41], however, side-chain packing on steric zipper regions is also important for some amyloid formation [42].

Despite this similar amyloid architecture, many (but not all [43]) amyloid peptides are unable to induce (a process termed cross-seeding) or co-assemble as amyloid with differing protein sequences, i.e. α -synuclein and β_2 -microglobulin cannot associate together to form amyloid fibrils. This indicates that side-chain interactions, and therefore sequence specificity, play a role in amyloid formation which is supported as sequence similarity strongly influences the formation of amyloid fibrils when inducing amyloid formation with differing peptides [42].

On close inspection of amyloid fibrils, heterogeneity in fine fibrillar structure is observed between fibrils formed not only from different precursor proteins, but also between fibrils formed from the same peptides. Figure 1.3 shows contrasting fibril structures created from a single sample of $A\beta_{40}$.

Studies involving a combination of cryo-EM and solid state NMR have confirmed this and have revealed more details on the heterogeneous structures of fibrils, such as varied

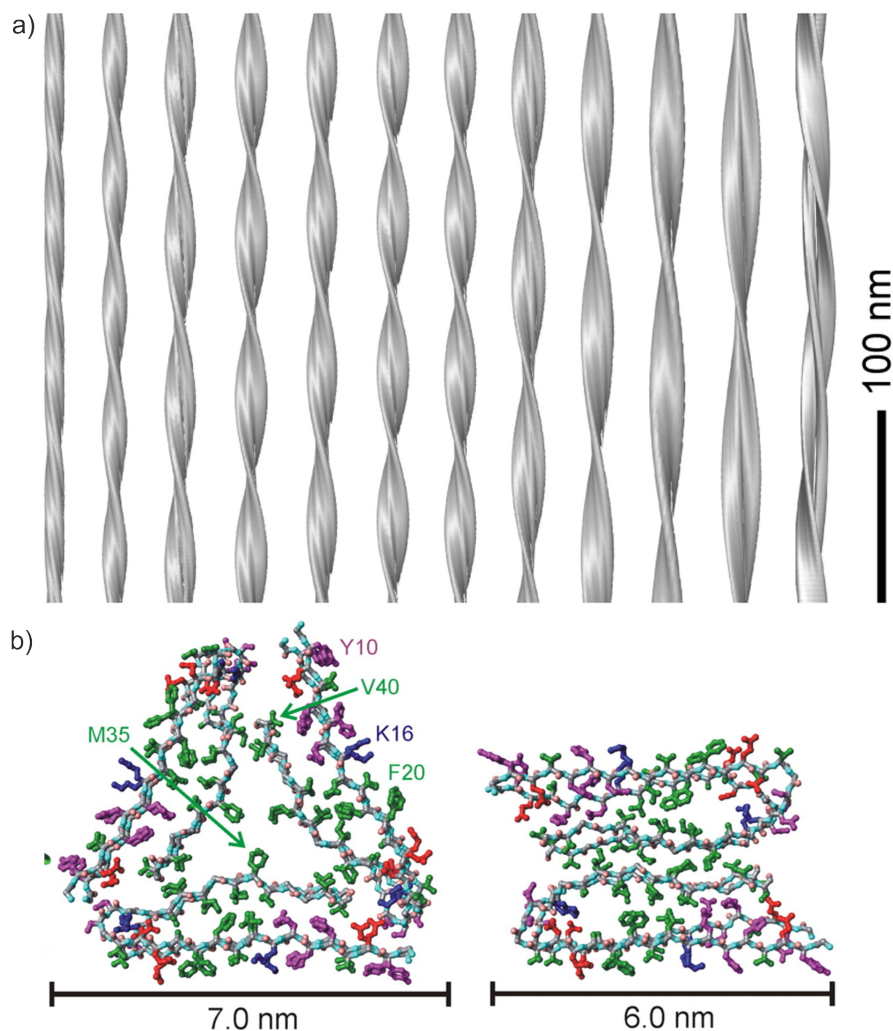


Figure 1.3: Great heterogeneity is observed in fine fibril structures.

a) Reconstructed models of 12 $A\beta_{40}$ fibrils based on cryo-EM data collected from a single sample. b) Atomic representations of 3Q and 2A fibril polymorphs of $A\beta_{9-40}$ viewed down the fibril axis with colour coded residue types: Hydrophobic (green), polar (purple), negatively-charged (red), and positively charged (blue). Backbone nitrogen and carbonyl oxygen atoms are cyan and pink. Adapted from [32, 44–46].

twist and pitch [32], arising from side-chain packing [47]. To date, many studies have shown the role of packing interactions of residues in forming protofilaments and their influence on morphology when combining into mature amyloid fibrils. Interestingly, the ability for different fibril morphologies to be created from the same amyloid peptide may be linked to variation in disease progression [48]. In Alzheimer's diseases, different morphologies have been observed which appear to correlate with different stages in the disease [48].

1.1.3 Current Understanding of the Mechanism of Amyloid Formation

The process by which soluble, monomeric peptides are converted, essentially irreversibly, into insoluble amyloid fibrils has been the focus of much research but remains a major question in the amyloid field. Current understanding of amyloid formation is that it does not occur via a simple, step-wise, linear process. Rather, the amyloid pathway is a playground of partially-folded peptide conformations with various degrees of disorder and folding. Monomers and oligomers sample a variety of forms, with a multitude of kinetic and thermodynamic factors contributing to the journey from monomer to fibril [1, 22]. Figure 1.4 presents a schematic for these processes.

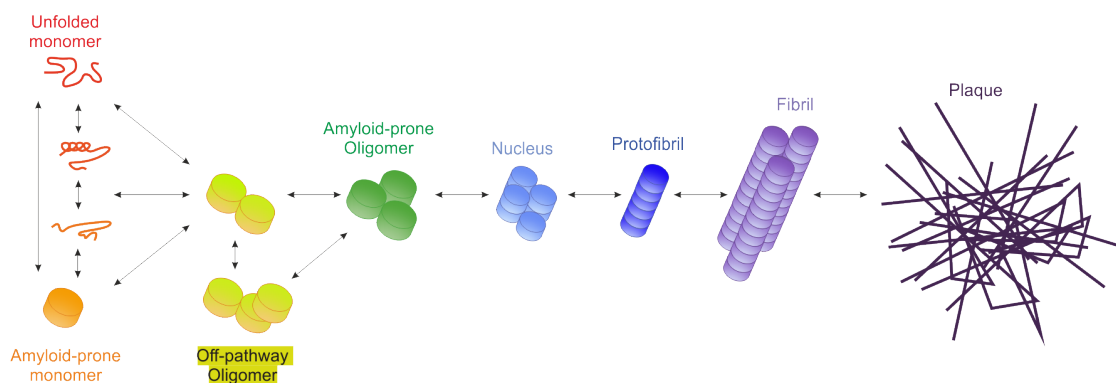


Figure 1.4: The amyloid formation pathway is complex.

The transition from a disordered (red) or folded (orange) monomers to form ordered fibrils (lilac) found in disease-associated plaques and deposits (purple) in multiple amyloid diseases consists of many interconverting states (including oligomers (yellow and green), nuclei (light blue), and protofibrils (light blue)), many of which remain undefined.

Firstly the monomeric amyloid peptide must adopt a conformation which is conducive to self-association (Figure 1.4(orange)) to form an amyloid-prone oligomer [49], (Figure 1.4(green)). For folded monomers the native fold may need to be partially or more fully unfolded to initiate amyloid formation. In the case of β_2 -microglobulin (the protein responsible for Dialysis Related Amyloidosis) the folded monomer is insufficient for fibril formation, as is evidenced from both *in vivo* [50] and *in vitro* [51–54] studies. However, in the presence of contributory factors such as copper ions [55, 56], collagen [57], heparin [58], or post translational modifications (e.g. cleavage of the six N-terminal residues) [59, 60], the structured β_2 -microglobulin monomer is perturbed and becomes a precursor to amyloid [61]. A key feature of this precursor is an exposed Pro32 converts from its native cis orientation to trans [62]. In order for an intrinsically disordered monomer

(Figure 1.4(red)) to become amyloidogenic (Figure 1.4(orange)), the conformational landscape (see Section 1.2.1) must be biased to promote the induction of amyloidogenic structures. In the case of $A\beta_{40}$ - an IDP - there is evidence that the extended chain must adopt a transient α -helix which then converts to a β -sheet (Figure 1.4(red-orange fade)), in order to participate in the amyloid formation pathway. Such structural transitions can be aided through interactions with other cellular components, for example, there is evidence that $A\beta_{40}$ associates with lipid bilayers to prompt aggregation, additionally interaction with metal ions can also encourage aggregation.

Amyloid-prone monomers associate together and result in a heterogeneous mixture of transient and dynamic oligomers which may be on- or off-pathway intermediates [63], (Figure 1.4(yellow)). This attribute of oligomers in the amyloid formation pathway makes their study highly complex and challenging. It is unclear whether different oligomeric species are able to inter-convert to reach an amyloid state or whether they must disassemble and re-assemble to form on-pathway intermediates [63–66].

With increasing oligomer size a nucleus (Figure 1.4(light blue)) forms in a process termed primary nucleation [66, 67]. A nucleus can be defined as the smallest aggregate whereby it is more energetically favourable to grow and sequester more monomers rather than dissociating into its constituent parts. Pre-nucleus sized oligomers are more likely to dissociate, especially in the presence of amyloid fibrils as the fibril stability (between the aggregate and the aqueous environment) drives the addition of monomer to fibril [67]. The formation of the aggregation-competent nucleus is kinetically disfavoured due to its high energy state. Nucleus formation is thus the rate-limiting phase of amyloid initiation and occurs during the lag phase of assembly, 1.5. The amyloid mechanism is generally accepted to be a ‘nucleated growth reaction’; essentially meaning that subsequent to nucleus formation, fast monomer association to the nucleus occurs [68] causing the fibril to grow as a protofibril (Figure 1.4(dark blue)), and thus the elongation phase of the process ensues. Evidence of the nucleated growth mechanism is observed (usually by Thioflavin T (ThT) fluorescence, see Section 1.4.1) by introducing pre-formed, aggregation-competent fibril seeds to a monomeric pool. This results in immediate elongation and amyloid fibril formation [69, 70], (Figure 1.4 and Figure 1.5(light purple)).

The primary method of elongation occurs when aggregation prone monomers bind to the ends of the elongating fibril. Molecular dynamic simulations indicate that on association,

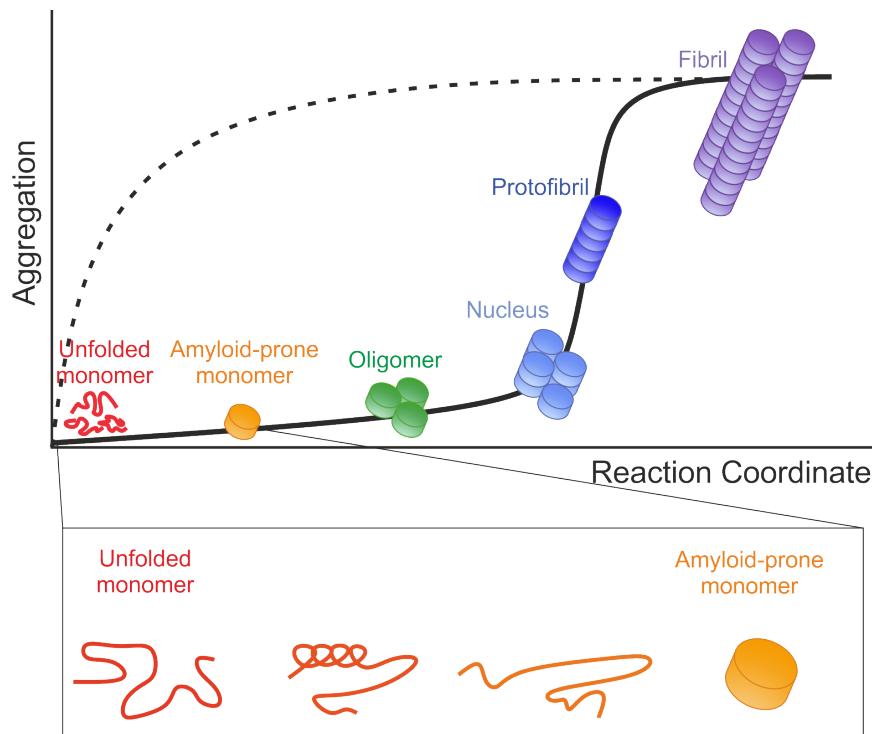


Figure 1.5: A generic ThT fluorescence profile of amyloid aggregation. A schematic to demonstrate the fluorescent output of ThT as a representation of fibril formation (solid line) from monomeric protein and when growth is seeded (dashed line) by the addition of seeds at the start of the reaction.

a structural rearrangement is induced resulting in full incorporation of the monomer to the fibril end [71]. As more monomers add to the growing aggregate, the aggregate becomes more thermodynamically stable and thus more monomers will associate to the growing fibril [72, 73].

Subsequently, a variety of secondary pathways can occur: secondary nucleation and fragmentation [67, 74]. Secondary nucleation happens when monomers bind to the surface of preexisting fibrils and a nucleus forms [75, 76]. The underlying molecular mechanism of this is not fully understood as it is unknown whether the nucleus remains attached to the side of the fibril or if it can dissociate to elongate independently [67]. Moreover, it is currently unknown whether secondary nucleation can occur at any point on the fibril surface or if a specific site is required. The current perspective of the field is in favour of specific sites due to the inability for cross-seeding of different amyloids [67, 77]. Residue-specific investigation into this effect (e.g. using NMR) would be impactful to aid the understanding of this phenomenon.

Fragmentation can also contribute to the rate of fibril formation. In this process, fibrils

break and expose two new ends from which elongation can occur [78, 79]. The extent of the significance of each of these processes varies between protein sequences. For example fragmentation has a negligible contribution to aggregation for A β ₄₀, whereas for prions it is the major method which determines disease progression [66, 80].

For each of these processes, the monomer conformation may play a key role with varying affinities for binding to each type of species present in the amyloid pathway. There is an need for greater understanding of how monomers interact with each of the species involved both directly and indirectly in the amyloid aggregation pathway. When the monomer species is intrinsically disordered, an additional layer of complexity is added and compounds challenges to study the heterogenous system of the amyloid pathway. If specific structural requirements of the monomer state were revealed which prevent, for example, monomer addition to an extending fibril, greater mechanistic understanding would be ascertained. This could ultimately lead to direction for therapeutic approaches for some of the many amyloid-associated diseases affecting human society.

1.1.4 Amyloid Diseases have an Immense Impact Globally

Amyloid diseases are some of the most prevalent health issues facing current society. According to the World Alzheimer Report 2018 [81], the number of people suffering from dementia (a generic term for a subset of amyloid diseases associated with amyloid deposition in the brain) worldwide is approximately 50 million and this figure is expected to rise to 152 million people by 2050 [81]!

Table 1.1 lists a selection of amyloid diseases, the dominant protein involved in fibril formation, and details any structural features in the monomer protein. Notably, over a third of the diseases listed are related to intrinsically disordered peptides, or peptides with intrinsically disordered regions, forming amyloid.

TABLE 1.1: Amyloid diseases and their associated proteins. Reproduced and adapted from [1].

Disease	Peptide	Residues	Native structure
Neurodegenerative diseases			
Neuroferritinopathy	Ferritin	175 or 183	All α

Disease	Peptide	Residues	Native structure
Spongiform encephalopathies	Prion protein or fragments thereof	253	Natively unfolded (residues 1-120) and α -helical (residues 121-230)
Parkinson disease	α -Synuclein	140	Natively disordered
Dementia with Lewy bodies	α -Synuclein	140	Natively disordered
Frontotemporal dementia with Parkinsonism	Tau	352–441	Natively disordered
Amyotrophic lateral sclerosis	Superoxide dismutase	153	All β , immunoglobulin-like
Huntington disease	Huntingtin with polyQ expansion	3,144	The polyQ-containing region is largely disordered
Spinocerebellar ataxias	Ataxins with polyQ expansion	816	All β , AXH domain (residues 562-694); the rest are unknown
Spinocerebellar ataxia 17	TATA box-binding protein with polyQ expansion	339	$\alpha+\beta$, TBP-like (residues 159-339); unknown (residues 1-158)
Spinal and bulbar muscular atrophy	Androgen receptor with polyQ expansion	919	All α , nuclear receptor ligand-binding domain (residues 669-919); the rest are unknown
Hereditary dentatorubral-pallidoluysian atrophy	Atrophin 1 with polyQ expansion	1,185	Unknown
Familial British dementia	ABri	23	Natively disordered
Familial Danish dementia	ADan	23	Natively disordered
Non-neuropathic systemic amyloidoses			

Disease	Peptide	Residues	Native structure
AL amyloidosis	Immunoglobulin light chains or fragments	~90	All β , immunoglobulin-like
AH amyloidosis	Immunoglobulin heavy chains or fragments	~220	All β , immunoglobulin-like
AA amyloidosis	Fragments of serum amyloid A protein	76-104	All α , unknown fold
Familial Mediterranean fever	Fragments of serum amyloid A protein	76-104	All α , unknown fold
Senile systemic amyloidosis	Wild-type transthyretin	127	All β , prealbumin-like
Familial amyloidotic polyneuropathy	Mutants of transthyretin	127	All β , prealbumin-like
Haemodialysis-related amyloidosis	β 2-Microglobulin	99	All β , immunoglobulin-like
ApoAI amyloidosis	N-terminal fragments of ApoAI	80-93	Natively disordered
ApoAII amyloidosis	N-terminal fragment of ApoAII	98	Unknown
ApoAIV amyloidosis	N-terminal fragment of ApoAIV	~70	Unknown
ApoCII amyloidosis	ApoCII	79	α +disordered
ApoCIII amyloidosis	ApoCIII	79	α +disordered
Finnish hereditary amyloidosis	Fragments of gelsolin mutants	71	Natively disordered
Lysozyme amyloidosis	Mutants of lysozyme	130	α + β , lysozyme fold
Fibrinogen amyloidosis	Variants of fibrinogen α -chain	27-81	Unknown

Disease	Peptide	Residues	Native structure
Icelandic hereditary cerebral amyloid angiopathy	Mutant of cystatin C	120	$\alpha+\beta$, cystatin-like
Non-neuropathic localized diseases			
Type II diabetes	Islet amyloid polypeptide (also known as amylin)	37	Natively disordered
Aortic media amyloidosis	Lectadherin C2-like domain	50	Unfolded
LECT2 amyloidosis	Leukocyte cell-derived chemotaxin 2	151	Unknown
Localized cutaneous amyloidosis	Gelactin 7	136	All β
Hypotrichosis simplex of the scalp	Corneodesmosin	529 (truncations cause amyloid)	Unknown
Calcifying epithelial odontogenic tumours	Odontogenic ameloblast-associated protein	153	Unknown
Senile seminal vesicle amyloidosis	Semenogelin 1	462	Unknown
Medullary carcinoma of the thyroid	Calcitonin	32	Natively disordered
Atrial amyloidosis	Atrial natriuretic factor	28	Natively disordered
Hereditary cerebral haemorrhage with amyloidosis	Mutants of amyloid- β peptide	40 or 42	Natively disordered

Disease	Peptide	Residues	Native structure
Pituitary prolactinoma	Prolactin	199	All α , four-helical cytokines
Injection-localized amyloidosis	Insulin	21 and 30	All α , insulin-like
Injection-localized amyloidosis	Enfuvirtide	36	Disordered
Aortic medial amyloidosis	Medin	50	Unknown
Hereditary lattice corneal dystrophy	Mainly C-terminal fragments of keratoepithelin	50-200	Unknown
Corneal amyloidosis associated with trichiasis	Lactoferrin	692	$\alpha+\beta$, periplasmic-binding protein like II
Cataract	-Crystallins	Variable	All β , -crystallin like
Calcifying epithelial odontogenic tumours	Unknown	~ 46	Unknown
Pulmonary alveolar proteinosis	Lung surfactant protein C	35	Unknown
Inclusion-body myositis	Amyloid- β peptide	40 or 42	Natively disordered
Cutaneous lichen amyloidosis	Keratins	Variable	Unknown

1.1.5 Amyloid Toxicity in Disease

It has been clear for the best part of four centuries (Figure 1.1) that fibrillar, amyloid deposits are linked to pathologies in disease [1, 82]. In the last 20 years, research focus has been adjusted towards identifying and structurally characterising proteinacious species. The current consensus of the field is that the oligomeric intermediates on- or off- the amyloid fibril pathway are more likely to be the main toxic species in amyloid disorders [83, 84], rather than mature fibrils [85].

Research focusing on oligomers formed from amyloidogenic proteins is particularly important in light of the general consensus that some of them act as toxic agents in amyloid disorders [82, 86–92]. Oligomeric species are generally formed from assembling partially-folded or partially-unfolded states which are highly heterogeneous. For folded proteins, a possible explanation of the hypothesised toxicity of some oligomers, is the exposure of chemical groups (namely from hydrophobic residues [93]) which would usually be protected in the folded core of the peptide. In fact greater toxicity of prefibrillar and oligomeric species relative to larger amyloid fibrils is not entirely surprising as the smaller species have a higher surface area to volume ratio and thus have more surface groups exposed per volume that are available to interact aberrantly with cellular components (membranes, organelles, other proteins, nucleotides etc.) causing disruption to cellular processes [12, 94]. Mature amyloid fibrils may, in fact, be relatively protective to cells acting as a reservoir to sequester the toxic species in inert, stable aggregates [95–97].

Despite this, there is contrasting evidence, indicating that mature fibrils can indeed infer toxicity and cellular disruption [98]. In dialysis-related amyloidosis, β_2 -microglobulin aggregates to form amyloid fibrils which are deposited in joints causing stress and dysfunction [99]. However, for neurodegenerative disorders, such as Alzheimer’s disease, no such correlation between the amount of fibrillar aggregates and disease severity has been observed [100, 101], e.g. in post-mortem analyses of Alzheimer’s disease patient brain samples [100]. This suggests that the cytotoxic, disease-causing species is not detectable as an aggregate [102].

For amyloidogenic IDPs, maintaining structural disorder may be important in preventing, or at least delaying, amyloid formation. Early oligomers of the disordered peptide, α -synuclein (involved in Parkinson’s Disease) are substantially disordered until a conformational change occurs in the oligomer as a whole adopts an on-pathway, β -sheet rich structure akin to an amyloid-like core [103]. This implies that gain of structure in oligomers may correlate with amyloid formation and the same may be true for monomer transitions.

1.1.6 Functional Roles of Amyloid

In the last two decades it has been realised that the amyloid fold is not restricted to protein aggregation disorders but can be found as functional fibrous structures produced by

bacteria and fungi, as well as in higher eukaryotes [2], Table 1.2. One of the most widely accepted roles of amyloid aggregation in biology is as part of a controlled response to address perturbed protein homeostasis [104] by allowing partially folded proteins to clump together in an inert state, i.e. hydrogen bond donors and acceptors can align to form hydrogen bonds, and hydrophobic regions can associate to minimise the unfavourable interaction with aqueous environments. In *E. coli* and *Salmonella spp*, amyloid fibrils are used in cell adhesion, as well as in biofilm formation [105]. Another bacteria, *Streptomyces coelicolor* which live in soil, produce functional amyloids called chaplins that bind to hydrophobic surfaces [106] and coat aerial hyphae assisting spore dispersal and the colonisation of surrounding soil [107]. In humans, amyloid can have roles involving interaction with secretory hormones (such as insulin) and in melanosomes where it facilitates and regulates the reactivity of melanin small molecule indolequinone precursors [106]. Furthermore, amyloids function in the human hemostatic system, factor XII can be activated by amyloids *in vitro* [108] and converts fibrinogen to fibrin fibres which are rich in β -sheets like amyloids [109].

TABLE 1.2: Functional amyloid in various organisms. Reproduced and adapted from [2].

Species	Protein	Function	Evidence
Bacteria			
<i>E. coli</i> , <i>Salmonella spp.</i>	Curli	Biofilm formation, host invasion	EM, Congo red, ThT, and CD
<i>Streptomyces coelicolor</i>	Chaplins	Modulation of water surface tension (i.e. development of aerial structures)	CD, ThT and EM
Fungi			
<i>Podospora anserine</i>	HET-s	Regulation of heterokaryon formation	EM, CD, FTIR, Congo red and NMR
<i>Saccharomyces cerevisiae</i>	URE2p	Regulation of nitrogen catabolism	Electron diffraction, X-ray, Congo red, EM and ThT
<i>S. cerevisiae</i>	Sup35p	Regulation of stop-codon read-through	EM, Congo red, CD and X-ray

Species	Protein	Function	Evidence
Most fungi	Hydrophobins	Fungal coat formation, modulation of adhesion and surface tension	AFM, CD, FTIR, ThT, NMR, Congo red and X-ray
Animalia			
Insects and fish	Chorion proteins	Structural and protective functions in the eggshell	Congo red, X-ray, EM, FTIR and CD
<i>Nephila clavipes</i>	Spidroins	Structural (i.e. spider silk)	EM and CD
<i>Homo sapiens</i>	Pmel17	Scaffolding and sequestration of toxic intermediates during melanin synthesis	X-ray, Congo red, EM and ThT

The presence of functional amyloids throughout domains of life [2, 110–115] prompts the questioning of the role of amyloid in the origins of life [116]. Over time some proteins have evolved to omit sequences with high amyloidogenic potential, such as strings of hydrophobic residues, or alternating sequences of polar and non-polar residues [41]. The fact that amyloidogenic proteins persist in biological organisms highlights the advantages for this structure in biology. In general, aggregation is a slow process (at physiological protein concentration), often taking years for disease to develop to present symptoms and thus there is little evolutionary pressure to select against aggregation-prone sequences at important evolutionary life stages. However, for functional amyloid often elaborate systems have evolved to control assembly such that it occurs rapidly and in the correct cellular location, e.g. Pmel17 [106].

1.2 Intrinsically Disordered Peptides

Previously, the view on protein folding was that a folded structure was essential for functionality. In many cases this holds true as protein function is enabled through structure, for example, specific 3D environments in active sites for enzyme catalysis and precise recognition features for some allosteric binding and transport [117]. However, 25 % of proteins expressed in humans are disordered, and approximately 50 % contain disordered stretches of at least 30 amino acids [118], bringing the role of disordered

peptides into the spotlight. The present view is that intrinsic disorder plays a role in signalling and various other cell processes, (discussed further in section 1.2.2) [117, 119, 120].

1.2.1 Defining Intrinsic Disorder

The term ‘Intrinsically Disordered Peptide’ has been defined as a peptide which possesses at least one region which does not have a fixed secondary or tertiary structure [118]. A limitation of this definition is that misfolded or unfolded proteins may also be lacking in fixed secondary or tertiary structures for part or all of their lifetime. For example, placement of ribonuclease A (the folded protein used in the famous folding experiments by Anfinsen *et al.*, [121]) in 8 M urea will yield a peptide chain lacking in secondary and tertiary structure, yielding an unfolded chain. The definition of an IDP has evolved over time as common features of IDPs have been observed.

A common misconception is to expect IDPs to exist as purely random coils. In reality, IDPs fleetingly sample different structural motifs and exist as a mixture of transient, partially folded states, which have low energy barriers allowing the rapid interconversion of conformers [122–127], Figure 1.6. Conformational preferences can be sequence specific and can depend on the previous conformation sampled by the IDP [120, 124].

In general, IDPs are characterised by having a high content of polar or charged residues [120] which can be viewed as ‘disorder-promoting’ residues: A, R, G, Q, S, P, E and K [128], and a low proportion of hydrophobic, uncharged residues [120]: W, C, F, I, Y, V, L, and N [128]. IDPs are usually geared towards exhibiting solubility in aqueous environments, hence the amino acid composition preferences. Additionally, the high net charges (causing electrostatic repulsion resulting from equally charged residues) and enhanced Proline content (causing steric prevention of close proximity) help to prevent self-association of the IDP [128]

1.2.1.1 Contrasting Disordered, Misfolded, and Unfolded Peptides

Using recent NMR methods and metadynamics simulations the energetic landscape of IDPs has been modelled and compared with that of a folded peptide and its unfolded, or misfolded derivatives [129].

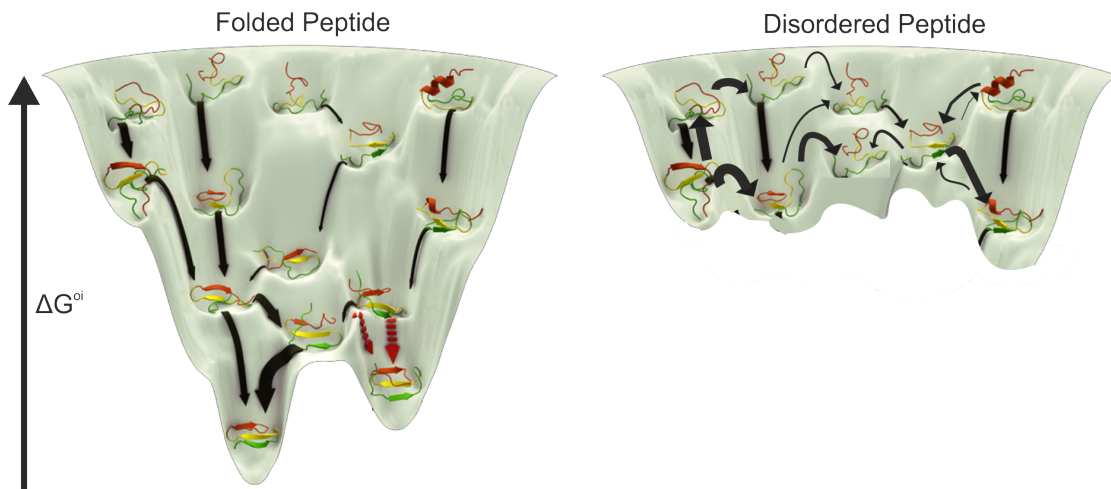


Figure 1.6: A schematic showing energy barriers between conformational states for folded peptides and IDPs.

The energy level profile for a typical folded protein (left) and an IDP (right). For the folded protein there is a clearly defined state which is most stable and therefore most of the protein will occupy this low energy state. However, for an IDP the landscape is much shallower with small energy barriers between many different conformers which the peptide can sample. Adapted from

<https://www.mpbenowitz.work/#/foldingproteins/>.

Protein folding today is visualised as an energy landscape with multiple routes to reach the lowest energy form of the protein [7, 130–132]. The potential folding paths, in line with the Levinthal Paradox [133], are restricted to occur via specific kinetically controlled folding routes to reduce the amount of potential folds a protein visits during folding to its native state [134]. This can be achieved through the use of chaperones (e.g. ER chaperone BiP), and restricted steric environments (e.g. the exit channel of the ribosome). Additionally the formation of key structural motifs early in the folding process can bias the rest of the conformational search to ensure highly efficient folding [133, 135–137].

As a natively folded protein folds from its high energy, unfolded state to achieve its most stable, low energy, fully folded conformation, it encounters transition state energy barriers (peaks on the energy landscape), as well as stable intermediate conformations (energy minima or troughs on the energy landscape). For intrinsically disordered peptides, it has been postulated by Granata *et al.*, [129] that the opposite trend is true: an IDP is most stable in a structure-less, state, when secondary structures are transiently sampled in the dynamic conformer equilibrium. As such, a key contrast for IDPs and folded peptides is that intermediate peptide conformations of IDPs are reached from

the global minimum through partial folding events, whereas for folded proteins, intermediate peptide conformations are attained from the global minimum through partial unfolding events [138–140]. IDPs are entropically stabilised whereas folded proteins are enthalpically stabilised.

Factors which alter the environment (e.g. changes in pH or temperature, or addition of small molecules which stabilise peptide conformations) can modulate the energy profile of different folded, and partially folded states altering the population distribution of a protein conformer landscape [12]. These intermediates may be on-pathway structures as the protein moves towards its favoured conformation, or they may be kinetically stable off-pathway forms [68, 141] in which the protein may become trapped. This is especially true for partially folded, or misfolded forms of folded proteins which may sit in deep energy troughs with high transition energy barriers. Accumulation of proteins in such states can lead to high local concentrations of partially folded proteins which renders aggregation more possible [68].

Increasing temperatures of IDP systems allows higher free energy states of IDPs to become more populated. As temperature increases, entropy also increases pushing the system to act more freely, however, the higher energy in the system makes higher energy conformers of IDPs more accessible and these can be more structured (and therefore compact) conformers of IDPs. This could be an explanation for the increased rates of aggregation of IDPs as temperatures increase [129].

Misfolded proteins (i.e. proteins which have failed to adopt the correct secondary and tertiary configurations of their native folded form) can have detrimental consequences in biological systems. Unlike IDPs, misfolded proteins have not evolved to exist in their environment and thus they are more likely to have unwanted interactions with other cell components. For example, a misfolded, or unfolded, protein is more likely to have hydrophobic residues exposed to an aqueous environment [138, 142, 143], this may lead to self-association with other exposed hydrophobic residues resulting in further misfolding. Alternatively, such residues may drive association with other unfolded or misfolded peptides initiating an aggregation mechanism [144], or such exposed residues may induce interactions with other cell components [138, 142, 143]. For these reasons cells have mechanisms to deal with and remove misfolded or unfolded species.

The primary mechanism to prevent damage incurred from incorrectly or incompletely folded proteins is to ensure that proper folding occurs initially through the use of chaperones in most stages of the peptide ‘life cycle’ (ie. folding, assembly, transport, degradation) [145]. Indeed, the primary response to a build up of misfolded or unfolded-structured proteins is to increase chaperone expression levels [146] via the Heat Shock Response [147, 148], for example, in *E. coli* this aids the association of misfolded proteins with chaperonins such as GroEL or GroES [146]. Alternative strategies include protein degradation through the Unfolded Protein Response, localisation into cellular compartments, and sequestering of peptides into relatively inert aggregates. In bacteria misfolded proteins are sequestered into inclusion bodies at the cell poles [149]. In eukaryotes, aggregates can be stored in one of two distinct compartments: the juxtannuclear quality control compartment (JUNQ) next to the nucleus, or the Insoluble Protein Deposit (IPOD) near the vacuole (in yeast) where the fate of trapped proteins is still undetermined [104]. Additionally, mammalian cells can also form specialised inclusion bodies; Russell (or Lewy) bodies to contain large amounts of ubiquitinated or phosphorylated proteins [150], and aggresomes which fuse to the lysosome to allow degradation of their proteinacious content [151, 152].

Although aggregation is generally regarded as an undesirable consequence of protein misfolding, there is speculation that if peptides aggregate to form an unreactive, stable structure when this may be a protective mechanism employed by cells to prevent further cell damage. Such aggregates may be amorphous or highly structured amyloid fibrils which were described in Section 1.1.

If amorphous aggregates form, they can be destroyed in eukaryotes through being engulfed by double-membraned autophagosomes which then fuse to the lysosome so their contents can be degraded [153], or ubiquitin-labelled aggregates can be destroyed by the 26S proteasome [153]. Alternatively, some cells can expel unwanted aggregates by exocytosis (then aggregates can be removed from blood is via receptor mediated uptake into cells whose protein degradation pathways are not saturated [154]), or through the creation of asymmetrical daughter cells, one of which contains aggregate material which then undergoes apoptosis, leaving an aggregate-free daughter cell [104]. Destruction of amyloid fibrils is more difficult owing to the immense stability as discussed in Section 1.1.2. There are however some examples of physiological methods to degrade amyloid

aggregates; for example, Insulin-degrading enzyme (IDE) has been shown to digest fibrillar insulin, glucagon, hIAPP and A β [155], as can neprilysin, a zinc-associated type II metalloprotease, [156].

An arising question from this is to consider how IDPs may elude these responses. Preliminary ideas suggest that recognition of exposed hydrophobic regions could be a key indicator of misfolded proteins. Chaperones mostly interact with unfolded or partially folded cytosolic proteins through mechanisms involving recognition of exposed hydrophobic areas [146] which would explain why IDPs, which are generally lacking in hydrophobic residues, are not cleared by the heat shock response cascade. This, in turn, raises the question of the homeostatic mechanisms involved in levels of IDPs and how IDPs are removed from cells if there is an error in their regulation? Thus far, Uversky *et al.*, [120], have speculated that IDPs may escape unwanted interactions via functional misfolding as a regulatory mechanism. This ignites questions on how a misfolded IDP can be distinguished from a misfolded structured peptide and ultimately begs the question of whether a peptide can misfold if there is no ‘correct’ fold to be adopted? Indeed, is an amyloid-prone conformer of A β ₄₀ misfolded, and what about a conformer which can form amorphous aggregates? Is an amyloid-prone IDP conformer closer to a folded protein than an IDP conformer which can only form amorphous aggregates? There are many questions still to be answered in the IDP field which are interesting to peruse, but are beyond the scope of this project.

1.2.2 Functional Disorder

In the last two decades, the importance of disorder in protein function has been realised. IDPs have been found to have roles in a wide variety of cellular functions including (but not limited to); mechanisms to sustain harsh environments [157], roles as interaction hubs or scaffolds to bring together multiple complex components [158], tunable regulatory factors affecting transcription levels and as transcription factors [159], enzymatic catalysis [160], regulation of protein synthesis [161], membrane curvature induction [162], and multiple others reviewed in [163, 164]. Figure 1.7 provides an overview of IDP functions. Indeed, time has become an important dimension in the characterisation of protein function due to disorder-to-folded transitions [165].

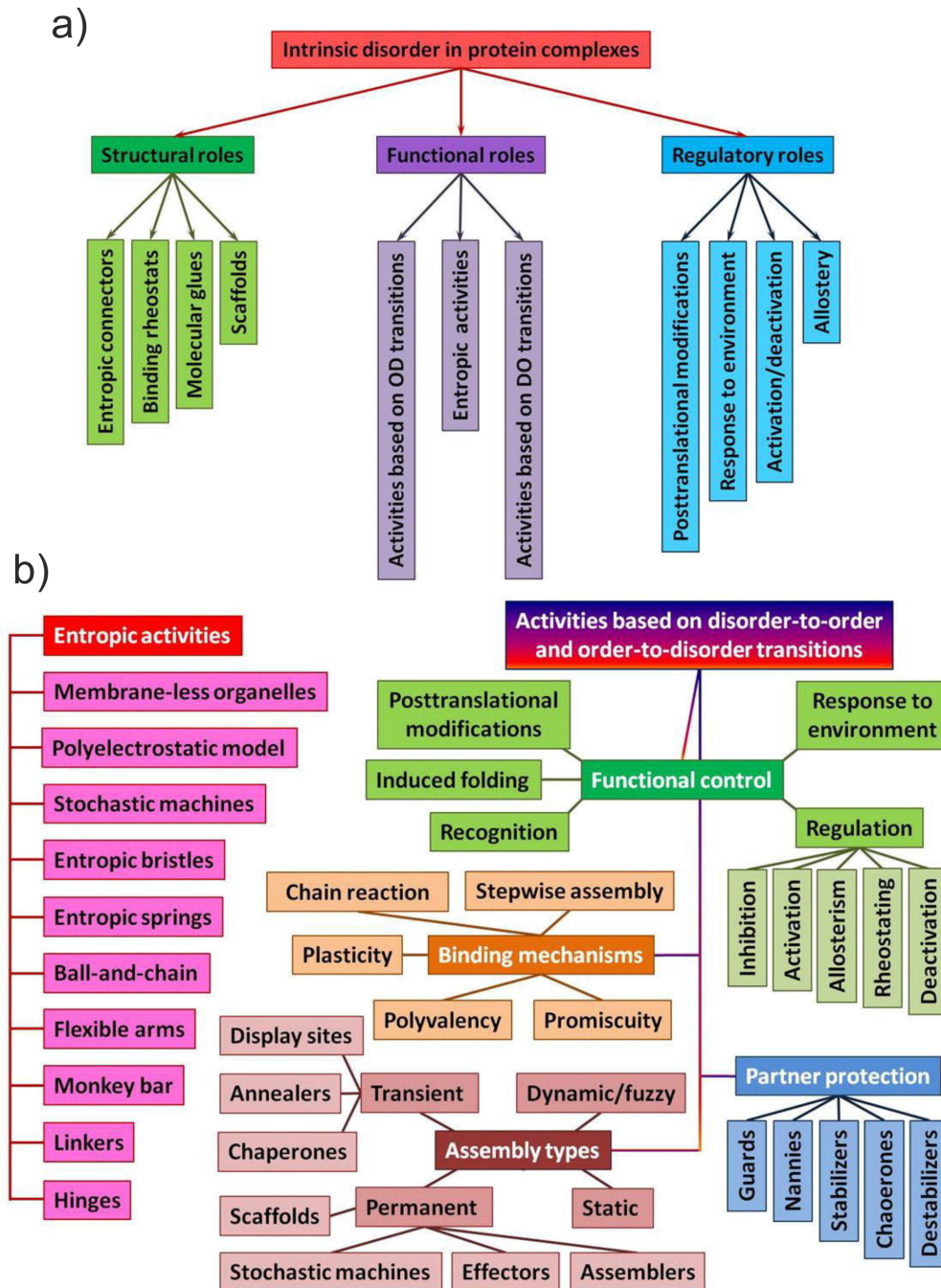


Figure 1.7: A summary of roles of IDPs.

a) Overview of structural (green), functional (purple), and regulatory (blue) roles of intrinsic disorder in protein complexes. b) Basic entropic activity and roles based on disorder-to-order transitions. Taken from [119].

One of the key features of IDP function is the ability to interact with a wide range of substrates, a property enabled through the high levels of IDP flexibility and dynamics [118]. For this reason IDPs can act as hub proteins, bringing together a variety of substrates. An impressive property for IDPs is how they can achieve interaction specificity despite

their wide variety of interaction partners [117, 166–169]. Rationalisation of this can be explained through the great sensitivity of IDPs to environmental conditions [170, 171] due to low energy barriers between conformers (see Section 1.2.1). IDPs interact weakly but specifically with substrates in what is termed interaction ‘fuzziness’ [172, 173]. The specificity of the interactions arise from the entropic force generated by intrinsically disordered segments interacting with substrates [174]. The binding energy is the sum of the favourable enthalpic binding interaction and the unfavourable restriction in IDP entropic flexibility upon binding. Interaction fuzziness can be beneficial, for example, in the HSR, IDPs play a role to interact with substrates which do not have a defined structure (owing to the misfolded nature of the proteins initiating the response). Such IDPs function as transcription factors and chaperones to trigger the plant version of the HSR [175].

Virtually all protein functions, whether folded or disordered, rely on interactions with other molecules, be they other proteins, lipids, polysaccharides, or small molecules [117]. In many cases, IDPs undergo coupled folding and binding due to the stability this interaction confers on one of the many conformations of an IDP [124]. The coupled folding and binding of proteins allows a much greater range of interactions within the same set of proteins, and therefore provides versatility. For example, different signalling proteins can bind to one receptor, leading to different reactions, and a given signalling protein can in turn bind to different receptors [124]. Due to the large solvent-accessible surface area of IDPs, such peptides/proteins have a large surface area for interaction with either multiple substrates which are distantly located [162] or, the extensive surface area can be wrapped around a single substrate. For example, p21 can bind to different cyclin dependent kinase proteins in different conformations [176], wrapping around a protein partner in order to protect the substrate from interactions with other proteins in the cell [177, 178].

IDPs may be the result of evolutionary mechanisms to develop finely tuned signalling and control systems in complex organisms [179]. This is based on the increasing prevalence of IDPs found in eukaryotic signalling pathways compared to in prokaryotes, Figure 1.8. It is possible that the complex signal regulation enabled by IDPs has provided an evolutionary gateway to higher organisms.

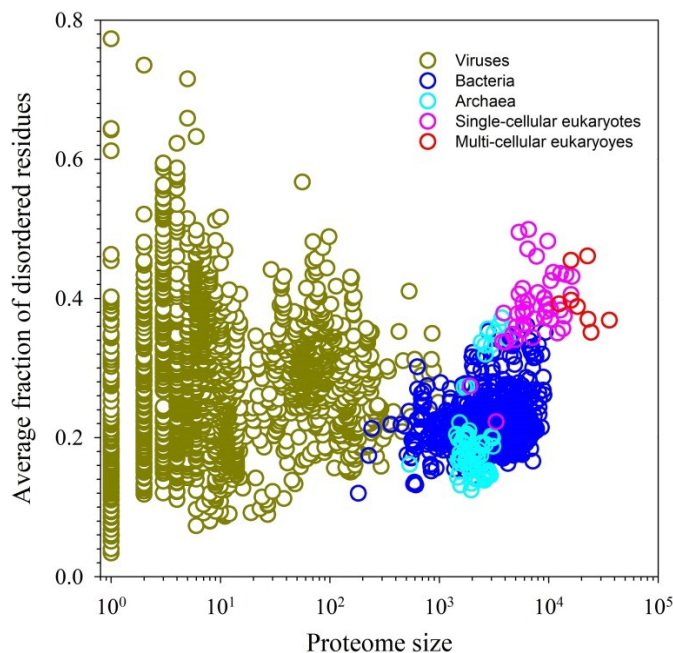


Figure 1.8: Prevalence of disorder in proteomes across different domains of life.

The fraction of IDPs or IDRs in proteomes of increasing size. Excluding viruses, as proteomes increase in size there is a trend that more disorder is observed. Taken from [180].

1.3 Intrinsic Disorder in Amyloid

1.3.1 Introducing $A\beta_{40}$: an important IDP in Alzheimer's Disease

$A\beta$ is the major proteinaceous component of extracellular Alzheimer's plaques [181–185], with the 40 residue $A\beta_{40}$ being the most abundant species present. *In vivo* the $A\beta_{40}$: $A\beta_{42}$ molar ratio is ~ 10 :1 [186–188] and there is evidence to suggest that the ratio between these two peptides can influence AD pathology [189, 190]. Although it is well evidenced that $A\beta_{42}$ is the most amyloidogenic form of $A\beta$ [191], the ratio of $A\beta_{40}$: $A\beta_{42}$ is a useful marker of Alzheimer's disease [192, 193], and the two peptides can interact to form amyloid as well as aggregating independently. Alzheimer's disease is responsible for two thirds of the 50 million cases of dementia worldwide [81]. As a progressive neurodegenerative disorder, Alzheimer's disease manifests as acute memory loss, cognitive decline and behavioural alterations [194] and is usually (but not always) associated with the presence of amyloid deposits, or plaques, in neural tissue [195]. As Alzheimer's disease is predicted to become more prevalent as the global population ages, the already high, socio-economic costs approximately \$1 trillion in the US alone [81])

are set to increase making research on the underlying biochemical causes and features of Alzheimer's disease an important field [82, 90].

$A\beta_{40}$ is an amphipathic peptide which has been confirmed as an IDP by solution NMR and circular dichroism experiments (CD) [196, 197]. The amino acid sequences for the main $A\beta$ peptides are shown in Figure 1.10. There is a range of $A\beta$ peptide lengths due to the unspecificity of cleavage from its precursor protein; amyloid precursor protein (APP), Figure 1.9. APP is expressed ubiquitously in many human cell types but is particularly abundant in the central nervous system [198, 199] reaching its highest expression level in synapses during early postnatal development [200] (when synapses and neuronal connections are formed [201, 202]). APP is an integral membrane protein with over four isoforms which range from 695 to 770 amino acids residues [203–206] and is highly glycosylated. APP is cleaved by a multitude of proteases to create many bio-molecules which have a broad range of cellular functions, of which many are still unclear [207]. For example, if α -secretase cleaves APP followed by λ -secretase then soluble C-terminal fragments (CTFs) called APP_α and APP_β can be formed which have neuroprotective effects (see [208, 209] and references therein). Additionally there is *in vitro* evidence for some cleavage products to have roles in the activation of adenylyl cyclase/PKA-dependent pathways [210]. The diversity of roles of many of the peptides produced from APP are mentioned in [203] and discussed more extensively in references therein.

To create $A\beta_{40}$ and other Alzheimer's-associated isoforms, APP is cleaved on the extracellular side by β -site APP cleavage enzyme (BACE), a β -secretase, to create the $A\beta$ N-terminal [181, 211]. Next a complex containing γ -secretase cleaves the intramembrane APP via hydrolysis to generate intrinsically disordered peptides of 39-43 residues in length Figure 1.10 (reviewed in [203, 205, 212]) which have varying structural propensities [213, 214]. The specificity of the γ -secretase is thought to be controlled by genetic variations in APP isoforms but the mechanism for this is unclear [205]. The distribution of cleavage products is not even: $A\beta_{40}$ makes up 90 % of the APP cleavage products, whereas $A\beta_{42}$ makes up 9 % [215]). The first 28 residues from the N-terminal of the cleaved proteins are from the extracellular domain of APP, and the remaining 11-15 are from the transmembrane domain [216]. This may become evident in structural analysis of $A\beta$ peptides.

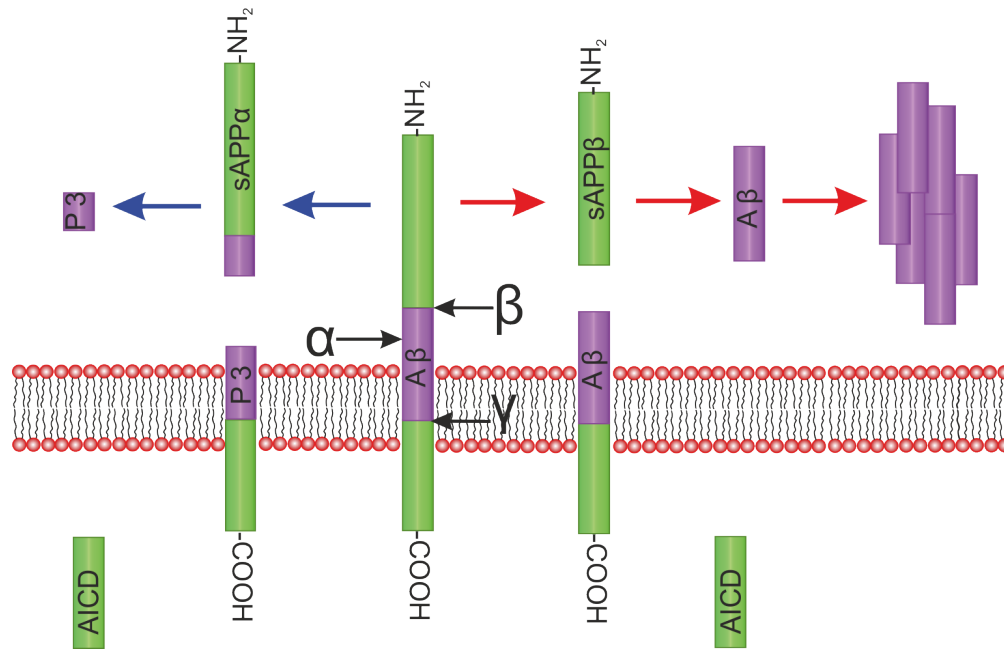


Figure 1.9: The proteolytic processing of APP.

APP can be cleaved by α -, β - and γ -secretases (the cleavage sites of these proteases are labelled in black on the full-length APP). Cleavage can lead to amyloidogenic (red arrows) or non-amyloidogenic (blue arrows) pathways. For the amyloidogenic pathway, β -secretase cleaves first releasing soluble APP β , next γ -secretase cleaves releasing A β extracellularly, and the amyloid precursor protein intracellular domain (AICD) intracellularly. In the non-amyloidogenic pathway, α -secretase cleaves within the A β sequence creating soluble APP and the membrane-tethered α APP-C terminal domain, which in turn is cleaved by γ -secretase releasing P3. The cell membrane is shown in red and black.

```

A $\beta$ 38: D A E F R H D S G Y E V H H Q K L V F F A E D V G S N K G A I I G L M V G G
A $\beta$ 39: D A E F R H D S G Y E V H H Q K L V F F A E D V G S N K G A I I G L M V G G V
A $\beta$ 40: D A E F R H D S G Y E V H H Q K L V F F A E D V G S N K G A I I G L M V G G V V
A $\beta$ 41: D A E F R H D S G Y E V H H Q K L V F F A E D V G S N K G A I I G L M V G G V V I
A $\beta$ 42: D A E F R H D S G Y E V H H Q K L V F F A E D V G S N K G A I I G L M V G G V V I A
A $\beta$ 43: D A E F R H D S G Y E V H H Q K L V F F A E D V G S N K G A I I G L M V G G V V I A T

```

Figure 1.10: Sequences of A β cleavage products.

Sequence differences at the C-terminal of A β caused by unspecific γ -secretase cleavage.

A β is not the sole peptide species associated with Alzheimer's disease. In Alzheimer's patients' brains, intracellular lesions are also often found, these are intracellular neurofibrillary tangles [217] with the major proteinaceous component being another IDP, Tau [218, 219]. Rather than study Tau alongside A β ₄₀, a different IDP (human Islet Amyloid Polypeptide, (hIAPP)) which is involved in Type II Diabetes Mellitus (TIIDM) was studied to add breadth of impact of this project. This peptide was chosen as there are links between Alzheimer's disease and TIIDM which are described in Section 1.3.3. Additionally there is evidence of A β codeposition with hIAPP in the islets of Langerhans

which suggests $A\beta$ may have a role in T1DM pathogenesis [220].

1.3.2 Introducing hIAPP: an important IDP in Type II Diabetes Mellitus

The extent of physiological roles of hIAPP in humans is still not fully defined, but it is known that hIAPP is associated with insulin and glucagon regulation as well as regulating the reactivity of small molecule indolequinone precursors of melanin, a skin pigment [106] in melanosome. The 37-residue peptide, Figure 1.11, has a hormonal role in influencing gastric emptying and satiation [221] by interacting with the Area Postrema of the brain which is located just outside of the blood-brain barrier [222]. hIAPP signals cause the stomach to slow gastric emptying [223], which delays absorption of glucose from the small intestine into the circulation, such functions have been reviewed extensively in rat models [224] and clinical studies [225, 226].

hIAPP: KCNTATCATQRLANFLVHSSNNFGAILSSTNVGSNTY-NH₂

Figure 1.11: The hIAPP peptide sequence.

The 37 amino acid sequence which composes hIAPP is shown. Important posttranslational modifications are highlighted; a Cys₂-Cys₇ disulfide bridge (blue) and an amidated C-terminus (green).

Due to the presence of hIAPP amyloid plaques located in the islets of Langerhans of pancreases in T1DM patients, studies of the effect of hIAPP on glucagon secretion, as well as the effect of hIAPP on insulin response to blood glucose level, have been performed. There are contradictory results concerning the effect of hIAPP on glucagon secretion: the majority agree that hIAPP acts in a complementary way to insulin and suggest hIAPP suppresses glucagon secretion by islet α -cells [224, 227, 228] and is generally accepted that hIAPP limits glucose-induced insulin production [229]. Indeed, in hIAPP knockout mice an elevation in glucose-stimulated insulin secretion is observed [230].

One major function of hIAPP is to prevent the self-association of insulin in β -cell insulin storage granules. β -cells require the storage of large amounts of hIAPP and insulin in preparation for fast release to quickly alter blood sugar levels via hormonal signalling. Association of hIAPP with insulin begins with their location in the human genome;

Insulin is located on the short arm of chromosome 11 and hIAPP is located on chromosome 12 which is thought to have been duplicated from chromosome 11 during evolution [231].

Insulin is stored as pro-insulin in these β -cell granules at concentrations of approximately 118 mM [232, 233] and, like hIAPP and its precursor pre-pro-hIAPP, has the potential to aggregate into amyloid aggregates. The ratio of pro-insulin:pre-pro-hIAPP in β -cell granules, under physiological conditions, is between 1:25 and 1:50. Susa *et al.*, [234] concluded that an insulin:hIAPP molar ratio between 1:5 and 1:100 would have strong inhibition of amyloid aggregation. The crystalline structures observed inside β -granules show a strictly ordered, hexameric, zinc-associated, pro-insulin core with a halo of pre-pro-hIAPP [235]. The two peptides mutually prevent each other from aggregating [229, 234, 236] despite both being able to form amyloid independently based on evidence from ThT fluorescence assays (see Section 1.4.1).

1.3.3 Links between Alzheimer's Disease and Type II diabetes Mellitus

There are epidemiological and physiological correlations between Alzheimer's disease and TIIDM, summarised in Figure 1.12. Epidemiology studies have shown that individuals with TIIDM have a 2 to 5 times greater risk of developing Alzheimer's disease than healthy patients [237–241], with approximately 70 % of TIIDM patients developing Alzheimer's disease within their lives [220, 242, 243]. There is clinical, transgenic, and physiological evidence for the $A\beta$ -hIAPP correlation based on long term population studies [237, 244], murine maze performance tests [245, 246], and resting-state functional magnetic resonance imaging [247, 248] studies respectively. Physiologically, both diseases are associated with amyloid formation and deposition [249]. Although $A\beta$ deposition mostly occurs in the brain there is evidence to suggest that $A\beta$ has a role in regulating the ability of peripheral tissues to respond to insulin [250–253].

Recently, many studies have identified the physiological actions of soluble hIAPP in brains, such as stimulating neuron growth and function, maintaining cerebral glucose homeostasis, inducing $A\beta$ degradation and inhibiting its neurotoxicity. However, during the progression of TIIDM, there is a decreased level of soluble hIAPP due to its aggregation. This reduction of soluble IAPP may result in loss of the protective effects of hIAPP on the brain and stimulating the progression of Alzheimer's disease [255]. In

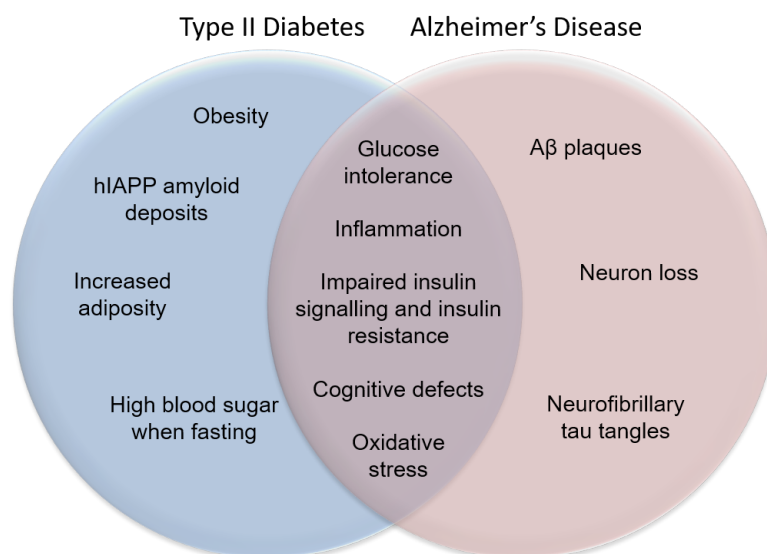


Figure 1.12: Physiological links between Alzheimer's disease and TIIDM. A Venn diagram showing some of the shared physiological impacts of TIIDM and Alzheimer's disease. [254].

accordance with this, it has been shown that elders with Alzheimer's disease have lower concentrations of soluble hIAPP in their plasma compared to healthy individuals in the same age group [255, 256].

1.3.4 A β_{40} and hIAPP interactions

hIAPP oligomers and mature fibrils are found deposited as independent plaques in the brain as well codeposited in A β neural plaques in the brains of TIIDM subjects with cognitive impairment [257–259]. Cross-seeding has been observed in *in vivo* studies [258, 260]. One study showed fibrillation from injection of either A β or hIAPP seeds leads to hIAPP fibril deposition in hIAPP transgenic mice [258]. There is a similar cross-seeding effect when A β transgenic mice were injected with hIAPP seeds [260]. hIAPP has 51 % sequence homology, and 27 % sequence identity to Amyloid- β_{42} [261, 262] (Figure 1.13) with segments important for self-aggregation displaying the greatest similarity [263]. Sequence similarity may permit cross-seeding and/or codeposition of these two peptides when they form amyloid.

There are two regions of hIAPP (residues 8 to 20 and residues 21 to 37) which have high binding affinity for A β [262]. Correspondingly, A β also has two regions (residues 11 to 21 and residues 23 to 37) with high binding affinity for hIAPP [262]. A low-nanomolar

A β ₄₂: D A E F R **H D S G Y E V H H** **Q K L V F F A** E D **V G S N K G A I I G L** M **V G** G V V I A
 hIAPP: **K C N T A T C A T** **Q R L A N F L** V H **S S N N F G A I L S S** T N **V G** S N T Y

Figure 1.13: Alignment of A β ₄₂ and hIAPP peptide sequences.

Identical residues are highlighted in bold and red, and similar residues in orange. The boxed residues correspond to the fibril spine residues according to [257].

affinity interaction between early non-fibrillar and non-toxic A β ₄₀ and hIAPP species, which was identified *in vitro*, has been shown to suppress cytotoxic self-association and amyloidogenesis by both A β ₄₀ and hIAPP [190] using mutagenesis experiments.

Interestingly, the transcription level of hIAPP in the brain is undetectable [259, 264] so it is thought that cerebral hIAPP is generated in the pancreatic β -cells and is transported to the brain [259]. hIAPP oligomers can cross the Blood Brain Barrier by inducing inflammatory cytokines to destroy the integrity of the barrier [265, 266]. Transgenic murine studies are ongoing to help reveal the TIIDM-AD link [220, 238, 267, 268].

A β ₄₀ and hIAPP appear to interact not only in their monomeric states, but also can interact once aggregated. A β ₄₀ fibrils cross-seed hIAPP fibril formation, suggesting that the 3D fibril structure of A β ₄₀ is able to template hIAPP aggregation [261]. The ability for the same peptide mimetics and small molecules to inhibit amyloid formation from hIAPP and A β also implies that their underlying, amyloid-prone conformer structures are similar [262], leading to the hypothesis that drugs to treat TIIDM could be used to treat Alzheimer's (reviewed in [269]).

1.3.5 Current understanding of the A β ₄₀ and hIAPP monomer roles in the amyloid pathway

As discussed in the previous sections, amyloid formation is an intricate process and involvement of an IDP as the monomer unit of aggregation add another layer of complexity. This project focused on two examples of amyloidogenic IDPs: hIAPP and A β ₄₀. Figure 1.14a shows structure prediction results and aggregation prediction for both peptides.

A β ₄₀ consists of a charged N-terminal region, followed by a hydrophobic central region and then a C-terminal domain, Figure 1.14b. The central region, sometimes referred to as the central hydrophobic core (CHC) is thought to be important for amyloid formation as it has been shown to form amyloid in isolation [24, 270], but the limits of this region are not definitive (e.g. residues 14-23 [271], 16-21 [272, 273] or 16 to 22 [274]).

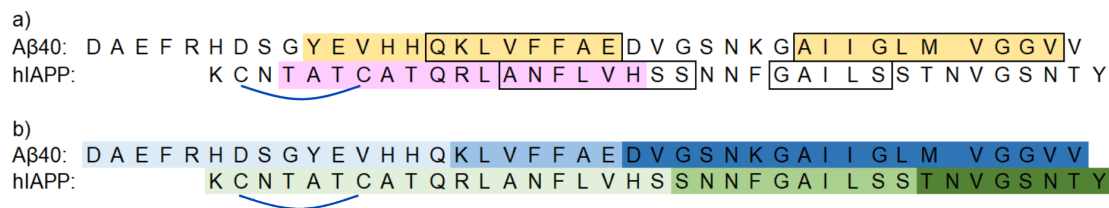


Figure 1.14: Structural predictions for A β ₄₀ and hIAPP.

a) Structural prediction (α -helical prediction in pink, β -sheet prediction in yellow) was calculated using PSIPRED (<http://bioinf.cs.ucl.ac.uk/psipred>) from University College London Department of Computer Science: Bioinformatics Group. AmyPred2 was used to find regions of predicted amyloidogenicity (black boxes)

(<http://aias.biol.uoa.gr/cgi-bin/AMYLPRD2>) which uses 10 separate prediction algorithms for amyloid propensity (including TANGO and WALTZ), consensus from 5 or more methods is required to determine a residue as being in an amyloidogenic region. b) Each peptide can be considered in three parts, A β ₄₀ has an N-terminal region (light blue), central hydrophobic region (mid blue), and C-terminal region (dark blue), and hIAPP also has an N-terminal region (light green), central hydrophobic region termed the ‘amyloidogenic region’ (mid green), and C-terminal region (dark green). The disulfide bridge is shown (blue) and the amidated C-terminus of hIAPP (green).

hIAPP has more structural features than A β ₄₀: a disulphide bridge between cysteines 2 and 7, and an amidated C-terminus, which are both important for amyloid aggregation [229]. The amino acid sequence of hIAPP can also be split roughly into three parts, Figure 1.14b: the N-terminal region, the amyloidogenic region, and the C-terminal region similarly to A β ₄₀. The N-terminal region, hIAPP₁₋₁₉, is able to bind to cell membranes [275]. Such an interaction can induce a transient, predominantly α -helical structure [276] to the otherwise randomly coiled peptide. This can bias the IDP conformation distribution prior to amyloid aggregation. hIAPP₂₀₋₂₉ is known as the amyloidogenic region [275], which is believed to lie at the inter-peptide interface when fibrillation occurs. Of this region of hIAPP, the shortest segment to form amyloid fibrils is NFGAIL [277] which is found to be essential for amyloid formation [229]. When comparing amyloidogenic hIAPP with non-amyloidogenic rat IAPP (rIAPP), 1.15, five residue substitutions are found in the amyloidogenic region and one substitution in the N-terminal region. This helps understand the lack of amyloid behaviour in the Pro-rich sequence. Interestingly, earlier isoforms of IAPP contain more Proline residues than hIAPP suggesting that in humans, hIAPP has developed the ability to aggregate due to an evolutionary driver, potentially this could well be for dense storage in β -granules. Finally, the C-terminal region of hIAPP is thought to positively modulate amyloid formation [275].



Figure 1.15: Sequence comparison of hIAPP and rIAPP. Altered residues are highlighted in blue. The disulfide bridge is shown in green and the amidated C-terminal in red.

Replica-exchange molecular dynamics (REMD) [278, 279], NMR [196, 280–285], electrospray ionisation ion mobility mass spectrometry (ESI-IMS-MS) [278, 286] and circular dichroism (CD) [197, 287–289] have all been used to gain insight into monomeric conformations of $A\beta_{40/42}$. Baumketner *et al.*, [278] used IMS-MS and REMD to categorise $A\beta_{42}$ conformations into three general groups. In each group the N-terminal part of the peptide exists mostly as loops and turns (e.g. A2-R5, A21-D23), but the groups differ in their propensity for structure in the hydrophobic C-terminal domain: greater propensity for α -helical structures, greater propensity for β -sheet structures, or a propensity for both types of structure [278]. Despite this, the ordered regions still only constitute 10-20 % of the total peptide sequence [278]. Prior NMR studies identified the CHC as having a high structural propensity to form α -helical fragments [196, 284] which is supported with MD simulations [279].

Molecular dynamics simulations on $A\beta_{40}$ based on NMR-guided metadynamics [290] were used to create a conformational landscape (Figure 1.16) of the IDP monomer and from this a library of structures which could be used as targets to design inhibitors which bind to $A\beta_{40}$ and prevent oligomerisation and fibrillation. The simulations are supported with biophysical data from size exclusion chromatography and pulse-field gradient NMR diffusion experiments to ascertain conformation diameters [129]. As expected for an IDP, the lowest energy states are least structured and as temperature increased, more structural motifs were simulated. The surface of the conformational landscape has many small undulations which enable the peptide to convert between different structures on minor energetic changes (*in vivo* such changes could be caused by the interaction of cell components or a change in ion concentration in the peptide environment).

Currently, it is unknown which structural propensities and features are essential for the initiation of $A\beta_{40}$ or hIAPP amyloid formation. The induction of α -helical structure in hIAPP has been linked to an increase in aggregation rate but it has not yet been probed on an atomic level, and it is not understood why this feature encourages amyloid

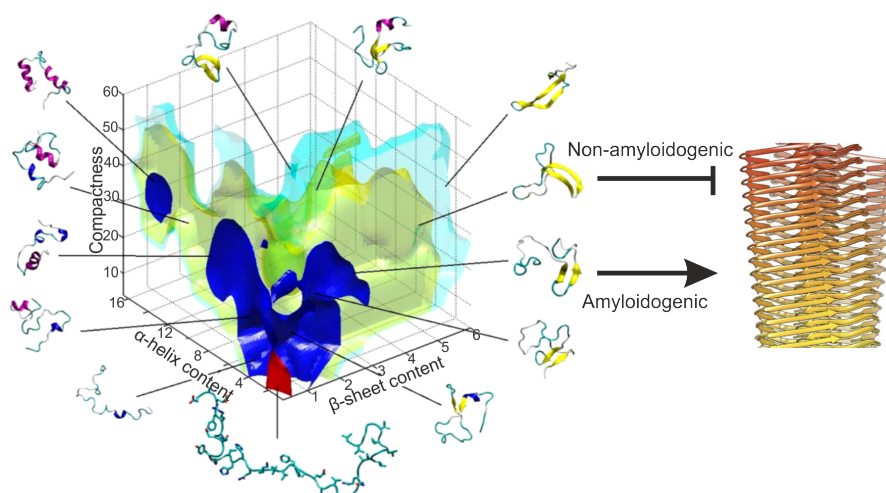


Figure 1.16: Free energy landscape predicted for A β ₄₀.

The free energy landscape shown is based on three variables (anti-parallel β -sheet content (X-axis), α -helical content (Y-axis) and number of hydrophobic contacts (or compactness, Z-axis)) used in an NMR-guided metadynamics simulation [129]. Levels of energy are discriminated at 5 (red), 10 (blue), 18 (yellow) and 25 kJ/mol (cyan) on the energy landscape whereas white regions are not visited as they have unsampled,

high free energies. Representative structures sampled during the simulation are illustrated outside the landscape in cartoon ribbon presentation. For increasing free energies, A β ₄₀ becomes more structured by populating both α -helical and β -sheet conformations. Some conformations are more prone to amyloid formation than others (black arrows). Adapted from [29, 129].

formation. Despite this, evidence of a transition of hIAPP to aggregate through β -sheet conformers without involving α -helical intermediates has been observed [291]. An α -helical structural transition has however also been noted in A β ₄₀ whereby a helical intermediate is formed prior to a β -sheet containing monomer which is amyloid-prone.

1.4 Strategies for Studying IDPs in Amyloid Formation: Approaches for Trapping Amyloid Species for Structural Analysis

The complex nature and incomplete understanding of both IDP conformational landscapes and the mechanism of amyloid formation makes studying IDP-amyloid transitions challenging, but potentially, enlightening. Much progress has been made in both fields and there is already a plethora of literature which combines them [292, 293]. Structural analysis can already be limited for structured amyloid precursors due to the timescale

of aggregation, the addition of monomer interconversion is yet more of a challenge. To aid the investigation of important monomer conformations of A β ₄₀ and hIAPP in their amyloid trajectory, specific conformations can be trapped, or stabilised to allow more time for structural analysis.

In the literature there are three major strategies which have been applied to trap, or skew, conformer population distributions of short-lived species on- or off- the amyloid pathway; use of peptide mimetics, peptide sequence mutagenesis, and small molecule stabilisation.

Using Peptide mimetics to investigate amyloid aggregation:

Peptide mimetics are usually peptides with similar sequences to the protein of interest, but are not compatible with further aggregation and thus can form and trap small oligomeric species. This approach has been used by Zhao *et al.* [275] and Westermarck *et al.* [229] to identify different functions of different parts of hIAPP in amyloid formation. Recently peptide mimetics have been used to study the interaction of hIAPP and insulin [294]. The hIAPP-fibrillating core (N₂₂FGAIL₂₇) fragment was used to inhibit insulin fibrillation [294]. NMR spectroscopy was used to analyse the inhibitory interaction at atomic resolution. Another study designed two small peptides (VVVVV and VIFYT) which, respectively, have a high and moderate predisposition for forming β -sheets, but both showed inhibitory behaviour in insulin amyloid aggregation [295]. In a study by Ratha *et al.*, [294], a derivative the N₂₂FGAIL₂₇ region created whereby the Ile was substituted for a residue mimetic, 2-aminobenzoic acid. This residue breaks β -sheet configurations and has been shown to prevent hIAPP from forming amyloid [296].

Using peptide sequence mutant or analogues to investigate amyloid:

Sequence alterations have also been insightful. Mutagenesis is generally a front-line approach for gaining information on peptide features and has been used in the amyloid field. A key example is the D76N mutant of β ₂-microglobulin which is a familial mutant leading to strongly enhanced amyloid aggregation [297, 298]. Pramlintide is an analogue of hIAPP which is currently used in the treatment of diabetes [299]. It prevents amyloid formation by binding to fibrils and preventing their elongation due to three proline substitutions (A25P, S28P, and S29P) which make pramlintide more similar to rIAPP (Figure 1.17) and prevent close β -sheet stacking.

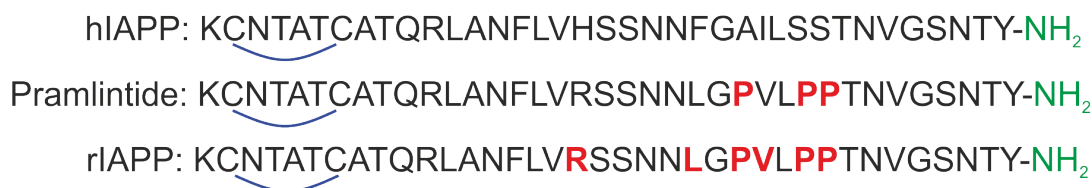


Figure 1.17: Sequence comparison of hIAPP, pramlintide and rIAPP.

Pramlintide differs by three residues from amyloidogenic hIAPP and non-amyloidogenic rIAPP. Residue substitution which are dissimilar to hIAPP are highlighted in red, the Cys2-Cys7 disulfide bridge is represented in blue, and the amidated C-terminus in green.

Altering residue side chains has also been used to probe for important chemistry in amyloid formation. For example, Abedini *et al.* [300] used acetylation (and truncation) experiments to show that if His18 of hIAPP is deprotonated, the rate of amyloid aggregation is faster than for the protonated form. At a monomer level, incorporation of additional chemistry into a peptide chain can be used to aid the study of amyloidogenic IDPs, for example, Click chemistry groups or groups for the addition of dye/FRET molecules. Or mutagenesis has been used to incorporate unnatural disulfide bridges to stabilise and bias peptide folds to encourage the formation of turns and secondary structural motifs which can be important in amyloid formation. Interestingly, work has been done to probe the importance of IDP sequence on amyloid propensity, Vadukul *et al.*, [301] used a combination of biophysical methods to observe changes in fibril morphology when the A β ₄₂ sequence was reverse or scrambled.

Use of small molecules to investigate amyloid:

Use of small molecules to probe amyloid formation is a vast area with a huge bank of scientific literature which is continually growing [302]. Small molecules have been used to bind and stabilise some conformations of IDPs [302, 303]. These compounds may act as inhibitors of aggregation by fixing the IDP monomer or oligomer in an off-pathway conformation, or may sterically exclude monomer addition to fibril forms. Alternatively compounds could accelerate amyloid formation by increasing the likelihood that the IDP samples an amyloid-prone conformation and thus increase the population of amyloidogenic forms. Many small molecules have been identified that affect the protein aggregation pathways. Of these, polyphenols, such as curcumin, EGCG, and resveratrol have been studied and shown to inhibit amyloid fibrillation [304–306]. In fact, certain

epigallocatechins have been used in clinical trials for the treatment of Alzheimers disease [307]. More recently, several quinones, such as benzoquinones, naphthoquinones, and anthraquinones, have been investigated and shown to modulate protein fibrillogenesis [304, 308, 309]. Small molecules do not effect all amyloid proteins in the same manner or to the same extent [302]. This is perhaps unsurprising given the breadth of proteins with amyloid-potential. Despite this, some large proteins can inhibit multiple amyloid proteins, e.g. C-Phycocyanin from *Spirulina* inhibits α -synuclein and $A\beta$ fibril formation [310], may share a common mode of action or may cause similar structural perturbations which can be analysed to shed light on important conformers in amyloid aggregation.

Additionally, there are many innovative methods, which can be used in conjunction with these three strategies, being developed to help explain the monomer and small oligomer phases of amyloid formation. Some examples of such methods are single molecule approaches (e.g. two colour coincidence [311, 312], fluorescence correction spectroscopy and FRET [313]); single molecule force measurements [314, 315], and novel mass spectrometry methods [316]. Furthermore various antibody-based approaches, reviewed by De Genst *et al.*, [317] have been used to stabilise partially structured species and folding intermediates of peptides involved in amyloid formation and Clark *et al.*, [252] developed a combinatorial method using two-photon scattering with time resolved fluorescence spectroscopy to create a novel way of monitoring the conformational dynamics of the early stages in aggregation of $A\beta$ (this is largely similar to CD but with enhanced sensitivity). In particular, NMR and MD methods are particularly suited to the study of IDPs.

Today there is an abundance of further biophysical methods which can be used in complementary analysis of amyloid formation mechanism. Table 1.3 lists some of these.

TABLE 1.3: Biophysical methods for monitoring IDP behaviour at various stages of amyloid formation. Adapted from [3–6] and references therein.

Technique	Applications	Species (Unfolded (U), Oligomeric (O), Aggregate (A))
Overall Structure/stoichiometry:		
TEM	Overall Shape	A
MS	Stoichiometry and important charge states	A O

Technique	Applications	Species (Unfolded, Oligomeric, Aggregate)
solid state NMR	Shape	A
Xray diffraction	Repetitive aggregate structure	A
chemical staining	Changes in surface exposure	A O U
H / D exchange	Changes in surface exposure	A O U
Cryo EM	Overall morphology	A
SDS + native PAGE	Stoichiometry	O U
DLS	Conformation	A O U
Specific structural info:		
solution NMR	Conformation,	O U
AFM	Formation/loss of secondary structure	O
H/D exchange	Highlight potential reactive hydrogens	A O U
Chemical crosslinking	Initial intermolecular interactions, surface exposure	O U
CD (near and far)	Formation/loss of secondary structure. Aromatic packing.	O U
Raman Resonance Spectroscopy	Surface exposure, aromatic interactions	O U
Intrinsic dynamics:		
Fluorescent probes (e.g. FRET, FPOP)	Degree of flexibility, rate of dis/association	A O U
ANS binding	Degree of flexibility, rate of dis/association	A O
solution NMR	Binding affinities and rates of folding	O U
AFM	Interaction strength	O U
H/D exchange	Surface exposure in alternating conformational states	A O U
EPR	Rate of dis/association	O

Technique	Applications	Species (Unfolded, Oligomeric, Aggregate)
Calorimetry	Rate of un/folding	O U

For this project a selection of these methods were chosen: ThT fluorometry, TEM, the β -lactamase tripartite assay, ESI-IMS-MS, and solution NMR. Choice of these methods is discussed in Chapter 3, Section 3.4. Provided here is a summary of how these methods have been used to study amyloidogenic IDPs.

1.4.1 ThT Fluorescence as a Reporter for Amyloid Aggregation *in vitro*

Although multiple dye-binding assays have been widely used to discover small molecule modulators of amyloid formation, use of the benzothiole dye Thioflavin-T (ThT) is by far the most popular [318, 319]. ThT can be added to an amyloidogenic system and changes in its fluorescence can indicate the extent of β -sheet formation. The popularity of the ThT fluorometry assay is likely due to its ease of use, small sample volumes, and the fact that a single experiment can provide a large amount of information about the system reaction kinetics [66]. The ThT assay is amenable to relatively high throughput data collection and thus is a commonly used as a screening technique.

In solution ThT emits a very low level of fluorescence (at 480 nm), however this increases greatly when the rotational freedom between its benzothiazole and dimethylaminobenzene ringed structures is limited. Associated with β -sheet conformations, such as those found within amyloid fibrils, is one type of interaction which can do this. Hence fibrillation can be monitored indirectly through the change in ThT fluorescence. Binding of ThT to amyloid fibrils, Figure 1.18, restricts the rotation of the benzothiazole and benzamidine rings of ThT which permits the fluorescence emission [320]. The interaction between ThT and β -sheet structures remains controversial [321–323] but the most widely accepted theory is that ThT can bind to β -sheet structures using a combination of electrostatic and hydrophobic interactions between ThT and the repetitive grooves of a β -fibril [324]. It is thought that ThT interacts hydrophobically with aromatic residues which are ≥ 4 β -strands apart and this restricts ring rotation on ThT and this enables fluorescence [321, 324, 325].

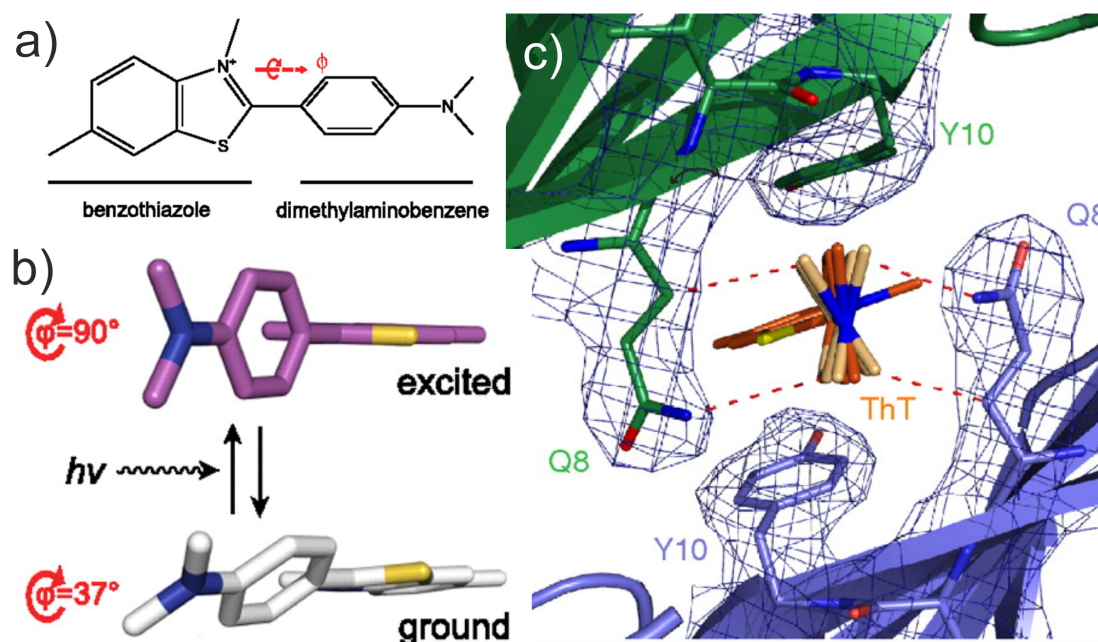


Figure 1.18: ThT ring orientation is restricted when bound to β -sheets.

a) the chemical structure of ThT. b) The orientation of the benzothiazole and dimethylaminobenzene structures differs when ThT is in its excited state. c) ThT (orange) between two β -sheets (green and blue) in a β_2 -microglobulin amyloid fibril showing restricted bond rotation. Adapted from [326].

Despite being the ‘Gold standard’ technique for monitoring aggregation, the ThT assay is not infallible. When used in conjunction with small molecules, compound-ThT interference can result in misleading fluorescence read outs. For example, a small molecule may interact directly with ThT and exhibit fluorescence regardless of the β -sheet content of the protein sample, or conversely, a compound may sequester and/or quench ThT fluorescence. Such interactions are particularly likely when screening aromatic compounds similar to many published amyloid inhibitors, e.g. EGCG, bexarotene, naphthoquinones etc. Additionally, there may be compound-peptide interactions which sterically block ThT from binding to β -sheet structures. For a screening assay, false positives which can be filtered out after further testing are less problematic than false negatives which could exclude hit compounds from analysis. For example, a false positive result is observed on the interaction of rifamycin with hIAPP in the presence of ThT [327]. Rifamycin interrupts the ThT-fibril interaction so no increase in fluorescence is observed implying inhibition of fibril formation. Use of additional biophysical methods, such as electron microscopy [328] or atomic force microscopy (AFM) [329] can be used subsequently to verify conclusions.

Interpretation of absolute levels of ThT fluorescence when bound to amyloid fibrils has been discussed extensively in the literature. There are conflicting claims on the correlation between fibril yield and ThT fluorescence. Some research shows a reproducible, linear correlation of fluorescence and fibril abundance (for example, Xue *et al.*, [330] showed this linear relationship between ThT intensity and $A\beta_{40+42}$ or prion protein Ure1 between protein concentrations of 0.2 to 500 μM). However, there are multiple factors which could disrupt this relationship. One of the major factors relevant to amyloid is the non-uniform affinity of ThT to bind to fibrils of differing morphology. As was discussed in Section 1.1, the structure of amyloid fibrils is heterogeneous and if the morphology of fibril created has a larger pitch or groove of altering depth then this could affect ThT affinity and fluorescence intensity. Work by Linse, Dobson and Knowles [66] developed models for fitting amyloid formation using ThT which enables interpretation of whether an aggregation process is dominated by fragmentation, primary, or secondary nucleation.

Recently the ThT assay has been used to probe the effects of compounds found in day-to-day life on $A\beta_{40}$ aggregation [331], such as caffeic acid in coffee, EGCG in green tea, resveratrol in red wine, and cumin in tumeric. Although a useful assay, there are flaws and next generation fluorophores are being developed, such as some curcumin analogues [332]. There are alternative dyes such as ANS and bisANS [333] and nezothiophenes which can discriminate oligomers and amyloid. Amyloid formation kinetics of other proteins, such as α -synuclein [334] and β_2 -microglobulin [335] have also been extensively studied using ThT fluorometry.

1.4.2 Testing Small Molecule effects on Amyloid Aggregation in a Physiological Environment

A notable *in vivo* study by Navarro *et al.* [336] developed a method of quantitative detection of amyloid within cells using a combination of confocal microscopy, fluorescence microscopy, and flow cytometry combined with a new dye called ProteoStat which can bind and discriminate intracellular amyloid aggregates in *E. coli*. A particularly useful *in vivo* method for the study of small molecules and their impact on aggregation, is the tripartite- β -lactamase assay [337]. This assay, based in the periplasm of *E. coli* cells, can be used as a small molecule screen and also to assess small molecule potency [337].

There are other *in vivo* assay options for investigating compound effects on aggregation in live cells but these experiments are limited to cytosolic environments [336, 338, 339]. These studies involved the fusion of aggregation-prone peptides to a reporter protein such as green fluorescent protein (GFP) [336, 338–340]. The folding of such a large reporter protein may influence peptide solubility and aggregation behaviour. The problem with this is that only certain compounds can cross the cell membrane leading to multiple false negative results. The presence of porins in the outer membrane of *E. coli* (and other Gram negative bacteria), the membrane barrier is permeable to molecules of up to approximately 600 Da [341]. A common theme for these assays is the genetic fusion of a protein of interest in between two domains of a reporter protein. This reporter may be a fluorescent protein [338, 339, 342] which can be detected directly or an enzymatic function which can be easily observed by indirect monitoring.

A schematic for the tripartite β -lactamase assay is shown in Figure 1.20. For this assay the peptide of interest, e.g. A β ₄₀ or hIAPP, is expressed into a linker region in between the two domains of β -lactamase (Figure 1.19. β -lactamase is often used as a reporter system due to its relatively small size (29 kDa) and monomeric nature [343]. The assay is based on the assumption that if the test protein inserted is able to aggregate with other β -lactamase tripartite fusions, the β -lactamase enzyme activity will be lost from the periplasm. Hence, when aggregation of the test protein occurs, β -lactamase activity is reduced and the bacteria are consequently more sensitive to β -lactam-containing antibiotics such as ampicillin or carbenicillin [337]. When the bacteria are grown in the presence of small molecule inhibitors of protein aggregation, antibiotic resistance is restored in a quantitative manner. For example, this assay has been implemented to screen for small molecule inhibitors of hIAPP aggregation [337] and an earlier variant has been used to screen for inhibitors of A β ₄₀ aggregation [344]. To date, the tripartite β -lactamase developed by Saunders *et al.* [337], is the only *in vivo* method that can be applied as a screen for the multitude of small molecules that cannot enter the cytoplasmic space.

A major benefit of this assay is that purified protein is not necessary which avoids time intensive steps in investigations. This meant the tripartite β -lactamase assay is amenable for investigation of hard-to-produce peptides which may be aggregation prone during the purification process. Furthermore, the assay can be used even when little structural or functional information about the peptide of interest is available, principally,

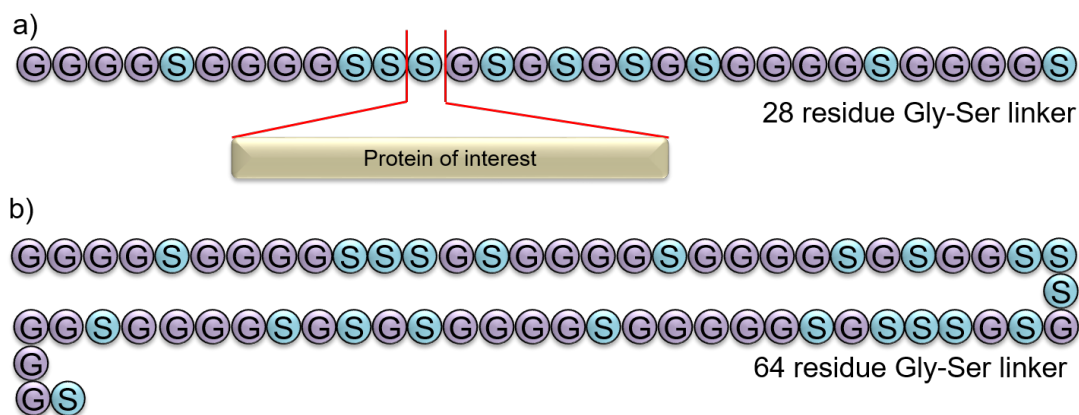


Figure 1.19: The Gly-Ser linker sequence between the two domains of β -lactamase
a) The sequence of the 28-residue linker and position of the test protein insert. b) The 64-residue linker sequence for control assay (for short peptides such as hIAPP or A β) whereby the linker is solely Gly-Ser

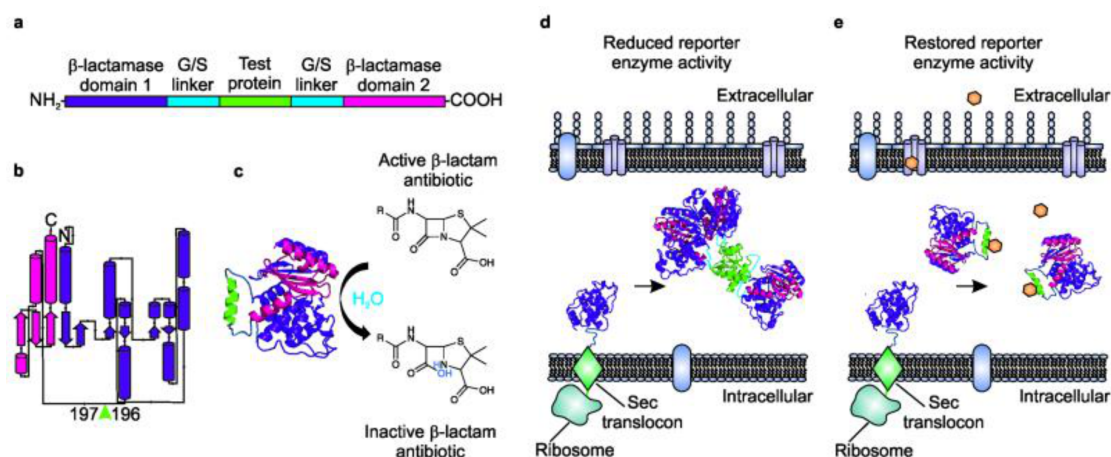


Figure 1.20: The tripartite β -lactamase assay can identify aggregation-prone sequences.
a) In this schematic the test protein (green) is inserted into a glycine/serine-rich linker (blue) within the loop region separating the two domains of β -lactamase (purple and pink). b) Clarification of where the inserted protein sits within the β -lactamase enzyme (green arrow). c) When β -lactamase can bring its two domains together, it can form the active site for β -lactam cleavage. d) When an aggregation-prone sequence is inserted β -lactamase enzymes are sequestered and the two β -lactamase domains are sterically prevented from forming the enzyme active site. e) Addition of a small molecule which inhibits aggregation of the inserted peptide can restore β -lactamase can function. Taken from [337].

the assay could be performed on a peptide for which only the primary sequence is known [345, 346]. Caveats to this assay included its ineffectiveness when compounds are highly toxic, or if a small molecule is able to stabilise a low order oligomeric state possibly allowing β -lactamase to still function as it is not so sterically hindered to prohibit the

formation of its active site [346].

1.4.3 The Value of Electron Microscopy in Amyloid Fibril Observation

There are various techniques which can be used to monitor the nature of mature aggregates as was indicated in Figure 1.1. Some aspects of mature fibrils lend themselves to biophysical analysis, such as their stability, and repetitive structures, where as others present challenges, such as polymorph heterogeneity and contrasting fine structures. Cryo-EM has propelled the extent of structural information which can be obtained from the study of fibrils to near atomic resolution, even for *ex vivo* samples [347, 348]. Other microscopy techniques, including the comparatively low resolution, transition electron microscopy (TEM), still have value as a rapid method to check for aggregate presence and overall morphology, i.e. amorphous or amyloid [337].

A caveat of TEM is the inability to accurately quantify aggregates species. The number of fibrils observed is difficult to quantify from EM techniques due to the varying lengths of fibrils observed, the inconsistent affinities of fibril morphologies to bind to the carbon grids or stain. Quantitative methods for fibril yields include sedimentation velocity AUC analysis, or RP-HPLC. Sedimentation velocity AUC analysis can characterise intermediate species in amyloid fibril formation in exceptional detail, particularly oligomers and protofibrils [349, 350]. RP-HPLC has been used to quantify early species in A β ₄₀ amyloid aggregation such as oligomers [351]. In 2014, Arosio *et al.*, [352] noted that many conventional methods for detecting amyloid forms were not sensitive to events taking place early in the lag phase. As described earlier, secondary nucleation plays a role in amyloid formation and it is important to note that low levels of some fibrillar species will be present in the early stages of amyloid formation. Quantification of such fibrillar species of A β ₄₂ has been measured using carefully conducted seeding calibrations and ThT fluorescence [352].

1.4.4 Use of Electrospray Ionisation Ion Mobility Spectrometry Mass Spectrometry (ESI-IMS-MS) to Observe Monomer and Small Oligomers in IDP ensembles

ESI-IMS-MS is one of the leading techniques for the study of heterogeneous, lowly populated, and transient species in biochemical reaction pathways [353, 354]. This is due to the specific ability to detect multiple species within a sample with great sensitivity even when species are low in concentration [316, 355, 356]. ESI-IMS-MS can separate ions not only by their mass:charge ratio, but also by their collisional-cross section area. This allows alternative conformational states of isobaric oligomers to be detected [316, 356, 357]. A further advantage of ESI-IMS-MS is the speed of data acquisition. This enables reaction progress to be monitored such as the disappearance of monomer and change in oligomer distribution as amyloid formation progresses [354]. The method has been used in the amyloid field [358, 359] and also in wider areas, such as in determining the reaction intermediates formed in chemical reactions [360].

In the amyloid field, ESI-IMS-MS has been demonstrated to be an ideal method for studying small compound interactions with intrinsically disordered peptides such as A β ₄₀ [358] and hIAPP [316]. In the most recent study by Young *et al.*, [358] the method was used to probe the binding mode and interaction stoichiometry (Figure 1.21) and to screen for small molecules which interact with monomeric and low oligomer forms of amyloidogenic peptides [316]. Despite the small sample requirements and great insight which this technique can provide on small molecule interaction and conformer distributions, one downfall is that all analysis is conducted in the gas phase rather than in a liquid solution and results thus need to be validated with other methods in solution.

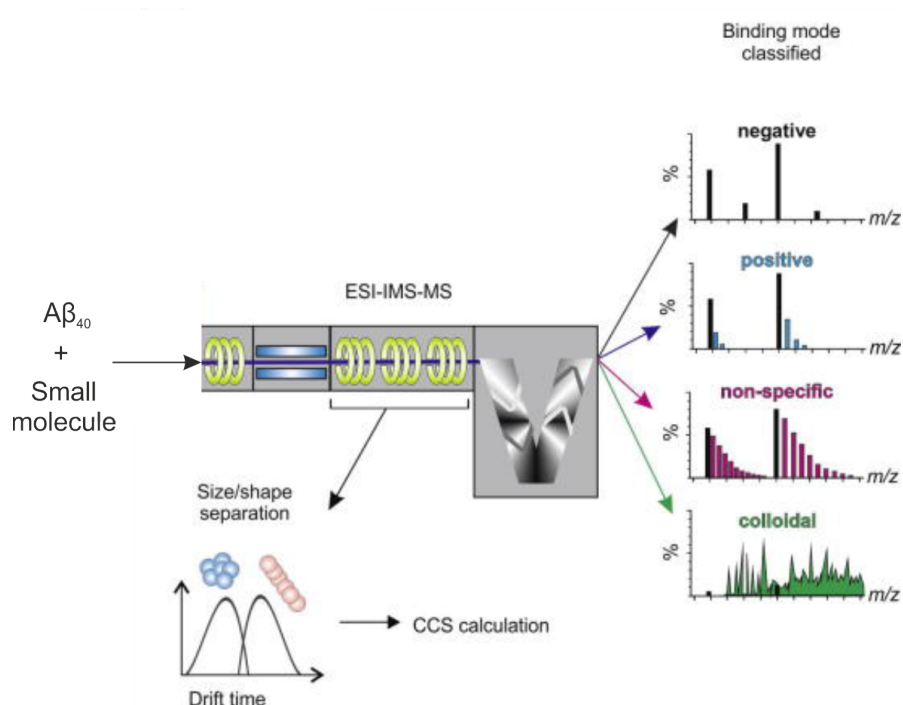


Figure 1.21: A schematic of the ESI-IMS-MS set up.

$A\beta_{40}$ was mixed with small molecules and the samples were infused into the mass spectrometer wherein separation occurs based on the mass to charge ratio (m/z) and collisional cross-sectional area (CCS) of the protein-small molecule complexes. Output data can generally be classified into four distinct outcomes: No small molecule interaction (black), specific small molecule interactions (blue), non-specific interaction (pink) or a colloidal mass wherein the compound bind to itself (green) based on [361].

Figure adapted from [358].

The power of ESI-MS in elucidating information on the early stages of amyloid formation was highlighted earlier with studies by Bleiholder *et al.*, [215]. Furthermore, IMS has been used, in conjunction with gas phase infra-red spectroscopy, to indicate that more expanded conformers, with a larger collisional cross-section (CCS), tend to contain more β -sheet and β -sheet-like architectures than smaller conformers [86, 92]. This observation implies the transition towards a fibril-like architecture may occur at a very early stage on the aggregation pathway for short amyloid-forming peptides.

1.4.5 Residue Specific Effects of Small Molecules Can be Monitored by Complementary NMR Methods

NMR spectroscopy is well-suited to the study of IDPs owing to their extensive flexibility and is highly compatible with small molecule-peptide interaction studies. Research on IDPs has led to development and adaptation of NMR techniques to extract structural information on these disordered states [362]. The selection of NMR methods available to IDP biologists is extensive (PRE, RDC, $T_{1,2}$, CPMG, Pulse-field gradients, NOEs, ^{13}C -direct detected experiments, $^1\text{H}^{15}\text{N}$ -HSQC, TROSY and anti-TROSY experiments) [363] and therefore a considered approach is required to select an complementary subset of techniques which can shed light on different peptide attributes. Often the information obtained by NMR can be interpreted using molecular modelling tools to generate conformational ensembles which represent IDP conformations [362]. Measurement and comparison of separate parameters can reveal insight into IDP behaviour which may be overlooked in a single type of analysis. Atomic level structural characterisation of IDP drug targets enables the development of more effective treatments [364, 365]. For example, small molecules have been designed to inhibit binding to IDP oncoprotein c-Myc [366], and to interfere with amyloid formation [364].

Assignment of chemical shifts of resonances of IDPs is essential for specific residue analysis. The intramolecular motions of IDPs cause slow relaxation rates giving rise to narrow linewidths which reduce spectral overlap. This is particularly useful given the narrow dispersion in the ^1H dimension of $^1\text{H}^{15}\text{N}$ -HSQC spectra of IDPs [367, 368] which can result in signal overlap. This can be problematic, but NMR methods have been developed to overcome spectral overlap issues. For example, 5D and 7D experiments were used to resolve signal overlap for the Tau protein (another amyloid IDP associated with Alzheimer's diseases) [369] but often resonance distributions for ^{13}C and ^{15}N nuclei can be exploited sufficiently to assign IDPs. Chemical shift changes of specific resonances on the addition of small molecule modulators of aggregation can pinpoint binding site locations, the binding affinities.

Secondary structure in IDPs is usually transient and confined to short segments [362]. Residual Dipolar Couplings (RDCs) and chemical shift perturbations are commonly used to infer information on secondary structure propensity due to their sensitivity to structure formation. For example, RDCs have been used to reveal structural information

on IDPs including α -synuclein [370] and $A\beta_{40}$ and fragments [371–373]. Interestingly there is a lack of literature demonstrating the use of RDCs to investigate IDPs in the presence of small molecules. Such experimentation would enable comparison of peptide properties in apo states and small molecule bound states. RDCs can provide insight into long-range intrapeptide interactions on up to a ms timescale [374, 375].

Where RDCs can indicate regions of structural propensity, temperature coefficients can indicate probability of involvement of backbone amides in hydrogen bonding [376, 377]. This correlates with secondary structure formation propensity and can lead to inference of flexibility along the backbone of an IDP. If an amide proton is involved in hydrogen bonding, indicative of secondary structure, there is a negative correlation between strength of hydrogen bond and the size of the temperature coefficient (a strong hydrogen bond gives rise to a small temperature coefficient) [376]. This is because it is more likely that amide protons in hydrogen bonds will not exchange with solvent hydrogens, and solvent exchange is very temperature dependent [378]. Again, there are few examples of using this parameter to monitor changes in structural conformations of IDPs on the addition of small molecules, but the method theoretically should be amenable to such measures. Okazaki *et al.*, [378] developed a method for classifying disorder in IDPs based on temperature coefficient scores which can aid the interpretation of measured values.

Heteronuclear relaxation experiments can probe peptide dynamics which is vital for consideration of IDPs. T_2 relaxation can give insight into ps-ns movements as well as on conformational exchange on the μ s-ms timescale [370, 379, 380]. T_2 relaxation is based on how quickly nuclei lose alignment after a magnetic pulse in the NMR spectrometer. If a peptide region is more flexible and able to move around more then the rate of relaxation will be fast, so T_2 will be shorter. This is explained in more detail in Chapter 5.

Taken together, these methods provide a detailed glimpse of IDP structural and dynamic properties which can indicate important transitions induced by small molecules. Used in conjunction with other methods, and if the small molecules can perturb amyloid aggregation, NMR can reveal important conformer steps in monomer folding necessary for amyloid aggregation. This topic has been extensively reviewed in [363, 381, 382] and many others.

1.5 Thesis Aims

Amyloid aggregation has a role in some of the most prevalent diseases in today's society. A great deal of research has focused on elucidating the key structures underpinning these diseases in the hope of revealing more about the mechanism of aggregation. The conformation of monomers in the amyloid pathway are particularly difficult to define structurally as many of the species are dynamic, existing only as transient states in a vastly heterogeneous population.

This thesis describes a multi-method approach which was used to investigate the aggregation of the amyloidogenic IDPs; $A\beta_{40}$ and hIAPP. Small molecules were then sought that are able to modulate the aggregation of $A\beta_{40}$.

Chapter three describes the construction of a method toolbox which was later used to screen and then evaluate the effects of 67 small molecules on amyloid formation of $A\beta_{40}$. Initially $A\beta_{40}$ and hIAPP were recombinantly expressed and purified as a prelude to testing small molecule effects on aggregation. The small molecule screening process must be relatively high throughput and data analysis will need to be efficient for revealing effects on amyloid formation. The toolbox will need to bring together a selection of methods which can then be used to probe small molecule effects on aggregation more thoroughly. On choosing which methods to be incorporated into the toolbox, key control experiments were conducted for each method to ensure compatibility with IDPs and small molecules. It is hoped that this toolbox will become an invaluable set of measures which can be used to find and then probe how specific small molecules can alter the amyloid aggregation pathway of IDPs. This will ultimately lead to greater understanding of amyloid diseases and may yield therapeutic directions in the future.

In chapter four, the method toolbox, was applied to screen a compound library to search for modulators of $A\beta_{40}$ aggregation. First a compound library for screening was selected using ROCS analysis of compound leads: 1,2-naphthoquinone, adapalene, bexarotene, MM3003, and UV11523. Next the screening method chosen in chapter three was used to find small molecules which perturb amyloid formation. Promising results from the screen were then investigated using the other methods in the toolbox (ESI-IMS-MS, TEM, quantified fibril yield assessment, and NMR).

In preparation for residue specific analysis of small molecule interactions with $A\beta_{40}$ chapter five describes a set of NMR methods which were used to define a set of structural parameters to describe the $A\beta_{40}$ apo conformational ensemble. Rather than bringing these measures together to create a modelled ensemble as has been performed already [129], the parameters will be used directly to compare with measures of $A\beta_{40}$ in the presence of small molecule modulators of amyloid aggregation. The purpose of this was to reveal any changes in structural propensity on the addition of small molecules. Direct comparison of $A\beta_{40}$ apo and small molecule bound measures were used to reveal key structural transitions which may be important in monomer transitions in amyloid formation.

Overall this work aimed to prepare a strategy for the structural investigation of monomeric, amyloidogenic IDPs, which are susceptible to the induction or stabilisation of semi-structured states on addition of small molecule compounds. Such information will clarify part of the enigma of how IDP monomers enter the amyloid pathway. Understanding amyloid formation will ultimately aid the development of future therapeutic approaches for the prevention of amyloid diseases in the future.

Chapter 2

Materials and Methods

2.1 Materials

2.1.1 Technical Equipment

Centrifuges

Avanti J-26XP Centrifuge (Beckman Coulter, Brea, CA, USA)

Eppendorf 5810R Centrifuge (Eppendorf, Hauppauge, NY, USA)

MiniSpin plus F-45-12-11 (Eppendorf, Hauppauge, NY, USA)

GenFuge 24D Centrifuge (Progen Scientific, London, UK)

Incubators, Mixers, and Shakers

Innova 43R shaking incubators (New Brunswick Scientific, NY, USA)

Innova 44R shaking incubators (New Brunswick Scientific, NY, USA)

Gallenkamp Economy Incubator Size 1 (Sanyo, Watford, UK)

Stuart Magnetic Stirrer SB161 (CamLab, Cambridge, UK)

Orbital Incubator S1500 (Stuart, Staffordshire, UK)

Orbital Incubator S1600 (Stuart, Staffordshire, UK)

Vortex Mixer SA8 (Stuart, Staffordshire, UK)

Tube Roller (Starlab, Milton Keynes, UK)

Protein Purification Equipment

AKTAprime plus (GE Healthcare, Buckinghamshire, UK)
HiLoad 26/600 Superdex 75 PG gel filtration column (GE Healthcare, Buckinghamshire, UK)
Superdex 75 10/300 gel GL filtration column (GE Healthcare, Buckinghamshire, UK)
Pharmacia Biotech XK 26 packable column (GE Healthcare, Buckinghamshire, UK)
Buhner funnel glas columns fo iapp prep vivaspins filters HPLC machine

Gel Electrophoresis Equipment

Techne Dri-Block DB-2A Heather (Bibby Scientific, Stone, UK)
UVITEC cambridge Nine Alliance Q9 Software (BioSPX, Abcoude, The Netherlands)
Slab Gel Electrophoresis Chamber AE-6450 (ATTO, Tokyo, Japan)
PowerPac Basic (Bio-Rad, Hercules, CA, USA)
KS-250 Basic Shaker (IKA Labortechnik, Oxford, UK)
UVITEC Cambridge Q9 Alliance (BioSPX, Abcoude, The Netherlands)
Vari-Gel midi system (CamLab, Cambridge, UK)

PCR thermocycler

T100 thermal cycler (Bio-Rad, CA, USA)

Spectrophotometers

UltraSpec 2100 pro UV/Visible Spectrophotometer (GE Healthcare, Buckinghamshire, UK)
UV-1800 UV/Vis Spectrophotometer (Shimadzu, Kyoto, Japan)
Nanodrop 2000 UV/Vis Spectrophotometer (Thermo Scientific, Surrey, UK)

Microplate readers

Fluostar OPTIMA Plate Reader (BMG Labtech, Aylesbury, UK)
CLARIOstar Plate Reader (BMG Labtech, Aylesbury, UK)
Corning Costar 3881 96 Well, Half Area with Clear Flat Bottom Polystyrene NBS Microplate (Corning Life Sci, The Netherlands)

Microscopes

JEOL JEM-1400 Transmission Electron Microscope (JEOL Ltd, Tokyo, Japan) with Gatan US1000XP 2k x 2k CCD camera (Gatan Inc., Pleasanton, USA)

Mass Spectrometers

Synapt high definition mass spectrometry (HDMS) quadrupole-time-of-flight mass spectrometer (Micromass UK Ltd., Waters Corp., Manchester, UK), equipped with a Triversa automated nano-electrospray ionisation (ESI) interface (Advion Biosciences, Ithaca, USA)

NMR Spectrometers

750 MHz NMR magnet (Oxford Instruments, Abingdon, UK)
QCI-P-cryoprobe and an Avance III HD console (Bruker Corp. Coventry, UK)

Kits

Wizard Plus SV Minipreps DNA Purification system (Promega, Hampshire, UK) Q5 Site-Directed Mutagenesis Kit (NEB, Hertfordshire, UK)

HPLC

Jupiter 5u C-18 300A column (Phenomenex)
ASI-100 Automated Sample Injector
FoxyJr automated fraction collector
HPLC machine: Dionex system consisting of a p580 pump with a PDA-100 Photodiode Array detector, an RF 2000 fluorescence detector and a DEGASYS DG-2410 equipment

Other

Ultrasonic Processor (Cole Parmer, St. Neots, UK)
Constant Cell Disruption Systems (Constant Systems, Northants, UK)
Grant JB1 Unstirred Waterbath (Grant Instruments, Shepreth, UK)
Ultrawave U50 Bath Ultrasonic (Ultrawave Ltd, Cardiff, UK)

Series 2100 Media Autoclave (Prestige Medical, Minworth, UK)
Heto PowerDry PL3000 Freeze drier (Thermo Scientific, Surrey, UK)
Snakeskin Pleated Dialysis Tubing: 3500 MWCO (Thermo Scientific, Surrey, UK)
Precisa 180A Scales (Precisa Ltd, West Lothian, UK)
Kern Electronic Scales PLS 360-3 (Kern, Northants, UK)
Satorius Electronic Scales TE 12000(Satorius, Surrey, UK)
Orion Versastar Pro pH meter (Thermo scientific, Surrey, UK)
TripleRed Purite Water System (Avidity Science, Bucks, UK)

2.1.2 Chemicals

A

Acetic acid, glacial (Fisher Scientific, Loughborough, UK)
Acrylamide 30 % (*v/v*) (Severn Biotech, Kidderminster, UK)
Adapalene (Merck, Gillingham, UK)
Agar (Fisher Scientific, Loughborough, UK)
Agarose (Melford Laboratories, Suffolk, UK)
L-(+)-Arabinose (Sigma Life Sciences, MO, USA)
Ammonium Chloride (¹⁵N) (Cambridge Isotope Libraries, UK)
Ammonium persulphate (APS) (Sigma Life Sciences, MO, USA)
Ammonium bicarbonate (Sigma Life Sciences, MO, USA)
Ampicillin sodium salt (Formedium, Norfolk, UK)

B

Benzamidine dihydrochloride (Sigma Life Sciences, MO, USA)
Bexarotene (Merck, Gillingham, UK)
Bromophenol blue (Sigma Life Sciences, MO, USA)

C

Carbenicillin disodium (Formedium, Norfolk, UK)
Calcium chloride (CaCl₂) (Melford Laboratories, Suffolk, UK)
Chloramphenicol (Sigma Life Sciences, MO, USA)

Compound 1-67 (Provided by Dr Richard Foster, University of Leeds, UK)

Compound A12a (ChemDiv, CA, USA)

Compound A13a (ChemDiv, CA, USA)

Compound A14a (ChemDiv, CA, USA)

Compound A21a (ChemBridge, CA, USA)

Compound Q06a (ChemBridge, CA, USA)

Coomassie Brilliant Blue (Fisher Scientific, Loughborough, UK)

D

Dithiothreitol (DTT) (Formedium, Norfolk, UK)

Deuterium oxide (D₂O) (Fluorochem, UK)

E

Ethanol (Sigma Life Sciences, MO, USA)

Ethidium bromide (EtBr) (Sigma Life Sciences, MO, USA)

Ethylenediaminetetraacetic acid (EDTA) (Fisher Scientific, Loughborough, UK)

G

Glucose (Fisher Scientific, Loughborough, UK)

Glucose (¹³C) (Cambridge Isotope Libraries, UK)

Glycerol (Fisher Scientific, Loughborough, UK)

Guanidine hydrochloride (Sigma Life Sciences, MO, USA)

H

HEPES (Sigma Life Sciences, MO, USA)

Hydrochloric acid (HCl) (Fisher Scientific, Loughborough, UK)

I

Instant Blue Stain (Expedeon Protein Solutions, UK)

Isopropanol (Fisher Scientific, Loughborough, UK)

Isopropyl -D-1-thiogalactopyranoside (IPTG) (Melford Laboratories, Suffolk, UK)

L

Lysogeny broth (LB), granulated (Melford Laboratories, Suffolk, UK)

M

Magnesium Sulfate (Melford Laboratories, Suffolk, UK)

N

1,2-Naphthoquinone (Merck, Gillingham, UK) (Melford Laboratories)

P

Phenylmethanesulfonyl fluoride (PMSF) (Sigma Life Sciences, MO, USA)

Potassium phosphate (monobasic) (Fisher Scientific, Loughborough, UK)

Precision plus protein dual colour standards protein ladder (Bio-Rad, CA, USA)

S

10 % SDS Solution (Severn Biotech Ltd, Kidderminster, UK)

Sodium azide (NaN_3) (Sigma Life Sciences, MO, USA)

Sodium chloride (NaCl) (Fisher Scientific, Loughborough, UK)

Sodium hydroxide (NaOH) (Fisher Scientific, Loughborough, UK)

Sodium dodecyl sulphate (SDS) (Severn Biotech, Kidderminster, UK)

Sodium phosphate dibasic, Na_2HPO_4 (Thermo Scientific, Surrey, UK)

Sodium phosphate monobasic, NaH_2PO_4 (Sigma Life Sciences, St. Louis, USA)

T

Terrific Broth (Melford Laboratories, Suffolk, UK)

Tetramethylethylenediamine (TEMED) (Sigma Life Sciences, MO, USA)

Thiamine (Merck, Gillingham, UK)

Tris (Fisher Scientific, Loughborough, UK)

Tetracycline (Formedium, Norfolk, UK)

U

Urea (MP biomedical, Loughborough, UK)

2.2 Methods

All buffers were filter sterilised using a 0.22 μm filter (Durapore). All water used was deionised and taken from a Purite system. All pHs were altered using 10 M NaOH (Fisher Scientific) and/or 34 % (*v/w*) HCl (Fisher Scientific).

2.2.1 Molecular Biology

2.2.1.1 *E. coli* Bacterial strains and plasmids

E. coli DH5 α (Invitrogen, Paisley, UK) F ϕ 80lacZ Δ M15 Δ (lacZYA-argF) U169 recA1 endA1 hsdR17 (rK, mK+) phoA supE44 λ thi-1 gyrA96 relA1

E. coli BL21 (DE3) (Stratagene, Cambridge, UK) F - dcm ompT hsdS(rB mB) gal λ (DE3)

E. coli BL21 (DE3) pLysS (Stratagene, Cambridge, UK) F - dcm ompT hsdS(rB mB) gal λ (DE3) [pLysS Camr]

A pETSAC plasmid encoding A β ₄₀ was provided by Dr Katie Stewart, University of Leeds. A pTXB1 plasmid encoding a quadripartite construct which contained hIAPP was provided by Prof. Andrew Miranker (University of Yale, USA) (was used for hIAPP expression). The tripartite β -lactamase construct was encoded in a pBM1 plasmid provided by Dr Janet Saunders (University of Leeds).

2.2.1.2 Preparation of competent *E. coli* cells

Communal stocks of competent cells are made using the following protocol. A 10 ml overnight culture is prepared using the desired cell strain. This was used to inoculate, at a ratio of 1:20, 100 ml LB which was shaken at 180 rpm, 37 °C until the OD₆₀₀ was 0.4-0.45. Cells were harvested at 4000 rpm (3220 xg), 4 °C for 10 min using a chilled A-4-62 Eppendorf rotor in a chilled Eppendorf centrifuge 5810R. The supernatant was discarded and the cell pellet gently resuspended in 10 ml of pre-chilled 100 mM CaCl₂ and incubated on ice for 10 min. Cells were harvested again by centrifugation in the same way and the supernatant was discarded. The cell pellet is resuspended in 2 ml

of 100 mM CaCl₂, 30 % (*v/v*) glycerol. The cell suspension was separated into 50 μ l aliquots in 1.5 ml eppendorf tubes and frozen on dry ice. Cells were stored at -80 °C.

2.2.1.3 LB medium and Agar Plate Preparation

LB medium was prepared in all instances by mixing LB powder with d.H₂O to create a 25 g/L solution in an appropriately sized conical flask (i.e. a 2 L flask for a 500 ml 1 L volume, a 250 ml flask for 100 ml volume, a 100 ml flask for a 50 ml solution) capped with a foam bung and foil. The flask was then autoclaved at 121 °C, 100 kPa for at least 20 minutes.

LB agar plates were prepared by mixing 1.5 mg agar and 2.5 mg of LB powder with 100 ml d.H₂O and then sterlising the solution via autoclaving at 121 °C, 100 kPa for 20 minutes. Once cooled to approximately 50 °C relevant antibiotics were added (100 μ g/ml ampicillin/carbenicillin for pTXB1 and pETSAC plasmids, or 10 μ g/ml tetracycline for pMB1 plasmids) and plates were poured in a sterile environment and left to solidify. Plates were wrapped in parafilm and stored at 5 °C until required but no longer than 6 weeks.

2.2.1.4 Transformation of *E. coli* cells

50 μ l aliquots of competent *E. coli* cells (see Section 2.2.1.2) were defrosted on ice for five minutes before 2 μ l of the construct-containing plasmid was added (pETSAC for A β ₄₀, pTXB1 for hIAPP, or pBM1 for β -lactamase constructs). After incubation on ice for 30 min with intermittent mixing, cells underwent heat shock for 45 s in a water bath (Stuart, SWB series) at 42 °C and were then returned to ice for 5 min. 500 μ l of sterile LB medium was added to the cells. The cell solution was incubated at 37 °C, 200 rpm (Stuart, Orbital incubator S150) for 30 minutes. 50 μ l of cell solution was plated onto LB agar plates (see Section 2.2.1.3) containing the relevant antibiotic and incubated overnight at 37 °C (Gallenkamp incubator).

2.2.1.5 Plasmid Amplification

Colonies of transformed *E. coli* DH5 α cells (see Section 2.2.1.4) present on antibiotic-containing LB agar plates (see Section 2.2.1.3) were selected and used to inoculate starter cultures (see Section 2.2.1.3) of 10–100 ml of LB medium which contained the relevant antibiotics (100 $\mu\text{g}/\text{ml}$ ampicillin/carbenicillin for cells containing pTXB1 or pETSAC plasmids, or 10 $\mu\text{g}/\text{ml}$ tetracycline for cells containing pMB1 plasmids). Starter cultures were grown overnight at 37 °C, 200 rpm (Stuart, orbital incubator S150). DNA was extracted and purified according to the kit protocols for either a miniprep (Promega) or midiprep (Qiagen). To determine the concentration of amplified DNA the absorbance at 260 nm was measured using a Nanodrop 2000 (Thermo Scientific) and used to determine DNA concentration: concentration ($\mu\text{g}/\text{ml}$) = $(A_{260} - A_{320}) \times 50 \mu\text{g}/\text{ml}$. A_{320} absorbance is a measure of the noise level and 50 $\mu\text{g}/\text{ml}$ is a standardised coefficient (an A_{260} equal to 1 is equivalent to 0.5 $\mu\text{g}/\text{ml}$ pure dsDNA). DNA was stored in an airtight container at -20 °C.

2.2.1.6 Agarose Gel Electrophoresis to Indicate DNA Size and DNA sequencing

To verify the production of complete plasmid amplification a sample of the DNA was subject to agarose gel electrophoresis. Agarose gels were made by dissolving 1.5 % (w/v) agarose in 1 x Tris-acetate-EDTA (TAE) buffer [40 mM tris HCl (Fisher Scientific), 20 mM acetic acid (Fisher Scientific), and 1 mM EDTA (Acros Organics), pH 7.5] and heating the solution using a microwave until the solution was transparent. Once cooled to approximately 45 °C, ethidium bromide (0.5 $\mu\text{g}/\text{ml}$) (Sigma Aldrich) was added. The gel was then poured into an 8 x 15 x 2.5 cm gel tray with a well comb, and allowed to solidify. The DNA sample was diluted in 10 x agarose loading buffer [2.5 mg/mL bromophenol blue (Sigma Aldrich), and 50 % (v/v) glycerol (Fisher Scientific)] and 30 μL was loaded into the gel well. Alongside the loaded lane, 5 μL of the 1 KB+ ladder solution was added [10 μL 1 KB+ ladder (NEB), 90 μL 10 mM tris, pH 8.5 (Fisher Scientific), and 20 μL 10x agarose loading buffer]. Agarose gel electrophoresis was carried out in 1 x TAE buffer at 100 V. Finally the gel was visualised using ultra violet (UV) illumination and photographed using a Syngene InGenius gel documentation system (Syngene, UK).

On observation of a band indicating successful plasmid amplification, another sample for the DNA was sent to Genewiz (formerly Beckman Cogenics) for sequence confirmation using commercial T7 primers:

Fwd: TAA-TAC-GAC-TCA-CTA-TAG-GG

Rev: CTA-GTT-ATT-GCT-CAG-CGG-TG

2.2.2 Protein Expression and Purification

2.2.2.1 Expression of unlabelled A β ₄₀

BL21 (DE3) cells were transformed with the pETSAC plasmid encoding A β ₄₀ (Section 2.2.1.4) and plated into 100 μ g/ml ampicillin/carbenicillin-containing LB agar (Section 2.2.1.3). At least 16 hours later a single colony was transferred from the agar plate into 100 mL of LB with 100 μ g/ml ampicillin/carbenicillin to create an inoculated starter culture under sterile conditions. These were incubated at 37 °C with shaking at 200 rpm overnight. 10 x 10 mL was removed from this culture and was used to inoculate 10 x 0.5 L sterile solutions of LB medium (prepared as detailed in Section 2.2.1.3). 100 μ g/mL ampicillin/carbenicillin was added prior to inoculation. The cultures were incubated at 37 °C, with 200 rpm agitation until the optical density at 600 nm (OD₆₀₀) reached 0.5-0.6. Protein expression was induced through the addition of 0.5 ml of 1 M isopropyl β -D-1-thiogalactopyranoside (IPTG) resulting in a final concentration of 1 mM IPTG. Cultures were then incubated for a further 3.5 h or until the OD₆₀₀ reached a plateau (typically around OD₆₀₀ = 1.2). Cells were harvested by centrifugation at 6000 x g for 15 min at 4 °C. The cell pellets were extracted and stored at -20 °C.

2.2.2.2 Expression of ¹⁵N/¹³C-labelled A β ₄₀

¹⁵N/¹³C-labelled, M9 minimal medium was used to culture *E. coli* BL21(DE3) cells which had been transformed with a pETSAC plasmid (Section 2.2.1.4) in order to generate ¹⁵N/¹³C-labelled A β ₄₀ for NMR experiments. M9 media was prepared as a 5x salts solution (15 g monobasic potassium phosphate (KH₂PO₄), 34 g anhydrous dibasic sodium phosphate (Na₂HPO₄), and 2.5 g sodium chloride (NaCl) made up to 1 L in d.H₂O) which was diluted five times with d.H₂O into conical flasks, i.e. for the starter

culture 10 ml of the 5x salts solution and 40 ml d.H₂O were poured into a 100 ml conical flask. This solution was sterlised via autoclaving at 121 °C, 100 kPa, for at least 20 minutes. The following components (all filtered using a 0.22 µm filter (Bio-rad)) were added immediately prior to inoculation of the 50 ml starter culture:

Component stock	Volume added to 50 ml	Volume added to 500 ml
100 mg/mL carbenicillin	50 µl	500 µl
1 M CaCl ₂	5 µl	50 µl
1 M MgSO ₄	100 µl	1 ml
20 % (w/v) ^{12/13} -glucose	0.5 ml	5 ml
20 % (w/v) ¹⁵ N-NH ₄ Cl	0.25 ml	2.5 ml
10 mg/mL thiamine	5 µl	50 µl

To inoculate the starter culture a single colony was taken from an LB-containing agar plate (as for expression in LB medium, Section 2.2.2.1) under sterile conditions. The 50 mL culture was incubated at 37 °C, with 200 rpm agitation for 24 h. At this time, 4 mL of the cell culture was extracted and used to inoculate each of 11 baffled 2 L flasks containing 500 mL of sterile M9 medium which had been prepared similarly as for the starter culture above (whereby the volumes of each component are scaled by a factor of 10 to maintain concentrations, Column 3 in the table above). Cultures were incubated overnight at 15 °c with 120 rpm shaking. In the morning, the temperature and shaking were increased to 37 °C and 180 rpm respectively. when the OD₆₀₀ reached 0.5-0.6, construct expression was induced using 0.5 mL of 1 M IPTG to each flask. The temperature was lowered to 24 °C and cultures were left shaking (at 180 rpm) overnight. Cells were harvested similarly to preparation in LB medium; centrifugation at 6000 x g for 15 min at 4 °C. The cell pellets were extracted and stored at -20 °C.

Expression was confirmed and yields were estimated using SDS-PAGE (Section 2.2.3).

2.2.2.3 Multistep Purification of A β ₄₀

A schematic workflow for the purification of A β ₄₀ can be found in Chapter 3, Figure 3.4. Throughout this process, purity was monitored using SDS-PAGE (Section 2.2.3).

Isolation and Lysis of A β ₄₀-containing Inclusion Bodies

12.5 mL of 1 x Buffer A was added to the cell pellet from Section 2.2.2.1. Approximately 0.5 mg DNase, 1 mM phenylmethanesulfonyl fluoride (PMSF) and 2 mM benzamidine were added to the suspension and mechanically stirred at 4 °C until an homogeneous

Buffer	Composition
10 x Buffer A	100 mM Tris-HCl (Fisher Scientific) 10 mM EDTA (Fisher Scientific) pH 8.5
1 x Buffer A	1:10 dilution of 10 x Buffer A in d.H ₂ O
Inclusion Body Solubiliser	8 M urea (MP Biomedicals) in 1 x Buffer A

solution was obtained (typically after 1 h). The solution was next passed through a blunt syringe needle (Terumo Global Pharmaceutical Solutions, NJ, USA) to increase homogeneity before sonication for 30 s (7.5 mm probe, 10 μ m amplitude). The homogenate was centrifuged at 30,000 x g for 15 min at 4 °C, and the supernatant was removed. The pelleted cell material was resolubilised in 12.5 ml 1 x Buffer A and the syringe homogenisation, sonication, and centrifugation processes were repeated once more. The pellet was lastly solubilised, using a magnetic stirrer, in cold (4 °C) inclusion body solubiliser until homogeneous (approximately 1 h). The suspension was sonicated and centrifuged a third time (as before) and the supernatant (containing solubilised A β ₄₀) was collected and diluted 1 in 4 with 1 x Buffer A to reduce the urea concentration from 8 M to 2 M in preparation for anion exchange purification.

Anion Exchange Purification using Q-Sepharose Resin

All the buffers used in the following steps of the A β ₄₀ purification were pre-cooled to 4 °C to reduce the aggregation potential of the peptide.

35 mL of Q-Sepharose Fast Flow resin (GE Healthcare) was equilibrated with 1 x Buffer A, before it was mixed with the 1 in 4 dilution of soluble cell lysate prepared in the previous section. Lysate and resin were incubated together for 30 min at 4 °C with gentle rocking. Positively charged peptides, including A β ₄₀ at pH 8, bind to the resin. Anion exchange purification of A β ₄₀ was then performed using a batch format to avoid problems associated with A β aggregation during column chromatography [383]. The batch purification was conducted in a 250 ml Büchner funnel, with Whatman 1 filter paper, fitted to a conical flask with a side arm. This arm was attached to a water-flow vacuum system. The loaded resin was poured into the Büchner funnel and the flow through was collected and set aside at 4 °C. The resin was washed twice with 50 ml pre-chilled 1 x Buffer A, containing 0 then 25 mM NaCl. Peptide elution was initiated with 5 x 50 ml washes of 1 x Buffer A containing 125 mM NaCl. Finally, a high-salt (1 x Buffer A, 250 mM NaCl) and high-salt with urea (1 x Buffer A, 250 mM NaCl, 8 M urea)

wash were applied to the resin to remove any remaining bound proteins. Each eluate was stored at 4 °C to avoid aggregation before buffer exchange into 50 mM ammonium bicarbonate by dialysis. Dialysis was conducted using 3,500 MWCO snake-skin dialysis tubing which was prepared by soaking in 50 mM ammonium bicarbonate. The Tubing was filled with the A β ₄₀-containing eluates and placed in 5 L of 50 mM ammonium bicarbonate with a total 4 x 5 L changes over 2 days. Fractions were then lyophilised.

The stored flow through was re-incubated with freshly equilibrated resin and subjected to the same batch anion exchange, buffer exchange, and lyophilisation processes (although only 3 x 50 ml elutions of 1 x buffer A containing 125 mM NaCl were used rather than 5 x 50 ml elutions due to time:yield compromise).

Size Exclusion Chromatography Purification of A β ₄₀

All SEC was performed at 4 °C. The lyophilised, partially-purified A β ₄₀ was resolubilised in 3-4 x 5 ml of 50 mM Tris-HCl, pH 8.5, containing 7 M guanidinium-HCl. The 5 ml solutions were aliquoted into 5 x 1.5 ml eppendorfs and centrifuged for 10 min at 14,000 rpm at 4 °C. The five aliquots were loaded together onto a pre-equilibrated (in 50 mM ammonium bicarbonate) HiLoad™ 26/60 Superdex 75 prep grade gel filtration column (GE Healthcare), connected to an ÄKTA prime Liquid Chromatography system. 50 mM ammonium bicarbonate was also the mobile phase in which the protein was eluted. The ÄKTA programme used is outlined in Table 2.1 and A β ₄₀ was eluted in a single peak at approximately 180 ml which was collected and lyophilised. The typical yield from this A β ₄₀ preparation was 5-6 mg/L culture.

Breakpoint (ml)	Flow Rate (ml/min)	Fraction Size (ml)	Injection Valve Position
0	2	0	Load
4	2	0	Inject
20	2	0	Load
50	2	4	Load
360	2	0	Load
362	0	0	Load

End

Table 2.1: The programme used to purify A β ₄₀ by SEC.

For some experiments, namely the ThT fluorometry assay $A\beta_{40}$, the purity of the peptide is essential for reproducibility of results as the assay is highly sensitive to contaminants. To prepare $A\beta_{40}$ for this assay, the lyophilised powder resulting for the SEC purification was subjected to another SEC run. 2.5-3.0 mg of lyophilised peptide was solubilised in 0.5 ml of 50 mM Tris-HCl, pH 8.5, containing 7 M analytical grade guanidinium-HCl (as previously, all buffers and SEC runs are conducted at 4 °C). This was centrifuged for 10 min at 14,000 rpm before being loaded onto a Superdex 75 GL column (GE Healthcare) which was pre-equilibrated with 50 mM ammonium bicarbonate. The ÄKTA programme was set so 1 ml fractions were collected as up to 0.4 ml/min of 50 mM ammonium bicarbonate flowed through the column. The $A\beta_{40}$ eluted in fractions 11-13 at approximately 1 hr depending on flow rate. $A\beta_{40}$ -containing fractions were immediately flash-frozen using dry ice and EtOH or in liquid nitrogen and lyophilised.

Yields were measured using absorbance at 280 nm using samples in a quartz cuvette. Samples were sent to the Mass Spectrometry facility to verify the final product and indicate final purity (approximately 98 % when two SEC steps were applied).

2.2.2.4 Expression of the hIAPP-containing Quadripartite Construct

The expression and purification protocols for recombinant hIAPP was based on the published protocol by Williamson and Miranker in 2007 [384] which is summarised in Figure 3.8 in Chapter 3.

BL21(DE3) cells transformed with the pTXB1 plasmid (Section 2.2.1.4) were selected from ampicillin/carbenicillin-containing LB agar plates (Section 2.2.1.3) and used to inoculate 100 ml LB medium with 100 μ g/ml ampicillin/carbenicillin. Cells were grown at 37 °C, 200 rpm (Stuart, Orbital Incubator S150) overnight. Glycerol stocks were prepared (0.5 ml of the overnight cultures were taken and added to 0.5 ml 30 % (*v/v*) glycerol and mixed). Glycerol stocks are stored at -80 °C and were used as an alternative for repetitive cell transformation.

4-10 ml of the overnight culture was taken and used to inoculate 1 L of sterile LB medium with 100 μ g/ml ampicillin. Cultures were grown at 37 °C, 200 rpm (Sanyo orbital incubator, Panasonic) until the OD_{600} was between 0.6-0.8 (measured using UV-micro cuvettes, Brand, Germany, and a Jenway spectrometry, Genova). At this point protein

expression was induced by addition of 1 ml of 1 M isopropyl β -D-1-thiogalactopyranoside (IPTG) (Formedium) to a final concentration of 1 mM and flasks were cooled to 15 °C (Innova 44, New Brunswick Scientific) and shaken overnight, 200 rpm. Cells are harvested after 15-20 hours by centrifugation at 5000 rpm (6238 xg) for 30 min, 4 °C, (using a JLA-8.1000 Beckman rotor in a Beckman Coulter Avanti J-26XP centrifuge) and the cell pellet was stored at -20 °C.

Expression was monitored using SDS-PAGE as detailed in Section 2.2.3.

2.2.2.5 Multistep purification of hIAPP

Cell Lysis and Removal of Insoluble Cellular Material

Buffer	Components
Equilibrium Buffer	20 mM HEPES (Sigma Aldrich), pH 8 0.1 mM EDTA (Acros Organics) 50 mM NaCl (Fisher Scientific) 2 M urea (MP Biomedicals)

The harvested cell pellet was resuspended in 20 ml Equilibrium buffer via gentle rocking (Stuart Roller Mixer) for approximately 30 min at 4 °C. 40 μ l of 50 mM phenylmethylsulfonyl fluoride (PMSF) (Sigma Aldrich) is added as well as 1-5 mg of bovine DNase1 (Sigma Aldrich). Sonication was used to lyse the cells using sonication (10 cycles of 15 s pulse, 45 s pause at 22 % amplitude). Lysed cells are then centrifuged at 20,000 rpm (48384 xg) for 30 min, 4 °C (JA25.50 Beckman rotor in a Beckman Coulter Avanti J-26XP centrifuge) to separate soluble and insoluble cell material. The pellet was discarded and the supernatant taken forward for the next steps in purification.

Chitin-Affinity Purification to Extract the Quadripartite Construct from Other Soluble Material

The supernatant was loaded onto a glass column of 2.8 cm diameter which was packed with a bed volume of 20 ml chitin beads (NEB). The column was equilibrated using d.H₂O followed by Equilibrium buffer (Section 2.2.2.5) prior to supernatant loading. The chitin resin was then washed with 300 ml of Equilibrium buffer to remove any unbound proteins.

C-terminal Amidation by Intein Cleavage

Buffer	Components
Cleavage Buffer	20 mM HEPES (Sigma Aldrich), pH 8.5 0.1 mM EDTA (Acros Organics) 50 mM NaCl (Fisher Scientific) 2 M urea (MP Biomedicals) 0.1 M DTT (Formedium) 2 M ammonium bicarbonate (Sigma Aldrich)

Three column volumes (3 x 20 ml) of Cleavage buffer were added quickly to the column. Before the final 20 ml of Cleavage buffer ran off of the column, the column was closed and incubated at 4 °C overnight. Protein was eluted from the column in three separate column volumes of Equilibrium buffer (Section 2.2.2.5), the first of which is taken forward for purification.

To regenerate the chitin resin for future purifications, the column was stripped of residual bound proteins using 0.3 M NaOH. Firstly three column volumes of 0.3 M NaOH were washed through the column. The column was then closed and the chitin beads incubated with the 0.3 M NaOH for 30 min. Subsequently seven column volumes of 0.3 M NaOH were flowed through the column to ensure no protein was left bound to the chitin beads. The column was finally washed using 20 column volumes of d.H₂O, and stored in 20 % (*v/v*) ethanol.

Buffer exchange and Filtration to Prepare for Release of hIAPP by V8 Cleavage

Buffer	Components
Dialysis Buffer 1	20 mM HEPES (Sigma Aldrich), pH 8 0.1 mM EDTA (Acros Organics) 2 M urea (MP Biomedicals) 50 mM NaCl (ThermoFisher Scientific)

In anticipation of the final cleavage of the protocol, the 20 ml first elution volume was dialysed in a 1000 Da MW cut off membrane (Spectra/Por 6) against 5 x 1 L of Dialysis buffer to remove ammonium bicarbonate and DTT. To prepare for V8 cleavage, the solution was concentrated (VIVASPIN 20, MWCO 3 kDa) using an A-4-62 Eppendorf rotor, in an Eppendorf centrifuge 5810R at 4000 rpm (3220 xg), 4 °C to 5 ml.

Site Directed Mutagenesis to Improve V8 cleavage Efficiency

Site Directed Mutagenesis (SDM) was carried out to change two glutamic acid residues in the leader sequence of the hIAPP expression construct to a glutamine and a histidine (E4Q and E5H). SDM was performed adhering to the protocol provided in the commercial Q5 kit (NEB).

Firstly, primers were designed using the NEB online tool (<http://nebasechanger.neb.com/>) and purchased from Eurofins MWG Operon (boldening denotes changed codons):

Primer	Sequence	Residues	% GC	T _m (°C)
Forward	AATGAAAATT CAAC ATGGCAACG CGAACC	29	41	56
Reverse	ATGTATATCTCCTTCTTAAAGTG	23	30	55

The primers were incorporated into the following reaction mixture in 0.2 ml PCR tubes:

Reagent	Volume (μ l)
Q5 Hot start high-fidelity master mix (2X)	12.5
10 μ M Forward primer	1.25
10 μ M Reverse primer	1.25
Template DNA (1-25 ng/ μ l)	1
Nuclease free water	9

The solution was subjected to the following Polymerase Chain Reaction (PCR) cycle:

Step	Temperature (°C)	Duration (s)
Initial denaturation	98	30
PCR	98	10
	50-72*	30
	72	kbx25
	72	120
Final extension	72	120
Hold	4	∞

*Annealing temperature was determined based on the mutagenic primers as calculated by NEBaseChanger (<http://nebasechanger.neb.com/>)

An agarose gel, Section 2.2.1.6, was used to confirm successful PCR. After confirmation of DNA of the correct molecular weight (\sim 7 kbs) the plamid was subjected to kinase digestion, ligation, and DpnI (KLD) enzyme treatment in a clean 0.2 ml PCR tube:

Reagent	Volume (μl)
PCR product	1
KLD reaction buffer (2x)	5
KLD enzyme mix (10x)	1
Nuclease free water	3

5 μl of the reaction product was used to transform competent *E. coli* DH5 α cells (Sections 2.2.1.2) using the protocol described in Section 2.2.1.4. An individual colony was picked and used to inoculate 10 ml LB medium with 100 $\mu\text{g}/\text{ml}$ ampicillin/carbenicillin. The culture was grown overnight at 37 °C, 180 rpm (Stewart orbital incubator, UK) A Pure Yield Plasmid Miniprep kit (Wizard) was used to extract plasmid DNA. Samples were subsequently sent to Genewiz (formerly Beckmen Cogenics), for sequence determination to verify the incorporation of the two amino acid substitutions.

E. coli BL21(DE3) cells were transformed with this plasmid as described in Section 2.2.1.4 and used to express the modified quaripartite construct in the same way as the original construct (Sections 2.2.2.4 and 2.2.2.5).

Release of hIAPP by V8 Cleavage and Separation by HPLC

2 mg of V8 protease (Endoproteinase Glu-C from *Staphylococcus aureus* V8, Sigma Aldrich) was added to the 5 ml sample and incubated at 4 °C for 1 hour with rocking, setting 18 on a mini see-saw rocker, SSM4, Stuart. The reaction was quenched by flash freezing using dry ice with ethanol (Sigma Aldrich) and then protein was lyophilised (Heto, PowerDry PL3000, Thermo Electron Scientific).

Buffer	Components
Eluant A	10 % (<i>v/v</i>) acetonitrile (Fisher Scientific)
	0.1 % (<i>v/v</i>) trifluoroacetic acid (Fisher Scientific)
Eluant B	90 % (<i>v/v</i>) acetonitrile (Fisher Scientific)
	0.1 % (<i>v/v</i>) trifluoroacetic acid (Fisher Scientific)

Next the leader (2.0 kDa) and hIAPP (3.9 kDa) peptides were separated using Reverse Phase High Performance Liquid Chromatography (RP-HPLC) using a Jupiter 5u C-18 300A column (Phenomenex). The HPLC apparatus used was Dionex system consisting of a p580 pump, ASI-100 automated sample injector, PDA-100 photodiode array detector, RF 2000 fluorescence detector, DEGASYS DG-2410, and FoxyJr automated

fraction collector. The lyophilised sample was dissolved in 300-500 μ l 100 % DMSO and loaded on to the column in multiple injections of volume no greater than 100 μ l. A gradient from 0 - 100 % Eluent B was applied and hIAPP was eluted in one 5 ml fraction between 16-17 min. The protein was then flash frozen and lyophilised.

The final step in the purification protocol was to oxidise and form the disulfide bond between Cys2 and Cys7 in hIAPP. This was attempted by dissolving the reduced hIAPP powder in 3 ml of 30 mM acetic acid, pH 5.3, forming a solution of \sim 0.215 mM hIAPP. H₂O₂ was added to a final concentration of 2 mM. The sample was incubated at 4 oC for 4–6 h and quenched by flash freezing and lyophilisation.

2.2.3 SDS-PAGE

Tris-Tricine buffered SDS-PAGE was used due to its aptitude for resolving small peptides (as low as 2 kDa in size) such as A β ₄₀ (4485 Da) and hIAPP (3907 Da). SDS-PAGE was used to monitor peptide purification throughout the expression and purification methods, as well as for measuring fibril yields. Gels were prepared as follows in all cases:

Component	Resolving gel (ml)	Stacking gel (ml)
30 % (<i>w/v</i>) acrylamide: 0.8 % (<i>w/v</i>) bisacrylamide (Severn Biotech Ltd.)	7.5	0.85
3 M tris-HCl (Fisher Scientific), 0.3 % (<i>w/v</i>) SDS (Sigma Aldrich), pH 8.45	5.0	1.55
Glycerol (Fisher Scientific)	2.0	0
10 % (<i>w/v</i>) ammonium persulfate (Sigma Aldrich)	0.1	0.1
TEMED (Sigma Aldrich)	0.01	0.01

Gels were placed vertically in a gel stand and seals were assured between buffer compartments. The following buffers were diluted to a 1x solution and added:

Buffer	Components
10x Anode buffer	242.3 g tris in 1 L d.H ₂ O, pH 8.8 (Fisher Scientific)
10x Cathode Buffer	tris-tricine-SDS running buffer, pH 8.3 (Alfa Aesor)

All electrophoresis was carried out at 35 mA and then increased to 70 mA once the gel front had moved through the stacking gel.

SDS-PAGE Sample Preparation and Staining

Buffer	Contents
4x SDS Loading Buffer	100 mM tris, pH 6.8 (Fisher Scientific) 4 % (<i>w/v</i>) sodium dodecyl sulfate (Sigma Aldrich) 0.2 % (<i>w/v</i>) bromophenol blue (Sigma Aldrich) 20 % (<i>v/v</i>) glycerol (Fisher Scientific)
2x SDS Loading Buffer	1:1 dilution of 4x SDS Loading Buffer in d.H ₂ O

A β ₄₀ gel samples (except fibril yield assays, see Section 2.2.5.3) were prepared as 20 μ l samples with a 1:1 ratio of sample to 2x SDS Loading buffer. Of these samples, 12 μ l (or 6 μ l when necessary to avoid overloading) was loaded into the SDS-PAGE gel alongside 6 μ l of PrecisionPlus ProteinTM Dual Xtra Standards protein ladder (Biorad).

For monitoring protein expression, 1 ml samples were taken from the expression cultures and pelleted by centrifugation at 14,100 xg (Eppendorf MiniSpin Plus) for 10 min at 4 °C. The pellet was resuspended in a volume of d.H₂O so that the OD₆₀₀ was equal to 1. This sample was then mixed to form a 1:1 ratio solution of sample to 2x SDS-PAGE as above.

After electrophoresis, gels were stained using Instant Blue (Biorad) overnight and de-stained for 2 h in d.H₂O before imaging. Gels were visualised using a Syngene InGenius gel documentation system (Syngene, UK).

Due to poor binding of hIAPP to SDS-Loading buffer and Instant Blue (Biorad), an alternative sample preparation method and stain were used. To prepare hIAPP samples, 5 μ l of 4 x LDS loading buffer (Biorad) with 8 M urea was added to 15 μ l of sample. Samples were boiled for four minutes and then spun briefly (Eppendorf Benchtop centrifuge 5418) to collect all condensation in the sample. 15 μ l of the prepared samples were loaded (except when this led to lane overloading, i.e. for supernatant samples with large amounts of protein, in which case 7.5 μ l of sample was loaded) in wells alongside 6 μ l of PrecisionPlus ProteinTM Dual Xtra Standards protein ladder (Biorad). After electrophoresis, the gels were stained using Coomassie Brilliant Blue as follows; Gels were submerged in fresh stain and microwaved for three 8 s bursts, with gentle shaking in between, before being left to stain for 20 minutes on a shaker (AOS manufacturing Ltd). The same procedure was carried out with a destaining solution (50 % (*v/v*) d.H₂O, 40 % (*v/v*) methanol (Fisher Scientific), and 10 % (*v/v*) acetic acid (Fisher Scientific)) and the gels were left gently shaking in destaining solution overnight. Gels were visualised using a Syngene InGenius gel documentation system (Syngene, UK).

2.2.4 Computational ROCS

Virtual screening was performed by Dr Charlotte H. Revill and Dr Richard J. Foster (University of Leeds). The structure of each of the five query molecules (1,2-naphthoquinone, adapalene, bexarotene, MM11253, UVI3003) was inputted into the virtual Rapid Overlay for Chemical Structures (vROCS) user interface and reduced to the lowest energy conformer using LigPrep [385]. This conformer was used as the query scaffold for *in silico* screening of an in-house library of 50,000 structurally diverse, small molecules using Rapid Overlay of Chemical Structures (ROCS) [385]. ROCS is a 3D method that compares the molecular steric arrangement of multiple compounds. The method can quickly identify potentially active compounds by shape comparison based on a smooth Gaussian-function fit model of structure volume comparison. Any volume mismatch is measured as an indication of compound dissimilarity. Additionally, the vROCS software can also incorporate a ROCS Combiscore assessment which compares the pharmacological characteristics of compounds and provides a measure of their shape similarity. 67 compounds were selected for screening based on a qualitative assessment of structural diversity by Dr Charlotte H. Revill.

2.2.5 Biophysical Techniques

2.2.5.1 ThT fluorometry

400 μL samples were prepared in 1.5 mL eppendorfs containing 100 μM thioflavin T (from a 0.2 μm filtered 1.2 M stock in $\text{d.H}_2\text{O}$), 20 μM $\text{A}\beta_{40}$ (from a 20 mg/mL stock in 100 % DMSO), 100 μM compound (from a 10 mM stock in 100 % DMSO) in 50 mM ammonium acetate, pH 6.8, and a 2 % (*v/v*) final concentration of DMSO. These were aliquoted into four 100 μl samples in wells on the same opaque, half area, 96-well plate and sealed with clear film. Plates were incubated in a FLUOstar OPTIMA plate reader for 21 hours at 37 °C without agitation. Fluorescence was excited using a 440 \pm 5 nm filter, and emission intensity was measured every 300 s using a 485 \pm 5 nm filter.

For compound titration ThT assays, the compound concentration was varied to 4 μM , 20 μM , or 200 μM .

2.2.5.2 Transmission Electron Microscopy Techniques

Samples were extracted from 96-well plates which were used to conduct the ThT fluorometry experiments at the end of the aggregation reaction. To prepare sample grids 10 μL of each sample was loaded onto a carbon-coated, copper specimen grid (Agar Scientific Ltd, UK) and left for 30 s before blotting against filter paper. The copper grids were subjected to irradiation used UV light prior to sample addition. Next 2 x 10 μL drops of H_2O were loaded to briefly wash the grid, before blotting again and staining with 10 μL 2 % (*w/v*) uranyl acetate for 30 s. The uranyl acetate had been centrifuged at 14000 rpm for 10 min to remove uranyl acetate precipitate. The grid was then finally blotted completely to leave negatively stained samples on the grids and allowed to dry completely in air. Incomplete blotting led to positive staining.

Transmission electron microscope images were acquired on a JEOL JEM-1400 transmission electron microscope (JEOL Ltd., Japan) equipped with a Gatan Orius camera or a Gatan Ultra Scan 1000 XP camera.

2.2.5.3 Measuring Fibril Yield

To quantify the extent of aggregation and SDS-PAGE method was used. To prepare samples, 100 μL of sample was removed from the 96-well plates in which the ThT fluorometry experiments were conducted. This was placed in a 200 μL eppendorf. 20 μL was removed and mixed with 7 μL of 4 x SDS-Loading buffer (Section 2.2.3) as the ‘Whole’ sample. The remaining 80 μL were subject to centrifugation at 14,000 rpm for 20 min to separate insoluble and soluble material. Using a precision tip, 20 μL from the top of the spun sample was removed and mixed with 7 μL of 4 x SDS-Loading buffer in a 200 μL eppendorf as the ‘Soluble’ sample. Using a precision tip the remaining 60 μL of liquid was removed from the centrifuged samples with care not to disturb pelleted material. The pellet was suspended in 80 μL of $\text{d.H}_2\text{O}$ and 20 μL was taken and mixed with 7 μL 4x SDS-Loading buffer in a separate 200 μL eppendorf as the ‘Pellet’ sample.

Each of the Whole, Soluble and Pellet samples were boiled for 10 min using a heat block set to 100 °C. Samples were briefly spun to collect any condensation within the eppendorf and then 20 μL was loaded onto an SDS-PAGE gel, Section 2.2.3. The gel was stained overnight in Instant Blue (Biorad) and destained for 2 h in $\text{d.H}_2\text{O}$ prior to imaging using

a Syngene InGenius gel documentation system (Syngene, UK). Image J, Fiji, was used to measure the band intensity. To enable gel-to-gel comparison, measurements were made relative to the density of the ‘Whole’ sample for each preparation.

2.2.5.4 ESI-IMS-MS

Protein desalting and mass analysis to confirm protein purity and mass was performed by LC-MS using a nanoACQUITY UPLC (Waters UK, Manchester, UK) interfaced to a Synapt G2S Q-IMT-TOF mass spectrometer (Waters UK, Manchester, UK) by Dr Rachel George in the Astbury Centre for Structural and Molecular Biology, Mass Spectrometry Facility.

All further mass spectrometry was carried out at the University of Leeds by Dr Patrick Knight and Dr Yong Xu using a Synapt high definition mass spectrometry (HDMS) quadrupole-time-of-flight mass spectrometer (Micromass UK Ltd., Waters Corp., Manchester, UK), equipped with a Triversa automated nano-electrospray ionisation (nESI) interface (Advion Biosciences, Ithaca, USA). To monitor ligand binding to $A\beta_{40}$, the peptide was dissolved in 20 mM ammonium acetate, pH 6.8 to form a 32 μM solution, and 10 mM stocks of compounds in 100 % DMSO were diluted into this to provide a final concentration of 160 μM . For analysis of these samples by nESI-MS, a sampling cone voltage of 30 V was used to preserve protein-ligand interactions, and a backing pressure of 1.6 mbar was applied. Data were acquired and processed by Dr Patrick Knight and Dr Yong Xu using MassLynx and Driftscope software. The m/z scale was calibrated with aqueous CsI cluster ions.

2.2.5.5 Nuclear Magnetic Resonance techniques

A. NMR Sample Preparation and Data Processing

For all NMR experiments, unless otherwise specified, the protein sample was composed of 50 μM ^{15}N -labelled, recombinant $A\beta_{40}$ (expressed and purified as described in Sections 2.2.2.1 and 2.2.2.3) from a 7 mg/ml stock in 10 mM NaOH, 20 mM sodium phosphate, 0.5 mM EDTA, 0.02 % (w/v) NaN_3 , 10 % D_2O , pH 7.4. Data were acquired at 4 °C using a 750 MHz spectrometer with an HCN triple resonance cryoprobe and Bruker

Advance III HD console. All raw NMR data were processed using nmrPipe [386] before further analysis, including peak fitting, using CCPNmr Analysis [387].

B. Optimisation of Sample Conditions for NMR Experiments

Analysis of the effects of pH, DMSO, temperature and buffer were carried out by obtaining $^1\text{H}^{15}\text{N}$ -HSQC experiments using a HN Enhanced Sensitivity HSQC pulse sequence [388, 389]. Spectra were recorded with 512 points in the indirect dimension (^{15}N) and 1024 points acquired in the direct dimension (^1H) and 2 scans. To monitor effects of pH, a single 50 μM $A\beta_{40}$ sample was prepared as described and split into four samples. The pH was decreased in three of the samples to pH 7.2, 7.0, and 6.8 using HCl. Samples were stored in ice before and after loading and acquisition in a 750 MHz spectrometer. To ensure no change in spectrum was caused by the increased time of incubation at 4 $^\circ\text{C}$ before acquisition, the first sample that was acquired (pH 7.4) was repeated at the end of all of the experiments to ensure no spectral alterations occurred. Each spectrum was processed in nmrPipe [386] and analysed using CCPNmr Analysis [387].

To monitor the effects of DMSO percentage on $A\beta_{40}$ a single, 450 μl sample was prepared as described at the start of Section 2.2.5.5, but excluding DMSO. A $^1\text{H}^{15}\text{N}$ -HSQC spectrum was acquired using a 750 MHz spectrometer with an HCN triple resonance cryoprobe and Bruker Advance III HD console. Spectra were recorded with 256 points in the indirect dimension (^{15}N) and 1024 points acquired in the direct dimension (^1H) and 8 scans. DMSO was titrated into the sample to 2 %, 4 %, 6 % and each acquired using the same acquisition procedure. Higher percentages caused deterioration in baseline shape evident using TopSpin.

Temperature effects on the $A\beta_{40}$ spectrum were monitored by acquiring multiple $^1\text{H}^{15}\text{N}$ -HSQC spectra for a single sample of $A\beta_{40}$. Spectra were recorded with 256 points in the indirect dimension (^{15}N) and 1024 points acquired in the direct dimension (^1H) and 8 scans. Acquisition was conducted at 37 $^\circ\text{C}$, 5 $^\circ\text{C}$, and then 37 $^\circ\text{C}$ again to ensure nother was no alteration to the sample over the course of the experiment.

Spectra quality of $A\beta_{40}$ in a solution of 50 mM ammonium acetate, pH 6.8, and in the buffer described at the out set of Section 2.2.5.5, were compared. For this, NMR lyophilised samples of $A\beta_{40}$ were solubilised directly in 50 mM ammonium acetate, pH 6.8, to create 50 μM peptide and a $^1\text{H}^{15}\text{N}$ -HSQC was acquired using a HN Enhanced

Sensitivity HSQC pulse sequence [388, 389]. Spectra were recorded with 256 points in the indirect dimension (^{15}N) and 1024 points acquired in the direct dimension (^1H) and 8 scans.

C. Backbone Assignment of $A\beta_{40}$

To assign the $A\beta_{40}$ $^1\text{H}^{15}\text{N}$ -HSQC spectrum, a triple labelled sample of $^1\text{H}^{13}\text{C}^{15}\text{N}$ - $A\beta_{40}$ was recombinantly expressed (Section 2.2.2.1), purified (Section 2.2.2.3), and prepared as described in Section 2.2.5.5A. Data were collected using a 950 MHz Bruker Ascend Aeon NMR spectrometer, Next-generation ultra-high field NMR magnet with actively shielded and with helium recycling technology, fitted with a TXO-cryoprobe (5mm) and operated using a Bruker Advance III HD console. The Bruker Best Trosy HNCA pulse sequence was used [389, 390]. The pulse sequence was run twice sequentially with 256 points in the indirect dimension (^{15}N), 128 points acquired in the direct dimension (^1H), and 1622 points for F3, the ^{13}C dimension. 16 scans were made for each experiment. The two spectra were combined using nmrPipe [386]. Assignment was conducted using CCPNmr Analysis [387] to identify sequential peaks. To validate assignments, published backbone assignments [367, 372, 391] were referenced.

D. Calculating $\Delta\delta\text{C}\alpha$ Chemical shifts

Using the $\delta^{13}\text{C}\alpha$ chemical shifts obtained from the Best Trosy HNCA experiments which was conducted for the assignment of the $A\beta_{40}$ peptide in the preceding section. The $\Delta\delta\text{C}\alpha$ Chemical shifts were automatically generated within CCPNmr Analysis. The software calculates the difference in measured $\delta\text{C}\alpha$ and the predicted chemical shift of the amide were it to be in a random coil [392, 393].

E. Measuring ^1HN Chemical Shift Temperature Coefficients

To calculate temperature coefficient values for each backbone amide in $A\beta_{40}$, a series of $^1\text{H}^{15}\text{N}$ -HSQC spectra were obtained using the 750 MHz spectrometer. Each spectrum was recorded with 256 points in the indirect dimension (^{15}N) and 1024 points acquired in the direct dimension (^1H) and 8 scans. $A\beta_{40}$ was expressed and purified as described in Sections 2.2.2.1 and 2.2.2.3, and a single sample was prepared in 20 mM sodium phosphate, pH 7.4, as described in Section 2.2.5.5A.

Data were acquired using a using a HN Enhanced Sensitivity HSQC pulse sequence [388, 389] at the following temperatures, in the presented sequence: 5 °C, 37 °C, 15 °C,

20 °C, 25 °C, 5 °C. Collection of spectra are 5 °C at the start and end of the experiment enabled spectral comparison to ensure peptide concentration was unaltered.

Spectra were processed using nmrPipe [386] and analysed using CCPNmr Analysis [387]. Spectra were referenced using water with the temperature correlation shift of -0.0119 ppm/° [394]. Peaks were picked on each spectrum in CCPNmr Analysis and the $\delta^{15\text{N}}$ positions were plotted, and linearly fit, for each residue. The gradient of the linear fit gives the $^1\text{H}^{\text{N}}$ chemical shift temperature coefficient for each residue.

F. Measurement of Residual Dipolar Couplings

To measure RDCs two $A\beta_{40}$ samples were prepared; an unaligned sample, and an aligned sample (whereby the peptide orientation is biased through interaction with an alignment medium). The unaligned sample was prepared as described in Section 2.2.5.5A. To prepare the aligned sample an alignment medium, bacteriophage Pf1, was used to bias the orientation of the $A\beta_{40}$ peptide ensemble.

Commercial bacteriophage Pf1 (NEB, UK) was supplied in 53 mg/ml in 10 mM potassium phosphate. In order to prepare the Pf1, it was precipitated out of the potassium phosphate using 1.25 M NaCl and centrifugation (1 hr at 30 °C, 14,100 xg in a microcentrifuge) to separate the soluble and insoluble fractions. The supernatant was discarded and the insoluble pellet washed three times in dH₂O before resuspension in 250 mM sodium phosphate, pH 7.4, over 2 hours at 4 °C. This was used to prepare a sample of $A\beta_{40}$ (Section 2.2.5.5A) with an addition of 26 mg/ml Pf1.

RDCs were measured using an in-phase-anti-phase (IPAP) amide HSQC experiment [395] set up with the aid of Dr Arnout Kalvada (University of Leeds) using the 750 MHz spectrometer (Section 2.2.5.5A). 640 points in the indirect dimension (^{15}N) and 1024 points in the direct dimension (^1H) were acquired 32 times (32 scans). Data were processed using nmrPipe [386] before further analysis using CCPNmr Analysis [387] for peak picking.

G. Measuring Transverse, R_2 , Relaxation Rates by NMR

R_2 rates were calculated from a set of T_2 relaxation experiments carried out at 750 MHz. Spectra were recorded with 160 points in the indirect dimension (^{15}N) and 2048 points acquired in the direct dimension (^1H) and 16 scans. R_2 is related to T_2 by the following:

$$R_2 = \frac{1}{T_2} \quad (2.1)$$

A sample of 50 μM $\text{A}\beta_{40}$ was prepared in 20 mM sodium phosphate according to Section 2.2.5.5A. Using this, a series of $^1\text{H}^{15}\text{N}$ -HSQC experiments - set up with the aid of Dr Arnout Kalvada (University of Leeds) using the 750 MHz spectrometer - were collected using a HN Enhanced Sensitivity HSQC pulse sequence [388, 389] with a range of time delays: 7.5, 14.9, 29.8, 44.7, 59.9, 74.5, 89.4, and 104.3 ms. Data were collected in a randomised order with two duplicate experiments (for delay times of 14.9 and 74.5 ms) for error estimation.

Peak intensities for each residue (measured using CCPNmr Analysis [387]) were plotted over time with error bars (which represent the error from the peak fitting). Data were fit to an exponential decay function to extract the R_2 as:

$$f(t) = Ae^{-t.R_2} \quad (2.2)$$

Where t is the delay time.

H. Measurement of heteronuclear Nuclear Overhauser Effects

Using a sample of 50 μM $\text{A}\beta_{40}$ in 20 mM sodium phosphate (fully described in Section 2.2.5.5A), heteronuclear NOE information was obtained. With the aid of Dr Arnout Kalvada (University of Leeds), two HSQC NOE experiments were set up. Data were acquired at 750 MHz at 5 °C using 148 points in the indirect dimension (^{15}N) and 248 points acquired in the direct dimension (^1H) and 48 scans. NMR data were processed using nmrPipe [386] and peak intensities were extracted, after peak fitting, using CCPNmr Analysis [387]. The ratio of the two intensities gives rise to the hetNOE value.

2.2.6 *In vivo* β -lactamase assay

Using the same transformation protocol as in Section 2.2.1.4 competent BL21(DE3) *E. coli* cells were made to take up an expression pMB1 plasmid (Figure 2.1a) containing the gene encoding either TEM1 β -lactamase with an hIAPP insert, $\text{A}\beta_{40/42}$ insert (βla -hIAPP or βla - $\text{A}\beta_{40/42}$ respectively or βla -construct generically) (Figure 2.1b) or

β -lactamase with a non-aggregative glycine/serine-rich linker (β la-linker) (Figure 2.1c). However, due to the different selection markers in the pMB1 plasmid and the pTXB1 plasmid 50 μ L of transformed cells were plated onto agar plates containing 10 μ g/mL tetracycline rather than agar containing ampicillin. Plates were incubated overnight at 37 °C. Single colonies were picked and used to inoculate 100 ml of LB containing 10 μ g/ml tetracycline overnight (37 °C, 200 rpm).

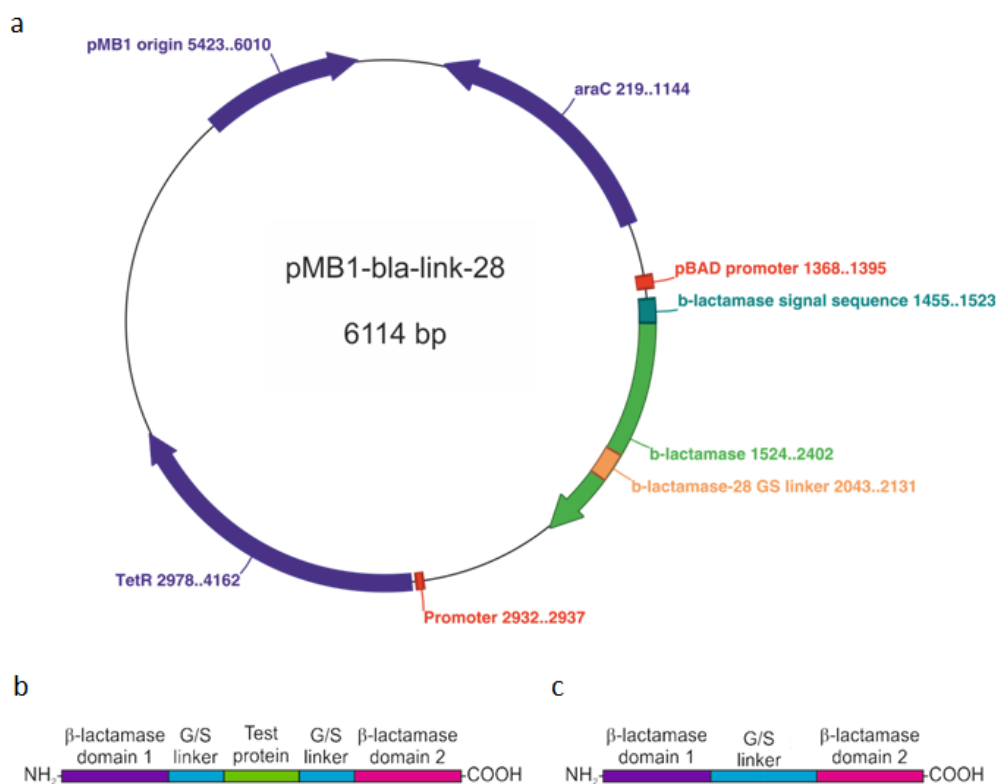


Figure 2.1: A map of the pMB1 plasmid encoding the β -lactamase construct. a) Map of the pMB1 plasmid into which the sequence encoding either β -lactamase with a Gly-Ser (non-aggregative) linker incorporated. The plasmid encodes for tetracycline resistance which is used for selection. The plasmid also encodes the L-arabinose operon which is transcribed when arabinose is present. Transcription of the inserted construct is under the control of the pBAD promoter which is part of the L-arabinose operon and is activated when arabinose is present, this arabinose is used to induce construct expression. Plasmid kindly provided by Professor J. Bardwell (Department of Biological Chemistry, University of Michigan, USA) and figure drawn by Dr J. Saunders, University of Leeds. b) Schematic of the β la-construct, where the ‘Test protein’ is either hIAPP, A β ₄₀ or A β ₄₂. Taken from [346]. c) Schematic of the β la-linker construct. Taken from [346].

The in vivo tripartite β -lactamase assay [337] was applied to study of the amyloid aggregation inhibition capacity of small molecule.

Two sterile 48 well plates (Greiner Bio-One, Germany) were prepared (one for β la-construct and one for β la-linker). Tetracycline (10 μ g/ml final concentration), filter sterilised arabinose (0.02 % (*w/v*) final concentration), and 200 μ M compound in 100 % DMSO (or pure DMSO) were added to 100 ml of sterile 1.5 % (*w/v*) agar cooled to 50 °C. 300 μ l was pipetted into each well in the first row of two 48-well plates. Filter sterilised ampicillin (10 mg/ml stock) was then added to the agar stock to give the required concentration for the next row of wells. This procedure was repeated until the plate contained 8 columns of agar containing increasing concentrations of ampicillin from 0 - 140 μ g/ml (20 μ g/ml increments) for β la-hIAPP. For the optimised assay for β la-A $\beta_{40/42}$ constructs the ampicillin increments were reduced to a lower range: 0, 2.5, 5, 10, 15, 20, 25, 30 μ g/ml in each column. Agar plates were left to set in a sterile environment.

The overnight cultures were used to inoculate fresh flasks of 100 ml sterile LB containing 10 μ g/ml tetracycline, which were incubated at 37 °C, 200 rpm. Once an OD₆₀₀ of 0.6 was reached the expression of β la-linker or β la-construct was induced by the addition of arabinose stock (final concentration of 0.02 % (*w/v*)). 392 μ l aliquots of the cultures were taken and mixed in 1.5 ml Eppendorf tubes with sterile LB and 10 mM stock compound stock to give a final volume of 400 μ l culture containing 200 μ M small molecule. These aliquots were incubated for 1 hour (37 °C, 200 rpm). Next, 100 μ l serial dilutions of 10-fold increments of these cells were made using filter sterilised 170 mM NaCl. 3 μ l of each cell dilution was spotted onto the prepared 48 well plates and incubated at 37 °C for 18 h. The maximal cell dilution at which growth can occur (MCD_{Growth}) was scored at each concentration of ampicillin on each plate. Scoring was done in a binary manner of either growth or no growth, where no growth is defined as agar wells with fewer than 10 colonies. To control for any intrinsic effect of small molecules on bacterial growth, the growth of *E. coli* BL21 (DE3) cells transformed with β la-linker in the absence or presence of small molecule was compared. Any effect on bacterial growth was subtracted from the β la-construct assay, at each concentration of ampicillin.

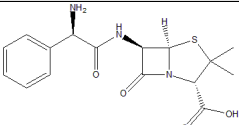
Chapter 3

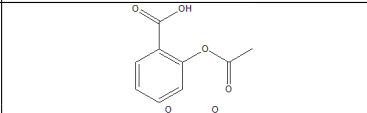
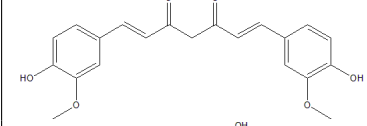
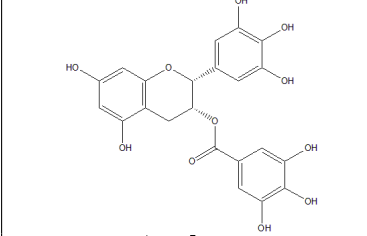
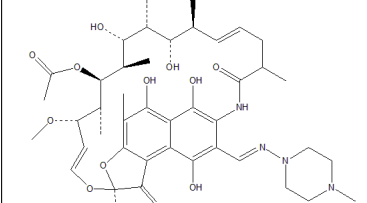
Creating a Toolbox of Methods to Study Small Molecule Effects on Amyloidogenic Peptides

3.1 Objectives

The primary aim of this project is to create a strategy, or toolbox of methods, which can be used to screen and investigate the effects of small compounds on IDP amyloid aggregation. This chapter describes the recombinant expression and purification of two IDPs, A β ₄₀ and hIAPP (Sections 3.2 and 3.3 respectively). It also outlines the rationale behind choosing each method which was incorporated into the toolbox (Section 3.4). Additionally, key optimisation steps and control experiments, which were conducted using published small molecules and antibiotics (Table 3.1 such as epigallocatechin-3-gallate (EGCG) and aspirin) are included in this chapter to demonstrate the effectiveness of each method (Section 3.5).

TABLE 3.1: Example small molecules used.

Compounds based on adapalene structure			
Name	Structure	Molecular formula	MW (Da)
Ampicillin		C ₁₆ H ₁₉ N ₃ O ₄ S	349

Continuation of Table 3.1			
Name	Structure	Molecular formula	MW (Da)
Aspirin		$C_9H_8O_4$	180
Curcumin		$C_{21}H_{20}O_6$	368
EGCG		$C_{22}H_{18}O_{11}$	458
Rifampicin		$C_{43}H_{58}N_4O_{12}$	822

$A\beta_{40}$ and hIAPP were chosen as exemplar amyloidogenic IDPs due to their roles in human diseases (Section 1.3.1) and because of the observed links between the two peptides which has been highlighted in the literature (Section 1.12). A key challenge in the production of amyloid peptides is preventing uncontrolled, irreversible aggregation during expression and purification. Published work shows that each of these peptides can be expressed and purified using contrasting approaches: $A\beta_{40}$ via an insoluble, inclusion body-based protocol [383], and hIAPP using a quadripartite construct method [384, 396] whereby the hIAPP sequence is surrounded by a solubility tag and additional domains for purification and post-translation modification steps.

3.2 Recombinant Expression and Purification of $A\beta_{40}$ from Insoluble Inclusion Bodies

The system used for producing $A\beta_{40}$ recombinantly in *E. coli* is summarised in the schematic in Figure 3.1. The $A\beta_{40}$ produced is in a close-to-native state as there are no post-translational modifications on human $A\beta_{40}$. However, there is an N-terminal

methionine (Met0) which has been shown not to affect fibril formation kinetics or fibril morphology [383]. In this chapter Met- $A\beta_{40}$ will be referred to as $A\beta_{40}$.

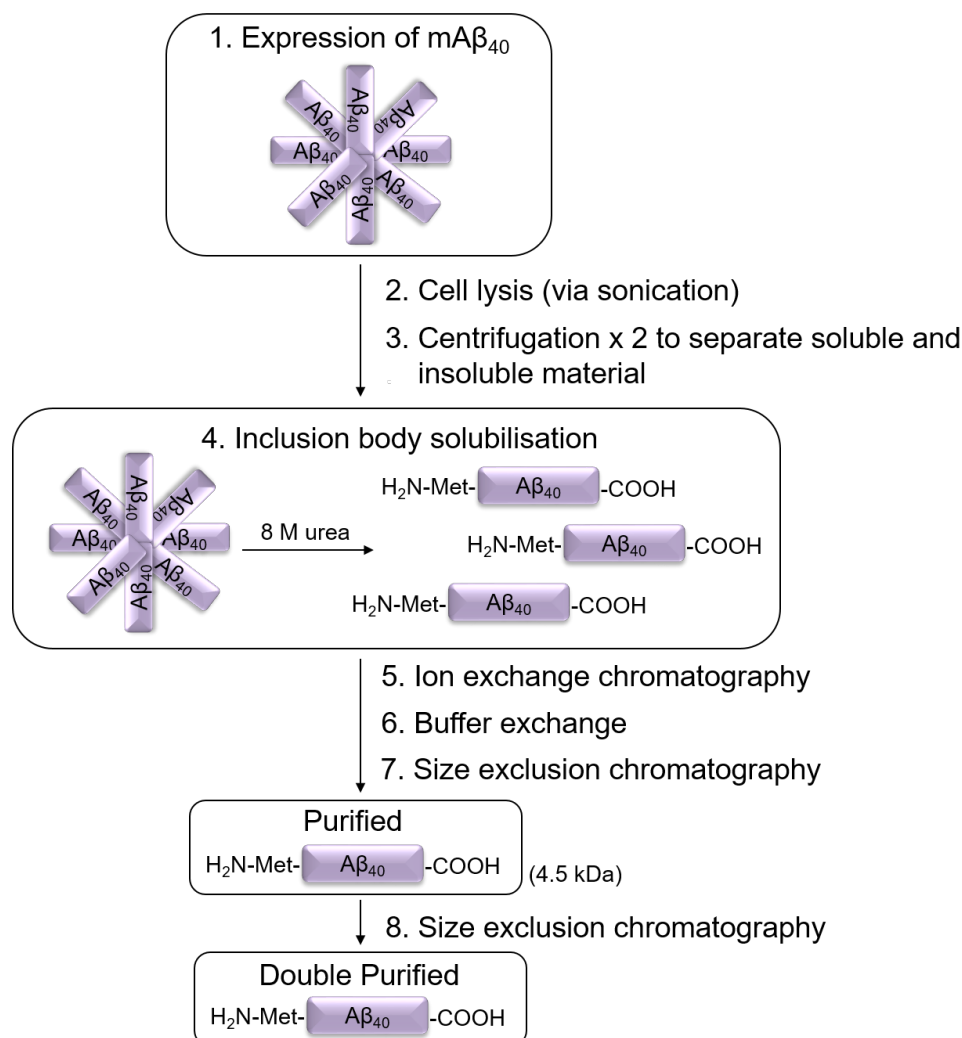


Figure 3.1: Expression and purification protocol for $A\beta_{40}$.
A schematic of steps followed to express and purify $A\beta_{40}$ (purple) from inclusion bodies (star-shaped arrangement).

$A\beta_{40}$ is expressed using *E. coli* transformed with a pETSAC plasmid (Section 2.2.1.4) which encoded $A\beta_{40}$ under the control of the T7 promoter. $A\beta_{40}$ expression was induced by addition of isopropyl β -D-1-thiogalactopyranoside (IPTG) as described in Section 2.2.2.1 leading to the formation of $A\beta_{40}$ inclusion bodies, Figure 3.1, (step 1). Cells were lysed (step 2) and the insoluble and soluble components separated by centrifugation (step 3). The insoluble inclusion bodies were solubilised using 8 M urea (step 4). To purify $A\beta_{40}$, batch ion exchange chromatography was conducted using Q-Sepharose resin (step 5), followed by buffer exchange (step 6), and either one or two size exclusion chromatography steps (steps 7 and 8).

Although the method described in detail in Section 2.2.2.1 was well established, a few optimisation steps were investigated for A β ₄₀ expression and the purification thereof.

3.2.1 Optimisation of Expression Conditions of A β ₄₀ to Maximise Yield

Initially the expression conditions for A β ₄₀ were varied to ensure efficient protein production. Growth medium and culture aeration were altered to find the highest yielding combination of conditions. The optical density for each culture variation was monitored, Figure 3.2, and the typical expression level for A β ₄₀ was shown via SDS-PAGE.

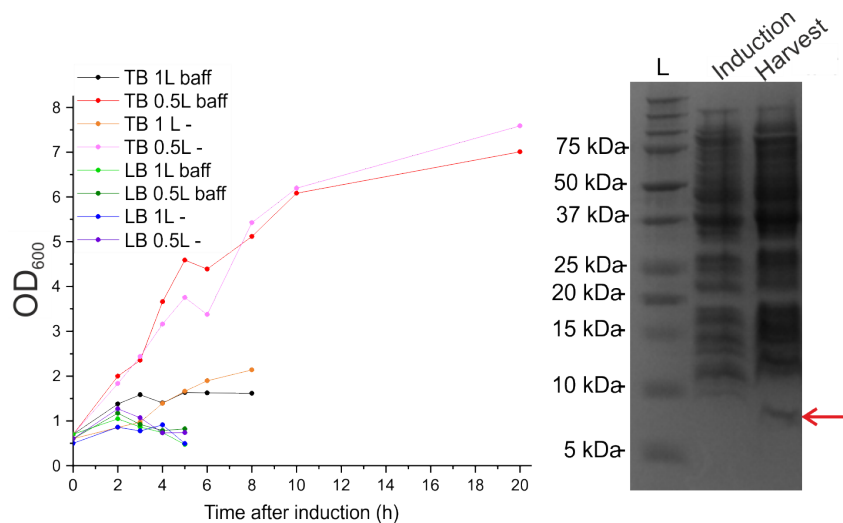


Figure 3.2: Expression of A β ₄₀ in various cultures.

Left: OD₆₀₀ of cultures of A β ₄₀ grown in either 0.5 L or 1 L of either LB or TB media, in baffled ‘baff’, or unbaffled, ‘-’, flasks. Right: Typical expression of A β ₄₀ (red arrow) is shown by SDS-PAGE at the time of induction and harvest. L = ladder.

From the plot, higher cell densities are attainable when using TB medium. This was improved further with a culture volume of 0.5 L rather than 1 L. This indicated that reducing the volume was more effective at improving the aeration of the growth culture than use of baffled flasks. A higher cell density meant there were more cells present which could express the A β ₄₀ peptide. However, it was also important to check the expression using SDS-PAGE as cell expression levels may alter when the cells are in high-density solutions. Similar expression levels were observed at the harvest time for each culture (data not shown), typical of that shown in Figure 3.2. Thus, the more cells in the solution, the higher the protein yield after the overnight incubation period.

As A β ₄₀ would eventually be required for NMR studies, it was important to ensure expression was possible in M9 minimal medium. In contrast to growth in LB media, the

growth period after induction with IPTG is incubated at 15 °C overnight rather than 37 °C for 2-4 hours. The results shown in Figure 3.3 show that a comparable yield can be obtained using ^{15}N - and $^{13}\text{C}^{15}\text{N}$ -labelled M9 media.

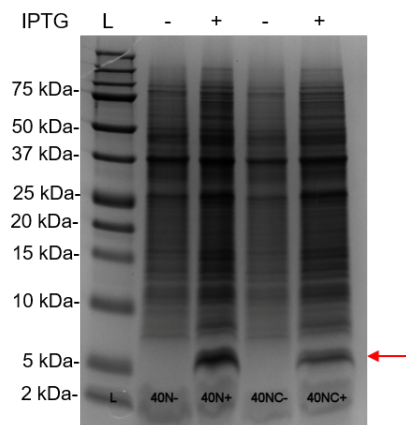


Figure 3.3: $A\beta_{40}$ can be expressed in labelled M9 medium.

An SDS-PAGE gel showing the expression levels of $A\beta_{40}$ (red arrow) in ^{15}N - (40N) or $^{15}\text{N}^{13}\text{C}$ -labelled (40NC) M9 media, before (-) and after(+), induction with IPTG.

For this work, the expression of unlabelled $A\beta_{40}$ was conducted in 0.5 L cultures of TB medium grown in baffled flasks. For isotopically-labelled samples (^{15}N - or $^{13}\text{C}^{15}\text{N}$ - $A\beta_{40}$), 0.5 L cultures of M9 medium were grown in baffled flasks.

3.2.2 Optimisation of Ion Exchange Chromatography in $A\beta_{40}$ Purification

High levels of $A\beta_{40}$ expression in inclusion bodies was essential as a starting material for the purification process. Despite reports of obtaining 10-20 mg/L yields using this purification method [383], the $A\beta_{40}$ yield obtained was 2-4 mg/L. To improve this the affinity purification step was probed and optimised.

Figure 3.4 shows a typical SDS-PAGE gel which tracks the purification throughout the steps in Figure 3.1. The gel shows some loss of $A\beta_{40}$ in the second supernatant fraction after two centrifugal separations, (see Section 2.2.2.3, and Figure 3.1 step 3). This was discarded as most of the $A\beta_{40}$ was retained in the inclusion body solubilisation solution (Figure 3.4, lane IC). This was loaded onto Q-Sepharose resin which binds to $A\beta_{40}$ through electrostatically-mediated interactions. Good binding was evident from the

decreased intensity of the $A\beta_{40}$ band in the flow through fraction (Figure 3.4, lane FT). Next, the resin was washed twice (Figure 3.4, lanes W1 and W2) to remove unbound protein contaminants. $A\beta_{40}$ was eluted from the resin in five batches of 125 mM NaCl, then the sixth fraction of 250 mM (Figure 3.4, lanes E1, E4, and E6*). After elution of $A\beta_{40}$, a 1 M NaCl solution was applied and collected to reveal any protein left on the resin (Figure 3.4, lane HS).

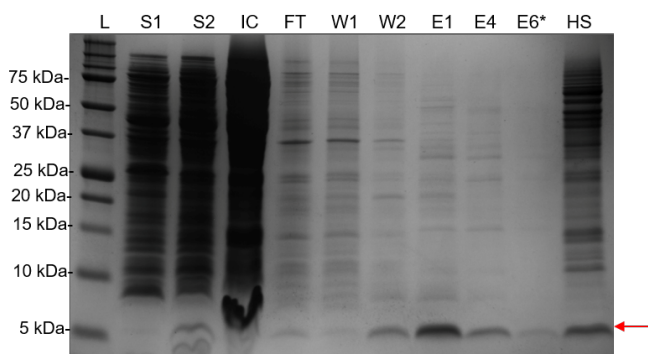


Figure 3.4: SDS-PAGE gel to show the protein profile at each stage in the $A\beta_{40}$ purification procedure.

$A\beta_{40}$ is indicated by the red arrow. Lanes are as follows: L=ladder, S1-supernatant after the first centrifugation step, S2=supernatant after the second centrifugation step, IC=inclusion body solubilisation solution, FT=flow through when loading the chitin resin, W1 and W2=wash fractions, E1-E6=elution fractions, HS=high salt-containing column wash. Gels were loaded as described in Section 2.2.3 whereby S1, S2, and IC are loaded with half as much sample as other lanes.

To optimise yield, the ‘flow through’ and ‘Wash 1’ fractions were collected and pooled. Re-application of these fractions to fresh Q-Sepharose resin and repetition of the wash steps and three elution volumes, Figure 3.5, increased the total $A\beta_{40}$ yield (of fully purified $A\beta_{40}$) to 5-7 mg/L.

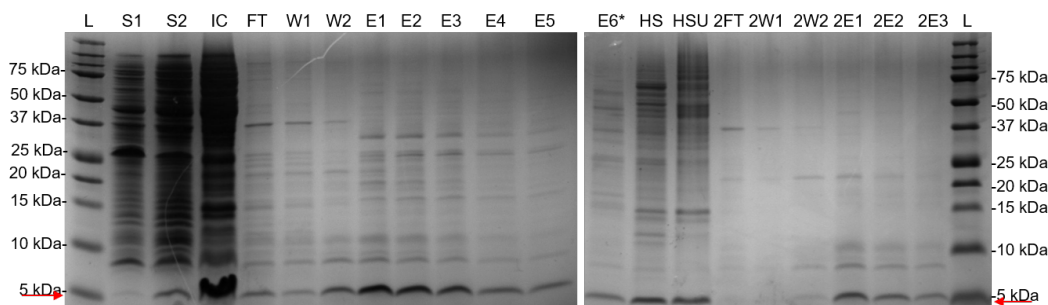


Figure 3.5: SDS-PAGE gel to show the protein profile at each stage in the optimised $A\beta_{40}$ purification procedure.

$A\beta_{40}$ indicated by red arrows. Lanes labelled as in Figure 3.4, additionally HSU=high salt and urea containing column wash. Samples collected on the second round of affinity chromatography are preceded with a ‘2’

Other optimisation steps were tested including increasing the number of elution fractions collected, and including fraction S2 (the supernatant after the second centrifugal separation) in the loading of the Q-Sepharose resin. As more elution fractions were collected, $A\beta_{40}$ was still present, however, the yield of protein in these latter fractions was low and caused the overall collection volume to increase. Combined, these decreased the time efficiency of the purification due to collection time and time for lyophilisation of the increased volume. Inclusion of S2 for resin loading caused severe reduction in the column flow rate, even under vacuum. This was possibly due to the nearly two-fold increase in non-target proteins in the resin mixture. Based on these findings it was decided not to include either of these amendments in the protocol.

To increase the time efficiency of the affinity ion exchange chromatography purification step, trials to improve the flow rate of liquid through the Q-Sepharose resin were conducted. The recommended method is to use a light vacuum created by running water through a T-tap attached to a büchner funnel flask to pull the unbound proteins in solution through the Q-Sepharose resin. Utilisation of a stronger force was tested using a vacuum pump, but this disrupted the resin- $A\beta_{40}$ interaction and decreased yield to a negligible level. Other flow optimisations could be tested such as use of a peristaltic pump, or controlled flow in an Äkta system, however, preliminary trials of these were not promising and thus not pursued in this work.

No further optimisation steps were taken to improve the published protocol. Thus the final improved purification yield of $A\beta_{40}$ was 5-7 mg/L.

3.2.3 Completion of A β ₄₀ purification

Subsequent to ion exchange chromatography, the A β ₄₀-containing solution undergoes buffer exchange into 50 mM ammonium bicarbonate to remove non-volatile salts (e.g. NaCl) and residual urea before lyophilisation. The final steps in the purification protocol was size-exclusion chromatography, Figure 3.6a. A β ₄₀ elutes as a single, resolved peak between 95–110 minutes (28–33 ml). Mass spectrometry (Figure 3.6c) confirms the production and purification of A β ₄₀ (sequence shown in Figure 3.6d).

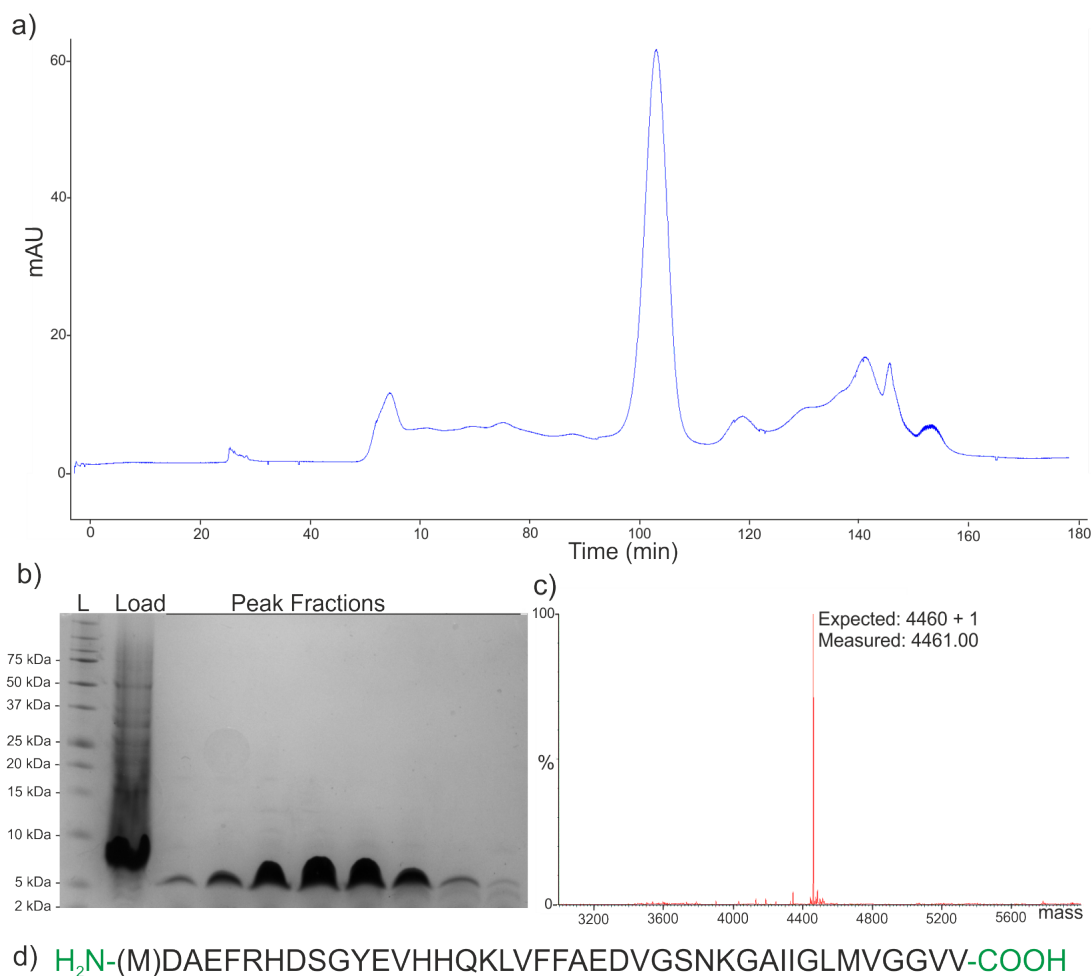


Figure 3.6: Confirmation of A β ₄₀ purification.

- a) Size Exclusion Chromatogram showing A β ₄₀ eluted as a single peak between 95–110 mins, with a flow rate of 0.3 ml/min. b) SDS-PAGE showing the proteins present in the sample before SEC (load) and in the collected peak seen in a (peak fractions). c) Mass spectrum to confirm peptide mass and infer identity as A β ₄₀. d) Amino acid sequence of A β ₄₀ purified with N- and C- termini highlighted in green.

3.2.4 Summary of A β ₄₀ Production

A β ₄₀ was successfully expressed and purified. Incorporation of the optimisation strategies discussed in this section led to an approximate 150 % increase in yield of A β ₄₀. However, the batch step of the purification process was still laborious and the time:yield ratio remained sub-optimal. Additionally the requirement to run two SEC steps was shown to be necessary for reproducibility in measuring aggregation kinetics (Section 3.5.1.3) but decreased protein yield by approximately 40 %. For other assays, the second SEC run was not necessary which was especially important for isotopically-labelled samples for NMR.

Recently a new approach to purifying A β ₄₀ was published which utilised RP-HPLC as the final step [397]. This method was modified in house (Dr M. Walko, University of Leeds) leading to nearly 10 mg/L peptide yield. This procedure is now being used routinely, but was not adopted here as it was published only recently in 2018 [397].

3.3 Production of IAPP for *in vitro* Aggregation Studies

The method for expression and purification of hIAPP used in this project was based on the protocol originally published by Williamson *et al.* [384]. This paper presents a method to express hIAPP as part of a quadripartite construct Figure 3.7a in *E. coli*. The plasmid containing the expression construct, which was used in this thesis, was kindly provided by Prof. A. Miranker at Yale University. Intrinsically disordered, wild-type hIAPP has two important post-translational, structural features: a disulfide bridge between Cysteines 2 and 7, and an amidated C-terminal (Figure 3.7b). These are both required for full biological activity when forming amyloid fibrils and for normal functions [229].

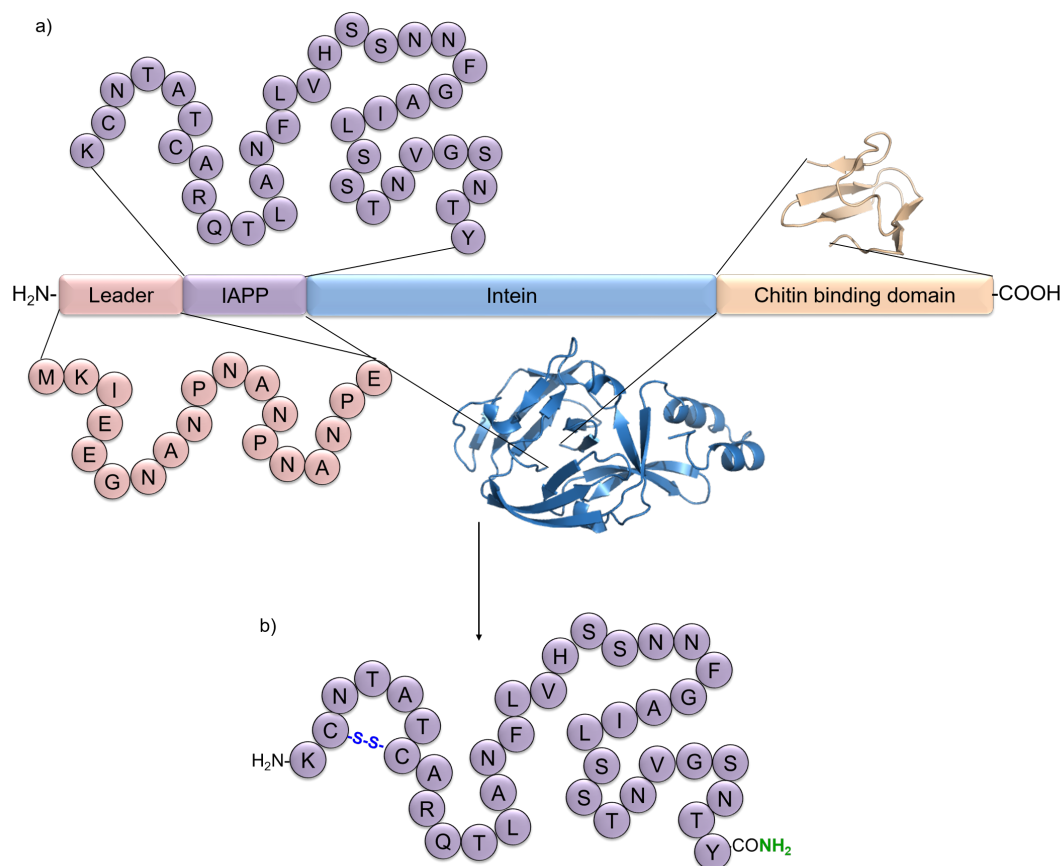


Figure 3.7: Anatomy of the quadripartite construct for the expression of hIAPP.

a) The schematic shows the quadripartite construct; leader sequence (pink), hIAPP sequence (purple), intein domain (blue), and chitin binding domain (orange). b) post translational modification to the hIAPP sequence. Amino acids are represented with circles, the Cys2-7 disulfide bridge is marked in blue and the amidated C-terminus in green.

The construct had already been designed to increase the solubility of hIAPP through the addition of an N-terminal leader domain. This leader domain contained codons which were highly expressed in *E. coli* (MKIEEG) [384] and a (NANP)₃ domain which had previously been used to increase the solubility of A β ₄₂ [398]. This 2 kDa leader sequence (Figure 3.7a) contains multiple proline residues which interfere with the formation of β -sheets [399], which are vital for fibril morphology and close packing of peptides. A Glutamic Acid residue was included at the C-terminus of the leader sequence, immediately adjacent to the N-terminal of the hIAPP codon sequence, to enable detachment of the leader from hIAPP using a V8 protease. V8 protease cleaves after acidic residues

(Aspartic Acid or Glutamic Acid) without leaving any additional residues N-terminal to hIAPP.

On the C-terminal side of hIAPP, an Mxe intein was incorporated as the third section of the quadripartite construct. An intein is a self-cleaving sequence; for this construct, a mini-intein of 198 residues from *Mycobacterium xenopi*gyrA has been used. The sequence included in the vector can undergo a thiol-mediated cleavage at its N-terminal, induced by a thiol reagent [400]. Cottingham *et al.* [401] showed that the addition of ammonium bicarbonate in the reducing, ‘intein cleavage buffer’, would result in the substitution of an amide group rather than a hydroxyl group at the point of cleavage, thus creating the amidated C-terminus of hIAPP. Finally a *Bacillus circulans* chitin binding domain is encoded at the C-terminal of the quadripartite construct to enable affinity chromatography in the purification process (Section 2.2.2.5).

Since the expression system uses *E. coli* (Section 2.2.2.4), the post-translational modifications must be incorporated in the multi-step purification process after expression, Figure 3.8. These post-translational modifications - and aggregation propensity of the peptide - has meant that hIAPP has been challenging to produce recombinantly and synthetically.

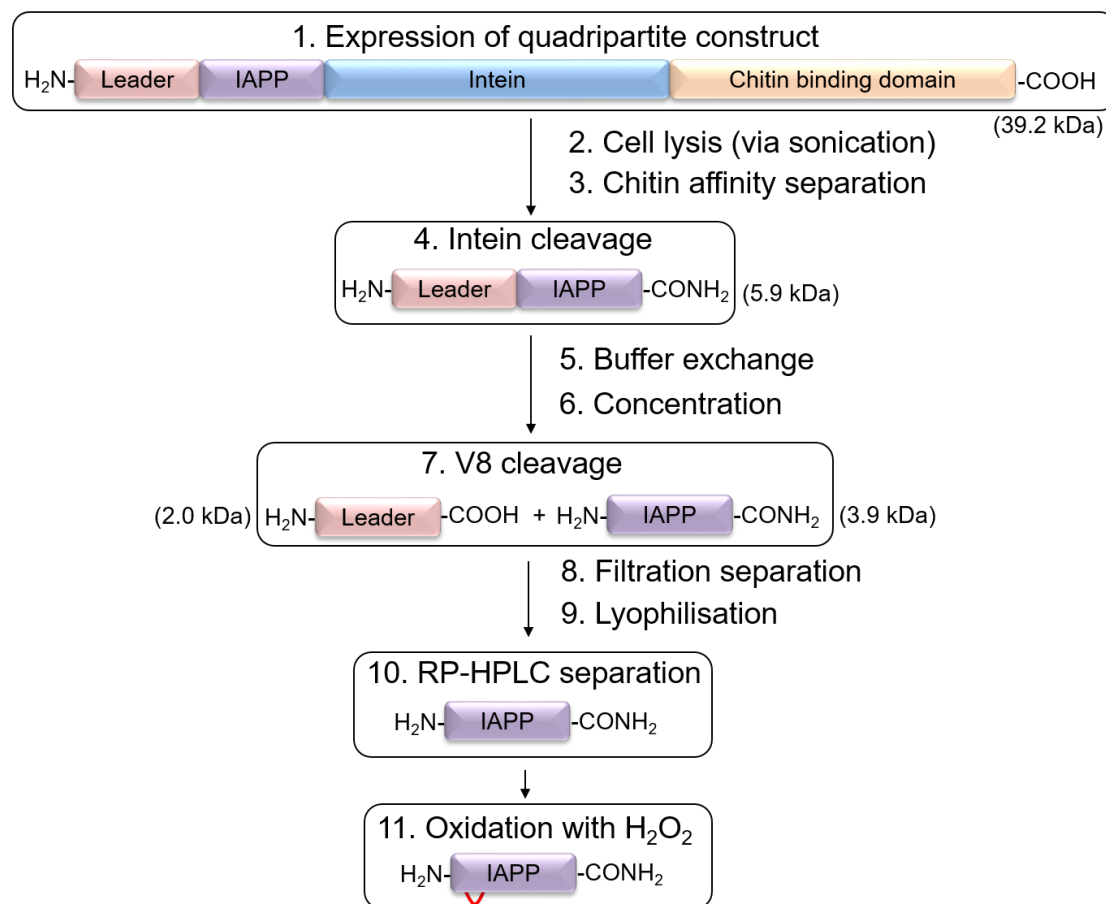


Figure 3.8: Workflow of the expression and purification of hIAPP.

Steps in the production protocol are summarised in the flow diagram and changes to the expression construct highlighted. The disulfide bridge between cys2-7 is represented in red.

After expression of the soluble construct, Figure 3.8 (step1), cells were lysed and the construct was purified from the cell lysate using centrifugation (step 2) followed by a chitin affinity step (step 3). Whilst on the chitin resin, the bound construct is incubated at 4 °C in the presence of 2 M ammonium bicarbonate and 0.1 M DTT to induce the intein cleavage reaction (step 4). The intein cleavage generates an amidated C-terminus on hIAPP and released the leader-hIAPP part of the construct leaving the chitin-binding domain and intein attached to the chitin resin. The amidated two-part construct (leader and hIAPP) was eluted from the column and undergoes filtration to remove any large species (such as low levels of co-eluted CBD-intein construct) and buffer exchange where salts were removed and the construct was exposed to a redox system, allowing the formation of the Cys2-Cys7 disulfide bridge in hIAPP (step 5).

The sample volume was reduced (step 6) in preparation for V8 cleavage. The leader sequence was then removed from hIAPP using the *Staphylococcus aureus* V8 protease (step 7) and then the solution was filtered again to remove the 29 kDa V8 protease from the 3.9 kDa hIAPP and 2.0 kDa leader sequence (step 8). The hIAPP and leader solution was lyophilised (step 9). The dried material was then suspended in 100 % DMSO and HPLC was used to separate the leader from hIAPP (step 10). Finally the disulfide bridge must be formed by an oxidising environment (step 11).

Optimisation of the expression and purification of hIAPP was necessary to obtain a high yield of the peptide required for this project. The original protocol was expected to yield 2.0 mg/L of hIAPP [384]. In 2015, an optimised version of the expression and purification was published [396]. This reported an improved yield of 2.5-3.0 mg/L of purified native hIAPP when recombinantly-expressed in 1 L of LB medium. This section describes the steps which were taken towards optimising the expression and purification of hIAPP for use in *in vitro* biophysical investigation into the mechanism of how IDPs form amyloid.

3.3.1 Recombinant Expression of hIAPP as a Soluble Quadripartite Construct

hIAPP was expressed recombinantly using *E. coli* which was transformed (Section 2.2.1.4) with a construct-encoding, pTXB1 plasmid, shown in Figure 3.9. This plasmid was kindly provided by Prof. A. Miranker (University of Yale, USA) [384].

In order to increase the yield of hIAPP obtained recombinantly, attempts were made to increase the over-expression of the four-part construct. This was done through optimisation of cell strain, growth medium, culture aeration, and length of incubation after induction.

3.3.1.1 Variation of Cell strain to Increase Peptide Expression Yield

Expression of the quadripartite construct in *E. coli* BL21(DE3) cells was controlled under a T7 promoter which can be manipulated simply using IPTG to induce a high level of protein expression [402]. The T7 promoter is commonly referred to as a 'leaky promoter' meaning that there is a low level of basal expression of the inserted construct

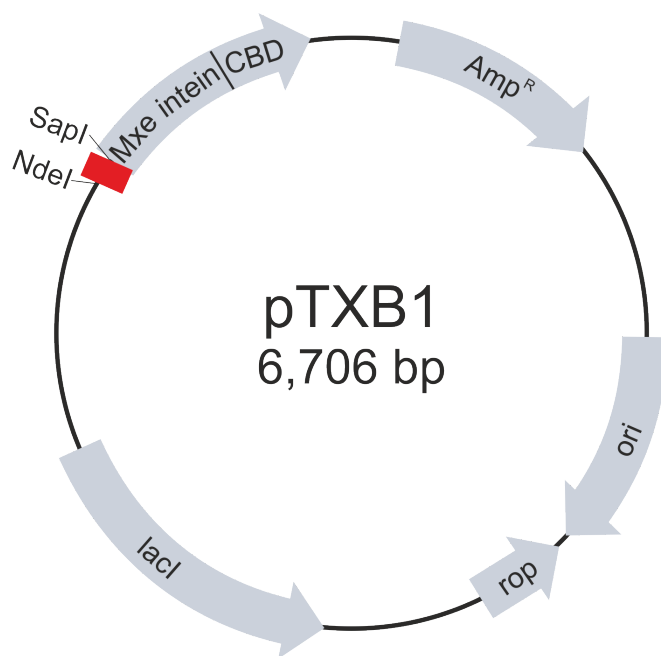


Figure 3.9: The pTXB1 plasmid encoding the hIAPP-containing quadripartite construct.

Bases encoding the leader and IAPP sequences were incorporated at the Multiple Cloning Site (red) using the NdeI and SapI restriction sites immediately 5' to the gene encoding the intein and the chitin binding domain (CBD). LacI, the Lac repressor is encoded and expressed to minimise basal expression at the T7 promoter site. There is a rop (Repressor of Primer) for regulation of plasmid copy number and an M13 phage origin of replication. The plasmid also has ampicillin resistance as a selection marker. The plasmid was kindly obtained from Prof. A. Miranker (University of Yale, USA) [384].

prior to IPTG addition. Other cell strains prevent 'leaky' expression, for example, *E. coli* BL21(DE3) pLysS, contain additional plasmids encoding phage T7 lysozyme, which is a strong repressor of the T7 promoter [403].

For toxic or bulky proteins, early protein production may hinder cell growth or health, leading to lower protein yields. Promoter leakage can be especially problematic if there are long time periods between culture inoculation and induction. Promoter leakage is commonly an issue for protein expression in minimal media where, due to the reduced availability of nutrients, growth rates are slower and thus the time required to reach optimal cell density is often extended.

For this project hIAPP needed to be prepared by a suitable method compatible with isotopic labelling. In order to achieve this, minimal medium must be used. To ascertain whether toxicity due to promoter leakage could be an issue for the quadripartite

construct a comparison of protein expression in BL21(DE3) cells and BL21(DE3) pLysS cells was performed.

Firstly cell transformations of BL21(DE3) and BL21(DE3) pLysS cells were conducted according to Section 2.2.1.4 whereby construct-encoding, pTXB1 plasmids were inserted into competent cells (Section 2.2.1.2) of each cell type via a heat-shock procedure (Section 2.2.1.4). BL21(DE3) and BL21(DE3) pLysS cells were plated onto solid agar containing 100 $\mu\text{g/ml}$ ampicillin/carbenicillin or 100 $\mu\text{g/ml}$ ampicillin/carbenicillin with 25 $\mu\text{g/ml}$ chloramphenicol respectively.

After plate incubation overnight at 37 °C, colony growth was observed and single colonies were selected and used to inoculate starter cultures of 100 ml LB medium containing the antibiotics as above. These cultures were incubated for 16 h at 37 °C with 200 rpm shaking for aeration. Next, 4 ml of the small cultures were transferred into 1 L of LB medium under the same conditions (Section 2.2.2.4). After 3-5 h the OD₆₀₀ reached 0.6 and 1 ml of 1 M IPTG was added in order to induce expression of the construct. Figure 3.10 shows the SDS-PAGE gels comparing the expression of the construct in BL21(DE3) and BL21(DE3)pLysS *E. coli* strains before and after induction.

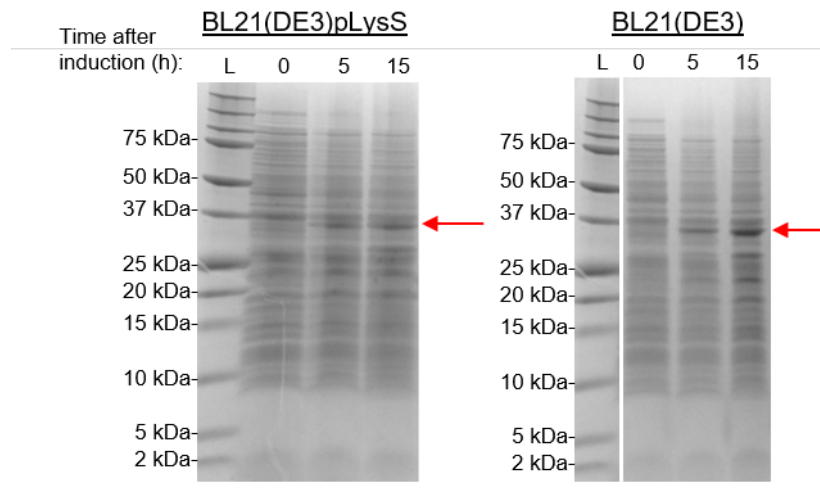


Figure 3.10: Expression of the quadripartite construct in different *E. coli* strains. SDS-PAGE showing the expression of the quadripartite construct in BL21(DE3)pLysS or BL21(DE3) cells grown in 1 L of LB medium in 2 L, non-baffled flasks. The final OD₆₀₀ for BL21(DE3)pLysS culture was 1.88 after 15 h, and 1.69 for BL21(DE3) cells.

Samples were taken at 0, 5, and 15 h after induction with IPTG and run on an SDS-PAGE gel. The red arrow highlights the quadripartite construct. L = ladder.

By comparing expression in BL21(DE3) pLysS cells and BL21(DE3) cells it was concluded that BL21(DE3)pLysS cells did not express the quadripartite construct as well as BL21(DE3) cells. Thus further optimisation of expression conditions was conducted in BL21(DE3) cells.

3.3.1.2 Optimisation of Growth Conditions for Efficient Peptide Production

To maximise yield, expression trials were conducted to find optimal conditions for cell growth and construct expression. Three variables were investigated; Type of medium (LB or M9), aeration by two methods (flask baffling and media volume), and growth time, Figure 3.11 and Table 3.2. Samples were prepared similarly to Section 3.3.1.1.

Gel	Volume (L)	Baffled flask?	Medium	Final OD ₆₀₀ (AU)
a	1	No	LB	1.69
b	0.5	No	LB	1.70
c	0.5	Yes	M9	2.27
d	0.5	Yes	LB	1.60
e	1	Yes	LB	1.57
f	0.5	No	M9	1.74
g	1	Yes	M9	1.79
h	1	No	M9	1.39

Table 3.2: hIAPP expression conditions and final OD₆₀₀.

Figure 3.11 shows the expression gels obtained when all the growth conditions in Table 3.2 were tested. In light of all the expression conditions investigated, optimal protein expression was performed using 1 L cultures of M9 media in baffled flasks.

To test whether 16 h was the optimum time for expression after induction three independent time trials were conducted. Cell cultures were left for up to 28 h to express the quadripartite construct (Figure 3.12). From the SDS-PAGE gels, maximal levels of expression were reached after approximately 15 h after induction of protein expression and maintained up to 28 h. The four-part construct (39.2 kDa) runs below the 37 kDa MW marker at approximately 30 kDa. Below the four-part construct there is a thinner band which likely represents the intein-CBD fragment only. This is created by the intein cleavage reaction occurring within the cells during the expression period. The leader-IAPP fragment is not visualised on the SDS-PAGE gel due to its poor ability to bind to the gel stains including coomassie blue [404] and references therein.

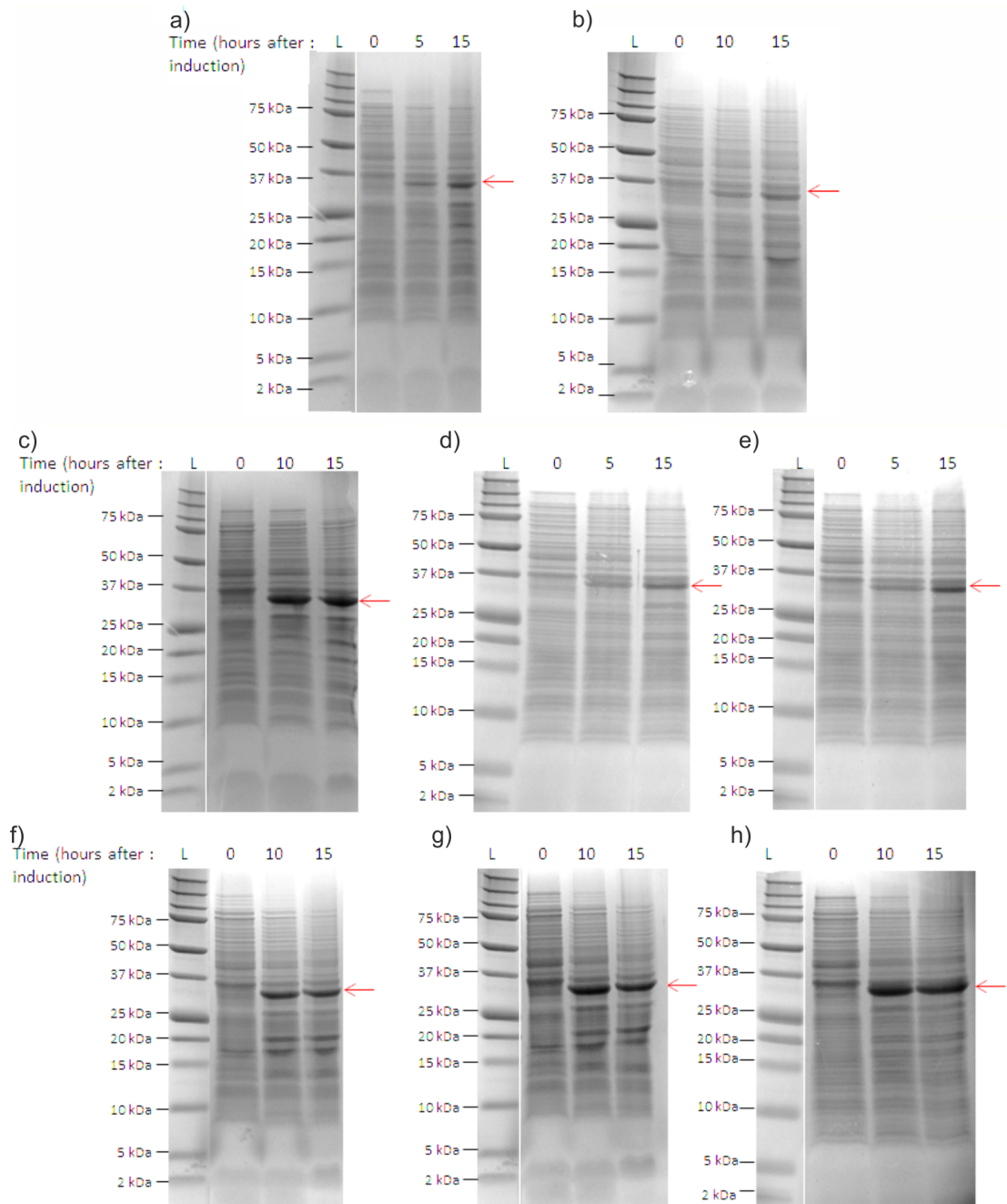


Figure 3.11: SDS-PAGE showing the effect of culture conditions on the expression of the quadripartite construct.

Samples were taken at 0, 5 or 10, and 15 h after induction with IPTG and run on an SDS-PAGE gel. The culture conditions and final OD_{600} are listed in Table 3.2. The red arrows highlights the quadripartite construct in each gel image. L = ladder.

An extension to the expression trials conducted would have been to test the effect of incubation temperature for protein expression. Caution to keep temperatures low in order to reduce protein degradation must be balanced with the need for the temperature to be

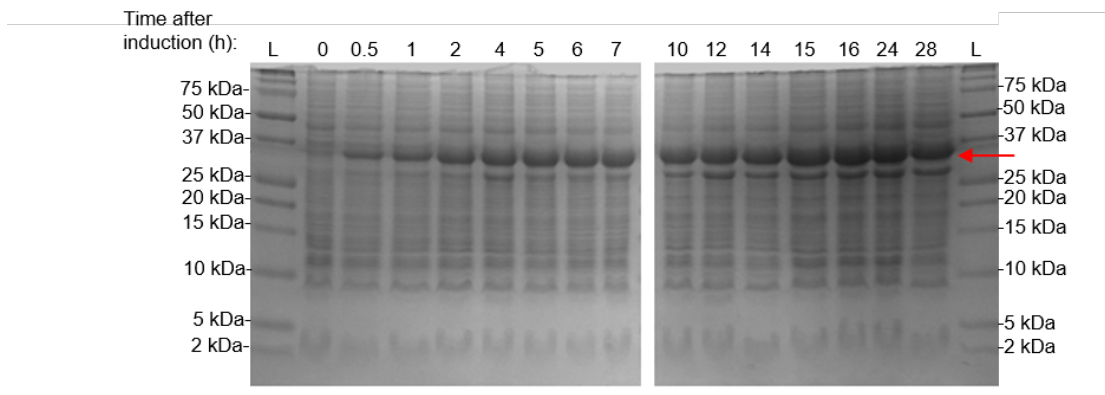


Figure 3.12: Time course of the expression of the quadripartite construct. Expression of the quadripartite construct (red arrow) was induced at $OD_{600} = 0.6$ by IPTG addition. Cultures were grown in 1 L of M9 in non-baffled flasks at 15 °C for the time shown. Samples were normalised to the optical density. L = ladder

high enough for protein expression and cell division to occur at an efficient rate. Preliminary investigations suggested that increasing the temperature to 37 °C after induction would produce yields of the quadripartite construct after 2 h that were comparable to the yields of the construct after approximately 8 hours when incubated at 15 °C (data not shown). The recommended temperature of 15 °C for the post-induction period [384] was used for protein expression in this project and cells were harvested after 15-20 h by centrifugation for 20 min at 5000 rpm to form a cell pellet which was stored at -20 °C.

3.3.2 Multi-step Purification of IAPP from the Soluble Quadripartite Construct

Once the quadripartite construct was reliably expressed to a significant yield the construct had to be purified and then the hIAPP fragment isolated. The multi-step purification method used is described in this subsection and optimisation steps tested and incorporated are discussed. Figure 3.8 summarised the purification protocol which is described in detail in Section 2.2.2.5.

Firstly cells were resuspended by stirring the cell pellet in 20 ml of 20 mM HEPES, 0.1 mM EDTA, 2 M urea, 50 mM NaCl, pH 8, at 4 °C. PMSF and DNase1 were added to prevent protein degradation. Once a homogeneous solution was obtained cells were lysed using sonication on ice (Section 2.2.2.4).

3.3.2.1 Optimising Flows for Chitin Affinity Purification

To separate the quadripartite construct from the cells two methods were used. Centrifugation was used to separate insoluble and soluble cell material and then the soluble fraction was applied to a chitin-resin column. The chitin resin interacted with the chitin-binding domain at the C-terminal of the quadripartite structure whereas other non-target proteins and cell components, flowed through the column.

Purification through the use of affinity tags is widely used as an efficient method to extract a protein of interest from a highly heterogeneous protein solution. For this protocol, chitin interaction with a chitin-binding domain was exploited. Chitin is a fibrous polysaccharide, often found in the exoskeletons of arthropods, which interacts with the aromatic residues in protein chitin-binding domains [405].

An open column was packed with 20 ml of chitin resin and the mixture of soluble proteins was loaded and washed using flows under gravitational force. This was a time intensive step which was optimised in various ways: separation of the soluble and insoluble protein fractions by more forceful centrifugation (Section 3.3.2.1A); increasing column width from 180 to 280 mm (but maintaining the column volume of 20 ml); alternatives to loading using gravity (peristaltic pump, and ÄKTA system, Section 3.3.2.1B).

Finally the recommended column washing procedure was optimised (Section 3.3.2.1C).

A. Preparing Harvested Cells for Application to the Chitin Affinity Column

The frozen pellet of cells was suspended in 20 ml of Equilibrium buffer and both PMSF and DNaseI were added (Section 2.2.2.5). The sample was left for 1 h with gentle agitation at 4 °C until a homogeneous solution was obtained. Cells were lysed (Figure 3.8, step 2) using a cell disrupter (Constant Systems, UK) at 30 kpsi and the lysate was subject to a centrifugation step to separate insoluble cell material from the soluble proteins. In the published protocol, this centrifugation step was performed at 5000 rpm (3220 xg). However, it was found that more stringent separation of the soluble and insoluble fractions could be achieved by increasing the force of the centrifugation step to 20,000 rpm (48384 xg) using a fixed angle Beckman JA25.50 rotor. This was important to enable more efficient loading of the supernatant (which contained the quadripartite construct) onto the chitin column.

B. Flow in the Chitin Affinity Column

Originally column flow rates were determined by gravity only. However, this was time intensive especially as there were multiple steps which required column flow: to load the supernatant, to wash off unbound proteins/components, and eventually to elute the amidated - and therefore cleaved - leader-hIAPP-CONH₂ construct. A more time-efficient method was investigated for the chitin affinity separation procedure (Figure 3.8, step 3).

Of the optimisation methods trialled the most successful was the alteration in the preparation of the soluble fraction (Section 2.2.2.5) and increasing the column diameter from 180 mm to 280 mm. The use of pumps to increase flow rates disrupted the chitin-peptide interaction and resulted in the presence of the quadripartite construct in the flow-through and wash fractions (data not shown) causing a lower yield. From these trials it was concluded that the column must be loaded, washed and eluted under gravitational flows due to the weakness of the chitin-peptide interaction.

C. Washing the Chitin Resin

The published protocol recommended 15 x 20 ml column volumes were required to wash the unbound protein from the chitin column. By monitoring the composition of each column volume used to wash the chitin resin (using SDS-PAGE shown in Figure 3.13) it was shown that the first three of the wash volumes were sufficient. Additional wash steps appeared to cause elution of some of the quadripartite construct which caused a reduction in hIAPP yield.

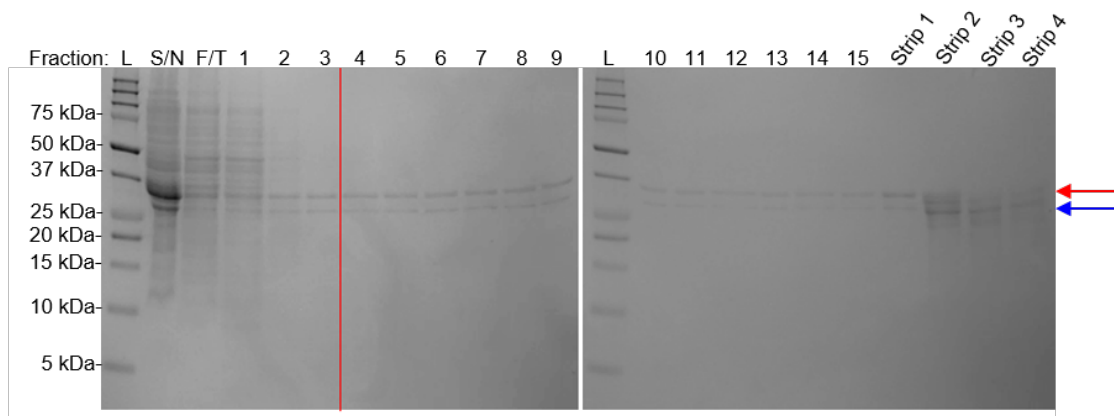


Figure 3.13: SDS-PAGE showing the protein contents of each wash step during chitin affinity purification.

The quadripartite construct (red arrow) and the intein-CBD construct (blue arrow) is detected in all wash steps indicating the chitin:CBD interaction is disrupted. The red line shows where the column is fully washed of unbound proteins. For all lanes, 13 μ l of sample was mixed with 5 μ l 4 x lithium dodecyl sulfate (LDS) loading buffer and 15 μ l was loaded on to the gel except for the supernatant (S/N) and flow-through (F/T) samples where only 7.5 μ l was loaded to avoid overloading.

As a result of these experiments, chitin-affinity purification was performed using more vigorously separated soluble and insoluble cellular protein fractions and only three wash volumes (3 x 20 ml) prior to intein cleavage were used.

3.3.2.2 Solubilisation of Buffer Salts in the Intein Cleavage Solution Solubilisation for C-terminal Amidation.

After washing the chitin column, the quadripartite construct remained bound to the chitin resin. The self-cleavage reaction of the intein (Figure 3.8, step 4) was initiated with the addition of 'Cleavage Buffer' (2 M ammonium bicarbonate, 0.1 M DTT, pH 8). Incubation in this buffer at 4 °C overnight results in amidation of the C-terminal Tyr residue on the leader-hIAPP construct. The intein-chitin-binding domain part of the construct remained attached to the chitin resin but the leader-IAPP-CONH₂ construct is free in solution and can be eluted from the column (Figure 3.14).

Figure 3.14 shows efficient cleavage at this step. However, practically there were inconsistencies in whether the ammonium bicarbonate stayed in solution during the overnight

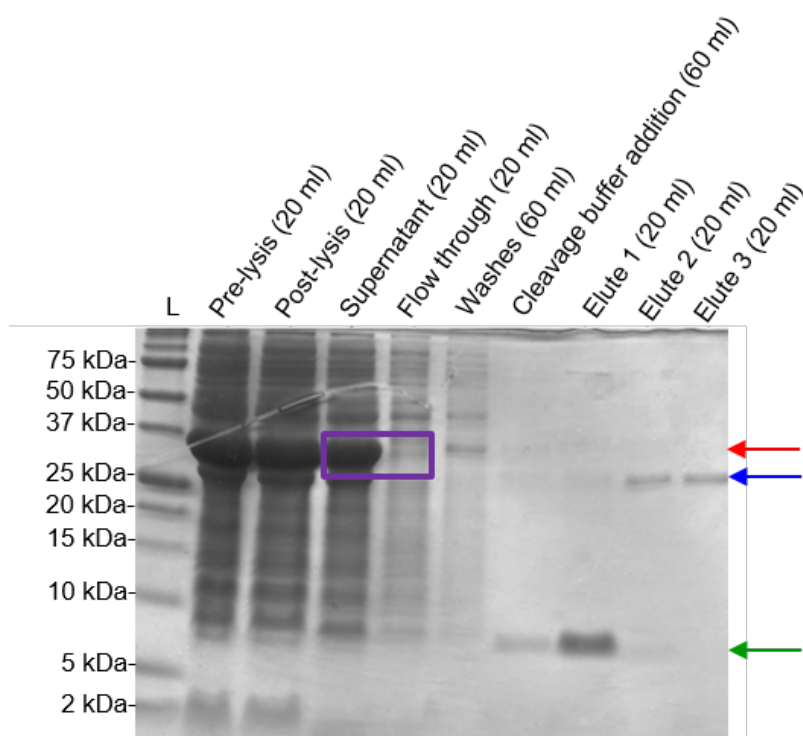


Figure 3.14: SDS-PAGE showing efficient production of the leader-hIAPP construct by intein cleavage.

Purification steps of hIAPP are shown. The purple box highlights the binding of the quadripartite construct (red arrow) to the chitin resin as little of the construct is present in the flow through fraction. Production of the leader-hIAPP construct (green arrow) is evident on addition of the cleavage buffer. The blue arrow shows the intein-chitin-binding-domain only construct.

incubation and even prior to addition to the column. Through increasing the pH of the Cleavage Buffer from pH 8 to pH 8.5, the solubility was improved and the method became more reproducible.

3.3.2.3 Optimisation of the Glu-C Endoprotease Cleavage for IAPP Release

Eluted fractions containing the leader-hIAPP-CONH₂ construct were dialysed in a 1000 Da MW cut off membrane into dialysis buffer (20 mM HEPES, 0.1 mM EDTA, 2M urea, 50 mM NaCl, pH 8) at 4 °C (Section 2.2.2.5, Figure 3.8, step 5) to remove ammonium bicarbonate and DTT. The sample was next passed through a 0.22 µm syringe filter to remove any large aggregates which may have formed.

The purification protocol suggested by Miranker and coworkers [384] suggested a V8:hiAPP (*w/w*) ratio of 25:1 to separate the leader sequence from the N-terminus of hiAPP-CONH₂. The V8 protease used was Endoproteinase Glu-C from *Staphylococcus aureus*. The more recently published protocol by Reif and coworkers [396] reported optimisation steps which led to a V8:hiAPP (*w/w*) ratio of 1:1. Since purchase of the V8 protease was costly, optimising its usage was a key focus. Optimisations were replicated in this work as follows.

Endoproteinase Glu-C V8 is a serine protease which cleaves on the carboxyl side of the acidic residues glutamic acid (E) and aspartic acid (D). The sequence of hiAPP is free from both of these amino acids but the leader sequence has three glutamic acid residues (Figure 3.7), only one of which is positioned N-terminal to the hiAPP sequence and is required to release full length hiAPP from the expression construct. Owing to this, site-directed mutagenesis was conducted (using a Q5 QuickChange kit 2.2.2.5) to remove the two additional glutamic acid residues and replace them with glutamine (E4Q) and histidine (E5H) (Figure 3.15) as suggested by Rodriguez-Camargo *et al.* [396].

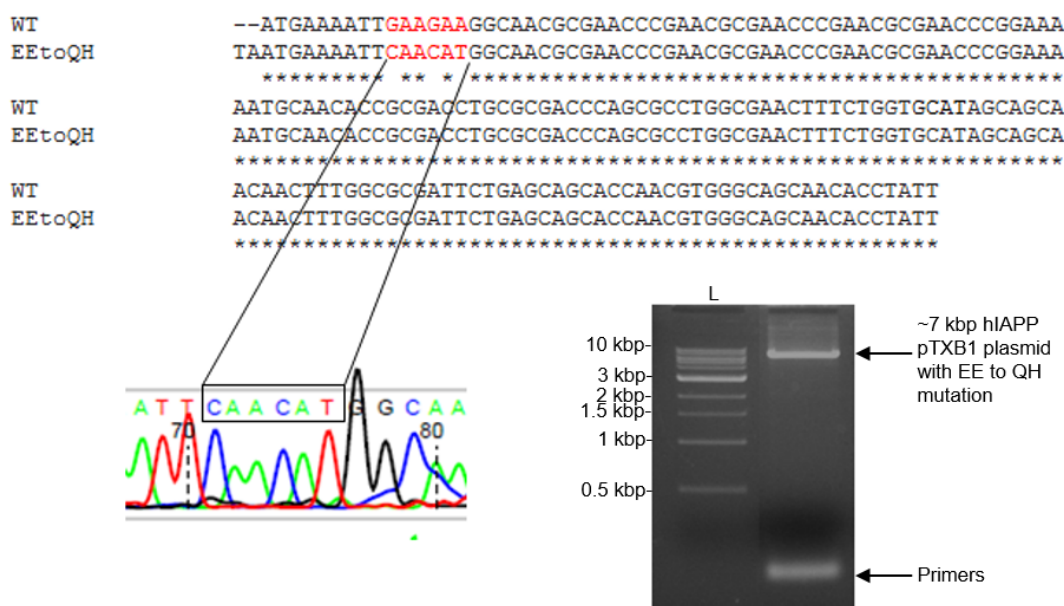


Figure 3.15: Site directed mutagenesis of the leader sequence.

Sequencing data from Beckman Cogenics confirms the incorporation of the substitutions GAAGAA (Glu-Glu) to CAACAT (Gln-His) in the leader sequence. The agarose gel shows the production of the plasmid after PCR amplification visualised by EtBr staining.

This substitution had the potential to reduce the number of unproductive catalysis

events of the V8 by reducing the number of catalysis sites available. The protocol by Reif and coworkers [396] recommended that additional sequence changes should also be made whereby Gly-Ile-Glu was incorporated into the leader sequence after the final Pro residue to enhance V8 cleavage (Figure 3.16). Rodriguez-Camargo *et al.* [396] found the Gly-Ile-Glu addition enhanced V8 protease activity, however, the converse was observed in this study (data not shown). Owing to this only the EE to QH mutation was incorporated, expressed, and purified according to Figure 3.8.

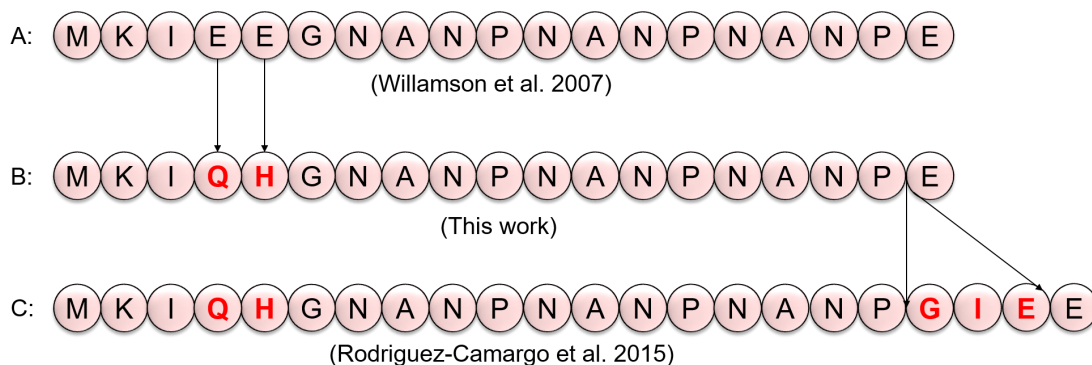


Figure 3.16: Variations on the N-terminal leader sequence to improve V8 cleavage. The amino acid code (pink circles) for the leader sequence is shown. Contrasts in sequence are highlighted in red lettering.

Other optimisations for the V8 cleavage step (Figure 3.8, step 7) were tested focusing on improving reaction conditions: the sample volume was decreased to 5 ml using centrifugation (Figure 3.8 step 6) and sample agitation and temperature were investigated.

Various spin columns were trialled with different membrane compositions to try and reduce loss of protein during concentration due to binding to the filter. The best performing filter tested was a 1 kDa MWCO VIVASPIN (Sartorius) spin column. Despite this, there was still significant loss of product at this step in the purification protocol.

Reduction of the sample volume increased collision probability, which was exacerbated by gentle solution agitation. Agitation is known to enhance the rate of enzyme catalysis, but also the rate of aggregation of many proteins, including hIAPP [406]. Owing to this the incubation period of the reaction was shortened.

Increasing the reaction temperature from 4 °C to 20 °C (as recommended by preliminary work on hIAPP by Dr M. Panya at the University of Leeds (personal communication)) improved the probability of successful binding and cleavage of the leader-hIAPP-CONH₂ construct with V8.

Figure 3.17 shows the final impact of the combined optimisations on the V8 cleavage of the leader-hIAPP-CONH₂ construct. As a result of the optimisation trials for all of the conditions considered, the V8 cleavage reaction was performed at 4 °C with gentle rocking. When 2 mg of enzyme is added to a concentrated leader-hIAPP-CONH₂ sample (based on the 1:1 hIAPP:V8 (*v/v*) suggested in [396] and the predicted final yield of 2 mg of hIAPP), the reaction appears to be complete after just 15 min (Figure 3.17). To alleviate the risk of amyloid formation, the duration of the V8 cleavage was shortened to 15 min.

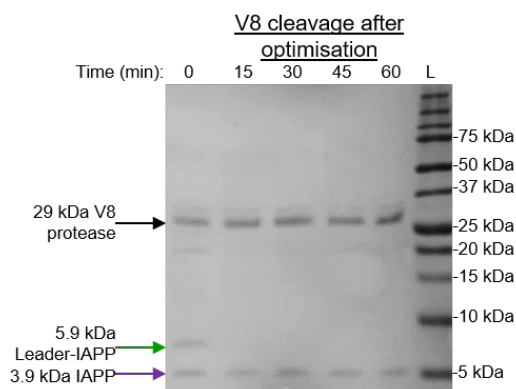


Figure 3.17: Optimisation of the V8 cleavage reaction to release hIAPP from the leader sequence.

An SDS-PAGE gel showing a time course of the V8 reaction after implementation of V8 cleavage optimisations. The band at 29 kDa represents V8 protease (black arrow).

Both gels show the presence of the leader-IAPP construct (green arrow) and the formation of the hIAPP peptide (purple arrow). The Leader sequence is not detectable as it cannot bind to Coomassie stain. All lanes were loaded with 15 μ l of sample (13 μ l sample and 5 μ l 4 x LDS loading buffer (Biorad)) which had been boiled for four minutes. L = ladder.

The V8 cleavage reaction was halted by removal of the large (29 kDa) V8 protease from the solution by filtration (Figure 3.8, step 8) using a VIVSPIN 5, 10 kDa MWCO tube. However, some loss of hIAPP was observed, possibly due to attachment to the filter membrane. Samples were lyophilised (Figure 3.8, step 9).

3.3.2.4 Separation of 4 kDa and 2 kDa Peptides using RP-HPLC

The final step in extracting hIAPP from the expression construct is to purify hIAPP-NH₂ from the cleaved leader sequence. RP-HPLC was used (Figure 3.8, step 10) to separate the two peptides on the basis of hydrophobicity using a gradient of increasing acetonitrile (ACN) concentration (Section 2.2.2.5). The absorbance at 280 nm was

monitored as liquid exited the column to detect protein elution. Owing to the lack of Trp residues and only a single Tyr, the absorbance at 280 nm of hIAPP is very low; $\epsilon_{\text{red}} = 1490 \text{ M}^{-1} \text{ cm}^{-1}$, $\epsilon_{\text{ox}} = 1615 \text{ M}^{-1} \text{ cm}^{-1}$ as determined by ExPASy - ProtParam tool [407]. This, combined with the limited loading volume of the HPLC system, created the need for a high concentration of hIAPP to be applied to the column in a small volume. Owing to the aggregation propensity of hIAPP, the peptide was solubilised in 100 % DMSO prior to application on the HPLC column to ensure the peptide remained monomeric. Care was taken as injection of 100 % DMSO onto the HPLC column may allow solubilised peptides to pass through the column without interacting with the column surface. To avoid this issue, multiple small injections (of up to 100 μl) of the DMSO solubilised sample were made (Section 2.2.2.5).

The earlier optimisation whereby the sample volume was reduced prior to buffer exchange (Section 2.2.2.5) was important to reduce the sample volume for loading onto the HPLC system. The smaller volume, which was lyophilised, produced a more dense dried material after lyophilisation, making suspension in small volumes of DMSO possible. Even with multiple injections, the maximum volume which can be loaded onto the HPLC column was 1.5 ml and at least 0.3 mg of hIAPP must be loaded onto the column to observe a convincing absorbance peak when IAPP eluted from the column.

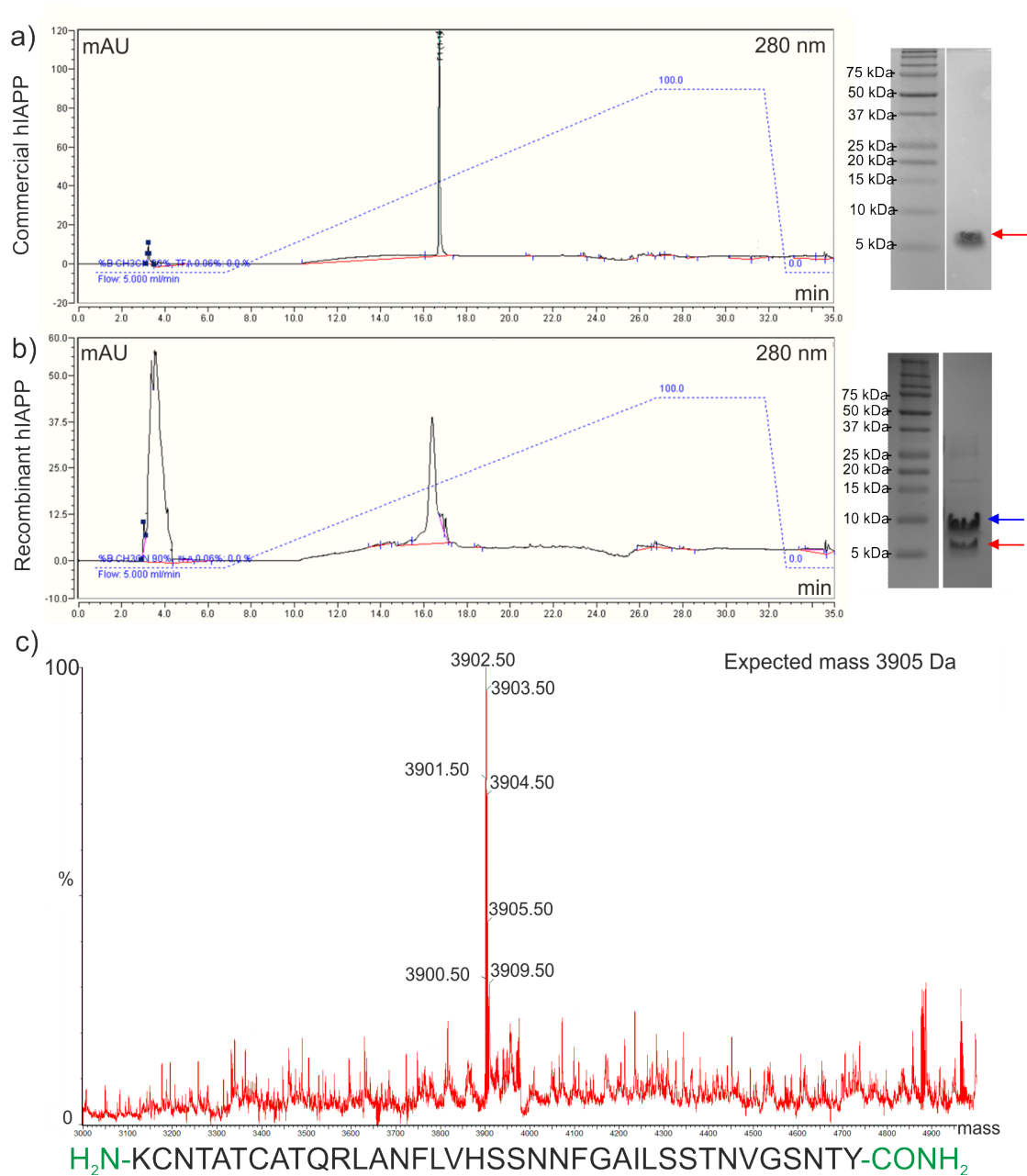


Figure 3.18: Separation of Leader and IAPP by RP-HPLC

a) A chromatogram showing the elution of 1 mg of commercial hIAPP from the RP-HPLC column. b) The chromatogram for recombinantly produced hIAPP. The blue dotted lines represent the acetonitrile gradient applied to the C18 column. The SDS-PAGE gels (right) show the contents of the major peaks of the chromatograms, hIAPP (red), and leader-hIAPP (blue). c) The mass spectrum of recombinantly purified hIAPP showing multiple impurities, with the hIAPP sequence below (N- and amidated-C-termini are highlighted in green).

Figure 3.18 (top) shows the elution profile of 1 mg of pure hIAPP (purchased from Sigma Aldrich) when applied to the C-18 column. Comparison of this to the chromatogram below which was obtained when approximately 0.3 mg of recombinant hIAPP and leader was applied to the same column. This suggests that hIAPP has been successfully produced and purified at a low level.

When the commercial hIAPP was applied to the RP-HPLC column a single, sharp peak is observed after 16.4 min indicating good purity and provides evidence that hIAPP can be observed using 280 nm wavelength light. On application of recombinantly-produced hIAPP a broader peak is observed with lower intensity despite application of the entire preparation. Use of SDS-PAGE showed the composition of this peak consisted of a mixture of hIAPP and uncleaved leader-hIAPP construct. There was no evidence of the leader sequence by SDS-PAGE or from the 280 nm absorbance trace as there are no aromatic residues in the sequence (refer to Figure 3.7). Absorbance detection at 220 nm revealed a peak eluting at 10.3 min (not shown) which is presumably the leader sequence. Thus RP-HPLC could be used to separate hIAPP from the leader sequence, however, preceding steps needed further optimisation to ensure all leader-hIAPP had been cleaved.

Due to the unsuccessful purification of hIAPP the final step in the purification protocol - oxidation by H₂O₂ (Figure 3.8, step 11) - was not conducted.

3.3.3 Methods to Measure hIAPP Concentration

Due to a lack of aromatic residues in the sequence of hIAPP, detection of the peptide using absorbance at a 280 nm wavelength was difficult with error-prone, very low readings measured. Potential problems with calculating the concentration of hIAPP from its A₂₈₀ is its low extinction coefficients; $\epsilon_{\text{ox}}=1615 \text{ M}^{-1}\text{cm}^{-1}$, $\epsilon_{\text{red}}=1490 \text{ M}^{-1}\text{cm}^{-1}$ (calculated using ExPASy ProtParam [407]). To confirm the validity of this calculated extinction coefficient, samples were sent for Quantitative Amino Acid Sequencing (Abingdon Heath Sciences, Birmingham, UK). Other absorbance techniques were trialled such as monitoring at 205 nm, 220 nm and use of the Bradford assay, but none proved to be reliable for the detection of hIAPP. This is consistent with the literature where the difficulties in quantifying small IDPs has been discussed [204].

Non-absorption-based methods were then considered. Detection of hIAPP by different stains which were compatible with SDS-PAGE could have been used routinely. IAPP appears to stain very poorly with QuickStain (Generon) on SDS-PAGE gels, but an improvement in staining sensitivity was observed when using Coomassie Brilliant Blue stain (Biorad). As a result of this finding, all gels on which hIAPP was loaded were stained using Coomassie Brilliant Blue rather than QuickStain (Generon), Section 2.2.3.

3.3.4 Summary of IAPP Production

The expression and purification of hIAPP from the soluble quadripartite construct was improved by this work. Optimal growth conditions were found to ensure reliable, good expression of the construct in BL21(DE3) cells. With more time the substitution of Thr to Cys at the third residue of the intein sequence would have been incorporated as there is evidence that this can improve the stability of the quadripartite construct [408]. This would decrease the amount of cleaved construct during expression.

Regarding the purification method, the alteration in cleavage buffer pH had a significant contribution to increasing the reproducibility of that part of the method. However, overall, the purification of hIAPP was generally unreliable and low-yielding, as well as time-intensive. Owing to the difficulties in producing hIAPP, the focus of this project moved solely to $A\beta_{40}$ which was able to be produced reliably and in sufficient quantity.

To pursue hIAPP studies in the future an alternative construct could be created. Use of a His tag rather than the Chitin-binding domain could enable use of a stronger affinity purification step. Additionally the leader sequence could be expanded for easier separation from hIAPP, e.g. through the use of filtration. An alternative approach could be to emulate the $A\beta_{40}$ preparation (see subsequent section) whereby hIAPP is expressed in an insoluble form. The incorporation of the intein sequence is however important for the amidation of the C-terminus. A lot of issues were encountered with the reproducibility of the V8 cleavage. Alternative enzymes which cleaved N-terminal to Lys or which could be used to create hIAPP with no additional amino acids was looked into, however, few alternatives were viable. Another route to this could be to express hIAPP with an N-terminal Met. Studies would be needed to ensure comparable behaviours with the wild-type. If this was the case, significant amounts of Met-hIAPP could be expressed and used for peptide-intensive biophysical methods.

3.4 Compilation of Methods to Study IDP Amyloid Formation

A plethora of methods have been applied to the study of amyloid proteins and IDPs [334, 409–411]. Small molecule approaches have already revealed insight in the aggregation processes of IDPs such as α -synuclein, hIAPP, and $A\beta_{40}$ (Section 1.4). Moreover, the breadth and number of methods that have been used to study amyloid (as discussed in Section 1.4) is ever increasing with novel approaches and method enhancements being developed continuously. New methods can probe previously untapped areas of amyloid formation. For example, Maity *et al.*, [412] developed a nanosecond fluorescence cross-correlation spectroscopy method to exploit changes in dynamics of hIAPP on the addition of small compounds in the probing of how structural disorder can be used for drug design. The level of active research in this field highlights the immense need for better understanding of amyloid formation. Additionally, continual improvement to established techniques (including single molecule [413] and fluorescence methods [414] as well as solid and solution NMR techniques reviewed in [415] but especially molecular dynamic simulations [416, 417]) has made these methods more versatile and increased their compatibility with numerous protein systems [418].

The purpose of this Section was to justify the selection and assimilation of methods for the toolbox, summarised in Figure 3.19, which can be implemented to investigate the effects of small molecules on IDP amyloid aggregation.

At the outset, it was necessary to select a method which could be used to screen small molecules for impact on $A\beta_{40}$ aggregation. There are a wide variety of screening techniques which could have been used including *in silico* based molecular simulations, *in vivo* methods (such as the tripartite β -lactamase assay [337]), or *in vitro* methods such as ESI-IMS-MS, or fluorescence-based assays [356]. For this work, a well-established, ThT-based assay was used [330, 419, 420]. This assay was amenable to high-throughput screening [410, 421, 422], and required small sample quantities. This assay generally highlights the presence of β -sheet aggregates [423] as well as revealing the kinetic profile of the aggregation reaction [424]. Subsequent to the use of this screening method, perturbations in the mechanism of amyloid aggregation can be inferred (as detailed in Section 1.4.1).

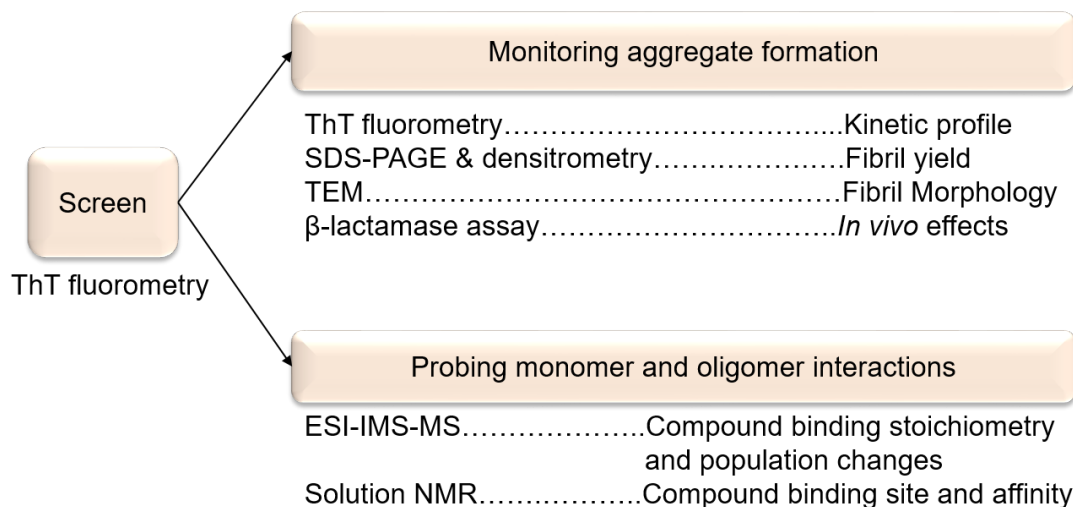


Figure 3.19: Compilation of methods for investigating small molecule effect on amyloid aggregation.

A schematic of the toolbox developed showing the incorporated methods and how they contribute information into the investigation of small molecule effects on amyloid aggregation.

On finding compounds which influence amyloid aggregation, a set of orthogonal methods was compiled to probe the small molecule effects on aggregation from complementary perspectives. To test the reproducibility of small molecule effects, a titration of compound concentration was included in the toolbox. Additionally this could reveal concentration dependent effects on ThT kinetics, for example, low concentrations of a compound may affect one stage of amyloid aggregation, whereas high concentration of a compound could form oligomeric states which perturb the amyloid aggregation in an alternative way. Continued use of the ThT assay for the titration investigation enables the kinetic profile of the aggregation reaction to be monitored.

To quantify the extent of aggregation and whether the addition of a specific compound could effect this, an SDS-PAGE-based fibril yield assay (reviewed in [289] and described in Section 2.2.5.3) was included in the toolbox. In the field the maximum fluorescence intensity in the ThT assay has been used to indicate fibril quantity [330]. However, there is debate regarding its reliability as a quantitative measure as maximum fluorescence levels in the ThT assay can be affected by: interactions between the small molecules with the ThT molecule; differences in binding affinity of ThT with different fibril polymorphs; competition between the small molecule and ThT for binding sites on fibrils; as well as variation based on the abundance of β -sheet formation.

In order to distinguish fibrillar and amorphous aggregates, transmission electron microscopy (TEM) was used. TEM was chosen as aggregate shapes can be observed directly. TEM can probe whether aggregates formed in the presence of small molecules can still adopt amyloid fibril morphology, or if amorphous aggregates are formed. Such behaviour could be achieved by pushing monomeric or small oligomeric conformations of A β ₄₀ into off-pathway states where amorphous aggregates are formed. TEM and the SDS-PAGE fibril yield assay complement each other well as SDS-PAGE fibril yield can report quantitatively on fibrils formed, and TEM reports qualitatively on aggregate morphology. For the purpose of this toolbox, TEM was used to note the presence or absence of fibrillar species, due to this the magnifications used did not probe the known multi-morphological states of A β ₄₀ fibrils.

The β -lactamase assay (Section 1.4.2) was chosen to add a more physiological aspect to the methods toolbox. The assay monitors small molecule ability to prevent aggregation of a peptide using ampicillin resistance as a reporter. This assay was chosen over other *in vivo* assays because it takes place in the periplasm of *E. coli* rather than in the cytosol. Cytosol-based assays can be misleading when using small molecules as some compounds have difficulty traversing the inner cell membrane. The β -lactamase assay provides a quantitative platform for identifying which small molecules can inhibit amyloid aggregation and to what extent.

To probe the effects small molecule modulators of aggregation had on the ensemble of small A β ₄₀ species (monomer and soluble oligomers) ESI-IMS-MS was used. This technique enabled the observation of distinct species of A β ₄₀ which were present in solution. Relative quantification is also possible with this technique and can probe whether a compound causes different states to be favoured or disfavoured. The ESI-IMS-MS method in the toolbox was developed and used previously by Dr L. Young at the University of Leeds to indicate compound binding and stoichiometries of small molecule:peptides interactions [356]. The method distinguishes species based on their oligomeric stage (monomeric, dimeric, hexameric etc.) and on the extent of species compaction (cross section correlation) [356]. Such observations can imply the mode of binding of the small molecule to the peptide, for example, if a 1:1 peptide:small molecule ratio is consistently observed, this may indicate there is a single specific binding site for the small molecule on the peptide. Conversely, the presence of a monomeric peptide bound to multiple copies of the small molecule can imply a non-specific binding

mode. This method provides a good indication of binding mode but cannot define the mode for certain. For example, if ESI-IMS-MS identifies that the peptide:small molecule stoichiometry is less than an arbitrary 1:4, this may be due to non-specific binding, or it could also occur by non-specific self-assembly of the small molecule in the gas phase. Nevertheless, this method was useful in combination with the other methods discussed to create a substantially-supported impression on the small molecule:peptide interaction *in vitro*.

Finally NMR was used to gain residue-specific, structural information. NMR was chosen as it is very suited to the study of disordered, dynamic and heterogeneous populations. To complete the toolbox of investigative methods to monitor small molecule effect on amyloid aggregation, NMR was used as a probe to find specific binding sites, and affinities of small molecule:peptide interactions. To do this $^1\text{H}^{15}\text{N}$ -HSQC experiments which revealed alterations in the chemical shifts of the backbone amide peaks of $\text{A}\beta_{40}$ on addition of small molecules were used. More extensive use of NMR to explore the conformational propensities of monomeric $\text{A}\beta_{40}$ is described in Chapter 5 where another, NMR-specific, methods approach is created and applied. Presentation of NMR optimisation steps and experimental details are excluded from this chapter as they are discussed in Chapter 5.

3.4.1 Summary and Outline of the Toolbox

In summary, these methods (Figure 3.19), have been chosen to create a multi-method approach for investigating how IDPs interact with aggregation-perturbing compounds. Biophysical methods which are compatible with heterogeneous systems are vital for comprehensive understanding of how IDPs form amyloid. The orthogonal methods selected can be used to investigate the nature of the amyloid-perturbation from different perspectives in order to build up a robust understanding of how a compound is affecting amyloid aggregation. In this work methods have been utilised and optimised for the study of IDPs with compounds to make progress towards elucidating important monomer conformations in the amyloid pathway.

Ultimately the combinatorial use of these methods can be used to gather evidence for the selection of compounds which have potential to reveal information on $\text{A}\beta_{40}$ monomer conformations on and around the $\text{A}\beta_{40}$ amyloid aggregation mechanism. Such promising

compounds could be used to subject $A\beta_{40}$ to more in depth investigation by NMR methods which are particularly suited to the study of IDPs.

3.5 Method Optimisation for Monitoring Small Molecule Effects on Amyloid Aggregation of Intrinsically Disordered Peptides

Once $A\beta_{40}$ had been produced, and the method strategy devised, it was important to optimise each of the methods in the toolbox and ensure compatibility with control compounds.

3.5.1 ThT Fluorometry to Screen for Small Molecule Effects on $A\beta_{40}$ Aggregation

As with most well established methods, there are many variations on how the ThT fluorometry assay is conducted. The precise method used in this thesis is described in Section 2.2.5.1 and is based on the method used in [425]. Modifications to this protocol are discussed in this section.

3.5.1.1 Validation of Fluorescence Detection Strategy

For this work, small molecules which perturb $A\beta_{40}$ formation need to be detected even if the effects are very subtle. ThT fluorescence was monitored using a single point in the centre of each well as a representative value for fluorescence intensity. To verify the validity of this method a complete wellscan was collected at the end of an aggregation experiment to assess aggregate distribution in the well.

Use of the Clariostar (BMG biotech) apparatus enabled measurement of ThT fluorescence at different locations within the same sample well. Experiments were conducted under quiescent conditions and thus the distribution of aggregates across each well were expected to be relatively even. Figure 3.20 shows the level of ThT fluorescence across four wells containing samples of 20 μM $A\beta_{40}$ in 50 mM ammonium acetate with 10

μM ThT, and two control wells containing buffer and ThT only (see Section 2.2.5.1). Samples had been incubated quiescently at 37 °C for 21 h.

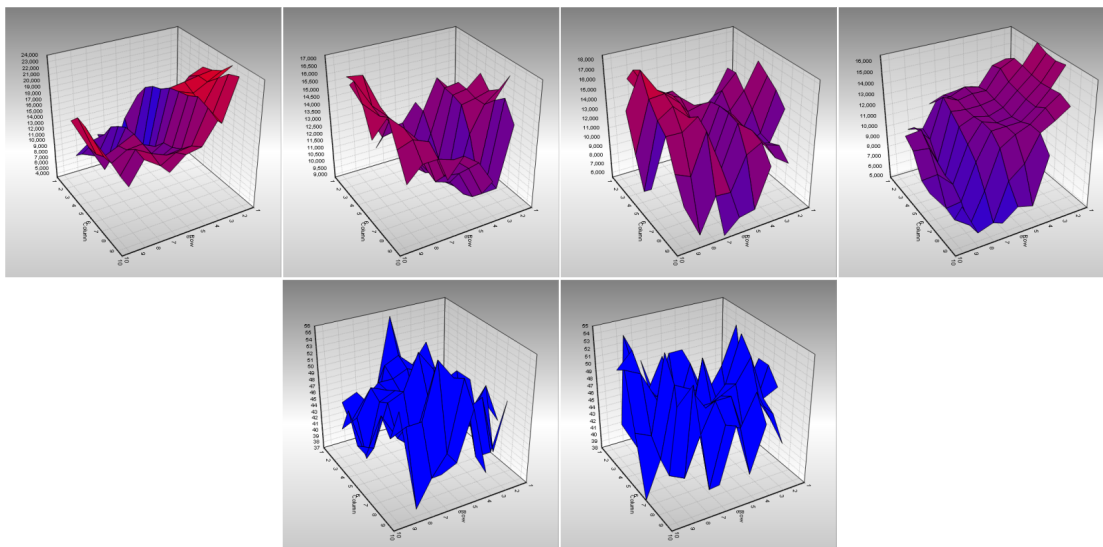


Figure 3.20: 3D representation of amyloid distribution in sample wells. The x-y plane represents the well surface with ThT fluorescence shown on the z-axis and through a colour gradient of low to high (blue-red) levels of ThT fluorescence.

As expected, there was a marked increase in fluorescence level for wells containing $A\beta_{40}$ indicating that aggregation had occurred. The surface levels shown in the graphs indicate that aggregate distribution across the wells is random. The intensity of ThT fluorescence of the single centre point of the wells was similar to the average of all the data collected on a full wellscan. Based on this, single point data collection was validated.

3.5.1.2 Assessment of the Effect of DMSO on $A\beta_{40}$ Aggregation

Many compound libraries store and provide compound stocks in DMSO due to its versatility as a solvent. As the methods toolbox was compiled specifically for use with small molecules, it was important to assess the effect of low levels of DMSO on the included methods. Moreover, it was essential to measure the effect DMSO had on peptide aggregation.

To this end, $A\beta_{40}$ aggregation was monitored using ThT fluorometry in presence of a titration of DMSO percentages, Figure 3.21.

Figure 3.21 implies that concentrations of up to 10 % (*v/v*) DMSO have no effect on the shape ThT curves which represent $A\beta_{40}$ aggregation. At 20 % (*v/v*) DMSO the ThT

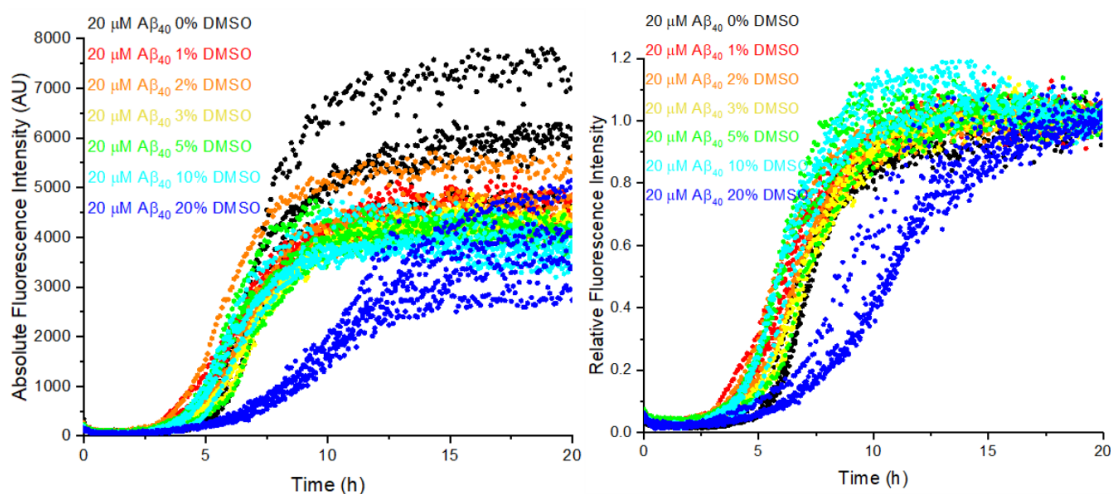


Figure 3.21: DMSO titration effects on $A\beta_{40}$ aggregation measured by ThT fluorescence. Graphs showing the absolute (left) and relative (right) fluorescence intensity measured when $A\beta_{40}$ aggregates in 50 mM ammonium acetate, pH 6.8, at 37 °C, under quiescent conditions with various percentages of DMSO; 0 % (*v/v*) (black), 1 % (*v/v*) (red), 2 % (*v/v*) (orange), 3 % (*v/v*) (yellow), 5 % (*v/v*) (green), 10 % (*v/v*) (cyan), and 20 % (*v/v*) (blue).

profile exhibits a longer lag time, and a shallower gradient implying DMSO may have interfered with elongation of $A\beta_{40}$ fibrils. Generally the maximum fluorescence level reached decreased as DMSO percentage increased.

This result contributed to the incorporation of 2 % (*v/v*) DMSO in all samples and controls in the toolbox. This ensured consistency across biophysical methods as this was high enough to permit addition of up to approximately 200 μM of compounds (from 10 mM stocks in 100 % DMSO) to peptide samples but low enough to avoid interference of DMSO with other biophysical methods (Sections 3.5.4.2, 3.5.5 and 5.1).

3.5.1.3 Assessment of Varying Preparations of $A\beta_{40}$

$A\beta_{40}$ aggregation is sensitive to the effects of impurities in sample preparation. Many methods are implemented in the sample preparation to ensure the starting material is monomeric which is vital for experimental reproducibility. For example the double SEC purification of $A\beta_{40}$ increases the reproducibility of observed ThT kinetics as contamination with oligomeric materials is removed [383]. Others have used 10 mM NaOH and sonication for this purpose [372].

To test the effects of sample preparation, ThT fluorometry was used to monitor $A\beta_{40}$ aggregation of three samples of $A\beta_{40}$ which were prepared differently, Figure 3.22. $A\beta_{40}$ was prepared in three ways; direct solubilisation in 50 mM ammonium acetate after one SEC or two purification steps, or from a 10 mM NaOH stock which was sonicated for 5 minutes in a water bath at 25 °C.

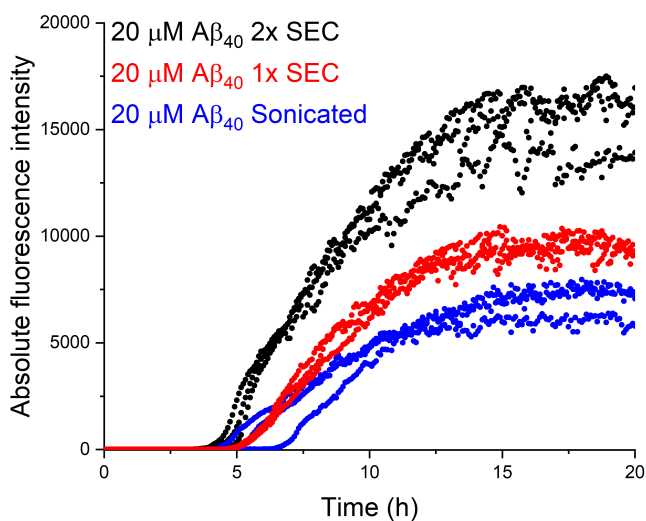


Figure 3.22: Effect of preparation methods of $A\beta_{40}$ on aggregation. ThT fluorescence of $A\beta_{40}$ aggregation when $A\beta_{40}$ is prepared from two sequential SEC purification runs (black), one SEC purification (red), or from a sonicated sample (blue). All samples contained 20 μM ammonium acetate, pH 6.8, 10 μM ThT, and 2 % (v/v) DMSO. Samples were monitored at 37 °C, quiescently.

Figure 3.22 shows there are differences in the kinetics observed when $A\beta_{40}$ is prepared in different ways and thus it is important that samples are prepared by exactly the same method for comparability. It was decided to use two rounds of SEC to prepare $A\beta_{40}$ to align with previous studies in our laboratory [425] and others [383].

3.5.1.4 Assurance of Sample Consistency through Testing of $A\beta_{40}$ Solubilisation Methods

Within a single ThT assay, experimental variation is observed between replicates (e.g. Figure 3.21). Minimisation of this variation would permit the detection of subtle changes in the $A\beta_{40}$ kinetic profiles caused by different small molecules. A possible cause of variation between sample replicates within a plate was the incomplete solubilisation of

lyophilised protein. Thus, an alternative $A\beta_{40}$ solubilisation approaches were considered.

At the end of the multi-step procedure for the purification of $A\beta_{40}$ (Section 2.2.2.3), the peptide is a dry, white powder. Owing to the aggregation propensity of $A\beta_{40}$, it is important to obtain complete solubilisation quickly on buffer addition to avoid areas of local high concentration which would initiate aggregation. However on solubilisation of this powder in aqueous buffers, e.g. 50 mM ammonium acetate, pH 6.8, insoluble flakes were observed. For non-amyloid samples, proteins can be left to go into solution over time or can be heated or agitated to encourage solubilisation. These are not possible with $A\beta_{40}$ due to its amyloidogenic potential.

To explore alternative solubilisation methods, $A\beta_{40}$ powder was solubilised in 100 % DMSO to form a 21 mg/ml solution and then diluted into the final buffer to form a solution of 20 μ M $A\beta_{40}$ in 50 mM ammonium acetate, pH 6.8, with 2 % (*v/v*) DMSO. DMSO was chosen as small molecule stocks are commonly solubilised in DMSO, thus would be in the sample buffer when probing small molecule effects on aggregation. Moreover, the results in Section 3.5.1.2 revealed that ThT fluorometry of $A\beta_{40}$ could tolerate DMSO addition upto 10 % (*v/v*).

Samples of 20 μ M $A\beta_{40}$ prepared by solubilisation directly into 50 mM ammonium acetate or via DMSO, are shown in Figure 3.23.

The data presented in Figure 3.23 show that both methods of $A\beta_{40}$ solubilisation lead to the measurement of similar ThT data. As the change in ThT profile was not significant, either method could be used for this project. Owing to the solvation efficiency of DMSO, solubilisation into 100 % DMSO - to form a 21 mg/ml (4.7 M) stock - was used in this work. This avoided the possibility of local high concentrations of $A\beta_{40}$ forming on solubilisation in aqueous buffer. Hence $A\beta_{40}$ is more likely to be monomeric at the start of the aggregation reaction

3.5.1.5 The Influences of Buffer Choice on Aggregation Kinetics

It is well known that aggregation kinetics can be highly sensitive to alterations in buffer conditions [426, 427]. The majority of the ThT fluorometric assays in this thesis are conducted in 50 mM ammonium acetate, pH 6.8, at 37 °C which is a compatible buffer

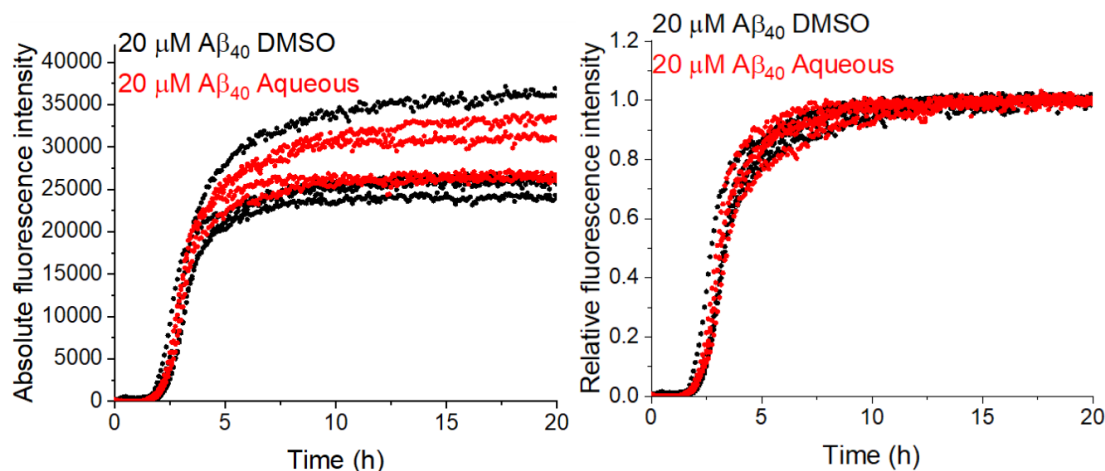


Figure 3.23: Effects of different solubilisation techniques on the reproducibility of amyloid aggregation kinetics.

Absolute (left) and relative (right) ThT fluorescence monitoring of $A\beta_{40}$ aggregation when the peptide is prepared by solubilisation in DMSO (black) prior to dilution into 50 mM ammonium acetate, pH 6.8, with 10 μM ThT or when $A\beta_{40}$ is solubilised directly in aqueous 50 mM ammonium acetate, pH 6.8, with 10 μM ThT (red).

for mass spectrometry and the creation of TEM grids. However, to align with optimised NMR conditions (Section 5.1) and published NMR data [372], $^1\text{H}^{15}\text{N}$ -HSQC experiments presented later in this thesis were performed in 20 mM sodium phosphate, pH 7.4, at 5 $^{\circ}\text{C}$. Owing to this it was important to monitor the effect of these changes in buffer on $A\beta_{40}$ aggregation to enable data interpretation between methods.

There are multiple contrasts between the two solutions: buffer components, pH, temperature, ionic strength, and peptide concentration. Determination of contributions from each contrasting component is not essential for this work. Rather, this section presents some controls to aid data interpretation later on (Section 4.6.1).

Firstly aggregation of 20 μM $A\beta_{40}$ in each buffer was monitored at 37 $^{\circ}\text{C}$.

With equal amounts of $A\beta_{40}$ present Figure 3.24 shows there is a shorter lag time for $A\beta_{40}$ aggregation in 50 mM ammonium acetate, pH 6.8 than for $A\beta_{40}$ in 20 mM sodium phosphate, pH 7.4 buffer. This could be due to the difference in ionic strengths of the two solutions. There was a stark difference in ionic strength of these buffers; 50 mM ammonium acetate had an ionic strength of 50 mM, whereas the 20 mM sodium phosphate buffer had an ionic strength of 3 M hence there are many more charged ions in the sodium phosphate buffer.

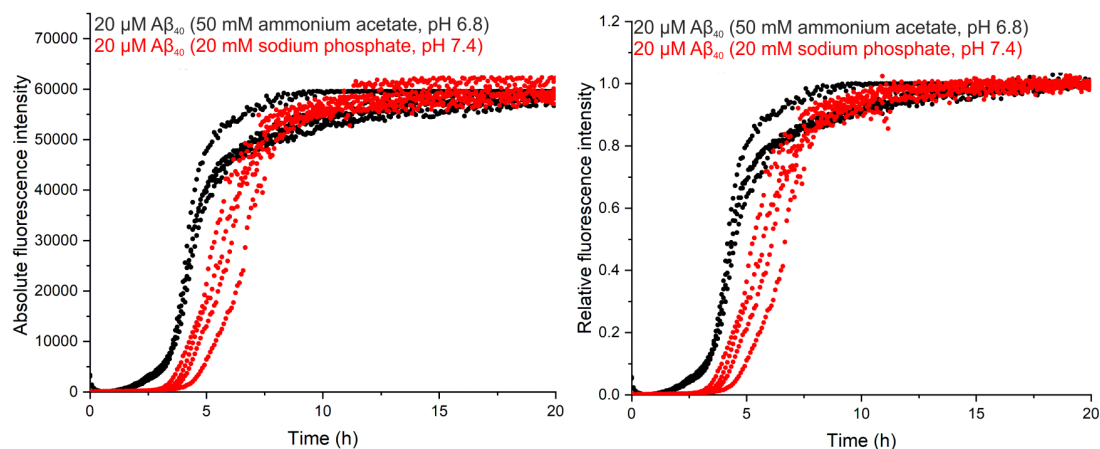


Figure 3.24: Effect of buffer on A β_{40} aggregation.

Absolute (left) and relative (right) fluorescence levels measured when A β_{40} aggregates under quiescent conditions at 37 °C in 50 mM ammonium acetate, pH 6.8 (black) or in 20 mM sodium phosphate, 0.02 % (*v/v*) NaN₃, 0.5 mM EDTA, pH 7.4 (red).

ThT fluorometry was also used to monitor A β_{40} aggregation in each buffer at varying temperatures, Figure 3.25.

As expected, A β_{40} aggregates more quickly at higher temperatures in both buffers as is evident from the decreased lag times at 37 °C. Interestingly there is a large increase in maximum fluorescence for A β_{40} in ammonium acetate at 37 °C which is not observed at the lower temperatures tested. This pattern is not evident in the sodium phosphate buffer samples. One possible explanation for this is that, at 37 °C in ammonium acetate buffer, A β_{40} forms β -sheet-containing fibrils with a morphology more conducive to ThT binding and enhanced fluorescence.

The lag time for A β_{40} at 37 °C (\sim 2.5 - 3.5 h) in ammonium acetate is comparable with Figure 3.24. For A β_{40} in sodium phosphate buffer at 37 °C the lag time is approximately 2 - 2.5 h, which is twice as fast as observed previously 4.0 - 6.5 h in Figure 3.24 which can be explained logically due to the higher protein concentration leading to faster aggregation. This concentration was tested to correlate with the NMR experimental concentration described later in Chapter 5.

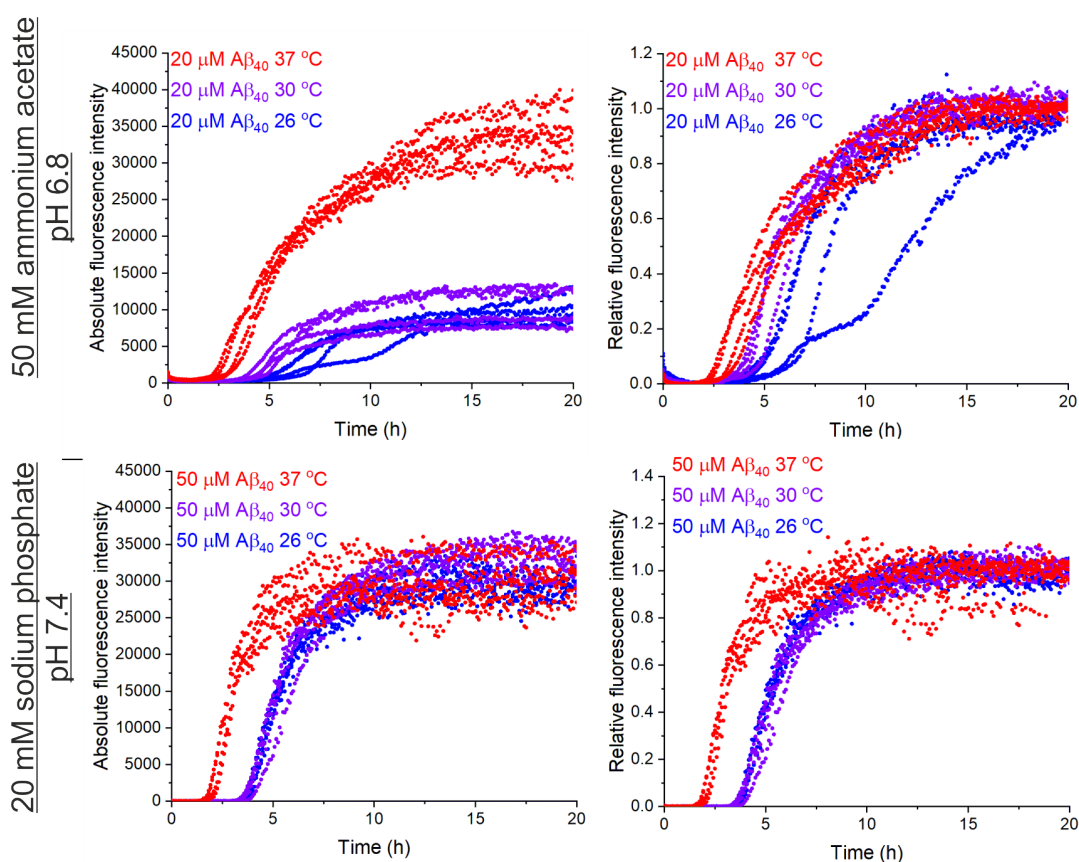


Figure 3.25: Effect of temperature on $A\beta_{40}$ aggregation in different buffers.

Absolute (left) and relative (right) fluorescence measured when $A\beta_{40}$ aggregates in either 50 mM ammonium acetate, pH 6.8 buffer (top), or 20 mM sodium phosphate, pH 7.4 (bottom) under quiescent conditions. Measurements of aggregation at 37 °C (red), 30 °C (purple), and 26 °C (blue) are shown on each graph.

3.5.1.6 Compatibility of ThT Fluorometry as an Indicator of Compound Effects on $A\beta_{40}$ Aggregation

There is a wealth of studies investigating how $A\beta_{40}$ aggregation is affected by the addition of small molecules. EGCG (a known inhibitor of $A\beta_{40}$ aggregation [381, 428]) and aspirin (a compound known not to affect $A\beta_{40}$ aggregation kinetics [429]) were used to demonstrate that the ThT fluorometric assay set-up was functional, Figure 3.26. Each compound was dissolved to form a 10 mM stock in 100 % DMSO to imitate the conditions of library compounds which will be used later in this work. The $A\beta_{40}$ peptide (which had been purified from two sequential SEC experiments) was also solubilised in 100 % DMSO before dilution in 50 mM ammonium acetate, pH 6.8. Data were recorded at 37 °C.

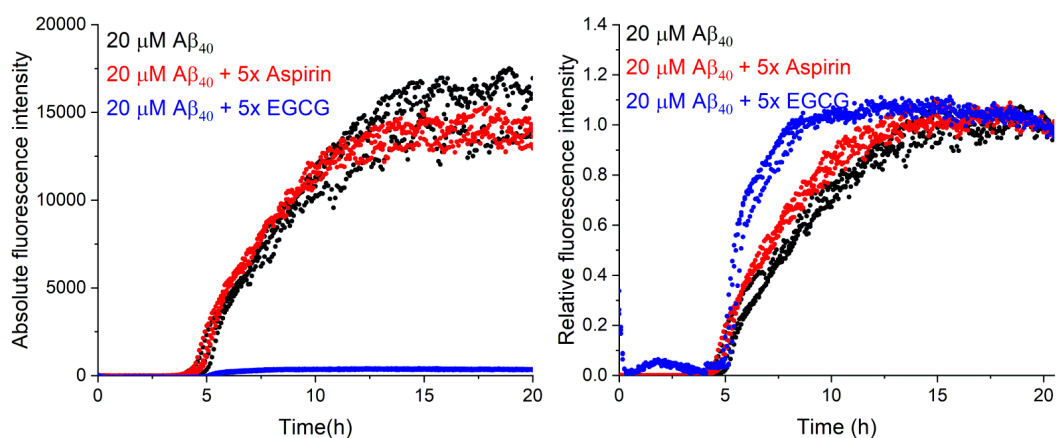


Figure 3.26: Monitoring effect of EGCG or aspirin on $A\beta_{40}$ aggregation by ThT fluorescence.

The absolute (left) and relative (right) ThT fluorescence profiles of $A\beta_{40}$ aggregation alone (black), or with 100 μM EGCG (blue) or 100 μM aspirin (red).

From the absolute fluorescence graph it is evident that the addition of EGCG prevents aggregation of $A\beta_{40}$ whereas aspirin has no effect. However, the effect of EGCG is masked in the normalised data, and in fact shows a faster rate for the fibril elongation. This highlights the need to monitor both absolute and relative fluorescence levels to maximise the information gain from ThT fluorometry.

3.5.2 Development of Quantification Strategies to Extract Objective Measures of Aggregation Kinetics from ThT fluorometry

After use of ThT fluorometry as a screening method to identify small molecules which perturb amyloid aggregation, the ThT assay can be used again to verify reliability of compound effects and to analyse the effects on the kinetic profile.

Qualitative assessment of the ThT fluorometry profiles was used as a fast and clear route to observe effects on $A\beta_{40}$ aggregation. However, this assessment was subjective and thus the extraction of measurable parameters - Maximum fluorescence, T_{50} , and lag time - which were altered by small molecule addition was necessary for more stringent use of the assay.

There are three main measures used: Maximum fluorescence, T_{50} , and lag time. The maximum fluorescence level is the steady-state intensity value once the reaction has

reached completion. The plateau observed is the fluorescence emitted at the final equilibrium of $A\beta_{40}$ in solution and in fibril form. In this work, the mean value of the final 20 data points measured was taken as the ‘maximum fluorescence level’. This could represent fibril yield [330], but owing to the unreliability of this - as previously discussed - should be regarded with care. As the reaction is usually fully aggregated after approximately six hours, continued measurement until 21 h enables any decay in fluorescence to be observed in case the fibrils or β -sheet rich aggregates formed are unstable. If such decay is detected qualitatively from the curve shape then alternate routes to measure the maximum fluorescence may be necessary. The fluorescence values on different plates can vary 10-fold meaning error values are not comparable. Thus all quantitative analyses were made relative to the mean of the $A\beta_{40}$ alone readings on each plate on normalised axes.

The T_{50} and lag time values are more linked. The T_{50} value is the time when the intensity of the fluorescence reached half of the maximum fluorescence level. If the data are normalised this is the time when the fluorescence reaches 0.5. In order to calculate the lag time a script was created where upon a tangential line was extended from the T_{50} coordinate to intersect with the x-axis (Figure 3.27a). Owing to noise in the data collected, there were some clear anomalies reported (Figure 3.27b). Other routes were considered for objectively calculating the lag time. Theoretically the T_{50} coordinate should fall at the centre of the exponential segment of the sigmoidal curve at which should also be the point of the maximum first differential (i.e. the steepest point on the graph). In real data the T_{50} (point of half maximum fluorescence) and the point of the maximum first differential often do not fully align. Owing to this difference, the script was altered to extend a line from the point of maximum first differential to the x-axis (Figure 3.27c). This provided a more accurate approximation of many of the lag times. For data sets where neither calculation of the lag time was suitable, linear fitting was used as is prominent in the field [76, 134, 430]. A major issue with linear fitting is that the linear portion of the collected data can be as little as 10 % of the data set and the boundaries of the linear portion must be monitored by eye which adds a level of subjectivity to the quantitative measure. In this work linear fitting has been used to obtain values of the lag time for curves which were not amenable to either of the aforementioned script methods of calculation.

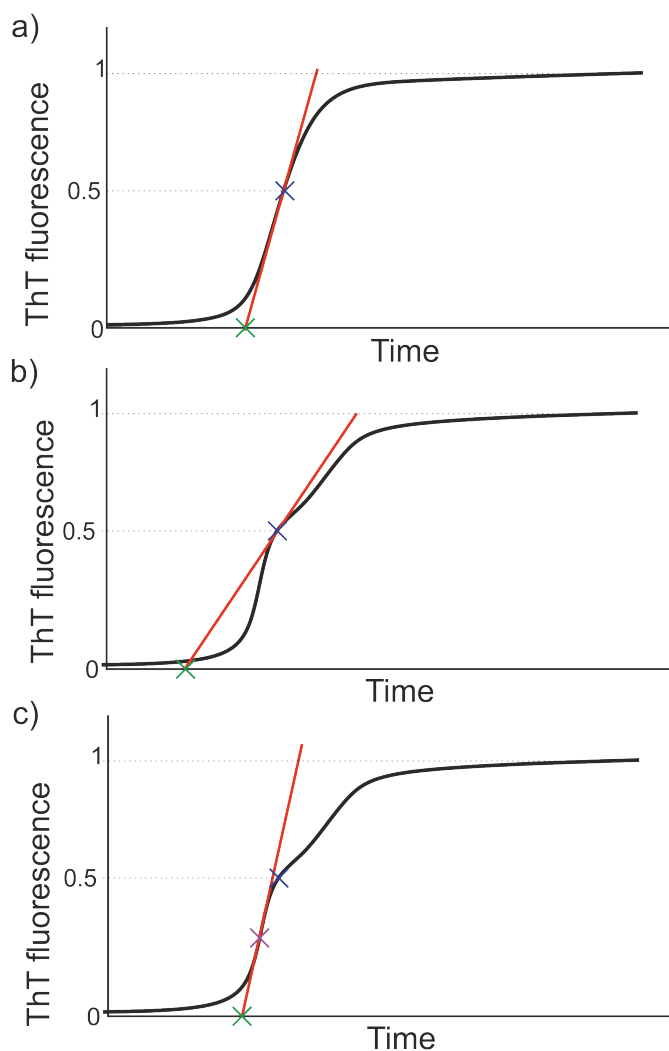


Figure 3.27: Schematic for lag time measurement

Illustrative ThT profiles demonstrating challenges in quantification measurement. The extended tangent (red line) is shown for the determination of lag time (green cross)

based on the T_{50} value (blue cross) in a) an ideal curve and b) a non-ideal curve whereby the method does not yield an accurate lag time approximation. c) Use of the maximum first differential (pink cross) to determine lag time.

3.5.3 Development of an SDS-PAGE-based Method to Measure the Yield of $A\beta_{40}$ Aggregation

To quantify the extent of aggregation, a fibril yield assay was developed from an established protocol used in our laboratory which relies on the different sedimentation properties of large aggregates (e.g. fibrils) and soluble species (e.g. monomer or small oligomers) when subjected to centrifugation. The simple technique consists of three stages: centrifugation (14,100 rpm, at 25 °C for 10 minutes) to separate insoluble and

soluble species, SDS-PAGE to visualise peptide location (i.e. in the insoluble or soluble phase), and densitometry to quantify the amount of peptide in each phase.

Optimisation steps which were implemented to achieve the reproducible assay results demonstrated in Figure 3.28 included consideration of sample containers, centrifugation speed, time, and temperature, use of precision Gel tips for phase separation, and amount of sample loaded onto the SDS-PAGE gel. Initially, the protocol had only been applied at the start and end of aggregation reactions, using samples directly transferred to and from ThT fluorometry plates. Attempts were made to quantitatively probe the extent of aggregation during different parts of the ThT fluorometry aggregation profile, but these were not successful.

Figure 3.28 shows an example of the fibril yield assay (described in detail in Section 2.2.5.3) used at the end of an aggregation reaction (21 h after 20 μ M $A\beta_{40}$ as solubilised in 50 mM ammonium acetate, pH 6.8, and incubated quiescently at 37 °C).

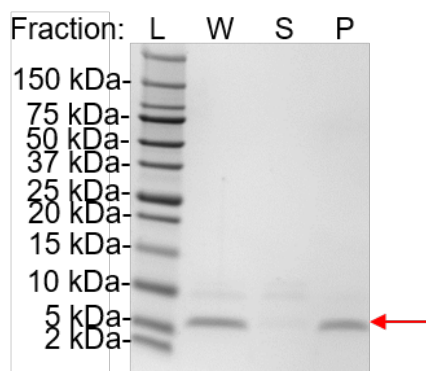


Figure 3.28: Demonstration of the Optimised Fibril Yield Sedimentation Assay.

SDS-PAGE gel showing the distribution of $A\beta_{40}$ (red arrow) at the end of an aggregation reaction. W = whole sample, S = soluble fraction, and P = the insoluble, pelleted fraction. L = ladder.

The gel image shows $A\beta_{40}$ in the ‘**W**hole’ sample taken before centrifugation. The whole sample was centrifuged to separate ‘**S**oluble’ and insoluble, or ‘**P**ellet’, samples. The ratio of band intensity of $A\beta_{40}$ in the Soluble and Pellet lanes indicates the extent of aggregation. The presence of strong band - corresponding to $A\beta_{40}$ - in the pellet sample indicated that essentially all of the peptide is present as insoluble aggregates.

3.5.4 Transmission Electron Microscopy to Qualitatively Observe Aggregate Forms

TEM was incorporated in to the methods toolbox to probe for formation of fibrillar aggregates as it can be used to directly observe aggregate forms. In this work TEM was conducted at 1,500x and 10,000x magnifications to image aggregate morphology. At these magnifications heterogeneous, fine fibril morphology (i.e. protofibril number, or twist pitch) cannot be observed, however, variation in gross fibril polymorphs can be noted (i.e. fibrillar or amorphous aggregates, and fibril lengths). As TEM was conducted using ThT fluorometry samples at the end of the reaction period (after 21 h of quiescent incubation at 37 °C), it was important to ensure that these samples were amenable to grid preparation (Section 2.2.5.2) and imaging, Figure 3.29.

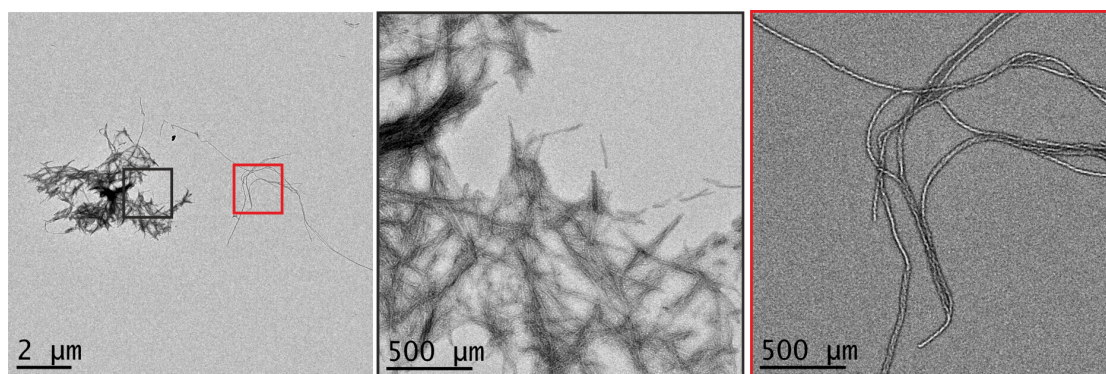


Figure 3.29: Gross morphology of $A\beta_{40}$ fibrils visualised by TEM

. TEM images of negatively stained carbon coated grids with samples of $A\beta_{40}$ taken directly from ThT analysis after 21 h. Left: A TEM image which captures two distinct fibril morphologies formed when $A\beta_{40}$ aggregates in 50 mM ammonium acetate, pH 6.8, 2 % (*v/v*) DMSO, 10 μ M ThT after 21 h at 37 °C. The image was taken at 1,500x magnification. Middle and right: 10,000x magnification images of the fibril morphologies, highlighted by black and red boxes.

This figure (Figure 3.29) shows two contrasting fibril deposits of $A\beta_{40}$ next to each other on the same grid. Highlighted in black are short (~ 200 – 500μ m), bunched fibrils, and in red, more disperse, elongated fibrils ($> 2 \text{ mm}$ in length) are observed. The images in this figure confirm that the $A\beta_{40}$ produced can form fibrillar aggregates, that the ThT samples are amenable to TEM imaging and that fibril heterogeneity occurs and can be observed.

3.5.4.1 Investigation of the Diversity of Fibril Morphology in Different Preparations using TEM

For some duplicate ThT experiments the final ThT signal observed was up to 10-fold more intense than for other replicates. There is contrasting evidence in the literature suggesting that such intensity changes could be caused by changes in fibril yield, or variation in ThT interaction with fibrils of different morphology. To check whether there were observable differences in morphology, TEM was conducted on two $A\beta_{40}$ samples, (Figure 3.30), one which exhibited a relatively low fluorescence intensity (5000 AU) and one which exhibited high fluorescence intensity (60,000 AU) for the same 20 μM $A\beta_{40}$ sample in 50 mM ammonium acetate, pH 6.8.

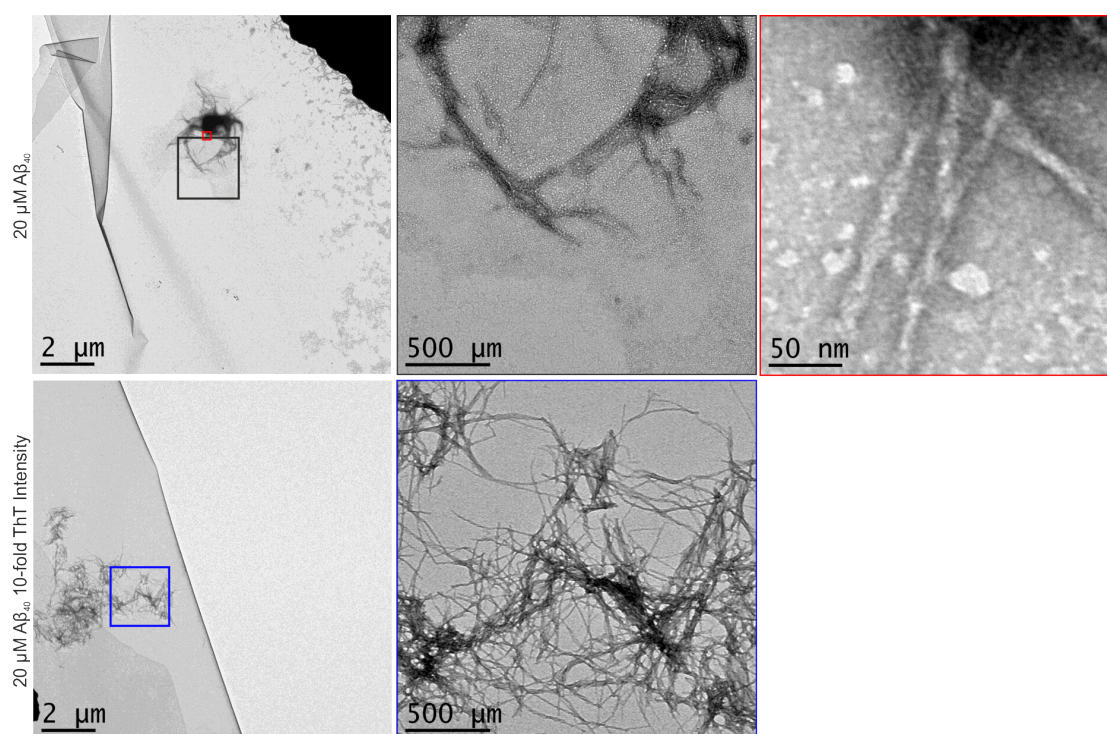


Figure 3.30: $A\beta_{40}$ aggregate morphology for different scales of ThT fluorescence. TEM images of negatively stained carbon coated grids with samples of $A\beta_{40}$ apo taken directly from ThT analysis after 21 h. Images on the top were from a ThT assay sample which gave a relatively low maximum ThT fluorescence (5000 AU) and images below were from a comparable ThT sample which gave a high ThT fluorescence (60,000 AU). Black, blue, and red boxes show magnified images.

Fibrillar aggregates are present in both samples, however are there differences in their distribution. For the low-intensity sample (Figure 3.30, top row) the fibril deposit is very clumped whereas the high-intensity sample (Figure 3.30, bottom) show well dispersed fibrils. This could affect ThT binding as there are more binding sites accessible in the

dispersed fibril sample, thus this could explain the higher fluorescence levels. Moreover, for the low-intensity sample, white circular deposits are visualised, (Zoomed image, Figure 3.30, red box). It has been suggested these are oligomers which could also be a contributing factor to the lower fluorescence observed as there was less protein in fibrils for ThT binding. Both the low-intensity and high-intensity samples were prepared similarly, and the grids were prepared after 21 h when a steady state of fluorescence was reached. The contrasts observed show the sensitivity of $A\beta_{40}$ amyloid formation to minor variations in sample preparation.

The sensitivity of $A\beta_{40}$ aggregation to subtle changes in solution implied the effect of different buffers - which influenced $A\beta_{40}$ aggregation kinetic reported by ThT fluorescence (Section 3.5.1) - was likely to influence $A\beta_{40}$ aggregate morphology. To test this, the aggregates formed under the ThT, fibril yield, and MS conditions (20 μM $A\beta_{40}$ in 50 mM ammonium acetate, pH 6.8), were compared to aggregates formed in NMR sample buffer (50 μM $A\beta_{40}$ in 20 mM sodium phosphate, pH 7.4) at a range of temperatures, Figure 3.31.

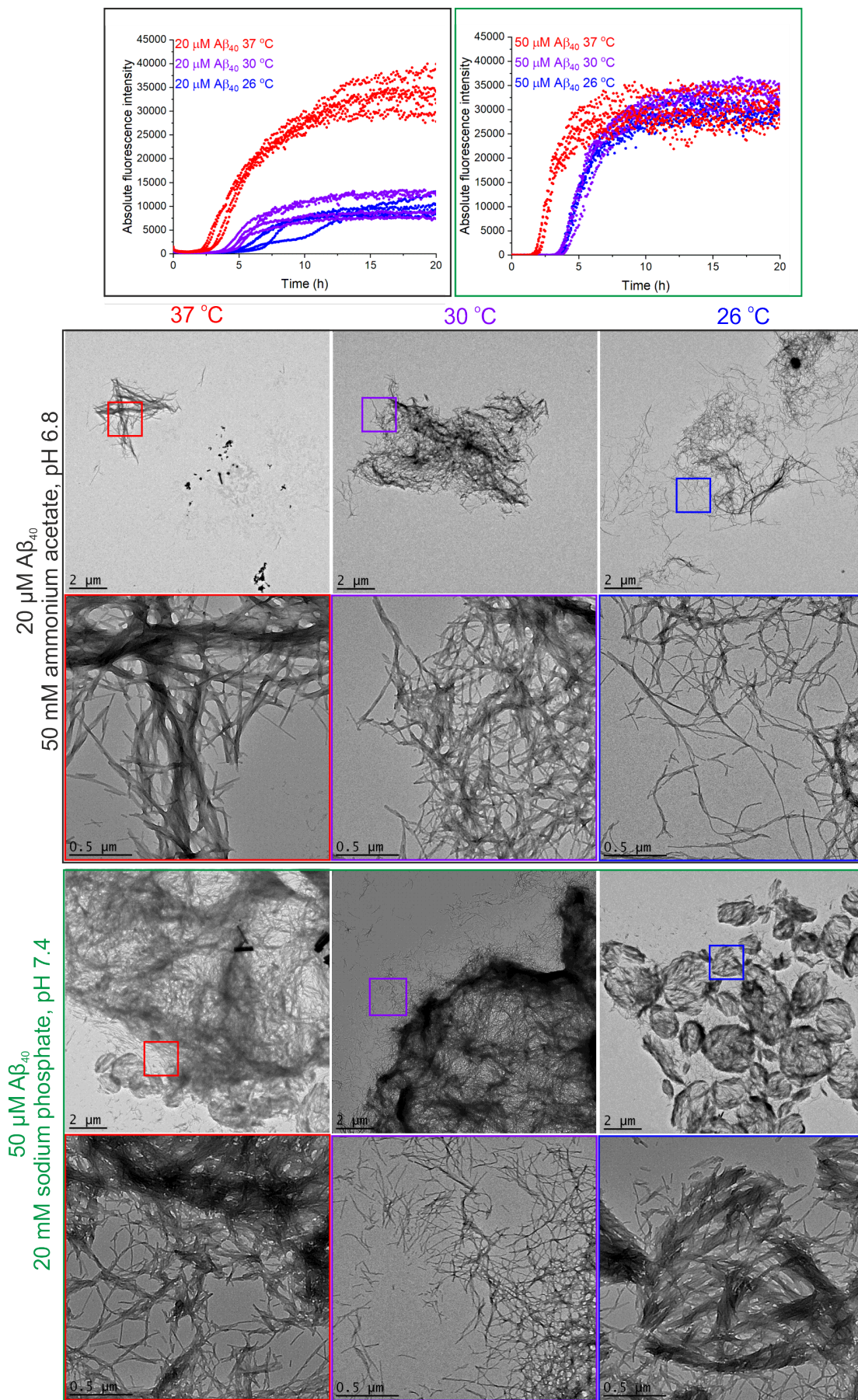


Figure 3.31: The effect of buffer on Aβ₄₀ aggregate morphology by TEM.

Caption on next page.

Figure 3.31: TEM images of A β ₄₀ aggregates on negatively-stained, carbon-coated grids. A β ₄₀ samples were prepared at either 20 μ M in 50 mM ammonium acetate, pH 6.8 (black boxes) or at 50 μ M in 20 mM sodium phosphate, pH 7.4 buffer (green boxes), in the presence of 2 % (*v/v*) DMSO and 10 μ M ThT. Samples were incubated quiescently at 37 °C (red), 30 °C (purple), or 26 °C (blue) for 21 h before grid preparation (Section 2.2.5.2). Top: A β ₄₀ aggregation profiles - by ThT fluorescence - reproduced from Figure 3.25. Bottom: TEM images of aggregates formed in each buffer at each temperature denoted. The top row of images in the black and green boxes were taken at 1,500x magnification and those below at 10,000x magnification.

The aggregation profiles recorded by ThT fluorescence in Section 3.5.1 are reproduced in this figure for convenience. The fibrils formed in ammonium acetate at each temperature tested are similar and are well dispersed within clusters. The fibrils observed at 10,000x magnification - for fibrils formed in ammonium acetate - at 37 °C (zoom of red box), are thicker (~20–45 nm) than those observed at the lower temperatures (10–15 nm). Fibrils which were formed in the sodium phosphate buffer contrast to those formed in ammonium acetate. Here the fibril clumps have more defined edges with lots of short (40–85 nm) fibrils forming ringed arrangements surrounding clusters of fibrils.

NMR data collection - later in this work - was conducted at 5 °C, however, no fibrils were observed in TEM samples prepared in NMR buffer at this temperature after one week.

Overall, these results confirm that fibrillar aggregates are formed in both the ammonium acetate buffer and the sodium phosphate buffer.

3.5.4.2 Investigation of Effect of DMSO on A β ₄₀ Aggregate Morphology

Investigation of DMSO effects on A β ₄₀ fibril morphology was conducted as it was the solvent that small molecules - which were used to modulate A β ₄₀ aggregation behaviour - are solubilised in. According to the ThT analysis (Section 3.5.1, and reproduced here for convenience) DMSO only perturbs fibril formation at 20 % (*v/v*) DMSO. However, TEM was performed to assess whether lower levels of DMSO can have effects which are invisible to ThT fluorometry. Figure 3.32 shows fibrils formed after 21 h of quiescent incubation at 37 °C of 20 μ M A β ₄₀ in 50 mM ammonium acetate, pH 6.8, with 10 μ M ThT, in the presence of increasing percentages of DMSO.

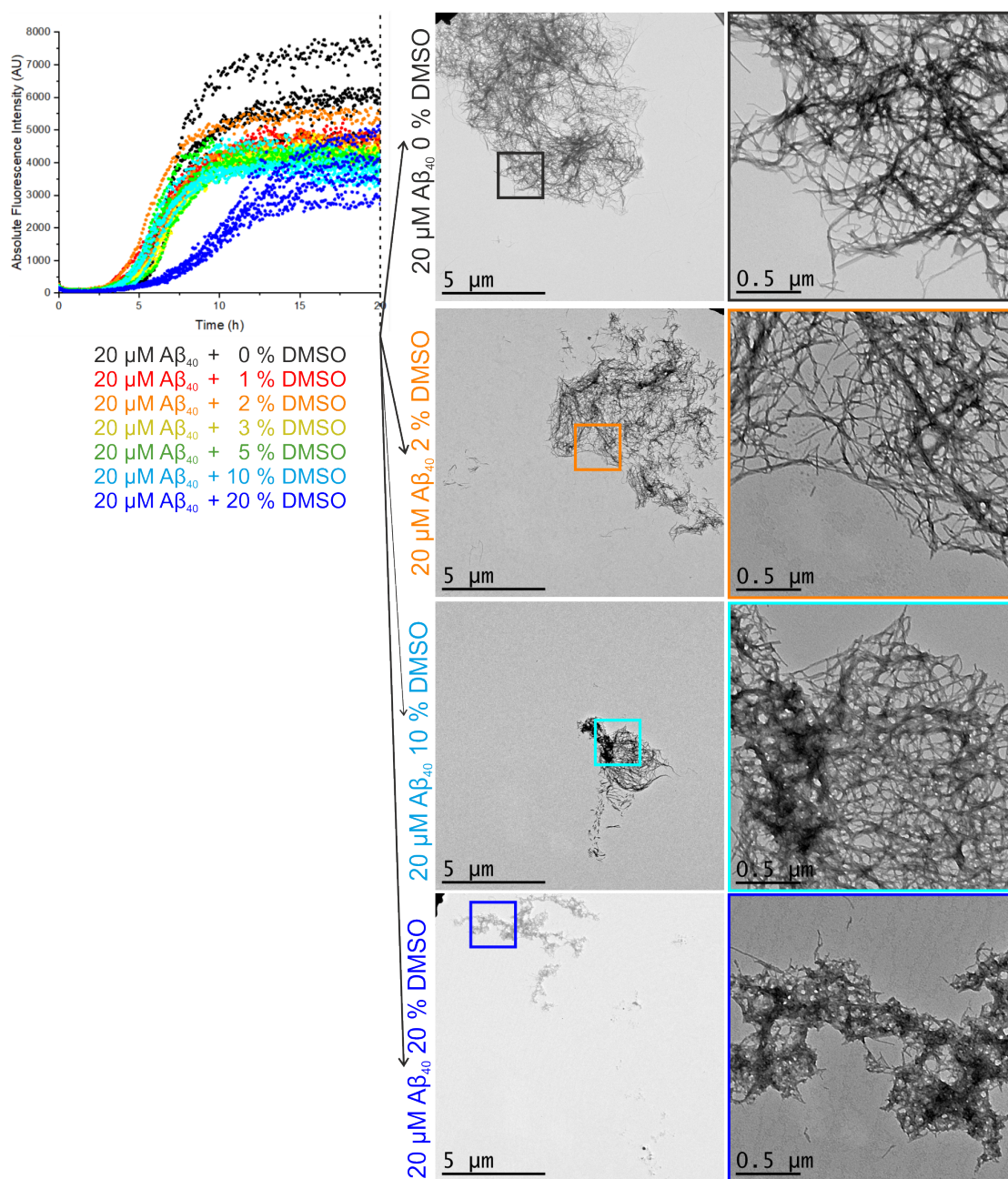


Figure 3.32: $\text{A}\beta_{40}$ aggregates formed in varying DMSO concentrations visualised by TEM.

The $\text{A}\beta_{40}$ aggregation profile by ThT fluorescence for the previous DMSO titration is reproduced here from Figure 5.5. TEM grids were made and imaged for various DMSO concentrations: 0 % (*v/v*) DMSO (black), 2 % (*v/v*) DMSO (orange), 10 % (*v/v*) DMSO (cyan), and 20 % (*v/v*) DMSO (blue).

Figure 3.32 shows that samples containing 0 %, 2 %, and 10 % (*v/v*) DMSO present typical fibrillar aggregates which are in well-dispersed clusters. In the presence of 20 %

(*v/v*) DMSO however, the aggregate clusters are more indicative of amorphous aggregates even though some fibrillar species are still clear.

The TEM data correlate well with the ThT fluorometry assay in Section 3.5.1 whereby DMSO shows no effect on A β_{40} aggregation up to 10 % (*v/v*) DMSO. Thus TEM was suitable for use in the toolbox as it was not perturbed by 2 % (*v/v*) DMSO which was present in small molecule-containing samples on application of the toolbox.

3.5.4.3 Comparison of Small Molecule Effects on A β_{40} Aggregates

Previously, TEM has been implemented to study the effects of small molecules on A β_{40} . To confirm that use of TEM was compatible with small molecule investigation of A β_{40} aggregation in this work, two compounds with well-documented effects on A β_{40} aggregation - Aspirin and EGCG - were used, Figure 3.33. As previously, ThT fluorometry samples which contained a 5:1 ratio of compound:peptide were used directly to create TEM grids.

Figure 3.33 shows representative images from samples of A β_{40} aggregates in the presence and absence of either Aspirin or EGCG (samples prepared from ThT fluorometry samples as previously described). The A β_{40} apo sample (black) shows two morphologies and is comparable to the A β_{40} apo samples previously shown (Figure 4.29). Aspirin shows no effect on A β_{40} aggregation by ThT fluorometry (reproduced in Figure 3.33), however when A β_{40} was left to aggregate in the presence of Aspirin the fibril morphology observed was surprisingly different; only thin fibrils of ~125–400 nm are observed. In contrast, when EGCG was present, aggregate heterogeneity was evident. The top panel shows within a single image the presence of short, clumped fibrils with a long narrow fibril across the grid. There is also evidence of oligomeric species, which were prevalent across the entire grid and exemplified in the middle panel. This is consistent with previous literature in that EGCG is known to cause A β_{40} to form off-pathway aggregates. The bottom panel shows an extended fibril indicating that not all of the A β_{40} is directed off of the amyloid pathway despite the significant decrease in ThT fluorescence when A β_{40} aggregates in the presence of EGCG (reproduced in Figure 3.33). This could explain the sigmoidal curve observed when ThT fluorescence was plotted on a relative scale (Figure 3.26).

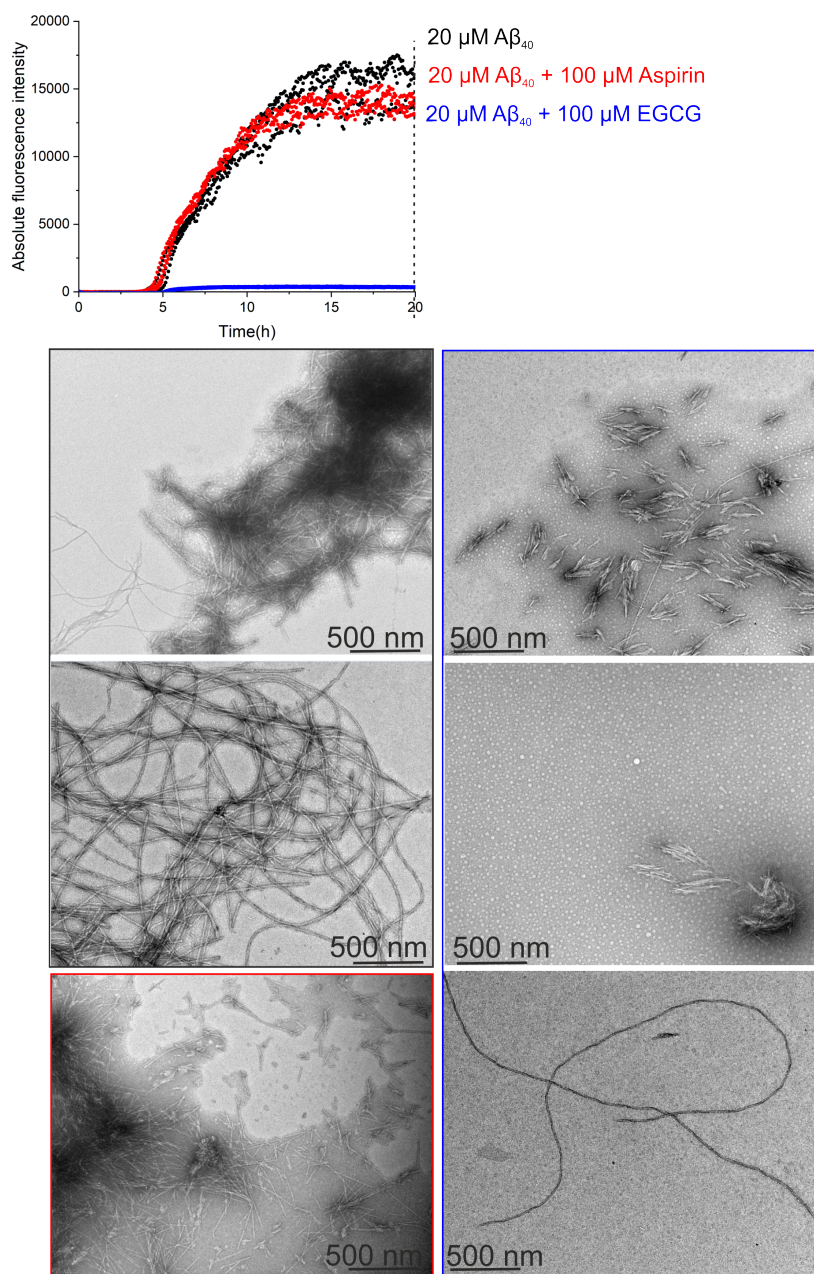


Figure 3.33: $A\beta_{40}$ aggregate morphology formed in the presence of EGCG or aspirin observed by TEM.

TEM images of $A\beta_{40}$ aggregates on negatively-stained, carbon-coated grids. Aggregates were formed from 20 μM $A\beta_{40}$ in the absence (black) or presence of 100 μM EGCG (red) or aspirin (blue) in 50 mM ammonium acetate, pH 6.8, 2 % (v/v) DMSO at 37 °C under quiescent conditions.

TEM is especially powerful in combination with ThT fluorometry data and thus is a vital part of the investigative toolbox.

3.5.5 ESI-IMS-MS Analysis of the Interactions Between Small Compounds and $A\beta_{40}$

ESI-IMS-MS was performed by Dr P. Knight and Dr Y. Xu at the University of Leeds using a published protocol [356] without optimisation. It was important to validate the reproducibility of the published method with the new samples of $A\beta_{40}$ prepared herein. The lyophilised powder was solubilised in 50 mM ammonium acetate, pH 6.8, to form a 32 μ M $A\beta_{40}$ solution. The results of ESI-IMS-MS analysis, in Figure 3.34, show the mass spectrum and drift scope of the newly prepared $A\beta_{40}$ sample.

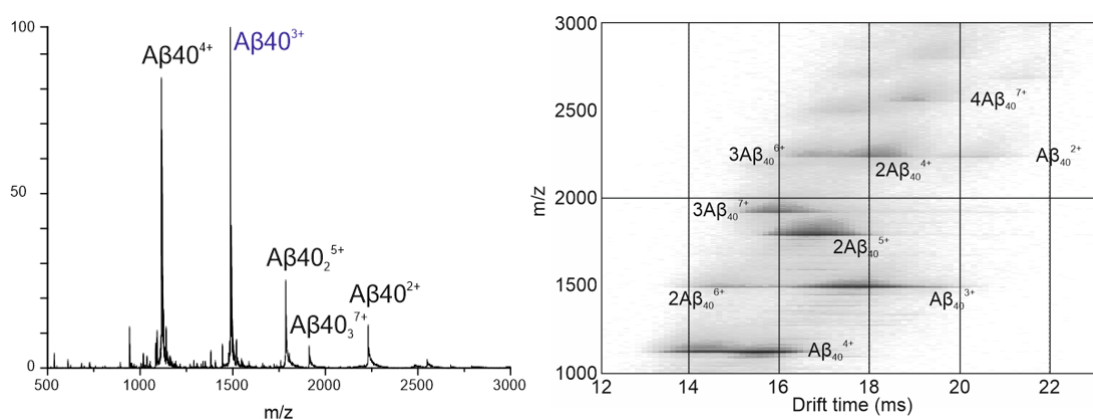


Figure 3.34: Mass spectrum and drift scope of $A\beta_{40}$.

Observation of $A\beta_{40}$ monomer, dimer, trimer and tetramer states by mass spectrometry using ESI-MS (left) and ESI-IMS-MS (right). Mass spectrometry was kindly conducted by Dr Patrick Knight (University of Leeds).

Figure 3.34 shows the expected profile of $A\beta_{40}$ [356]. There is evidence of the monomer in different charge states as well as low order oligomers; dimers, trimers and tetramers. There is also evidence of larger oligomers, but these have poorer resolution. Using IMS, the collisional cross section of species has been extracted. Analysis of these data indicated the presence of two conformations of the $A\beta_{40}^{4+}$ monomer. This is evident in the drift scope by the extended band for $A\beta_{40}^{4+}$. More compact species have a shorter drift time than more extended conformers.

Evidently ESI-IMS-MS is a powerful technique for investigation of species formed in the early stages in $A\beta_{40}$ aggregation. Following the protocol developed by Young et al. [358], two compounds - EGCG and Aspirin - were added at a 5:1 compound:peptide ratio into the $A\beta_{40}$ sample. These compounds were EGCG which is known to inhibit $A\beta_{40}$ aggregation, and aspirin which is expected not to interact with $A\beta_{40}$, Figure 3.35.

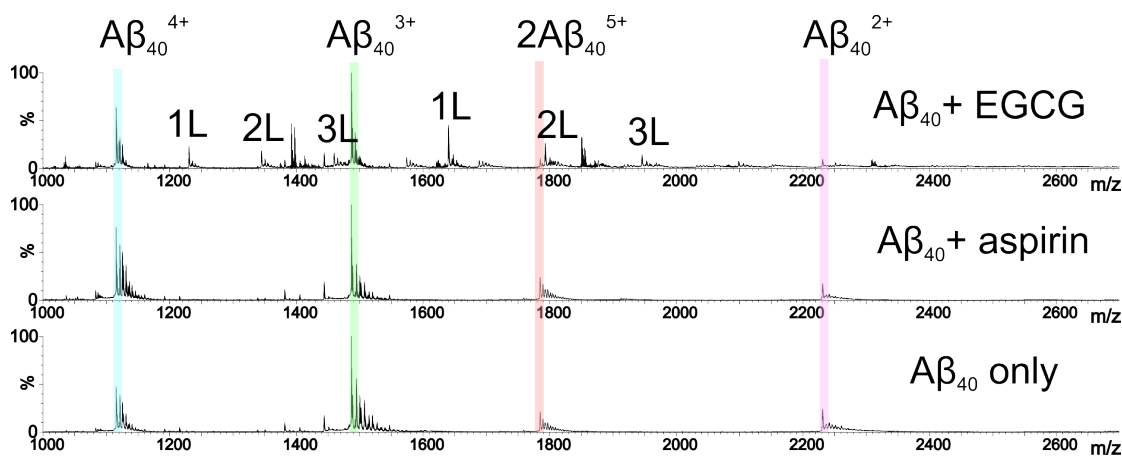


Figure 3.35: ESI-MS of $A\beta_{40}$ in the presence of EGCG or Aspirin.

$32 \mu\text{M}$ $A\beta_{40}$ was mixed at a 5:1 compound:peptide ratio in 50 mM ammonium acetate, pH 6.8 and applied to ESI-MS. Vertical bars highlighting $A\beta_{40}$ monomer with different charge states indicated (blue, green, and pink), and a dimer (red). L = ligand. Mass spectrometry was kindly conducted by Dr Yong Xu (University of Leeds).

The ESI-MS results show evidence of multiple copies of EGCG binding to $A\beta_{40}$ which is similar to published data [316], and no evidence that aspirin binds to $A\beta_{40}$. According to [316] EGCG exhibited behaviour showing non-specific binding as multiple copies of the small molecule bound to $A\beta_{40}$, implying there is more than one binding site. Conversely, EGCG may have interacted with $A\beta_{40}$ a single, specific binding site and then associated to more copies of EGCG, possibly through aromatic ring stacking interactions.

Incorporation of ESI-IMS-MS into the toolbox added insight into the stoichiometry of small molecule interactions with monomer and oligomer states. Moreover, drift scope analysis revealed the effects small molecules have on monomer and oligomer populations.

3.5.6 Tripartite $A\beta$ -lactamase Assay to Provide *in vivo* Information on $A\beta_{40}$

The final method in the toolbox is the β -lactamase tripartite assay [337], described in detail in Section 1.4.2. This provides a perspective into small molecule effects on peptide aggregation in the *E. coli* periplasm. Originally developed to screen for mutants with enhanced stability [431, 432], it was later applied to probe small molecule effects on hIAPP aggregation, [337]. A great benefit of this assay is that it does not require purified protein. However, without additional information provided by the other methods in the toolbox, the mechanism of compound action cannot be deduced.

Figure 3.36 shows the effect on *E. coli* growth when hIAPP is inserted into the β -lactamase construct compared to when a non-aggregation-prone Gly-Ser linker is included. The results show that the incorporation of hIAPP into β -lactamase reduces the ampicillin resistance of the bacteria. This implies that aggregation of hIAPP inactivates β -lactamase in the periplasm. The steric hindrance caused, prevents the two domains of the enzyme from coming together and therefore the ability to cleave the β -lactam ring in ampicillin is lost. On the addition of 200 μ M curcumin, a known hIAPP inhibitor [433, 434], some of the ampicillin resistance was regained as shown by the increase in maximum cell dilution where growth was still observed. This suggested that curcumin could interfere with and limit the extent of hIAPP aggregation as was consistent with published literature [433, 434].

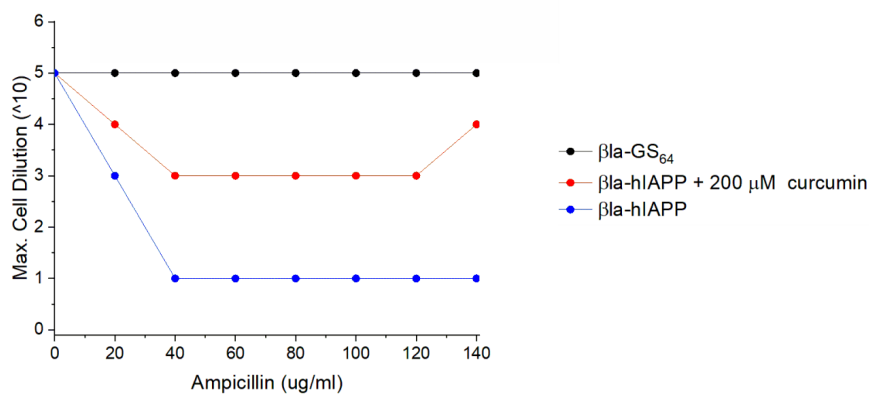


Figure 3.36: Demonstration of the tripartite β -lactamase assay with hIAPP and curcumin.

The effect of incorporation of the hIAPP sequence in the β -lactamase construct on cell survival (blue) and a non-aggregative Gly-Ser linker (black). The effect on cell growth when 200 μ M curcumin is added to the β -lactamase construct (red) shows some restoration of cell survival. n=1.

Since the focus of this thesis moved to $A\beta_{40}$ the DNA sequence of $A\beta_{40}$ was inserted into the β -lactamase construct. Preliminary results indicated that the assay needed some optimisation in order to be used to investigate compound effects on $A\beta_{40}$ aggregation. On incorporation of $A\beta_{40}$ into the construct, the bacteria were highly susceptible to ampicillin and no growth was observed after the second increment of ampicillin was added (Figure 3.37), even when the cell concentration was not diluted. It was important to observe the level of cell growth so any improvements made by compounds could be quantified.

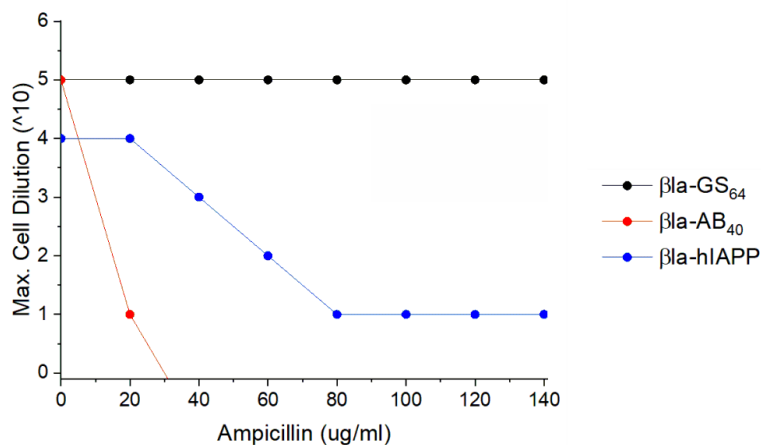


Figure 3.37: A comparison of the Tripartite β -lactamase assay with a hIAPP or $A\beta_{40}$ insert.

Effect on cell survival when the Gly-Ser linker is in the β -lactamase construct (black), and when it is replaced with either hIAPP (blue), or $A\beta_{40}$ (red). n=1.

The conditions which were varied included the reduction in percentage of arabinose used to induce expression of the construct. This was trialled under the hypothesis that there would be a lower concentration of $A\beta_{40}$ -containing β -lactamase in the periplasm if less was expressed, leading to a reduction in aggregation. To this end, the length of the incubation period after induction of expression before plating the bacteria onto solid agar was also reduced. After multiple optimisation trials, the most successful change was to decrease the amount of ampicillin added. Reducing the increment concentration from 20 μ g/ml to 2.5-5 μ g/ml created assay conditions conducive to measurement, Figure 3.38. The assay was concurrently optimised for use with $A\beta_{42}$ to enable possible extensions to this work.

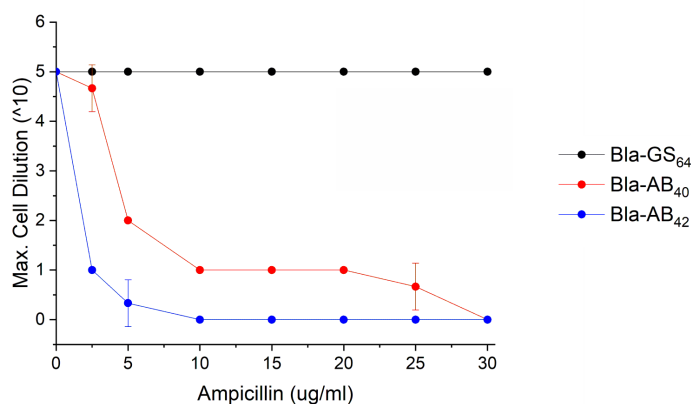


Figure 3.38: Optimised tripartite β -lactamase assay for use with an $A\beta_{40}$ insert
 Cell survival levels observed for the β -lactamase constructs with 2.5-5 $\mu\text{g/ml}$ increments of ampicillin are added. $n=3$.

Once the assay was optimised, EGCG and aspirin were used to test whether a distinction could be observed between the two compounds in the β -lactamase assay. As a positive control, a titration of EGCG was applied to the assay, Figure 3.39.

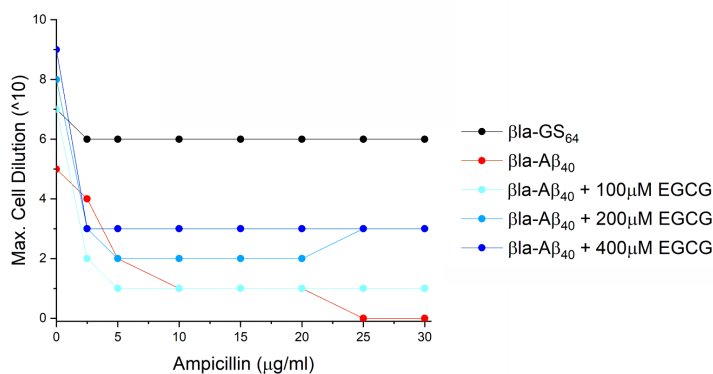


Figure 3.39: A titration of EGCG in the $A\beta_{40}$ tripartite β -lactamase assay
 Effect of EGCG on $A\beta_{40}$ aggregation through cell survival. $n=1$.

This figure showed that as more EGCG was added, there was more cell survival at higher cell dilutions. This implied that EGCG did indeed disrupt the aggregation of $A\beta_{40}$. As a negative control, 200 μM aspirin was also tested in the assay as shown in Figure 3.40 where there is little alteration observed in the growth levels of cells with the $A\beta_{40}$ β -lactamase construct in the presence or absence of aspirin, suggesting that aspirin does not interfere with $A\beta_{40}$ aggregation.

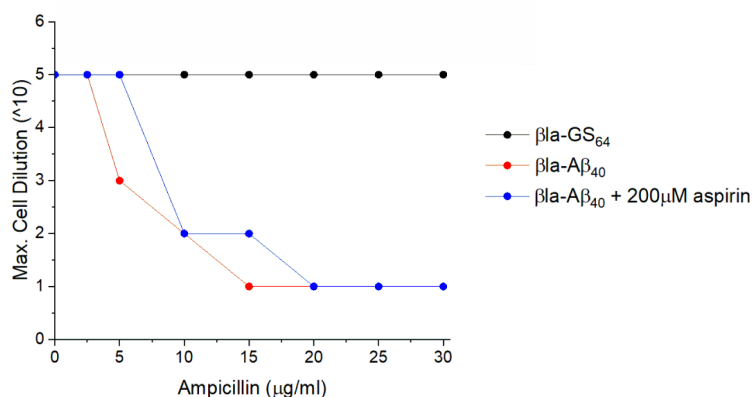


Figure 3.40: Cell survival monitored using the tripartite β -lactamase assay in the presence of aspirin

The effect of aspirin on $A\beta_{40}$ aggregation monitored indirectly using the optimised tripartite β -lactamase assay. $n=1$.

The β -lactamase assay was optimised for use with $A\beta_{40}$ and tested using EGCG and aspirin. The assay was therefore included in the methods toolbox as it probed unique information on whether small molecules can affect $A\beta_{40}$ aggregation in a more complex environment.

3.6 Discussion

The overall aim of work in this chapter was to collate a complementary set of methods to form a toolbox which could be applied as a work strategy in further research. The brief for creation of the toolbox was that it needed to be able to screen for and verify small molecule effects on amyloid aggregation and it needed to be compatible with the study of small amyloidogenic IDPs. To this end, the work presented in this chapter has not only brought together this toolbox, but has demonstrated its use and suitability for purpose.

At the outset, two small amyloidogenic IDPs, $A\beta_{40}$ and hIAPP, were selected as exemplar peptides on which the toolbox could be applied. Purification of these peptides enabled their use as a tool to aid in the preparation and optimisation of the toolbox. Both IDPs had been purified in the literature by contrasting multistep purification methods [383, 384, 396]. Although optimisation of various steps enabled effective purification

of $A\beta_{40}$, hIAPP was more elusive and thus it was decided only to proceed with $A\beta_{40}$ for this project. Further optimisation to the current hIAPP purification protocol should focus on ensuring complete cleavage of the leader-hIAPP construct and stringent separation of the leader-hIAPP-CONH₂ construct from hIAPP-CONH₂. This could be done through thorough optimisation of the Endoproteinase Glu-C V8 enzyme cleavage step, either by condition optimisation or further alterations in construct sequence to promote V8 interaction. An alternative strategy could be to use a different cleavage enzyme. Similarly to the $A\beta_{40}$ preparation, the addition of an N-terminal amino acid may not perturb aggregation but may improve purification success. For example the addition of an N-terminal Met can be found on many recombinantly produced peptides, and there are strategies for its removal if it influences peptide behaviour [435]. However, exploration of this route may be impeded by the inability to successfully produce native hIAPP which would be need for construct comparison. Such comparison would therefore rely on the purchase or production of synthetic peptides.

Purification of $A\beta_{40}$ was much more successful and the optimisation steps taken improved yield from 2–4 mg/L to 5–7 mg/L, namely the reapplication of the flowthrough and wash 1 fractions to chitin resin. Further optimisation of the $A\beta_{40}$ purification to reduce the temporal inefficiencies during the ion exchange step could be investigated. As mentioned previously, recent publications by Warner *et al.*, [436] and Huang *et al.*, [397] developed a RP-HPLC method to purify recombinant $A\beta_{40}$ (and $A\beta_{42}$). This method was quicker and higher yielding than the purification strategy used in this work but owing to the time of publication, and the effect of peptide preparation on aggregation kinetics - observed by ThT fluorescence shown in this chapter-, the method was not implemented in this study.

On successful purification of $A\beta_{40}$, the methods which make up the toolbox were chosen. Consideration of the orthogonal perspectives which each method could provide was paramount to the creation of an efficient methods strategy to investigate small molecule effects on $A\beta_{40}$, the example amyloid IDP.

Firstly the screening method chosen was the ThT fluorescence assay. Use of this assay to monitor amyloid aggregation kinetics is prevalent in the literature [321, 323, 425, 437] (and references therein) and have been used to assess small molecule effects on amyloid peptides [304, 438–441] including $A\beta_{40}$ [442, 443]. The assay was amenable to

be relatively high throughput making it suitable for use as a screen. In spite of its speed, the assay is highly data efficient in that a large amount of information can be interpreted from the ThT fluorescence data including whether aggregation is inhibited or enhanced, and if so whether the small molecule is acting during primary nucleation, secondary nucleation or elongation [76, 134]. As discussed in section 1.4.1 and in this chapter, the ThT assay is not infallible but has a propensity for false positive results when screening for small molecule inhibitors of amyloid aggregation. This was not problematic as other methods in the toolbox, such as TEM - which shows the qualitative morphology of the aggregates formed-, and the SDS-PAGE fibril yield assay - which quantified the aggregated species-, were able to verify implication reported by ThT fluorescence.

The assembled toolbox entailed both TEM and the SDS-PAGE fibril yield assay. Additionally the β -lactamase tripartite assay was included to provide more physiological insight into whether a small molecule could influence $A\beta_{40}$ aggregation. Together these methods could robustly confirm whether a small molecule was indeed able to affect $A\beta_{40}$ aggregation. The final part of the toolbox included methods which could provide insight into the ensemble of $A\beta_{40}$. ESI-IMS-MS was incorporated to reveal binding stoichiometry and oligomer distribution, and $^1\text{H}^{15}\text{N}$ -HSQC were used to probe for residue-specific information such as binding site and binding affinity. On amalgamation of data provided by all of these methods, an informed decision could be made on which compounds to take forward for extensive structural investigation by NMR (Chapter 5).

This chapter presented how each the methods were optimised for use in the toolbox and key controls were conducted using EGCG and Aspirin to verify that the toolbox could be used to find small molecule modulators of aggregation. For example, the $A\beta_{40}$ insert in the tripartite β -lactamase assay increased the sensitivity of the *E. coli* to ampicillin, the concentration of which was therefore decreased. Also buffer conditions and peptide preparation methods were considered, such as techniques to ensure peptide species were monomeric at the start of experimentation. Moreover, methods to quantify the data were developed, for example, determination of the lag time.

These experiments have demonstrated the readiness of the toolbox for monitoring compound effects on $A\beta_{40}$ aggregation. In the next chapter the toolbox will be applied to compounds which have not been studied for effects on $A\beta_{40}$ aggregation with the aim of demonstrating the application of the tool box on compounds with unknown effects on

A β ₄₀ aggregation. This toolbox also has the potential to identify novel compounds which affect A β ₄₀ aggregation which could direct later research in the field and ultimately lead to a better understanding of the A β ₄₀ aggregation mechanism.

Chapter 4

Screening for Novel Modulators of $A\beta_{40}$ Aggregation

4.1 Objectives

The previous chapter highlighted that the investigation of amyloidogenic, intrinsically disordered peptides (IDPs), such as hIAPP and $A\beta_{40}$, was possible with careful optimisation of well-established, biophysical techniques. In this chapter these methods were implemented together as a robust work-flow to identify small molecules which affect the aggregation of $A\beta_{40}$. After identifying small molecules which affect $A\beta_{40}$ amyloid aggregation, the effects the compound has on aggregation were probed. This ultimately contributes to the identification of conformations of $A\beta_{40}$ which are important for promoting or perturbing the $A\beta_{40}$ amyloid aggregation mechanism. For example, a small molecule which causes an increased rate of aggregation may cause this by skewing the conformation probability distribution of $A\beta_{40}$ into a more aggregation-prone state. On the other hand, if the small molecule stabilises an on - or off-pathway state, the rate of aggregation observed will be reduced. Irrespective of the nature of the effect on the aggregation rate, the ability of a small molecule to cause a change in aggregation in itself is of interest and could reveal more information on the mechanism of amyloid aggregation.

In order to proceed, a considered collection of small molecules were selected. Based on previous literature [444] and work conducted by Dr K. Stewart, Dr L. Young, and Dr

J. Saunders at the University of Leeds [356], five molecules were chosen as query compounds to be used in focused screening. The first part of this chapter details why these compounds were chosen and how the initial library of compounds was selected based on the query compounds. This focus was used to bias a large *in silico* screen towards finding inhibitors of A β_{40} aggregation, thereby increasing the likelihood of discovering a small molecule which had an effect on A β_{40} aggregation.

After compound selection, an initial screen was conducted using the Thioflavin-T (ThT) fluorometry assay described previously (Section 2.2.5.1) and a subset of the molecules was chosen based on the qualitative and quantitative effects on aggregation observed in the initial screen as described in Section 3.5.2. The multi-method approach described in Chapter 3 (and summarised in Figure 4.1) was used to produce orthogonal data sets which confirmed robustly which small molecules affected the aggregation of A β_{40} reliably and provided insight as to how the compound might be interacting with A β_{40} .

On the completion of these analyses, compounds which show the ability to perturb amyloid aggregation reliably may be used as future tools in the study of the A β_{40} aggregation mechanism.

4.2 Introducing Focused Screening and Compound Library Selection using ROCS.

It is impossible to test every compound in existence for an ability to modulate amyloid formation. A considered subset of compounds must be chosen to focus research endeavours in order to make the study viable, if not comprehensive. This study used focused screening to create and justify the selection of a small library of compounds based on structural similarity to compounds which were already known to modulate A β_{40} aggregation.

Compound screening is the process by which a large quantity of small molecules are evaluated as part of a methodical survey for their suitability for a specific role or purpose. A screen utilises known analytical assays with relevant controls to yield a reliable biological result but lacks the rigour used in the final method, e.g. screening data are rarely produced in triplicate. Development of screening assays to a high-throughput

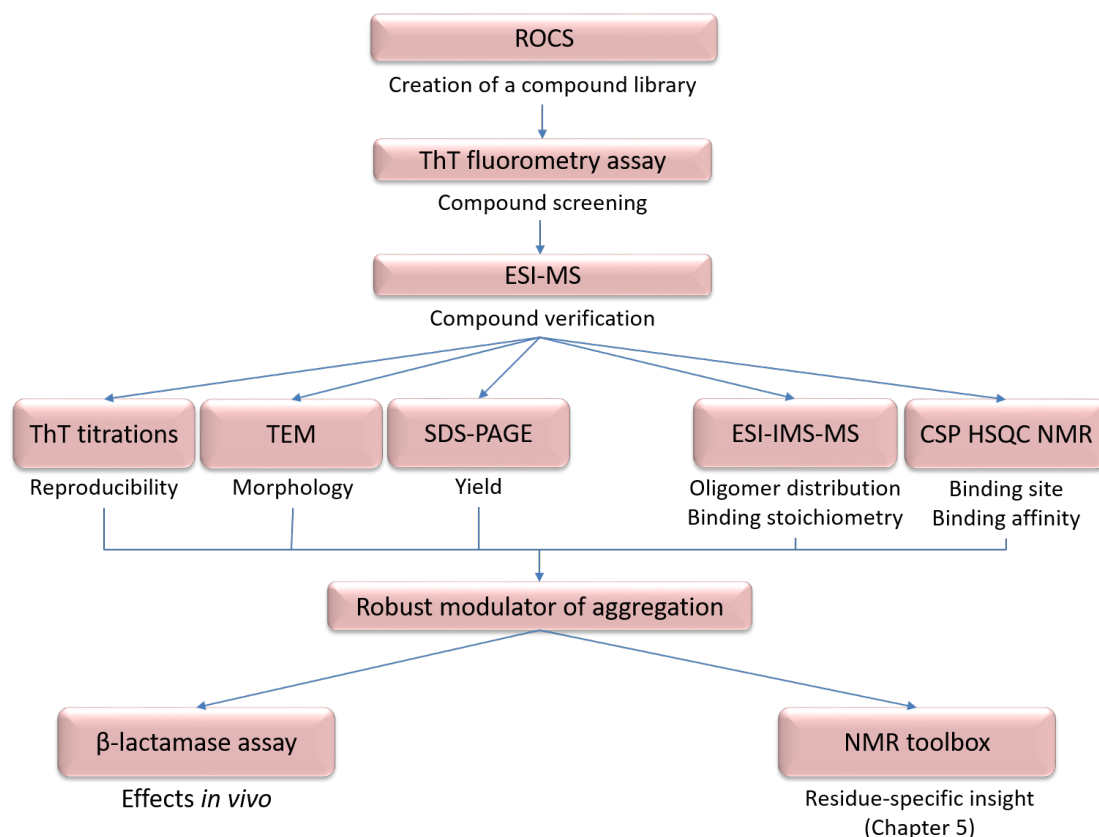


Figure 4.1: The multi-method approach to find and verify compounds which robustly modulate amyloid aggregation.

format has been implemented widely with debatable levels of success [445], from biochemical research to use within the pharmaceutical industry. Generally high-throughput (HTP) compound screening will have a hit rate of approximately 0.1 % but this can be increased when used strategically in combination with methods such as rational design, modelling, fragment screening, and prior biochemical knowledge about the system. Focused screening is an effective strategy for improving the hit rate of HTP screens to approximately 10 %. It is achieved by biasing the starting library of compounds so it is not fully randomised. Prior knowledge of compound relationships, molecular structure, interactions, chemistry, and/or reactivity can be used to skew the library towards the attribute which is being investigated.

Rapid Overlay of Chemical Structures (ROCS) analysis [446] was used to bias the screen. ROCS analysis identifies compounds which occupy a similar 3D molecular space to a query molecule e.g. a known inhibitor of amyloid aggregation. In this study, in collaboration with Dr Richard Foster (University of Leeds), five query molecules (see Section 4.2.1) were compared separately to all 50,000 members of the structurally diverse,

in-house molecular library. This led to the production of a 67-member library of small molecules which was screened biochemically for effects on $A\beta_{40}$ aggregation.

4.2.1 Selection of Known Modulators of $A\beta_{40}$ Aggregation as a Basis for Library Production

To use ROCS, a known structure (or ‘query compound’) was required for steric comparison to other compounds in the in-house library. As selection of the query compound ultimately dictated the region of compound space which was explored, it was essential to choose a compound - or set of compounds - carefully.

There is a plethora of compounds which have been noted in the field for inhibitory effects on $A\beta_{40}$ aggregation (reviewed in [381, 447–449]). Some of the more commonly cited compounds, such as EGCG, resveratrol, and curcumin, have been thoroughly investigated [381, 448, 450] and could have been used as seed molecules for the creation of a compound library. However, in light of recent publication by Habchi et al. [444], the following compounds were chosen to seed a new library of compounds which could be screened for amyloid modulatory effects. Choosing the less well-characterised molecules gave rise to the potential of exploring an exciting new area of amyloid biochemistry, with great potential which justified this more risky strategy.

Bexarotene first appeared in the literature in 1995 [451] as a potent retinoid X receptor ligand which induced apoptosis in Leukemia cells. Since then it has become an FDA-approved drug for the treatment of cutaneous T-cell lymphoma. In 2012, Crammer *et al.* [452], published that oral administration of bexarotene to an AD model mouse could stimulate physiological $A\beta$ clearance mechanisms resulting in the rapid reversal of cognitive, social and olfactory deficits leading to improved neural circuit function. This effect was hypothesised to be due to an increased level of ApoE expression caused by retinoid X receptor (RXR) stimulation. Since then there has been interest in repurposing the compound as a potential treatment for Alzheimer’s Disease [453, 454]. This led to research into the mechanism of how bexarotene can restore cognitive functions in AD models. There is evidence for bexarotene to act in a range of mechanisms including inhibiting cholesterol binding to β -amyloid peptides and the prevention of Ca^{2+} -permeable amyloid pore formation [455, 456], and direct interaction of bexarotene with $A\beta_{42}$ and $A\beta_{25-35}$ [455], as well as the amyloid precursor protein transmembrane

domain causing alterations in its helical conformation[457]. Recently the interaction of bexarotene with A β_{42} was studied and it was shown that bexarotene could suppress the primary nucleation reaction of amyloid fibril formation[443]. This is supported by other researchers using ThT and AFM methods[458]. Docking studies revealed that the basic residues His13 and Lys16 of A β are important for interaction with bexarotene [459].

As bexarotene had originally been developed primarily to interact with the RXR, it is possible that the structure of bexarotene could be optimised for interaction with A β . Since the primary species with which bexarotene interacts are transient [443], it was not possible to use traditional structure-based drug development strategies (such as molecular docking, substrate-based or structure-based design [460]) to develop similar compounds. Quasi-structure-based drug discovery (QSBDD) was implemented [444] which assumes there are some shared structural features among the binding targets of bexarotene, i.e. there are areas of similarity between A β primary nuclei and RXRs. From this, it can be hypothesised that other RXR ligands (both agonists and antagonists) may be able to interact with A β primary nuclei.

Physiologically, RXRs form DNA-binding heterodimers with retinoid A receptors (RARs) which are ligand-controlled transcription factors[461]. Ligands which bind to RARs can affect the dimerisation of RXR and RAR, reviewed in [462], by well characterised interactions [462, 463]. Due to this relationship, ligands which interact with RARs have also been considered. From work by Habchi et al. [444] a total of four, structurally-diverse compounds were chosen including an agonist and antagonist for RXRs (bexarotene and UVI3003) and RARs (adapalene and MM11253), respectively. UVI3003 is a selective antagonist of RXRs and was suggested as a valuable tool to study RXR function [464]. Adapalene is an FDA-approved drug for treating mild to moderate acne but has also been shown to have retinoid activity (reviewed in [465]). Finally MM11253 is a selective antagonist of retinoic acid receptor (RAR) leading to the inhibition of the growth of oral squamous carcinoma cells [466]. The structures of the molecules are shown in Figure 4.2.

The final molecule selected for use as a starting compound was 1,2-naphthoquinone. Early work on rifampicin [318] suggested that the naphthoquinone group may be responsible for the ability of rifampicin to inhibit A β_{40} aggregation. In 2007, Necula et

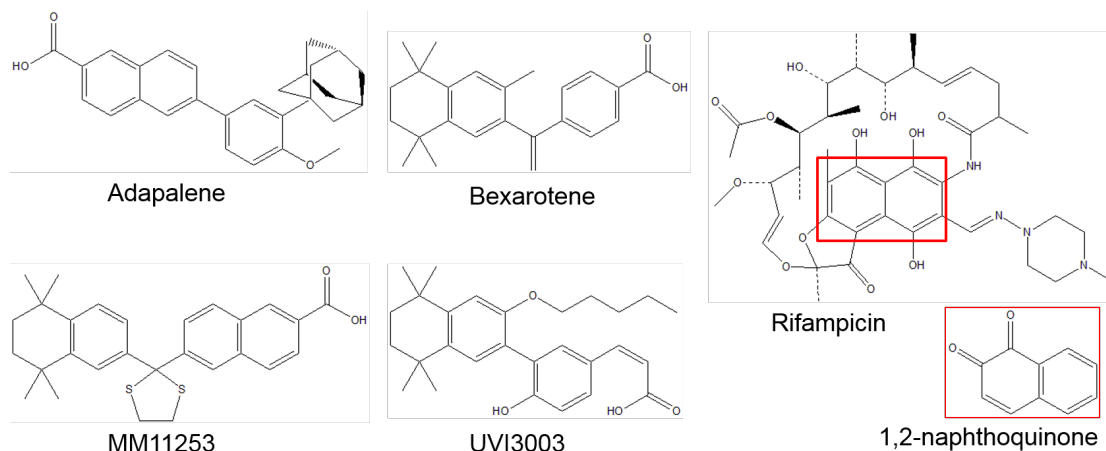


Figure 4.2: Structures of the five query compounds used as a root for the screening library.

Rifampicin is included as 1,2-naphthoquinone was based on part of this structure (red outline).

al. [467] published that 1,2-naphthoquinone could inhibit $A\beta_{42}$ oligomer formation aggregation using immuno-dot blot assays. However, in the same paper they used ThT fluorescence, light scattering and TEM to show that although 1,2-naphthoquinone could prevent oligomer formation, fibrillation still occurred. This suggested that the compound may be causing amyloid to form by a different mechanism compared with the apo protein which forms amyloid via immuno-binding oligomers. Work conducted by Nikki Green and Dr K. Stewart at the University of Leeds indicated that 1,2-naphthoquinone could also delay $A\beta_{40}$ oligomerisation during the amyloid aggregation process. The ability of a compound to alter the amyloid pathway could stabilise an alternative monomeric conformation or oligomeric structure that may reveal specific features of the $A\beta_{40}$ - $A\beta_{40}$ interaction.

Selection of five query compounds (bexarotene, adapalene, MM11253, UVI3003, and 1,2-naphthoquinone) broadens the diversity of compound steric space which can be accessed and assessed in this study. In collaboration with Dr Richard Foster (University of Leeds), each query compound was used to search for compounds with similar spatial arrangements within the 50,000 member in-house library *in silico* to create a smaller library that was suitable for biochemical analysis.

4.2.2 Compound Library Creation using ROCS

Through the use of ROCS (Figure 4.3) a selection of 67 compounds was chosen based on the query compounds chosen in the previous section (Tables 4.1 to 4.4). All the compounds were selected from the in-house library to be used in biochemical screening. Compounds were supplied as 10 mM stocks in 100 % DMSO and stored in air-tight Eppendorfs at -20 °C. Compound selection was based on the ‘ROCS Combiscore’ (the default comparator of the ROCS programme) with a sensitivity to maintaining structural and chemical diversity within the 67-member screening library. The ROCS Combiscore measures the similarity of the compound shapes as well as the pharmacophoric features [421].

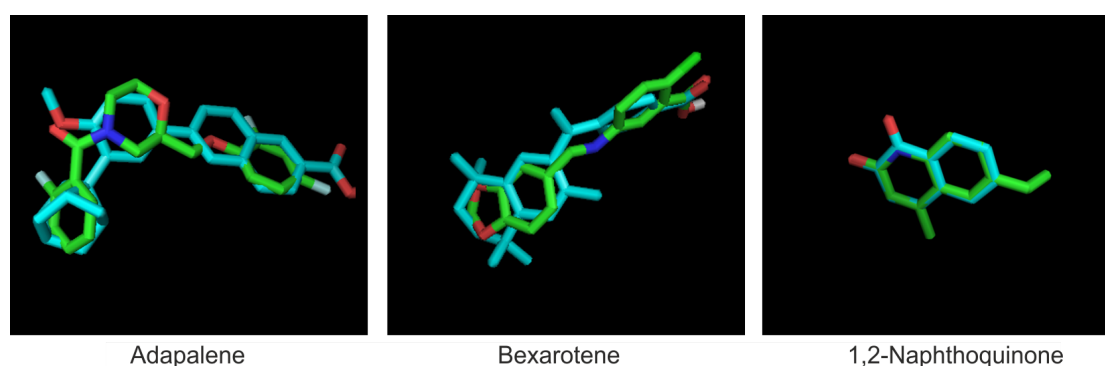


Figure 4.3: Examples of structural comparison using ROCS.

Query compounds (blue) adapalene (left), bexarotene (middle) and 1,2-naphthoquinone (right) overlaid with library compounds (green) during ROCS.

Adapted from images taken by Dr C. H. Reville.

Molecules with similar steric forms as the query molecules were then checked for PAINS (Pan-assay interference compound) motifs. PAINS molecules are defined by their activity across a range of assay platforms and against a multitude of proteins such as metal chelation, chemical aggregation, redox, compound fluorescence, cystine oxidation, and promiscuous binding. All PAINS molecules found in the ROCS analysis were excluded to increase the likelihood that any observed effects on amyloid aggregation were a result of direct interaction between the small molecule and A β_{40} . A notable exception to this is the query molecule 1,2-naphthoquinone.

The final library of compounds for screening for A β_{40} amyloid aggregation modulatory activity are shown in Tables 4.1 to 4.4. Many thanks are owed to Dr C. H. Reville and Dr

R. J. Foster (University of Leeds) for conducting the ROCS and selecting the 67-member library.

The selected compounds:

TABLE 4.1: Selected compounds based on the structure of adapalene.

Compounds based on adapalene structure			
ID	Structure	MW (Da)	LogP
Adapalene		413	6.25
A1		351	3.21
A2		359	2.57
A3		377	0.93
A4		431	1.85
A5		388	3.02
A6		345	2.78
A7		376	3.98
A8		362	2.15
A9		409	4.63

Continuation of Table 4.1			
ID	Structure	MW	LogP
A10		421	3.78
A11		361	4.02
A12		407	1.72
A13		366	3.99
A14		337	3.60
A15		344	3.28
A16		382	1.00
A17		355	3.99
A18		355	2.20
A19		369	2.76
A20		269	5.01

Continuation of Table 4.1			
ID	Structure	MW	LogP
A21		375	4.30
A22		385	1.23

TABLE 4.2: Selected compounds based on the structure of bexarotene.

Compounds based on bexarotene structure			
ID	Structure	MW (Da)	LogP
Bexarotene		348	6.38
B1		326	3.12
B2		314	3.34
B3		287	2.51
B4		371	4.22
B5		325	0.94
B6		306	3.26
B7		323	3.55

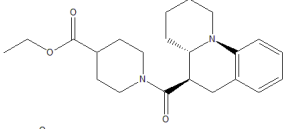
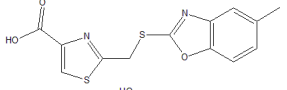
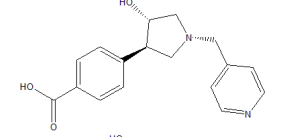
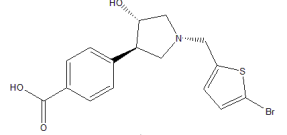
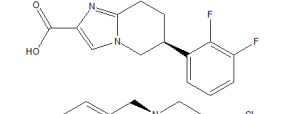
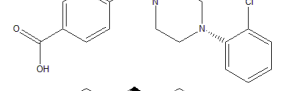
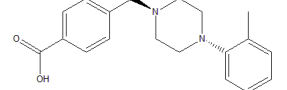
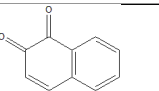
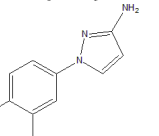
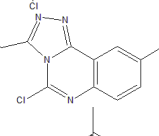
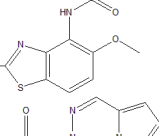
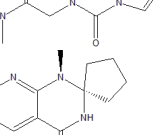
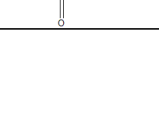
Continuation of Table 4.2			
ID	Structure	MW	LogP
B8		370	3.25
B9		306	2.96
B10		298	1.21
B11		382	2.62
B12		278	2.51
B13		331	3.80
B14		310	3.62

TABLE 4.3: Selected compounds based on the structure of 1,2-naphthoquinone.

Compounds based on 1,2-naphthoquinone structure			
ID	Structure	MW (Da)	LogP
1,2-NQ		158	1.50
Q1		288	2.71
Q2		263	2.47
Q3		236	1.23
Q4		248	1.03
Q5		217	1.44

Continuation of Table 4.3			
ID	Structure	MW	LogP
Q6		287	3.22
Q7		305	2.29
Q8		221	0.87
Q9		152	1.67
Q10		251	0.77
Q11		265	1.15
Q12		277	1.44
Q13		218	2.00
Q14		204	1.64
Q15		219	2.98
Q16		238	2.57
Q17		191	1.57
Q18		209	-0.09
Q19		203	0.39
Q20		273	0.04
Q21		207	2.01
Q22		187	3.14

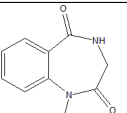
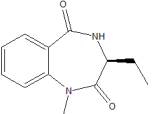
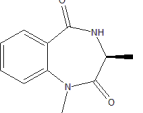
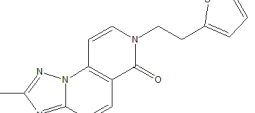
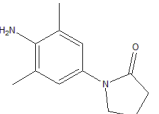
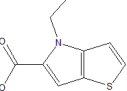
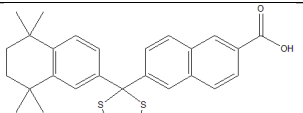
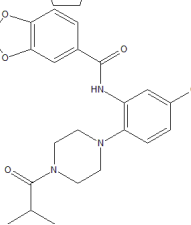
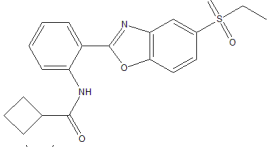
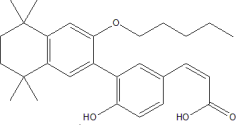
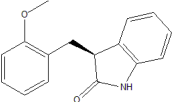
Continuation of Table 4.3			
ID	Structure	MW	LogP
Q23		190	0.05
Q24		218	1.06
Q25		204	0.53
Q26		311	1.45
Q27		205	3.13
Q28		195	2.21

TABLE 4.4: Selected compounds based on the structure of MM11253 and UVI3003.

Compounds based on MM11253 or UVI3003 structures			
ID	Structure	MW (Da)	LogP
MM11253			-
M01		430	3.56
M02		384	3.44
UVI3003			-
U01		253	02.88

The partition coefficients, logP, have been included and provide a measure of the hydrophobicity of each compound. LogP values are a component of Lipinski's Rule of 5 and represent the lipophilicity of a drug which is important for its solubility, absorption, membrane penetration, and distribution. For an oral drug, the logP should be less than five, however, a drug targeting the central nervous system should ideally be less lipophilic and have a logP of less than two. Such levels of lipophilicity make it more likely for the drug to move across lipid membranes rather than solubilising and remaining in the lipid phase.

The 67 compounds listed formed the library which was subjected to biochemical analysis for effects on A β_{40} aggregation. The following sections detail the initial biochemical screening of these compounds for their ability to perturb A β_{40} aggregation (using the Thioflavin-T fluorometric assay), followed by aggregation assessments from orthogonal perspectives to probe the compound mechanism of effect on the amyloid mechanism.

4.3 Screening for Compounds which Modulate A β_{40} Aggregation using Thioflavin-T Fluorescence

4.3.1 Initial screening of 67 compounds for A β_{40} modulatory behaviour

The compound screening method in the toolbox (devised in Chapter 3) was a ThT fluorescence-based assay (described in Section 1.4.1 and justified in Section 3.5.1). This assay reported on the aggregation kinetics of A β_{40} aggregation by fluorescence emission at 480 nm. As described previously (Section 1.4.1), the assay was compatible with the use of compounds solubilised in DMSO (Section 3.5.1).

To screen the 67-member library for effects on A β_{40} aggregation, a series of 96-well plates were prepared. On each plate nine compounds were tested alongside a compound-free, A β_{40} sample positive control (Figure 4.4). Each sample was prepared as 20 μ M A β_{40} (from a 4.7 M stock in 100 % (*v/v*) DMSO), in 50 μ M ammonium acetate, pH 6.8, with 10 μ M ThT (from a 1.2 M stock in H₂O), and 100 μ M compound (from a 10 mM stock in 100 % (*v/v*) DMSO). The final DMSO percentage was adjusted to 2 % (*v/v*) DMSO. Each compound sample was aliquotted into four wells in one column of a 96-well plate (Figure 4.4) and an A β_{40} -free negative control was applied to the two wells below.

Plates were incubated quiescently at 37 °C and fluorescence was measured every 300 s for 21 h using a FLUOstar OPTIMA plate reader.

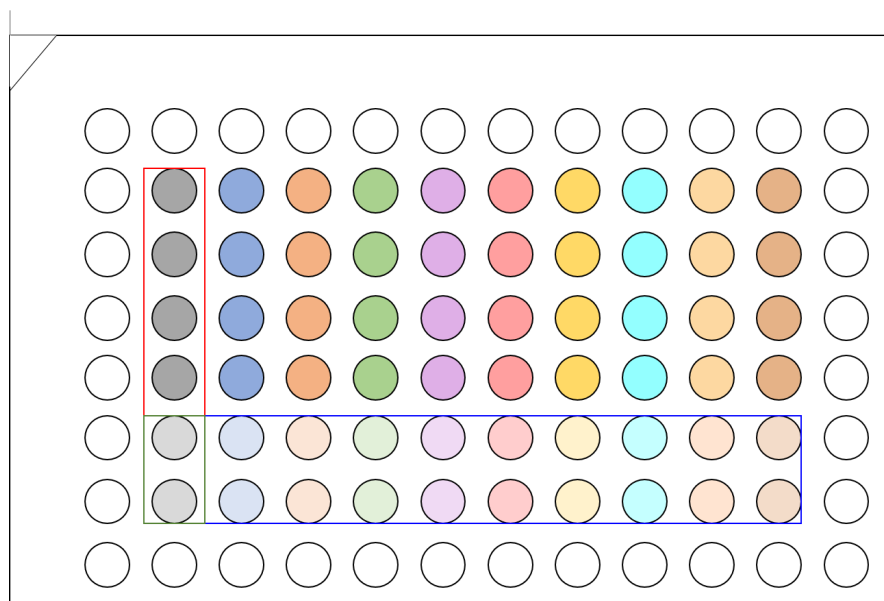


Figure 4.4: The 96-well plate layout used in the ThT screen.

The wells in the red box contain $A\beta_{40}$ only in buffer as a positive aggregation control. Wells in the blue box contain no $A\beta_{40}$ to ensure the compounds do not interact with ThT causing it to fluoresce, and wells in the green box contain no small molecule and no $A\beta_{40}$ as a negative control. The wells around the edge of the plate were filled with 100 μl of 50 mM ammonium acetate, pH 6.8 buffer only to ensure consistency in environmental conditions for peripheral sample wells.

Initially, the assay was conducted to probe $A\beta_{40}$ aggregation behaviour in the presence of the parent compounds adapalene, bexarotene, and 1,2-naphthoquinone (MM11253 and UVI3003 were unobtained), Figure 4.5. Data were plotted on an absolute fluorescence intensity scale as well as on relative axes. This is because the absolute intensity values can vary between experimental runs and thus without normalisation, plate-to-plate comparison would not be possible.

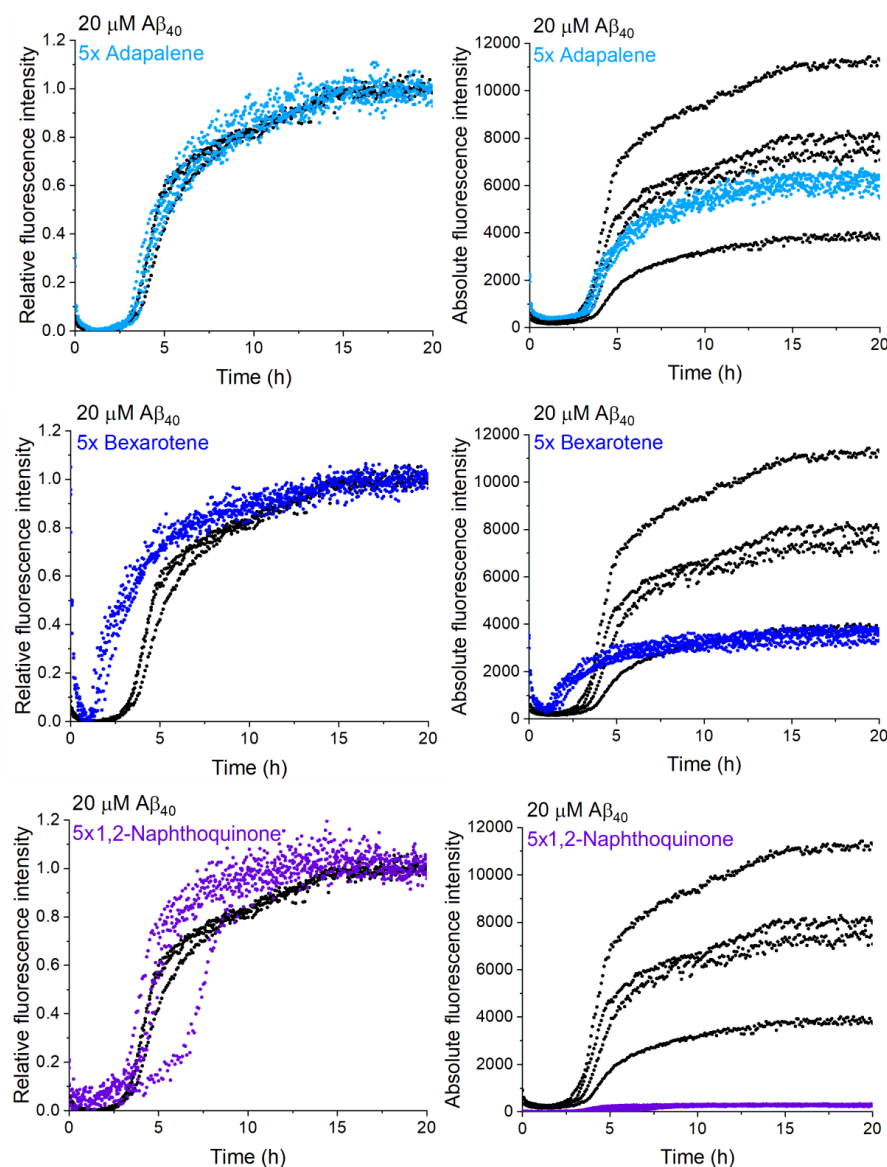


Figure 4.5: Compound screening by ThT fluorescence.

Each graph shows the aggregation kinetics for 20 μM $\text{A}\beta_{40}$ (black) and 20 μM $\text{A}\beta_{40}$ with 100 μM of each query compound 1,2-NQ (purple), adapalene (light blue), and bexarotene (dark blue). There are four examples in each trace taken from within a single experiment on the same plate. The left-hand column shows the normalised data and the right-hand column shows the absolute absorbance values. All samples are in 50 mM ammonium acetate, pH 6.8, 2 % (v/v) DMSO, 37 $^{\circ}\text{C}$, under quiescent conditions.

Adapalene - which was chosen as a query compound based on its interaction with retinoid receptors like bexarotene - showed no effect on $\text{A}\beta_{40}$ kinetics (by ThT fluorescence) but bexarotene and 1,2-naphthoquinone both affected the fluorescence measured.

Bexarotene has been shown to have an inhibitory effect on $A\beta_{40}$ aggregation, observable as an extension of the lag time observed by ThT fluorometry [458], however, the converse is observed here. For $A\beta_{40}$ - under the specified conditions - the lag time shortens by approximately 2 h. This difference may be explained by the different mechanisms which dominate $A\beta_{40}$ and $A\beta_{42}$ amyloid aggregation: primary or secondary nucleation respectively. The aim of work in this Chapter was to find small molecule modulators of the mechanism of $A\beta_{40}$ aggregation, which is evident here. Eventual structural investigation of bexarotene-induced monomer conformations may highlight important folds or chemical interactions which are important in the amyloid mechanism. 1,2-naphthoquinone did not affect the lag time observed but it did dramatically reduce the maximum level of fluorescence measured (by approximately 97 %). This behaviour was akin to that of EGCG (Section 3.5.1) and was subsequently probed using other methods in the toolbox. The dramatic effect of 1,2-naphthoquinone was encouraging for finding new small molecule inhibitors of $A\beta_{40}$ aggregation through the ROCS-generated library based on this compound.

The kinetic aggregation profiles of $A\beta_{40}$ in the presence and absence of the 67 compounds in the screening library are shown in Figures 4.6 to 4.11. ThT plots in this chapter are presented as normalised fluorescence levels to aid flow and clarity of the work (absolute intensity plots are found in Appendix A.1). During investigation and data processing, absolute values were quantified and have been included when conveying a notable effect such as for $A\beta_{40}$ in the presence of 5x 1,2-naphthoquinone.

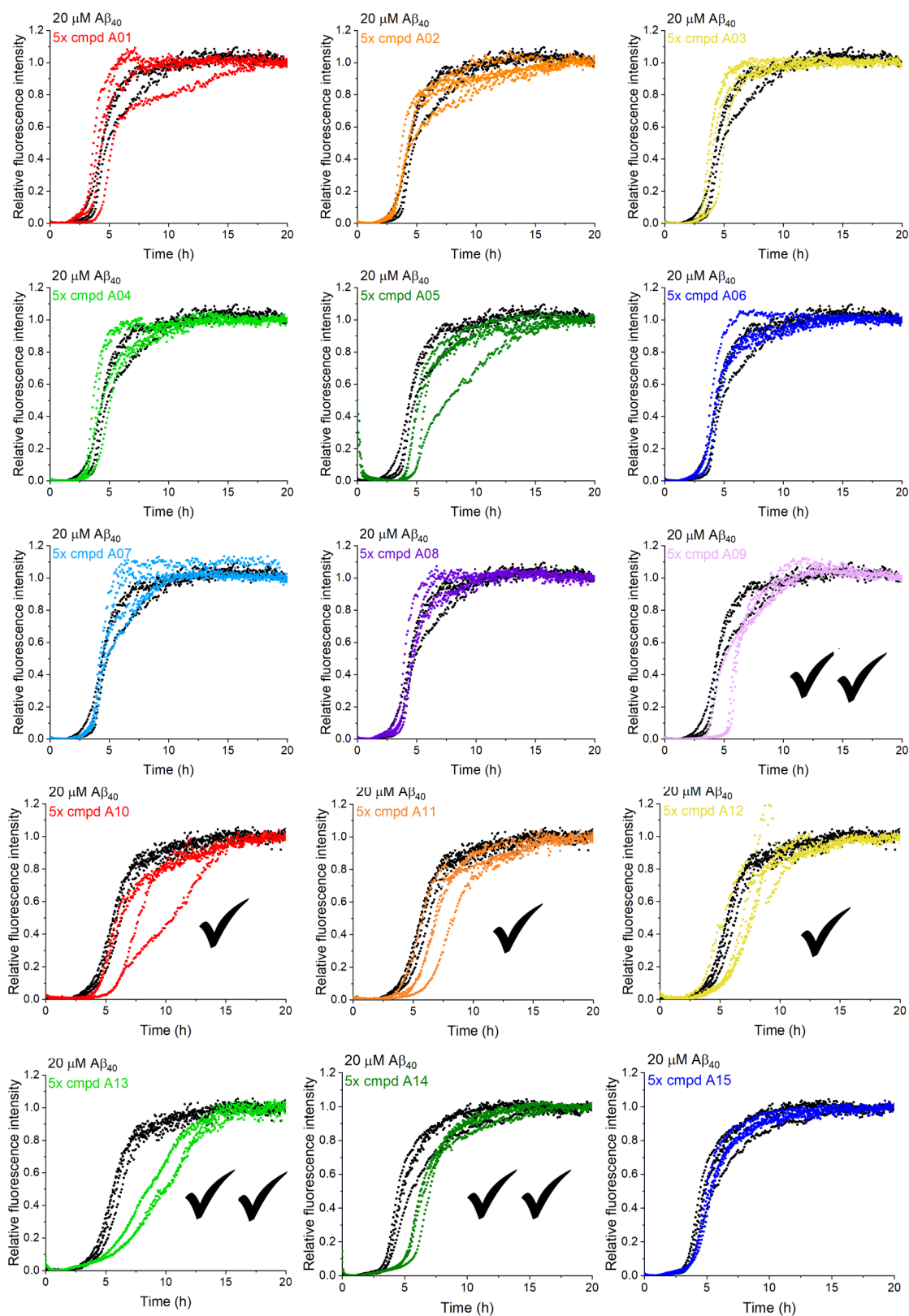


Figure 4.6: Screening by ThT fluorescence of compounds A01-A15.

Each graph shows four replicates of the aggregation kinetics for 20 μM $\text{A}\beta_{40}$ in 50 mM ammonium acetate, pH 6.8, 2% (*v/v*) DMSO (black), 10 μM ThT (black) and 100 μM of each adapalene-based compound (colours). There are four examples of each trace.

Traces where a clear (double tick) or moderate (single tick) qualitative effect on aggregation is observed are indicated.

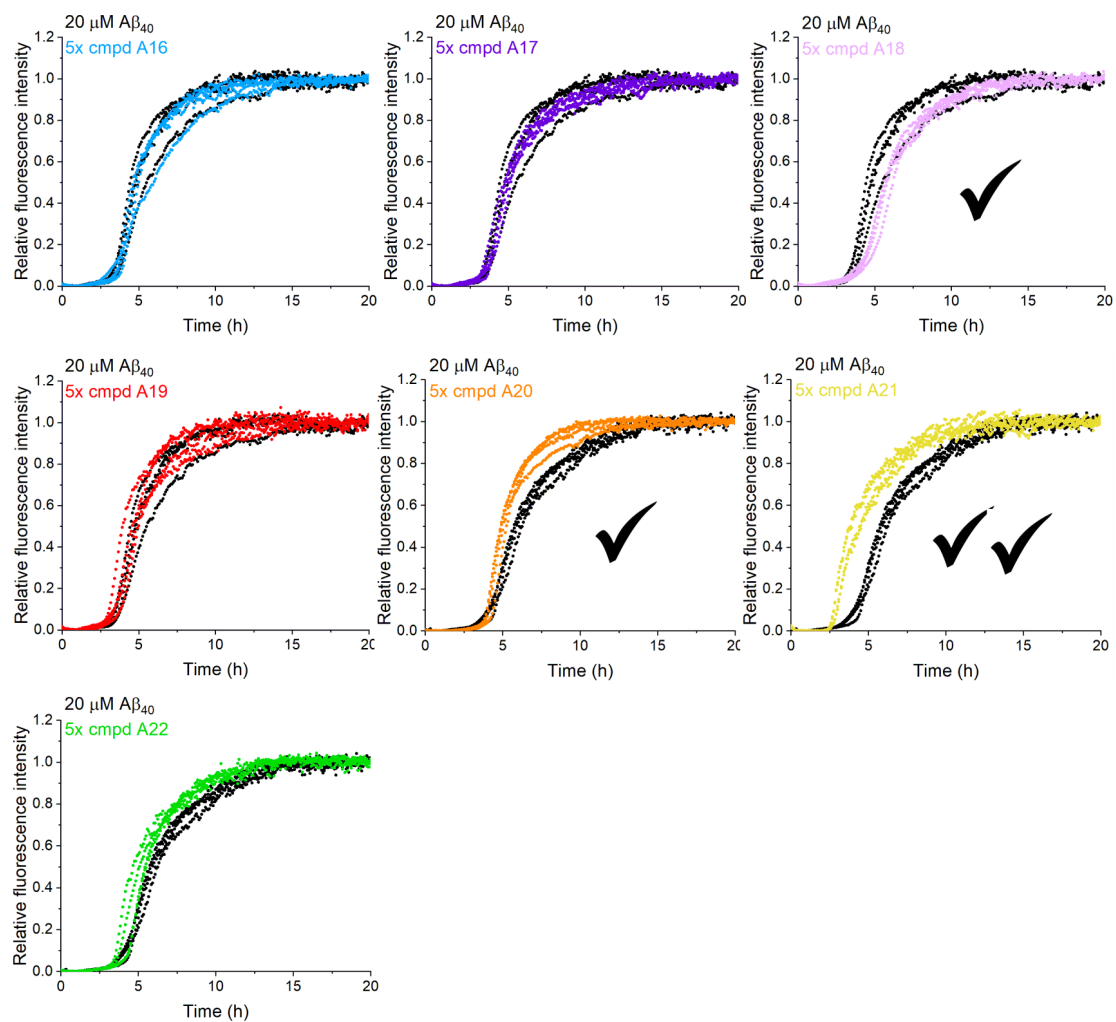


Figure 4.7: Further screening by ThT fluorescence of compounds A16-A22.

As described in Figure 4.6.

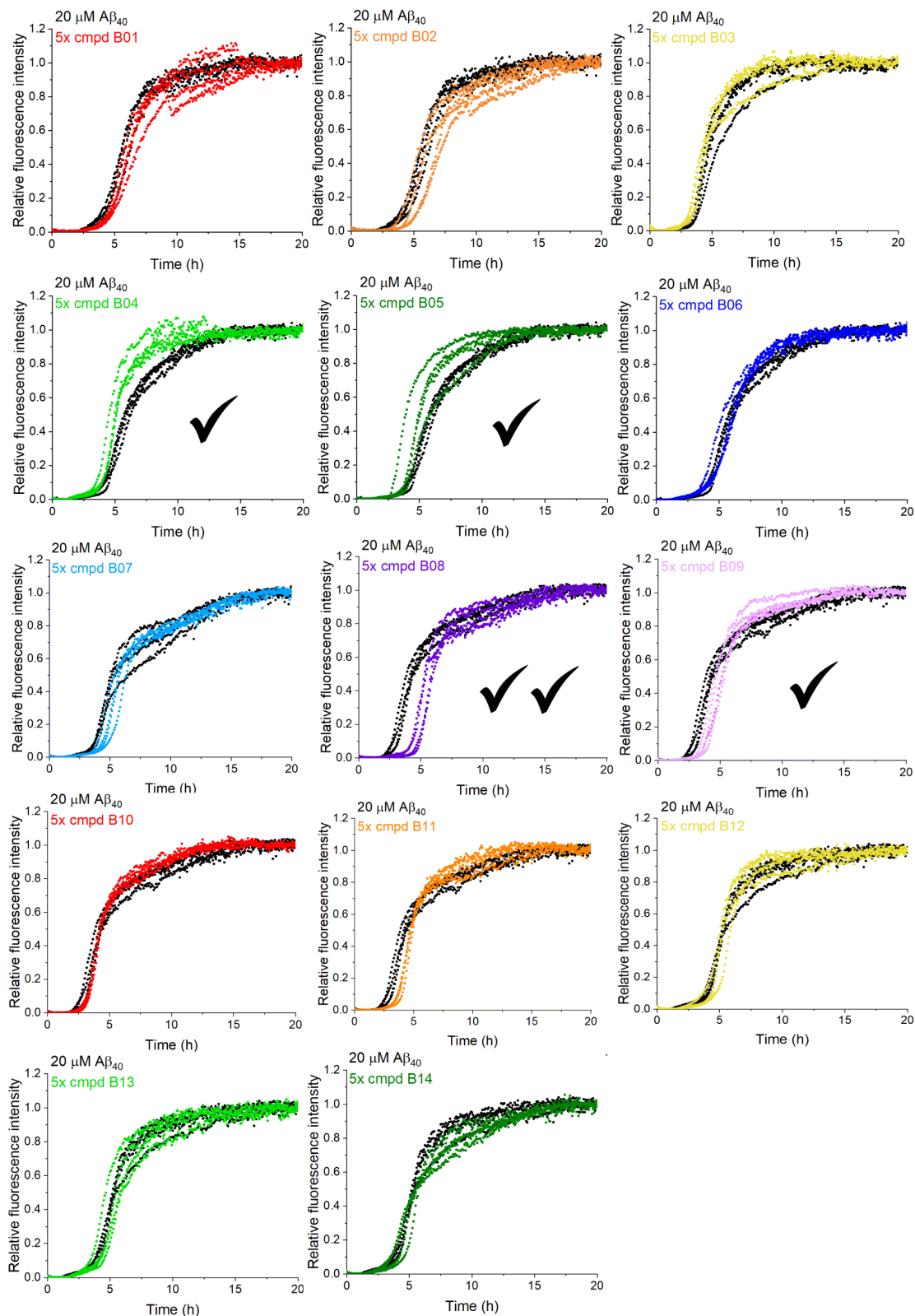


Figure 4.8: Screening by ThT fluorescence of compounds B01-B14.

As described in Figure 4.6 except the colours represent bexarotene-based compounds.

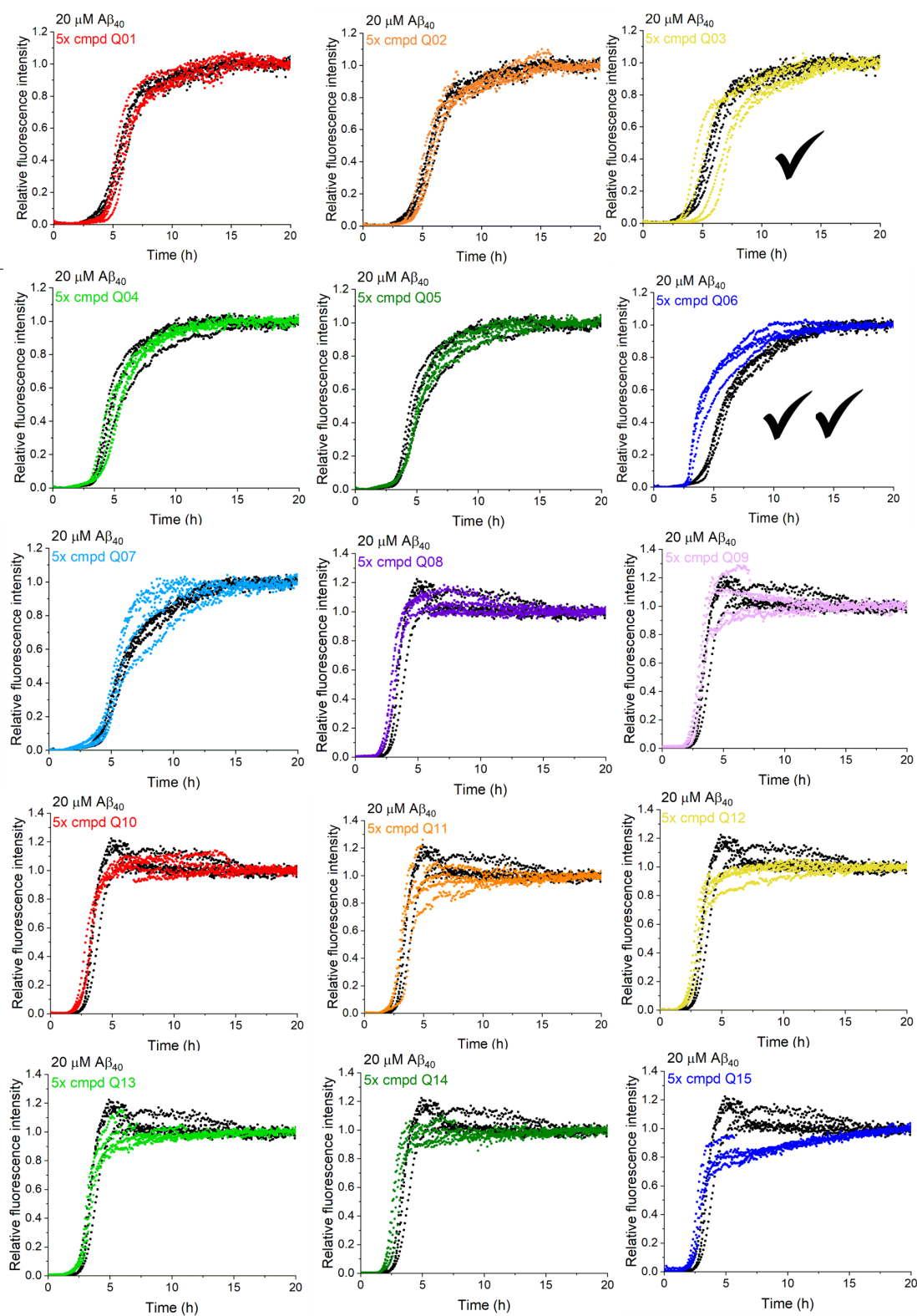


Figure 4.9: Screening by ThT fluorescence of compounds Q01-Q15.

As described in Figure 4.6 except the colours represent 1,2-naphthoquinone-based compounds.

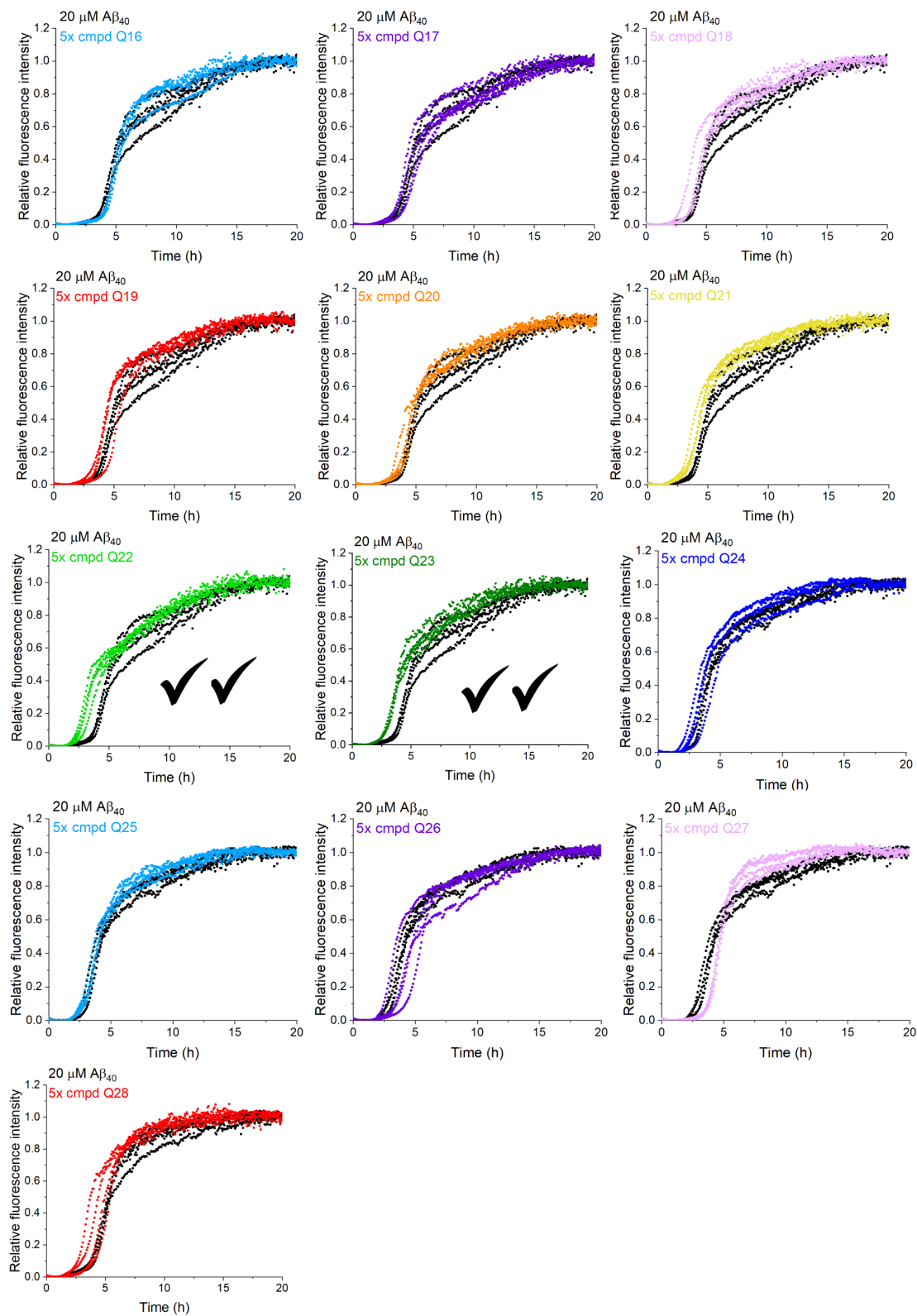


Figure 4.10: Further screening by ThT fluorescence of compounds Q16-Q28.

As described in Figure 4.9.

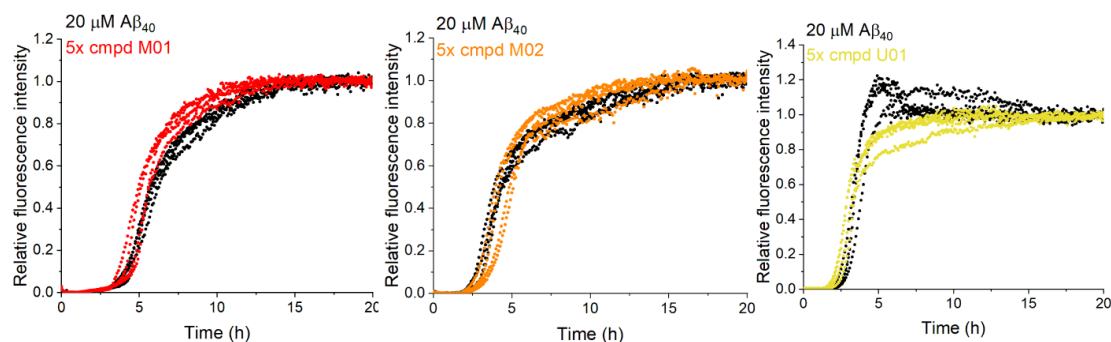


Figure 4.11: Screening by ThT fluorescence of compounds M01, M02, and U01.

As described in Figure 4.6 except the colours represent compounds based either MM11253 (M01, M02) or UVI3003 (U01).

Each graph shows the kinetic profile of $A\beta_{40}$ aggregation in the presence of a test compound compared with the $A\beta_{40}$ apo aggregation profile measured on the same 96-well plate. The differences in the kinetics of the $A\beta_{40}$ apo and $A\beta_{40}$ with compound aggregation profiles can be interpreted by visual inspection of the fibril growth curves [64].

As expected for a screen, the majority (75 %) of the compounds did not exhibit an effect on $A\beta_{40}$ kinetics by ThT fluorescence. However, eight compounds clearly perturbed aggregation (A09, A13, A14, A21, B08, Q06, Q22, and Q23), and a further 11 showed possible effects (A10, A11, A12, A18, A20, A22, B04, B05, B09, and Q03).

For example, compound A14 had an effect where the exponential increase in ThT fluorescence was delayed due to an increased lag time. According to Knowles *et al.*, [64], this indicated that compound A14 was acting at the primary nucleation stage of aggregation making it less likely that $A\beta_{40}$ monomers will come together and form oligomers which would seed fibril growth. This effect was also observed for A09, A10, A11, A12 and B08, and to some extent for A18, B09, Q03. Conversely, compounds A21, Q06, Q22, and Q23 (and possibly A20, B04, and B05) reduced the lag time observed by ThT fluorescence, indicating that the interaction of $A\beta_{40}$ with these molecules promoted amyloid aggregation. This could be achieved through influencing $A\beta_{40}$ conformation, and encouraging the adoption of amyloid-prone conformers leading to the self-association of $A\beta_{40}$.

Another type of perturbation was observed for compound A13 (and possibly A10). Here the shape of the $A\beta_{40}$ aggregation profile is altered from the typical sigmoidal curve

associated with amyloid aggregation. The gradient of the fluorescence increase was shallower indicating a reduced rate of elongation and/or secondary nucleation had been caused by the addition of A13 [64].

Based on the qualitative data collected there were a range of compounds which could have been taken forward for further investigation of their effects on $A\beta_{40}$ aggregation. To aid decision making, more objective, quantitative parameters were measured - based on the ThT screening data presented here - to enable justified compound selection.

4.3.2 Quantitative Analysis of Compound Effects on $A\beta_{40}$ Aggregation Profiles

Qualitative assessment of curve shape has typically been used to identify modulators of amyloid formation. In this thesis quantitative limits were also implemented for molecule selection based on the $A\beta_{40}$ aggregation profiles - monitored by ThT fluorescence-. The following section discusses how eight compounds were chosen for further biochemical study based on qualitative and quantitative analysis of the initial ThT screening data.

As described in the preceding chapter (section 3.5.2), three quantitative measures were considered. Firstly, the effect of the compound on the lag time was monitored as an indication of whether the compounds can interfere with the primary nucleation phase of amyloid aggregation. Secondly, the time taken to reach 50 % of the maximum fluorescence level, T_{50} , was used as an indication of the compound effects on elongation or secondary nucleation processes. Lastly, the maximum fluorescence level was measured to indicate aggregate yield or perturbed fibril morphology. To enable inter-plate comparison, all measures calculated relatively by division of the parameter value by that of the $A\beta_{40}$ apo sample from the same 96-well plate.

To measure the lag time a tangential line was extended from the steepest point on the curve (maximum first differential) to intersect with the x-axis. This was calculated using a script written by Emma Cawood (University of Leeds) and refinement of this script is noted in Section 3.5.2. The point of intersection was used as the 'lag time' and in the majority of cases this value gave a sensible approximation of the end of the lag time when compared qualitatively with the curve shape. Clear outliers and erroneous measures - caused by noise in the acquired data - were removed from analysis and such data

points were remeasured using linear fitting to the steepest part of the sigmoidal curve in OriginPro version 2018b. Use of linear fitting was less accurate than using the tangent to the maximum first differential as the linear portions of curves were variable and in some cases accounted for only around 10 % of the measured data. Figure 4.12 presents the relative changes to the lag time and statistically different data are highlighted based on a t-test ($P < 0.05$). Data are plotted according to their parent compound rather than in the randomised order they were screened.

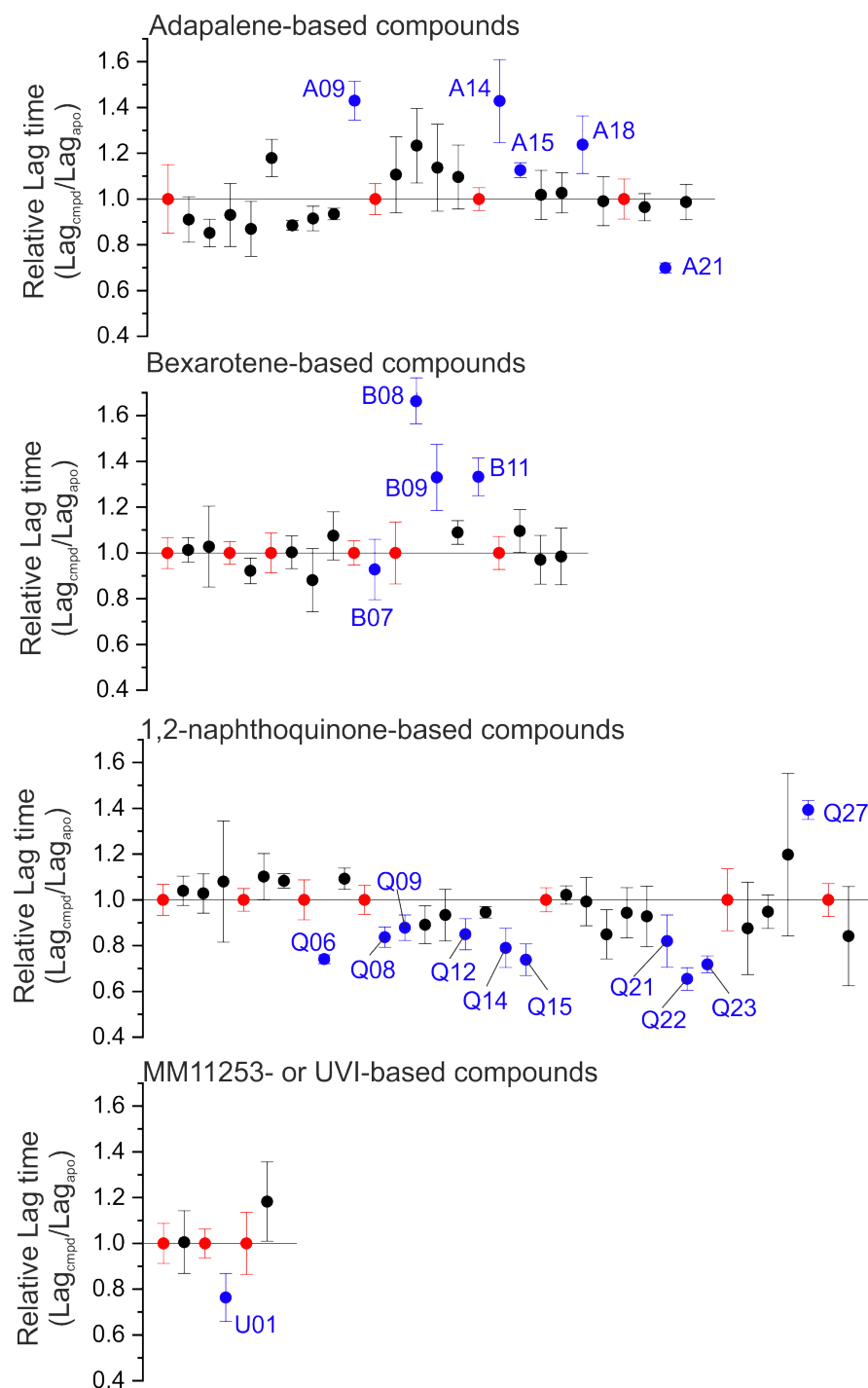


Figure 4.12: A plot of the relative lag times for $A\beta_{40}$ aggregation in the presence of each compound.

The mean of the relative effects that each compound had on the lag time observed for $A\beta_{40}$ aggregation are plotted (black) in numerical compound order (i.e. A01–A22, in the bottom graph the compound order is M01, U01, M02) compared to the $A\beta_{40}$ apo control (red) on the same 96-well plate. Error bars which show the standard deviation and compounds which affect the lag time significantly according to the student t-test ($P < 0.05$) are labelled (blue).

Compounds which show no effect on the lag time of $A\beta_{40}$ aggregation are located close to the $y = 1$ line on the plots in Figure 4.12. Compounds which have had a significant impact on the $A\beta_{40}$ aggregation lag time are labelled in blue. For example, compounds A09, B08, and Q27 increased the length of the lag phase relative to $A\beta_{40}$ alone. This implied these compounds were able to delay the formation of amyloid-prone species. Conversely, compounds A21, Q22, and U01 had the opposite effect and decreased the relative lag time of $A\beta_{40}$ aggregation, possibly through promotion of formation or destabilisation of amyloid precursor conformations.

The effects of each compound on the T_{50} (Figure 4.13) were also quantified. The T_{50} value (time taken to reach 50 % of the maximum fluorescence level) can be influenced by perturbations in curve gradient and the start time of the exponential increase in fluorescence which are caused by elongation or secondary nucleation and primary nucleation of amyloid aggregation respectively. The contributions from these can be deconvoluted by additionally measuring the relative change in lag time as described to separate the primary nucleation contribution to T_{50} measures.

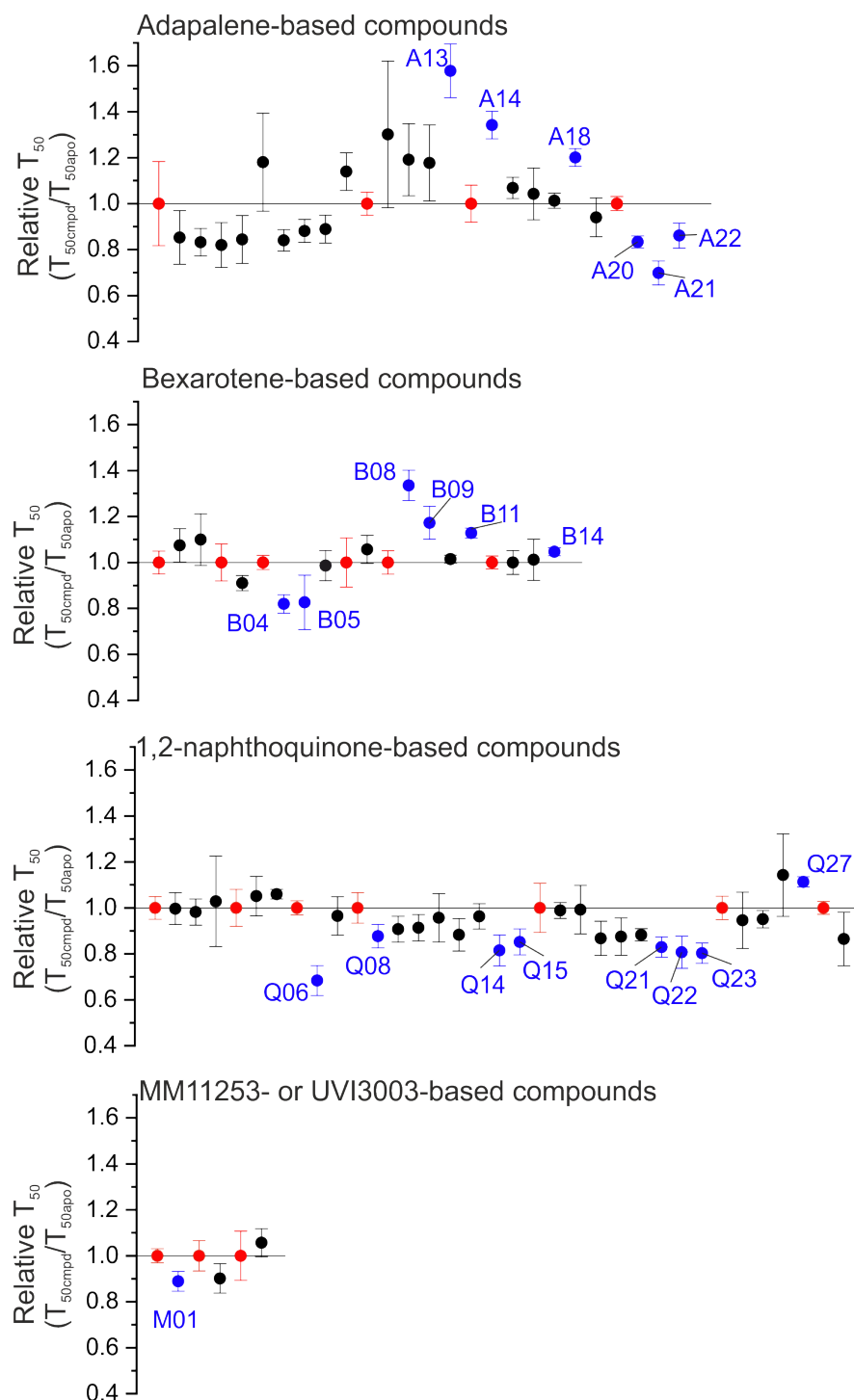


Figure 4.13: A plot of the relative T_{50} for $A\beta_{40}$ aggregation in the presence of each compound.

The mean of the relative effects that each compound had on the T_{50} observed for $A\beta_{40}$ aggregation are plotted (black) in numerical compound order (i.e. A01–A22, in the bottom graph the compound order is M01, U01, M02) compared to the $A\beta_{40}$ apo control (red) on the same 96-well plate. Error bars which show the standard deviation and compounds which affect the lag time significantly according to the student t-test ($P < 0.05$) are labelled (blue).

Compounds which had an effect on the T_{50} values ($P < 0.05$) of $A\beta_{40}$ aggregation are labelled in blue. Interestingly, the majority of compounds based on 1,2-naphthoquinone which have an effect on aggregation decrease the T_{50} value, which implied these compounds, such as Q06, Q14, and Q23, increase the propensity of $A\beta_{40}$ to aggregate, which is contrary to the effects of 1,2-naphthoquinone (Figure 4.5). Four of the six compounds based on bexarotene which showed a significant effect on relative T_{50} - of $A\beta_{40}$ aggregation - increased the T_{50} time and thus were indicative of inhibitory effects, which is the converse to the effect bexarotene (Figure 4.5).

Lastly, the effects of each compound on maximum fluorescence intensity were probed (Figure 4.14). There is a multitude of contributing and hard to control factors which affect the level of ThT fluorescence such as heterogeneity of fibrils and aggregates formed, their affinity to bind ThT, or synergistic or antagonistic contributions to the fluorescence emitted. However, for published inhibitors of $A\beta_{40}$ aggregation, the absolute fluorescence level is an indication of aggregation inhibition; this was demonstrated for 1,2-naphthoquinone in Figure 4.5. Maximum fluorescence levels can be used tentatively to imply the extent of aggregation which could be tested more reliably using the SDS-PAGE-based fibril yield assay in the toolbox (Section 3.5.3) or may be more affected by a compound-induced change in fibril morphology (which could be tested more reliably using TEM (Section 3.5.4).

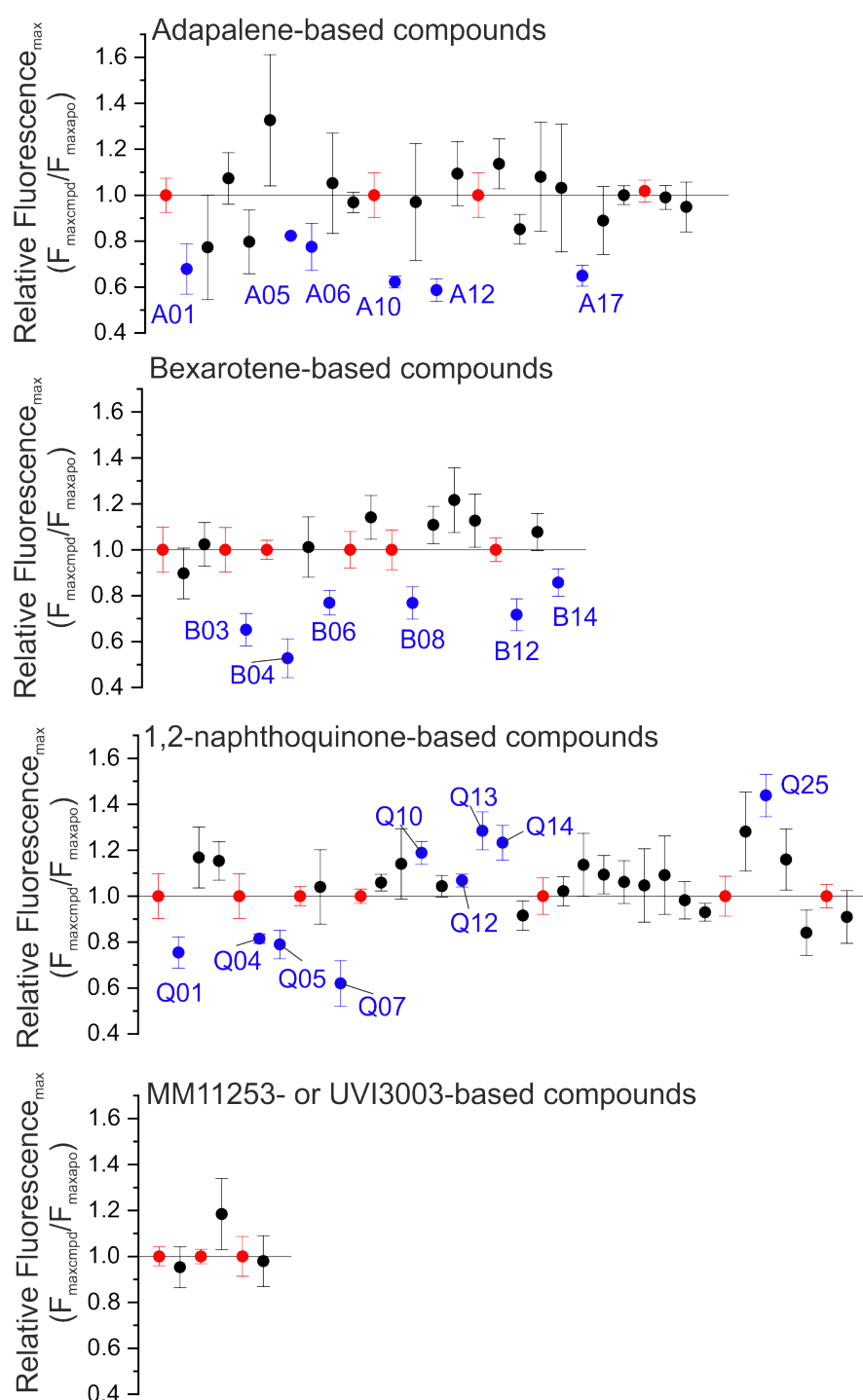


Figure 4.14: A plot of the relative final fluorescence intensities for $A\beta_{40}$ aggregation in the presence of each compound.

The mean of the relative effects that each compound had on the final fluorescence intensities observed for $A\beta_{40}$ aggregation are plotted (black) in numerical compound order (i.e. A01–A22, in the bottom graph the compound order is M01, U01, M02) compared to the $A\beta_{40}$ apo control (red) on the same 96-well plate. Error bars which show the standard deviation and compounds which affect the lag time significantly according to the student t-test ($P < 0.05$) are labelled (blue).

Many of the compounds which had a significant effect on the maximum fluorescence intensity ($P < 0.05$, highlighted in blue) showed a negative impact. This could indicate that fewer β -sheet containing aggregates have been formed. Alternatively, these molecules may interfere with ThT fluorescence when in the presence of β -folds. This can be examined in more detail on application of toolbox methods. Some compounds (such as Q10–14 and Q25) showed the opposite; an increase in maximum fluorescence intensity was observed compared with $A\beta_{40}$ alone. From conducting fibril yield experiments (Section 3.5.3) it is known that the yield of $A\beta_{40}$ into fibrils is greater than 90 %, therefore there must be a contribution from variation in fibril morphology leading to greater ThT fluorescence.

Figure 4.15 collates and represents the qualitative and quantitative data obtained for each compound. Actual quantitative measures are included in Appendix A.2. Using multiple measures (ThT signal shape, lag time, T_{50} , and maximum ThT signal) as an indication of compound effect on $A\beta_{40}$ aggregation increased the probability that compounds which were selected for further analysis would have genuine effects on aggregation.

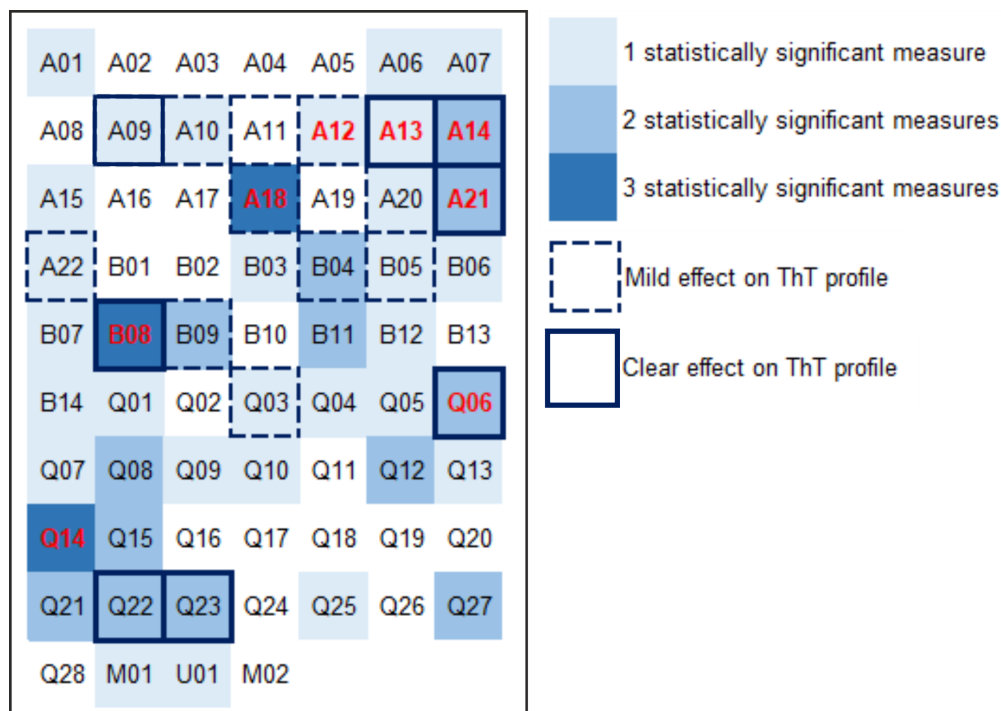
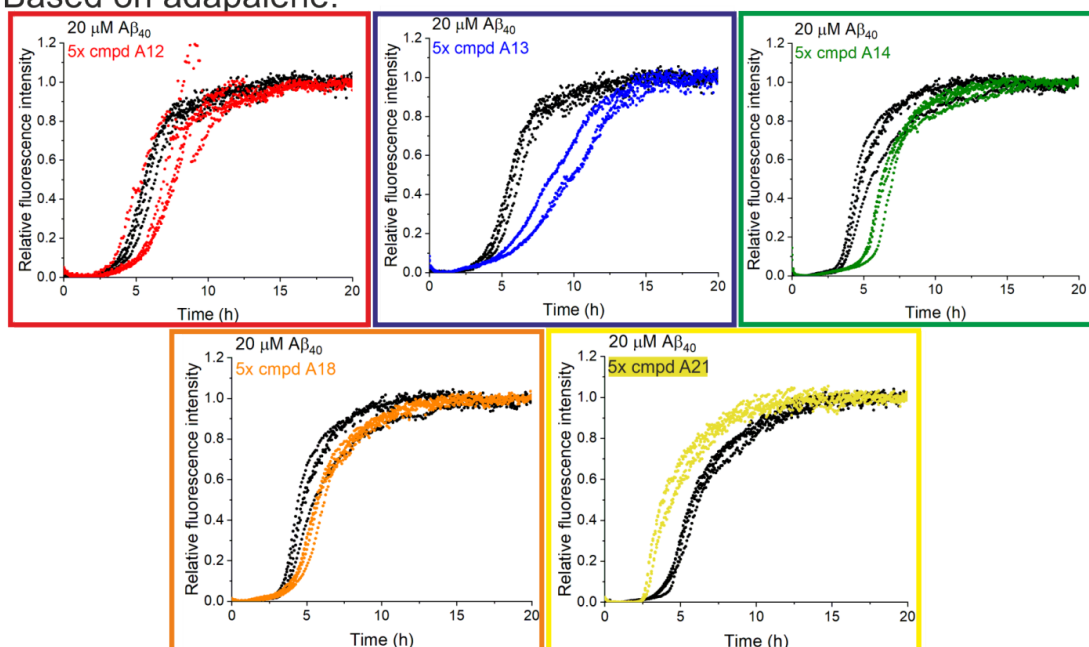


Figure 4.15: A heat map to represent extent of evidence of aggregation for each compound to perturb $A\beta_{40}$ aggregation.

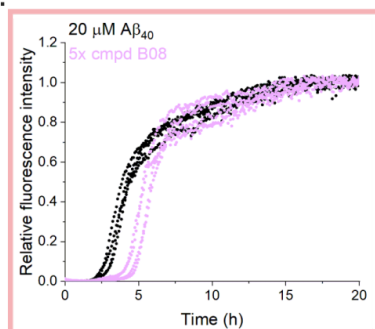
Each compound is represented by its screening name (i.e. A01). The number of statistically significant quantitative measures of aggregation perturbation are represented as shade of blue: one measure (light blue), two measures (mid-blue), or all three measures (dark blue). The extent of the qualitative indication of perturbation is represented: possible perturbation (dashed outline), or clear perturbation (solid outline). Compounds which were chosen for further analysis are shown in red text.

From this summary, eight compounds (highlighted in red) were selected for more detailed investigation of their effects on $A\beta_{40}$ aggregation; A12, A13, A14, A18, A21, B08, Q06, Q14. The ThT curves for each of these compounds are reproduced in Figure 4.16 (copied from Figures 4.6 to 4.11) for clarity. Figure 4.16 also introduces the compound colour identity which will be used throughout the rest of the chapter as a visual aid. The subsequent figure (Figure 4.17) shows enlarged structures of the compounds.

Based on adapalene:



Based on bexarotene:



Based on 1,2-naphthoquinone:

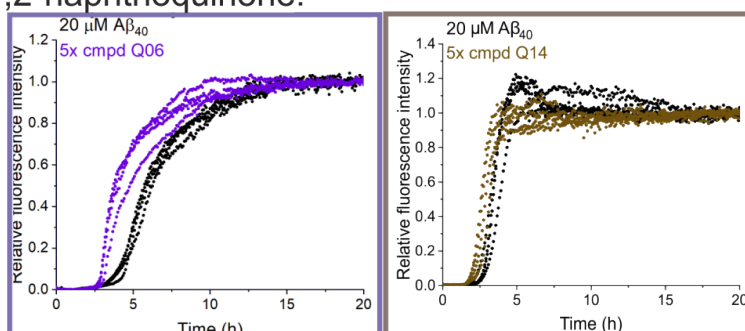


Figure 4.16: Summary of the eight compounds selected for further investigation. Reproduction of the screening results for eight compounds which are likely to be modulators of $\text{A}\beta_{40}$ aggregation and will be studied further.

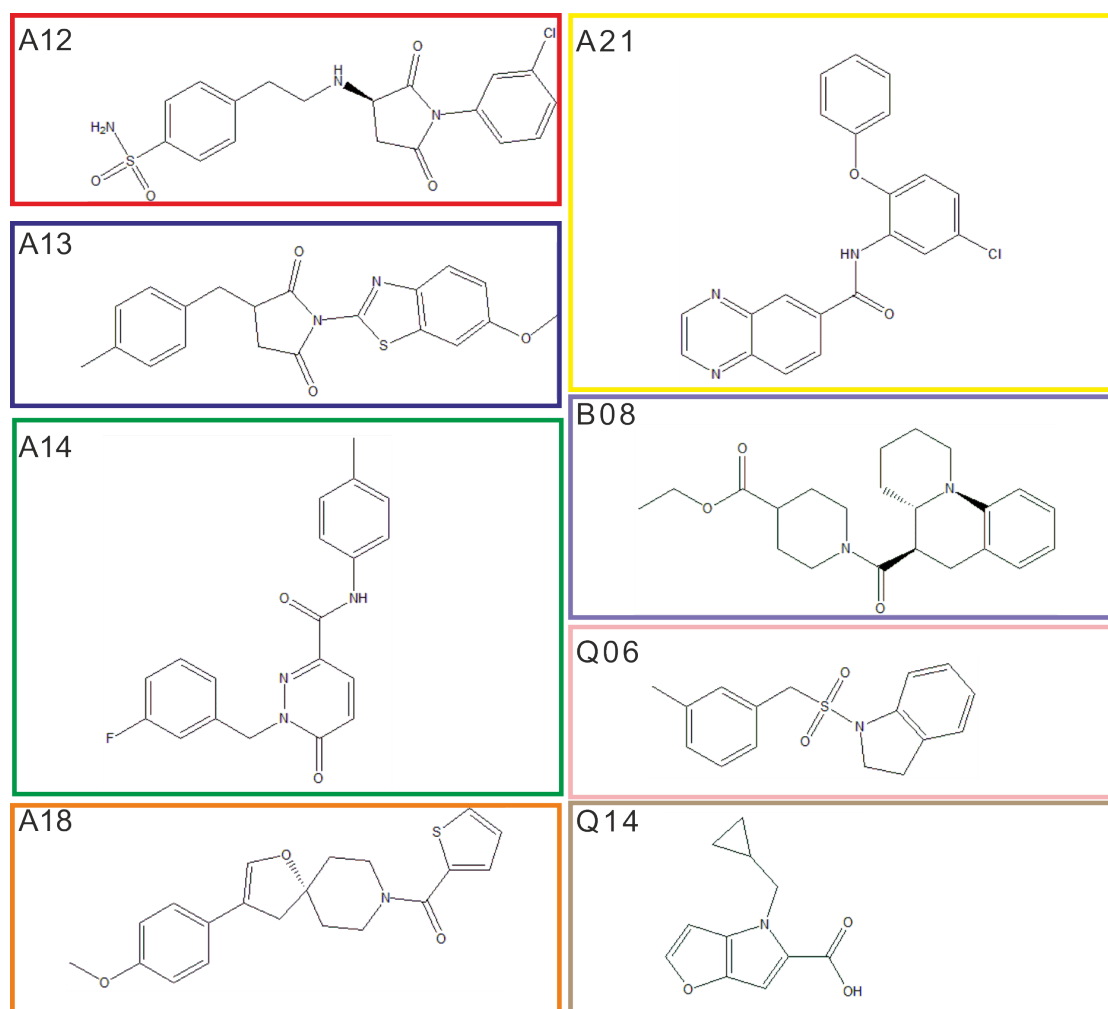


Figure 4.17: The chemical structures of each of the eight compounds selected for further investigation.

These compounds were taken forward for more detailed investigation to discover whether the effects on aggregation which were observed by ThT were reproducible, and whether other methods revealed additional insight into the mechanism of how these compounds modulated $A\beta_{40}$ aggregation.

4.3.2.1 Confirmation of Compound Identity by Mass Spectrometry

When working with molecules from compound libraries it is good practice to check the mass of the compounds which are provided to the laboratory from the library. This is because many compounds can be unstable after prolonged storage even under optimal library management. Storage of powdered compounds tends to be problematic in large scale libraries [468] due to varying powder properties (i.e. density, hygroscopicity). The

most common solution for the disparity in solid compound properties is to create standardised samples in uniform, automation-friendly vials. Typically compounds are stored at a high concentration and solubilised in DMSO [469]. DMSO is highly hygroscopic thus samples should be stored under humidity-controlled conditions to limit the potential oxidation of the stored compound. Based on the length of time spent in DMSO at a storage facility, some compounds may degrade or be chemically modified by the time they are required for biochemical screening.

Mass spectrometry was used to detect whether there were any impurities, degradation, or chemically-modified species present in the stock solution. The eight compounds were diluted from the 100 % DMSO stocks provided by the library to 2 % DMSO solutions in 50 mM ammonium acetate, pH 6.8. These solutions underwent liquid chromatography mass spectrometry (LC-MS) examination (using a 10–90 % (*v/v*) acetonitrile gradient in 0.1 % (*v/v*) TFA) conducted and processed by Dr Yong Xu (University of Leeds). The results of the analyses are presented in the top panels of Figures 4.18 to 4.24.

There were multiple mass discrepancies evident and low purity of stock compounds. To eliminate the possibility of modification and contamination during the LC-MS process, commercially-available, powdered versions of the compounds were purchased from the original library suppliers and 10 mM aliquots in 100 % (*v/v*) DMSO were created. These were stored at -20 °C in air-tight Eppendorf tubes before application to the same LC-MS analysis conducted and processed by Dr Yong Xu (University of Leeds), presented in the bottom panels of Figures 4.18 to 4.24. The new samples are denoted with an ‘a’ following the compound number to distinguish them from the library samples. It was not possible to purchase compounds A18a, B08a, or Q14a.

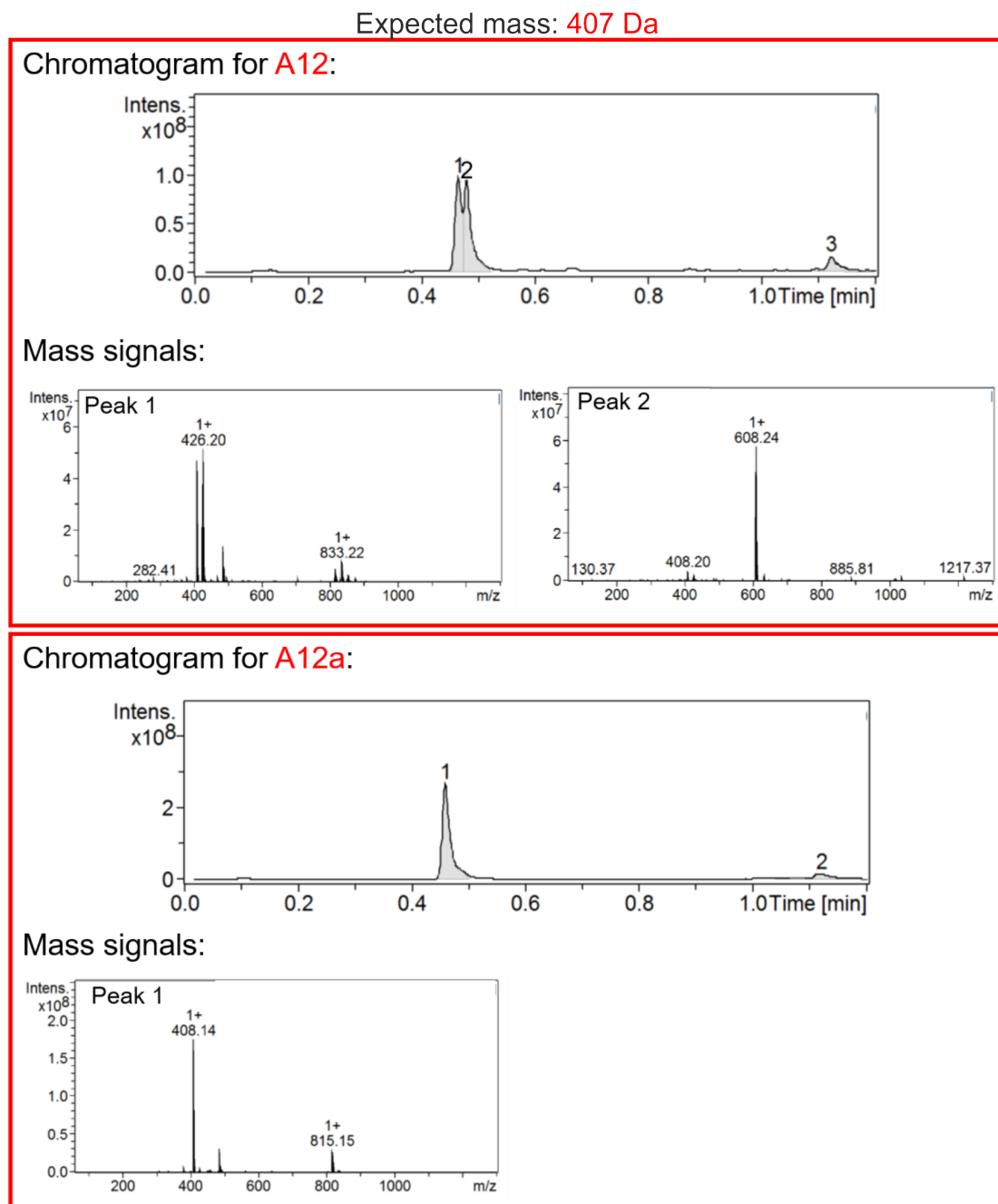


Figure 4.18: LC chromatogram and MS spectra of library compound A12 and commercial compound A12a.

LC chromatogram and MS of each peak present on the LC chromatogram for A12 (top) and A12a (bottom).

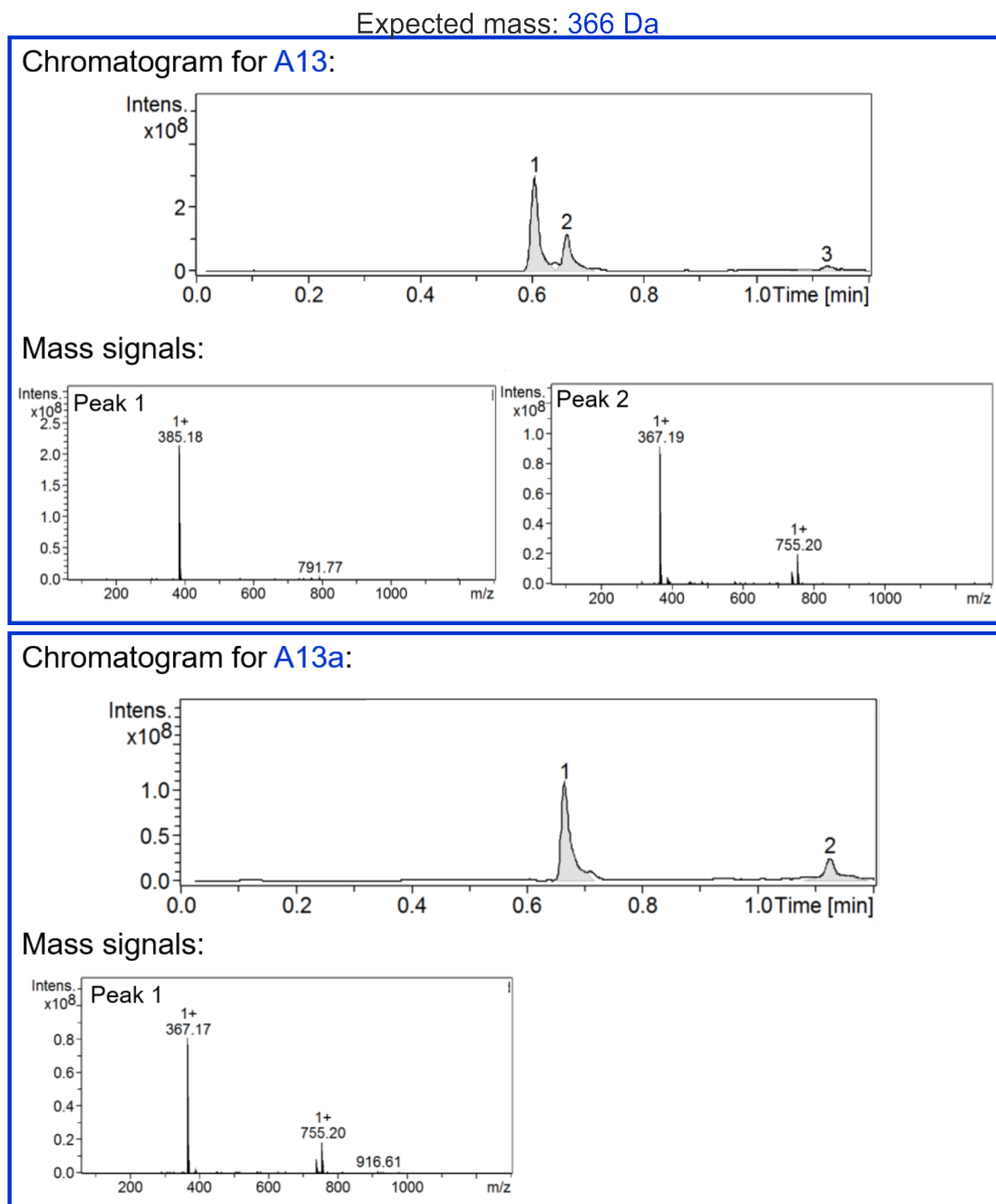


Figure 4.19: LC chromatogram and MS spectra of library compound A13 and commercial compound A13a.

LC chromatogram and MS of each peak present on the LC chromatogram for A13 (top) and A13a (bottom).

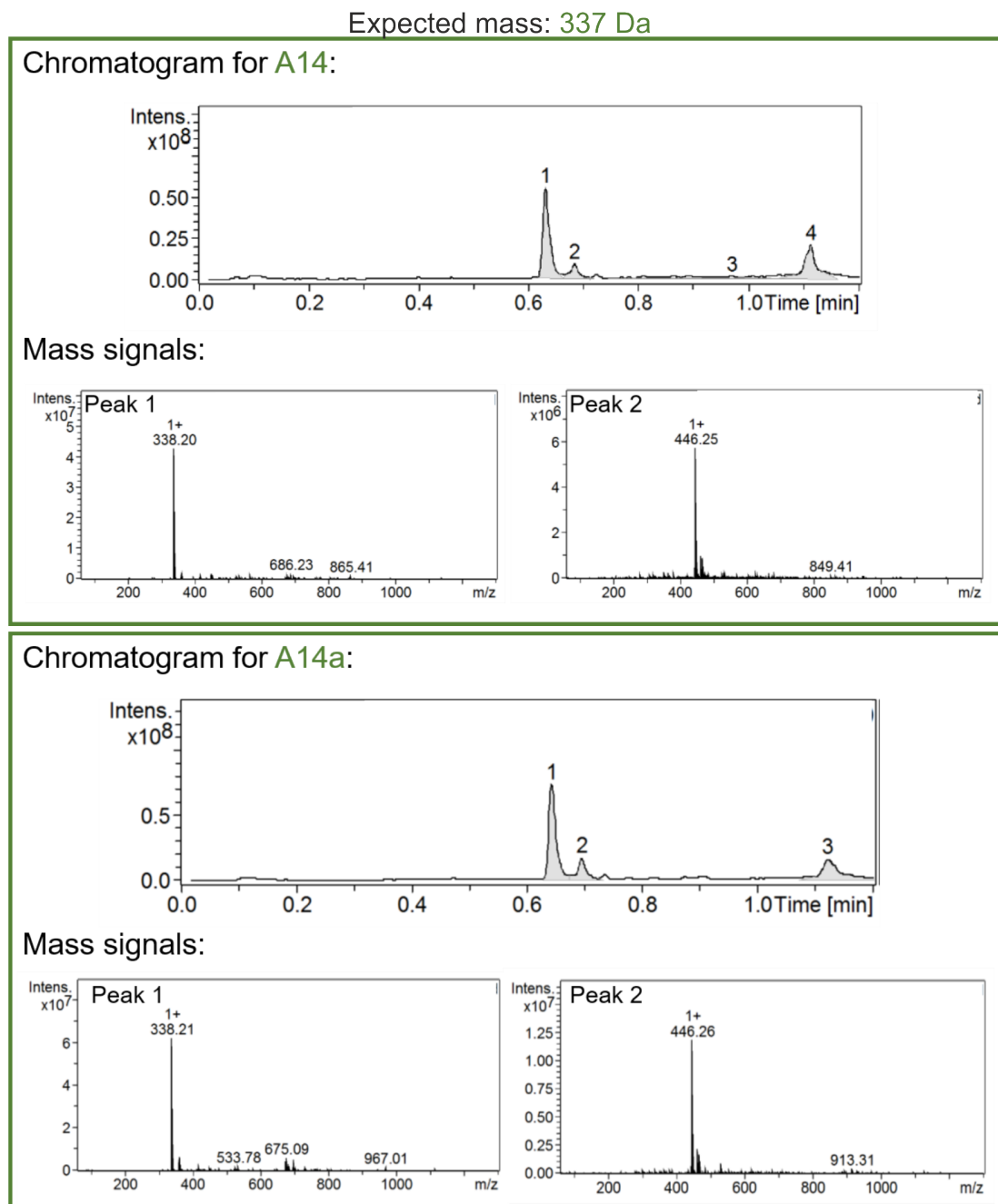


Figure 4.20: LC chromatogram and MS spectra of library compound A14 and commercial compound A14a.

LC chromatogram and MS of each peak present on the LC chromatogram for A14 (top) and A14a (bottom).

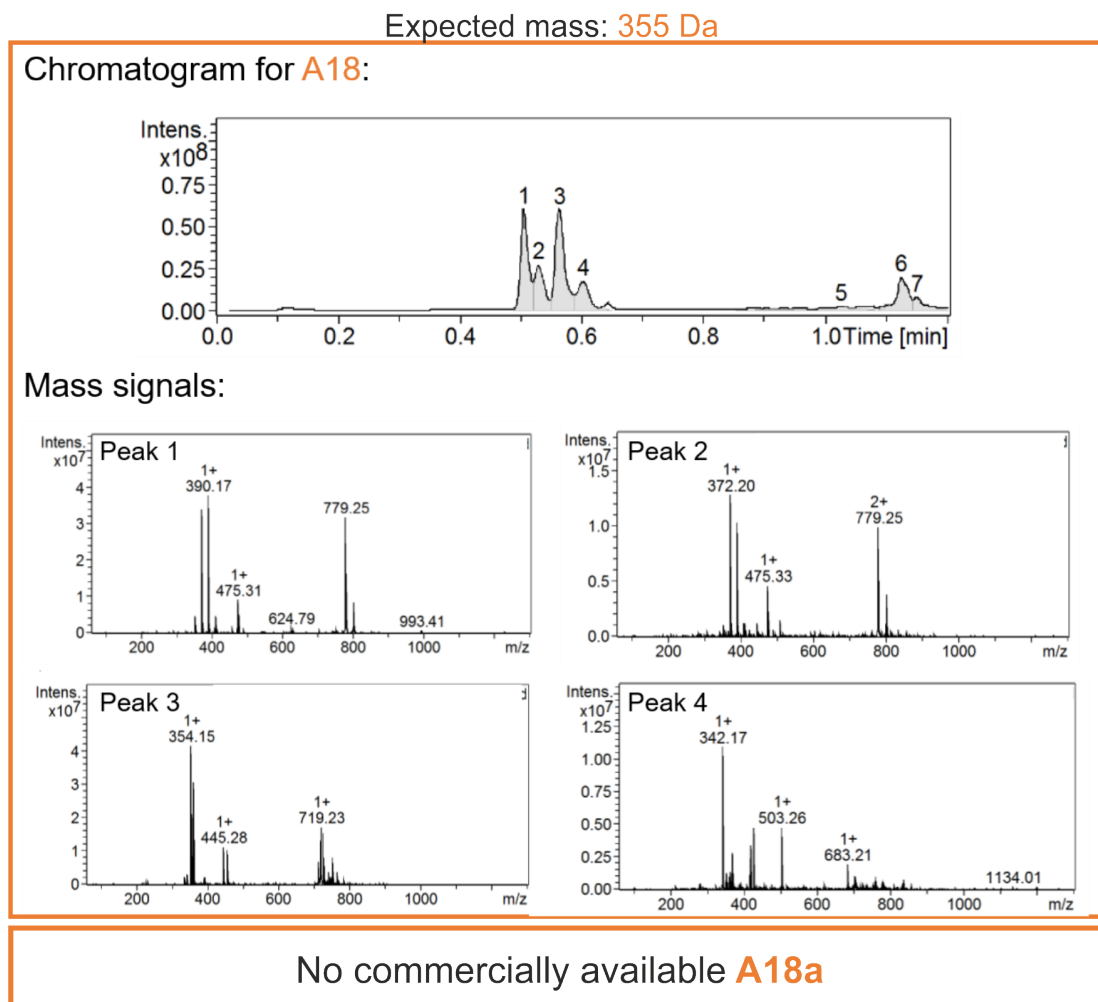


Figure 4.21: LC chromatogram and MS spectra of library compound A18 and commercial compound A18a.

LC chromatogram and MS of each peak present on the LC chromatogram for A18 (top) and A18a (bottom).

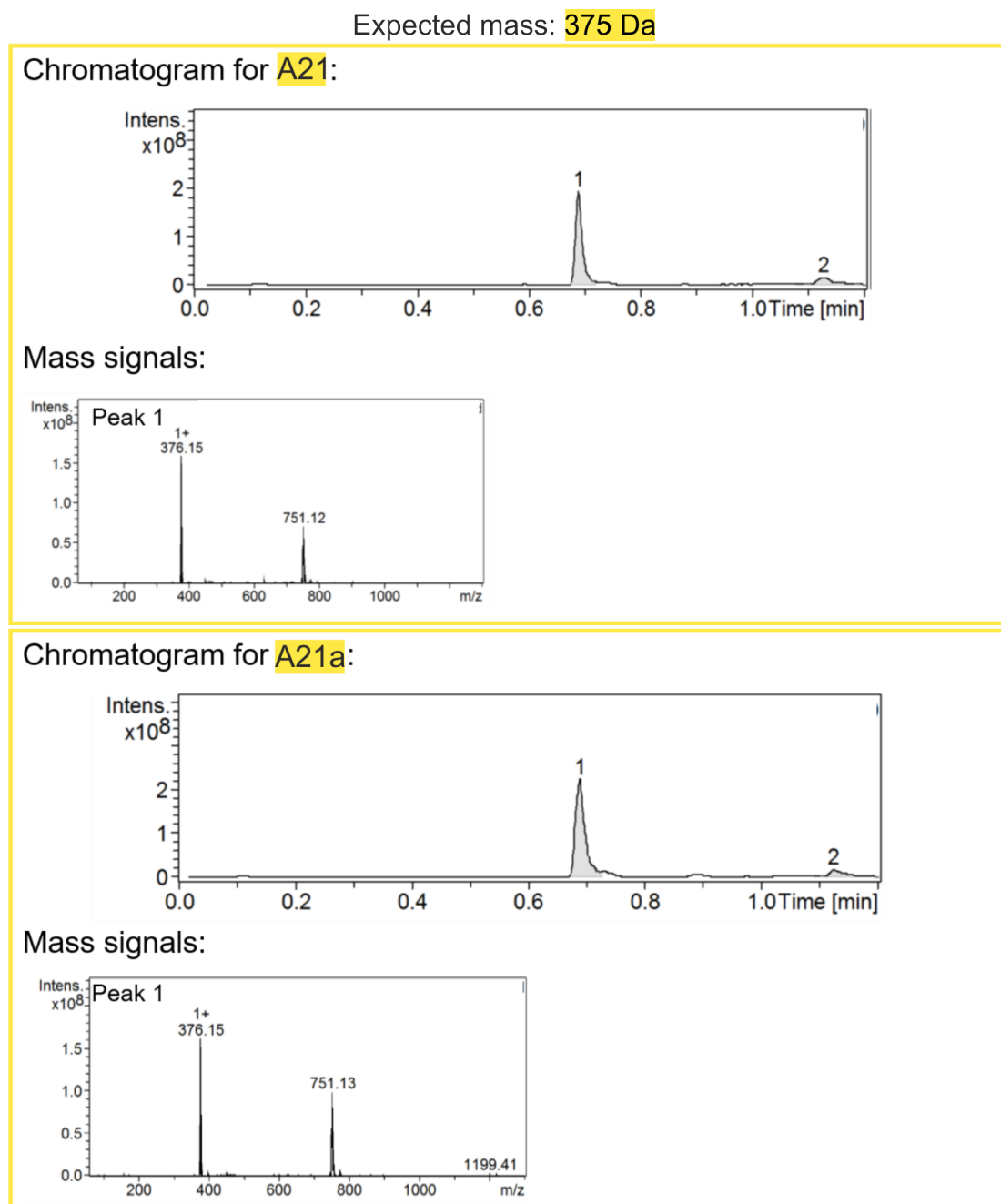


Figure 4.22: LC chromatogram and MS spectra of library compound A21 and commercial compound A21a.

LC chromatogram and MS of each peak present on the LC chromatogram for A21 (top) and A21a (bottom).

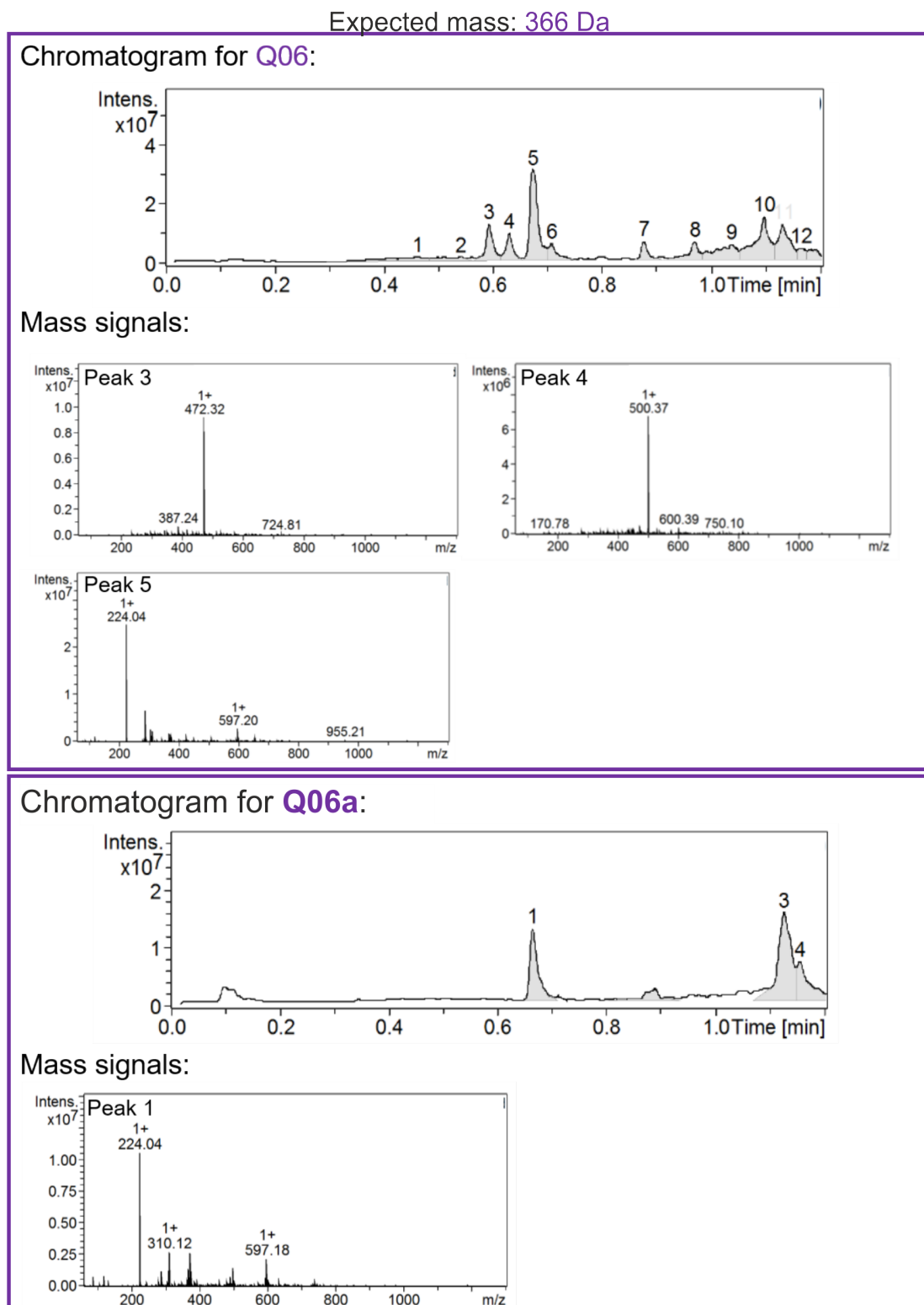


Figure 4.23: LC chromatogram and MS spectra of library compound Q06 and commercial compound Q06a.

LC chromatogram and MS of each peak present on the LC chromatogram for Q06 (top) and Q06a (bottom).

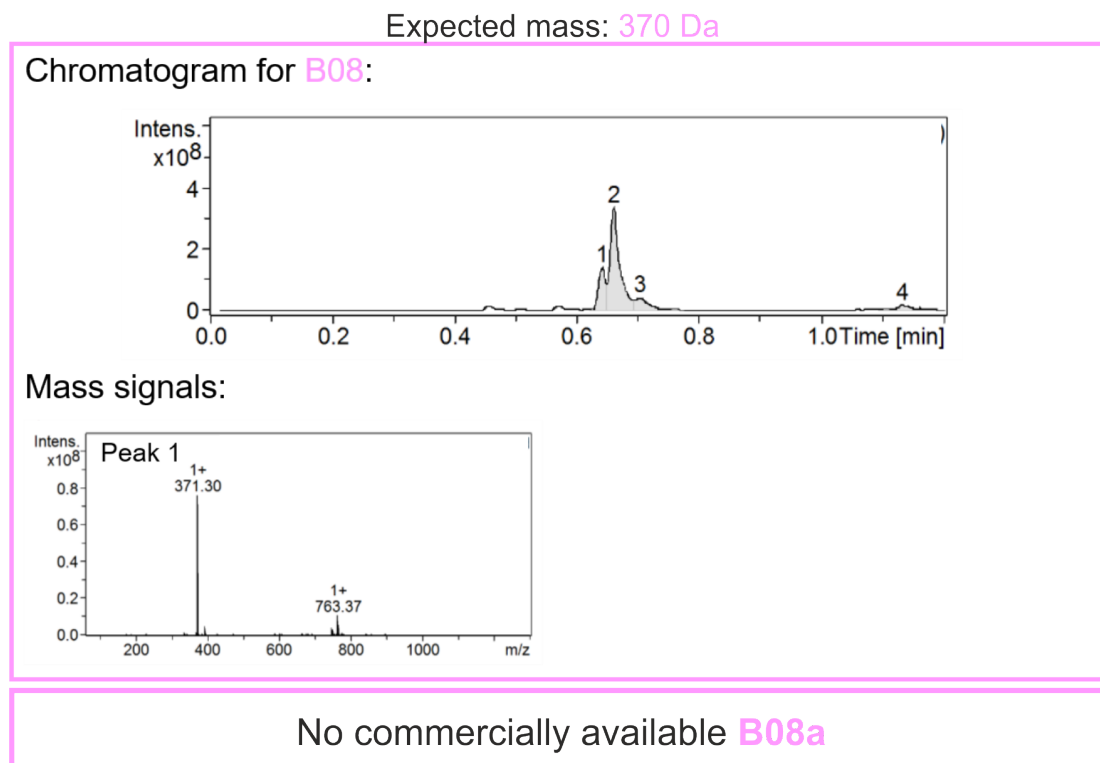


Figure 4.24: LC chromatogram and MS spectra of library compound B08 and commercial compound B08a.

LC chromatogram and MS of each peak present on the LC chromatogram for B08 (top) and B08a (bottom).

These data are summarised in Table 4.5.

TABLE 4.5: Mass spectrometry analysis of compound molecular weight.

Compound (expected MW)	Structure	Library MW	Commercial MW
A12 (407)		407, 425, 607	407
A13 (366)		384, 366	366
A14 (337)		337, 445	337, 445

Continuation of Table 4.5			
Compound (expected MW)	Structure	Library MW	Commercial MW
A18 (355)		371, 389, 353, 341	N/A
A21 (376)		375	375
Q06 (287)		471, 499, 223, more peaks	223, 309
B08 (370)		370	N/A
Q14 (205)		None present	N/A

The LC chromatogram for compound A12 (expected mass 407 Da) showed a doublet peak indicating sample impurity (Figure 4.18). A 407 Da species was present in low abundance in the second of the two peaks. However, this peak was dominated by major species with a MW of 607 Da which, based on the relative peak intensity, is approximately 10x more present than A12. The preceding peak was caused by a 425 Da product which is hypothesised to be an oxidised form of compound A12 (as the mass increase of 18 Da could correspond to H₂O). For A12a, a single species was present with the expected mass of 407 Da, and a dimeric form is observed in low abundance. The minor peak in the A12a corresponds to a dimeric form of the compound.

Similarly, the LC chromatogram for compound A13 (expected mass 366 Da) also showed two peaks (Figure 4.19). A13 was present in the second peak, whereas, the preceding peak (~ 3 x the intensity of the compound-containing peak) corresponded to a 384 Da compound which is presumably an oxidised form of A13. The A13a LC chromatogram also showed a single peak corresponding to the expected (protonated) mass of 367 Da.

The A13a spectrum shows a minor population with a mass of 754 Da which is probably a dimeric form of A13a with a sodium adduct.

Unlike the previous two compounds, the LC chromatogram for A14 (expected mass 337 Da) revealed that the desired compound was the major species in the sample (Figure 4.20, top, peak 1). Despite this, there was evidence of impurities present and a second peak was evident on the LC chromatogram corresponding to a 445 Da contaminant. The major species present for A14a was the correct mass, 337 Da, however there is an additional species at 445 Da. This species was also present in the library compound A14 at a similar level. This could indicate that this compound was prone to reaction with the air or in DMSO to form this higher MW species, or that during LC-MS some of the 337 Da is modified.

Multiple masses were detected for compound A18 (expected mass 355 Da). A18 was present in the second major peak (peak 3, Figure 4.21). However, within this peak there were contaminant species making up approximately 40 % of the total population. Furthermore, the additional peaks in the LC chromatogram corresponded to other contaminant species. Only one of the identified masses was less than the expected mass of A18 indicating degradation was not a major cause of sample contamination. A18 was not commercially available.

Compound A21 (expected mass 375 Da) was present in a pure form as was evident from the single peak observed on the LC chromatogram (Figure 4.22). The peak at 750 Da corresponds to a dimer form of A21. Similarly, commercial A21a appeared to contain only the expected compound and its dimeric form.

Analysis of compound Q06 (expected mass 287 Da) showed species of various masses but none which corresponded to Q06 (Figure 4.23). LC-MS for the purchased compound Q06a revealed the presence of multiple masses. Although fewer species were evident than in the library Q06 sample some of the species detected are of the same MW, e.g. 223 Da and 309 Da. There was no evidence of a 287 Da species which would have corresponded to the expected compound.

The LC chromatogram for compound B08 (expected mass 370 Da) presented three overlapping peaks which implied there were multiple species present in the sample (Figure

4.24). However, the mass analysis reproducibly showed that peaks 1, 2 and 3 all corresponded to the same mass, 370 Da, with a different retention time. The compound may be able to form different rotamer or isomer states which have different affinities for the hydrophobic surface of the LC column. A minor population of a 762 Da species was present which was hypothesised to be a B08 dimer with a sodium ion adduct. B08 was not available commercially.

Compound Q14 was analysed but no mass signals were detected above the noise level by LC-MS, additionally, Q14 was not available commercially.

From comparison of the LC-MS traces of library compounds and purchased compounds, it was apparent that many of the library compounds had encountered some modification or contamination during the long storage period in DMSO in the compound library e.g. compounds A12, A13, A18, Q06, and Q14. As these library compounds were not the same as the commercial compounds, the commercial compounds were subjected to the ThT fluorometry screening assay (Figure 4.25) to screen the commercial compounds for effects on A β_{40} aggregation. A14a and A21a - which are equivalent to A14 and A21 respectively - were also screened.

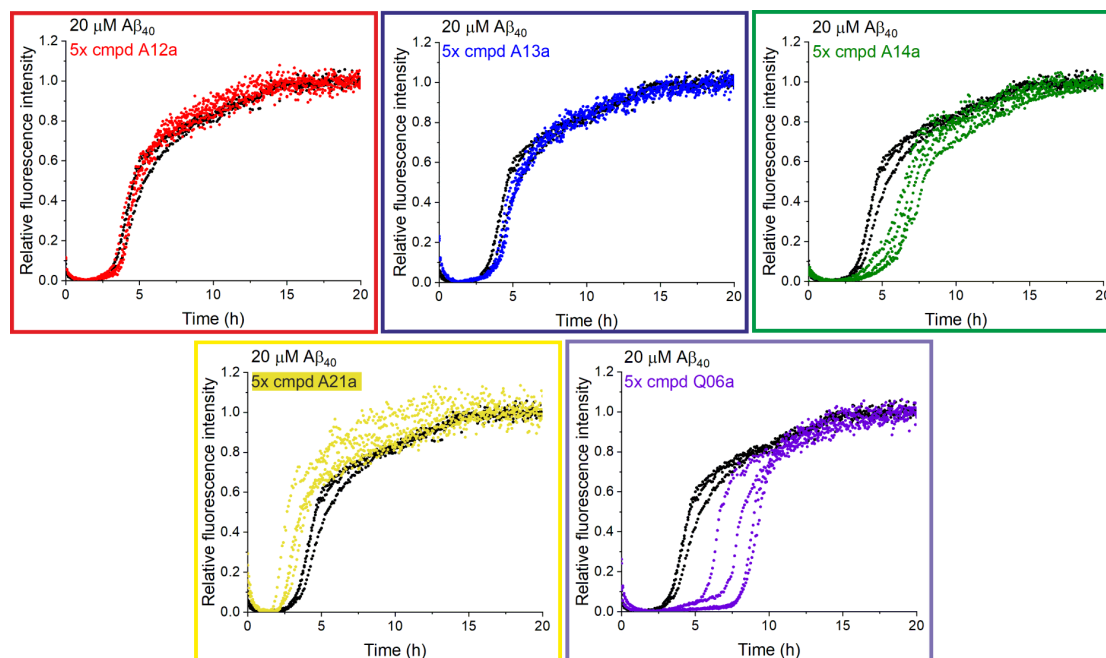


Figure 4.25: ThT fluorometry screen of the new commercial compounds.

Each graph shows the aggregation kinetics for 20 μM $\text{A}\beta_{40}$ apo (black) and 20 μM $\text{A}\beta_{40}$ with 100 μM of each purchased compound; A12a (red), A13a (blue), A14a (green), A21a (yellow), and Q06a (purple) in 50 mM ammonium acetate, pH 6.8, 2 % (*v/v*) DMSO with 10 μM ThT. There are four replicates of each.

From Figure 4.25 there was evidence of amyloid perturbation by compounds A14a, A21a and Q06a. A12a and A13a showed no effect on $\text{A}\beta_{40}$ aggregation by ThT fluorometry. A12a does not exhibit the increased lag time observed for A12. This could be because the 608 MW species in A12 was the active compound rather than the 407 Da compound which is pure in A12a. The additional 384 Da species in A13 may have affected the elongation rate of $\text{A}\beta_{40}$ (observed in Figure 4.16) in a way which A13a (366 Da) cannot, or the 384 and 366 Da species may have interacted together in order to influence $\text{A}\beta_{40}$ aggregation kinetics.

Comparison of A14a and A21a to A14 and A21 in Figure 4.16 show the same behaviour whereby A14 and A14a delay $\text{A}\beta_{40}$ aggregation by ~ 2 h and A21 and A21a promote $\text{A}\beta_{40}$ aggregation by ~ 2 h. This was expected as the LC-MS analysis showed that the commercial compounds were the same as the library compounds (Figures 4.20 and 4.22). Q06a showed a strikingly different effect on $\text{A}\beta_{40}$ aggregation by increasing the lag time (by 3–5 h) compared with Q06 which showed a decreased lag time (by 2–3 h). This

discrepancy was understandable as Q06 was very impure and Q06a contained different molecular weight species.

All five of the commercial compounds were taken forward for application of further toolbox methods to demonstrate the ability of the toolbox to differentiate small molecule modulators of aggregation by a stringent and robust approach. Investigation of the original library compounds was not continued due to the uncertain nature of the active species in the compound samples; determination of which was beyond the scope of this project. Moreover, limited supply of library compounds meant that further application in the toolbox would have been limited.

4.4 Verification of Compound-mediated effects on Amyloid Aggregation using a Multi-method Approach

In this section, toolbox methods are used to verify the effects of the selected compounds (A12a, A13a, A4a, A21a, and Q06a) on $A\beta_{40}$ aggregation. Firstly, reproducibility of effects was explored using a titration of compound:peptide ratios in the ThT fluorometry assay. Next, an SDS-PAGE-based assay was used to detect aggregate species and to quantify the amount of insoluble material produced at the end of the aggregation reaction. Finally, TEM is used to investigate aggregate morphology of $A\beta_{40}$ formed in the presence of each compound.

4.4.1 Assessment of the Reproducibility of Compound-Induced Modulation of $A\beta_{40}$ Aggregation using Titration Effects

Validation of compound effects - for the compounds A12a, A13a, A14a, A21a, and Q06a - on $A\beta_{40}$ was achieved through ligand titration ThT fluorometry assays. This technique reported on the reproducibility of effects each compound had on $A\beta_{40}$ aggregation kinetics, as well as determining whether there was a dose-dependent relationship between compound concentration and effect on $A\beta_{40}$ aggregation.

A deviation on the screening assay was used where the ratio of compound: $A\beta_{40}$ was varied to 5:1, 1:1 and 1:5. The $A\beta_{40}$ concentration was kept constant at 20 μ M across

all of the experiments and the amount of compound was varied to achieve the aforementioned ratios. The experimental procedure was the same as in the initial screen whereby a 96-well plate format was used, ThT fluorescence was monitored every 300 s, and the experimental conditions (37 °C, quiescent) and buffer conditions (50 μ M ammonium acetate, pH 6.8, 2 % (*v/v*) DMSO, 10 μ M ThT) were the same. Plates were also set up similarly to those in the screen with four wells of each compound concentration mixed with A β_{40} , and four wells of the A β_{40} apo control.

The titration experiments were initially conducted in triplicate for one of the query compounds, 1,2-naphthoquinone, Figure 4.26 to demonstrate the method.

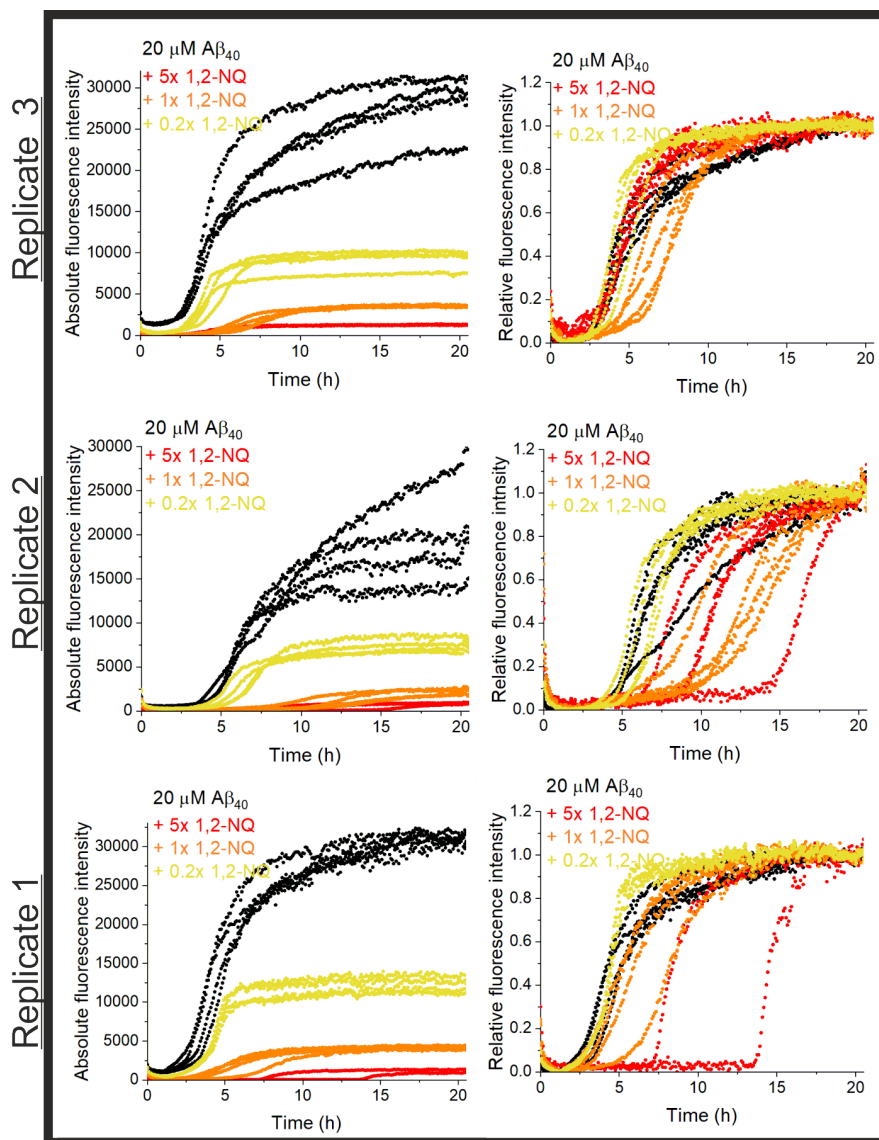


Figure 4.26: Titration analysis of 1,2-naphthoquinone on $A\beta_{40}$ aggregation. Absolute (left) and relative (right) plots of triplicate repeats of ThT fluorometry to monitor effect of a 5:1 (red), 1:1 (orange) and 1:5 (yellow) molar ratios of 1,2-naphthoquinone to $A\beta_{40}$ (black) on aggregation. Buffer and reaction conditions were the same as in the screen, and described in Section 2.2.5.1.

Plots of absolute ThT fluorescence revealed a clear titratable effect in the maximum fluorescence level attained when the 1,2-naphthoquinone: $A\beta_{40}$ was varied. Increased levels of 1,2-naphthoquinone showed a more drastic suppression of the fluorescence level attained. This could be due to a lower fibril yield or a greater change in fibril morphology which binds poorly to ThT. The relative plots revealed sigmoidal curves suggesting β -sheet formation occurs and reached a plateau which may be indicative of amyloid formation.

Moreover the relative plots revealed the dose-dependent effect 1,2-naphthoquinone had on the lag time more clearly. In all replicates, a 1x molar ratio of 1,2-naphthoquinone appeared to delay aggregation but the extent of this effect varied between experiments. In the second and third replicate the 5x molar excess of 1,2-naphthoquinone exacerbated this effect. The general trend observed was that spread in lag time increased as the lag time extended, consistent with stochastic nucleation [470].

Subsequent to the 1,2-naphthoquinone titration experiment, the ratios of compound:peptide were adjusted (from 5:1,1:1, 1:5 to 1:1, 1:5, 1:10 compound:A β_{40} while the *v/v* DMSO percentage remained constant at 2 %) for the compound investigation. The hypothesis to justify this was based on the expectation that adding a large excess of compound would augment the effects observed on A β_{40} aggregation kinetics reported on by ThT fluorescence, Figure 4.27.

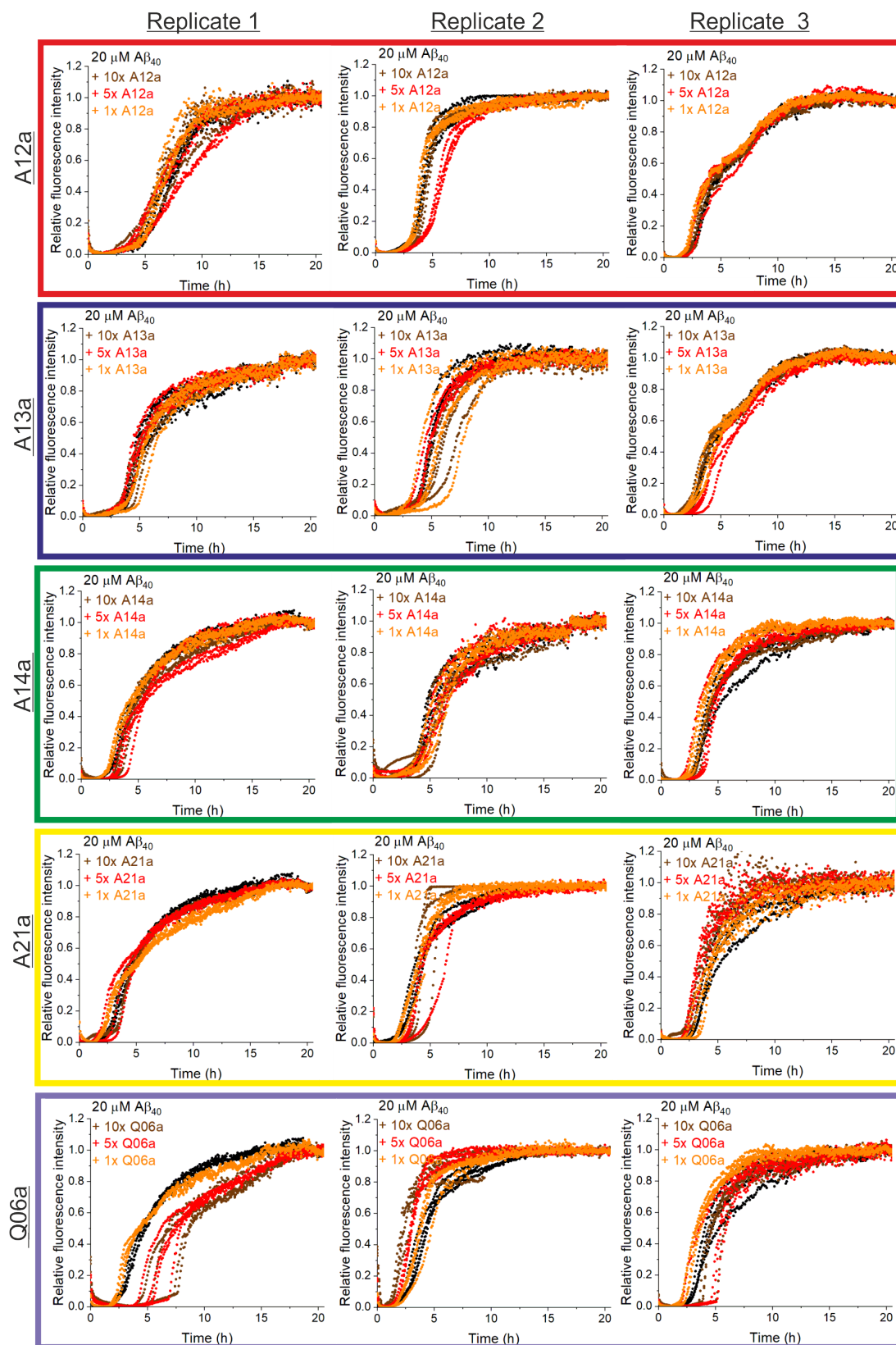


Figure 4.27: Titration analysis of the commercial compounds on $A\beta_{40}$ aggregation. Relative plots of triplicate repeats of ThT fluorometry to monitor effect of a 10:1 (brown), 5:1 (red) and 1:1 (orange) molar ratios of compound to $A\beta_{40}$ (black) on aggregation; A12a (red box), A13a (blue box), A14a (green box), A21a (yellow box), and Q06a (purple box). Buffer and reaction conditions were the same as in the screen, and described in Section 2.2.5.1.

From Figure 4.27, few large, reproducible trends were observed on the effect of the compounds on ThT fluorescence. The qualitative analysis of the curve shape revealed the effects observed in the screening assay to be very small and higher compound: $A\beta_{40}$ ratios may have been necessary to cause more reproducible effects on $A\beta_{40}$ aggregation. From these data it was unlikely that the selected compounds would be promising modulators of $A\beta_{40}$ aggregation.

4.4.2 Quantification of the Extent of Aggregation of $A\beta_{40}$ in the Presence of Each Compound

Thus far, only a single technique (based on ThT fluorescence) had been used to probe compound interference in $A\beta_{40}$ aggregation. Use of alternative methods in conjunction with the ThT fluorometric assay enabled different aspects of the compound- $A\beta_{40}$ interaction to be investigated.

The maximum fluorescence level reported in the ThT assay can be misleading due to the multitude of contributing factors (discussed in Section 1.4.1). To measure the extent of aggregation of $A\beta_{40}$, the SDS-PAGE-based fibril assay was used (described in Section 2.2.5.3 and demonstrated in Section 3.5.3).

At the end of the ThT reaction (20 μM $A\beta_{40}$ in 50 mM ammonium acetate, pH 6.8, 2 % (*v/v*) DMSO, 10 μM ThT, 21 h quiescent incubation at 37 °C), samples were removed from the 96-well plate and transferred into Eppendorf tubes. Samples were taken from the solution before and after centrifugation for 20 minutes at 14,000 rpm in a benchtop microfuge. This centrifugation caused large species, such as aggregates and insoluble oligomers, to form a pellet at the base of the tube whilst soluble species remained in the supernatant. Samples from the insoluble and soluble fractions were run on an SDS-PAGE gel alongside a non-centrifuged sample which represented the protein in the whole sample, Figure 4.28a. Measurement of band intensity by densitometry (using Fiji software, Section 2.2.5.3) was used to quantify how much protein aggregated in the presence of each compound as a relative percentage of the ‘whole’ sample. The assay was first applied to three of the query molecules - adapalene, bexarotene, and 1,2-naphthoquinone - (Figure 4.28b) which the screen (Section 4.3.1) was based upon. This suggested that after 21 h under the conditions described, $A\beta_{40}$ existed predominantly as insoluble - presumably aggregate - forms in the presence of each parent molecule. The

fibril yield assay was then applied to compounds A12a, A13a, A14a, A21a and Q06a (Figure 4.28c).

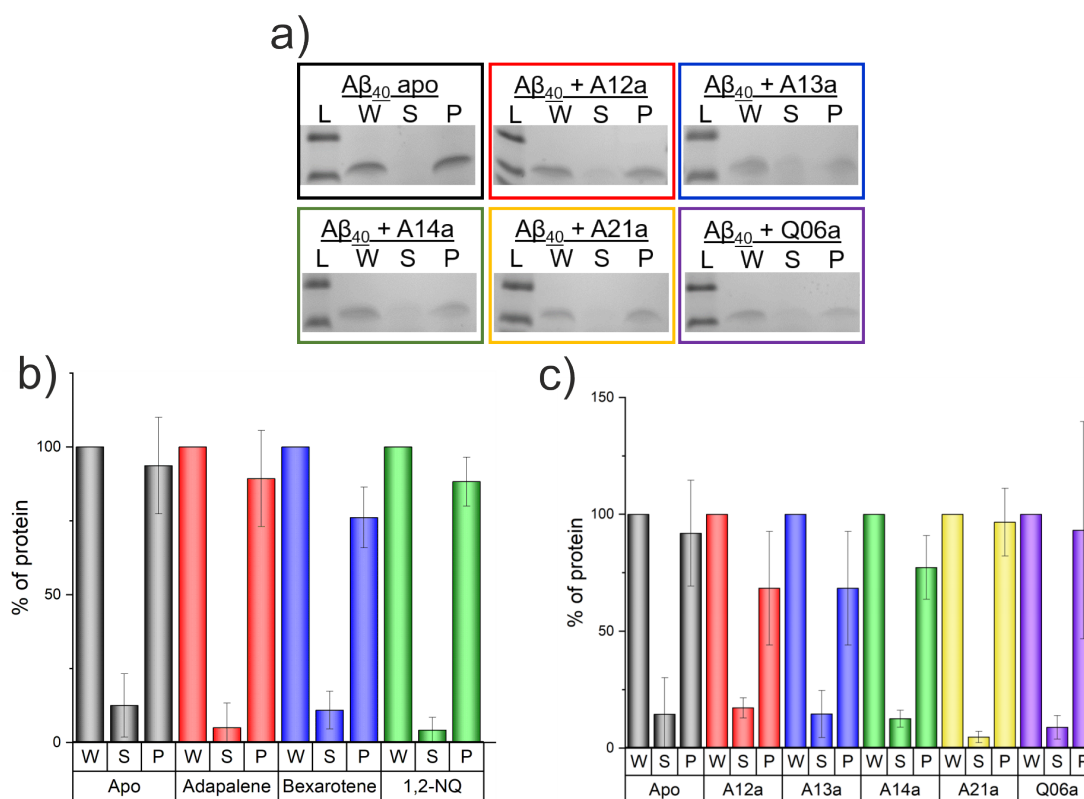


Figure 4.28: Application of the SDS-PAGE fibril yield assay.

a) SDS-PAGE gel for Whole (W), soluble (S), and pelleted (P) protein samples of 20 μM $\text{A}\beta_{40}$ in the absence of compound (black), and in the presence of A12a (red), A13a (blue), A14a (green), A21a (yellow), and Q06a (purple) after 21 h incubation at 37 $^{\circ}\text{C}$, in 50 mM ammonium acetate, pH 6.8, 2 % (*v/v*) DMSO and 10 μM ThT. b and c) Relative amounts of $\text{A}\beta_{40}$ in the Whole (W), soluble (S), and pelleted (P) protein samples of the query molecules (b) based on densitometry and the commercial compound leads (c). Error bars represent standard deviation.

Figure 4.28 showed that the majority of $\text{A}\beta_{40}$ was present in the insoluble pellet (P) fractions rather than in soluble (S) states irrespective of whether any compound was present. Each bar is plotted relative to the band intensity for the whole (W) sample prior to centrifugation. There were no significant differences ($P < 0.05$) in the proportion of $\text{A}\beta_{40}$ in the soluble and pellet fractions with each of the compounds compared to the apo state - using a 5x molar excess of compound tested here-. Thus none of the compounds

investigated can prevent 20 μM $\text{A}\beta_{40}$ forming insoluble aggregates in 50 mM ammonium acetate, pH 6.8, with 2 % (*v/v*) DMSO and 10 μM ThT over 21 h at 37 °C.

4.4.3 $\text{A}\beta_{40}$ forms Fibrillar Aggregates in the Presence and Absence of Compounds

To assess qualitatively whether the aggregate species of $\text{A}\beta_{40}$ were influenced by the addition of 5x molar excess of compounds A12a, A13a, A14a, A21a and Q06a, TEM was used. Samples were taken directly from the 96-well plates used in the ThT fluorometry experiments after 21 h of quiescent incubation at 37 °C (20 μM $\text{A}\beta_{40}$ in 50 mM ammonium acetate, pH 6.8, 2 % (*v/v*) DMSO. with 10 μM ThT). These samples were fixed onto carbon-coated grids and negatively stained using uranyl acetate. As the samples were all taken after 21 h of incubation at 37 °C the aggregation reaction had reached completion and presence of aggregates were implied by fibril yield results (Section 4.4.2). Moreover, ThT fluorometry (Figure 4.16) implied these aggregates were β -sheet rich. Samples were imaged to show whether amyloid-like fibrils were present or whether the compound had caused the $\text{A}\beta_{40}$ to aggregate in a colloidal manner.

Figures 4.29 and 4.30 show images - at 1500x magnification and 10,000x magnification - of representative aggregate morphology observed for $\text{A}\beta_{40}$ apo, and with each compound under investigation including 1,2-naphthoquinone.

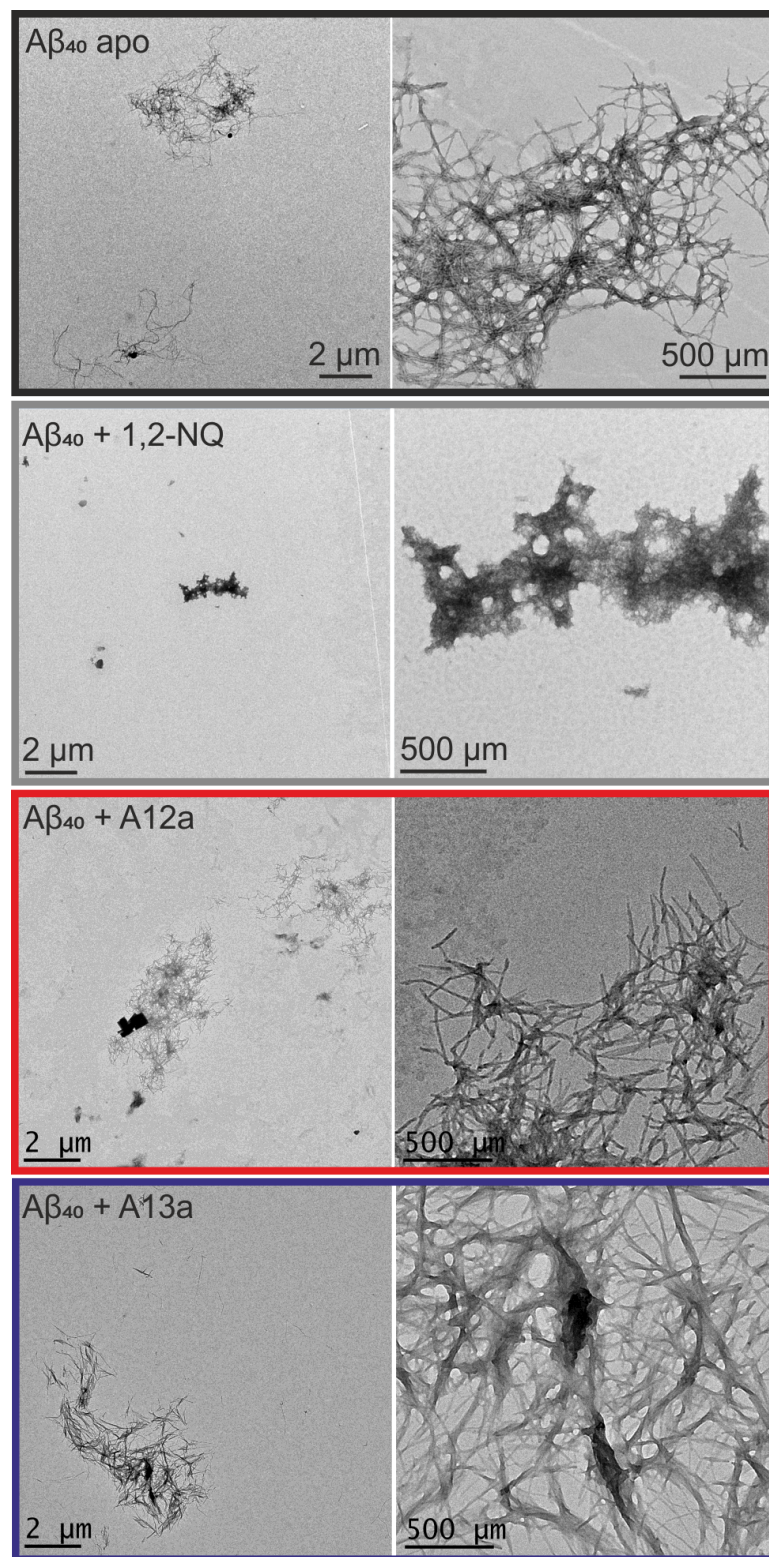


Figure 4.29: Transmission electron micrographs of $A\beta_{40}$ aggregates in the absence or presence of compounds.

Samples were taken directly from ThT assay samples (Section 2.2.5.2) and fixed onto carbon-coated EM grids which were negatively stained using 2 % uranyl acetate.

Images were taken at 1500x magnification (left) and 10,000x magnification (right). $A\beta_{40}$ aggregates formed in the absence of compounds (black box) is shown and in the presence of 5x molar excess of 1,2-naphthoquinone (grey box), A12a (red bx), A13a (blue box). Imaged according to Section 2.2.5.2.

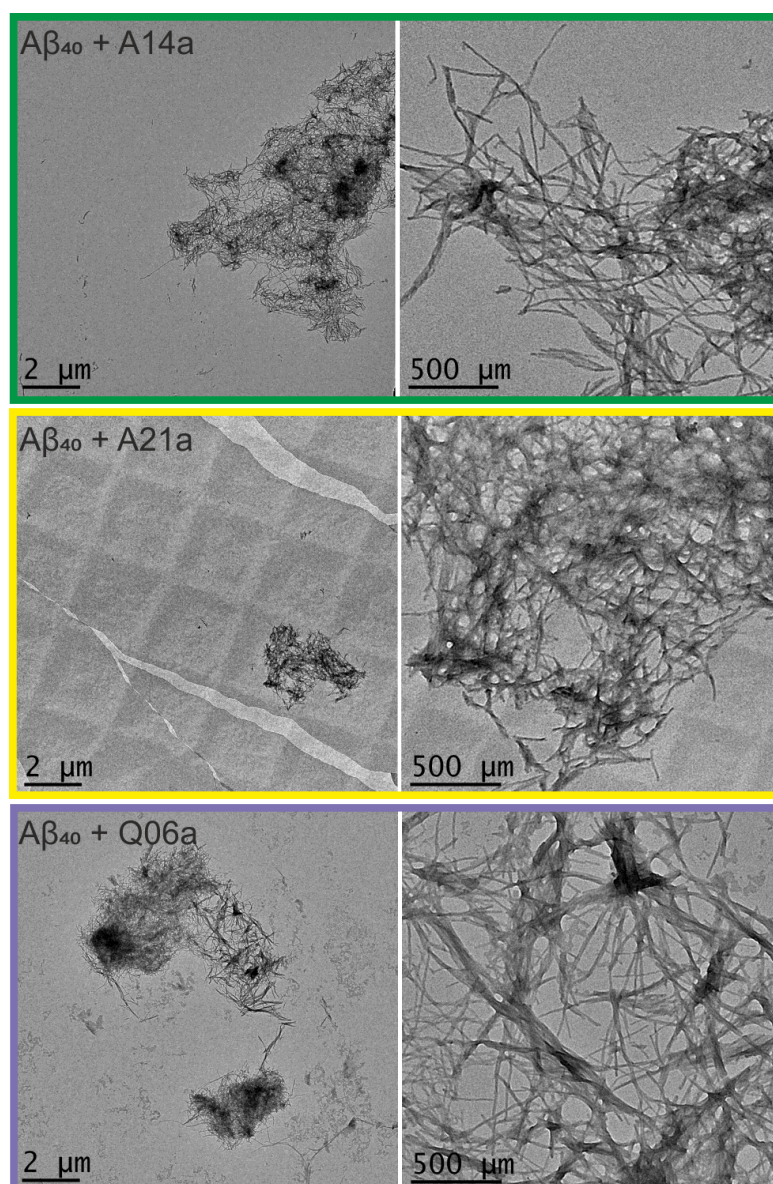


Figure 4.30: Transmission electron micrographs of $A\beta_{40}$ aggregates in the absence or presence of compounds (continued).

As for Figure 4.29 but the compounds present were A14a (green box), A21a (yellow box), and Q06a (purple box).

As expected there was evidence of fibrillar species of $A\beta_{40}$ in the apo sample, which was typical of amyloid formation. Such species were also observed for aggregates formed in the presence of 5x molar excesses of A12a, A13a, A14a, A21a and Q06a. The fibril morphology appeared largely consistent with fibrils with widths of 1-20 nm observed. When 5x 1,2-naphthoquinone was present no fibrillar aggregates were observed. Instead,

amorphous masses were detected and the grid was predominantly covered with circular colourations (Figure 4.31) which may be off pathway aggregates.

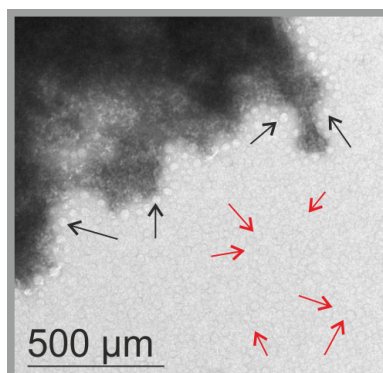


Figure 4.31: Observation by TEM of circular species formed by $A\beta_{40}$ in the presence of 1,2-naphthoquinone.

TEM image of aggregate or oligomer morphology noted when $A\beta_{40}$ was incubated quiescently at 37 °C in the presence of a 5x molar excess of 1,2-naphthoquinone in 50 mM ammonium acetate, pH 6.8, 2 % (*v/v*) DMSO, and 10 μ M ThT. Black arrows indicate circular species close to the amorphous aggregate, and red arrows highlight circular species which were noted across the grid.

Combination of the TEM data with the ThT, and fibril yield results presented in the previous two sections indicated that none of the novel compounds affected $A\beta_{40}$ aggregation under the conditions used, but 1,2-naphthoquinone pushed $A\beta_{40}$ off of the amyloid pathway.

4.5 Probing the Interaction between Small Molecules and $A\beta_{40}$ Species

4.5.1 Probing the Molecular Interaction between Compounds and $A\beta_{40}$ by ESI-IMS-MS to Indicate Binding Mode

Subsequent to the verification that aggregation occurred in the presence of all the investigated compounds, the focus was then directed on whether the compounds bound to $A\beta_{40}$ monomers. This was investigated using electrospray ionisation-ion mobility spectrometry-mass spectrometry (ESI-IMS-MS). This method also probed the compound binding mode; specific, non-specific, or colloidal interaction with the peptide [421].

Compounds (solubilised in 100 % DMSO) were mixed with aqueous $A\beta_{40}$ monomer in 50 mM ammonium acetate, pH 6.8, at a 5:1 (compound: $A\beta_{40}$) molar ratio and then analysed immediately by Dr P. Knight and Dr Y. Xu (University of Leeds). Fast analysis ensured that monomeric species were observed which was desirable as the binding mode of the compounds with monomeric (and low oligomeric forms of) $A\beta_{40}$ was of interest in this study. ESI-IMS-MS investigation was conducted on the query compounds adapalene, bexarotene and 1,2-naphthoquinone (Figure 4.32) and on the five novel compounds (Figure 4.33) which were identified in the screen (Section 4.3.1).

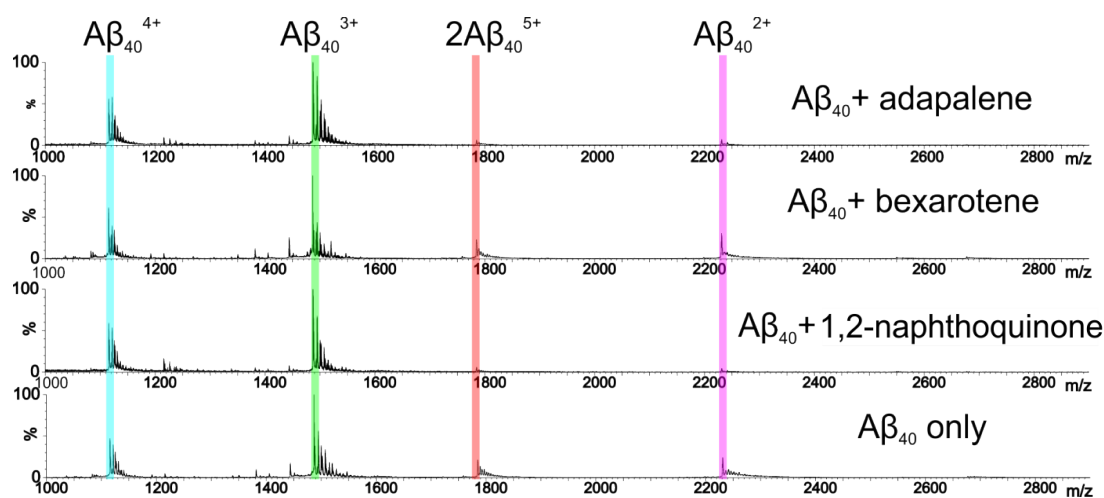


Figure 4.32: Mass spectra of $A\beta_{40}$ in the presence of query compounds.

ESI-MS was conducted by Dr P. Knight and Dr Y. Xu, University of Leeds. 20 μM $A\beta_{40}$ in 50 mM ammonium acetate, pH 6.8 in the absence (bottom) or presence of 100 μM compound were analysed. The coloured lines show $A\beta_{40}$ species.

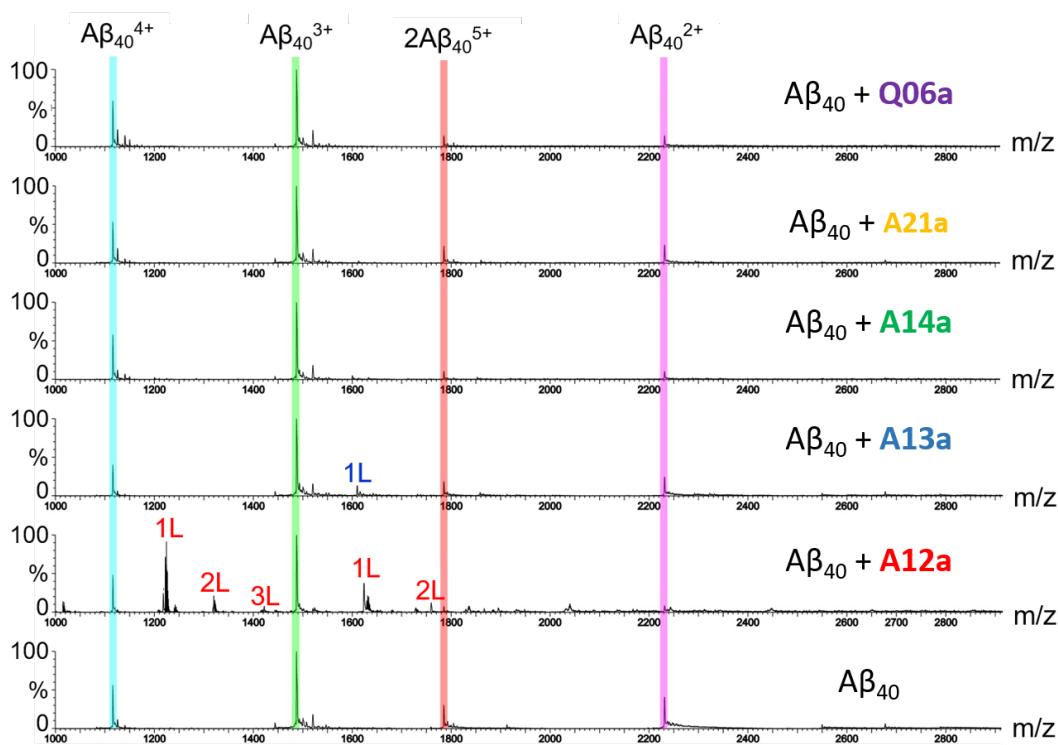


Figure 4.33: ESI-Mass spectra of $A\beta_{40}$ in the presence of lead compounds.

ESI-MS was conducted by Dr P. Knight and Dr Y. Xu, University of Leeds. $20 \mu\text{M}$ $A\beta_{40}$ in 50 mM ammonium acetate, pH 6.8 in the absence (bottom) or presence of $100 \mu\text{M}$ compound were analysed. The coloured lines show $A\beta_{40}$ species. Compound (or ligand) binding is labelled 'L'.

Figure 4.33 shows that in the apo state $A\beta_{40}$ was present as monomeric, and dimeric forms. On some repeats trimeric species were also observed (data not shown). The dimer was present when each compound is added. In the presence of 5x molar excess of query compounds adapalene, bexarotene, or 1,2-naphthoquinone, no binding was observed. Additionally, no $A\beta_{40}$ -compound interaction was observed on the addition of 5x molar excess of A14a, A21a or Q06a.

In the presence of 5x molar excess of A12a, the abundance of the $A\beta_{40}$ dimer was lower than in other samples which implied that compound A12a may interfere with the self-association of the peptide. However, this was inconsistent with the observed ThT kinetics in Figure 4.25 where no effect on lag time was observed (an increased lag time would have been indicative of an ability to interrupt monomer association). This observation can be justified hypothetically due to the time scale of each of the

experiments; for ESI-IMS-MS the effect of A12a could be short-lived and thus over the course of the ThT reaction have little impact on the measured lag time.

The addition of compound A12a to $A\beta_{40}$ showed multiple copies (one two or three) of the compound bound to the 3+ and 4+ charge states of monomeric $A\beta_{40}$ but not to the 2+ state. This was suggestive of a non-specific interaction between A12a and $A\beta_{40}$, with the more highly charged species. To test this hypothesis the experiment was repeated using a 1:1 molar ratio of $A\beta_{40}$:compound. The abundance of observed bound compound was reduced with a maximum of only two ligands bound to $A\beta_{40}$ monomer (Figure 4.34). This supported a non-specific interaction between A12a and $A\beta_{40}$ at the higher molar ratios used.

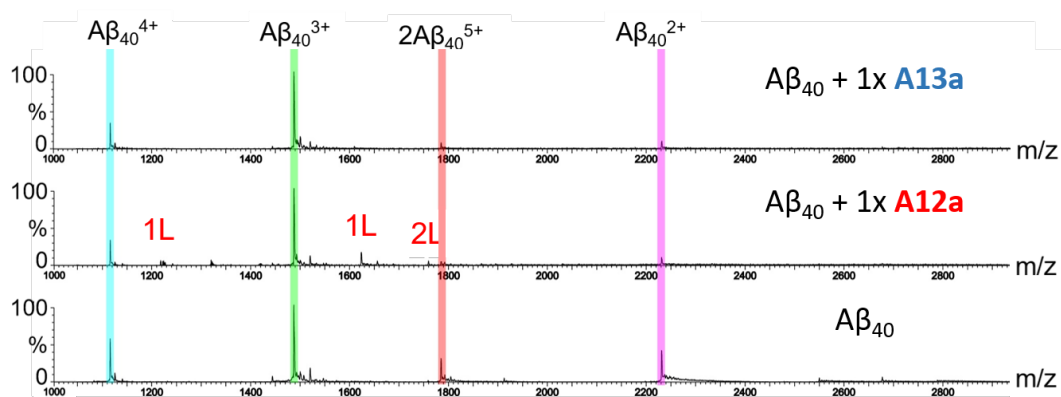


Figure 4.34: ESI-Mass spectra of $A\beta_{40}$ in the presence of different compounds.

ESI-MS was conducted by Dr P. Knight and Dr Y. Xu, University of Leeds. 20 μM $A\beta_{40}$ in 50 mM ammonium acetate, pH 6.8 in the absence (bottom) or presence of 20 μM A13a (top) or A14a (middle) were analysed. The coloured lines show $A\beta_{40}$ species.

Compound (or ligand) binding is labelled 'L'.

Addition of a 5x molar excess of A13a showed a low level of 1:1 complex with the $A\beta_{40}$ monomer suggestive of (possibly weak) binding but no effect on aggregation was observed by ThT, TEM, fibril yield, nor when a lower (1x) molar ratio of compound: $A\beta_{40}$ was analysed by ESI-MS.

4.6 Probing for Potential Molecular Interactions between Compounds and A β_{40} by NMR

A robust method for detecting an interaction between a small molecule and a peptide is to use NMR [363, 471]. As discussed previously, A β_{40} is well suited to study by NMR due to its small and flexible nature. Measurement of chemical shift perturbations (CSP) of the backbone amide resonances in the A β_{40} $^1\text{H}^{15}\text{N}$ -HSQC spectrum - caused on compound addition - can reveal residue-specific information, for example, CSP may reveal compound binding sites. The A β_{40} $^1\text{H}^{15}\text{N}$ -HSQC spectrum has previously been assigned and published [364, 372]. Furthermore, effects of some small molecules on the spectrum have also been studied, for example EGCG [428] (Figure 4.35).

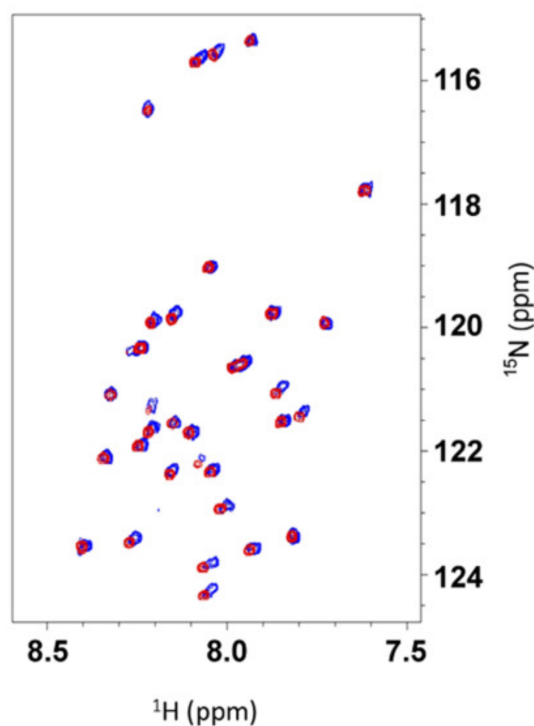


Figure 4.35: Effect of EGCG on $^1\text{H}^{15}\text{N}$ -HSQC spectra of A β_{40} .

$^1\text{H}^{15}\text{N}$ -HSQC of 50 μM A β_{40} in 50 mM phosphate buffer, pH 7.4 at 5 $^\circ\text{C}$ apo (red) or with a 3x molar excess of EGCG (blue). Reproduced from [428].

To aid interpretation of $^1\text{H}^{15}\text{N}$ -HSQC spectra collected, the assigned A β_{40} apo spectrum is shown (Figure 4.36). Chapter 5 describes extensive condition optimisation of NMR buffers - hence the buffer change from ammonium acetate to sodium phosphate in this section - and the assignment process used.

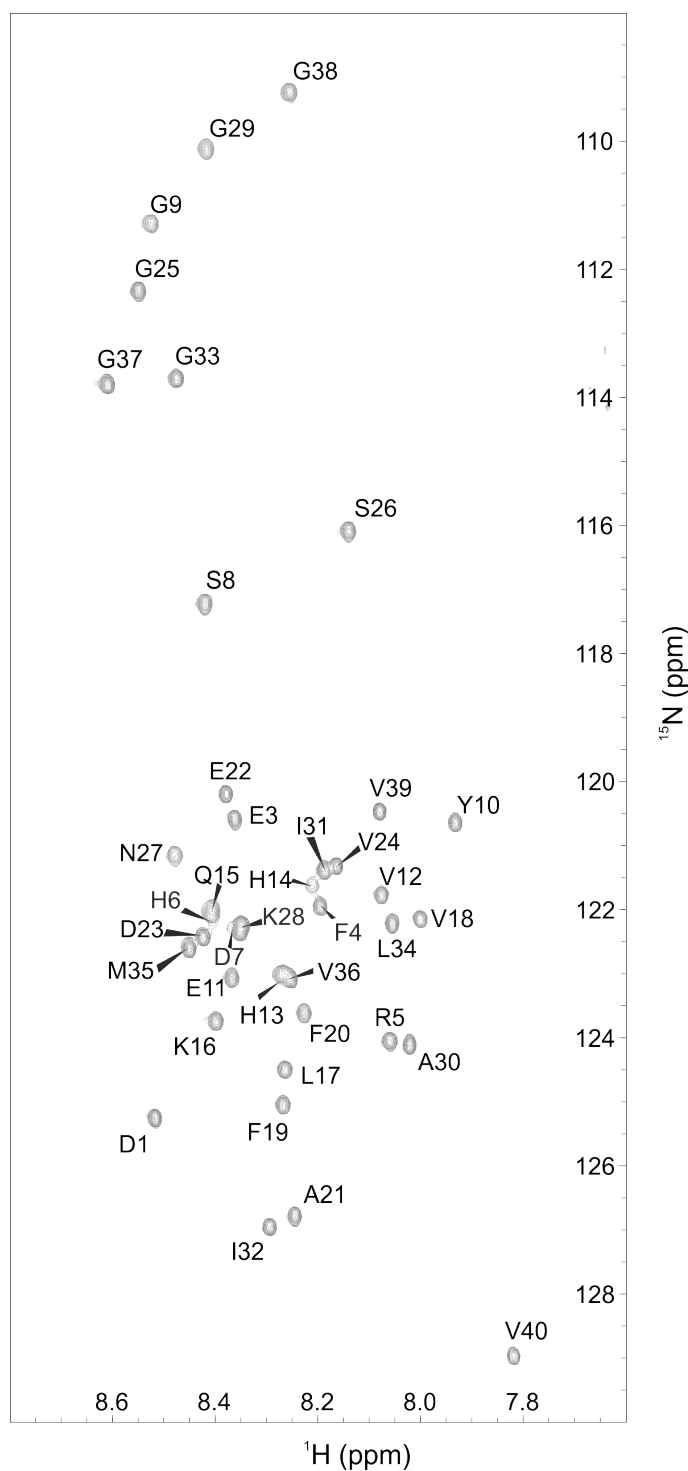


Figure 4.36: Assigned HSQC spectrum for A β_{40} .

¹H¹⁵N-HSQC spectra recorded using a 750 MHz Bruker spectrometer. 50 μ M A β_{40} was solubilised in 20 mM sodium phosphate buffer, pH 7.4, containing 10 % D₂O, 0.02 % (v/v) NaN₃, 0.5 mM EDTA, and 2 % (v/v) DMSO at 5 °C. Peaks were assigned as described in Section 5.1.4.

$^1\text{H}^{15}\text{N}$ -HSQC spectra were then collected for A β_{40} in the presence of a 3:1 compound to peptide ratio (similarly to [428]) of each of the available query compounds (Figure 4.37). A 3:1 ratio of compound:peptide was used based on work by Fusco *et al.*, [428], to minimise compound self-association at the higher concentration. Given that the peptide concentration had increased from 20 μM to 50 μM , the compound concentration would be very high to maintain a 5:1 ratio (250 μM). If a compound bound to or near a backbone amide, it would have caused an alteration in the magnetic environment around the nuclei and this would have been evident as a CSP for the corresponding resonance.

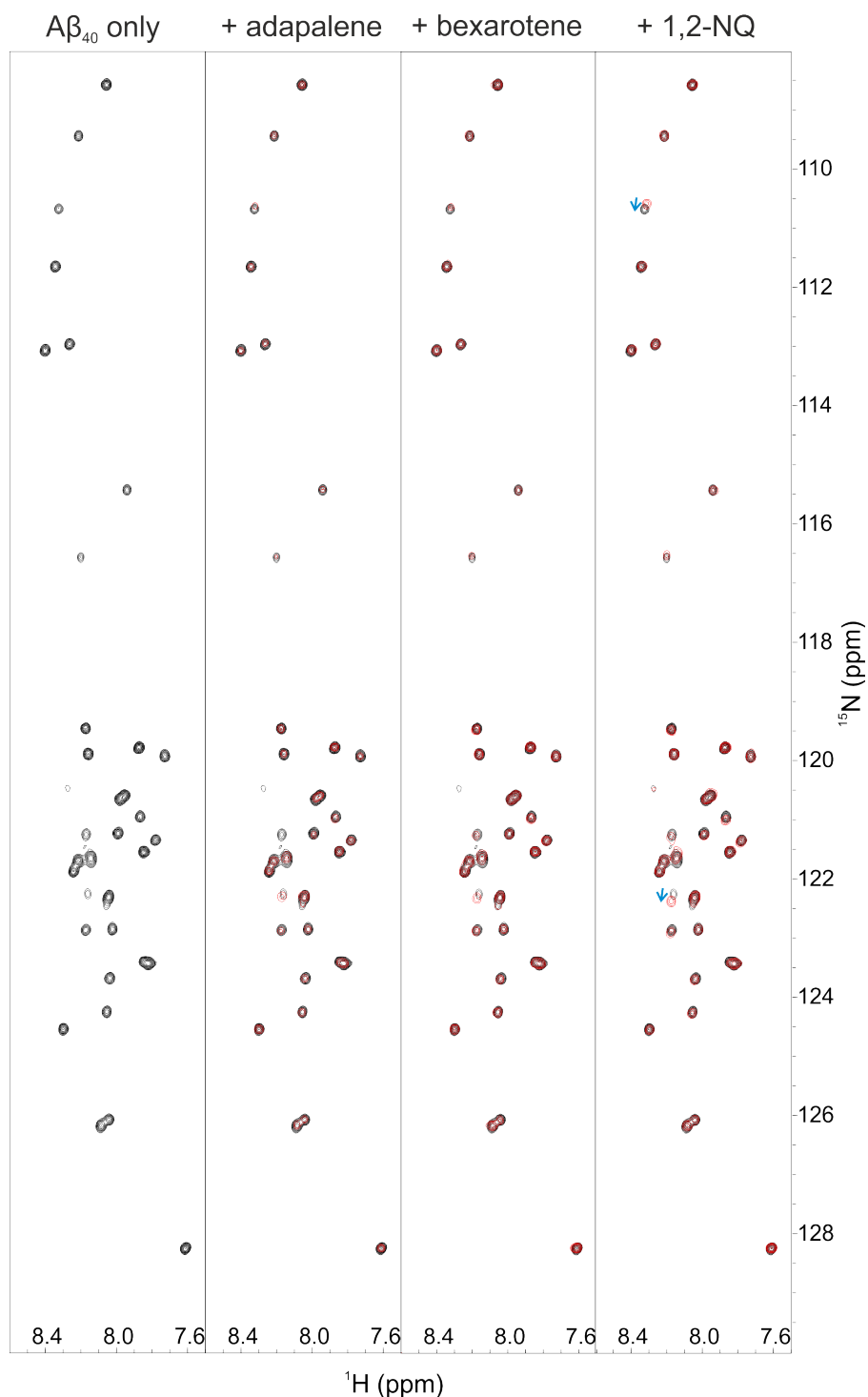


Figure 4.37: HSQC to detect chemical shift perturbations of $A\beta_{40}$ in the presence of A12a.

HSQC spectra recorded using a 750 MHz Bruker spectrometer. 50 μM $A\beta_{40}$ was solubilised in 20 mM sodium phosphate buffer, pH 7.4, containing 10 % D_2O , 0.02 % (v/v) NaN_3 , and 0.5 mM EDTA at 5 $^{\circ}C$. 150 μM of each compound was added to the $A\beta_{40}$ sample as labelled and the spectrum (red) was overlaid with the apo (black) spectrum to detect chemical shift perturbations.

No chemical shift perturbations were observed on the addition of adapalene or bexarotene, and only Gly9 and Glu11 shift (Figure 4.37, blue arrows) when 1,2-naphthoquinone is added. Previously in the literature it has been shown that bexarotene does not interact with the A β_{40} monomer in order to affect aggregation [472]. The results collected here concur.

To explore whether any of the lead compounds interacted with A β_{40} under the conditions used (20 mM sodium phosphate buffer, pH 7.4, containing 10 % D₂O, 0.02 % (v/v) NaN₃, and 0.5 mM EDTA at 5 °C), ¹H¹⁵N-HSQC spectra were recorded for A β_{40} in the presence of 150 μ M A12a, A13a, A14a, A21a, or Q06a (Figures 4.38 and 4.39).

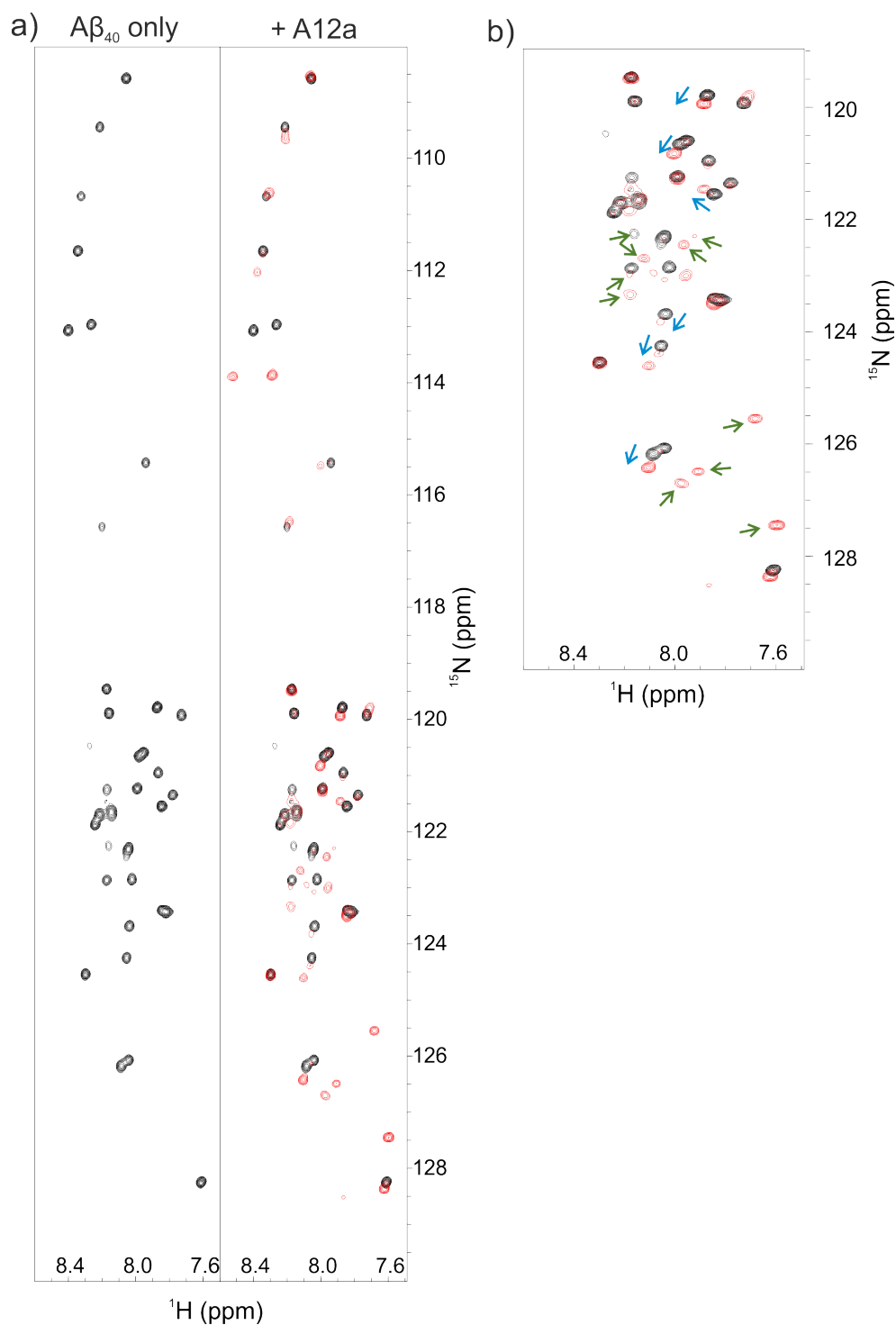


Figure 4.38: $^1\text{H}^{15}\text{N}$ -HSQC to detect chemical shift perturbations of $\text{A}\beta_{40}$ in the presence of A13a.

a) $^1\text{H}^{15}\text{N}$ -HSQC spectra were recorded as for Figure 4.37. $150\ \mu\text{M}$ A12a was added to the $\text{A}\beta_{40}$ sample and the spectrum (red) was overlaid with the apo (black) spectrum to detect chemical shift perturbations. . b) Zoomed in region of (a) with chemical shift changes (blue arrows) and new resonance appearances (green arrows) to the $\text{A}\beta_{40}$ spectrum on addition of a 3x molar excess of A12a.

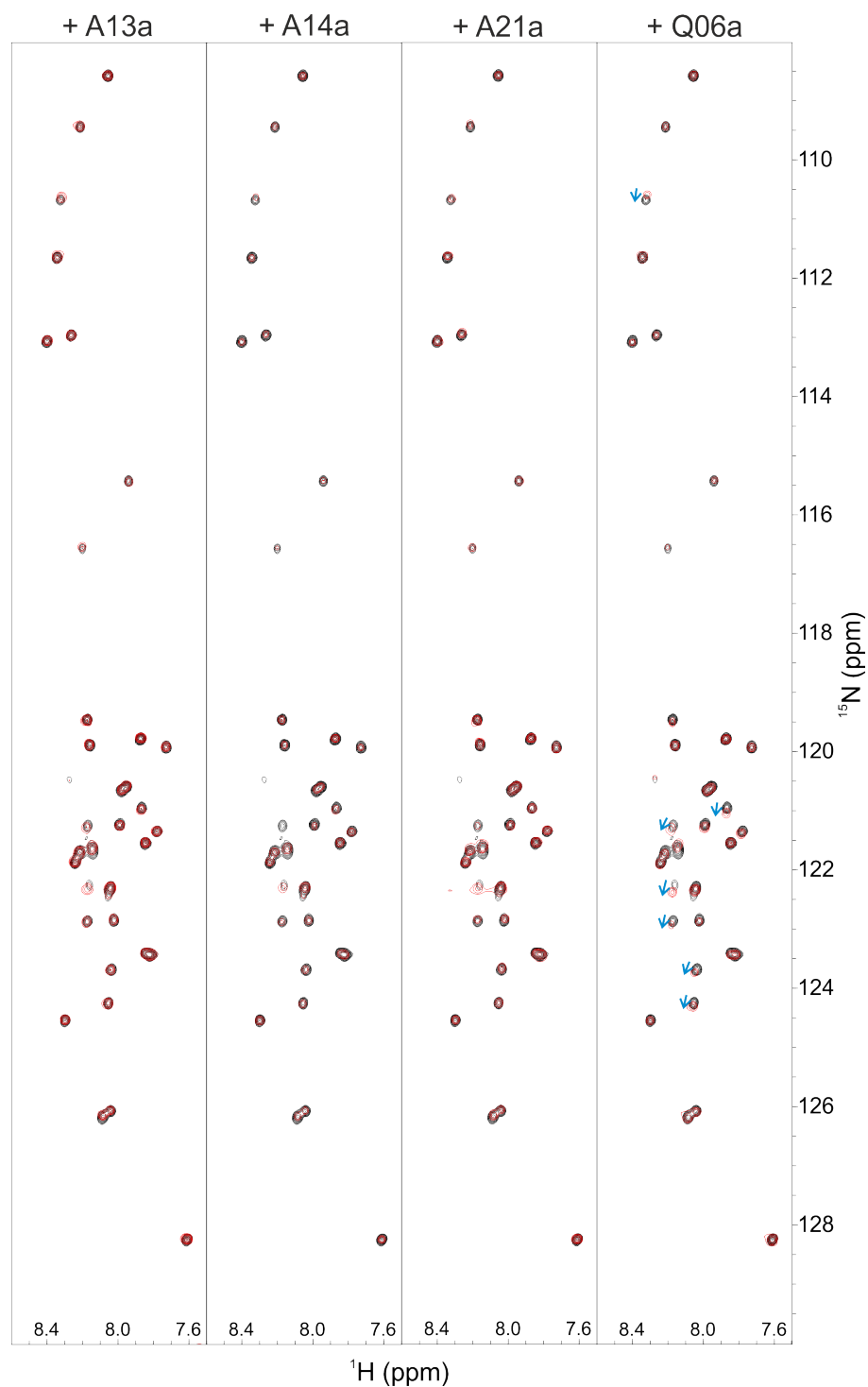


Figure 4.39: $^1\text{H}^{15}\text{N}$ -HSQC to detect chemical shift perturbations of $\text{A}\beta_{40}$ in the presence of other lead compounds.

$^1\text{H}^{15}\text{N}$ -HSQC spectra were recorded as for Figure 4.37. 150 μM A13a, A14a, a21a or Q06a was added to the $\text{A}\beta_{40}$ sample and the spectrum (red) was overlaid with the apo (black) spectrum to detect chemical shift perturbations. Chemical shift changes are highlighted (blue arrows).

The $^1\text{H}^{15}\text{N}$ -HSQC spectra of $\text{A}\beta_{40}$ in the presence or absence of compound A12a are distinct. There is evidence of peak shifts as well as evidence of some peak splitting which is indicative of multiple conformations being populated and exchanging slowly with each other. Compounds A13a, A14a and A21a show no perturbation in the chemical shifts of the $\text{A}\beta_{40}$ $^1\text{H}^{15}\text{N}$ -HSQC spectrum which provides further evidence that these compounds do not bind to $\text{A}\beta_{40}$.

Q06a showed peak shifts for seven residues - Gly9, Glu11, Val12, Gln15, Lys16, Leu17 and Phe19- (Figure 4.39, blue arrows). This could indicate a region of $\text{A}\beta_{40}$ which interacted with Q06a. However, this region surrounded two histidines (His13 and His14) which are very sensitive to mild pH changes, thus care must be taken to verify that the effect seen is not due to pH.

In spite of the chemical shift perturbations observed for Q06a, other methods in the toolbox showed there was no reproducible effect on $\text{A}\beta_{40}$ aggregation, and that Q06a did not interact with $\text{A}\beta_{40}$ (under ESI-MS conditions). Moreover, the expected mass (287 Da) was not present on ESI-MS of the compound alone (Figure 4.23) and extensive investigation to identify the active molecule would have been necessary; this was beyond the scope of this project. On the other hand, A12a showed a more pronounced influence on the $\text{A}\beta_{40}$ $^1\text{H}^{15}\text{N}$ -HSQC spectrum and there was evidence of compound binding from ESI-MS (Section 4.5.1). Due to this, A12a was chosen as the most promising lead compound.

4.6.1 Analysis of Promising Compound A12a in Modulating $\text{A}\beta_{40}$ Aggregation and Discovery of Compound Stability

Since the chemical shift changes caused by compound A12a were most drastic it was decided that further residue-specific investigation of this compound with $\text{A}\beta_{40}$ was justified in order to locate specific residues which may interact with the compound. The initial stage of this was to assign the $\text{A}\beta_{40}$ + A12a spectrum. Upon remaking the NMR sample, however, the chemical shift differences were no longer observed. To investigate whether compound instability could be a cause of this finding, an aliquot of 10 mM A12a in 100 % DMSO was exposed to air at room temperature over a period of two weeks. At multiple time points the sample was subject to mass spectrometry (conducted by Owen Cornwell, University of Leeds). The results of this are shown in Figure 4.40.

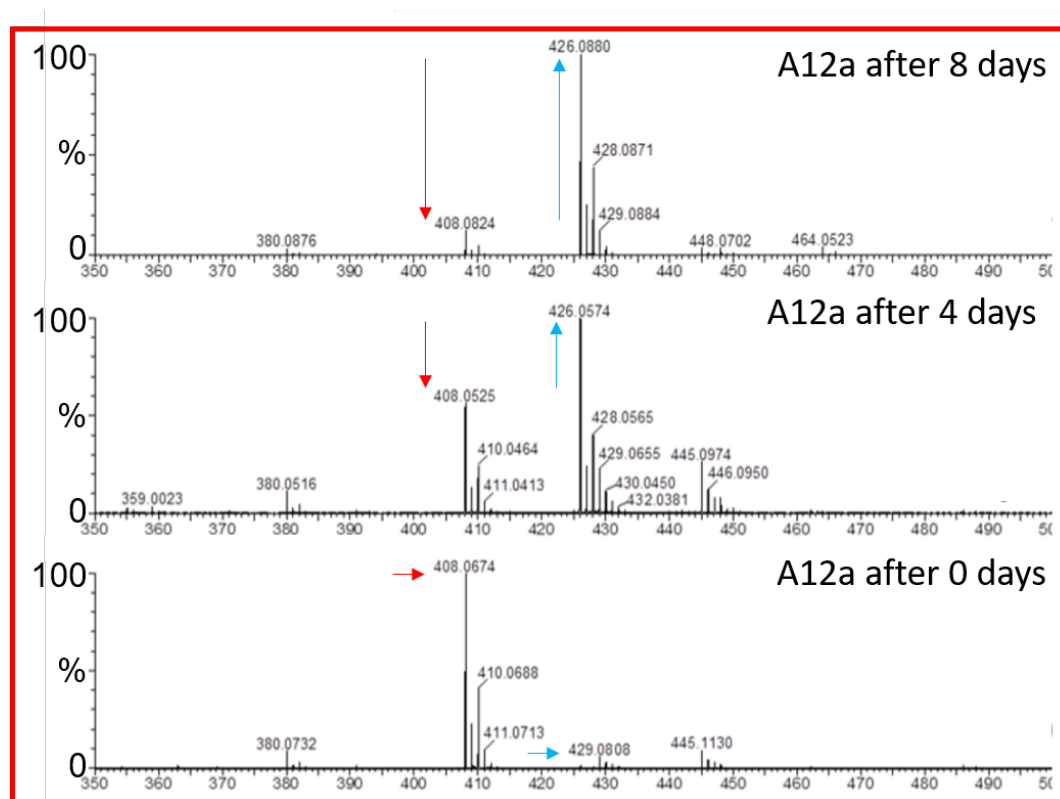


Figure 4.40: ESI-mass spectra of the hydrolysis of A12a.

ESI-mass spectra of A12a initially (bottom), after 4 (middle), and after 8 (top) days of exposure to air. The red arrows highlight the expected 407 Da mass of the compound and the blue arrows highlight the increase in 425 Da oxidised product over time.

From this analysis it is evident that the 407 Da compound A12a is prone to modification on contact with the air. On the initial day of exposure to air the compound exists as a majority in the expected form. However by day four a modified, 425 Da product is already the dominant species and by eight days the original compound is barely present. The 425 species is 18 Da larger than the expected mass of A12a and is likely to be a hydrolysed product (Figure 4.41). The 444 Da species present after four days of air-exposure is undetermined. Due to the hygroscopicity of DMSO it was possible that when stock aliquots of A12a in DMSO are thawed, opened, and re-frozen there was opportunity for water to enter the solution and hydrolyse the compound (Figure 4.41).

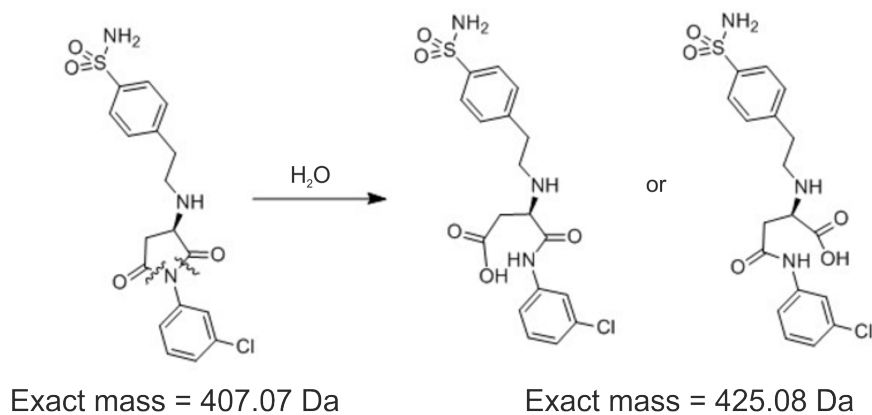


Figure 4.41: Predicted hydrolysed product of A12a.

To explore whether the hydrolysed A12a product affected $A\beta_{40}$ $^1\text{H}^{15}\text{N}$ -HSQC CSPs - and thus explain the irreproducibility of the CSPs observed (Figure 4.38) - $^1\text{H}^{15}\text{N}$ -HSQC were collected for $A\beta_{40}$ in solution with 3x molar excess of A12a which had been exposed to the air for zero, four, or eight days (Figure 4.42). To complement this, ThT fluorometry was also used to probe discrepancy in how A12a and the oxidised A12a compound impacted $A\beta_{40}$ aggregation kinetics.

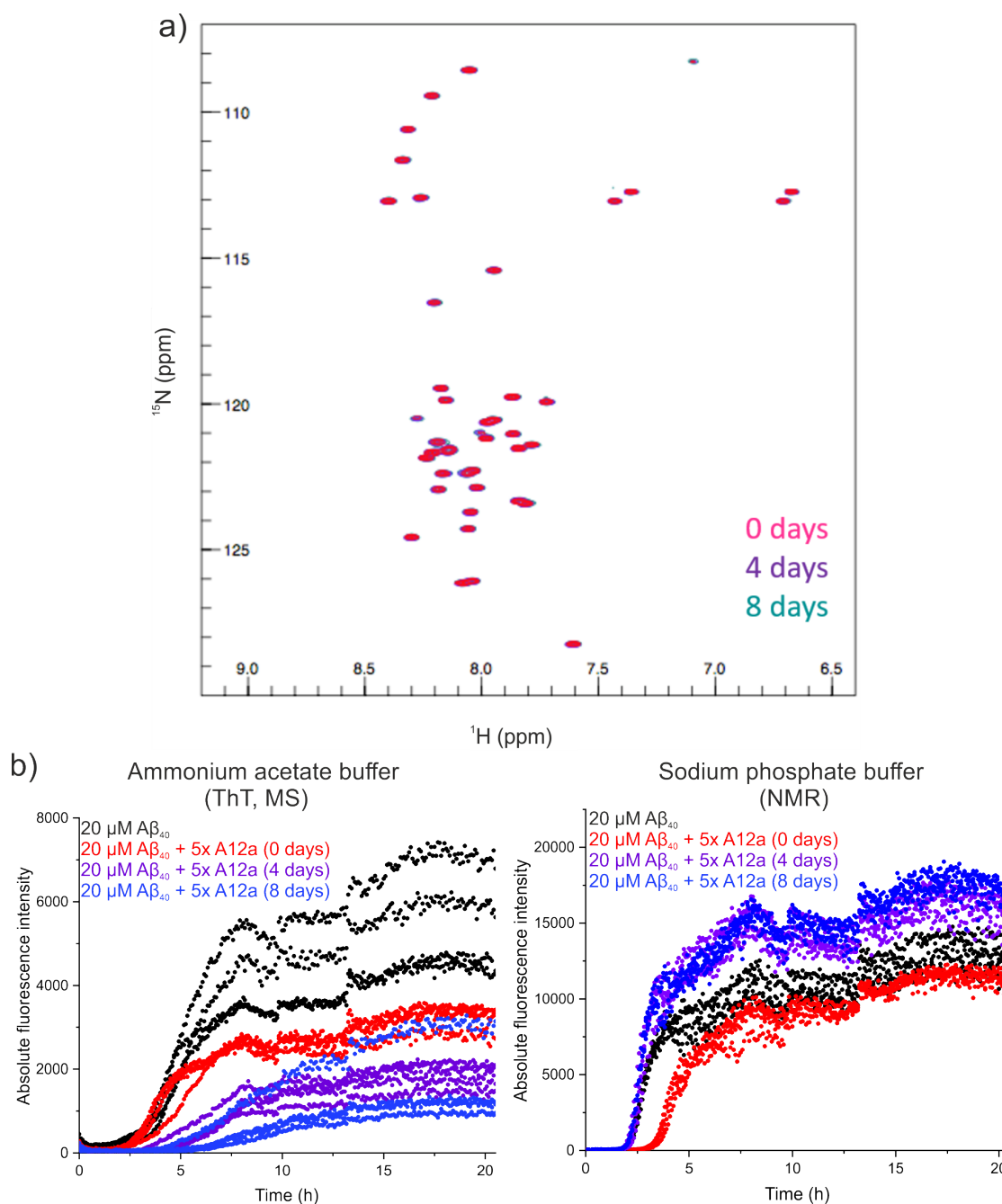


Figure 4.42: $^1\text{H}^{15}\text{N}$ -HSQC and ThT fluorescence investigation of the effect of compound A12a on $\text{A}\beta_{40}$ aggregation as it undergoes hydrolysis.

a) The $^1\text{H}^{15}\text{N}$ -HSQC spectra presented were recorded using a 750 MHz Bruker spectrometer. $50\ \mu\text{M}$ $\text{A}\beta_{40}$ was solubilised in 20 mM sodium phosphate buffer, pH 7.4, containing 10 % D_2O , 0.02 % (v/v) NaN_3 , and 0.5 mM EDTA at $5\ ^\circ\text{C}$. To each sample of $\text{A}\beta_{40}$ $150\ \mu\text{M}$ A12a was added after either 0 (red), 4 (purple), or 8 (blue) days. b) ThT fluorescence analysis of the effect of zero, four, or eight days old A12a on $\text{A}\beta_{40}$ aggregation. Analysis was conducted at $37\ ^\circ\text{C}$, quiescently with $20\ \mu\text{M}$ $\text{A}\beta_{40}$ in the ammonium acetate buffer used previously for ThT analysis, MS, and TEM (50 mM ammonium acetate, pH 6.8, with 2 % (v/v) DMSO and $10\ \mu\text{M}$ ThT) and the sodium phosphate buffer used for NMR in (b).

The HSQC spectra showed no perturbation in chemical shifts for any of the A12a samples, thus, hydrolysed A12a was not responsible for the irreproducibility of the CSP observed. In contrast, the A β_{40} aggregation profiles reported on by ThT fluorescence show a dose-dependent effect on the extent of A12a hydrolysis in ammonium acetate buffer, whereby more hydrolysis leads to an increased lag time and reduced maximum fluorescence. In sodium phosphate, the converse is observed whereby only the unmodified A12a can increase the lag time of A β_{40} .

Although this investigation did not reveal the cause of the irrepressible effects on A β_{40} $^1\text{H}^{15}\text{N}$ -HSQC spectra, it did highlight an additional criterion which could be added to the toolbox. It is well known that amyloid aggregation is sensitive to buffer conditions. Testing whether compounds are able to modulate A β_{40} aggregation under a range of buffer conditions would add a new level of stringency to the toolbox.

4.7 Discussion

The purpose of this chapter was to demonstrate the applicability of the method toolbox developed in Chapter 3. Work was geared to identify a novel compound, or set of compounds, which could modulate A β_{40} aggregation and then to probe how this modulation was achieved. Although unsuccessful in identifying a new modulator of A β_{40} aggregation, the testing of the toolbox conducted demonstrated the suitability of method chosen and even highlighted an addition criteria for compounds which could improve of the toolbox stringency (Figure 4.43).

The journey from library choice to being able to make an informed decision on compound impact on A β_{40} aggregation has been documented in this chapter. The initial library of compounds was chosen based on a focused screen using ROCS analysis. This was followed by a ThT fluorometry screen to choose a subset of molecules for more detailed investigation. Based on this screen, mass analysis was conducted on compounds of interest to check the integrity of the library samples and commercial versions of the compounds were purchased where possible. During this stage of the investigation there were indications of compound instability as many of the library compound contained unexpected masses, often in addition to the expected mass, but in the case of compound Q06 the expected mass was not observed. As Q06 was still absent from the purchased

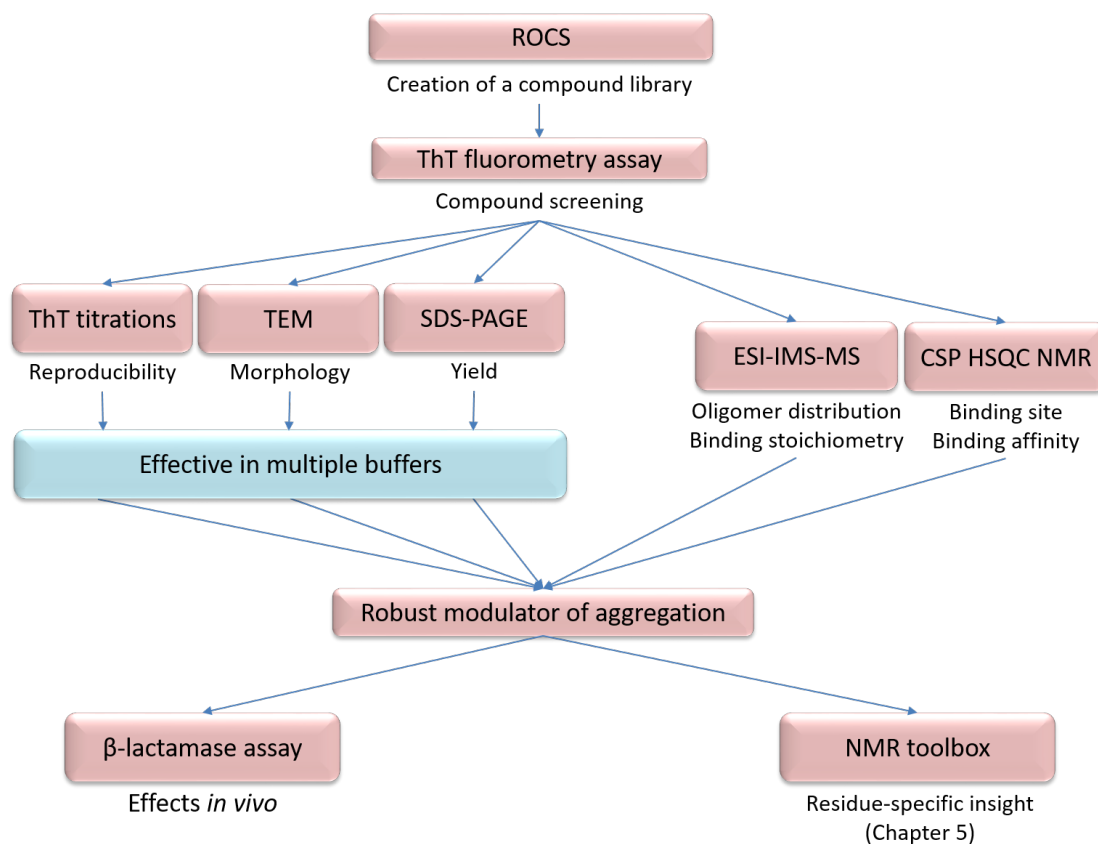


Figure 4.43: The improved toolbox strategy for finding robust modulators of amyloid aggregation.

The new step to ensure effectiveness of compounds in different buffers is highlighted in blue.

form of this compound it is a clear indication that either Q06 was highly unstable or that it was not amenable to ESI-MS analysis on the acetonitrile gradient. Despite mass discrepancies it was interesting to investigate how the compounds could affect $A\beta_{40}$ aggregation. The variation in compound structures was now broader than had originally been planned as many of the library compound structures were clearly divergent from the original query molecules.

The reproducibility of effects observed by compounds on $A\beta_{40}$ aggregation was poor when studied by ThT fluorometry. This projected some uncertainty onto whether the ThT screen was an optimal method to use as the first step in finding potential inhibitors of $A\beta_{40}$. Nevertheless, the use of ThT fluorometry was justified due to its high false positive rate as it would have been problematic to use a more stringent assay in the first instance of compound testing due to the risk of obtaining false negative results. These could have resulted in the exclusion of promising aggregation modulators from further

investigation. False positive results are easily identified from the additional experiments in the toolbox as discussed in Chapter 3. The alterations in the $A\beta_{40}$ aggregation kinetics observed by ThT fluorometry were minor in comparison to the effects of query compound 1,2-naphthoquinone - the published inhibitor of amyloid aggregation. It was possible therefore that the effects compounds had on the ThT profiles in the initial screen were too small despite the significance indicated by the student t-test. Although a significant inhibition or promotion affect on aggregation would have been interesting to study - and to probe how a compound could cause such a large effect - the small changes detected on $A\beta_{40}$ kinetics may have indicated more subtle alterations in the $A\beta_{40}$ monomer conformation which would be identified using NMR. Based on the work conducted in this chapter it may be worthwhile to derive threshold levels of perturbations observed by ThT fluorometry. However, a balance must be struck in order to not exclude compounds which can cause reproducible small changes in amyloid aggregation. This could be achieved by requiring compounds to enter the screen multiple times.

As the ThT assay was only a single approach to detecting effects on $A\beta_{40}$ aggregation, the investigation was continued using the selection of structural methods proposed in the previous chapter (and outlined in Figure 4.43) which provided insight into $A\beta_{40}$ aggregation from orthogonal perspectives. Use of TEM showed that none of the compounds prevented $A\beta_{40}$ forming fibrillar aggregates by the end point of the reactions and the SDS-PAGE fibril yield assay showed that aggregates were formed reproducibly.

The ESI-MS was a useful indication of interaction between the compounds and $A\beta_{40}$. After the ESI-MS, compound A12a was most interesting as an intereaction between A12a an $dA\beta_{40}$ was observed. Ideally, a compound hit would have exhibited specific binding to $A\beta_{40}$ and its site of interaction could then have been probed in subsequent NMR experiments. Had this been the case, $^1\text{H}^{15}\text{N}$ -HSQC experiments would have been carried out using a titration of compound concentrations in order to measure a binding affinity. If the binding affinity was too high to be observed by NMR, then alternative methods, such as surface plasmon resonance could have been considered, optimised and used.

The observation of A12a effects on the $A\beta_{40}$ spectrum by NMR was exciting. Although

compound stability issues prevented further investigation into the A12a-A β_{40} interaction and how A β_{40} conformation was affected, it demonstrated that the use of $^1\text{H}^{15}\text{N}$ -HSQC spectra was a useful tool to use as an indication of compound-A β_{40} interaction. The instability of the compounds investigated, namely A12a, explains some of the irreproducibility of results and some of the discrepancies in compound effects, e.g. when compounds could promote aggregation in one instance and then delay aggregation in another repeat of the experiment. This is possibly due to different compound species and population distributions being present in the compound stocks. The difficulty in working with these compounds makes them non-ideal candidates for future study into the mechanism of A β_{40} aggregation. Closer investigation as to why Q06a affected the A β_{40} $^1\text{H}^{15}\text{N}$ -HSQC spectrum could have been interesting but work was needed to identify the compound identity.

Through the investigation into A12a stability, the contrasts in compound effects on A β_{40} in different buffers were highlighted. Some of the methods in the toolbox were more suited to different buffers, for example, ESI-IMS requires a volatile, low-ionic buffer such as ammonium acetate. However, for NMR, the volatile nature of ammonium acetate caused concerns over sample ‘bubbling’ on application of magnetic pulses. For NMR, sodium phosphate is ideal as it can be pH-ed using mono- and di-basic forms rather than typical use of NaOH/HCl which increases salt content. Due to this, an additional step in the toolbox was suggested whereby compounds were tested for effects on A β_{40} aggregation in different buffers to monitor the stringency of compound robustness.

At this stage, compound profiles were assessed to decide whether any of the lead compounds were reliable modulators of A β_{40} aggregation. For the compound investigated, it was decided that none of the compounds were robust modulators of amyloid aggregation and thus did not warrant further investigation to assess *in vivo* effects - using the β -lactamase assay - or for residue-specific profiling by NMR investigation.

Despite not identifying a novel modulator of amyloid aggregation, the testing of the toolbox has been worthwhile as it has led to the improvement of the toolbox strategy which can be applied in the future to other sets of compounds.

Chapter 5

Residue Specific Investigation into the Intrinsically Disordered $A\beta_{40}$ Peptide

The methods toolbox which was brought together in Chapter 3, and applied in Chapter 4, focused on a combination of complementary techniques to identify small molecules which could modulate $A\beta_{40}$ aggregation. This chapter set out to prepare the framework for study into how these small molecules caused their effects on $A\beta_{40}$ aggregation at a residue-specific level using NMR techniques. Hence this chapter brings together an NMR-based strategy which can probe the influence of small molecules on amyloidogenic IDPs. To demonstrate the techniques, and to create a set of data for future comparative analysis, the structural and dynamic properties of $A\beta_{40}$ (without small molecules) are measured under optimised conditions which are suitable for small molecule addition later.

As discussed in the introduction, IDPs do not exist solely as a random coil, but instead are an ensemble of transiently inter-converting states. Characterisation of the $A\beta_{40}$ monomer ensemble has been conducted previously using a combinatorial approach including multiple structural methods, e.g. CD and NMR, to generate parameters which have been used in molecular modelling. Conformational ensembles are excellent resources for understanding the behaviour of IDPs such as $A\beta_{40}$ monomer. However, the

nature of the modelled, landscape inherently means that measured parameters are averaged and precise data are moulded into an overall, snapshot of structural probabilities. The purpose of this work is to be able to characterise the precise difference in ensemble properties on addition of small molecules - which can perturb amyloid formation. As the A β ₄₀ monomer exists as a heterogeneous, dynamic ensemble, a variety of NMR techniques must be implemented to probe different attributes of the peptide - such as structural features, structural preferences and dynamic regions-. Assimilating a set of experimental data which are highly sensitive to even subtle structural or dynamic perturbations in A β ₄₀ - which occur on small molecule addition - will yield insight into key features of the amyloid formation pathway of the peptide.

All NMR measures are an ensemble average of all the A β ₄₀ molecules in solution. In a calculated energy landscape, small changes in conformation stability may be overlooked or subsumed into the general error of the predictions. However, directly comparing parameter measures ensures small changes can be noted and not overlooked. This is the power of such a sensitive technique. This work will act as a reference to future work in the amyloid field, especially related to small molecule perturbations in A β ₄₀ conformation in the early stages of aggregation.

One of the major benefits of using NMR to probe the A β ₄₀ conformation ensemble is that residue specific information can be obtained and different thermodynamic and kinetic properties can be monitored. Firstly different buffer conditions were tested to ensure A β ₄₀ could be monitored along the entire length of the peptide distinguishing features of the N-, C-terminal regions and central regions of the peptide chain. Section 5.1 depicts the effects of two buffer compositions, pH, temperature, and DMSO. A DMSO titration was conducted in order to ensure compatibility of the A β ₄₀ apo methods and measurements with future A β ₄₀ investigations with small molecules.

Narrow dispersion in the ¹H dimension of the NMR ¹H¹⁵N-HSQC spectrum can indicate intrinsic disorder in a peptide because the flexible chain yields little variation in backbone amide environments (i.e. most interact only with their neighbouring residues and have a similar level of exposure to the solvent, and consequently to hydrogen exchange with the solvent).

To probe conformational features and the structural propensity of the A β ₄₀ backbone and to reveal deviations from random coil conformations, three methods were used:

$\delta C\alpha$ chemical shifts (Section 5.2.1), which constitute an empirically based method to predict regions of secondary structure; temperature coefficients of backbone ¹H amide shifts (Section 5.2.2), which reveals probability of participation in hydrogen bonding; and residual dipolar couplings (RDCs) (Section 5.2.3) which are very sensitive probes of secondary structures propensity.

To monitor the fast (ps-ns) and slow (μ s-ms) dynamic movements of the A β ₄₀ peptide, R₂ measurements (or T₂ measurements, as R₂=1/T₂) (Section 5.3.1) and heteronuclear NOEs (hetNOEs) (Section 5.3.2) were collected, as described in Section 2.2.5.5. Examples of motions which occur on fast dynamic timescale include bond rotations and vibrations, whereas slower motions include binding, folding and unfolding events [367, 379, 473]).

These methods were chosen as they can inform on multiple, complementary, aspects of A β ₄₀ behaviour. Together the methodological approach is sensitive to small effects on A β ₄₀ structural propensity and dynamics [474–476]. The approach has the potential to reveal major and even very subtle perturbations in the A β ₄₀ ensemble caused by small molecule addition. Future application of this work has the potential to reveal key structural transitions for specific regions of the peptide which may be vital in the amyloid aggregation mechanism. Ultimately, it is a potential tool to direct small molecule design for either therapeutic or further investigatory studies.

5.1 Prerequisites to the study of A β ₄₀ by NMR

5.1.1 Optimisation of Sample Conditions for NMR Investigation

In order to maximise the information gained from NMR investigation, it was important to select conditions which would provide well-resolved peaks for the majority of the backbone amides of A β ₄₀. It is well known in the literature that both amyloid formation and IDP behaviour are greatly affected by buffer conditions such as salt concentration, ionic strength, pH, temperature, as well as peptide concentration. In this project, buffer salts, temperature, and pH were varied to find optimal conditions for NMR data collection as described in this section.

5.1.1.1 Comparing Ammonium Acetate and Sodium Phosphate as Buffers for NMR Samples

To ascertain whether A β ₄₀ could yield clear NMR signals, ¹⁵N-labelled A β ₄₀ was recombinantly expressed and purified (see Sections 2.2.2.1 and 2.2.2.3). To aid comparison with previous work in this thesis, the peptide was solubilised in the same buffer used in the ThT, MS and TEM studies described in Chapters 3 and 4; 50 mM ammonium acetate, pH 6.8. Figure 5.1a shows the ¹H¹⁵N-HSQC spectrum for 50 μ M A β ₄₀, at 37 °C. This spectrum showed 30 resolved peaks corresponding to 30 backbone amides out of a potential 40. Even at this initial, pre-optimised stage, it was promising that A β ₄₀ would be amenable to NMR investigation.

With an aim to increase the appearance of more amide resonances an alternative buffer was tested: 20 mM sodium phosphate buffer (Figure 5.1b). The sodium phosphate buffer was chosen based on work by Newby *et al.*, [372] which presents A β ₄₀ apo ¹H¹⁵N-HSQC spectra with 38 peaks evident (26 well-resolved peaks, 8 partially-overlapped peaks, and 4 substantially-overlapped peaks).

Overall, both spectra were very similar indicating that the peptide adopts conformations which are similar in both buffers. Notably each of the spectra presented in Figure 5.1 show good dispersion in the ¹⁵N dimension, but are only narrowly dispersed in the ¹H dimension which is indicative of an intrinsically disordered peptide. As there was precedent in the literature using A β ₄₀ in a sodium phosphate buffer [372], 20 mM sodium phosphate was taken forward as the buffer to optimise for residue specific NMR investigation of A β ₄₀. The reason for this precedent is because phosphate is a non-protonated buffer and therefore does not obscure protein signals.

5.1.1.2 Effect of Temperature on the ¹H¹⁵N-HSQC A β ₄₀ Spectrum

Next, the effect of temperature on signal intensity was tested. It was important to acquire data under conditions which gave rise to intense peaks to minimise acquisition time which is particularly important for an aggregation prone system such as that of A β ₄₀. Figure 5.2 shows the change in ¹H¹⁵N-HSQC spectra when acquired at 5 °C and 37 °C.

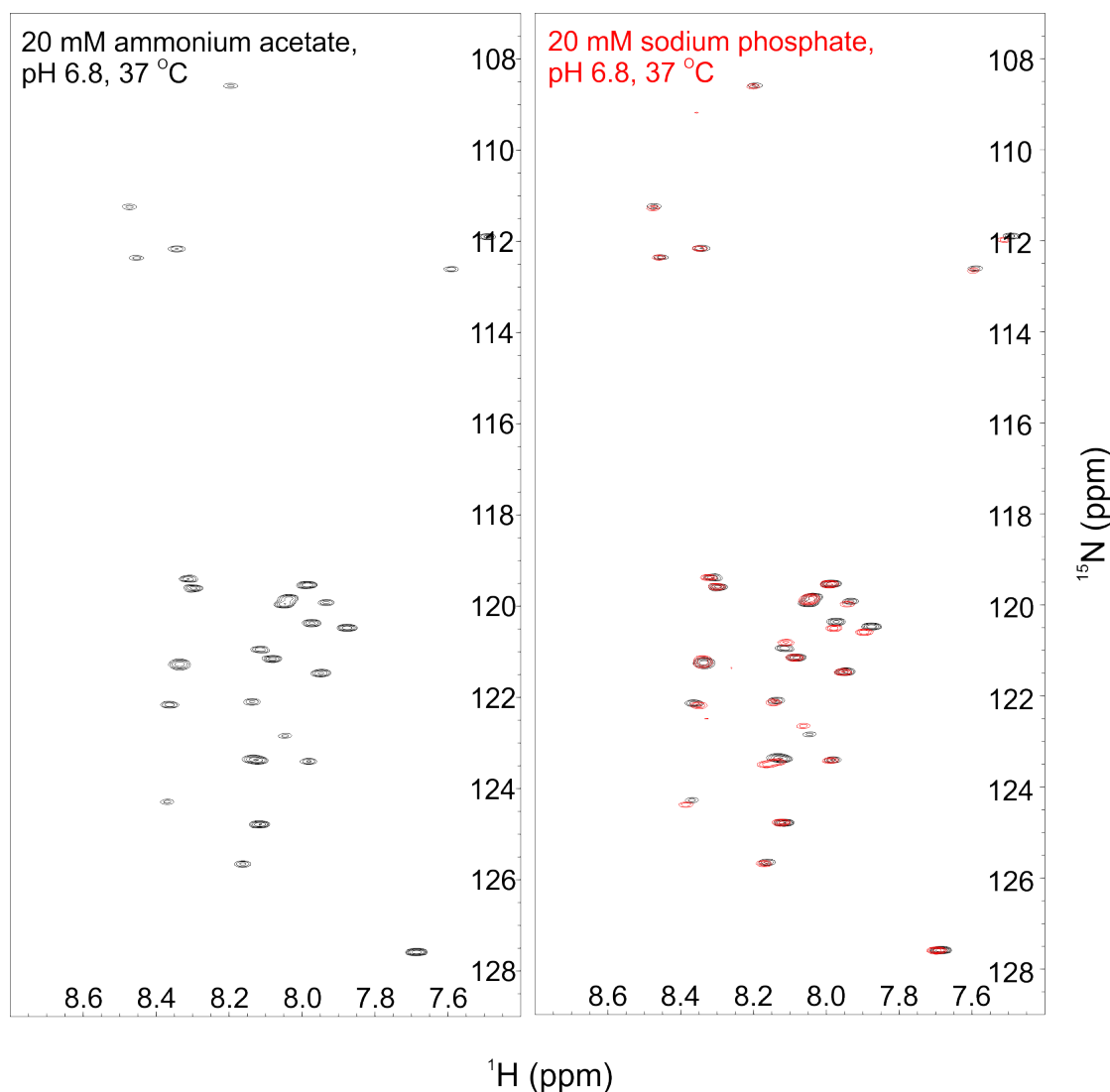


Figure 5.1: Preliminary $^1\text{H}^{15}\text{N}$ -HSQC spectra of A β ₄₀ in different salt solutions a) 50 mM A β ₄₀ in 50 mM ammonium acetate, pH 6.8, 37 °C, with 10 % D₂O. b) Figure a (black) overlaid with the HSQC spectrum of 50 mM A β ₄₀ in 20 mM sodium phosphate, 0.5 mM EDTA, 0.02 % (*w/v*) NaN₃, pH 6.8, 37 °C (red). All spectra were acquired using a 750 MHz spectrometer with a TCI-cryoprobe; ^1H -optimised triple resonance NMR inverse probe and Bruker Avance III HD console.

In globular proteins, increased temperatures usually lead to greater signal intensity because of faster tumbling, and therefore faster R_2 relaxation rates leading to sharper peaks with narrower linewidths. In contrast, the opposite is typical for IDPs as significant line broadening occurs at higher temperatures. Line broadening is observed as a result of the fast exchange of $^1\text{H}^{\text{N}}$ protons with water. As expected, a decrease in peak intensity was observed for A β ₄₀ as the temperature was increased to 37 °C. Thus, the best spectrum quality was observed when data were acquired at 5 °C. In conclusion from this experiment, further NMR investigation was conducted at 5 °C.

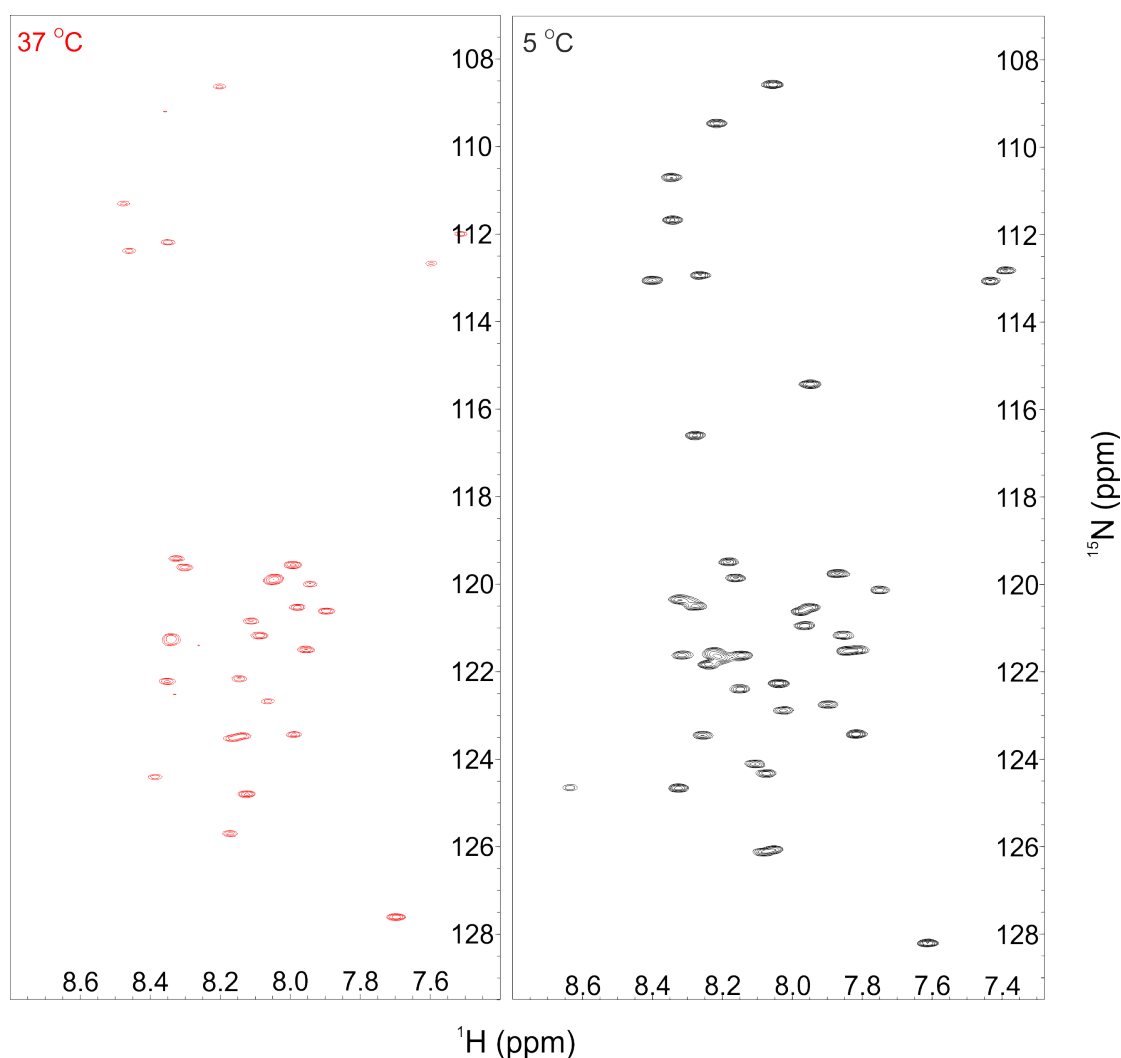


Figure 5.2: Comparison of $^1\text{H}^{15}\text{N}$ -HSQC spectra of A β_{40} at high and low temperatures. $^1\text{H}^{15}\text{N}$ -HSQC spectrum of 50 mM A β_{40} in 20 mM sodium phosphate, 0.5 mM EDTA, 0.02 % (*w/v*) NaN $_3$, pH 6.8, with 10 % D $_2$ O acquired at either 37 °C (left panel, red) or the same sample acquired at 5 °C (right panel, black). Both spectra were acquired using a 750 MHz spectrometer with a TCI-cryoprobe; 1H-optimised triple resonance NMR inverse probe and Bruker Avance III HD console.

5.1.1.3 Effect of pH on the $^1\text{H}^{15}\text{N}$ -HSQC A β_{40} Spectrum

Next, a pH titration between 6.8 and 7.4 was conducted (Figure 5.3) using the conditions previously optimised: 20 mM sodium phosphate buffer, at 5 °C. Altering the pH may enable separation of some overlapping peaks, for example, His residues are very sensitive to pH as they can experience different protonation states close to physiological pH and thus a change in the nuclei magnetic environment is experienced. This is represented on the $^1\text{H}^{15}\text{N}$ -HSQC spectrum as a chemical shift change.

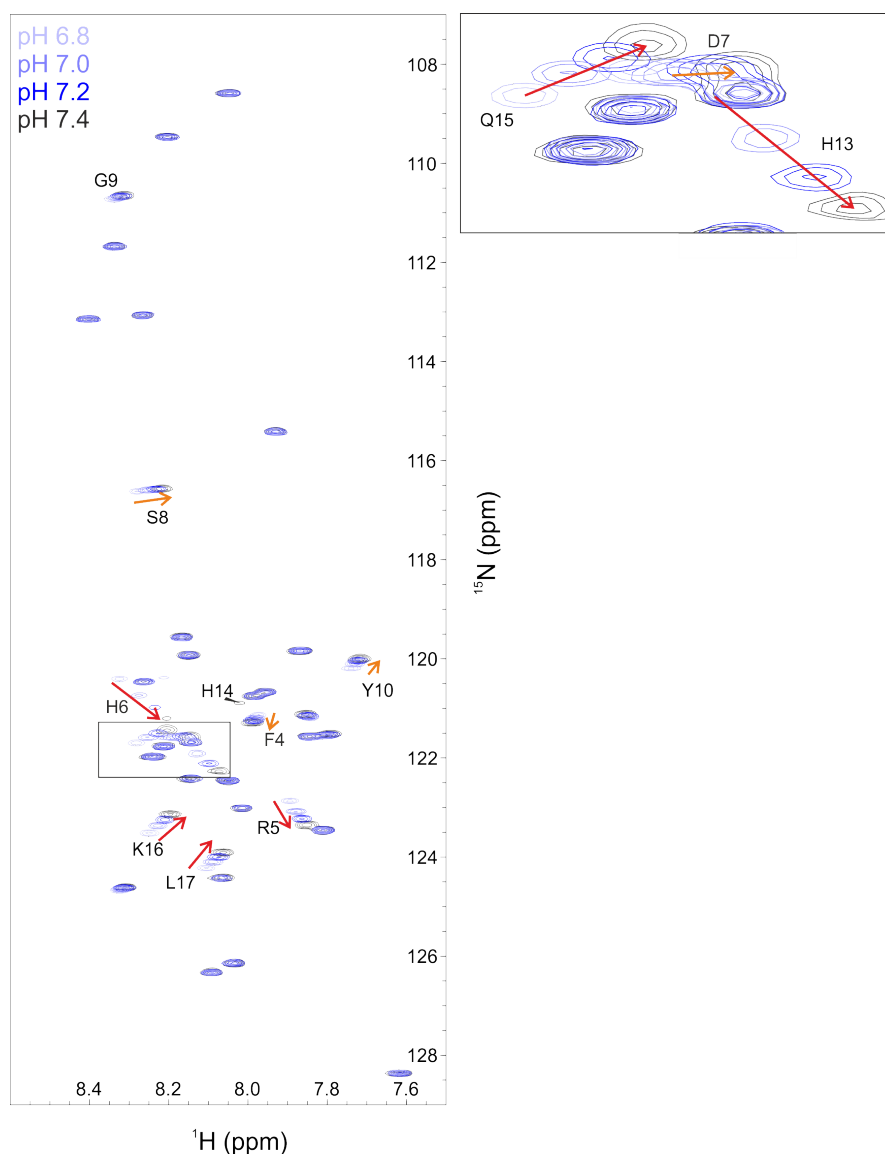


Figure 5.3: A β_{40} $^1\text{H}^{15}\text{N}$ -HSQC spectra dependence on pH.

^1H - ^{15}N -HSQC spectrum of 50 mM A β_{40} in 20 mM sodium phosphate, 0.5 mM EDTA, 0.02 % (*w/v*) NaN $_3$, 5 °C, with 10 % D $_2$ O across a pH gradient: pH 6.8 (light blue), pH 7.0 (mid-blue), pH 7.2 (dark blue), pH 7.4 (black). Red arrows and peak labels highlight resonances which are affected by pH and the zoom in region (black box) shown in the top right clarifies the movement of some of the overlapping amide signals. Samples were made as described in 2.2.5.5 and the pH adjusted using 10 mM NaOH and HCl. All spectra were acquired using a 750 MHz spectrometer with a TCI-cryoprobe; 1H-optimised triple resonance NMR inverse probe and Bruker Avance III HD console.

As expected, there are large shifts observed for Histidine residues (His6, His 13, and

His14) and the sequential amino acids (Arg5, Asp7, Ser8, Gly9, Tyr10, and Gln15, Lys16, Leu17) likely to be caused by the change in Histidine protonation.

The lower limit of this pH titration was chosen for consistency with ThT, ESI-IMS-MS, and TEM data in the previous chapter, and the upper limit was chosen based on conditions used in a published investigation of A β_{40} by Newby *et al.*, [372]. Newby *et al.*, published the pK^H values of His6, His13, and His14 in A β_{40} (without the N-terminal methionine) as 6.85, 6.81, and 6.79 respectively. In fact, the paper [372] goes onto quantify the extent of protonation for each Histidine at pH 6.8, \sim 50 % chance of protonation, and pH 7.4, \sim 20-25 % chance of protonation. This is consistent with the chemical shift changes observed in this study.

It was decided to conduct further NMR experiments at pH 7.4 as most peaks were well resolved with strong peak intensity. Moreover, aligning pH with previous work in the field enabled comparison of results.

5.1.2 Ensuring Stability of the A β_{40} Peptide for the Time Period Required for NMR Data Acquisition

For some NMR experiments, including 3D experiments and relaxation measurements, long acquisition times are needed to obtain the necessary resolution and sensitivity. This is especially true when measuring IDP parameters which are likely to exhibit very small changes. To investigate whether A β_{40} would be suitable for long experimentation the peak intensity of the A β_{40} sample was monitored over 16 hours, Figure 5.4, using ¹H¹⁵N-HSQC spectra.

In contrast to the ThT assays presented in Chapter 4, Section 4.6.1, Figure 5.4 suggests that A β_{40} is stable in 20 mM sodium Phosphate, pH 7.4, 5 °C as the peak intensity only decreases by a maximum of \sim 20 %. There are no chemical shift perturbations or new resonances detected suggesting the absence of conformational changes over this time period. This finding suggests that monomeric A β_{40} is the most populated species over 16 h under the NMR conditions. Based on this experiment, these buffer conditions would be suitable for the study of A β_{40} using long NMR procedures, including 3D experiments for spectral assignment in Section 5.1.4, R₂, and hetNOE relaxation measurements (Section 5.3.1 and Section 5.3.2).

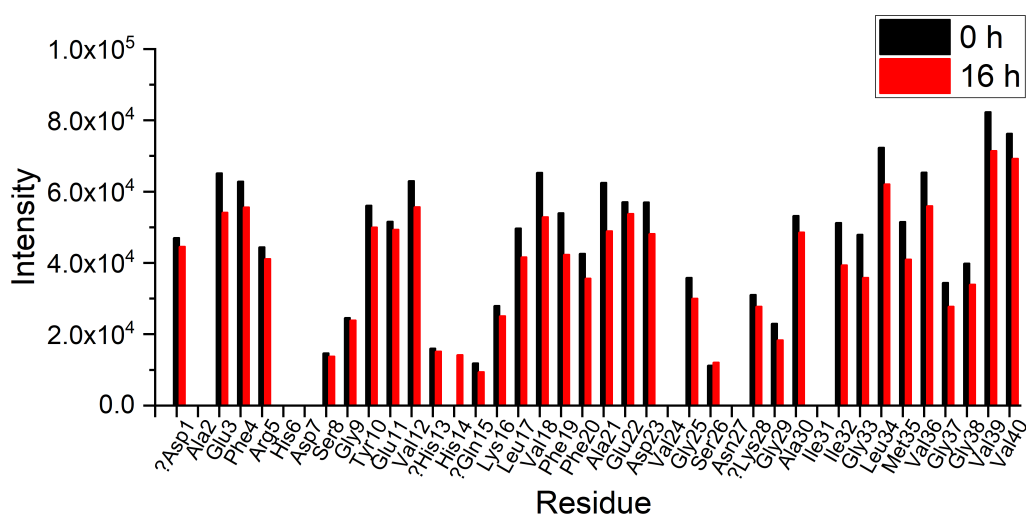


Figure 5.4: Stability of A β_{40} in optimised buffer conditions.

Change in peak intensity of the ^1H - ^{15}N -HSQC spectrum of 50 mM A β_{40} in 20 mM sodium phosphate, 0.5 mM EDTA, 0.02 % (*w/v*) NaN₃, pH 7.4, 5 °C, with 10 % D₂O over 16 h (red) compared to the initial spectrum at 0 h (black). All spectra were acquired using a 750 MHz spectrometer with a TCI-cryoprobe; ^1H -optimised triple resonance NMR inverse probe and Bruker Avance III HD console.

5.1.3 The Effect of DMSO on A β_{40} Conformation

A requirement of the methodological approach devised in this chapter is its compatibility with small molecule presence in samples of A β_{40} . DMSO (a weakly acidic, polar, and aprotic compound) is a largely universal solvent. Due to this, DMSO is commonly used to solubilise small molecules in high-throughput compound screening [477], as has been implemented in this thesis in Chapter 4 which used small compounds stock solutions in DMSO. Thus, to compare measured parameters between A β_{40} and A β_{40} in the presence of small molecules, a small amount (< 10 % (*v/v*) of the sample volume) of DMSO must be included in the buffer composition.

To measure the extent of spectral perturbation caused by DMSO, a titration of DMSO percentages was conducted. Figure 5.5, shows a titratable effect is observed for chemical shift position on increasing the DMSO percentage of the sample from 0 % to 6 % (*v/v*). Only small perturbations were observed upon DMSO titration suggesting that the presence of up to 6 % (*v/v*) DMSO does not significantly change A β_{40} conformation. As all of the compounds listed in Chapter 4 were solubilised in 100 % DMSO before

incorporation into A β ₄₀ samples, DMSO was present in all of the samples. In Chapter 4 the majority of samples contained 2 % (*v/v*) DMSO, thus 2 % (*v/v*) DMSO was selected for A β ₄₀ analysis for consistency.

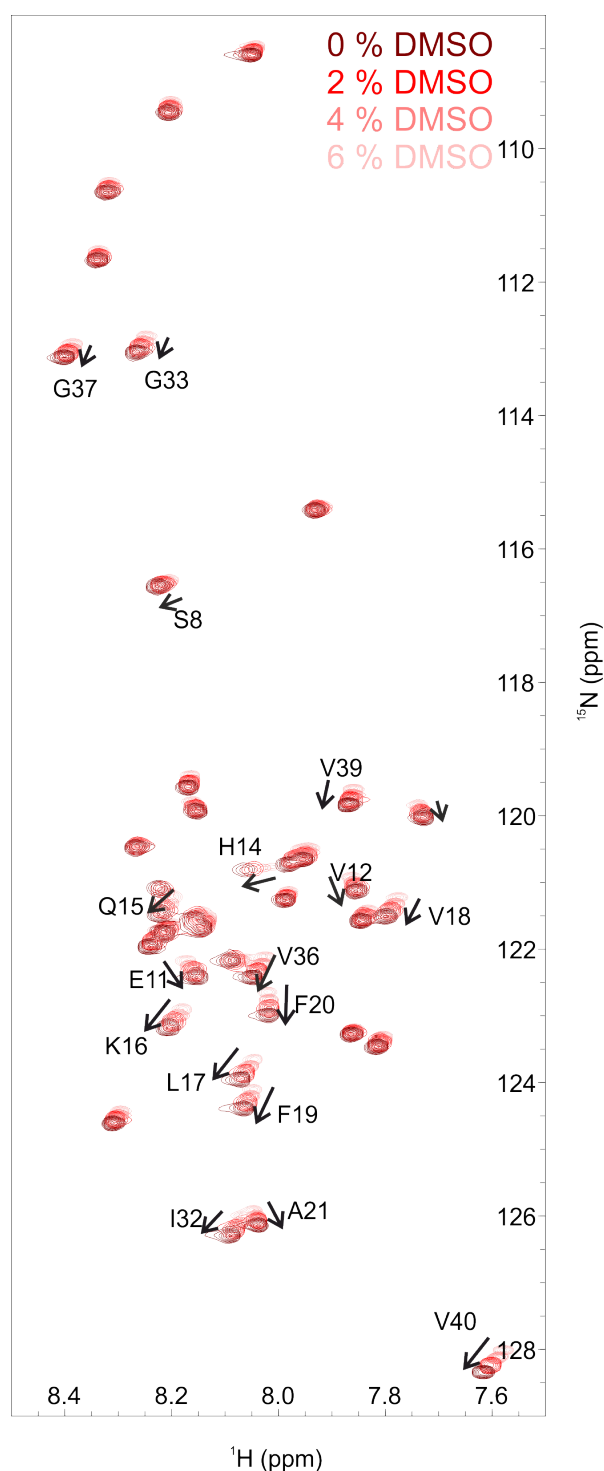


Figure 5.5: Monitoring the effect of DMSO percentage on the ^1H - ^{15}N -HSQC spectrum of A β ₄₀.

^1H - ^{15}N -HSQC spectra of 50 mM A β ₄₀ in 20 mM sodium phosphate, 0.5 mM EDTA, 0.02 % (*w/v*) NaN₃, pH 7.4, 5 °C, with 10 % D₂O across a gradient of DMSO: 0 % (dark red), 2 % (*v/v*) (red), 4 % (*v/v*) (pink), and 6 % (*v/v*) (light pink). Black arrows and resonance labels highlight changes in chemical shifts of some residues. All spectra were acquired using a 750 MHz spectrometer with a TCI-cryoprobe; ^1H -optimised triple resonance NMR ‘inverse’ probe and Bruker Avance III HD console.

As a result of the preceding work to optimise buffer conditions for NMR data collection the following composition was used for sample preparation: 50 μ M A β ₄₀, 20 mM sodium phosphate buffer including 0.02 % (*w/v*) NaN₃, 0.5 mM EDTA, 10 % D₂O, 2 % DMSO (*v/v*), at pH 7.4.

5.1.4 Backbone Amide Assignment of A β ₄₀

NMR spectral assignment for globular proteins and IDPs is well established with multiple methods which can be used [478, 479]. These methods tend to rely on coherence transfer steps between backbone ¹³C and ¹⁵N nuclei as well as associated ¹H nuclei. For A β ₄₀, good assignment was achieved from standard 3D assignment methods, due to its small size.

The backbone assignment of A β ₄₀ was previously published under varying conditions [367, 372, 480–482], including those similar to the optimised sample conditions used in this work [372]. Due to the nature of IDPs and their great sensitivity to small environmental changes, validation of previous assignment of the recombinantly expressed A β ₄₀ was performed (Figure 5.6 and Table 5.1) using a 3D Best Trosy HNCA experiment described in Section 2.2.5.5. Comparison to published spectra, and pH dependence behaviour observed previously was used to validate the assignments.

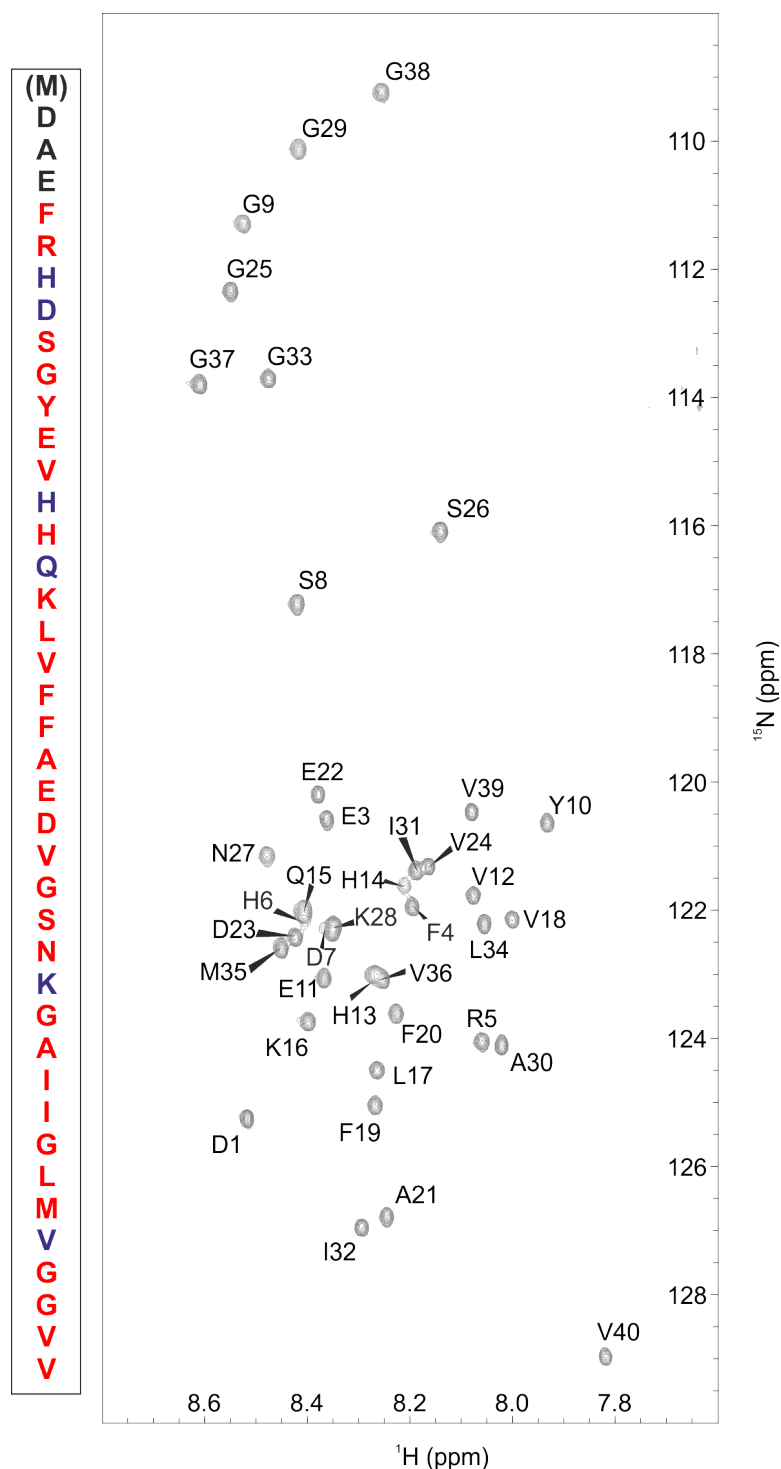


Figure 5.6: Assigned $^1\text{H}^{15}\text{N}$ -HSQC spectrum of A β ₄₀.

Left: Vertical sequence of A β ₄₀ showing extent of assigned amides (red), overlapping amides (blue) and unassigned amides (black). Right: Assigned ^1H - ^{15}N -HSQC spectrum of 50 mM A β ₄₀ in 20 mM sodium phosphate, 0.5 mM EDTA, 0.02 % (*w/v*) NaN₃, pH 7.4, 5 °C, 2 % (*v/v*) DMSO with 10 % D₂O. Acquired using a 950 MHz Bruker Ascend Aeon, Next-generation ultra-high field NMR magnet with a TXO-cryoprobe or a TCI-cryoprobe; ^1H -optimised triple resonance NMR inverse probe and Bruker Avance III HD console.

TABLE 5.1: Table of ¹H, ¹⁵N, and ¹³C values for each residue in A β ₄₀. Resonances are given in ppm and those preceded by a 't' indicate that these assignments are tentative.

Residue	¹ HN	¹⁵ N	¹³ C _{α}
Met0	-	-	t51.530
Asp1	t8.517	t125.273	t49.807
Ala2	-	-	-
Glu3	8.360	120.638	53.670
Phe4	8.196	121.953	54.796
Arg5	8.060	124.074	52.591
His6	8.406	122.236	53.350
Asp7	8.349	122.275	51.047
Ser8	8.417	117.240	56.112
Gly9	8.525	111.323	42.381
Tyr10	7.932	120.639	55.278
Glu11	8.369	123.075	53.576
Val12	8.074	121.766	59.819
His13	8.271	123.016	53.143
His14	8.210	121.662	53.329
Gln15	8.405	122.055	52.914
Lys16	8.398	123.754	53.390
Leu17	8.264	124.512	52.123
Val18	7.995	122.153	58.953
Phe19	8.269	125.062	54.452
Phe20	8.227	123.621	54.346
Ala21	8.244	126.797	49.364
Glu22	8.378	120.221	53.614
Asp23	8.424	122.441	51.105
Val24	8.164	121.335	59.796
Gly25	8.550	112.362	42.489
Ser26	8.140	116.104	55.553
Asn27	8.480	121.154	50.249
Lys28	8.351	122.325	53.733
Gly29	8.418	110.140	42.156

Continuation of Table 5.1			
Residue	¹ H _N	¹⁵ N	¹³ C _α
Ala30	8.021	124.129	49.432
Ile31	8.188	121.386	58.067
Ile32	8.294	126.969	58.168
Gly33	8.476	113.720	42.148
Leu34	8.056	122.254	52.116
Met35	8.451	122.623	52.223
Val36	8.253	123.078	59.567
Gly37	8.610	113.819	42.204
Gly38	8.255	109.277	42.072
Val39	8.080	120.484	59.478
Val40	7.818	128.990	60.782

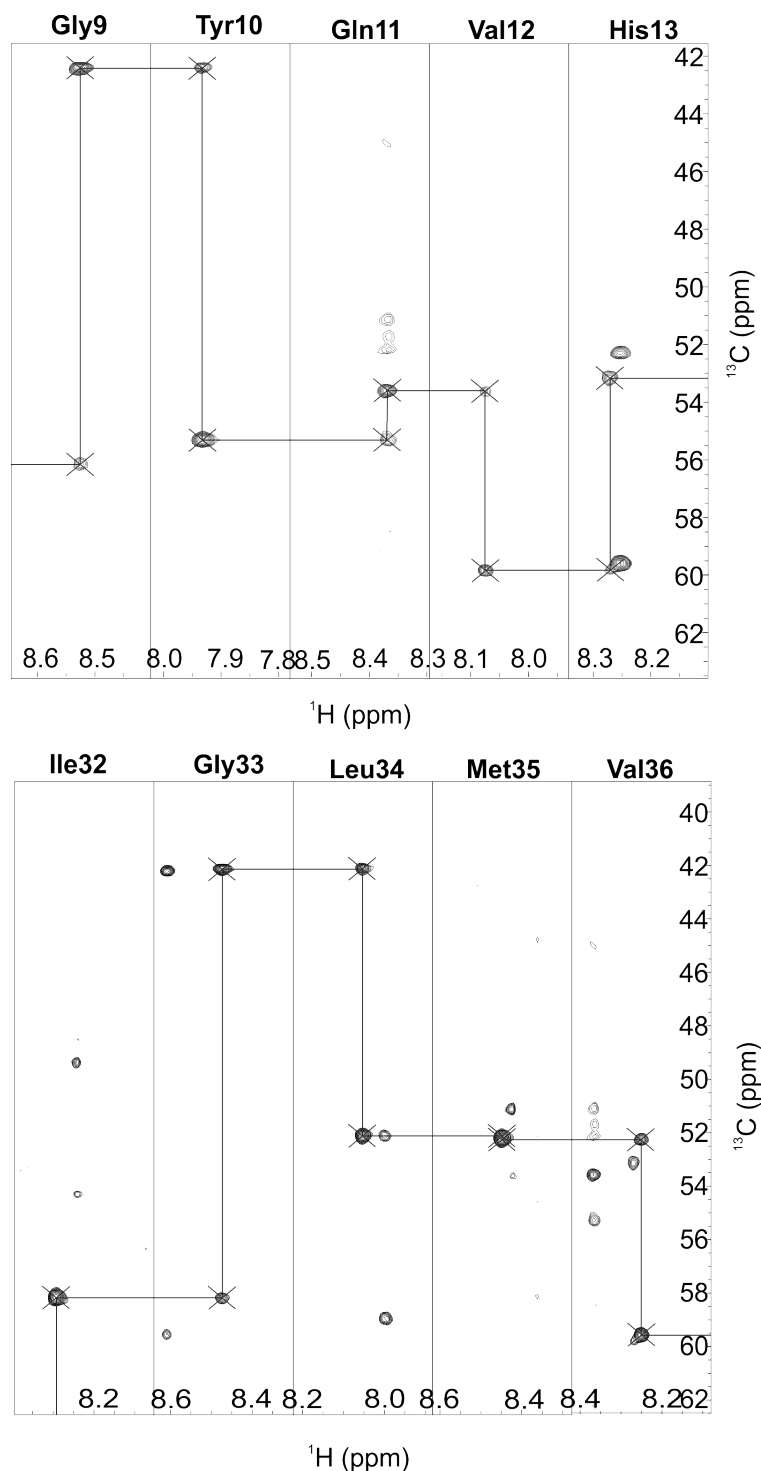


Figure 5.7: Examples of how A β_{40} spectral assignment was conducted.

Two examples of how backbone assignments were performed using a HNCA experiment of 50 mM A β_{40} in 20 mM sodium phosphate, 0.5 mM EDTA, 0.02 % (*w/v*)

NaN₃, pH 7.4, 5 °C, 2 % (*v/v*) DMSO with 10 % D₂O. Acquired using a 950 MHz

Bruker Ascend Aeon, Next-generation ultra-high field NMR magnet with a TXO-cryoprobe or a TCI-cryoprobe; ^1H -optimised triple resonance NMR inverse probe and Bruker Avance III HD console. The most intense peak in each strip corresponds to the 'i' and the weaker peak is the 'i-1' residue which enables matching up of strips to permit assignment. For Met35 the i and i-1 peaks overlap which is confirmed by the alignment of Leu34i peak and Val26i-1 peaks.

The unassigned resonance has been tentatively assigned to Asp1 though may represent Met0 (as the A β_{40} used in this study has an N-terminal Methionine). However, as an i-1 peak is detected (Figure 5.8) it is more likely to represent Asp1 than Met0 as generally the N-terminal amide experiences too great line broadening from hydrogen exchange with the solvent to give a detectable resonance. Macao *et al.*, [391] published 2D amide spectra for A β_{40} and Met-A β_{40} . For the peptide with the N-terminal methionine a peak is observed in a similar location to the unassigned peak whereas the A β_{40} spectrum shows no resonance here. Whether this resonance represents Met0 or Asp1 is non-vital for this investigation as it can be used to represent a marker for the far N-terminal region of the peptide (in further analyses this resonance will be referred to as tentative Asp1 (tAsp1)).

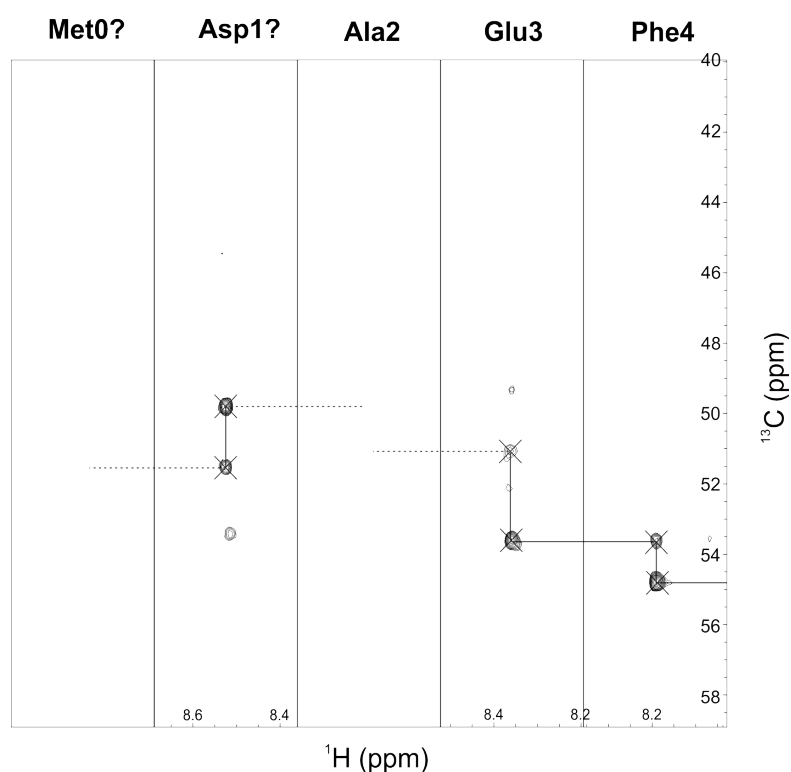


Figure 5.8: Evidence for the tentative assignment of Asp1.

Due to the lack of correlation between the the i-1 peak observed for Glu3 and the peaks for the unassigned resonance, Ala2 can be ruled out, leaving only Met0 or Asp1.

Sample and data collection as in Figure 5.7.

38 out of the 41 residues were assigned using the HNCA data (Figure 5.6) from detection of i and i-1 peaks in the HNCA spectra, Figure 5.7. Ala2 was not observed and there was one unassignable resonance remaining. Of these 38 residues, six are overlapping

so will be excluded from NMR analysis: His6 and Gln15, Asp7 and Lys28, His13 and Val36. Thus for further NMR analysis there is an expected 80 % sequence coverage.

In summary, there is almost complete assignment of the A β ₄₀ peptide and a significant amount of well resolved peaks making this an appropriate system to profile how well a complementary set of NMR methods can be used to investigate IDP conformers. The subsequent sections in this chapter show how, using a combination of NMR techniques, a precise and detailed comparative set of parameters of an IDP can be ascertained. On identification of small molecules which can influence amyloid aggregation, these parameters can be compared to ligand-bound states of A β ₄₀ to reveal specific regions of the peptide which experience either a change in structural propensity or flexibility.

5.2 Characterisation of residue-specific structural propensity in IDPs

This work strives to collate a method strategy for the investigation of important conformer or structural motifs. To this end, structural investigation of A β ₄₀ by NMR techniques was conducted as described in this section.

5.2.1 Predicting Secondary Structure using $\delta^{13}\text{C}\alpha$ Chemical Shifts

Chemical shifts can be good reporters of backbone conformation and there has been focus to develop approaches to exploit this to probe local structural propensities of IDPs (reviewed in [483]). Such approaches use deviations from empirically defined random coil values to imply local geometries and to quantify secondary structure propensities [484–486]. As previously mentioned, the ^1H dispersion observed for A β ₄₀ is narrow which is indicative of an IDP. $\delta^{13}\text{C}\alpha$ chemical shifts can provide further insight into secondary structure. Using the HNCA data used for spectral assignment (Figure 5.1.4), the $\Delta\delta^{13}\text{C}\alpha$ chemical shifts can be calculated using the following equation:

$$\Delta\delta C\alpha = \delta C\alpha_i - \delta C\alpha_{\text{random coil}} \quad (5.1)$$

Where $\delta C\alpha_i$ is the $\delta C\alpha$ position obtained from the experimental data, and $\delta C\alpha_{\text{random coil}}$ is the $\delta C\alpha$ position predicted if that $C\alpha$ atom was part of a random coil. For this analysis, $\Delta\delta^{13}C\alpha$ chemical shifts were calculated within CCPNAnalysis which bases random coil chemical shifts prediction on [392, 393].

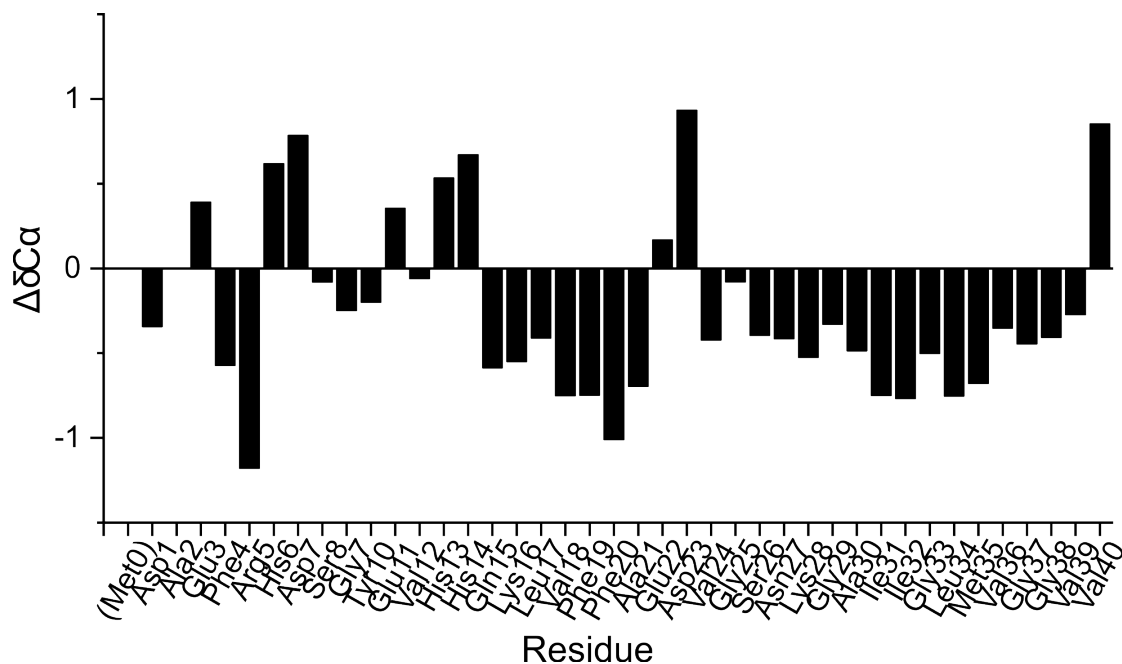


Figure 5.9: Backbone conformation indication from $^{13}C\alpha$ chemical shifts.

$\delta^{13}C\alpha$ values for each residue in $A\beta_{40}$ calculated in CCPNAnalysis whereby the $^{13}C\alpha$ chemical shifts are subtracted from the predicted values had the peptide existed as an entirely random coil.

Residues involved in α -helices have $\delta^{13}C\alpha$ chemical shifts of greater than 2 ppm [376] whereas residues within β -sheets exhibit negative values less than -2 ppm [376]. Figure 5.9 shows the majority of the $\delta^{13}C\alpha$ chemical shifts are within 2 ppm of zero showing strong evidence for intrinsic disorder across the length of the peptide.

NMR $^{13}C\alpha$ chemical shift analysis will be a fast way to extract initial indications of α -helical perturbations on addition of small molecules using previously acquired data. Notwithstanding, this is only a predictive mechanism based on empirical evidence and thus structural propensity needs to be measured specifically using other methods as described in the subsequent sections.

5.2.2 Hydrogen-bonding and Secondary Structure Indications from Temperature Coefficients

The probability of elements of secondary structure forming can be predicted for each residue. Measurement of the extent to which the ¹H-chemical shift of amide protons is perturbed across a temperature gradient can indicate residues which are more likely to be involved in intramolecular, backbone hydrogen bonding opposed to those involved in solvent hydrogen bonding [378, 487–490]. These parameters are known as ¹H^N-chemical shift temperature coefficients (¹H^N-CSTC) and can be used to distinguish intrinsically disordered regions from structured regions of a peptide. ¹H^N-CSTCs are able to shed light on hydrogen bonding due to the thermal expansions in bond length which occur as temperature increases [378]. Larger expansions are more likely between backbone amides and surrounding water molecules than between backbone amide-amide hydrogen bonds due to the less restricted movement of the solvent.

¹H¹⁵N-HSQC spectra were collected across a temperature gradient (5 °C, 15 °C, 20 °C, 25 °C, and 37 °C) and are presented in Figure 5.10a. The spectra are referenced as described in Section 2.2.5.5 and resonances show the expected upfield shift which is typically observed on temperature increase for IDP spectra.

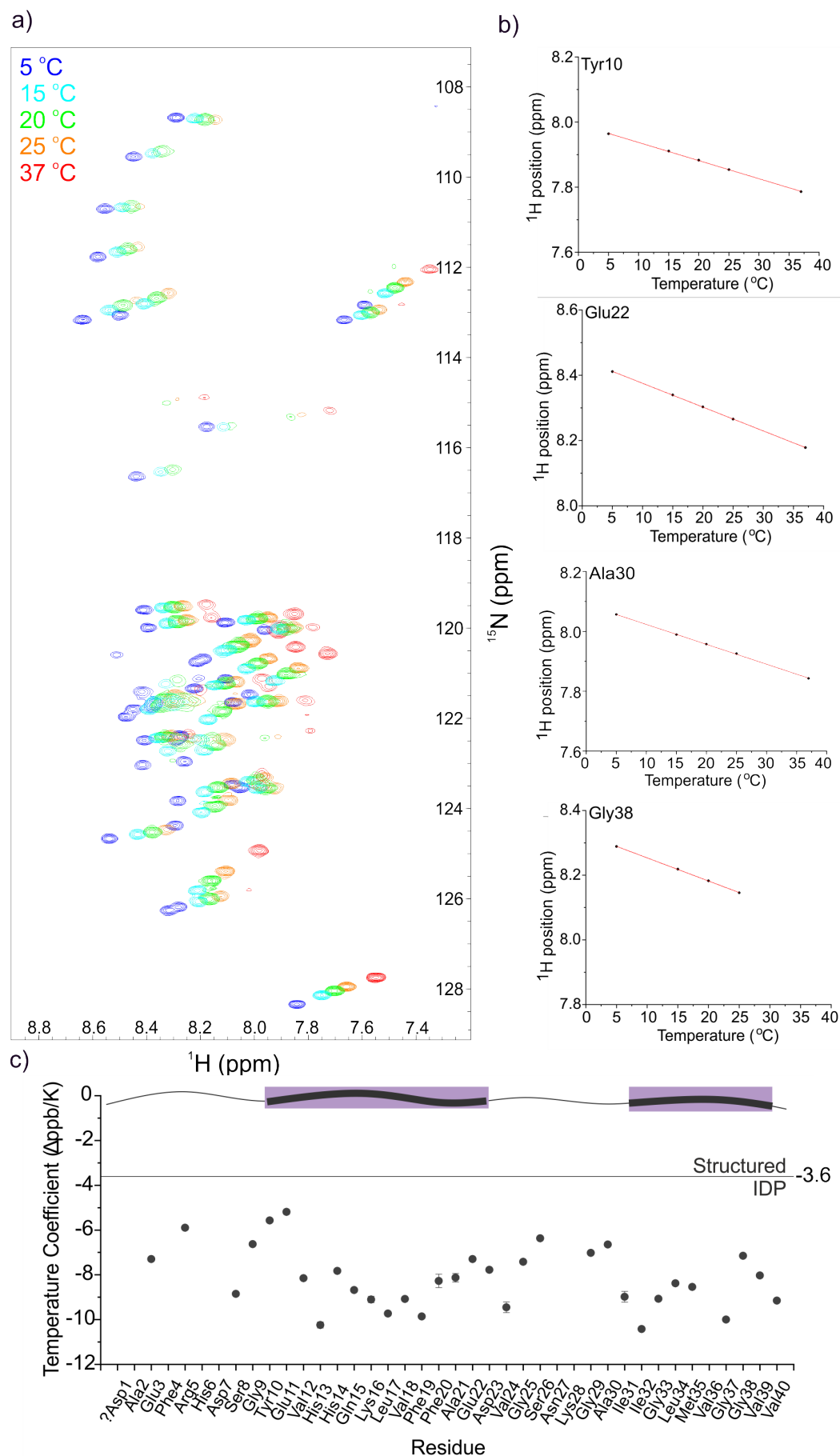


Figure 5.10: a) ^1H - ^{15}N -HSQC spectra of 50 mM A β ₄₀ in 20 mM sodium phosphate, 0.5 mM EDTA, 0.02 % (*w/v*) NaN₃, pH 7.4, 2 % (*v/v*) DMSO, with 10 % D₂O across a temperature gradient: 5 °C (cyan), 15 °C (blue), 20 °C (green), 25 °C (orange), and 37 °C (red). All spectra were referenced using the water peak position and the ^1H temperature factor -0.0119 ppm/° [376] acquired using a 750 MHz spectrometer with a TCI-cryoprobe; ^1H -optimised triple resonance NMR inverse probe and Bruker Avance III HD console. b) Exemplar plots of the linear correlation between ^1H chemical shift position and temperature increase for each resonance (the complete set are in Appendix B.1). The gradient of the linear fit is the temperature correlation coefficient plotted in (c). -3.6 is an empirical cut off value to imply disorder [378]. Predicted regions of structural propensity (think lines) are shown in the purple schematic.

From Figure 5.10a, the temperature titration enables clear peak monitoring for most of the resonances observed in the original 5 °C despite the change in chemical shift position. Monitoring the change in peak position in the ^1H dimension shows a linear dependence on temperature for each residue, a selection of examples are presented in Figure 5.10b. The intensity of some peaks become too low for detection at higher temperatures due to increased exchange with water but there are enough data points for most residues to plot a reliable linear fit which can be used to calculate the $^1\text{H}^{\text{N}}$ -CSTC values (Figure 5.10c).

The more negative the $^1\text{H}^{\text{N}}$ -CSTC is, the less likely the amide is involved in a hydrogen bond. The purpose of using $^1\text{H}^{\text{N}}$ -CSTCs in this study is as a predictor of regions which may be more prone to forming secondary structure. However, as the distinction between structured and unstructured regions is not fully equivalent to hydrogen bonded or non-hydrogen bonded states, an empirically derived threshold value of - 3.6 ppb/K was used in Figure 5.10, to distinguish intrinsically disordered regions [378]. From the data presented, no regions of secondary structure are evident, indeed the $^1\text{H}^{\text{N}}$ -CSTCs for all residues are well into the disordered segment of the graph.

To summarise, based on $^1\text{H}^{\text{N}}$ -CSTC analysis, the entirety of A β ₄₀ is intrinsically disordered with no regions indicating propensity to form Hydrogen-bonded secondary structure elements. The conformational flexibility and dynamics can be inferred from the lack of secondary structure elements as loops and random coils are more likely to exhibit fast flexible movement than rigid α -helices or β -sheets.

5.2.3 Characterisation of Residual Secondary Structure Elements in A β_{40} using RDCs

Use of RDCs as an indicator of structural propensity for regions of an IDP has many advantages over other methods including $\Delta\delta C\alpha$ predictions and $^1\text{H}^{\text{N}}$ -CSTCs. For many IDPs, measurement of RDCs can be used as a highly sensitive tool to obtain residue-specific structural propensities and are commonly used for structural ensemble calculations and MD simulations of IDPs [415] as they can yield insight into conformer interchange on up to a ms timescale and are sensitive to transient long-range interactions [362, 374, 375]. A current trend is to use RDCs to study unfolded proteins [491–494], akin to an IDP, for example, efforts have been made to monitor the conformational space of urea-denatured ubiquitin [491, 495]. Measured RDC values are averages of the whole ensemble of dipolar interactions within a protein, including all protein conformers interconverting at time scales faster than the inverse of RDC values (1/RDC s) [495]. RDCs were used in this work to contribute to the backbone investigation of A β_{40} by mapping regions of structural propensity. Future studies can analyse how the pattern of structural propensity is altered by the addition of compounds which perturb amyloid aggregation.

The method exploits the dependence of dipolar coupling of an NH backbone amide on its vector orientation with respect to the magnetic field vector [362, 375]. RDCs in IDPs are very sensitive to local structure propensities. RDCs provide valuable information about the conformational properties of proteins, including IDPs, and reports on both local and long range structure [363]. RDCs are a measure of the through-space dipolar interaction between two nuclei, given by Equation 5.2.

$$D_{ij} = -\frac{\gamma_i\gamma_j h\mu_0}{4\pi^2 r^3} \left(\frac{3\cos^2\theta - 1}{2} \right) \quad (5.2)$$

where γ_i , γ_j are the gyromagnetic ratios of each nucleus, h , Plank's constant, μ_0 the permeability of a vacuum, r , the distance between nuclei i and j , and θ the orientation of the nuclear vector within the external magnetic field. RDCs contain information on long range angular information of internuclear vectors. In isotropic solutions proteins are free to tumble randomly, thus θ can take all possible values and hence the dipolar coupling, D_{ij} , in Equation 5.2 averages to zero. RDCs arise when the tumbling of proteins

is restricted, reducing the range of values θ can take, and thus giving rise to a non-zero dipolar coupling. Restriction of tumbling can be achieved by adding an alignment medium to a protein sample, for example a filamentous bacteriophage, polyacrylamide gel, or lipid bicelles [496], Figure 5.11a.

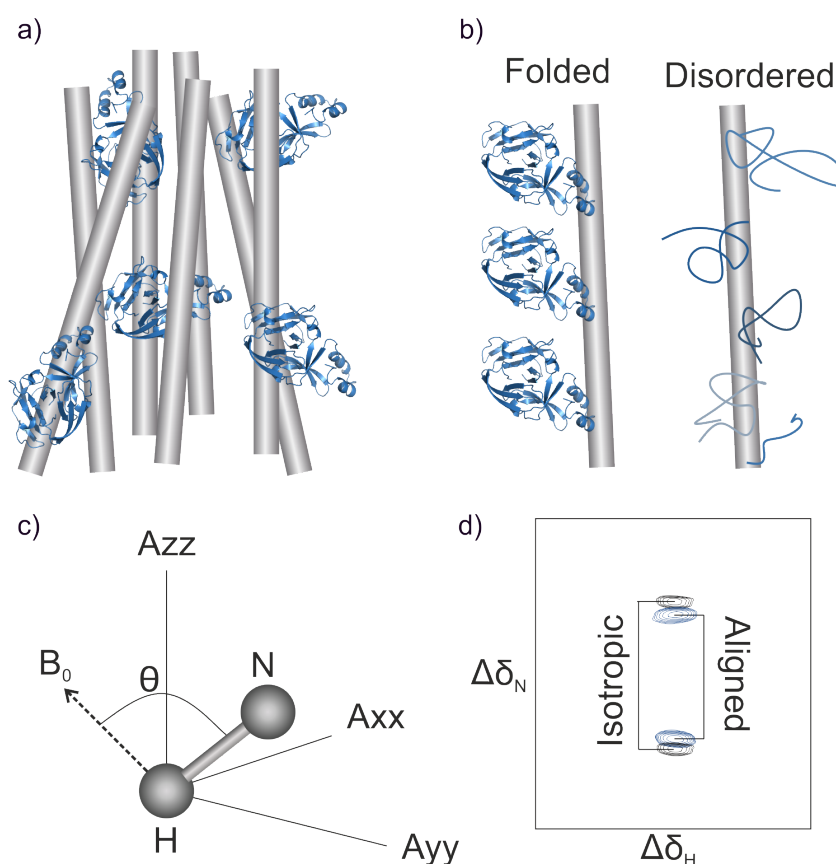


Figure 5.11: Representation of how RDCs are measured from protein samples.

a) Addition of an alignment medium (grey cylinders) to a protein solution (blue protein, PDB: 1AM2, [497]) restricts the protein tumbling. b) Interactions between the alignment medium and folded proteins biases protein orientation. Interaction of the medium with disordered proteins still permits peptide chain flexibility. c) For folded proteins, the angle θ is non-zero due to the biased orientation of the protein in the magnetic field. d) An undecoupled HSQC spectrum in isotropic and aligned solutions. RDCs are calculated by the different in splitting of the aligned and isotropic peaks.

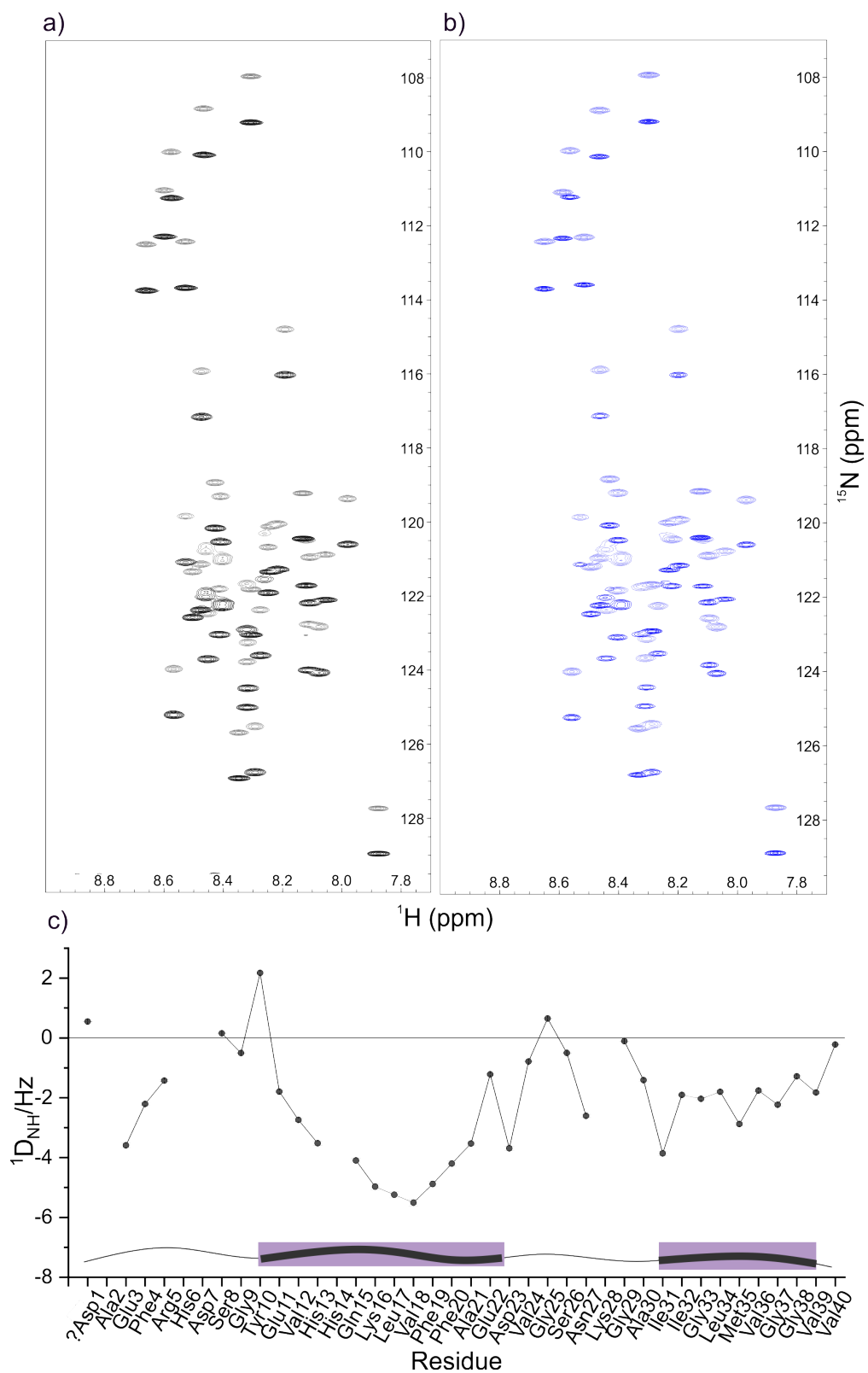
In this study, protein tumbling was restricted using filamentous bacteriophage Pf1 (Section 2.2.5.5), a commonly used alignment medium [496]. When in solution, proteins will associate with the Pf1 meaning their orientation will be biased in a specific way. The angle, θ which a heteronuclear bond vector takes whilst in this orientation, is measured relative to the external magnetic field, B_0 (Figure 5.11c). For folded proteins a large percentage of the population will adopt the same orientation (Figure 5.11b) so θ is heavily biased providing a large RDC. For an IDP - or for an unfolded protein [498]- the

flexibility and lack of defined structure still permits great variation in vector orientation with respect to B_0 even though they interact with the Pf1 matrix (Figure 5.11b). Thus for IDPs, the angles θ can adopt are only slightly biased and the RDC is close to zero. The RDC for each vector is calculated from the probability of alignment. RDCs are typically measured using inphase-antiphase (IPAP) sequences which separate the up- and downfield components of the J-coupled doublet, (Figure 5.11d) [363, 499].

Due to the flexibility of IDPs, they generally align parallel to the external magnetic field in an extended conformation. This gives rise to negative RDCs for the majority of the peptide. The termini usually have RDCs very close to zero due to their dynamic freedom, thus a shallow, bowl-shaped curve is expected [363, 498, 500, 501].

Due to the sensitivity of IDPs to buffer conditions, care must be taken to ensure the IDP conformational ensemble is not majorly perturbed by the addition of the alignment medium. Pf1 filamentous bacteriophage was used previously in work by Newby *et al.*, [372] which probed the relationship between alignment medium and $A\beta_{40}$, which concluded that Pf1 did not majorly perturb the $A\beta_{40}$ peptide [372].

Figure 5.12 shows the dipolar splitting of the unaligned (Figure 5.12a) and aligned (Figure 5.12b) samples of $A\beta_{40}$ (prepared as optimised in Section 5.1 and described in Section 2.2.5.5) which were collected using standard interleaved Bruker IPAP experiments. The spectra show the decoupled ‘up and down’ peaks which are usually combined in a HSQC spectrum. The magnitude of the dipolar coupling depends on the angle between the internuclei vector (HN) and the external magnetic field as well as the internuclei distance. As the dipolar interaction is between two covalently bonded nuclei, the internuclear distance is mostly fixed and mainly the orientation dependence influences the RDC [495].

Figure 5.12: RDC probes of A β_{40} structural propensity.

(Figure legend continued on the following page) .

Figure 5.12: a) Overlaid ‘up (grey) and down (black)’ spectra of A β_{40} in the optimised sample buffer: 50 mM A β_{40} in 20 mM sodium phosphate, 0.5 mM EDTA, 0.02 % (*w/v*) NaN₃, pH 7.4, 5 °C, 2 % (*v/v*) DMSO with 10 % D₂O. b) Overlaid ‘up (light blue) and down (blue)’ spectra of A β_{40} in the optimised sample buffer as in (a) with 26 mg/ml Pfl alignment medium. c) RDC values: Differences in splitting between peaks in (a) and (b) converted from ppm to Hz. Predicted regions of structural propensity (thick lines) are shown in the purple schematic. RDC data were collected using a 750 MHz spectrometer with a TCI-cryoprobe; ¹H-optimised triple resonance NMR inverse probe and Bruker Avance III HD console.

Figure 5.12c shows the RDCs for each backbone amide in A β_{40} . A region of increased structural propensity is observed between Tyr10-Ala21 which correlated well with the structure prediction (purple boxes). Additionally there is a region of possible structural propensity nearer the C terminus, Ile31-Gly38, which also corresponds well to predictions. Furthermore, the RDCs measured here show good agreement of published RDCs by Newby (*et al.*, [372], (Figure 5.13).

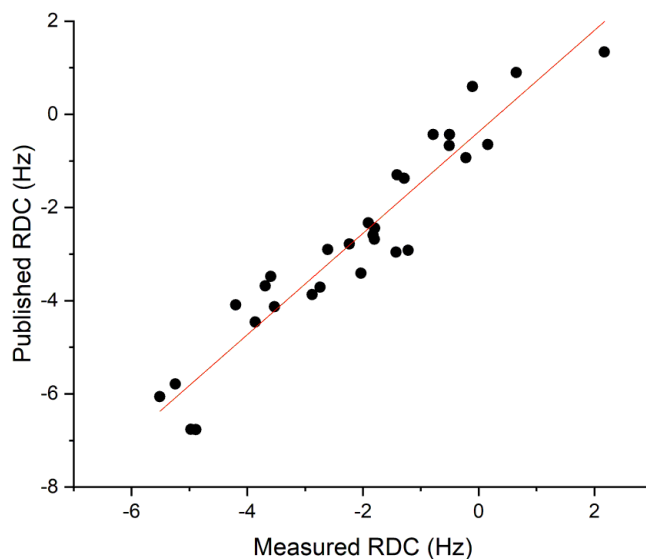


Figure 5.13: Correlation of experimental and published RDCs.

Comparison of measured RDC values from experimental data and those published by Newby *et al.*, [372]. Sample conditions in the published work differed only in the absence of 2 % (*v/v*) DMSO. Excellent correlation was observed, $R^2 = 0.912$ (3 s.f.).

Of the methods used to probe A β_{40} structural propensity, RDCs are the most sensitive, noting regions which were not highlighted by CSTCs or $\Delta\delta C\alpha$ methods.

5.3 Characterisation of residue-specific dynamics in IDPs

One of the key characteristics of IDPs is their innate flexibility. Along the peptide chain different regions will have different degrees of motion which can be modulated for IDP functions, e.g. to tune the affinity for target recognition or the formation of dynamic complexes in different environments [502, 503]. When investigating an amyloidogenic IDP it is therefore of interest to be able to extract measurable parameters on the dynamics of protein flexibility as well as conformer inter-conversion behaviour [362]. Figure 5.14 shows a selection of NMR methods which can provide information on differing types of peptide flexibility.

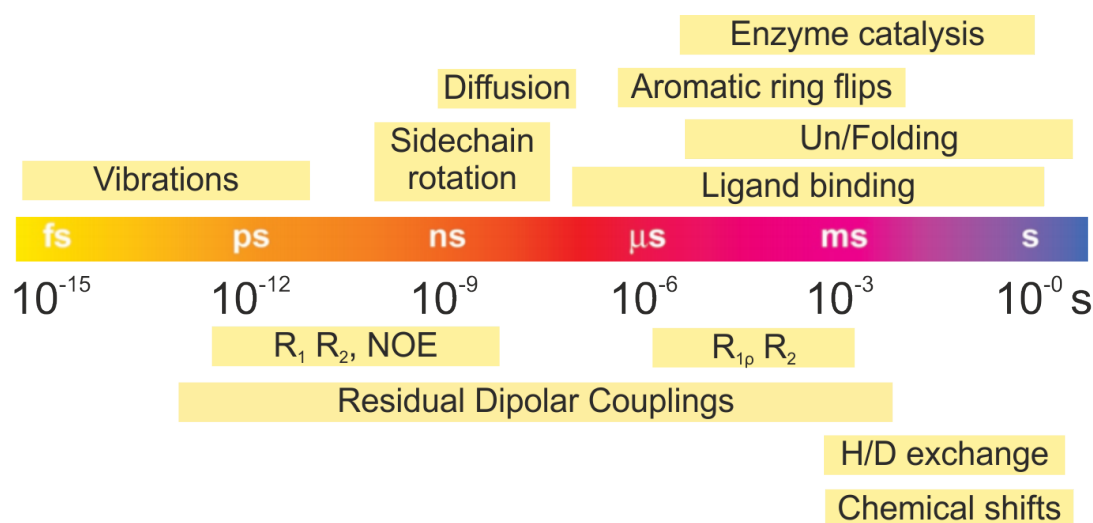


Figure 5.14: Diverse NMR methods to collect data on different dynamic timescales.

These can highlight how flexible specific regions in the A β_{40} sequence are and can be used to compare with the same measurements in the presence of small molecules which perturb amyloid formation. Such comparators may reveal necessary flexible regions for amyloid formation. Here, transverse relaxation rates and heteronuclear NOEs are described as these measures were collected to probe motions on ps-ns and μ s-ms timescales.

5.3.1 T₂ Measurements to probe ps-ns and μ s-ms Conformational Dynamics of A β_{40}

Characterisation of an IDP would not be complete without considering the dynamic flexibility of the system. Fast (ps-ns) timescale motions of the local polypeptide chain can be monitored by ¹⁵N spin relaxation experiments: ¹⁵N-R₁, R₂ and ¹⁵N-¹H^N NOEs. ¹⁵N-R₂ times are also sensitive to rotational correlation time and chemical exchange caused by larger peptide motions on the μ s-ms e.g. conformational exchange [379]. Due to this R₂ values were collected to reveal information on bond rotations and vibrations (ps-ns movements) and folding and eventually ligand binding interactions (μ s-ms motions).

Nucleus spin relaxation is caused by fluctuations in the local magnetic field arising from molecular reorientation. Thus relaxation depends on overall rotation of the peptide within the magnetic field, B₀, and internal fluctuations of individual bonds. The T₂ is the lifetime of coherent transverse (x-y) magnetisation and T₂ measurements are generally used to investigate protein dynamics. To measure T₂, a set of HSQC spectra are recorded with different delay times, t (Figure 5.15).

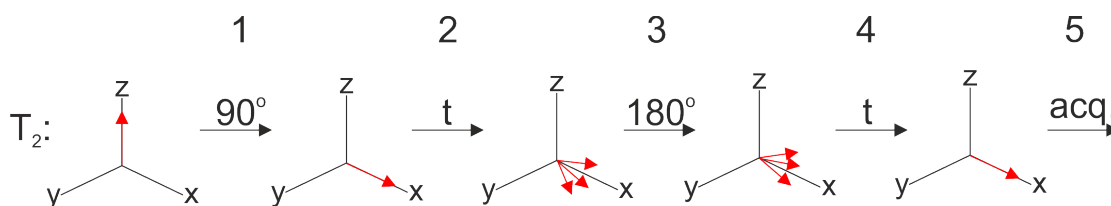


Figure 5.15: Schematic of transverse relaxation which gives rise to R₂ rates.

Step 1: A 90° pulse being applied to the equilibrium sample along the positive z-axis.

This puts the signal onto the x-y plane where it can be detected. Step2: After the pulse is applied, the sample is left for a period of time, t, during which the sample disperses as it relaxes back towards its equilibrium position along the positive z-axis.

Step 3: A 180° pulse is applied to mirror the spins around the x-axis. Step 4: After time, t, again all the spins should return to the coherent alignment along the positive x-axis. Step 5: Comparison of the intensity of the signal on the x-axis after step 1 and step 5 can indicate the extent to which contributing signals spread out during time, t, and thus indicate flexibility.

For this experiments, the time delay, t, after the initial 90° pulse was varied to 7.5, 14.9, 29.8, 44.7, 59.9, 74.5, 89.4, and 104.3 ms. R₂ values were calculated, Figure 5.16a by

fitting the amide proton peak intensities to monoexponential decay functions (Figure 5.16b) for each resonance. Standardised errors of 2 % were used based on common protocols in NMR and their agreement with errors calculated from the difference of duplicate peak intensities using relaxation delays of 14.9 and 74.5 ms. The overall trend observed in the R_2 values shows there is more flexibility in the terminal regions than in the central region which is typical for an IDP (Figure 5.16a). The R_2 profile of A β ₄₀ (Figure 5.16a) shows typical IDP behaviour which is comparable to published data [372].

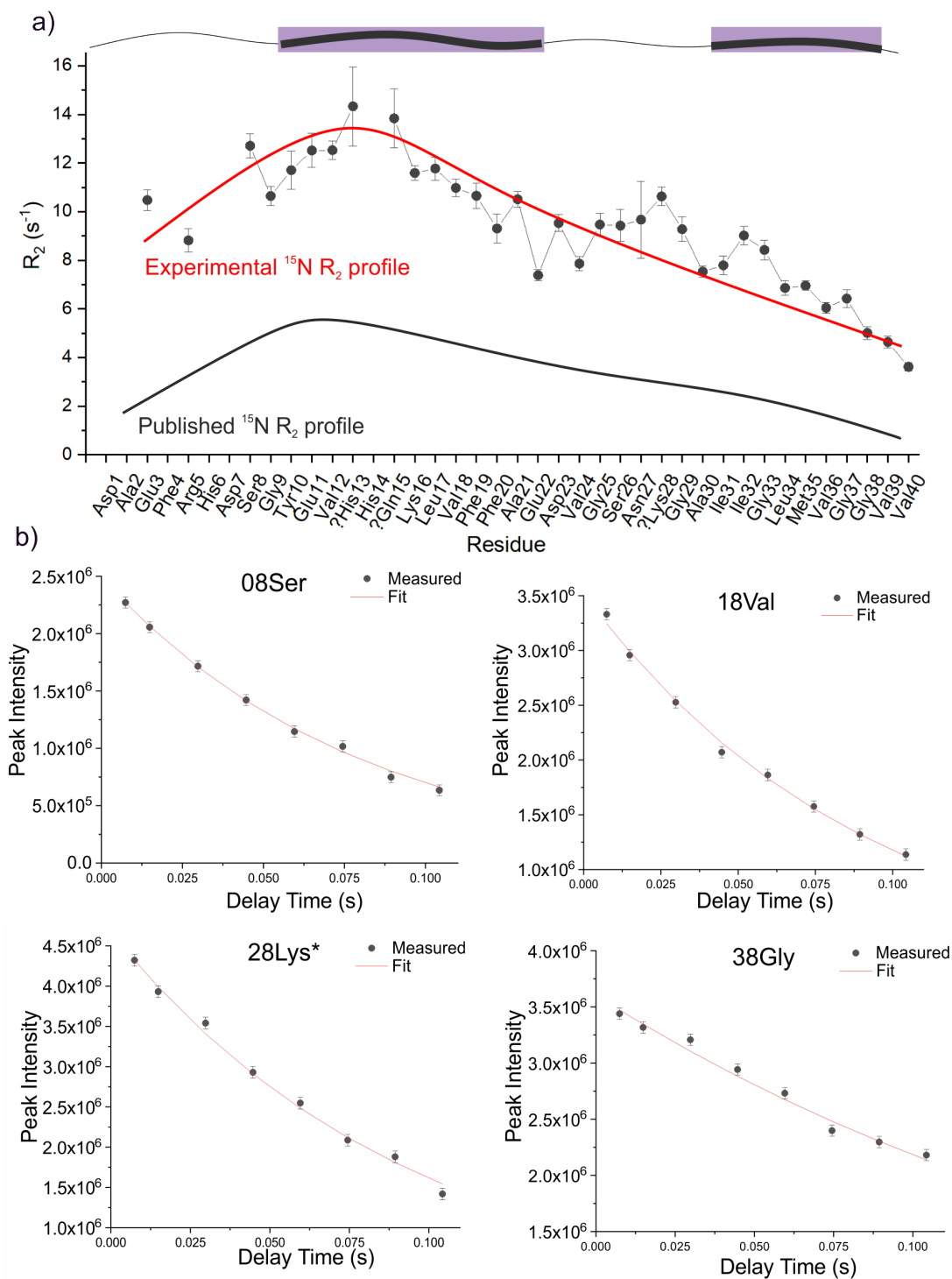
Figure 5.16: R_2 rates for backbone amides in $A\beta_{40}$ to indicate ps-ns dynamics.*(Figure legend continued on the following page)*

Figure 5.16: a) Transverse relaxation rates for each backbone amide bond in A β ₄₀ with a qualitative trend line (red) to which echos the same trend as from published data (black) [these are not a quantitative fits, instead they show overall shape]. b) Experimental fit to a relaxation decay for several representative residues (teh complete seat are in Appendix B.2). Data were collected using a standard Bruker experiment protocol whereby multiple HSQC spectra are acquired using various delay times (7.5, 14.9, 29.8, 44.7, 59.9, 74.5, 89.4, and 104.3 ms). The sample consisted of 50 mM A β ₄₀ in the optimised sample buffer: 20 mM sodium phosphate, 0.5 mM EDTA, 0.02 % (*w/v*) NaN₃, pH 7.4, 5 °C, 2 % (*v/v*) DMSO with 10 % D₂O.

5.3.2 Heteronuclear NOEs to probe ps-ns Dynamics

To obtain information on the motion of individual backbone amides, ¹⁵N-¹H-heteronuclear Nuclear Overhauser Effects (¹⁵N-¹H-hetNOEs) were measured. Backbone ¹⁵N-¹H-hetNOEs provide information on the motion of individual N-H bond vectors [415], specifically, on a ps-ns timescale. Amides which undergo motion that is faster than the overall rotation correlation time of the peptide in solution (i.e. ps-ns motions such as vibrations and side chain rotations) show a decreased ¹⁵N-¹H-hetNOE intensity relative to those collected for other, more restrained backbone regions. For example, decreased values are often found at the N- and C-terminals of an IDP. Conversely, increased ¹⁵N-¹H-hetNOEs indicate areas which are less dynamic [415, 504].

¹⁵N-¹H-hetNOEs are a measure of the change in the steady state population of the ¹⁵N spin when the attached proton is saturated.

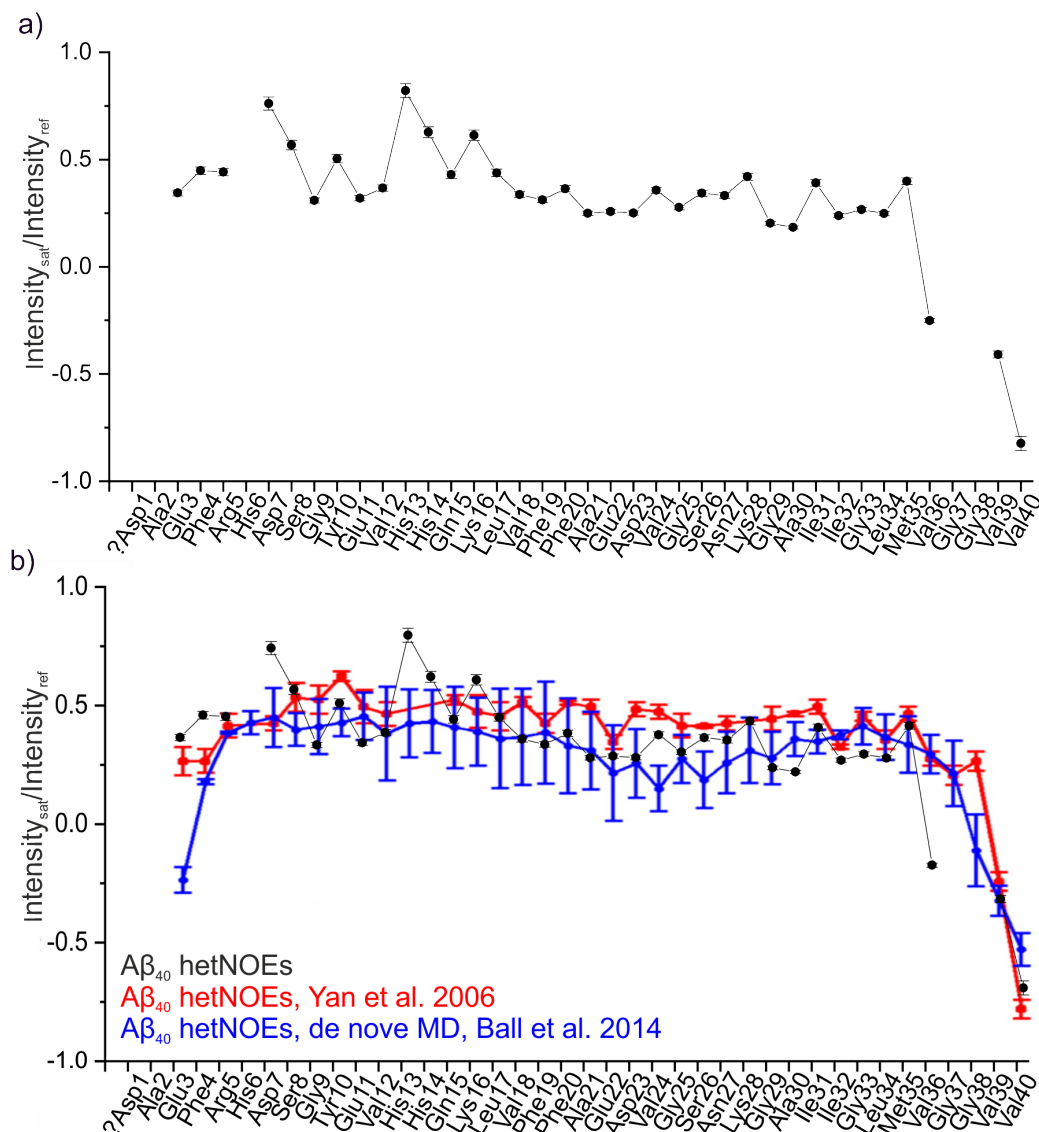


Figure 5.17: Heteronuclear NOEs for $A\beta_{40}$.

a) Heteronuclear NOE values for each backbone amide of $A\beta_{40}$ (calculated by: $\text{Intensity}_{\text{saturated}}/\text{Intensity}_{\text{equilibrium}}$). Data were collected for 50 mM $A\beta_{40}$ in the optimised sample buffer: 20 mM sodium phosphate, 0.5 mM EDTA, 0.02 % (*w/v*) NaN_3 , pH 7.4, 5 °C, 2 % (*v/v*) DMSO with 10 % D_2O and acquired using a 750 MHz spectrometer with a TCI-cryoprobe; ^1H -optimised triple resonance NMR inverse probe and Bruker Avance III HD console. b) Overlay of experimental data with published hetNOEs for $A\beta_{40}$, adapted from [415].

The low (~ 0.5) ^1H - ^{15}N heteronuclear NOE values shown in Figure 5.17a, suggest that the $A\beta_{40}$ backbone is incredibly dynamic on the ps-ns timescale. The experimental hetNOEs collected are superimposed on data originally collected by Yan *et al.*, [505]

and presented alongside simulated values by Ball *et al.*, [415] in Figure 5.17b. This shows that the data collected correlates well with the experimental data by Yan *et al.*. However, both lack evidence of flexibility at the N terminus which was expected for the peptide chain, and predicted in MD simulations [415]. Interestingly, hetNOEs collected by Rezaei-Ghaleh *et al.*, [367] detected negative values for Arg3, as predicted, under very similar conditions to those used in this study. Excluding the N terminus, the hetNOE values are similar in each set of work, including the work by Resaei-Ghalei and coworkers. In this work, the hetNOEs measured indicated that the N-terminus is similarly dynamic to the central part of the peptide chain. The small values measured (less than 1) indicate dynamics on the ps-ns timescale [367]. The C-terminus shows negative hetNOE values indicating an area with a high likelihood of ps-ns, rotational and vibrational motions. The large hetNOEs measured for Asp7 and His13 are most likely to be an artefact from exchange or data processing. This is because these residues are overlapped with other peaks which are more dominant (Lys28 and Val36 respectively) and thus there are multiple resonances contributing to the intensity measured.

5.4 Discussion

In this chapter, an NMR-based strategy for investigating the structural and dynamic properties of small IDPs has been assembled. The purpose of this strategy was for use in future studies of IDP-small molecule interactions. It was designed to follow on from the methods toolbox developed in Chapter 3 to probe how a small molecule modulator of IDP aggregation was able to influence - structurally and dynamically - the monomeric peptide. This was based on the hypothesis that a small molecule, which reproducibly and robustly affects IDP amyloid aggregation, may perturb aggregation through an ability to bias the conformational population distribution of the monomer (Figure 5.18).

Figure 5.18 clarifies the chapter aims. On addition of a small molecule to an IDP ensemble, the molecule may interact and skew the peptide distribution as it may favour a specific state or be more inclined to adopt a partial fold (thick lines). Some of these states which are more populated may be prone to amyloid formation (e.g. the conformation induced by the red molecule). In this case, the methods strategy in this chapter can be applied to the ensemble to extract specific parameters to reveal which regions of the peptide are acting differently to when they are in an apo population. This

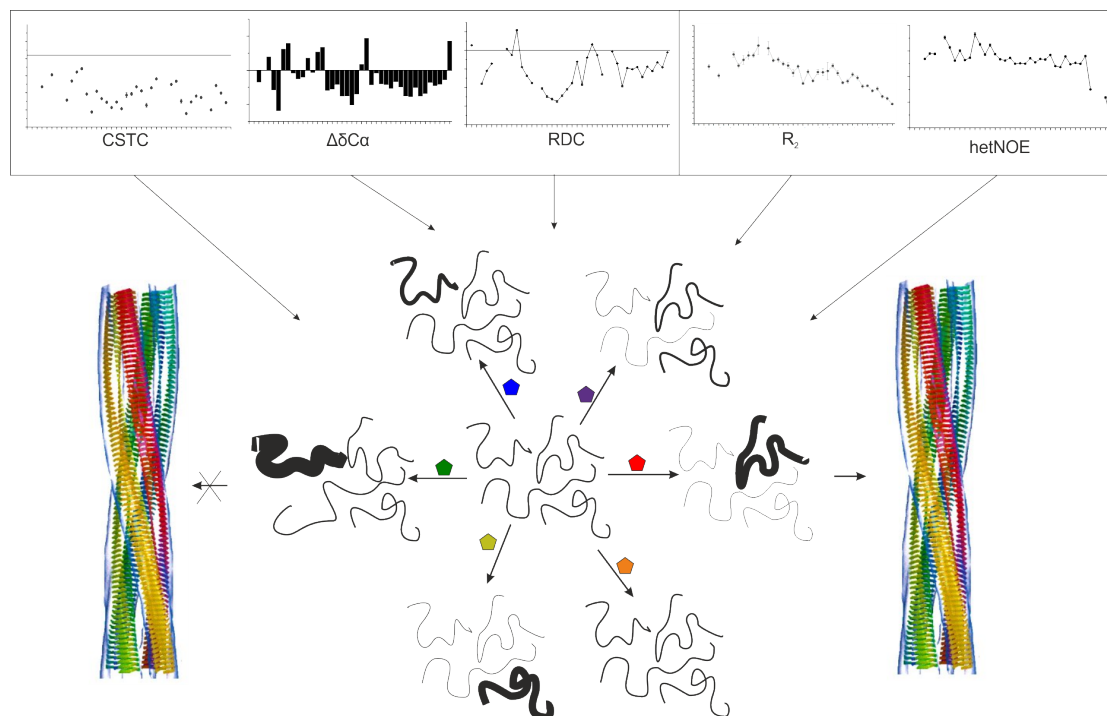


Figure 5.18: Schematic of investigation into how small molecules may influence conformation distribution of $A\beta_{40}$.

The methods used in the toolbox contribute information to help build up a structural and dynamic understanding to gain insight into peptide behaviour are Small molecules are represented by the coloured shapes. Line thickness indicates population size. [506]

analysis could reveal important structural transitions on the IDP-to-oligomer-competent monomer journey. In contrast, if a small molecule acts to inhibit amyloid formation (e.g. the green molecule), application of the methods strategy will probe structural and dynamic changes of a conformation which is not amyloidogenic. This can yield insight to structural features which could prevent amyloid formation. For all future comparative studies, a parameter base for the IDP without any small molecules present would be necessary. This has been provided in this chapter for future studies of $A\beta_{40}$.

Work presented here sets up the foundation for future studies which will monitor structural and dynamic features of $A\beta_{40}$ - the exemplar amyloidogenic IDP used in this work - in the presence of small molecules. This can be achieved using the set of NMR methods compiled herein to collect comprehensive data that can be used to monitor peptide behaviour.

To probe structural properties, $\delta^{13}C\alpha$ predictions were used in combination with $^1H^N$ -CSTCs and RDCs. Of these RDCs has the greatest sensitivity for structural propensities - as evidenced in Section 5.2.3) - but cannot differentiate different types of secondary

structure. $\delta^{13}\text{C}\alpha$ predictions complement the RDC data as they can provide a possible distinction between β -sheet and α -helical forms. It will be interesting to monitor whether small molecules which perturb aggregation are able to alter the A β ₄₀ conformer enough to make these predictions $\delta^{13}\text{C}\alpha$. $^1\text{H}^{\text{N}}$ -CSTCs were included as an indication of how probable it is for each backbone amide to participate in peptide secondary structure.

For dynamic investigation, transverse relaxation rates (R_2) and hetNOEs were included in the strategy. Both of these methods are able to shed light on ps-ns movements and thus data can be validated. R_2 rates are also sensitive to μs -ms motions thus a broad range of dynamic timescales can be probed using this strategy.

To complete the toolbox, a method to collect and analyses RDCs collected in different alignment media should be included. This would permit the determination of the ns-ms timescale dynamics and filled the gap between very fast (ns-ps dynamics inferred from R_2 values) and slower motions (ms-s dynamics inferred from chemical shift perturbations) of A β ₄₀ [507]. Moreover, observing how concentration affects A β ₄₀ parameters could be a good way to probe structural changes. In the case of R_2 rates, higher concentrations of A β ₄₀ are more likely to yield information on important areas of the peptide for oligomerisation and protein-protein interactions. To further structural investigation, deeper analysis and experimentation into $^1\text{H}^{\text{N}}$ -CSTC data could have been conducted to deconvolute the contribution from the rate of tumbling (rotational correlation time) and the rate of exchange using TROSY and antiTROSY spectra.

The data collected have been similar to previous work on A β ₄₀ [367, 372] showing that the optimised conditions -which are suitable for small molecule addition - do not perturb A β ₄₀ dramatically despite the known sensitivity of IDPs to environmental conditions.

Often such studies compile measured parameter data to construct ensemble models or conformational landscapes, however, in this study parameters were purposely analysed in isolation to avoid loss of the finer nuances of the peptide. With this, precise, quantitative comparisons can be made in future studies involving small molecules. The assignment of 90 % of the A β ₄₀ peptide has led to near-complete data set collection for each parameter monitored.

The value of this work will be realised upon its application to small molecule:A β ₄₀ investigations and small molecule studies on other amyloidogenic IDPs. The strategy

may also be applied to broader investigative strategies, such as the investigation of substituted and mutant IDPs, truncated peptides, and peptide mimetics. For example, the strategy could be used to probe the structural and dynamic properties of different lengths of A β , or to reveal the importance of certain aromatic or charged residues in an IDP sequence.

The methods presented here were used together to create structural and dynamic conclusions about the A β ₄₀ backbone. Although their true value will be revealed on comparison of parameters with small molecule containing systems. In subsequent studies the techniques implemented here can be used to directly compare localised (within the peptide chain) effects of the compound on specific aspects of A β ₄₀.

Chapter 6

Concluding Remarks

6.1 Summary of Findings

Amyloid diseases are some of the most common afflictions in society causing huge burden to sufferers, healthcare providers, and families [81]. Despite the prevalence of Alzheimer's disease, the major neurodegenerative disorder in dementia [81], the understanding the first steps in the aggregation mechanism which is linked to the disease, are still remains elusive. An explanation for this is due to the substantial challenges in studying the heterogeneous, transient populations of low-order amyloid intermediates (monomers and oligomers) involved in amyloid formation which is compounded by the dynamic conformational heterogeneity of IDPs.

Considering IDP populations as a landscape of conformational probabilities is perhaps the clearest way to realise the extent of the intricacies within the system. Definition of every conformation in the landscape can be predicted using ensemble calculations molecular modelling methods [508, 509]. However, due to the delicate sensitivity of IDP behaviour and structural propensity to minor changes in buffer conditions, transferable value of such landscapes is limited between studies. The work described in this thesis aimed to set up a methods toolbox to probe for small molecule modulators of the aggregation of IDPs - using hIAPP and A β_{40} as exemplar peptides - followed by an NMR-based methods strategy to explore how these small molecules could cause such effects. The eventual hope of this work is that it will be implemented to reveal important structural transitions required for IDP entry into the amyloid pathway.

Small molecules can bias the conformer probability distribution of IDP populations, potentially increasing or decreasing the predominance of species with certain structural traits (e.g. by stabilising a short α -helical segment in a terminal region of an IDP) which are important for either promoting or preventing amyloid progression. Such structures can be identified using the methods presented in this work and can reveal important structural transitions in amyloid progression.

The value of this project lies in the decision of creating a balanced toolbox of methods from the extensive range of methods which could have been applied to the IDP system. The toolboxes of methods which have been brought together in this thesis (in Chapter 3 for small molecule selection and initial structural implication, applied in Chapter 4, and Chapter 5 for precise structural assessment at a residue-level resolution) can be used to build up a comprehensive impression of IDP behaviour from multiple, complementary perspectives.

Initially, methods which could identify perturbations in the rates of amyloid formation had to be selected and their compatibility with small molecule addition was tested (Chapter 3). Use of methods which indicated amyloid formation of $A\beta_{40}$, such as the ThT assay, TEM, and fibril yield measures, were combined with ESI-MS and $^1H^{15}N$ -HSQC NMR experiments to yield monomer and oligomer level indications of compound-peptide interactions. Each method examined how the addition of a small molecule can influence aggregation from a differing perspective; ThT can reveal information on the kinetics of the reaction and whether the small molecule is interfering within the lag phase, possibly interacting with monomers and small oligomers, or whether the small molecule perturbs amyloid formation at the secondary nucleation stage; TEM reveals aggregate morphology; and fibril yield quantifies the extent of aggregation. ESI-MS showed the stoichiometry of the peptide-compound interaction, and $^1H^{15}N$ -HSQC NMR had the potential to reveal interaction sites and binding affinity.

Use of the toolbox of methods was demonstrated using $A\beta_{40}$ as presented in Chapters 3 and 4. To enable this, work was conducted to optimise the expression and purification procedures for this peptide. Optimisation improved peptide yields from 2-4 mg/L to 4-6 mg/L of pure $A\beta_{40}$. Within the last year a new approach to the purification of $A\beta_{40}$ has been published. This method uses HPLC and can achieve a yield of up to 9 mg/L [397]. At the outset, a second amyloidogenic IDP, hIAPP, was also going to be

used to demonstrate the versatility of the method toolbox, however, issues with hIAPP purification prevented this.

To increase the possible impact of the work conducted here, small molecule selection was considered. To demonstrate the use of the method toolbox, any of the wealth of known small molecule inhibitors of amyloid aggregation could have been used as a test system. Indeed, Chapter 3 demonstrates how the methods were optimised for use with $A\beta_{40}$ in the presence of small molecules which have already received a large amount of research attention: EGCG (as a known amyloid inhibitor) [328, 510, 511] and aspirin (as a negative control) [429]. Chapter 4 had the potential to discover a novel small molecule which could perturb $A\beta_{40}$ amyloid aggregation. Although this did not occur on this application of the methods toolbox, the screening and testing approach is ready for application to other compound libraries and different known modulators of amyloid aggregation can be used to direct screening.

The selected compound library used in Chapter 4 for *in silico* screening was an extensive in house library at the University of Leeds, Department of Chemistry, and compounds were selected from it for *in vitro* screening based on structural similarity to known modulators of amyloid aggregation and their derivatives; 1,2-naphthoquinone, bexarotene, MM3003, and UV11532 [444]. The ThT assay was used for screening due to its relatively high-throughput, and information rich nature. Lead compounds identified were then tested for amyloid-modulatory effects using the toolbox of methods from Chapter 3. This was vital to validate the effects seen in the screening assays. Overall, Chapter 4 clearly showed how the toolbox can be applied to a new, small molecule discovery and testing investigation.

Finally, a selection of NMR methods were compiled to form a strategic investigation approach in how small molecules may alter monomer conformation dynamics. Similarly to the methods toolbox used to identify small molecule modulators of amyloid formation, the NMR approach assembled in Chapter 5 is a multi-method plan which can evaluate how small molecules effect IDPs from complementary perspectives. The NMR approach was applied to $A\beta_{40}$ apo state to obtain a set of parameters which can be compared to those measured when the approach is applied to a small molecule-containing system. Had a new small molecule modulator of amyloid aggregation been identified, the method approach that was compiled in Chapter 5 could have been used to glean sequence-specific

impressions of how the small molecule was perturbing the IDP. This will reveal delicate changes in the structural propensities of each region of the A β ₄₀ peptide induced by small molecules which alter the amyloidogenic properties of the IDP.

6.2 Future Work

The power of the work conducted in this thesis comes from its future applicability, not only to other small molecule libraries, but to other amyloidogenic IDP systems, for example, Tau, α -synuclein, hIAPP, and length variants of A β .

The toolbox of methods in Chapter 3, could be applied to alternative compound libraries for screening and robust assessment of effect on aggregation. The small molecule screening, and complementary validation methods, can be applied to further carefully selected compound libraries with a view to identify compounds which can alter the progression of amyloid formation. Furthermore, this could lead to the identification of novel compounds, whose effects on amyloid have not previously been considered. More importantly, application of the methodological strategy in Chapter 5 to other small molecule libraries (whether novel or known modulators of amyloid) has the potential to reveal important conformers in the amyloid pathway and mechanistic insight. This may be of particular interest for therapeutic development to find target structures for drug interactions. In extension to this, investigation of the peptide-compound interaction would also yield valuable direction for therapeutic development; a method toolbox for such study by NMR has recently been published [512].

The ability to transfer the methods selected here for use on other IDP systems give this work a wide breadth of impact. Not only would this give specific insight into various disease pathogenesis, but it also would allow the comparison of monomer transitions between amyloid disorders. Such comparative analysis may reveal key folding or interaction events which are essential for amyloid formation.

As new methods are developed, it will become important to include or substitute IDP-optimised methods for those currently in the toolbox. Care must be taken as the toolboxes could be expanded with many methods and technical approaches. To prevent devaluation of the work in this thesis, methods should only be added to the toolbox if they can provide a new perspective on the monomer conformations to avoid collection of

overlapping information. Despite this, one experiment which should ideally be included in the toolbox in Chapter 5, is to test for regions involved in monomer-monomer interaction by monitoring the dependence of the $A\beta_{40}$ $^1\text{H}^{15}\text{N}$ -HSQC spectrum on peptide concentration. This could also show the oligomeric state of $A\beta_{40}$.

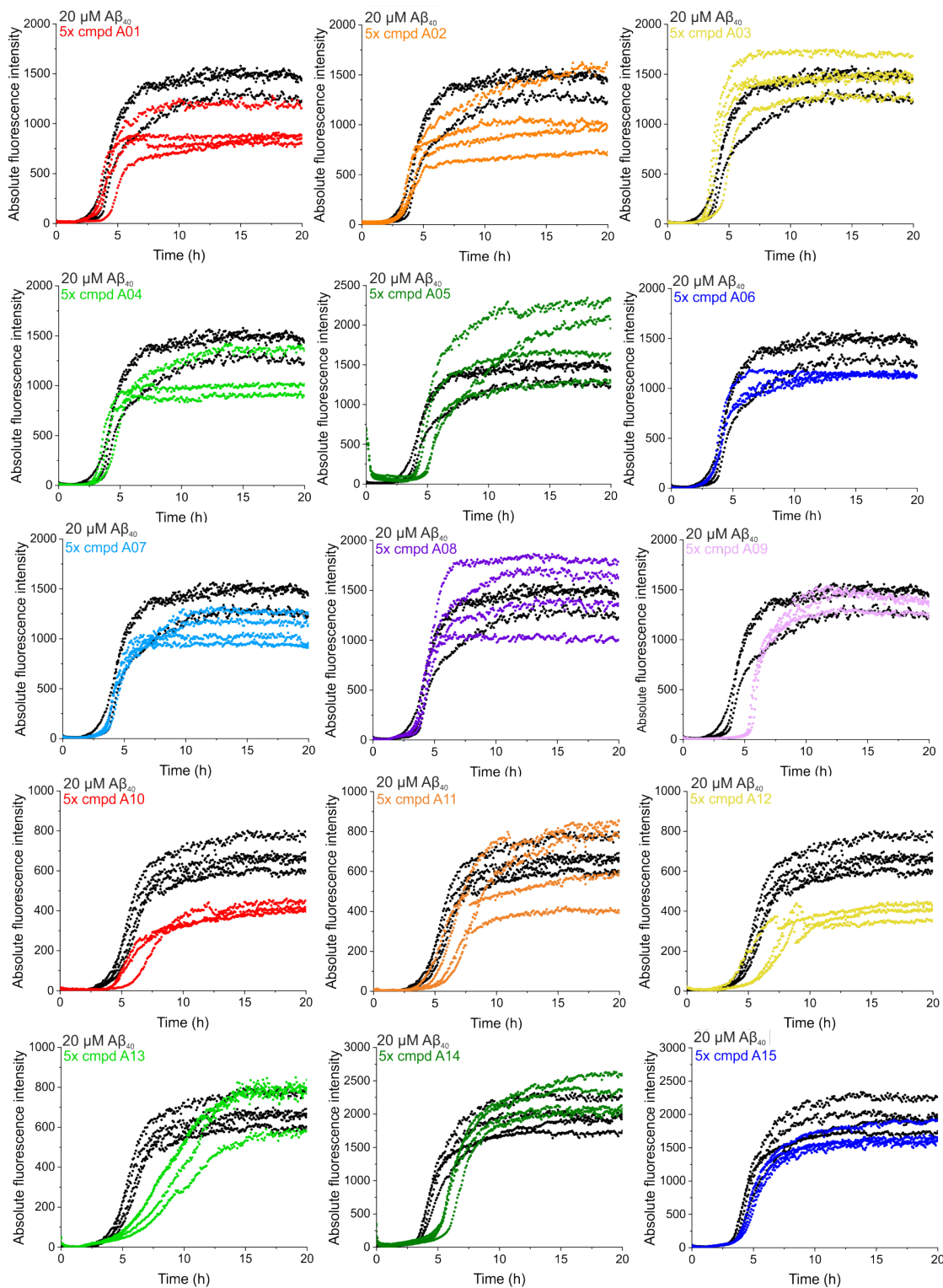
In summary, presented in this thesis are two methodological strategies; one to identify and validate small molecule modulators of amyloid aggregation (which has been applied to the study of $A\beta_{40}$), and one for detailed, comparative analysis of the structural and dynamic properties of amyloidogenic IDPs in conjunction with the identified small molecules (which has been fully prepared for small molecule additions to the tested $A\beta_{40}$ apo system). Use of these strategies will enable the discovery of important transient monomer conformers of IDPs and low order oligomers which affect amyloid formation. Such knowledge will help to piece together the puzzle of how and why IDPs such as $A\beta_{40}$ swap their highly-entropic and disordered conformations for rigid, ordered amyloid fibrils.

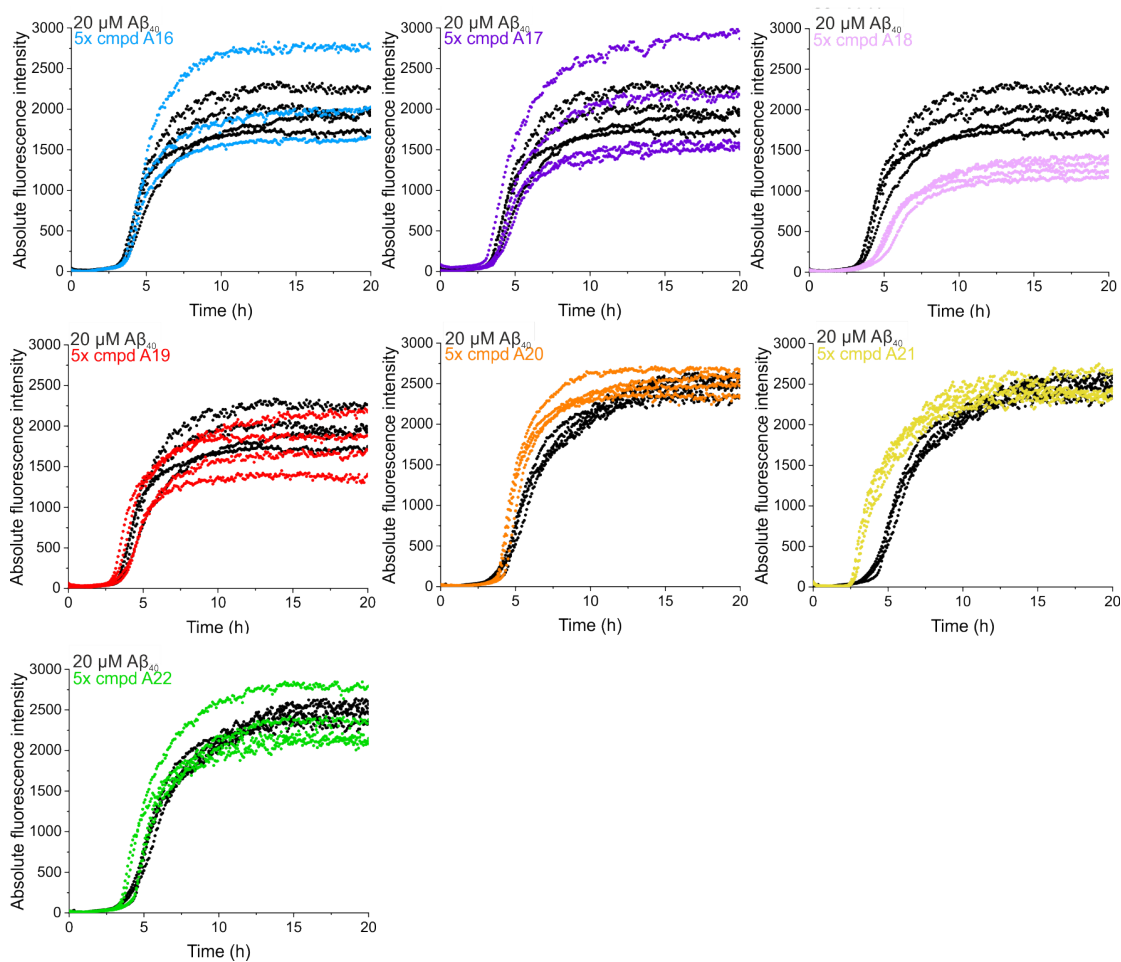
Appendix A

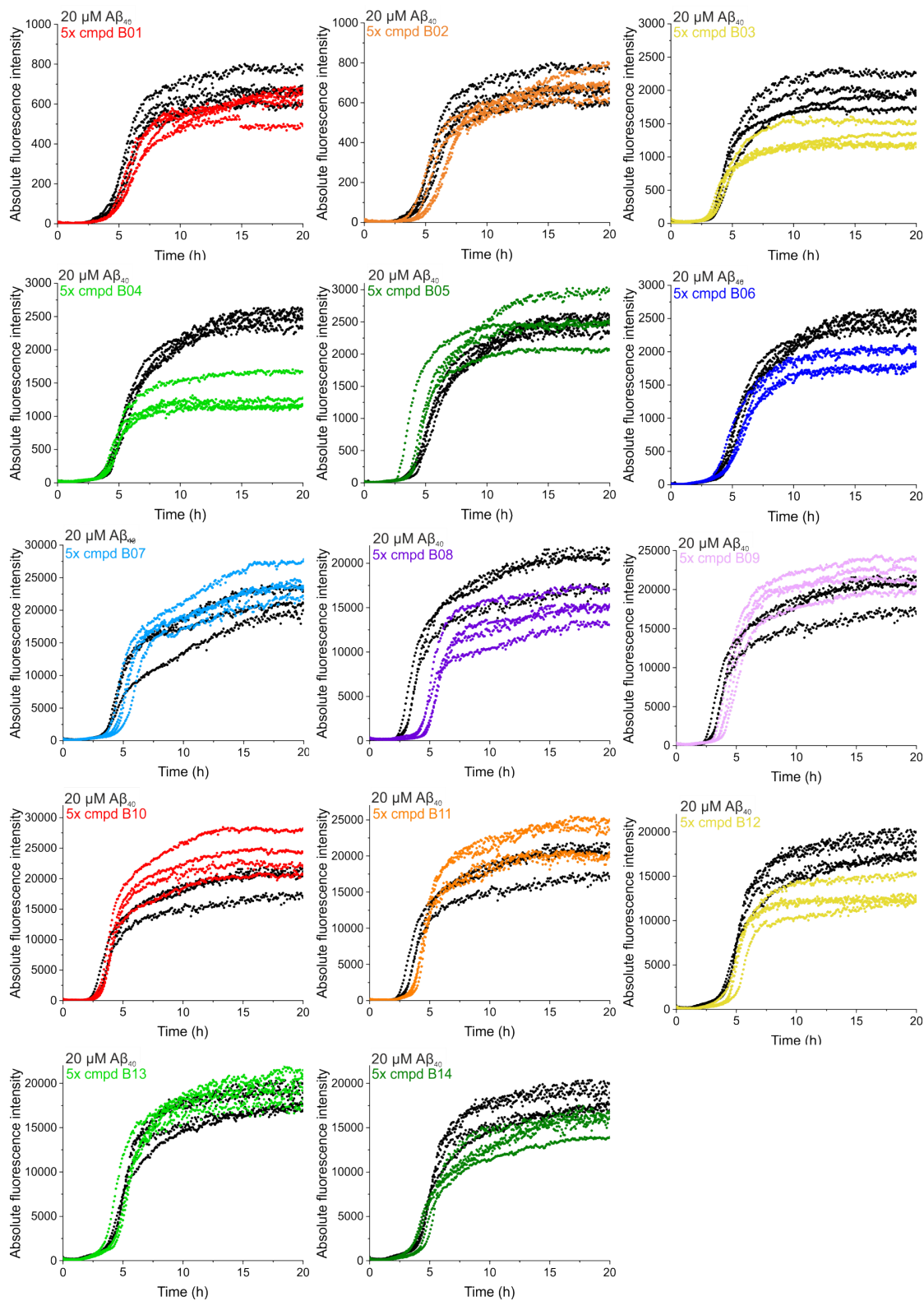
Appendix A

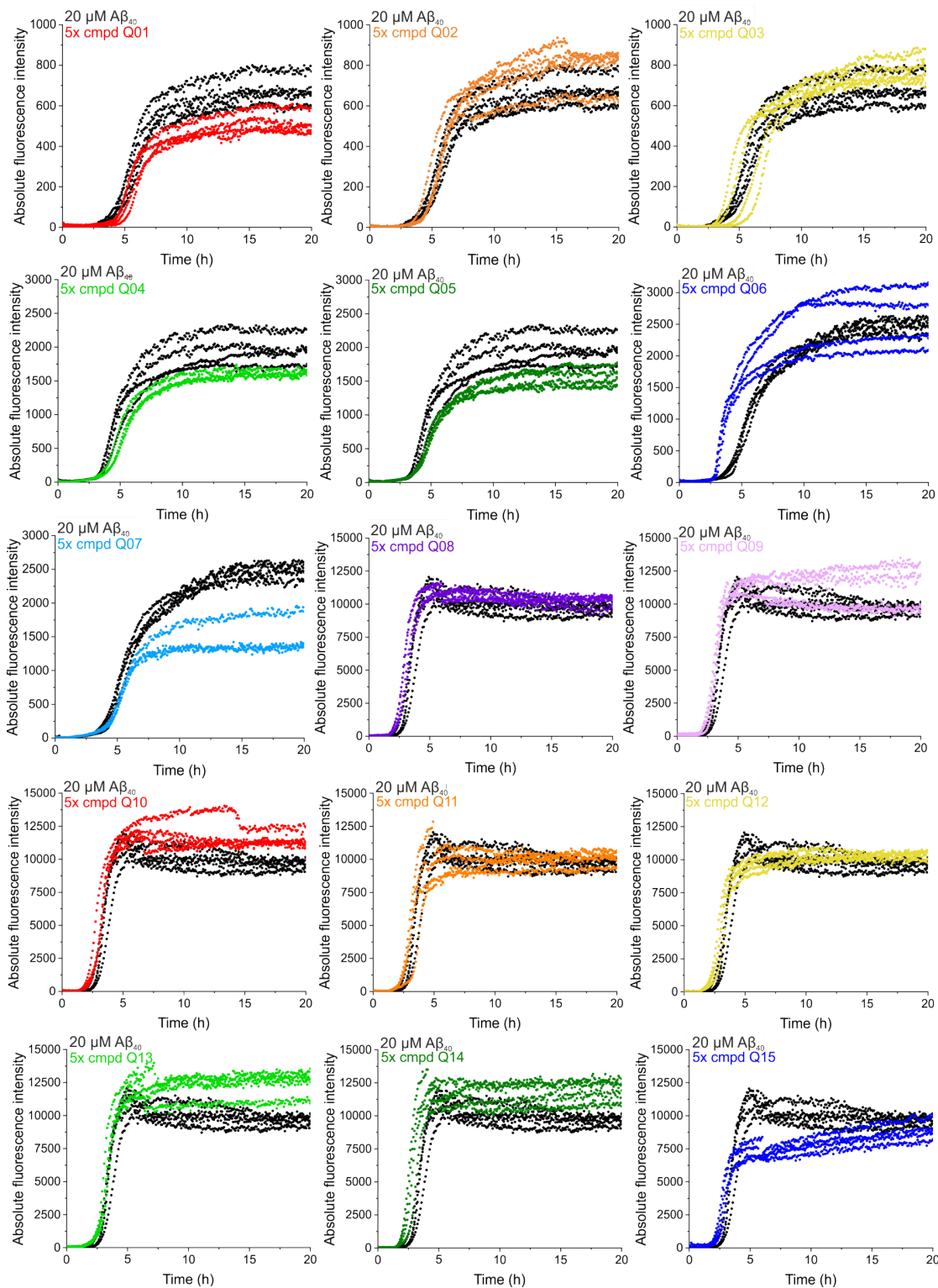
A.1 Absolute ThT fluorescence measured for $A\beta_{40}$ aggregation in the presence of each compound screened

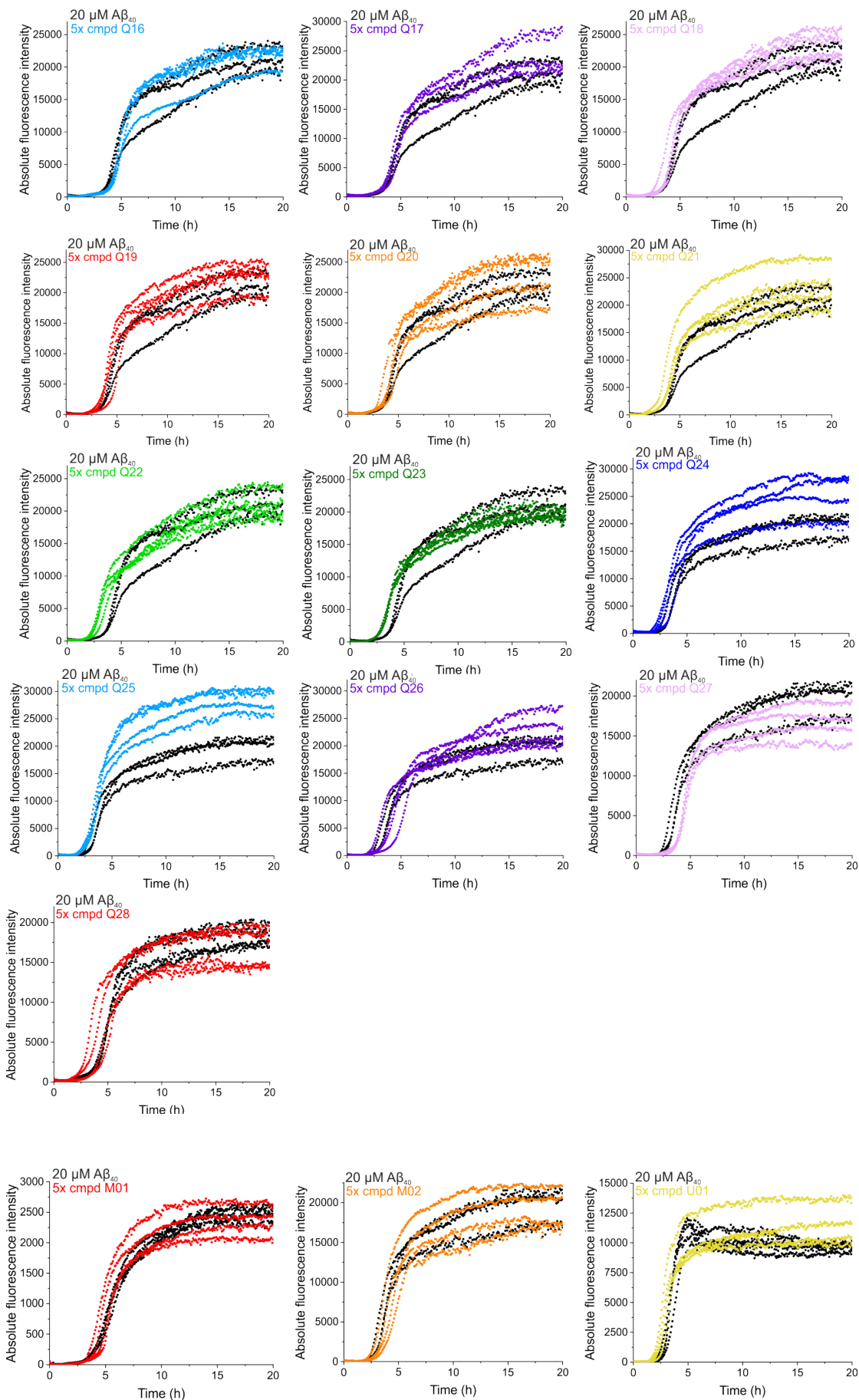
Absolute fluorescence intensity of ThT fluorescence to monitor $A\beta_{40}$ aggregation in the presence of each of the 67 compounds in the screening library.











A.2 T-test values for quantitative analysis of the ThT screen

TABLE A.1: Table of t-test values

T-test values			
Compound	Lag time	T ₅₀	Max. Fluorescence
Compounds based on adapalene			
A01	0.420	0.283	0.014
A02	0.162	0.181	0.219
A03	0.575	0.183	0.448
A04	0.283	0.247	0.142
A05	0.119	0.309	0.164
A06	0.235	0.193	0.029
A07	0.388	0.319	0.042
A08	0.484	0.358	0.753
A09	0.013	0.274	0.632
A10	0.344	0.157	0.003
A11	0.062	0.091	0.855
A12	0.284	0.126	0.002
A13	0.324	0.000	0.376
A14	0.008	0.001	0.156
A15	0.010	0.249	0.069
A16	0.796	0.613	0.629
A17	0.660	0.807	0.860
A18	0.023	0.008	0.001
A19	0.891	0.409	0.321
A20	0.580	0.000	0.640
A21	0.001	0.000	0.804
A22	0.852	0.009	0.471
Compounds based on bexarotene			
B01	0.806	0.193	0.271
B02	0.810	0.211	0.776
B03	0.118	0.124	0.002
B04	0.973	0.001	0.000

Continuation of Table A.1			
Compound	Lag time	T ₅₀	Max. Fluorescence
B05	0.253	0.049	0.889
B06	0.379	0.752	0.001
B07	0.035	0.455	0.138
B08	0.000	0.000	0.021
B09	0.028	0.015	0.211
B10	0.328	0.651	0.104
B11	0.011	0.007	0.236
B12	0.211	1.000	0.001
B13	0.700	0.837	0.210
B14	0.856	0.050	0.020
Compounds based on 1,2-naphthoquinone			
Q01	0.494	0.945	0.012
Q02	0.672	0.699	0.127
Q03	0.631	0.817	0.084
Q04	0.166	0.479	0.040
Q05	0.051	0.260	0.019
Q06	0.002	0.000	0.694
Q07	0.158	0.525	0.002
Q08	0.011	0.043	0.075
Q09	0.046	0.115	0.169
Q10	0.120	0.140	0.001
Q11	0.410	0.570	0.234
Q12	0.031	0.081	0.031
Q13	0.219	0.486	0.001
Q14	0.014	0.015	0.003
Q15	0.003	0.026	0.086
Q16	0.594	0.867	0.746
Q17	0.916	0.933	0.291
Q18	0.072	0.129	0.262
Q19	0.454	0.158	0.474
Q20	0.411	0.115	0.710

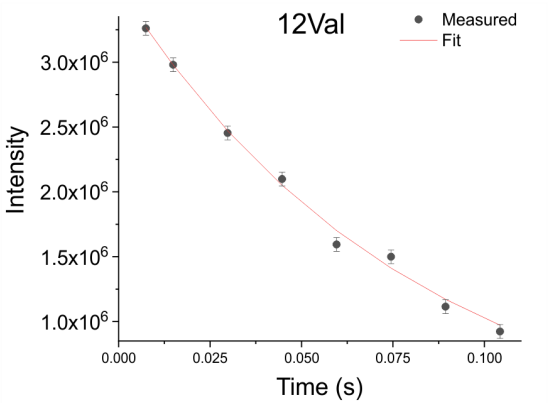
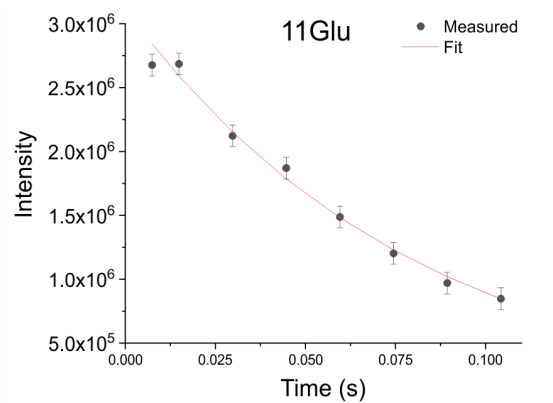
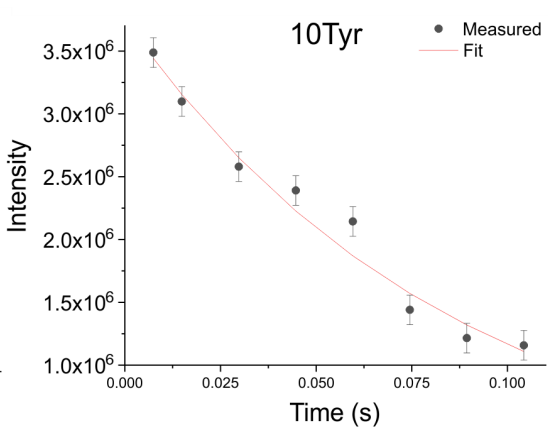
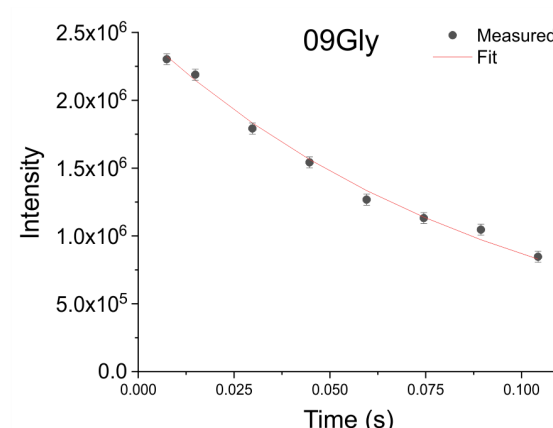
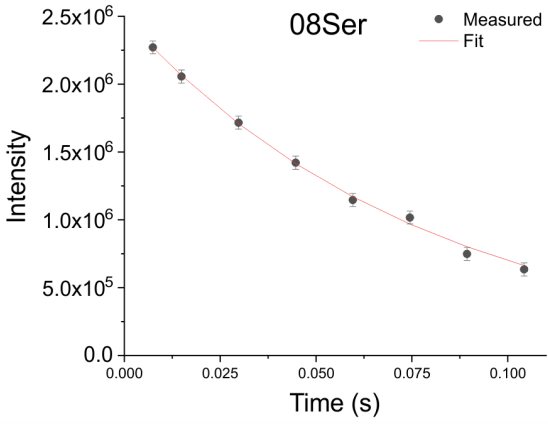
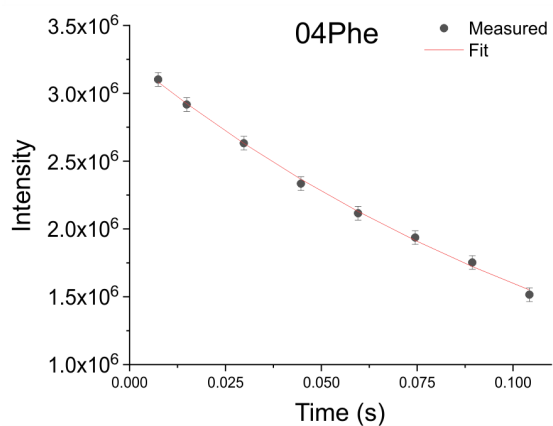
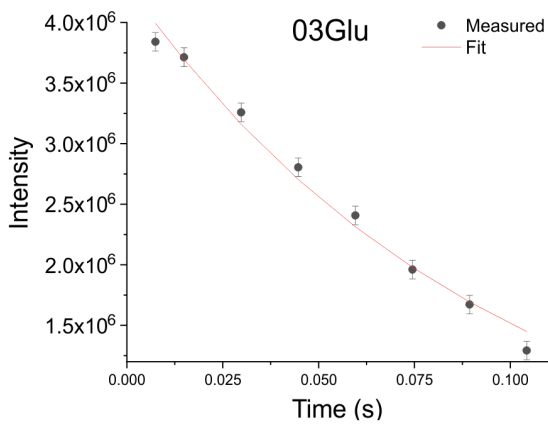
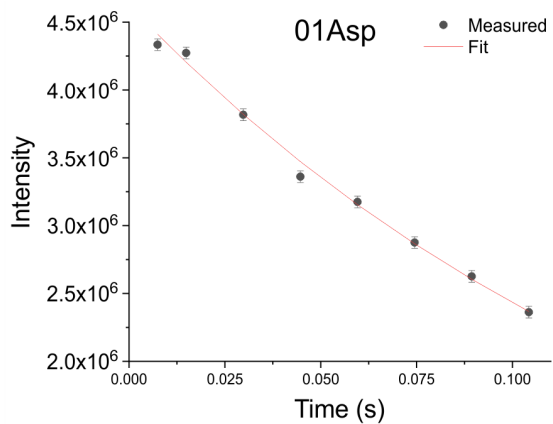
Continuation of Table A.1			
Compound	Lag time	T ₅₀	Max. Fluorescence
Q21	0.048	0.044	0.499
Q22	0.000	0.040	0.817
Q23	0.000	0.026	0.251
Q24	0.410	0.505	0.080
Q25	0.582	0.227	0.003
Q26	0.403	0.233	0.188
Q27	0.003	0.012	0.119
Q28	0.275	0.098	0.259
Compounds based on UVI3003 or MM11253			
M01	0.955	0.011	0.433
U01	0.016	0.114	0.089
M02	0.200	0.308	0.832

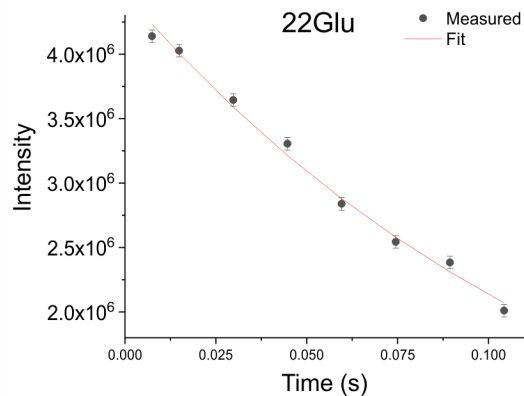
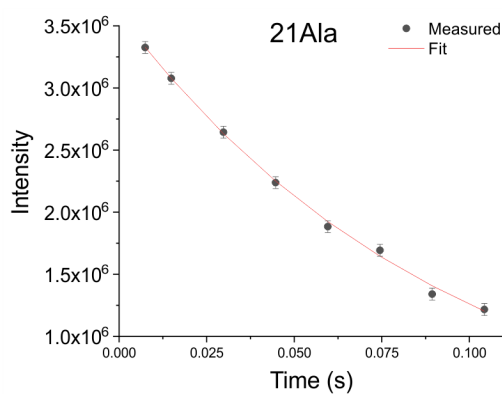
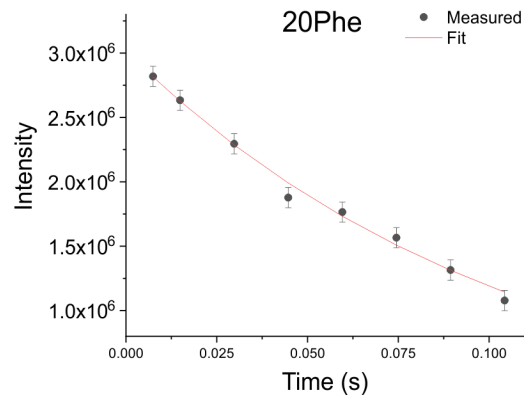
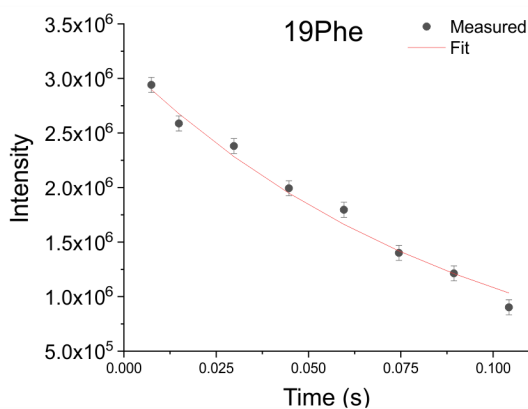
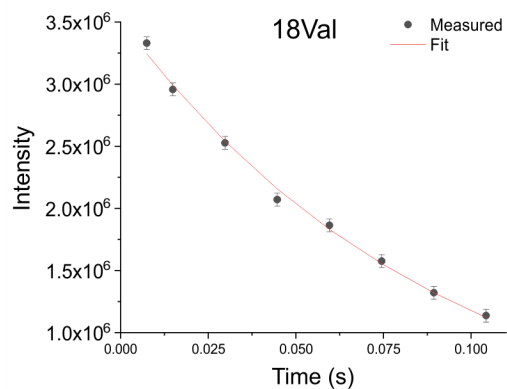
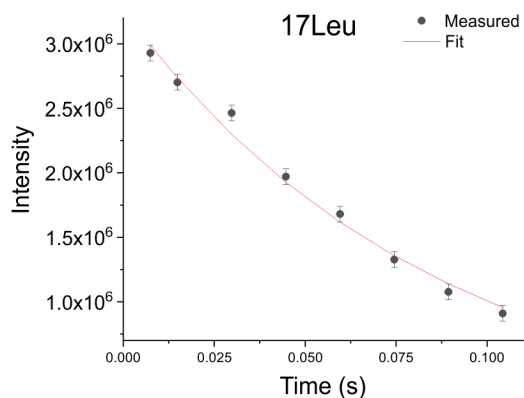
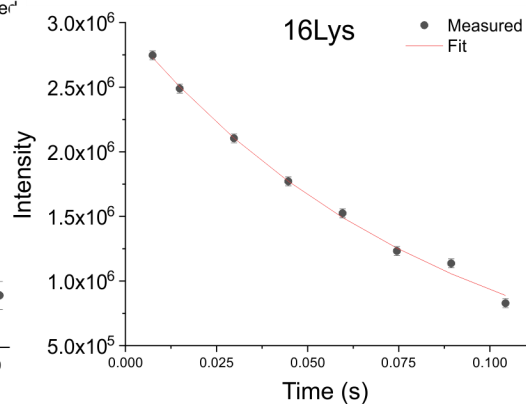
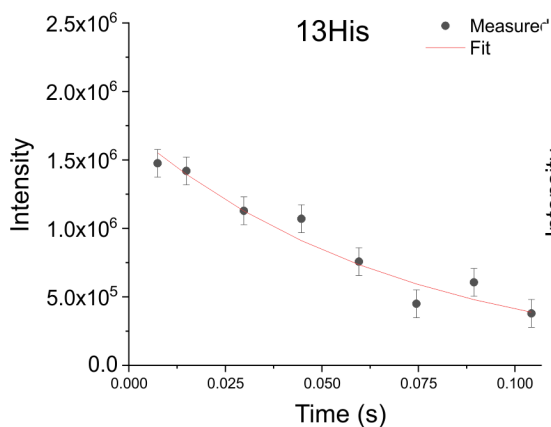
Appendix B

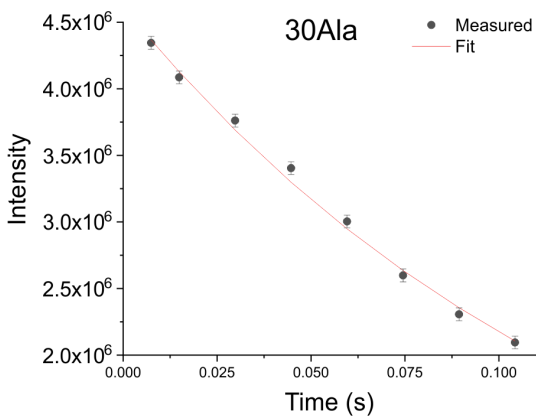
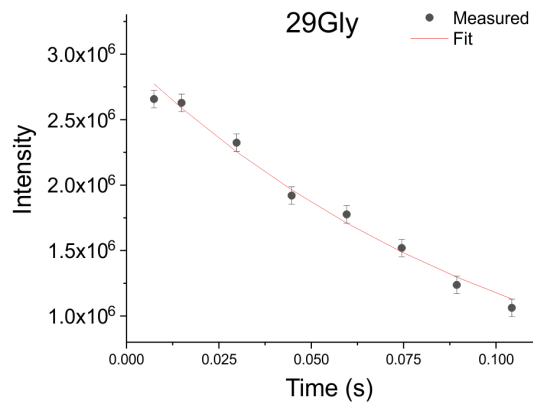
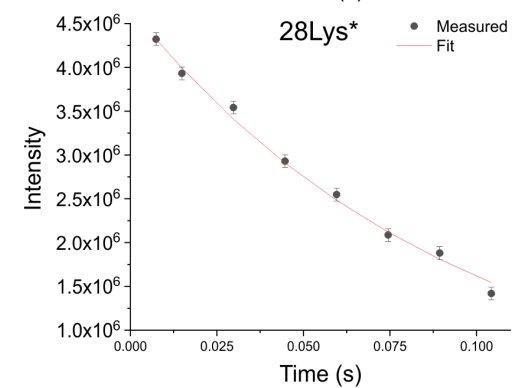
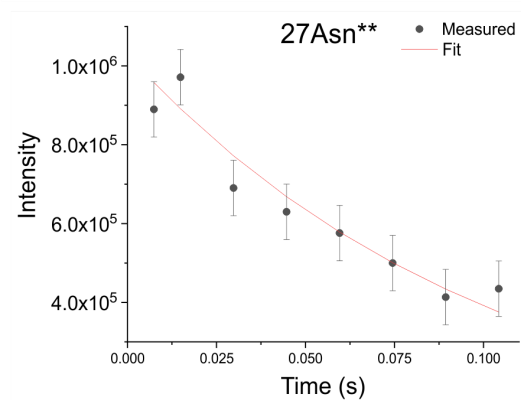
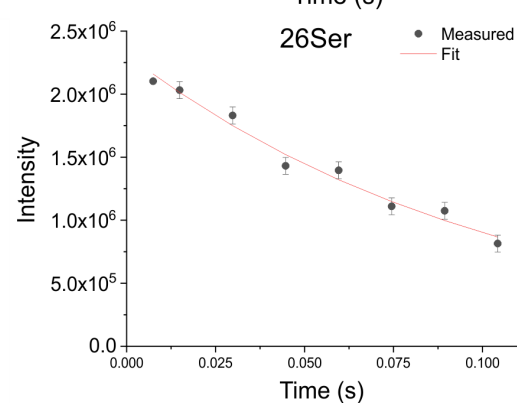
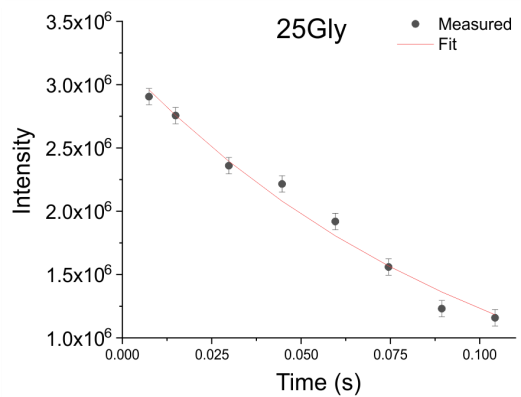
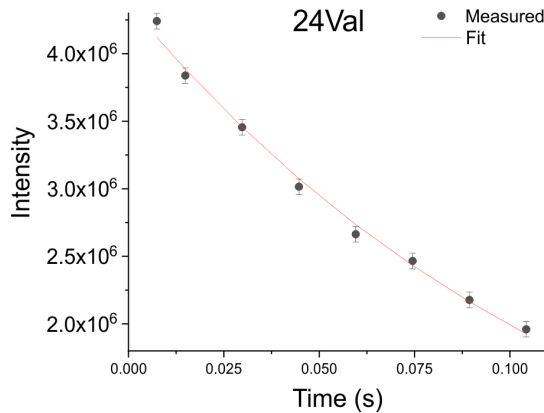
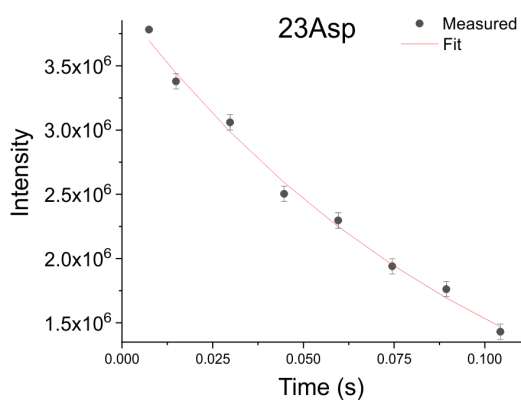
Appendix B: NMR parameters

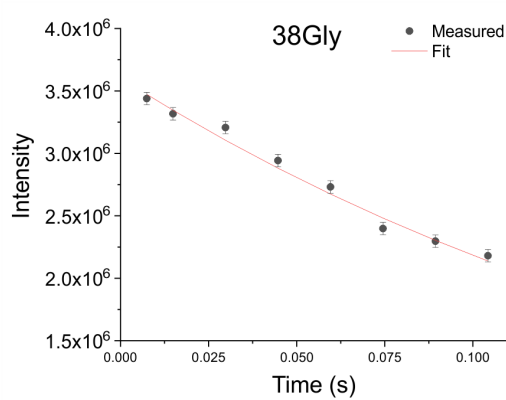
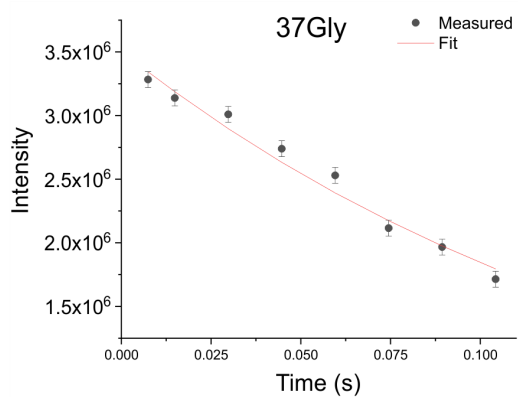
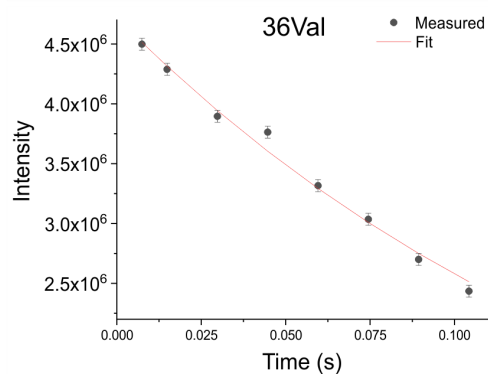
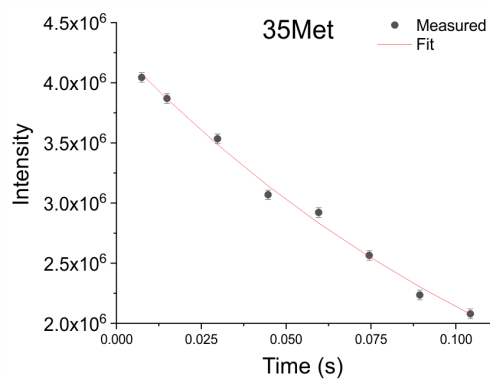
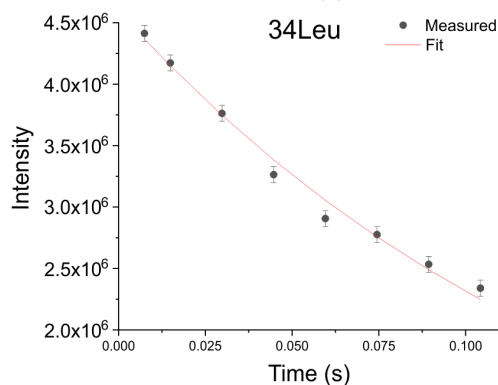
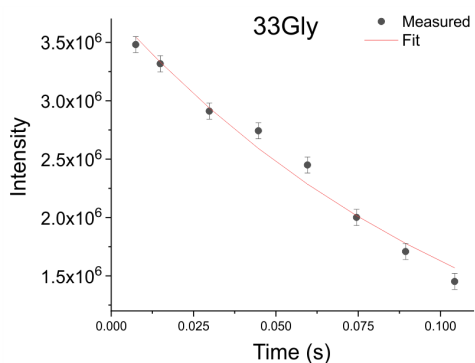
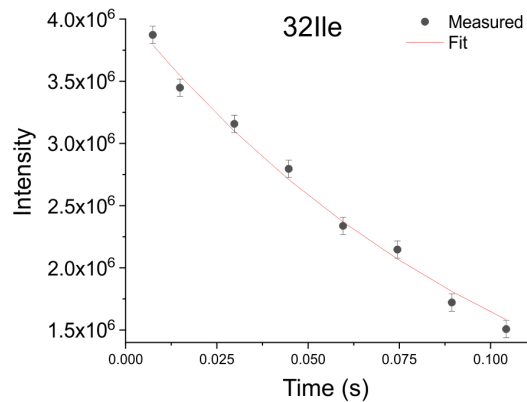
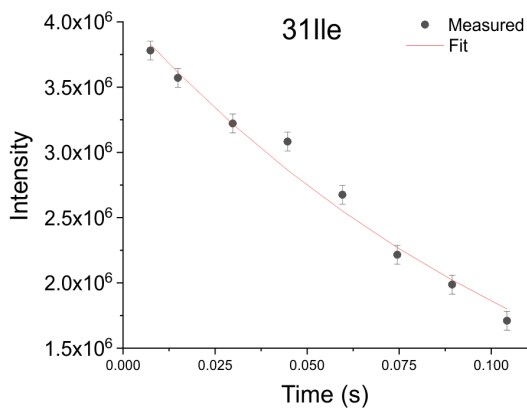
B.1 Data for calculating temperature coefficients

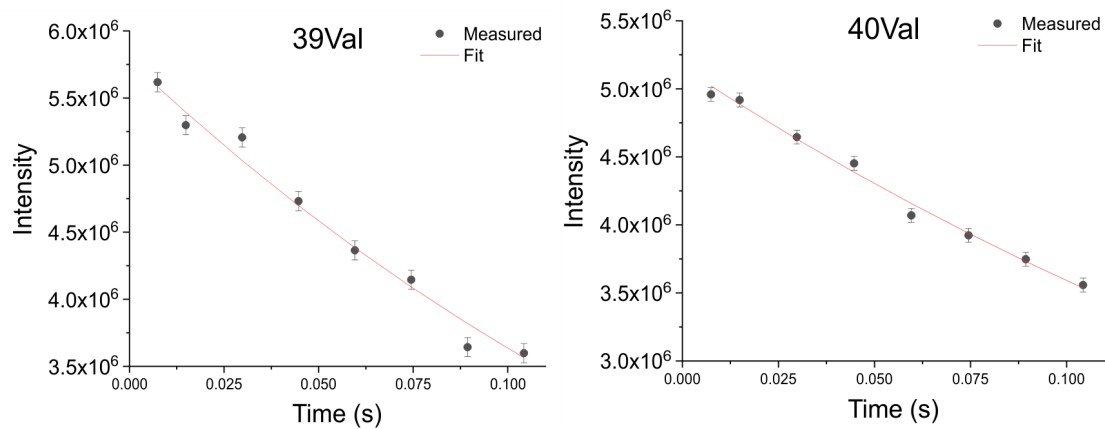
Plots of peak intensity after different delay times for the calculation of R_2 measures of each backbone amide of $A\beta_{40}$.





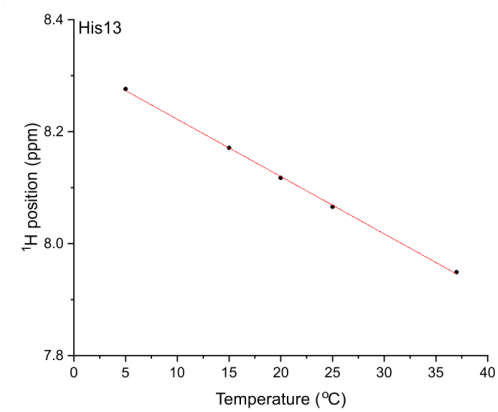
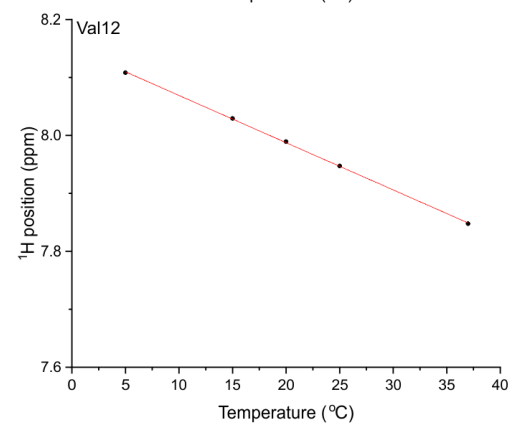
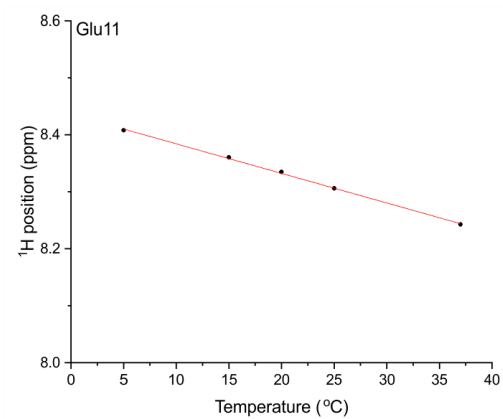
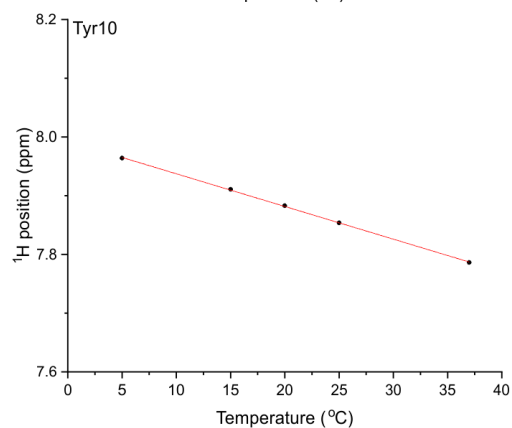
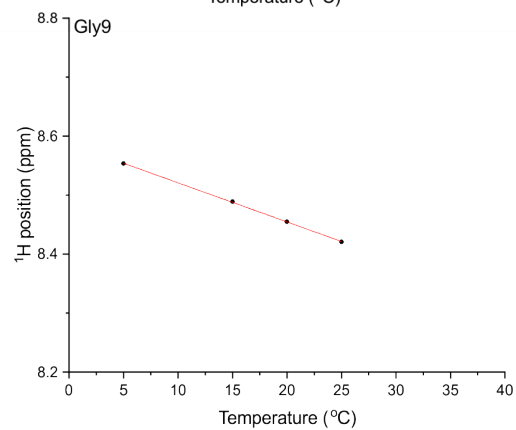
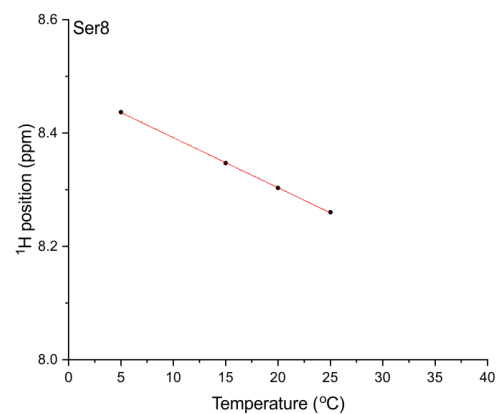
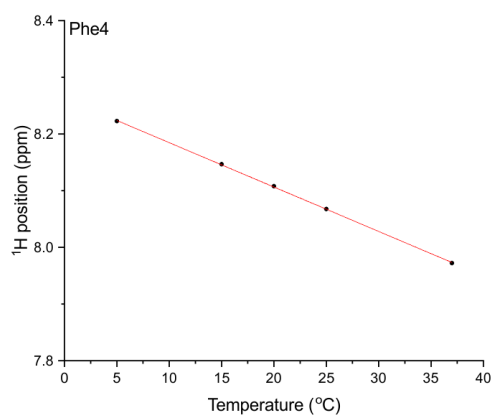
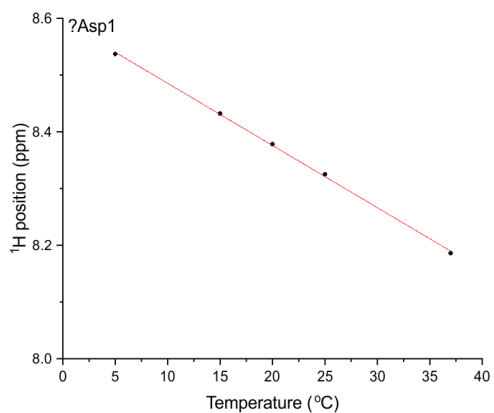


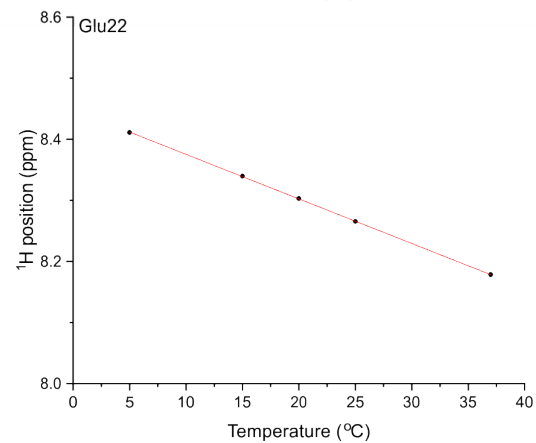
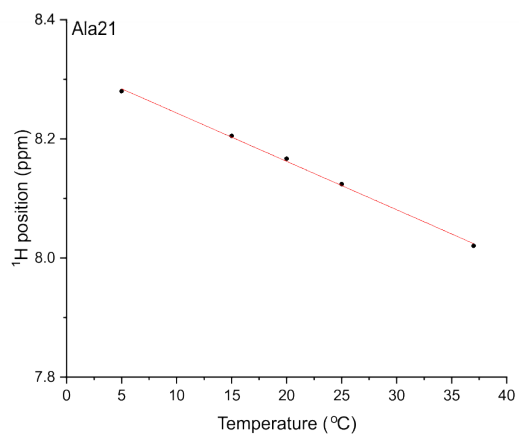
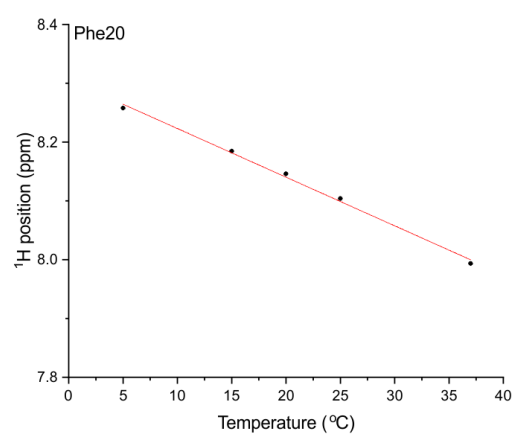
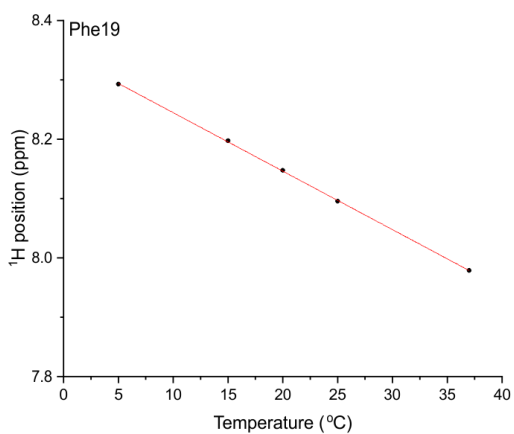
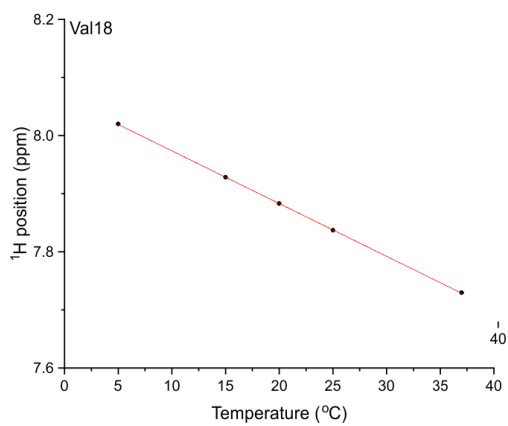
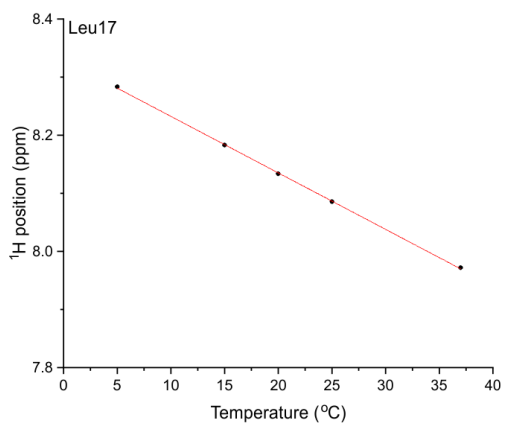
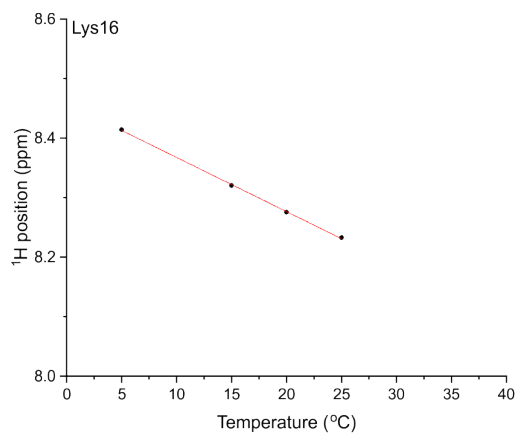
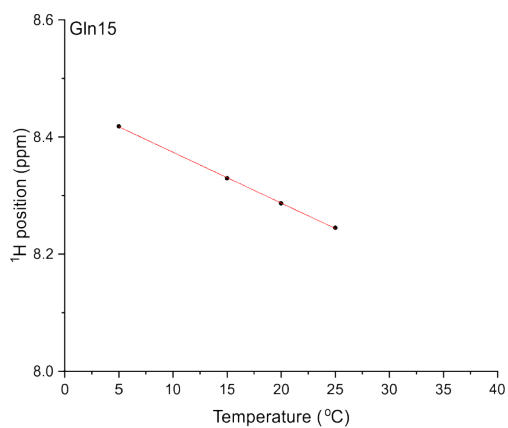


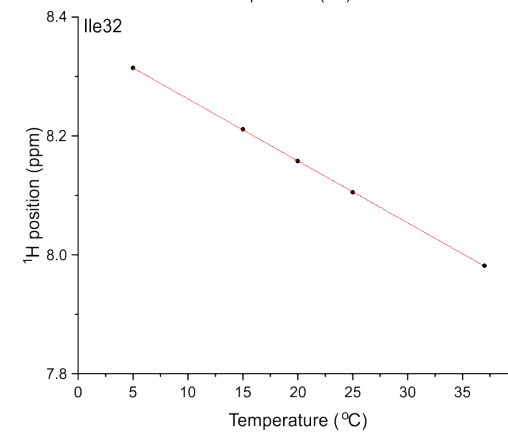
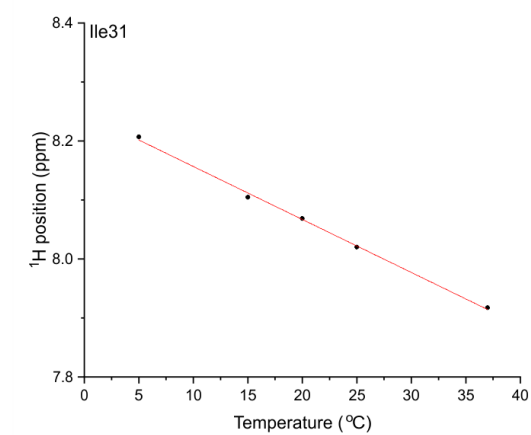
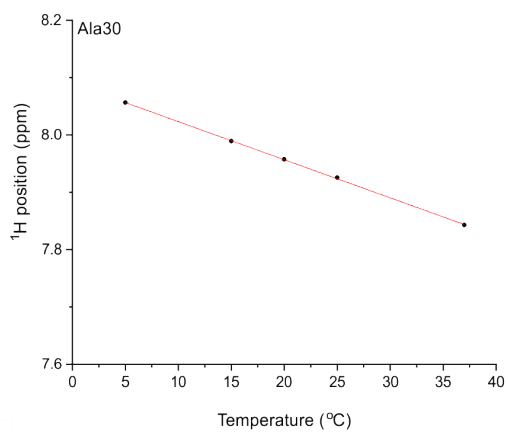
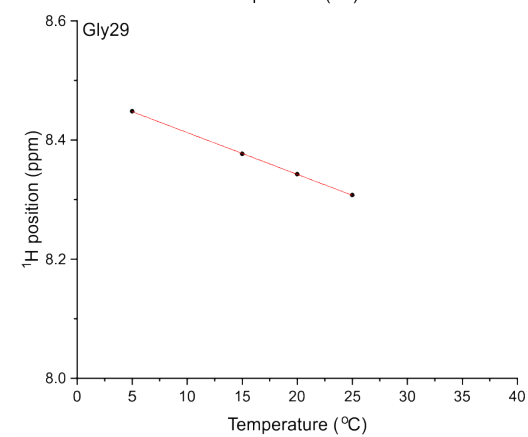
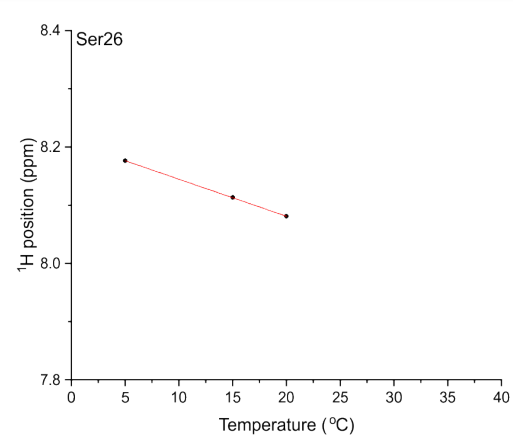
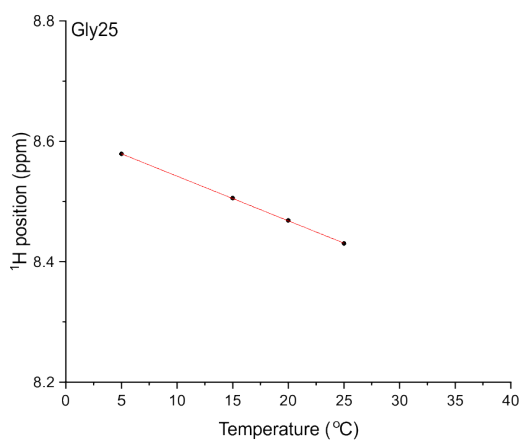
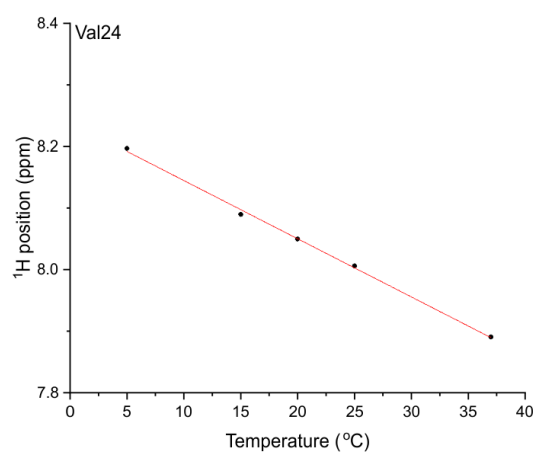
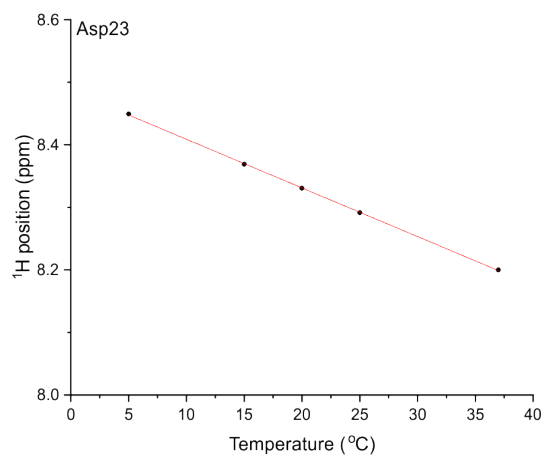


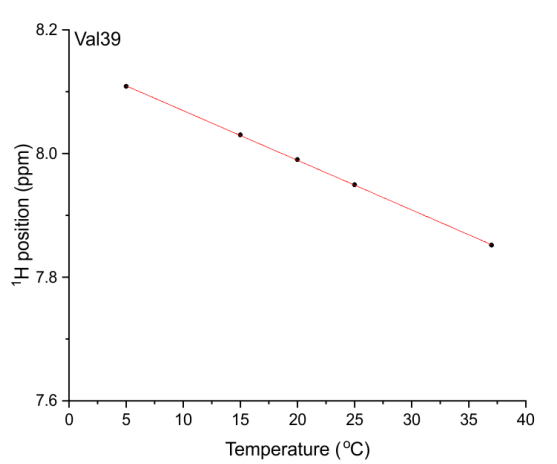
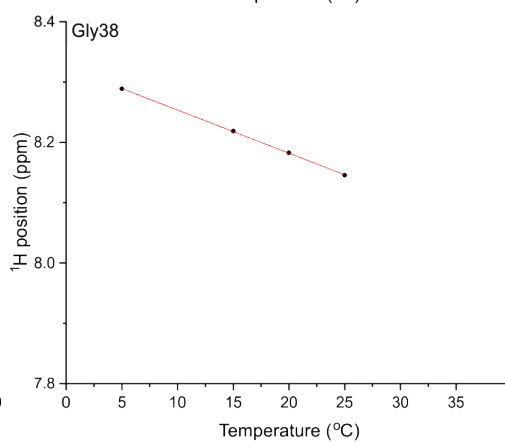
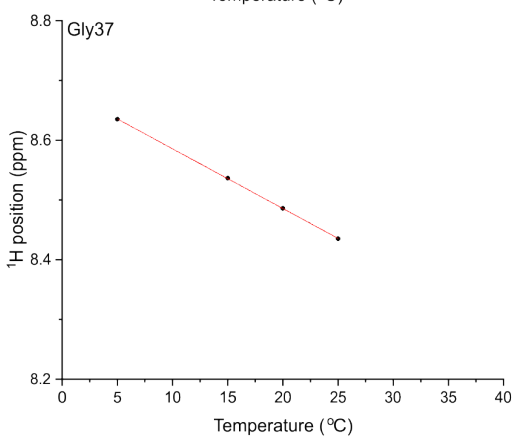
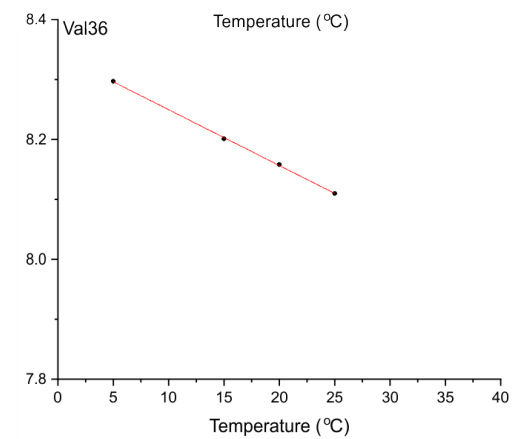
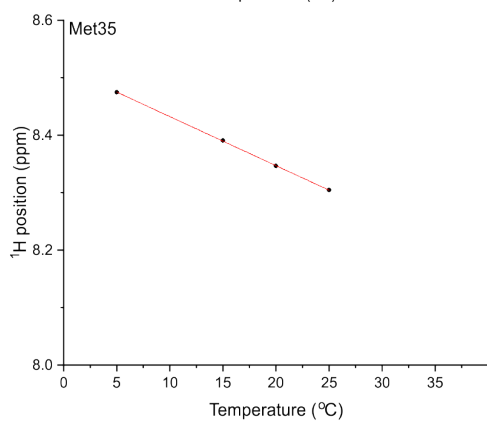
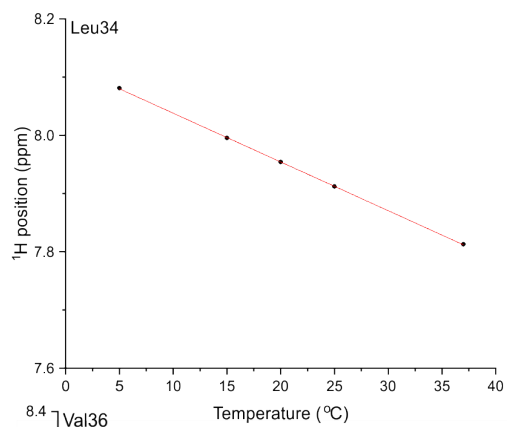
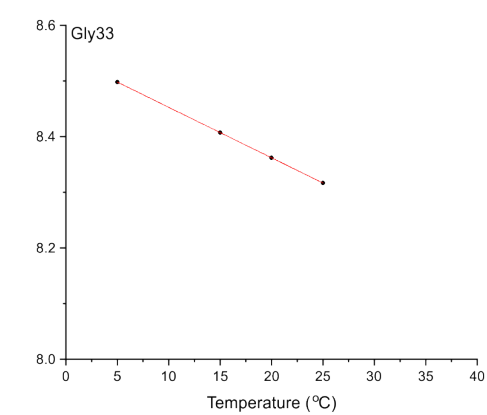
B.2 Data for calculating R_{2s}

Plots of ^1H -chemical shift perturbations across a range of temperatures for the calculation of $^1\text{H}^{\text{N}}$ -CSTCs of $A\beta_{40}$ backbone amides.









Bibliography

- [1] M. G. Iadanza, M. P. Jackson, E. W. Hewitt, N. A. Ranson, and S. E. Radford. A new era for understanding amyloid structures and disease. *Nat. Rev. Mol. Cell Biol.*, 19(12):755–773, Dec 2018.
- [2] D. M. Fowler, A. V. Koulov, W. E. Balch, and J. W. Kelly. Functional amyloid—from bacteria to humans. *Trends Biochem. Sci.*, 32(5):217–224, May 2007.
- [3] T. R. Jahn, O. S. Makin, K. L. Morris, K. E. Marshall, P. Tian, P. Sikorski, and L. C. Serpell. The common architecture of cross-beta amyloid. *J. Mol. Biol.*, 395(4):717–727, Jan 2010.
- [4] A. I. Bartlett and S. E. Radford. An expanding arsenal of experimental methods yields an explosion of insights into protein folding mechanisms. *Nat. Struct. Mol. Biol.*, 16(6):582–588, Jun 2009.
- [5] Z. Hamrang, N. J. Rattray, and A. Pluen. Proteins behaving badly: emerging technologies in profiling biopharmaceutical aggregation. *Trends Biotechnol.*, 31(8):448–458, Aug 2013.
- [6] W. Wang. Protein aggregation and its inhibition in biopharmaceutics. *Int J Pharm*, 289(1-2):1–30, Jan 2005.
- [7] T. Eichner and S. E. Radford. A diversity of assembly mechanisms of a generic amyloid fold. *Mol. Cell*, 43(1):8–18, Jul 2011.
- [8] A. C. Woerner, F. Frotin, D. Hornburg, L. R. Feng, F. Meissner, M. Patra, J. Tatzelt, M. Mann, K. F. Winklhofer, F. U. Hartl, and M. S. Hipp. Cytoplasmic protein aggregates interfere with nucleocytoplasmic transport of protein and RNA. *Science*, 351(6269):173–176, Jan 2016.

- [9] Q. Guo, C. Lehmer, A. Martinez-Sanchez, T. Rudack, F. Beck, H. Hartmann, M. Perez-Berlanga, F. Frottin, M. S. Hipp, F. U. Hartl, D. Edbauer, W. Baumeister, and R. Fernandez-Busnadiego. In Situ Structure of Neuronal C9orf72 Poly-GA Aggregates Reveals Proteasome Recruitment. *Cell*, 172(4):696–705, Feb 2018.
- [10] C. Campanella, A. Pace, C. Caruso Bavisotto, P. Marzullo, A. Marino Gammazza, S. Buscemi, and A. Palumbo Piccionello. Heat Shock Proteins in Alzheimer’s Disease: Role and Targeting. *Int J Mol Sci*, 19(9), Sep 2018.
- [11] J. D. Sipe, M. D. Benson, J. N. Buxbaum, S. I. Ikeda, G. Merlini, M. J. Saraiva, and P. Westermark. Amyloid fibril proteins and amyloidosis: chemical identification and clinical classification International Society of Amyloidosis 2016 Nomenclature Guidelines. *Amyloid*, 23(4):209–213, Dec 2016.
- [12] F. Chiti and C. M. Dobson. Protein misfolding, functional amyloid, and human disease. *Annu. Rev. Biochem.*, 75:333–366, 2006.
- [13] S. Auer, F. Meersman, C. M. Dobson, and M. Vendruscolo. A generic mechanism of emergence of amyloid protofilaments from disordered oligomeric aggregates. *PLoS Comput. Biol.*, 4(11):e1000222, Nov 2008.
- [14] Webster P. Taddei N. Clark A. Stefani M. Ramponi G. Dobson C. M. Chiti, F. Designing conditions for in vitro formation of amyloid protofilaments and fibrils. *Proc Natl Acad Sci USA*, 7(96):3590–3594, Mar 1999.
- [15] J. I. Guijarro, M. Sunde, J. A. Jones, I. D. Campbell, and C. M. Dobson. Amyloid fibril formation by an SH3 domain. *Proc. Natl. Acad. Sci. U.S.A.*, 95(8):4224–4228, Apr 1998.
- [16] B. Urbanc, L. Cruz, S. Yun, S. V. Buldyrev, G. Bitan, D. B. Teplow, and H. E. Stanley. In silico study of amyloid beta-protein folding and oligomerization. *Proc. Natl. Acad. Sci. U.S.A.*, 101(50):17345–17350, Dec 2004.
- [17] L. Goldschmidt, P. K. Teng, R. Riek, and D. Eisenberg. Identifying the amyloids, proteins capable of forming amyloid-like fibrils. *Proc. Natl. Acad. Sci. U.S.A.*, 107(8):3487–3492, Feb 2010.
- [18] C. M. Dobson. Principles of protein folding, misfolding and aggregation. *Semin. Cell Dev. Biol.*, 15(1):3–16, Feb 2004.

- [19] D. S. Eisenberg and M. R. Sawaya. Structural Studies of Amyloid Proteins at the Molecular Level. *Annu. Rev. Biochem.*, 86:69–95, 06 2017.
- [20] M. Sunde and C. Blake. The structure of amyloid fibrils by electron microscopy and X-ray diffraction. *Adv. Protein Chem.*, 50:123–159, 1997.
- [21] O. S. Makin and L. C. Serpell. Structures for amyloid fibrils. *FEBS J.*, 272(23): 5950–5961, Dec 2005.
- [22] T. P. Knowles, M. Vendruscolo, and C. M. Dobson. The amyloid state and its association with protein misfolding diseases. *Nat. Rev. Mol. Cell Biol.*, 15(6): 384–396, Jun 2014.
- [23] D. Eisenberg and M. Jucker. The amyloid state of proteins in human diseases. *Cell*, 148(6):1188–1203, Mar 2012.
- [24] H. Inouye, P. E. Fraser, and D. A. Kirschner. Structure of beta-crystallite assemblies formed by Alzheimer beta-amyloid protein analogues analysis by x-ray diffraction. *Biophys. J.*, 64(2):502–519, Feb 1993.
- [25] L. C. Serpell. Alzheimer’s amyloid fibrils: structure and assembly. *Biochim. Biophys. Acta*, 1502(1):16–30, Jul 2000.
- [26] P. Westermark, M. D. Benson, J. N. Buxbaum, A. S. Cohen, B. Frangione, S. Ikeda, C. L. Masters, G. Merlini, M. J. Saraiva, and J. D. Sipe. A primer of amyloid nomenclature. *Amyloid*, 14(3):179–183, Sep 2007.
- [27] R. Khurana, V. N. Uversky, L. Nielsen, and A. L. Fink. Is Congo red an amyloid-specific dye? *J. Biol. Chem.*, 276(25):22715–22721, Jun 2001.
- [28] S. K. Maji, L. Wang, J. Greenwald, and R. Riek. Structure-activity relationship of amyloid fibrils. *FEBS Lett.*, 583(16):2610–2617, Aug 2009.
- [29] S. M. Chafekar, F. Baas, and W. Scheper. Oligomer-specific A β toxicity in cell models is mediated by selective uptake. *Biochim. Biophys. Acta*, 1782(9):523–531, Sep 2008.
- [30] A. K. Chamberlain, C. E. MacPhee, J. Zurdo, L. A. Morozova-Roche, H. A. Hill, C. M. Dobson, and J. J. Davis. Ultrastructural organization of amyloid fibrils by atomic force microscopy. *Biophys. J.*, 79(6):3282–3293, Dec 2000.

- [31] S. B. Malinchik, H. Inouye, K. E. Szumowski, and D. A. Kirschner. Structural analysis of Alzheimer's beta(1-40) amyloid: protofilament assembly of tubular fibrils. *Biophys. J.*, 74(1):537–545, Jan 1998.
- [32] J. Meinhardt, C. Sachse, P. Hortschansky, N. Grigorieff, and M. Fandrich. Abeta(1-40) fibril polymorphism implies diverse interaction patterns in amyloid fibrils. *J. Mol. Biol.*, 386(3):869–877, Feb 2009.
- [33] M. Saiki, S. Honda, K. Kawasaki, D. Zhou, A. Kaito, T. Konakahara, and H. Morii. Higher-order molecular packing in amyloid-like fibrils constructed with linear arrangements of hydrophobic and hydrogen-bonding side-chains. *J. Mol. Biol.*, 348(4):983–998, May 2005.
- [34] E. Nugent, C. F. Kaminski, and G. S. Kaminski Schierle. Super-resolution imaging of alpha-synuclein polymorphisms and their potential role in neurodegeneration. *Integr Biol (Camb)*, 9(3):206–210, 03 2017.
- [35] Robert Tycko. Molecular-Level Insights into Amyloid Polymorphism from Solid-State Nuclear Magnetic Resonance. In *Bio-nanoimaging: Protein Misfolding and Aggregation*, pages 37–46. 2013. ISBN 9780123944313. doi: 10.1016/B978-0-12-394431-3.00004-3.
- [36] C. Seuring, J. Verasdonck, P. Ringler, R. Cadalbert, H. Stahlberg, A. Bockmann, B. H. Meier, and R. Riek. Amyloid Fibril Polymorphism: Almost Identical on the Atomic Level, Mesoscopically Very Different. *J Phys Chem B*, 121(8):1783–1792, 03 2017.
- [37] T. Sneideris, K. Milto, and V. Smirnovas. Polymorphism of amyloid-like fibrils can be defined by the concentration of seeds. *PeerJ*, 3:e1207, 2015.
- [38] M. R. Sawaya, S. Sambashivan, R. Nelson, M. I. Ivanova, S. A. Sievers, M. I. Apostol, M. J. Thompson, M. Balbirnie, J. J. Wiltzius, H. T. McFarlane, A. Madsen, C. Riek, and D. Eisenberg. Atomic structures of amyloid cross-beta spines reveal varied steric zippers. *Nature*, 447(7143):453–457, May 2007.
- [39] R. Nelson, M. R. Sawaya, M. Balbirnie, A. ?. Madsen, C. Riek, R. Grothe, and D. Eisenberg. Structure of the cross-beta spine of amyloid-like fibrils. *Nature*, 435(7043):773–778, Jun 2005.

- [40] A. G. Palmer. Nmr probes of molecular dynamics: overview and comparison with other techniques. *Annu Rev Biophys Biomol Struct*, 30:129–155, 2001.
- [41] E. Monsellier and F. Chiti. Prevention of amyloid-like aggregation as a driving force of protein evolution. *EMBO Rep.*, 8(8):737–742, Aug 2007.
- [42] M. R. Krebs, L. A. Morozova-Roche, K. Daniel, C. V. Robinson, and C. M. Dobson. Observation of sequence specificity in the seeding of protein amyloid fibrils. *Protein Sci.*, 13(7):1933–1938, Jul 2004.
- [43] C. J. Sarell, P. G. Stockley, and S. E. Radford. Assessing the causes and consequences of co-polymerization in amyloid formation. *Prion*, 7(5):359–368, 2013.
- [44] A. K. Paravastu, R. D. Leapman, W. M. Yau, and R. Tycko. Molecular structural basis for polymorphism in Alzheimer’s beta-amyloid fibrils. *Proc. Natl. Acad. Sci. U.S.A.*, 105(47):18349–18354, Nov 2008.
- [45] A. T. Petkova, R. D. Leapman, Z. Guo, W. M. Yau, M. P. Mattson, and R. Tycko. Self-propagating, molecular-level polymorphism in Alzheimer’s beta-amyloid fibrils. *Science*, 307(5707):262–265, Jan 2005.
- [46] A. T. Petkova, W. M. Yau, and R. Tycko. Experimental constraints on quaternary structure in Alzheimer’s beta-amyloid fibrils. *Biochemistry*, 45(2):498–512, Jan 2006.
- [47] M. Fandrich and C. M. Dobson. The behaviour of polyamino acids reveals an inverse side chain effect in amyloid structure formation. *EMBO J.*, 21(21):5682–5690, Nov 2002.
- [48] W. Qiang, W. M. Yau, J. X. Lu, J. Collinge, and R. Tycko. Structural variation in amyloid- fibrils from Alzheimer’s disease clinical subtypes. *Nature*, 541(7636):217–221, 01 2017.
- [49] A. Sicorello, S. Torrassa, G. Soldi, S. Gianni, C. Travaglini-Allocatelli, N. Taddei, A. Relini, and F. Chiti. Agitation and high ionic strength induce amyloidogenesis of a folded PDZ domain in native conditions. *Biophys. J.*, 96(6):2289–2298, Mar 2009.
- [50] F. Gejyo, S. Odani, T. Yamada, N. Honma, H. Saito, Y. Suzuki, Y. Nakagawa, H. Kobayashi, Y. Maruyama, and Y. Hirasawa. Beta 2-microglobulin: a new

- form of amyloid protein associated with chronic hemodialysis. *Kidney Int.*, 30(3):385–390, Sep 1986.
- [51] S. L. Myers, S. Jones, T. R. Jahn, I. J. Morten, G. A. Tennent, E. W. Hewitt, and S. E. Radford. A systematic study of the effect of physiological factors on beta2-microglobulin amyloid formation at neutral pH. *Biochemistry*, 45(7):2311–2321, Feb 2006.
- [52] S. Yamamoto, K. Hasegawa, I. Yamaguchi, S. Tsutsumi, J. Kardos, Y. Goto, F. Gejyo, and H. Naiki. Low concentrations of sodium dodecyl sulfate induce the extension of beta 2-microglobulin-related amyloid fibrils at a neutral pH. *Biochemistry*, 43(34):11075–11082, Aug 2004.
- [53] N. A. Athanasou, B. Puddle, and B. Sallie. Highly sulphated glycosaminoglycans in articular cartilage and other tissues containing beta 2 microglobulin dialysis amyloid deposits. *Nephrol. Dial. Transplant.*, 10(9):1672–1678, 1995.
- [54] T. Ookoshi, K. Hasegawa, Y. Ohhashi, H. Kimura, N. Takahashi, H. Yoshida, R. Miyazaki, Y. Goto, and H. Naiki. Lysophospholipids induce the nucleation and extension of beta2-microglobulin-related amyloid fibrils at a neutral pH. *Nephrol. Dial. Transplant.*, 23(10):3247–3255, Oct 2008.
- [55] C. J. Morgan, M. Gelfand, C. Atreya, and A. D. Miranker. Kidney dialysis-associated amyloidosis: a molecular role for copper in fiber formation. *J. Mol. Biol.*, 309(2):339–345, Jun 2001.
- [56] J. Villanueva, M. Hoshino, H. Katou, J. Kardos, K. Hasegawa, H. Naiki, and Y. Goto. Increase in the conformational flexibility of beta 2-microglobulin upon copper binding: a possible role for copper in dialysis-related amyloidosis. *Protein Sci.*, 13(3):797–809, Mar 2004.
- [57] A. Relini, C. Canale, S. De Stefano, R. Rolandi, S. Giorgetti, M. Stoppini, A. Rossi, F. Fogolari, A. Corazza, G. Esposito, A. Gliozzi, and V. Bellotti. Collagen plays an active role in the aggregation of beta2-microglobulin under physiopathological conditions of dialysis-related amyloidosis. *J. Biol. Chem.*, 281(24):16521–16529, Jun 2006.
- [58] A. Relini, S. De Stefano, S. Torrassa, O. Cavalleri, R. Rolandi, A. Gliozzi, S. Giorgetti, S. Raimondi, L. Marchese, L. Verga, A. Rossi, M. Stoppini, and V. Bellotti.

- Heparin strongly enhances the formation of beta2-microglobulin amyloid fibrils in the presence of type I collagen. *J. Biol. Chem.*, 283(8):4912–4920, Feb 2008.
- [59] V. Bellotti, M. Stoppini, P. Mangione, M. Sunde, C. Robinson, L. Asti, D. Braccaccio, and G. Ferri. Beta2-microglobulin can be refolded into a native state from ex vivo amyloid fibrils. *Eur. J. Biochem.*, 258(1):61–67, Nov 1998.
- [60] G. Esposito, R. Michelutti, G. Verdone, P. Viglino, H. Hernandez, C. V. Robinson, A. Amoresano, F. Dal Piaz, M. Monti, P. Pucci, P. Mangione, M. Stoppini, G. Merlini, G. Ferri, and V. Bellotti. Removal of the N-terminal hexapeptide from human beta2-microglobulin facilitates protein aggregation and fibril formation. *Protein Sci.*, 9(5):831–845, May 2000.
- [61] F. Chiti, P. Mangione, A. Andreola, S. Giorgetti, M. Stefani, C. M. Dobson, V. Bellotti, and N. Taddei. Detection of two partially structured species in the folding process of the amyloidogenic protein beta 2-microglobulin. *J. Mol. Biol.*, 307(1):379–391, Mar 2001.
- [62] Theodoros K. Karamanos, Clare L. Pashley, Arnout P. Kalverda, Gary S. Thompson, Maxim Mayzel, Vladislav Y. Orekhov, and Sheena E. Radford. A Population Shift between Sparsely Populated Folding Intermediates Determines Amyloidogenicity. *Journal of the American Chemical Society*, 138(19):6271–6280, may 2016. ISSN 0002-7863. doi: 10.1021/jacs.6b02464.
- [63] E. Hellstrand, B. Boland, D. M. Walsh, and S. Linse. Amyloid -protein aggregation produces highly reproducible kinetic data and occurs by a two-phase process. *ACS Chem Neurosci*, 1(1):13–18, Jan 2010.
- [64] G. Meisl, J. B. Kirkegaard, P. Arosio, T. C. Michaels, M. Vendruscolo, C. M. Dobson, S. Linse, and T. P. Knowles. Molecular mechanisms of protein aggregation from global fitting of kinetic models. *Nat Protoc*, 11(2):252–272, Feb 2016.
- [65] K. P. Nilsson. Small organic probes as amyloid specific ligands—past and recent molecular scaffolds. *FEBS Lett.*, 583(16):2593–2599, Aug 2009.
- [66] S. I. Cohen, S. Linse, L. M. Luheshi, E. Hellstrand, D. A. White, L. Rajah, D. E. Otzen, M. Vendruscolo, C. M. Dobson, and T. P. Knowles. Proliferation of amyloid-42 aggregates occurs through a secondary nucleation mechanism. *Proc. Natl. Acad. Sci. U.S.A.*, 110(24):9758–9763, Jun 2013.

- [67] M. Tornquist, T. C. T. Michaels, K. Sanagavarapu, X. Yang, G. Meisl, S. I. A. Cohen, T. P. J. Knowles, and S. Linse. Secondary nucleation in amyloid formation. *Chem. Commun. (Camb.)*, 54(63):8667–8684, Aug 2018.
- [68] T. R. Jahn and S. E. Radford. Folding versus aggregation: polypeptide conformations on competing pathways. *Arch. Biochem. Biophys.*, 469(1):100–117, Jan 2008.
- [69] D. N. Dean, P. Rana, R. P. Campbell, P. Ghosh, and V. Rangachari. Propagation of an A Dodecamer Strain Involves a Three-Step Mechanism and a Key Intermediate. *Biophys. J.*, 114(3):539–549, Feb 2018.
- [70] M. Stefani. Protein misfolding and aggregation: new examples in medicine and biology of the dark side of the protein world. *Biochim. Biophys. Acta*, 1739(1):5–25, Dec 2004.
- [71] T. Gurry and C. M. Stultz. Mechanism of amyloid- fibril elongation. *Biochemistry*, 53(44):6981–6991, Nov 2014.
- [72] R. A. Rodriguez, L. Y. Chen, G. Plascencia-Villa, and G. Perry. Thermodynamics of Amyloid- Fibril Elongation: Atomistic Details of the Transition State. *ACS Chem Neurosci*, 9(4):783–789, Apr 2018.
- [73] R. R. Kopito. Aggresomes, inclusion bodies and protein aggregation. *Trends Cell Biol.*, 10(12):524–530, Dec 2000.
- [74] Samuel I.A. Cohen, Michele Vendruscolo, Mark E. Welland, Christopher M. Dobson, Eugene M. Terentjev, and Tuomas P.J. Knowles. Nucleated polymerization with secondary pathways. I. Time evolution of the principal moments. *Journal of Chemical Physics*, 135(6), 2011. ISSN 00219606. doi: 10.1063/1.3608916.
- [75] F. Ferrone. Analysis of protein aggregation kinetics. *Meth. Enzymol.*, 309:256–274, 1999.
- [76] S. Linse. Monomer-dependent secondary nucleation in amyloid formation. *Biophys Rev*, 9(4):329–338, Aug 2017.

- [77] R. Cukalevski, X. Yang, G. Meisl, U. Weininger, K. Bernfur, B. Frohm, T. P. J. Knowles, and S. Linse. The A40 and A42 peptides self-assemble into separate homomolecular fibrils in binary mixtures but cross-react during primary nucleation. *Chem Sci*, 6(7):4215–4233, Jul 2015.
- [78] G. Meisl, L. Rajah, S. A. I. Cohen, M. Pfammatter, A. ?ari?, E. Hellstrand, A. K. Buell, A. Aguzzi, S. Linse, M. Vendruscolo, C. M. Dobson, and T. P. J. Knowles. Scaling behaviour and rate-determining steps in filamentous self-assembly. *Chem Sci*, 8(10):7087–7097, Oct 2017.
- [79] T. P. Knowles, C. A. Waudby, G. L. Devlin, S. I. Cohen, A. Aguzzi, M. Vendruscolo, E. M. Terentjev, M. E. Welland, and C. M. Dobson. An analytical solution to the kinetics of breakable filament assembly. *Science*, 326(5959):1533–1537, Dec 2009.
- [80] M. Tanaka, S. R. Collins, B. H. Toyama, and J. S. Weissman. The physical basis of how prion conformations determine strain phenotypes. *Nature*, 442(7102):585–589, Aug 2006.
- [81] World Alzheimer Report 2018 Alzheimer’s Disease International. <https://www.alz.co.uk/research/WorldAlzheimerReport2018.pdf>, 2018. Accessed: 2019-01-02.
- [82] F. Chiti and C. M. Dobson. Protein Misfolding, Amyloid Formation, and Human Disease: A Summary of Progress Over the Last Decade. *Annu. Rev. Biochem.*, 86:27–68, 06 2017.
- [83] P. Salahuddin, M. T. Fatima, A. S. Abdelhameed, S. Nusrat, and R. H. Khan. Structure of amyloid oligomers and their mechanisms of toxicities: Targeting amyloid oligomers using novel therapeutic approaches. *Eur J Med Chem*, 114:41–58, May 2016.
- [84] N. Benseny-Cases, O. Klementieva, and J. Cladera. In vitro oligomerization and fibrillogenesis of amyloid-beta peptides. *Subcell. Biochem.*, 65:53–74, 2012.
- [85] B. Penke, F. Bogar, G. Paragi, J. Gera, and L. Fulop. Key Peptides and Proteins in Alzheimer’s Disease. *Curr. Protein Pept. Sci.*, Jan 2019.

- [86] W. Hoffmann, G. von Helden, and K. Pagel. Ion mobility-mass spectrometry and orthogonal gas-phase techniques to study amyloid formation and inhibition. *Curr. Opin. Struct. Biol.*, 46:7–15, 10 2017.
- [87] R. Kaye, E. Head, J. L. Thompson, T. M. McIntire, S. C. Milton, C. W. Cotman, and C. G. Glabe. Common structure of soluble amyloid oligomers implies common mechanism of pathogenesis. *Science*, 300(5618):486–489, Apr 2003.
- [88] R. Kaye, E. Head, F. Sarsoza, T. Saing, C. W. Cotman, M. Necula, L. Margol, J. Wu, L. Breydo, J. L. Thompson, S. Rasool, T. Gurlo, P. Butler, and C. G. Glabe. Fibril specific, conformation dependent antibodies recognize a generic epitope common to amyloid fibrils and fibrillar oligomers that is absent in prefibrillar oligomers. *Mol Neurodegener*, 2:18, Sep 2007.
- [89] R. Kaye and C. A. Lasagna-Reeves. Molecular mechanisms of amyloid oligomers toxicity. *J. Alzheimers Dis.*, 33 Suppl 1:67–78, 2013.
- [90] D. J. Selkoe and J. Hardy. The amyloid hypothesis of Alzheimer’s disease at 25 years. *EMBO Mol Med*, 8(6):595–608, 06 2016.
- [91] U. Sengupta, A. N. Nilson, and R. Kaye. The Role of Amyloid- Oligomers in Toxicity, Propagation, and Immunotherapy. *EBioMedicine*, 6:42–49, Apr 2016.
- [92] J. Y. Seo, S. S. Lim, J. Kim, K. W. Lee, and J. S. Kim. Alantolactone and Isoalantolactone Prevent Amyloid 25-35 -induced Toxicity in Mouse Cortical Neurons and Scopolamine-induced Cognitive Impairment in Mice. *Phytother Res*, 31(5):801–811, May 2017.
- [93] H. Shi, B. Kang, and J. Y. Lee. Zn(2+) effect on structure and residual hydrophobicity of amyloid -peptide monomers. *J Phys Chem B*, 118(35):10355–10361, Sep 2014.
- [94] J. Janson, R. H. Ashley, D. Harrison, S. McIntyre, and P. C. Butler. The mechanism of islet amyloid polypeptide toxicity is membrane disruption by intermediate-sized toxic amyloid particles. *Diabetes*, 48(3):491–498, Mar 1999.
- [95] G. Gorbenko, V. Trusova, M. Giryh, E. Adachi, C. Mizuguchi, and H. Saito. Interactions of Lipid Membranes with Fibrillar Protein Aggregates. *Adv. Exp. Med. Biol.*, 855:135–155, 2015.

- [96] J. Kumar, R. Namsechi, and V. L. Sim. Structure-Based Peptide Design to Modulate Amyloid Beta Aggregation and Reduce Cytotoxicity. *PLoS ONE*, 10(6):e0129087, 2015.
- [97] A. D. Williams, M. Segal, M. Chen, I. Kheterpal, M. Geva, V. Berthelier, D. T. Kaleta, K. D. Cook, and R. Wetzel. Structural properties of A β protofibrils stabilized by a small molecule. *Proc. Natl. Acad. Sci. U.S.A.*, 102(20):7115–7120, May 2005.
- [98] W. Qiang, W. M. Yau, and J. Schulte. Fibrillation of amyloid peptides in the presence of phospholipid bilayers and the consequent membrane disruption. *Biochim. Biophys. Acta*, 1848(1 Pt B):266–276, Jan 2015.
- [99] J. Floege and G. Ehlerding. Beta-2-microglobulin-associated amyloidosis. *Nephron*, 72(1):9–26, 1996.
- [100] P. E. Spies, M. M. Verbeek, M. J. Sjogren, F. E. de Leeuw, and J. A. Claassen. Alzheimer biomarkers and clinical Alzheimer disease were not associated with increased cerebrovascular disease in a memory clinic population. *Curr Alzheimer Res*, 11(1):40–46, Jan 2014.
- [101] D. J. Irwin and H. I. Hurtig. The Contribution of Tau, Amyloid-Beta and Alpha-Synuclein Pathology to Dementia in Lewy Body Disorders. *J Alzheimers Dis Parkinsonism*, 8(4), 2018.
- [102] M. Stefani. Structural features and cytotoxicity of amyloid oligomers: implications in Alzheimer’s disease and other diseases with amyloid deposits. *Prog. Neurobiol.*, 99(3):226–245, Dec 2012.
- [103] H. A. Lashuel, C. R. Overk, A. Oueslati, and E. Masliah. The many faces of α -synuclein: from structure and toxicity to therapeutic target. *Nat. Rev. Neurosci.*, 14(1):38–48, 01 2013.
- [104] J. Tyedmers, A. Mogk, and B. Bukau. Cellular strategies for controlling protein aggregation. *Nat. Rev. Mol. Cell Biol.*, 11(11):777–788, Nov 2010.
- [105] M. R. Chapman, L. S. Robinson, J. S. Pinkner, R. Roth, J. Heuser, M. Hammar, S. Normark, and S. J. Hultgren. Role of *Escherichia coli* curli operons in directing amyloid fiber formation. *Science*, 295(5556):851–855, Feb 2002.

- [106] D. M. Fowler, A. V. Koulov, C. Alory-Jost, M. S. Marks, W. E. Balch, and J. W. Kelly. Functional amyloid formation within mammalian tissue. *PLoS Biol.*, 4(1):e6, Jan 2006.
- [107] E. B. Sawyer, D. Claessen, M. Haas, B. Hurgobin, and S. L. Gras. The assembly of individual chaplin peptides from *Streptomyces coelicolor* into functional amyloid fibrils. *PLoS ONE*, 6(4):e18839, Apr 2011.
- [108] E. Bramanti, E. Benedetti, A. Sagripanti, F. Papineschi, and E. Benedetti. Determination of secondary structure of normal fibrin from human peripheral blood. *Biopolymers*, 41(5):545–553, Apr 1997.
- [109] O. Kranenburg, B. Bouma, L. M. Kroon-Batenburg, A. Reijerkerk, Y. P. Wu, E. E. Voest, and M. F. Gebink. Tissue-type plasminogen activator is a multiligand cross-beta structure receptor. *Curr. Biol.*, 12(21):1833–1839, Oct 2002.
- [110] C. M. Dobson. Protein misfolding, evolution and disease. *Trends Biochem. Sci.*, 24(9):329–332, Sep 1999.
- [111] J. Greenwald and R. Riek. On the possible amyloid origin of protein folds. *J. Mol. Biol.*, 421(4-5):417–426, Aug 2012.
- [112] O. Carny and E. Gazit. A model for the role of short self-assembled peptides in the very early stages of the origin of life. *FASEB J.*, 19(9):1051–1055, Jul 2005.
- [113] J. Greenwald, M. P. Friedmann, and R. Riek. Amyloid Aggregates Arise from Amino Acid Condensations under Prebiotic Conditions. *Angew. Chem. Int. Ed. Engl.*, 55(38):11609–11613, 09 2016.
- [114] A. J. Geddes, K. D. Parker, E. D. Atkins, and E. Beighton. "Cross-beta" conformation in proteins. *J. Mol. Biol.*, 32(2):343–358, Mar 1968.
- [115] W. T. Astbury and A. Street. X-ray Studies of the Structure of Hairm Wool and Related Fibres. *I. General. Phil. Trans. R. Soc.*, 230:75–101, 1932.
- [116] L. Jaeken. The neglected functions of intrinsically disordered proteins and the origin of life. *Prog. Biophys. Mol. Biol.*, 126:31–46, 07 2017.
- [117] V. N. Uversky. Functions of short lifetime biological structures at large: the case of intrinsically disordered proteins. *Brief Funct Genomics*, Jul 2018.

- [118] A. K. Dunker, I. Silman, V. N. Uversky, and J. L. Sussman. Function and structure of inherently disordered proteins. *Curr. Opin. Struct. Biol.*, 18(6):756–764, Dec 2008.
- [119] V. N. Uversky. The multifaceted roles of intrinsic disorder in protein complexes. *FEBS Lett.*, 589(19 Pt A):2498–2506, Sep 2015.
- [120] V. N. Uversky. Intrinsically disordered proteins may escape unwanted interactions via functional misfolding. *Biochim. Biophys. Acta*, 1814(5):693–712, May 2011.
- [121] C. B. ANFINSEN, E. HABER, M. SELA, and F. H. WHITE. The kinetics of formation of native ribonuclease during oxidation of the reduced polypeptide chain. *Proc. Natl. Acad. Sci. U.S.A.*, 47:1309–1314, Sep 1961.
- [122] V. N. Uversky. Mysterious oligomerization of the amyloidogenic proteins. *FEBS J.*, 277(14):2940–2953, Jul 2010.
- [123] P. Tompa, G. E. Tusnady, P. Friedrich, and I. Simon. The role of dimerization in prion replication. *Biophys. J.*, 82(4):1711–1718, Apr 2002.
- [124] H. J. Dyson and P. E. Wright. Intrinsically unstructured proteins and their functions. *Nat. Rev. Mol. Cell Biol.*, 6(3):197–208, Mar 2005.
- [125] K. Tompa, M. Bokor, and P. Tompa. Wide-line NMR and protein hydration. *Methods Mol. Biol.*, 895:167–196, 2012.
- [126] V. N. Uversky. Disorder in the lifetime of a protein. *Intrinsically Disord Proteins*, 1(1):e26782, 2013.
- [127] K. A. Dill and J. L. MacCallum. The protein-folding problem, 50 years on. *Science*, 338(6110):1042–1046, Nov 2012.
- [128] C. J. Oldfield and A. K. Dunker. Intrinsically disordered proteins and intrinsically disordered protein regions. *Annu. Rev. Biochem.*, 83:553–584, 2014.
- [129] D. Granata, F. Baftizadeh, J. Habchi, C. Galvagnion, A. De Simone, C. Camilloni, A. Laio, and M. Vendruscolo. The inverted free energy landscape of an intrinsically disordered peptide by simulations and experiments. *Sci Rep*, 5:15449, Oct 2015.
- [130] K. L. Morris and L. C. Serpell. X-ray fibre diffraction studies of amyloid fibrils. *Methods Mol. Biol.*, 849:121–135, 2012.

- [131] P. G. Wolynes. Evolution, energy landscapes and the paradoxes of protein folding. *Biochimie*, 119:218–230, Dec 2015.
- [132] K. A. Dill and H. S. Chan. From Levinthal to pathways to funnels. *Nat. Struct. Biol.*, 4(1):10–19, Jan 1997.
- [133] C. Levinthal. How to Fold Graciously University of Illinious Press. In: Proceedings of a Meeting held at Allerton House, Monticello, Illinois, Monticello, Illinois, 1969.
- [134] S. Linse and B. Linse. Protein folding through kinetic discrimination. *J. Am. Chem. Soc.*, 129(27):8481–8486, Jul 2007.
- [135] C. Levinthal. Are there pathways for protein folding? *Extrait du Journal de Chimie Physique*, 65(1):44, 1968.
- [136] R. Zwanzig, A. Szabo, and B. Bagchi. Levinthal’s paradox. *Proc. Natl. Acad. Sci. U.S.A.*, 89(1):20–22, Jan 1992.
- [137] D. Raimondi, G. Orlando, R. Pancsa, T. Khan, and W. F. Vranken. Exploring the Sequence-based Prediction of Folding Initiation Sites in Proteins. *Sci Rep*, 7(1):8826, Aug 2017.
- [138] P. Neudecker, P. Robustelli, A. Cavalli, P. Walsh, P. Lundstrom, A. Zarrine-Afsar, S. Sharpe, M. Vendruscolo, and L. E. Kay. Structure of an intermediate state in protein folding and aggregation. *Science*, 336(6079):362–366, Apr 2012.
- [139] A. De Simone, A. Dhulesia, G. Soldi, M. Vendruscolo, S. T. Hsu, F. Chiti, and C. M. Dobson. Experimental free energy surfaces reveal the mechanisms of maintenance of protein solubility. *Proc. Natl. Acad. Sci. U.S.A.*, 108(52):21057–21062, Dec 2011.
- [140] D. Thirumalai and G. Reddy. Protein thermodynamics: Are native proteins metastable? *Nat Chem*, 3(12):910–911, Nov 2011.
- [141] J. Schonbrun and K. A. Dill. Fast protein folding kinetics. *Proc. Natl. Acad. Sci. U.S.A.*, 100(22):12678–12682, Oct 2003.
- [142] M. J. Feige, S. Groscurth, M. Marciniowski, Z. T. Yew, V. Truffault, E. Paci, H. Kessler, and J. Buchner. The structure of a folding intermediate provides insight into differences in immunoglobulin amyloidogenicity. *Proc. Natl. Acad. Sci. U.S.A.*, 105(36):13373–13378, Sep 2008.

- [143] R. Moulick and J. B. Udgaonkar. Identification and Structural Characterization of the Precursor Conformation of the Prion Protein which Directly Initiates Misfolding and Oligomerization. *J. Mol. Biol.*, 429(6):886–899, 03 2017.
- [144] I. Moreno-Gonzalez and C. Soto. Misfolded protein aggregates: mechanisms, structures and potential for disease transmission. *Semin. Cell Dev. Biol.*, 22(5):482–487, Jul 2011.
- [145] M. Beissinger and J. Buchner. How chaperones fold proteins. *Biol. Chem.*, 379(3):245–259, Mar 1998.
- [146] R. M. Vabulas, S. Raychaudhuri, M. Hayer-Hartl, and F. U. Hartl. Protein folding in the cytoplasm and the heat shock response. *Cold Spring Harb Perspect Biol*, 2(12):a004390, Dec 2010.
- [147] D. C. Henstridge, M. Whitham, and M. A. Febbraio. Chaperoning to the metabolic party: The emerging therapeutic role of heat-shock proteins in obesity and type 2 diabetes. *Mol Metab*, 3(8):781–793, Nov 2014.
- [148] R. I. Morimoto. Regulation of the heat shock transcriptional response: cross talk between a family of heat shock factors, molecular chaperones, and negative regulators. *Genes Dev.*, 12(24):3788–3796, Dec 1998.
- [149] A. I. Gragerov, E. S. Martin, M. A. Krupenko, M. V. Kashlev, and V. G. Nikiforov. Protein aggregation and inclusion body formation in *Escherichia coli* rpoH mutant defective in heat shock protein induction. *FEBS Lett.*, 291(2):222–224, Oct 1991.
- [150] D. Ebrahimi-Fakhari, L. J. Saidi, and L. Wahlster. Molecular chaperones and protein folding as therapeutic targets in Parkinson’s disease and other synucleinopathies. *Acta Neuropathol Commun*, 1:79, Dec 2013.
- [151] M. Stefani and C. M. Dobson. Protein aggregation and aggregate toxicity: new insights into protein folding, misfolding diseases and biological evolution. *J. Mol. Med.*, 81(11):678–699, Nov 2003.
- [152] X. Zhang and S. B. Qian. Chaperone-mediated hierarchical control in targeting misfolded proteins to aggresomes. *Mol. Biol. Cell*, 22(18):3277–3288, Sep 2011.
- [153] U. Woehlbier and C. Hetz. Modulating stress responses by the UPRosome: a matter of life and death. *Trends Biochem. Sci.*, 36(6):329–337, Jun 2011.

- [154] A. R. Wyatt, J. J. Yerbury, R. A. Dabbs, and M. R. Wilson. Roles of extracellular chaperones in amyloidosis. *J. Mol. Biol.*, 421(4-5):499–516, Aug 2012.
- [155] R. G. Bennett, W. C. Duckworth, and F. G. Hamel. Degradation of amylin by insulin-degrading enzyme. *J. Biol. Chem.*, 275(47):36621–36625, Nov 2000.
- [156] S. Howell, J. Nalbantoglu, and P. Crine. Neutral endopeptidase can hydrolyze beta-amyloid(1-40) but shows no effect on beta-amyloid precursor protein metabolism. *Peptides*, 16(4):647–652, 1995.
- [157] V. N. Uversky. Intrinsically disordered proteins and their environment: effects of strong denaturants, temperature, pH, counter ions, membranes, binding partners, osmolytes, and macromolecular crowding. *Protein J.*, 28(7-8):305–325, Oct 2009.
- [158] M. S. Cortese, V. N. Uversky, and A. K. Dunker. Intrinsic disorder in scaffold proteins: getting more from less. *Prog. Biophys. Mol. Biol.*, 98(1):85–106, Sep 2008.
- [159] H. J. Dyson and P. E. Wright. Role of Intrinsic Protein Disorder in the Function and Interactions of the Transcriptional Coactivators CREB-binding Protein (CBP) and p300. *J. Biol. Chem.*, 291(13):6714–6722, Mar 2016.
- [160] E. Z. Eisenmesser, D. A. Bosco, M. Akke, and D. Kern. Enzyme dynamics during catalysis. *Science*, 295(5559):1520–1523, Feb 2002.
- [161] I. Gelis, A. M. Bonvin, D. Keramisanou, M. Koukaki, G. Gouridis, S. Karamanou, A. Economou, and C. G. Kalodimos. Structural basis for signal-sequence recognition by the translocase motor SecA as determined by NMR. *Cell*, 131(4):756–769, Nov 2007.
- [162] W. F. Zeno, U. Baul, W. T. Snead, A. C. M. DeGroot, L. Wang, E. M. Lafer, D. Thirumalai, and J. C. Stachowiak. Synergy between intrinsically disordered domains and structured proteins amplifies membrane curvature sensing. *Nat Commun*, 9(1):4152, 10 2018.
- [163] N. Tokuriki and D. S. Tawfik. Protein dynamism and evolvability. *Science*, 324(5924):203–207, Apr 2009.
- [164] V. N. Uversky. Unreported intrinsic disorder in proteins: Building connections to the literature on IDPs. *Intrinsically Disord Proteins*, 2(1):e970499, 2014.

- [165] J. Rydberg, L. Baltzer, and V. Sarojini. Intrinsically unstructured proteins by design-electrostatic interactions can control binding, folding, and function of a helix-loop-helix heterodimer. *J. Pept. Sci.*, 19(8):461–469, Aug 2013.
- [166] A. K. Dunker, J. D. Lawson, C. J. Brown, R. M. Williams, P. Romero, J. S. Oh, C. J. Oldfield, A. M. Campen, C. M. Ratliff, K. W. Hipps, J. Ausio, M. S. Nissen, R. Reeves, C. Kang, C. R. Kissinger, R. W. Bailey, M. D. Griswold, W. Chiu, E. C. Garner, and Z. Obradovic. Intrinsically disordered protein. *J. Mol. Graph. Model.*, 19(1):26–59, 2001.
- [167] M. Arbesu, G. Iruela, H. Fuentes, J. M. C. Teixeira, and M. Pons. Intramolecular Fuzzy Interactions Involving Intrinsically Disordered Domains. *Front Mol Biosci*, 5:39, 2018.
- [168] S. Wu, D. Wang, J. Liu, Y. Feng, J. Weng, Y. Li, X. Gao, J. Liu, and W. Wang. The Dynamic Multisite Interactions between Two Intrinsically Disordered Proteins. *Angew. Chem. Int. Ed. Engl.*, 56(26):7515–7519, Jun 2017.
- [169] R. Sharma, Z. Raduly, M. Miskei, and M. Fuxreiter. Fuzzy complexes: Specific binding without complete folding. *FEBS Lett.*, 589(19 Pt A):2533–2542, Sep 2015.
- [170] A. Bah and J. D. Forman-Kay. Modulation of Intrinsically Disordered Protein Function by Post-translational Modifications. *J. Biol. Chem.*, 291(13):6696–6705, Mar 2016.
- [171] M. J. Lee and M. B. Yaffe. Protein Regulation in Signal Transduction. *Cold Spring Harb Perspect Biol*, 8(6), Jun 2016.
- [172] P. Tompa and M. Fuxreiter. Fuzzy complexes: polymorphism and structural disorder in protein-protein interactions. *Trends Biochem. Sci.*, 33(1):2–8, Jan 2008.
- [173] M. Fuxreiter and P. Tompa. Fuzzy complexes: a more stochastic view of protein function. *Adv. Exp. Med. Biol.*, 725:1–14, 2012.
- [174] N. D. Keul, K. Oruganty, E. T. Schaper Bergman, N. R. Beattie, W. E. McDonald, R. Kadirvelraj, M. L. Gross, R. S. Phillips, S. C. Harvey, and Z. A. Wood. The entropic force generated by intrinsically disordered segments tunes protein function. *Nature*, 563(7732):584–588, 11 2018.

- [175] D. E. Wetzler, F. Fuchs Wightman, H. A. Bucci, J. Rinaldi, J. J. Caramelo, N. D. Iusem, and M. M. Ricardi. Conformational plasticity of the intrinsically disordered protein ASR1 modulates its function as a drought stress-responsive gene. *PLoS ONE*, 13(8):e0202808, 2018.
- [176] M. K. Yoon, D. M. Mitrea, L. Ou, and R. W. Kriwacki. Cell cycle regulation by the intrinsically disordered proteins p21 and p27. *Biochem. Soc. Trans.*, 40(5):981–988, Oct 2012.
- [177] T. Mittag and J. D. Forman-Kay. Atomic-level characterization of disordered protein ensembles. *Curr. Opin. Struct. Biol.*, 17(1):3–14, Feb 2007.
- [178] M. A. Breidenbach and A. T. Brunger. Substrate recognition strategy for botulinum neurotoxin serotype A. *Nature*, 432(7019):925–929, Dec 2004.
- [179] J. Kuriyan and D. Eisenberg. The origin of protein interactions and allostery in colocalization. *Nature*, 450(7172):983–990, Dec 2007.
- [180] A. L. Darling and V. N. Uversky. Intrinsic Disorder and Posttranslational Modifications: The Darker Side of the Biological Dark Matter. *Front Genet*, 9:158, 2018.
- [181] R. J. O’Brien and P. C. Wong. Amyloid precursor protein processing and Alzheimer’s disease. *Annu. Rev. Neurosci.*, 34:185–204, 2011.
- [182] N. Ida, C. L. Masters, and K. Beyreuther. Rapid cellular uptake of Alzheimer amyloid betaA4 peptide by cultured human neuroblastoma cells. *FEBS Lett.*, 394(2):174–178, Sep 1996.
- [183] Y. Qi-Takahara, M. Morishima-Kawashima, Y. Tanimura, G. Dolios, N. Hirotsu, Y. Horikoshi, F. Kametani, M. Maeda, T. C. Saido, R. Wang, and Y. Ihara. Longer forms of amyloid beta protein: implications for the mechanism of intramembrane cleavage by gamma-secretase. *J. Neurosci.*, 25(2):436–445, Jan 2005.
- [184] A. E. Roher, Y. M. Kuo, C. Esh, C. Knebel, N. Weiss, W. Kalback, D. C. Luehrs, J. L. Childress, T. G. Beach, R. O. Weller, and T. A. Kokjohn. Cortical and leptomeningeal cerebrovascular amyloid and white matter pathology in Alzheimer’s disease. *Mol. Med.*, 9(3-4):112–122, 2003.

- [185] H. Welander, J. Franberg, C. Graff, E. Sundstrom, B. Winblad, and L. O. Tjernberg. Abeta43 is more frequent than Abeta40 in amyloid plaque cores from Alzheimer disease brains. *J. Neurochem.*, 110(2):697–706, Jul 2009.
- [186] S. G. Younkin. Evidence that A beta 42 is the real culprit in Alzheimer’s disease. *Ann. Neurol.*, 37(3):287–288, Mar 1995.
- [187] D. J. Selkoe. Translating cell biology into therapeutic advances in Alzheimer’s disease. *Nature*, 399(6738 Suppl):23–31, Jun 1999.
- [188] K. N. Dahlgren, A. M. Manelli, W. B. Stine, L. K. Baker, G. A. Krafft, and M. J. LaDu. Oligomeric and fibrillar species of amyloid-beta peptides differentially affect neuronal viability. *J. Biol. Chem.*, 277(35):32046–32053, Aug 2002.
- [189] J. Kim, L. Onstead, S. Randle, R. Price, L. Smithson, C. Zwizinski, D. W. Dickson, T. Golde, and E. McGowan. Abeta40 inhibits amyloid deposition in vivo. *J. Neurosci.*, 27(3):627–633, Jan 2007.
- [190] L. M. Yan, A. Velkova, M. Tatarek-Nossol, E. Andreetto, and A. Kapurniotu. IAPP mimic blocks Abeta cytotoxic self-assembly: cross-suppression of amyloid toxicity of Abeta and IAPP suggests a molecular link between Alzheimer’s disease and type II diabetes. *Angew. Chem. Int. Ed. Engl.*, 46(8):1246–1252, 2007.
- [191] K. H. Lim, H. H. Collver, Y. T. Le, P. Nagchowdhuri, and J. M. Kenney. Characterizations of distinct amyloidogenic conformations of the Abeta (1-40) and (1-42) peptides. *Biochem. Biophys. Res. Commun.*, 353(2):443–449, Feb 2007.
- [192] P. Lewczuk, N. Lelental, P. Spitzer, J. M. Maler, and J. Kornhuber. Amyloid-42/40 cerebrospinal fluid concentration ratio in the diagnostics of Alzheimer’s disease: validation of two novel assays. *J. Alzheimers Dis.*, 43(1):183–191, 2015.
- [193] G. Siegel, H. Gerber, P. Koch, O. Bruestle, P. C. Fraering, and L. Rajendran. The Alzheimer’s Disease -Secretase Generates Higher 42:40 Ratios for -Amyloid Than for p3 Peptides. *Cell Rep*, 19(10):1967–1976, 06 2017.
- [194] V. Rangachari, D. N. Dean, P. Rana, A. Vaidya, and P. Ghosh. Cause and consequence of A - Lipid interactions in Alzheimer disease pathogenesis. *Biochim Biophys Acta Biomembr*, 03 2018.

- [195] G. G. Glenner, C. W. Wong, V. Quaranta, and E. D. Eanes. The amyloid deposits in Alzheimer's disease: their nature and pathogenesis. *Appl Pathol*, 2(6):357–369, 1984.
- [196] L. Hou, H. Shao, Y. Zhang, H. Li, N. K. Menon, E. B. Neuhaus, J. M. Brewer, I. J. Byeon, D. G. Ray, M. P. Vitek, T. Iwashita, R. A. Makula, A. B. Przybyla, and M. G. Zagorski. Solution NMR studies of the A beta(1-40) and A beta(1-42) peptides establish that the Met35 oxidation state affects the mechanism of amyloid formation. *J. Am. Chem. Soc.*, 126(7):1992–2005, Feb 2004.
- [197] M. D. Kirkitadze, M. M. Condrón, and D. B. Teplow. Identification and characterization of key kinetic intermediates in amyloid beta-protein fibrillogenesis. *J. Mol. Biol.*, 312(5):1103–1119, Oct 2001.
- [198] D. J. Selkoe, M. B. Podlisny, C. L. Joachim, E. A. Vickers, G. Lee, L. C. Fritz, and T. Oltersdorf. Beta-amyloid precursor protein of Alzheimer disease occurs as 110- to 135-kilodalton membrane-associated proteins in neural and nonneural tissues. *Proc. Natl. Acad. Sci. U.S.A.*, 85(19):7341–7345, Oct 1988.
- [199] M. Shoji, T. E. Golde, J. Ghiso, T. T. Cheung, S. Estus, L. M. Shaffer, X. D. Cai, D. M. McKay, R. Tintner, and B. Frangione. Production of the Alzheimer amyloid beta protein by normal proteolytic processing. *Science*, 258(5079):126–129, Oct 1992.
- [200] B. De Strooper and W. Annaert. Proteolytic processing and cell biological functions of the amyloid precursor protein. *J. Cell. Sci.*, 113 (Pt 11):1857–1870, Jun 2000.
- [201] H. S. Hoe, Z. Fu, A. Makarova, J. Y. Lee, C. Lu, L. Feng, A. Pajoohesh-Ganji, Y. Matsuoka, B. T. Hyman, M. D. Ehlers, S. Vicini, D. T. Pak, and G. W. Rebeck. The effects of amyloid precursor protein on postsynaptic composition and activity. *J. Biol. Chem.*, 284(13):8495–8506, Mar 2009.
- [202] Z. Wang, B. Wang, L. Yang, Q. Guo, N. Aithmitti, Z. Songyang, and H. Zheng. Presynaptic and postsynaptic interaction of the amyloid precursor protein promotes peripheral and central synaptogenesis. *J. Neurosci.*, 29(35):10788–10801, Sep 2009.

- [203] E. Montagna, M. M. Dorostkar, and J. Herms. The Role of APP in Structural Spine Plasticity. *Front Mol Neurosci*, 10:136, 2017.
- [204] O. Coskuner-Weber and V. N. Uversky. Insights into the Molecular Mechanisms of Alzheimer's and Parkinson's Diseases with Molecular Simulations: Understanding the Roles of Artificial and Pathological Missense Mutations in Intrinsically Disordered Proteins Related to Pathology. *Int J Mol Sci*, 19(2), Jan 2018.
- [205] M. P. Mattson. Pathways towards and away from Alzheimer's disease. *Nature*, 430(7000):631–639, Aug 2004.
- [206] T. Matsui, M. Ingelsson, H. Fukumoto, K. Ramasamy, H. Kowa, M. P. Frosch, M. C. Irizarry, and B. T. Hyman. Expression of APP pathway mRNAs and proteins in Alzheimer's disease. *Brain Res.*, 1161:116–123, Aug 2007.
- [207] C. Priller, T. Bauer, G. Mitteregger, B. Krebs, H. A. Kretzschmar, and J. Herms. Synapse formation and function is modulated by the amyloid precursor protein. *J. Neurosci.*, 26(27):7212–7221, Jul 2006.
- [208] R. J. Andrew, K. A. Kellett, G. Thinakaran, and N. M. Hooper. A Greek Tragedy: The Growing Complexity of Alzheimer Amyloid Precursor Protein Proteolysis. *J. Biol. Chem.*, 291(37):19235–19244, 09 2016.
- [209] S. Chasseigneaux and B. Allinquant. Functions of A, sAPP and sAPP : similarities and differences. *J. Neurochem.*, 120 Suppl 1:99–108, Jan 2012.
- [210] P. F. Copenhaver and D. Kogel. Role of APP Interactions with Heterotrimeric G Proteins: Physiological Functions and Pathological Consequences. *Front Mol Neurosci*, 10:3, 2017.
- [211] C. Haass, C. Kaether, G. Thinakaran, and S. Sisodia. Trafficking and proteolytic processing of APP. *Cold Spring Harb Perspect Med*, 2(5):a006270, May 2012.
- [212] V. W. Chow, M. P. Mattson, P. C. Wong, and M. Gleichmann. An overview of APP processing enzymes and products. *Neuromolecular Med.*, 12(1):1–12, Mar 2010.
- [213] O. Wise-Scira, L. Xu, T. Kitahara, G. Perry, and O. Coskuner. Amyloid- peptide structure in aqueous solution varies with fragment size. *J Chem Phys*, 135(20): 205101, Nov 2011.

- [214] A. Vandersteen, E. Hubin, R. Sarroukh, G. De Baets, J. Schymkowitz, F. Rousseau, V. Subramaniam, V. Raussens, H. Wenschuh, D. Wildemann, and K. Broersen. A comparative analysis of the aggregation behavior of amyloid-peptide variants. *FEBS Lett.*, 586(23):4088–4093, Nov 2012.
- [215] C. Bleiholder and M. T. Bowers. The Solution Assembly of Biological Molecules Using Ion Mobility Methods: From Amino Acids to Amyloid -Protein. *Annu Rev Anal Chem (Palo Alto Calif)*, 10(1):365–386, 06 2017.
- [216] M. F. M. Sciacca, C. Tempra, F. Scollo, D. Milardi, and C. La Rosa. Amyloid growth and membrane damage: Current themes and emerging perspectives from theory and experiments on A and hIAPP. *Biochim Biophys Acta Biomembr*, Mar 2018.
- [217] E. M. Mandelkow and E. Mandelkow. Tau in Alzheimer’s disease. *Trends Cell Biol.*, 8(11):425–427, Nov 1998.
- [218] I. Grundke-Iqbal, K. Iqbal, Y. C. Tung, M. Quinlan, H. M. Wisniewski, and L. I. Binder. Abnormal phosphorylation of the microtubule-associated protein tau (tau) in Alzheimer cytoskeletal pathology. *Proc. Natl. Acad. Sci. U.S.A.*, 83(13):4913–4917, Jul 1986.
- [219] C. L. Masters, G. Simms, N. A. Weinman, G. Multhaup, B. L. McDonald, and K. Beyreuther. Amyloid plaque core protein in Alzheimer disease and Down syndrome. *Proc. Natl. Acad. Sci. U.S.A.*, 82(12):4245–4249, Jun 1985.
- [220] N. Wijesekara, R. Ahrens, M. Sabale, L. Wu, K. Ha, G. Verdile, and P. E. Fraser. Amyloid- and islet amyloid pathologies link Alzheimer’s disease and type 2 diabetes in a transgenic model. *FASEB J.*, 31(12):5409–5418, 12 2017.
- [221] I. Chapman, B. Parker, S. Doran, C. Feinle-Bisset, J. Wishart, C. W. Lush, K. Chen, C. Lacerte, C. Burns, R. McKay, C. Weyer, and M. Horowitz. Low-dose pramlintide reduced food intake and meal duration in healthy, normal-weight subjects. *Obesity (Silver Spring)*, 15(5):1179–1186, May 2007.
- [222] G. Christopoulos, G. Paxinos, X. F. Huang, K. Beaumont, A. W. Toga, and P. M. Sexton. Comparative distribution of receptors for amylin and the related peptides calcitonin gene related peptide and calcitonin in rat and monkey brain. *Can. J. Physiol. Pharmacol.*, 73(7):1037–1041, Jul 1995.

- [223] P. J. Wookey, T. A. Lutz, and S. Andrikopoulos. Amylin in the periphery II: An updated mini-review. *ScientificWorldJournal*, 6:1642–1655, Dec 2006.
- [224] B. R. Gedulin, C. M. Jodka, K. Herrmann, and A. A. Young. Role of endogenous amylin in glucagon secretion and gastric emptying in rats demonstrated with the selective antagonist, AC187. *Regul. Pept.*, 137(3):121–127, Dec 2006.
- [225] M. Samsom, L. A. Szarka, M. Camilleri, A. Vella, A. R. Zinsmeister, and R. A. Rizza. Pramlintide, an amylin analog, selectively delays gastric emptying: potential role of vagal inhibition. *Am. J. Physiol. Gastrointest. Liver Physiol.*, 278(6):G946–951, Jun 2000.
- [226] A. Vella, J. S. Lee, M. Camilleri, L. A. Szarka, D. D. Burton, A. R. Zinsmeister, R. A. Rizza, and P. D. Klein. Effects of pramlintide, an amylin analogue, on gastric emptying in type 1 and 2 diabetes mellitus. *Neurogastroenterol. Motil.*, 14(2):123–131, Apr 2002.
- [227] A. Young. Inhibition of gastric emptying. *Adv. Pharmacol.*, 52:99–121, 2005.
- [228] D. F. Kruger, C. L. Martin, and C. E. Sadler. New insights into glucose regulation. *Diabetes Educ*, 32(2):221–228, 2006.
- [229] P. Westermark, A. Andersson, and G. T. Westermark. Islet amyloid polypeptide, islet amyloid, and diabetes mellitus. *Physiol. Rev.*, 91(3):795–826, Jul 2011.
- [230] S. Gebre-Medhin, H. Mulder, M. Pekny, G. Westermark, J. Tornell, P. Westermark, F. Sundler, B. Ahren, and C. Betsholtz. Increased insulin secretion and glucose tolerance in mice lacking islet amyloid polypeptide (amylin). *Biochem. Biophys. Res. Commun.*, 250(2):271–277, Sep 1998.
- [231] S. J. Wimalawansa. Amylin, calcitonin gene-related peptide, calcitonin, and adrenomedullin: a peptide superfamily. *Crit Rev Neurobiol*, 11(2-3):167–239, 1997.
- [232] E. T. Jaikaran, M. R. Nilsson, and A. Clark. Pancreatic beta-cell granule peptides form heteromolecular complexes which inhibit islet amyloid polypeptide fibril formation. *Biochem. J.*, 377(Pt 3):709–716, Feb 2004.
- [233] P. Rorsman and E. Renstrom. Insulin granule dynamics in pancreatic beta cells. *Diabetologia*, 46(8):1029–1045, Aug 2003.

- [234] A. C. Susa, C. Wu, S. L. Bernstein, N. F. Dupuis, H. Wang, D. P. Raleigh, J. E. Shea, and M. T. Bowers. Defining the molecular basis of amyloid inhibitors: human islet amyloid polypeptide-insulin interactions. *J. Am. Chem. Soc.*, 136(37):12912–12919, Sep 2014.
- [235] P. Westermark, Z. C. Li, G. T. Westermark, A. Leckstrom, and D. F. Steiner. Effects of beta cell granule components on human islet amyloid polypeptide fibril formation. *FEBS Lett.*, 379(3):203–206, Feb 1996.
- [236] Y. C. Kudva, C. Mueske, P. C. Butler, and N. L. Eberhardt. A novel assay in vitro of human islet amyloid polypeptide amyloidogenesis and effects of insulin secretory vesicle peptides on amyloid formation. *Biochem. J.*, 331 (Pt 3):809–813, May 1998.
- [237] B. R. Ott. Cognition and behavior in patients with Alzheimer’s disease. *J Genet Specif Med*, 2(3):63–69, 1999.
- [238] Yun Zhang and Weihong Song. Islet amyloid polypeptide: Another key molecule in alzheimers pathogenesis? *Progress in Neurobiology*, 153:100 – 120, 2017. ISSN 0301-0082.
- [239] J. A. Luchsinger, A. Pablos-Mendez, C. Knirsch, D. Rabinowitz, and S. Shea. Antibiotic use and risk of ischemic stroke in the elderly. *Am. J. Med.*, 111(5):361–366, Oct 2001.
- [240] A. Ott, R. P. Stolk, A. Hofman, F. van Harskamp, D. E. Grobbee, and M. M. Breteler. Association of diabetes mellitus and dementia: the Rotterdam Study. *Diabetologia*, 39(11):1392–1397, Nov 1996.
- [241] R. Peila, B. L. Rodriguez, and L. J. Launer. Type 2 diabetes, APOE gene, and the risk for dementia and related pathologies: The Honolulu-Asia Aging Study. *Diabetes*, 51(4):1256–1262, Apr 2002.
- [242] P. Bharadwaj, N. Wijesekara, M. Liyanapathirana, P. Newsholme, L. Ittner, P. Fraser, and G. Verdile. The Link between Type 2 Diabetes and Neurodegeneration: Roles for Amyloid-, Amylin, and Tau Proteins. *J. Alzheimers Dis.*, 59(2):421–432, 2017.

- [243] Y. Yang and W. Song. Molecular links between Alzheimer's disease and diabetes mellitus. *Neuroscience*, 250:140–150, Oct 2013.
- [244] Z. Arvanitakis, R. S. Wilson, J. L. Bienias, D. A. Evans, and D. A. Bennett. Diabetes mellitus and risk of Alzheimer disease and decline in cognitive function. *Arch. Neurol.*, 61(5):661–666, May 2004.
- [245] G. J. Biessels, A. Kamal, I. J. Urban, B. M. Spruijt, D. W. Erkelens, and W. H. Gispen. Water maze learning and hippocampal synaptic plasticity in streptozotocin-diabetic rats: effects of insulin treatment. *Brain Res.*, 800(1):125–135, Jul 1998.
- [246] E. Planel, Y. Tatebayashi, T. Miyasaka, L. Liu, L. Wang, M. Herman, W. H. Yu, J. A. Luchsinger, B. Wadzinski, K. E. Duff, and A. Takashima. Insulin dysfunction induces in vivo tau hyperphosphorylation through distinct mechanisms. *J. Neurosci.*, 27(50):13635–13648, Dec 2007.
- [247] W. Xia, S. Wang, Z. Sun, F. Bai, Y. Zhou, Y. Yang, P. Wang, Y. Huang, and Y. Yuan. Altered baseline brain activity in type 2 diabetes: a resting-state fMRI study. *Psychoneuroendocrinology*, 38(11):2493–2501, Nov 2013.
- [248] H. Zhou, W. Lu, Y. Shi, F. Bai, J. Chang, Y. Yuan, G. Teng, and Z. Zhang. Impairments in cognition and resting-state connectivity of the hippocampus in elderly subjects with type 2 diabetes. *Neurosci. Lett.*, 473(1):5–10, Mar 2010.
- [249] G. Verdile, K. N. Keane, V. F. Cruzat, S. Medic, M. Sabale, J. Rowles, N. Wijesekara, R. N. Martins, P. E. Fraser, and P. Newsholme. Inflammation and Oxidative Stress: The Molecular Connectivity between Insulin Resistance, Obesity, and Alzheimer's Disease. *Mediators Inflamm.*, 2015:105828, 2015.
- [250] M. Vandal, P. J. White, G. Chevrier, C. Tremblay, I. St-Amour, E. Planel, A. Marette, and F. Calon. Age-dependent impairment of glucose tolerance in the 3xTg-AD mouse model of Alzheimer's disease. *FASEB J.*, 29(10):4273–4284, Oct 2015.
- [251] M. Jimenez-Palomares, J. J. Ramos-Rodriguez, J. F. Lopez-Acosta, M. Pacheco-Herrero, A. M. Lechuga-Sancho, G. Perdomo, M. Garcia-Alloza, and I. Cozar-Castellano. Increased A production prompts the onset of glucose intolerance and insulin resistance. *Am. J. Physiol. Endocrinol. Metab.*, 302(11):E1373–1380, Jun 2012.

- [252] J. R. Clarke, N. M. Lyra E Silva, C. P. Figueiredo, R. L. Frozza, J. H. Ledo, D. Beckman, C. K. Katashima, D. Razolli, B. M. Carvalho, R. Frazao, M. A. Silveira, F. C. Ribeiro, T. R. Bomfim, F. S. Neves, W. L. Klein, R. Medeiros, F. M. LaFerla, J. B. Carvalheira, M. J. Saad, D. P. Munoz, L. A. Velloso, S. T. Ferreira, and F. G. De Felice. Alzheimer-associated A oligomers impact the central nervous system to induce peripheral metabolic deregulation. *EMBO Mol Med*, 7(2):190–210, Feb 2015.
- [253] Y. Zhang, B. Zhou, B. Deng, F. Zhang, J. Wu, Y. Wang, Y. Le, and Q. Zhai. Amyloid- induces hepatic insulin resistance in vivo via JAK2. *Diabetes*, 62(4):1159–1166, Apr 2013.
- [254] J. M. Walker and F. E. Harrison. Shared Neuropathological Characteristics of Obesity, Type 2 Diabetes and Alzheimer’s Disease: Impacts on Cognitive Decline. *Nutrients*, 7(9):7332–7357, Sep 2015.
- [255] B. L. Adler, M. Yarchoan, H. M. Hwang, N. Louneva, J. A. Blair, R. Palm, M. A. Smith, H. G. Lee, S. E. Arnold, and G. Casadesus. Neuroprotective effects of the amylin analogue pramlintide on Alzheimer’s disease pathogenesis and cognition. *Neurobiol. Aging*, 35(4):793–801, Apr 2014.
- [256] W. Q. Qiu and H. Zhu. Amylin and its analogs: a friend or foe for the treatment of Alzheimer’s disease? *Front Aging Neurosci*, 6:186, 2014.
- [257] P. Krotee, J. A. Rodriguez, M. R. Sawaya, D. Cascio, F. E. Reyes, D. Shi, J. Hattne, B. L. Nannenga, M. E. Oskarsson, S. Philipp, S. Griner, L. Jiang, C. G. Glabe, G. T. Westermark, T. Gonen, and D. S. Eisenberg. Atomic structures of fibrillar segments of hIAPP suggest tightly mated β -sheets are important for cytotoxicity. *Elife*, 6, 01 2017.
- [258] M. E. Oskarsson, J. F. Paulsson, S. W. Schultz, M. Ingelsson, P. Westermark, and G. T. Westermark. In vivo seeding and cross-seeding of localized amyloidosis: a molecular link between type 2 diabetes and Alzheimer disease. *Am. J. Pathol.*, 185(3):834–846, Mar 2015.
- [259] K. Jackson, G. A. Barisone, E. Diaz, L. W. Jin, C. DeCarli, and F. Despa. Amylin deposition in the brain: A second amyloid in Alzheimer disease? *Ann. Neurol.*, 74(4):517–526, Oct 2013.

- [260] I. Moreno-Gonzalez, G. Edwards Iii, N. Salvadores, M. Shah Nawaz, R. Diaz-Espinoza, and C. Soto. Molecular interaction between type 2 diabetes and Alzheimer's disease through cross-seeding of protein misfolding. *Mol. Psychiatry*, 22(9):1327–1334, 09 2017.
- [261] B. O'Nuallain, A. D. Williams, P. Westermark, and R. Wetzel. Seeding specificity in amyloid growth induced by heterologous fibrils. *J. Biol. Chem.*, 279(17):17490–17499, Apr 2004.
- [262] E. Andreetto, L. M. Yan, M. Tatarek-Nossol, A. Velkova, R. Frank, and A. Kapurniotu. Identification of hot regions of the Abeta-IAPP interaction interface as high-affinity binding sites in both cross- and self-association. *Angew. Chem. Int. Ed. Engl.*, 49(17):3081–3085, Apr 2010.
- [263] A. Kapurniotu. Amyloidogenicity and cytotoxicity of islet amyloid polypeptide. *Biopolymers*, 60(6):438–459, 2001.
- [264] S. Srodulski, S. Sharma, A. B. Bachstetter, J. M. Brelsfoard, C. Pascual, X. S. Xie, K. E. Saatman, L. J. Van Eldik, and F. Despa. Neuroinflammation and neurologic deficits in diabetes linked to brain accumulation of amylin. *Mol Neurodegener*, 9:30, Aug 2014.
- [265] W. A. Banks, A. J. Kastin, L. M. Maness, W. Huang, and J. B. Jaspan. Permeability of the blood-brain barrier to amylin. *Life Sci.*, 57(22):1993–2001, 1995.
- [266] G. V. Chaitanya, W. E. Cromer, S. R. Wells, M. H. Jennings, P. O. Couraud, I. A. Romero, B. Weksler, A. Erdreich-Epstein, J. M. Mathis, A. Minagar, and J. S. Alexander. Gliovascular and cytokine interactions modulate brain endothelial barrier in vitro. *J Neuroinflammation*, 8:162, Nov 2011.
- [267] M. A. Chishti, D. S. Yang, C. Janus, A. L. Phinney, P. Horne, J. Pearson, R. Strome, N. Zuker, J. Loukides, J. French, S. Turner, G. Lozza, M. Grilli, S. Kunicki, C. Morissette, J. Paquette, F. Gervais, C. Bergeron, P. E. Fraser, G. A. Carlson, P. S. George-Hyslop, and D. Westaway. Early-onset amyloid deposition and cognitive deficits in transgenic mice expressing a double mutant form of amyloid precursor protein 695. *J. Biol. Chem.*, 276(24):21562–21570, Jun 2001.
- [268] J. Janson, W. C. Soeller, P. C. Roche, R. T. Nelson, A. J. Torchia, D. K. Kreutter, and P. C. Butler. Spontaneous diabetes mellitus in transgenic mice expressing

- human islet amyloid polypeptide. *Proc. Natl. Acad. Sci. U.S.A.*, 93(14):7283–7288, Jul 1996.
- [269] K. Akter, E. A. Lanza, S. A. Martin, N. Myronyuk, M. Rua, and R. B. Raffa. Diabetes mellitus and Alzheimer’s disease: shared pathology and treatment? *Br J Clin Pharmacol*, 71(3):365–376, Mar 2011.
- [270] P. E. Fraser, L. K. Duffy, M. B. O’Malley, J. Nguyen, H. Inouye, and D. A. Kirschner. Morphology and antibody recognition of synthetic beta-amyloid peptides. *J. Neurosci. Res.*, 28(4):474–485, Apr 1991.
- [271] L. O. Tjernberg, A. Pramanik, S. Bjorling, P. Thyberg, J. Thyberg, C. Nordstedt, K. D. Berndt, L. Terenius, and R. Rigler. Amyloid beta-peptide polymerization studied using fluorescence correlation spectroscopy. *Chem. Biol.*, 6(1):53–62, Jan 1999.
- [272] P. D. Gorevic, E. M. Castano, R. Sarma, and B. Frangione. Ten to fourteen residue peptides of Alzheimer’s disease protein are sufficient for amyloid fibril formation and its characteristic x-ray diffraction pattern. *Biochem. Biophys. Res. Commun.*, 147(2):854–862, Sep 1987.
- [273] G. W. Preston, S. E. Radford, A. E. Ashcroft, and A. J. Wilson. Covalent cross-linking within supramolecular peptide structures. *Anal. Chem.*, 84(15):6790–6797, Aug 2012.
- [274] K. Tao, J. Wang, P. Zhou, C. Wang, H. Xu, X. Zhao, and J. R. Lu. Self-assembly of short a(16-22) peptides: effect of terminal capping and the role of electrostatic interaction. *Langmuir*, 27(6):2723–2730, Mar 2011.
- [275] J. Zhao, X. Yu, G. Liang, and J. Zheng. Structural polymorphism of human islet amyloid polypeptide (hIAPP) oligomers highlights the importance of interfacial residue interactions. *Biomacromolecules*, 12(1):210–220, Jan 2011.
- [276] J. A. Williamson, J. P. Loria, and A. D. Miranker. Helix stabilization precedes aqueous and bilayer-catalyzed fiber formation in islet amyloid polypeptide. *J. Mol. Biol.*, 393(2):383–396, Oct 2009.
- [277] K. Tenidis, M. Waldner, J. Bernhagen, W. Fischle, M. Bergmann, M. Weber, M. L. Merkle, W. Voelter, H. Brunner, and A. Kapurniotu. Identification of a

- penta- and hexapeptide of islet amyloid polypeptide (IAPP) with amyloidogenic and cytotoxic properties. *J. Mol. Biol.*, 295(4):1055–1071, Jan 2000.
- [278] A. Baumketner and J. E. Shea. Free energy landscapes for amyloidogenic tetrapeptides dimerization. *Biophys. J.*, 89(3):1493–1503, Sep 2005.
- [279] F. Massi, J. W. Peng, J. P. Lee, and J. E. Straub. Simulation study of the structure and dynamics of the Alzheimer’s amyloid peptide congener in solution. *Biophys. J.*, 80(1):31–44, Jan 2001.
- [280] J. P. Lee, E. R. Stimson, J. R. Ghilardi, P. W. Mantyh, Y. A. Lu, A. M. Felix, W. Llanos, A. Behbin, M. Cummings, and M. Van Crielinge. ¹H NMR of A beta amyloid peptide congeners in water solution. Conformational changes correlate with plaque competence. *Biochemistry*, 34(15):5191–5200, Apr 1995.
- [281] J. Danielsson, A. Andersson, J. Jarvet, and A. Graslund. ¹⁵N relaxation study of the amyloid beta-peptide: structural propensities and persistence length. *Magn Reson Chem*, 44 Spec No:S114–121, Jul 2006.
- [282] S. Zhang, K. Iwata, M. J. Lachenmann, J. W. Peng, S. Li, E. R. Stimson, Y. Lu, A. M. Felix, J. E. Maggio, and J. P. Lee. The Alzheimer’s peptide a beta adopts a collapsed coil structure in water. *J. Struct. Biol.*, 130(2-3):130–141, Jun 2000.
- [283] N. D. Lazo, M. A. Grant, M. C. Condrón, A. C. Rigby, and D. B. Teplow. On the nucleation of amyloid beta-protein monomer folding. *Protein Sci.*, 14(6):1581–1596, Jun 2005.
- [284] R. Riek, P. Guntert, H. Dobeli, B. Wipf, and K. Wuthrich. NMR studies in aqueous solution fail to identify significant conformational differences between the monomeric forms of two Alzheimer peptides with widely different plaque-competence, A beta(1-40)(ox) and A beta(1-42)(ox). *Eur. J. Biochem.*, 268(22): 5930–5936, Nov 2001.
- [285] S. G. Itoh, M. Yagi-Utsumi, K. Kato, and H. Okumura. Effects of a Hydrophilic/Hydrophobic Interface on Amyloid- Peptides Studied by Molecular Dynamics Simulations and NMR Experiments. *J Phys Chem B*, Dec 2018.
- [286] S. L. Bernstein, T. Wyttenbach, A. Baumketner, J. E. Shea, G. Bitan, D. B. Teplow, and M. T. Bowers. Amyloid beta-protein: monomer structure and early

- aggregation states of Abeta42 and its Pro19 alloform. *J. Am. Chem. Soc.*, 127(7): 2075–2084, Feb 2005.
- [287] D. M. Walsh, D. M. Hartley, Y. Kusumoto, Y. Fezoui, M. M. Condron, A. Lomakin, G. B. Benedek, D. J. Selkoe, and D. B. Teplow. Amyloid beta-protein fibrillogenesis. Structure and biological activity of protofibrillar intermediates. *J. Biol. Chem.*, 274(36):25945–25952, Sep 1999.
- [288] T. H. Huang, D. S. Yang, N. P. Plaskos, S. Go, C. M. Yip, P. E. Fraser, and A. Chakrabartty. Structural studies of soluble oligomers of the Alzheimer beta-amyloid peptide. *J. Mol. Biol.*, 297(1):73–87, Mar 2000.
- [289] G. Bitan, E. A. Fradinger, S. M. Spring, and D. B. Teplow. Neurotoxic protein oligomers—what you see is not always what you get. *Amyloid*, 12(2):88–95, Jun 2005.
- [290] D. Granata, C. Camilloni, M. Vendruscolo, and A. Laio. Characterization of the free-energy landscapes of proteins by NMR-guided metadynamics. *Proc. Natl. Acad. Sci. U.S.A.*, 110(17):6817–6822, Apr 2013.
- [291] J. Tan, J. Zhang, Y. Luo, and S. Ye. Misfolding of Human Islet Amyloid Polypeptide at Lipid Membrane Populates through β -Sheet Conformers without Involving β -Helical Intermediates. *J. Am. Chem. Soc.*, Jan 2019.
- [292] C. P. B. Yiu and Y. W. Chen. From Disorder to Mis-Order: Structural Aspects of Pathogenic Oligomerization in Conformational Diseases. *Protein Pept. Lett.*, 24(4):307–314, 2017.
- [293] T. S. Choi, J. Y. Han, C. E. Heo, S. W. Lee, and H. I. Kim. Electrostatic and hydrophobic interactions of lipid-associated β -synuclein: The role of a water-limited interfaces in amyloid fibrillation. *Biochim Biophys Acta Biomembr*, Feb 2018.
- [294] B. N. Ratha, R. K. Kar, S. Kalita, S. Kalita, S. Raha, A. Singha, K. Garai, B. Mandal, and A. Bhunia. Sequence specificity of amylin-insulin interaction: a fragment-based insulin fibrillation inhibition study. *Biochim Biophys Acta Proteins Proteom*, 1867(4):405–415, Jan 2019.
- [295] M. K. Siddiqi, P. Alam, T. Iqbal, N. Majid, S. Malik, S. Nusrat, A. Alam, M. R. Ajmal, V. N. Uversky, and R. H. Khan. Elucidating the Inhibitory Potential of

- Designed Peptides Against Amyloid Fibrillation and Amyloid Associated Cytotoxicity. *Front Chem*, 6:311, 2018.
- [296] A. Paul, S. Kalita, S. Kalita, P. Sukumar, and B. Mandal. Disaggregation of Amylin Aggregate by Novel Conformationally Restricted Aminobenzoic Acid containing / and / Hybrid Peptidomimetics. *Sci Rep*, 7:40095, 01 2017.
- [297] M. Leri, F. Bemporad, R. Oropesa-Nunez, C. Canale, M. Calamai, D. Nosi, M. Ramazzotti, S. Giorgetti, F. S. Pavone, V. Bellotti, M. Stefani, and M. Bucciantini. Molecular insights into cell toxicity of a novel familial amyloidogenic variant of 2-microglobulin. *J. Cell. Mol. Med.*, 20(8):1443–1456, 08 2016.
- [298] C. L. Pashley, E. W. Hewitt, and S. E. Radford. Comparison of the aggregation of homologous 2-microglobulin variants reveals protein solubility as a key determinant of amyloid formation. *J. Mol. Biol.*, 428(3):631–643, Feb 2016.
- [299] S. Edelman, H. Maier, and K. Wilhelm. Pramlintide in the treatment of diabetes mellitus. *BioDrugs*, 22(6):375–386, 2008.
- [300] A. Abedini and D. P. Raleigh. The role of His-18 in amyloid formation by human islet amyloid polypeptide. *Biochemistry*, 44(49):16284–16291, Dec 2005.
- [301] D. M. Vadukul, O. Gbajumo, K. E. Marshall, and L. C. Serpell. Amyloidogenicity and toxicity of the reverse and scrambled variants of amyloid- 1-42. *FEBS Lett.*, 591(5):822–830, 03 2017.
- [302] R. Cuchillo and J. Michel. Mechanisms of small-molecule binding to intrinsically disordered proteins. *Biochem. Soc. Trans.*, 40(5):1004–1008, Oct 2012.
- [303] J. Michel and R. Cuchillo. The impact of small molecule binding on the energy landscape of the intrinsically disordered protein C-myc. *PLoS ONE*, 7(7):e41070, 2012.
- [304] M. K. Siddiqi, P. Alam, S. Malik, N. Majid, S. K. Chaturvedi, S. Rajan, M. R. Ajmal, M. V. Khan, V. N. Uversky, and R. H. Khan. Stabilizing proteins to prevent conformational changes required for amyloid fibril formation. *J. Cell. Biochem.*, Sep 2018.

- [305] K. Ono, K. Hasegawa, H. Naiki, and M. Yamada. Anti-amyloidogenic activity of tannic acid and its activity to destabilize Alzheimer's beta-amyloid fibrils in vitro. *Biochim. Biophys. Acta*, 1690(3):193–202, Nov 2004.
- [306] J. Bieschke, J. Russ, R. P. Friedrich, D. E. Ehrnhoefer, H. Wobst, K. Neugebauer, and E. E. Wanker. EGCG remodels mature alpha-synuclein and amyloid-beta fibrils and reduces cellular toxicity. *Proc. Natl. Acad. Sci. U.S.A.*, 107(17):7710–7715, Apr 2010.
- [307] Q. Nie, X. G. Du, and M. Y. Geng. Small molecule inhibitors of amyloid peptide aggregation as a potential therapeutic strategy for Alzheimer's disease. *Acta Pharmacol. Sin.*, 32(5):545–551, May 2011.
- [308] M. Convertino, R. Pellarin, M. Catto, A. Carotti, and A. Caffisch. 9,10-Anthraquinone hinders beta-aggregation: how does a small molecule interfere with Abeta-peptide amyloid fibrillation? *Protein Sci.*, 18(4):792–800, Apr 2009.
- [309] P. Bermejo-Bescos, S. Martin-Aragon, K. L. Jimenez-Aliaga, A. Ortega, M. T. Molina, E. Buxaderas, G. Orellana, and A. G. Csak. In vitro anti-amyloidogenic properties of 1,4-naphthoquinones. *Biochem. Biophys. Res. Commun.*, 400(1):169–174, Sep 2010.
- [310] Y. Liu, B. Jovcevski, and T. L. Pukala. C-Phycocyanin from *Spirulina* Inhibits -Synuclein and Amyloid- Fibril Formation but Not Amorphous Aggregation. *J. Nat. Prod.*, 82(1):66–73, Jan 2019.
- [311] A. Orte, R. Clarke, and D. Klenerman. Single-molecule two-colour coincidence detection to probe biomolecular associations. *Biochem. Soc. Trans.*, 38(4):914–918, Aug 2010.
- [312] N. Cremades, S. I. Cohen, E. Deas, A. Y. Abramov, A. Y. Chen, A. Orte, M. Sandal, R. W. Clarke, P. Dunne, F. A. Aprile, C. W. Bertocini, N. W. Wood, T. P. Knowles, C. M. Dobson, and D. Klenerman. Direct observation of the interconversion of normal and toxic forms of -synuclein. *Cell*, 149(5):1048–1059, May 2012.
- [313] A. Orte, R. W. Clarke, and D. Klenerman. Single-molecule fluorescence coincidence spectroscopy and its application to resonance energy transfer. *Chemphyschem*, 12(3):491–499, Feb 2011.

- [314] W. S. Gosal, S. L. Myers, S. E. Radford, and N. H. Thomson. Amyloid under the atomic force microscope. *Protein Pept. Lett.*, 13(3):261–270, 2006.
- [315] Z. Lv, R. Roychaudhuri, M. M. Condrón, D. B. Teplow, and Y. L. Lyubchenko. Mechanism of amyloid -protein dimerization determined using single-molecule AFM force spectroscopy. *Sci Rep*, 3:2880, Oct 2013.
- [316] L. M. Young, P. Cao, D. P. Raleigh, A. E. Ashcroft, and S. E. Radford. Ion mobility spectrometry-mass spectrometry defines the oligomeric intermediates in amylin amyloid formation and the mode of action of inhibitors. *J. Am. Chem. Soc.*, 136(2):660–670, Jan 2014.
- [317] E. De Genst, A. Messer, and C. M. Dobson. Antibodies and protein misfolding: From structural research tools to therapeutic strategies. *Biochim. Biophys. Acta*, 1844(11):1907–1919, Nov 2014.
- [318] T. Tomiyama, S. Asano, Y. Suwa, T. Morita, K. Kataoka, H. Mori, and N. Endo. Rifampicin prevents the aggregation and neurotoxicity of amyloid beta protein in vitro. *Biochem. Biophys. Res. Commun.*, 204(1):76–83, Oct 1994.
- [319] H. A. Lashuel, D. M. Hartley, D. Balakhaneh, A. Aggarwal, S. Teichberg, and D. J. Callaway. New class of inhibitors of amyloid-beta fibril formation. Implications for the mechanism of pathogenesis in Alzheimer’s disease. *J. Biol. Chem.*, 277(45):42881–42890, Nov 2002.
- [320] V. I. Stsiapura, A. A. Maskevich, V. A. Kuzmitsky, V. N. Uversky, I. M. Kuznetsova, and K. K. Turoverov. Thioflavin T as a molecular rotor: fluorescent properties of thioflavin T in solvents with different viscosity. *J Phys Chem B*, 112(49):15893–15902, Dec 2008.
- [321] M. Biancalana, K. Makabe, A. Koide, and S. Koide. Molecular mechanism of thioflavin-T binding to the surface of beta-rich peptide self-assemblies. *J. Mol. Biol.*, 385(4):1052–1063, Jan 2009.
- [322] M. Groenning. Binding mode of Thioflavin T and other molecular probes in the context of amyloid fibrils-current status. *J Chem Biol*, 3(1):1–18, Mar 2010.

- [323] K. Gade Malmos, L. M. Blancas-Mejia, B. Weber, J. Buchner, M. Ramirez-Alvarado, H. Naiki, and D. Otzen. ThT 101: a primer on the use of thioflavin T to investigate amyloid formation. *Amyloid*, 24(1):1–16, Mar 2017.
- [324] P. K. Singh, A. K. Mora, and S. Nath. Ultrafast fluorescence spectroscopy reveals a dominant weakly-emissive population of fibril bound thioflavin-T. *Chem. Commun. (Camb.)*, 51(74):14042–14045, Sep 2015.
- [325] V. I. Stsiapura, A. A. Maskevich, V. A. Kuzmitsky, K. K. Turoverov, and I. M. Kuznetsova. Computational study of thioflavin T torsional relaxation in the excited state. *J Phys Chem A*, 111(22):4829–4835, Jun 2007.
- [326] L. S. Wolfe, M. F. Calabrese, A. Nath, D. V. Blaho, A. D. Miranker, and Y. Xiong. Protein-induced photophysical changes to the amyloid indicator dye thioflavin T. *Proc. Natl. Acad. Sci. U.S.A.*, 107(39):16863–16868, Sep 2010.
- [327] F. Meng, P. Marek, K. J. Potter, C. B. Verchere, and D. P. Raleigh. Rifampicin does not prevent amyloid fibril formation by human islet amyloid polypeptide but does inhibit fibril thioflavin-T interactions: implications for mechanistic studies of beta-cell death. *Biochemistry*, 47(22):6016–6024, Jun 2008.
- [328] D. E. Ehrnhoefer, J. Bieschke, A. Boeddrich, M. Herbst, L. Masino, R. Lurz, S. Engemann, A. Pastore, and E. E. Wanker. EGCG redirects amyloidogenic polypeptides into unstructured, off-pathway oligomers. *Nat. Struct. Mol. Biol.*, 15(6):558–566, Jun 2008.
- [329] B. Ren, Y. Liu, Y. Zhang, Y. Cai, X. Gong, Y. Chang, L. Xu, and J. Zheng. Genistein: A Dual Inhibitor of Both Amyloid and Human Islet Amylin Peptides. *ACS Chem Neurosci*, 9(5):1215–1224, May 2018.
- [330] C. Xue, T. Y. Lin, D. Chang, and Z. Guo. Thioflavin T as an amyloid dye: fibril quantification, optimal concentration and effect on aggregation. *R Soc Open Sci*, 4(1):160696, Jan 2017.
- [331] R. S. Mancini, Y. Wang, and D. F. Weaver. Phenylindanes in Brewed Coffee Inhibit Amyloid-Beta and Tau Aggregation. *Front Neurosci*, 12:735, 2018.

- [332] T. Sato, M. Hotsumi, K. Makabe, and H. Konno. Design, synthesis and evaluation of curcumin-based fluorescent probes to detect A fibrils. *Bioorg. Med. Chem. Lett.*, 28(22):3520–3525, Dec 2018.
- [333] N. D. Younan and J. H. Viles. A Comparison of Three Fluorophores for the Detection of Amyloid Fibers and Prefibrillar Oligomeric Assemblies. ThT (Thioflavin T); ANS (1-Anilinonaphthalene-8-sulfonic Acid); and bisANS (4,4'-Dianilino-1,1'-binaphthyl-5,5'-disulfonic Acid). *Biochemistry*, 54(28):4297–4306, Jul 2015.
- [334] A. I. Sulatskaya, N. P. Rodina, M. I. Sulatsky, O. I. Povarova, I. A. Antifeeva, I. M. Kuznetsova, and K. K. Turoverov. Investigation of -Synuclein Amyloid Fibrils Using the Fluorescent Probe Thioflavin T. *Int J Mol Sci*, 19(9), Aug 2018.
- [335] A. I. Sulatskaya, N. P. Rodina, D. S. Polyakov, M. I. Sulatsky, T. O. Artamonova, M. A. Khodorkovskii, M. M. Shavlovsky, I. M. Kuznetsova, and K. K. Turoverov. Structural Features of Amyloid Fibrils Formed from the Full-Length and Truncated Forms of Beta-2-Microglobulin Probed by Fluorescent Dye Thioflavin T. *Int J Mol Sci*, 19(9), Sep 2018.
- [336] S. Navarro and S. Ventura. Fluorescent dye ProteoStat to detect and discriminate intracellular amyloid-like aggregates in Escherichia coli. *Biotechnol J*, 9(10):1259–1266, Oct 2014.
- [337] J. C. Saunders, L. M. Young, R. A. Mahood, M. P. Jackson, C. H. Revill, R. J. Foster, D. A. Smith, A. E. Ashcroft, D. J. Brockwell, and S. E. Radford. An in vivo platform for identifying inhibitors of protein aggregation. *Nat. Chem. Biol.*, 12(2):94–101, Feb 2016.
- [338] A. F. McKoy, J. Chen, T. Schupbach, and M. H. Hecht. A novel inhibitor of amyloid (A) peptide aggregation: from high throughput screening to efficacy in an animal model of Alzheimer disease. *J. Biol. Chem.*, 287(46):38992–39000, Nov 2012.
- [339] W. Kim, Y. Kim, J. Min, D. J. Kim, Y. T. Chang, and M. H. Hecht. A high-throughput screen for compounds that inhibit aggregation of the Alzheimer's peptide. *ACS Chem. Biol.*, 1(7):461–469, Aug 2006.

- [340] J. S. Lee, J. Ryu, and C. B. Park. High-throughput analysis of Alzheimer's beta-amyloid aggregation using a microfluidic self-assembly of monomers. *Anal. Chem.*, 81(7):2751–2759, Apr 2009.
- [341] G. M. Decad and H. Nikaido. Outer membrane of gram-negative bacteria. XII. Molecular-sieving function of cell wall. *J. Bacteriol.*, 128(1):325–336, Oct 1976.
- [342] C. Wurth, N. K. Guimard, and M. H. Hecht. Mutations that reduce aggregation of the Alzheimer's Abeta42 peptide: an unbiased search for the sequence determinants of Abeta amyloidogenesis. *J. Mol. Biol.*, 319(5):1279–1290, Jun 2002.
- [343] T. Wehrman, B. Kleaveland, J. H. Her, R. F. Balint, and H. M. Blau. Protein-protein interactions monitored in mammalian cells via complementation of beta-lactamase enzyme fragments. *Proc. Natl. Acad. Sci. U.S.A.*, 99(6):3469–3474, Mar 2002.
- [344] L. L. Lee, H. Ha, Y. T. Chang, and M. P. DeLisa. Discovery of amyloid-beta aggregation inhibitors using an engineered assay for intracellular protein folding and solubility. *Protein Sci.*, 18(2):277–286, Feb 2009.
- [345] L. Foit. Optimising protein stability and folding in vivo PhD thesis. PhD thesis, 2010.
- [346] J. C. Saunders. An In Vivo Platform for Identifying Protein Aggregation Inhibitors PhD thesis. PhD thesis, 2014.
- [347] C. Terry, R. L. Harniman, J. Sells, A. Wenborn, S. Joiner, H. R. Saibil, M. J. Miles, J. Collinge, and J. D. F. Wadsworth. Structural features distinguishing infectious ex vivo mammalian prions from non-infectious fibrillar assemblies generated in vitro. *Sci Rep*, 9(1):376, Jan 2019.
- [348] M. G. Iadanza, R. Silvers, J. Boardman, H. I. Smith, T. K. Karamanos, G. T. Debelouchina, Y. Su, R. G. Griffin, N. A. Ranson, and S. E. Radford. The structure of a 2-microglobulin fibril suggests a molecular basis for its amyloid polymorphism. *Nat Commun*, 9(1):4517, 10 2018.
- [349] C. l. e. L. Pham, Y. F. Mok, and G. J. Howlett. Sedimentation velocity analysis of amyloid fibrils. *Methods Mol. Biol.*, 752:179–196, 2011.

- [350] Y. F. Mok, G. J. Howlett, and M. D. Griffin. Sedimentation Velocity Analysis of the Size Distribution of Amyloid Oligomers and Fibrils. *Meth. Enzymol.*, 562: 241–256, 2015.
- [351] D. Du, A. N. Murray, E. Cohen, H. E. Kim, R. Simkovsky, A. Dillin, and J. W. Kelly. A kinetic aggregation assay allowing selective and sensitive amyloid- quantification in cells and tissues. *Biochemistry*, 50(10):1607–1617, Mar 2011.
- [352] P. Arosio, R. Cukalevski, B. Frohm, T. P. Knowles, and S. Linse. Quantification of the concentration of A42 propagons during the lag phase by an amyloid chain reaction assay. *J. Am. Chem. Soc.*, 136(1):219–225, Jan 2014.
- [353] A. E. Ashcroft. Recent developments in electrospray ionisation mass spectrometry: noncovalently bound protein complexes. *Nat Prod Rep*, 22(4):452–464, Aug 2005.
- [354] L. A. Woods, S. E. Radford, and A. E. Ashcroft. Advances in ion mobility spectrometry-mass spectrometry reveal key insights into amyloid assembly. *Biochim. Biophys. Acta*, 1834(6):1257–1268, Jun 2013.
- [355] C. Wu, W. F. Siems, G. R. Asbury, and H. H. Hill. Electrospray ionization high-resolution ion mobility spectrometry-mass spectrometry. *Anal. Chem.*, 70(23): 4929–4938, Dec 1998.
- [356] L. M. Young, J. C. Saunders, R. A. Mahood, C. H. Revill, R. J. Foster, A. E. Ashcroft, and S. E. Radford. ESI-IMS-MS: A method for rapid analysis of protein aggregation and its inhibition by small molecules. *Methods*, 95:62–69, Feb 2016.
- [357] H. Hernandez and C. V. Robinson. Determining the stoichiometry and interactions of macromolecular assemblies from mass spectrometry. *Nat Protoc*, 2(3):715–726, 2007.
- [358] L. M. Young, L. H. Tu, D. P. Raleigh, A. E. Ashcroft, and S. E. Radford. Understanding co-polymerization in amyloid formation by direct observation of mixed oligomers. *Chem Sci*, 8(7):5030–5040, Jul 2017.
- [359] D. C. da Silva and L. M. T. R. Lima. Physico-chemical properties of co-formulated fast-acting insulin with pramlintide. *Int J Pharm*, 547(1-2):621–629, Aug 2018.
- [360] N. Lespes, E. Pair, C. Maganga, M. Bretier, V. Tognetti, L. Joubert, V. Levacher, M. Hubert-Roux, C. Afonso, C. Loutelier-Bourhis, and J. F. Briere. A Unique

- (3+2) Annulation Reaction between Meldrum's Acid and Nitrones: Mechanistic Insight by ESI-IMS-MS and DFT Studies. *Chemistry*, 24(16):4086–4093, Mar 2018.
- [361] T. Daubenfeld, A. P. Bouin, and G. van der Rest. A deconvolution method for the separation of specific versus nonspecific interactions in noncovalent protein-ligand complexes analyzed by ESI-FT-ICR mass spectrometry. *J. Am. Soc. Mass Spectrom.*, 17(9):1239–1248, Sep 2006.
- [362] S. Kosol, S. Contreras-Martos, C. Cedeno, and P. Tompa. Structural characterization of intrinsically disordered proteins by NMR spectroscopy. *Molecules*, 18(9):10802–10828, Sep 2013.
- [363] T. K. Karamanos, A. P. Kalverda, G. S. Thompson, and S. E. Radford. Mechanisms of amyloid formation revealed by solution NMR. *Prog Nucl Magn Reson Spectrosc*, 88-89:86–104, Aug 2015.
- [364] N. Rezaei-Ghaleh, M. Blackledge, and M. Zweckstetter. Intrinsically disordered proteins: from sequence and conformational properties toward drug discovery. *Chembiochem*, 13(7):930–950, May 2012.
- [365] G. R. Lamberto, A. Binolfi, M. L. Orcellet, C. W. Bertoncini, M. Zweckstetter, C. Griesinger, and C. O. Fernandez. Structural and mechanistic basis behind the inhibitory interaction of PcTS on alpha-synuclein amyloid fibril formation. *Proc. Natl. Acad. Sci. U.S.A.*, 106(50):21057–21062, Dec 2009.
- [366] D. I. Hammoudeh, A. V. Follis, E. V. Prochownik, and S. J. Metallo. Multiple independent binding sites for small-molecule inhibitors on the oncoprotein c-Myc. *J. Am. Chem. Soc.*, 131(21):7390–7401, Jun 2009.
- [367] N. Rezaei-Ghaleh, E. Andreetto, L. M. Yan, A. Kapurniotu, and M. Zweckstetter. Interaction between amyloid beta peptide and an aggregation blocker peptide mimicking islet amyloid polypeptide. *PLoS ONE*, 6(5):e20289, 2011.
- [368] H. J. Dyson and P. E. Wright. Unfolded proteins and protein folding studied by NMR. *Chem. Rev.*, 104(8):3607–3622, Aug 2004.

- [369] R. L. Narayanan, U. H. Durr, S. Bibow, J. Biernat, E. Mandelkow, and M. Zweckstetter. Automatic assignment of the intrinsically disordered protein Tau with 441-residues. *J. Am. Chem. Soc.*, 132(34):11906–11907, Sep 2010.
- [370] C. Narayanan, K. Bafna, L. D. Roux, P. K. Agarwal, and N. Doucet. Applications of NMR and computational methodologies to study protein dynamics. *Arch. Biochem. Biophys.*, 628:71–80, 08 2017.
- [371] D. J. Rosenman, C. R. Connors, W. Chen, C. Wang, and A. E. Garcia. A monomers transiently sample oligomer and fibril-like configurations: ensemble characterization using a combined MD/NMR approach. *J. Mol. Biol.*, 425(18):3338–3359, Sep 2013.
- [372] F. N. Newby, A. De Simone, M. Yagi-Utsumi, X. Salvatella, C. M. Dobson, and M. Vendruscolo. Structure-Free Validation of Residual Dipolar Coupling and Paramagnetic Relaxation Enhancement Measurements of Disordered Proteins. *Biochemistry*, 54(46):6876–6886, Nov 2015.
- [373] K. S. Usachev, A. V. Filippov, O. N. Antzutkin, and V. V. Klochkov. Use of a combination of the RDC method and NOESY NMR spectroscopy to determine the structure of Alzheimer’s amyloid A10-35 peptide in solution and in SDS micelles. *Eur. Biophys. J.*, 42(11-12):803–810, Dec 2013.
- [374] P. Krolak-Salmon. [What use of biological markers for the diagnosis of Alzheimer’s disease and associated disorders?]. *Psychol Neuropsychiatr Vieil*, 8(1):25–31, Mar 2010.
- [375] N. Tjandra and A. Bax. Direct measurement of distances and angles in biomolecules by NMR in a dilute liquid crystalline medium. *Science*, 278(5340):1111–1114, Nov 1997.
- [376] D. S. Wishart, C. G. Bigam, J. Yao, F. Abildgaard, H. J. Dyson, E. Oldfield, J. L. Markley, and B. D. Sykes. ^1H , ^{13}C and ^{15}N chemical shift referencing in biomolecular NMR. *J. Biomol. NMR*, 6(2):135–140, Sep 1995.
- [377] J. H. Tomlinson and M. P. Williamson. Amide temperature coefficients in the protein G B1 domain. *J. Biomol. NMR*, 52(1):57–64, Jan 2012.

- [378] H. Okazaki, N. Matsuo, T. Tenno, N. Goda, Y. Shigemitsu, M. Ota, and H. Hiroaki. Using ^1H N amide temperature coefficients to define intrinsically disordered regions: An alternative NMR method. *Protein Sci.*, 27(10):1821–1830, Oct 2018.
- [379] L. E. Kay, D. A. Torchia, and A. Bax. Backbone dynamics of proteins as studied by ^{15}N inverse detected heteronuclear NMR spectroscopy: application to staphylococcal nuclease. *Biochemistry*, 28(23):8972–8979, Nov 1989.
- [380] A. G. Palmer. Dynamic properties of proteins from NMR spectroscopy. *Curr. Opin. Biotechnol.*, 4(4):385–391, Aug 1993.
- [381] R. Ahmed and G. Melacini. A solution NMR toolset to probe the molecular mechanisms of amyloid inhibitors. *Chem. Commun. (Camb.)*, 54(37):4644–4652, May 2018.
- [382] J. Huang and A. D. MacKerell. Force field development and simulations of intrinsically disordered proteins. *Curr. Opin. Struct. Biol.*, 48:40–48, 02 2018.
- [383] D. M. Walsh, E. Thulin, A. M. Minogue, N. Gustavsson, E. Pang, D. B. Teplow, and S. Linse. A facile method for expression and purification of the Alzheimer’s disease-associated amyloid beta-peptide. *FEBS J.*, 276(5):1266–1281, Mar 2009.
- [384] J. A. Williamson and A. D. Miranker. Direct detection of transient alpha-helical states in islet amyloid polypeptide. *Protein Sci.*, 16(1):110–117, Jan 2007.
- [385] Maestro. CD-ROM. LLC, NY, USA: Schrödinger, 2014-2.
- [386] F. Delaglio, S. Grzesiek, G. W. Vuister, G. Zhu, J. Pfeifer, and A. Bax. NMRPipe: a multidimensional spectral processing system based on UNIX pipes. *J. Biomol. NMR*, 6(3):277–293, Nov 1995.
- [387] W. F. Vranken, W. Boucher, T. J. Stevens, R. H. Fogh, A. Pajon, M. Llinas, E. L. Ulrich, J. L. Markley, J. Ionides, and E. D. Laue. The CCPN data model for NMR spectroscopy: development of a software pipeline. *Proteins*, 59(4):687–696, Jun 2005.
- [388] J. Schleucher, M. Schwendinger, M. Sattler, P. Schmidt, O. Schedletzky, S. J. Glaser, O. W. Sørensen, and C. Griesinger. A general enhancement scheme in heteronuclear multidimensional NMR employing pulsed field gradients. *J. Biomol. NMR*, 4(2):301–306, Mar 1994.

- [389] S. Grzesiek and A. Bax. Measurement of amide proton exchange rates and NOEs with water in $^{13}\text{C}/^{15}\text{N}$ -enriched calcineurin B. *J. Biomol. NMR*, 3(6):627–638, Nov 1993.
- [390] E. Lescop, P. Schanda, and B. Brutscher. A set of BEST triple-resonance experiments for time-optimized protein resonance assignment. *J. Magn. Reson.*, 187(1):163–169, Jul 2007.
- [391] B. Macao, W. Hoyer, A. Sandberg, A. C. Brorsson, C. M. Dobson, and T. Hard. Recombinant amyloid beta-peptide production by coexpression with an affibody ligand. *BMC Biotechnol.*, 8:82, Oct 2008.
- [392] S. Schwarzingler, G. J. Kroon, T. R. Foss, J. Chung, P. E. Wright, and H. J. Dyson. Sequence-dependent correction of random coil NMR chemical shifts. *J. Am. Chem. Soc.*, 123(13):2970–2978, Apr 2001.
- [393] D. S. Wishart and B. D. Sykes. Chemical shifts as a tool for structure determination. *Meth. Enzymol.*, 239:363–392, 1994.
- [394] D. S. Wishart, C. G. Bigam, A. Holm, R. S. Hodges, and B. D. Sykes. ^1H , ^{13}C and ^{15}N random coil NMR chemical shifts of the common amino acids. I. Investigations of nearest-neighbor effects. *J. Biomol. NMR*, 5(1):67–81, Jan 1995.
- [395] F. Cordier, A. J. Dingley, and S. Grzesiek. A doublet-separated sensitivity-enhanced HSQC for the determination of scalar and dipolar one-bond J-couplings. *J. Biomol. NMR*, 13(2):175–180, Feb 1999.
- [396] D. C. Rodriguez Camargo, K. Tripsianes, T. G. Kapp, J. Mendes, J. Schubert, B. Cordes, and B. Reif. Cloning, expression and purification of the human Islet Amyloid Polypeptide (hIAPP) from *Escherichia coli*. *Protein Expr. Purif.*, 106:49–56, Feb 2015.
- [397] S. Yoo, S. Zhang, A. G. Kreutzer, and J. S. Nowick. An Efficient Method for the Expression and Purification of A(M1-42). *Biochemistry*, 57(26):3861–3866, 07 2018.
- [398] H. Dobeli, N. Draeger, G. Huber, P. Jakob, D. Schmidt, B. Seilheimer, D. Stuber, B. Wipf, and M. Zulauf. A biotechnological method provides access to aggregation

- competent monomeric Alzheimer's 1-42 residue amyloid peptide. *Biotechnology (N. Y.)*, 13(9):988–993, Sep 1995.
- [399] C. M. Venkatachalam and G. N. Ramachandran. Conformation of polypeptide chains. *Annu. Rev. Biochem.*, 38:45–82, 1969.
- [400] M. W. Southworth, K. Amaya, T. C. Evans, M. Q. Xu, and F. B. Perler. Purification of proteins fused to either the amino or carboxy terminus of the *Mycobacterium xenopi* gyrase A intein. *BioTechniques*, 27(1):110–114, Jul 1999.
- [401] I. R. Cottingham, A. Millar, E. Emslie, A. Colman, A. E. Schnieke, and C. McKee. A method for the amidation of recombinant peptides expressed as intein fusion proteins in *Escherichia coli*. *Nat. Biotechnol.*, 19(10):974–977, Oct 2001.
- [402] J. W. Dubendorff and F. W. Studier. Creation of a T7 autogene. Cloning and expression of the gene for bacteriophage T7 RNA polymerase under control of its cognate promoter. *J. Mol. Biol.*, 219(1):61–68, May 1991.
- [403] F. W. Studier. Use of bacteriophage T7 lysozyme to improve an inducible T7 expression system. *J. Mol. Biol.*, 219(1):37–44, May 1991.
- [404] S. Contreras-Martos, H. H. Nguyen, P. N. Nguyen, N. Hristozova, M. Macossay-Castillo, D. Kovacs, A. Bekesi, J. S. Oemig, D. Maes, K. Pauwels, P. Tompa, and P. Lebrun. Quantification of Intrinsically Disordered Proteins: A Problem Not Fully Appreciated. *Front Mol Biosci*, 5:83, 2018.
- [405] M. Hashimoto, T. Ikegami, S. Seino, N. Ohuchi, H. Fukada, J. Sugiyama, M. Shirakawa, and T. Watanabe. Expression and characterization of the chitin-binding domain of chitinase A1 from *Bacillus circulans* WL-12. *J. Bacteriol.*, 182(11):3045–3054, Jun 2000.
- [406] C. L. Ladner-Keay, B. J. Griffith, and D. S. Wishart. Shaking alone induces de novo conversion of recombinant prion proteins to β -sheet rich oligomers and fibrils. *PLoS ONE*, 9(6):e98753, 2014.
- [407] ExpASY ProtParam. <https://web.expasy.org/protparam/>, 2018. Accessed: 2019-01-06.

- [408] C. Cui, W. Zhao, J. Chen, J. Wang, and Q. Li. Elimination of in vivo cleavage between target protein and intein in the intein-mediated protein purification systems. *Protein Expr. Purif.*, 50(1):74–81, Nov 2006.
- [409] S. A. Bondarev, K. S. Antonets, A. V. Kajava, A. A. Nizhnikov, and G. A. Zhouravleva. Protein Co-Aggregation Related to Amyloids: Methods of Investigation, Diversity, and Classification. *Int J Mol Sci*, 19(8), Aug 2018.
- [410] S. Giorgetti, C. Greco, P. Tortora, and F. A. Aprile. Targeting Amyloid Aggregation: An Overview of Strategies and Mechanisms. *Int J Mol Sci*, 19(9), Sep 2018.
- [411] P. Forouzanmehr, A. Abbaspour, C. Fang, M. Cabrerizo, D. Loewenstein, R. Duara, and M. Adjouadi. A survey on applications and analysis methods of functional magnetic resonance imaging for Alzheimer’s disease. *J. Neurosci. Methods*, 317:121–140, Apr 2019.
- [412] B. K. Maity, V. Vishvakarma, D. Surendran, A. Rawat, A. Das, S. Pramanik, N. Arfin, and S. Maiti. Spontaneous Fluctuations Can Guide Drug Design Strategies for Structurally Disordered Proteins. *Biochemistry*, 57(28):4206–4213, 07 2018.
- [413] P. R. Banerjee and A. A. Deniz. Shedding light on protein folding landscapes by single-molecule fluorescence. *Chem Soc Rev*, 43(4):1172–1188, Feb 2014.
- [414] A. Nath and E. Rhoades. A flash in the pan: dissecting dynamic amyloid intermediates using fluorescence. *FEBS Lett.*, 587(8):1096–1105, Apr 2013.
- [415] K. A. Ball, D. E. Wemmer, and T. Head-Gordon. Comparison of structure determination methods for intrinsically disordered amyloid- peptides. *J Phys Chem B*, 118(24):6405–6416, Jun 2014.
- [416] S. J. Moore, K. Sonar, P. Bharadwaj, E. Deplazes, and R. L. Mancera. Characterisation of the Structure and Oligomerisation of Islet Amyloid Polypeptides (IAPP): A Review of Molecular Dynamics Simulation Studies. *Molecules*, 23(9), Aug 2018.

- [417] E. Peng, N. Todorova, and I. Yarovsky. Effects of forcefield and sampling method in all-atom simulations of inherently disordered proteins: Application to conformational preferences of human amylin. *PLoS ONE*, 12(10):e0186219, 2017.
- [418] A. Bhowmick, D. H. Brookes, S. R. Yost, H. J. Dyson, J. D. Forman-Kay, D. Gunter, M. Head-Gordon, G. L. Hura, V. S. Pande, D. E. Wemmer, P. E. Wright, and T. Head-Gordon. Finding Our Way in the Dark Proteome. *J. Am. Chem. Soc.*, 138(31):9730–9742, 08 2016.
- [419] A. I. Sulatskaya, A. V. Lavysh, A. A. Maskevich, I. M. Kuznetsova, and K. K. Turoverov. Thioflavin T fluoresces as excimer in highly concentrated aqueous solutions and as monomer being incorporated in amyloid fibrils. *Sci Rep*, 7(1):2146, 05 2017.
- [420] R. Crespo, E. Villar-Alvarez, P. Taboada, F. A. Rocha, A. M. Damas, and P. M. Martins. What Can the Kinetics of Amyloid Fibril Formation Tell about Off-pathway Aggregation? *J. Biol. Chem.*, 291(4):2018–2032, Jan 2016.
- [421] L. M. Young, J. C. Saunders, R. A. Mahood, C. H. Reville, R. J. Foster, L. H. Tu, D. P. Raleigh, S. E. Radford, and A. E. Ashcroft. Screening and classifying small-molecule inhibitors of amyloid formation using ion mobility spectrometry-mass spectrometry. *Nat Chem*, 7(1):73–81, Jan 2015.
- [422] L. P. Jameson, N. W. Smith, and S. V. Dzyuba. Dye-binding assays for evaluation of the effects of small molecule inhibitors on amyloid (a) self-assembly. *ACS Chem Neurosci*, 3(11):807–819, Nov 2012.
- [423] C. Wu, M. Biancalana, S. Koide, and J. E. Shea. Binding modes of thioflavin-T to the single-layer beta-sheet of the peptide self-assembly mimics. *J. Mol. Biol.*, 394(4):627–633, Dec 2009.
- [424] D. Hall, J. Kardos, H. Edskes, J. A. Carver, and Y. Goto. A multi-pathway perspective on protein aggregation: implications for control of the rate and extent of amyloid formation. *FEBS Lett.*, 589(6):672–679, Mar 2015.
- [425] K. L. Stewart and S. E. Radford. Amyloid plaques beyond A: a survey of the diverse modulators of amyloid aggregation. *Biophys Rev*, 9(4):405–419, Aug 2017.

- [426] D. Narang, A. Singh, H. M. Swasthi, and S. Mukhopadhyay. Characterization of Salt-Induced Oligomerization of Human 2-Microglobulin at Low pH. *J Phys Chem B*, 120(32):7815–7823, 08 2016.
- [427] G. M. Moriarty, M. P. Olson, T. B. Atieh, M. K. Janowska, S. D. Khare, and J. Baum. A pH-dependent switch promotes α -synuclein fibril formation via glutamate residues. *J. Biol. Chem.*, 292(39):16368–16379, 09 2017.
- [428] G. Fusco, M. Sanz-Hernandez, F. S. Ruggeri, M. Vendruscolo, C. M. Dobson, and A. De Simone. Molecular determinants of the interaction of EGCG with ordered and disordered proteins. *Biopolymers*, 109(10):e23117, Aug 2018.
- [429] L. H. Tu, H. Noor, P. Cao, and D. P. Raleigh. Aspirin, diabetes, and amyloid: re-examination of the inhibition of amyloid formation by aspirin and ketoprofen. *ACS Chem. Biol.*, 9(7):1632–1637, Jul 2014.
- [430] T. Weiffert, G. Meisl, P. Flagmeier, S. De, C. J. R. Dunning, B. Frohm, H. Zetterberg, K. Blennow, E. Portelius, D. Klenerman, C. M. Dobson, T. P. J. Knowles, and S. Linse. Increased Secondary Nucleation Underlies Accelerated Aggregation of the Four-Residue N-Terminally Truncated A42 Species A5-42. *ACS Chem Neurosci*, Mar 2019.
- [431] L. Foit, A. Mueller-Schickert, B. S. Mamathambika, S. Gleiter, C. L. Klaska, G. Ren, and J. C. Bardwell. Genetic selection for enhanced folding in vivo targets the Cys14-Cys38 disulfide bond in bovine pancreatic trypsin inhibitor. *Antioxid. Redox Signal.*, 14(6):973–984, Mar 2011.
- [432] L. Foit, J. S. George, B. W. Zhang, C. L. Brooks, and J. C. Bardwell. Chaperone activation by unfolding. *Proc. Natl. Acad. Sci. U.S.A.*, 110(14):E1254–1262, Apr 2013.
- [433] A. S. Pithadia, A. Bhunia, R. Sribalan, V. Padmini, C. A. Fierke, and A. Ramamoorthy. Influence of a curcumin derivative on hIAPP aggregation in the absence and presence of lipid membranes. *Chem. Commun. (Camb.)*, 52(5):942–945, Jan 2016.
- [434] A. Pithadia, J. R. Brender, C. A. Fierke, and A. Ramamoorthy. Inhibition of IAPP Aggregation and Toxicity by Natural Products and Derivatives. *J Diabetes Res*, 2016:2046327, 2016.

- [435] Y. D. Liao, J. C. Jeng, C. F. Wang, S. C. Wang, and S. T. Chang. Removal of N-terminal methionine from recombinant proteins by engineered *E. coli* methionine aminopeptidase. *Protein Sci.*, 13(7):1802–1810, Jul 2004.
- [436] C. J. A. Warner, S. Dutta, A. R. Foley, and J. A. Raskatov. A Tailored HPLC Purification Protocol That Yields High-purity Amyloid Beta 42 and Amyloid Beta 40 Peptides, Capable of Oligomer Formation. *J Vis Exp*, (121), 03 2017.
- [437] Y. Shi, W. Lv, A. Jiao, C. Zhang, and J. Zhang. A Novel Pentapeptide Inhibitor Reduces Amyloid Deposit Formation by Direct Interaction with hIAPP. *Int J Endocrinol*, 2019:9062032, 2019.
- [438] S. U. B. Farrukh, I. Javed, A. Q. Ather, A. H. Emwas, M. Alazmi, X. Gao, G. A. Chotana, T. P. Davis, P. C. Ke, and R. S. Z. Saleem. Synthesis and identification of novel pyridazinylpyrazolone based diazo compounds as inhibitors of human islet amyloid polypeptide aggregation. *Bioorg. Chem.*, 84:339–346, Mar 2019.
- [439] M. F. M. Sciacca, V. Romanucci, A. Zarrelli, I. Monaco, F. Lolicato, N. Spinella, C. Galati, G. Grasso, L. D’Urso, M. Romeo, L. Diomede, M. Salmona, C. Bongiorno, G. Di Fabio, C. La Rosa, and D. Milardi. Inhibition of A Amyloid Growth and Toxicity by Silybins: The Crucial Role of Stereochemistry. *ACS Chem Neurosci*, 8(8):1767–1778, 08 2017.
- [440] H. Ramshini, M. mohammad zadeh, and A. Ebrahim-Habibi. Inhibition of amyloid fibril formation and cytotoxicity by a chemical analog of Curcumin as a stable inhibitor. *Int. J. Biol. Macromol.*, 78:396–404, 2015.
- [441] N. N. Jha, R. Kumar, R. Panigrahi, A. Navalkar, D. Ghosh, S. Sahay, M. Mondal, A. Kumar, and S. K. Maji. Comparison of α -Synuclein Fibril Inhibition by Four Different Amyloid Inhibitors. *ACS Chem Neurosci*, 8(12):2722–2733, 12 2017.
- [442] T. Rho, M. S. Choi, M. Jung, H. W. Kil, Y. D. Hong, and K. D. Yoon. Identification of fermented tea (*Camellia sinensis*) polyphenols and their inhibitory activities against amyloid-beta aggregation. *Phytochemistry*, 160:11–18, Apr 2019.
- [443] J. Habchi, P. Arosio, M. Perni, A. R. Costa, M. Yagi-Utsumi, P. Joshi, S. Chia, S. I. Cohen, M. B. Muller, S. Linse, E. A. Nollen, C. M. Dobson, T. P. Knowles, and M. Vendruscolo. An anticancer drug suppresses the primary nucleation reaction

- that initiates the production of the toxic A42 aggregates linked with Alzheimer's disease. *Sci Adv*, 2(2):e1501244, Feb 2016.
- [444] J. Habchi, S. Chia, R. Limbocker, B. Mannini, M. Ahn, M. Perni, O. Hansson, P. Arosio, J. R. Kumita, P. K. Challa, S. I. Cohen, S. Linse, C. M. Dobson, T. P. Knowles, and M. Vendruscolo. Systematic development of small molecules to inhibit specific microscopic steps of A42 aggregation in Alzheimer's disease. *Proc. Natl. Acad. Sci. U.S.A.*, 114(2):E200–E208, 01 2017.
- [445] R. Macarron, M. N. Banks, D. Bojanic, D. J. Burns, D. A. Cirovic, T. Garyantes, D. V. Green, R. P. Hertzberg, W. P. Janzen, J. W. Paslay, U. Schopfer, and G. S. Sittampalam. Impact of high-throughput screening in biomedical research. *Nat Rev Drug Discov*, 10(3):188–195, 03 2011.
- [446] OpenEye Scientific Software, 2018. URL <http://www.eyesopen.com/>.
- [447] N. R. Jabir, F. R. Khan, and S. Tabrez. Cholinesterase targeting by polyphenols: A therapeutic approach for the treatment of Alzheimer's disease. *CNS Neurosci Ther*, 24(9):753–762, 09 2018.
- [448] S. N. Bukhari and I. Jantan. Synthetic Curcumin Analogs as Inhibitors of - Amyloid Peptide Aggregation: Potential Therapeutic and Diagnostic Agents for Alzheimer's Disease. *Mini Rev Med Chem*, 15(13):1110–1121, 2015.
- [449] D. M. A. Oliver and P. H. Reddy. Small molecules as therapeutic drugs for Alzheimer's disease. *Mol. Cell. Neurosci.*, 96:47–62, Mar 2019.
- [450] B. A. Q. Gomes, J. P. B. Silva, C. F. R. Romeiro, S. M. Dos Santos, C. A. Rodrigues, P. R. Goncalves, J. T. Sakai, P. F. S. Mendes, E. L. P. Varela, and M. C. Monteiro. Neuroprotective Mechanisms of Resveratrol in Alzheimer's Disease: Role of SIRT1. *Oxid Med Cell Longev*, 2018:8152373, 2018.
- [451] Marcus F. Boehm, Lin Zhang, Lin Zhi, Michael R. McClurg, Elain Berger, Murriel Wagoner, Dale E. Mais, Carla M. Suto, Peter J. A. Davies, Richard A. Heyman, and Alex M. Nadzan. Design and synthesis of potent retinoid x receptor selective ligands that induce apoptosis in leukemia cells. *Journal of Medicinal Chemistry*, 38(16):3146–3155, 1995. doi: 10.1021/jm00016a018. URL <https://doi.org/10.1021/jm00016a018>.

- [452] P. E. Cramer, J. R. Cirrito, D. W. Wesson, C. Y. Lee, J. C. Karlo, A. E. Zinn, B. T. Casali, J. L. Restivo, W. D. Goebel, M. J. James, K. R. Brunden, D. A. Wilson, and G. E. Landreth. ApoE-directed therapeutics rapidly clear β -amyloid and reverse deficits in AD mouse models. *Science*, 335(6075):1503–1506, Mar 2012.
- [453] W. J. Strittmatter. Medicine. Old drug, new hope for Alzheimer’s disease. *Science*, 335(6075):1447–1448, Mar 2012.
- [454] F. M. LaFerla. Preclinical success against Alzheimer’s disease with an old drug. *N. Engl. J. Med.*, 367(6):570–572, Aug 2012.
- [455] J. Fantini, C. Di Scala, N. Yahi, J. D. Troadec, K. Sadelli, H. Chahinian, and N. Garmy. Bexarotene blocks calcium-permeable ion channels formed by neurotoxic Alzheimer’s β -amyloid peptides. *ACS Chem Neurosci*, 5(3):216–224, Mar 2014.
- [456] C. Di Scala, H. Chahinian, N. Yahi, N. Garmy, and J. Fantini. Interaction of Alzheimer’s β -amyloid peptides with cholesterol: mechanistic insights into amyloid pore formation. *Biochemistry*, 53(28):4489–4502, Jul 2014.
- [457] F. Kamp, H. A. Scheidt, E. Winkler, G. Basset, H. Heinel, J. M. Hutchison, L. M. LaPointe, C. R. Sanders, H. Steiner, and D. Huster. Bexarotene Binds to the Amyloid Precursor Protein Transmembrane Domain, Alters Its β -Helical Conformation, and Inhibits β -Secretase Nonselectively in Liposomes. *ACS Chem Neurosci*, 9(7):1702–1713, Jul 2018.
- [458] P. D. Q. Huy, N. Q. Thai, Z. Bednarikova, L. H. Phuc, H. Q. Linh, Z. Gazova, and M. S. Li. Bexarotene Does Not Clear Amyloid Beta Plaques but Delays Fibril Growth: Molecular Mechanisms. *ACS Chem Neurosci*, 8(9):1960–1969, 09 2017.
- [459] Z. Mirza and M. A. Beg. Possible Molecular Interactions of Bexarotene - A Retinoid Drug and Alzheimer’s A Peptide: A Docking Study. *Curr Alzheimer Res*, 14(3):327–334, 2017.
- [460] A. D. Andricopulo, L. B. Salum, and D. J. Abraham. Structure-based drug design strategies in medicinal chemistry. *Curr Top Med Chem*, 9(9):771–790, 2009.

- [461] X. K. Zhang, B. Hoffmann, P. B. Tran, G. Graupner, and M. Pfahl. Retinoid X receptor is an auxiliary protein for thyroid hormone and retinoic acid receptors. *Nature*, 355(6359):441–446, Jan 1992.
- [462] A. le Maire, S. Alvarez, P. Shankaranarayanan, A. R. Lera, W. Bourguet, and H. Gronemeyer. Retinoid receptors and therapeutic applications of RAR/RXR modulators. *Curr Top Med Chem*, 12(6):505–527, 2012.
- [463] L. Altucci, M. D. Leibowitz, K. M. Ogilvie, A. R. de Lera, and H. Gronemeyer. RAR and RXR modulation in cancer and metabolic disease. *Nat Rev Drug Discov*, 6(10):793–810, Oct 2007.
- [464] V. Nahoum, E. Perez, P. Germain, F. Rodriguez-Barrios, F. Manzo, S. Kammerer, G. Lemaire, O. Hirsch, C. A. Royer, H. Gronemeyer, A. R. de Lera, and W. Bourguet. Modulators of the structural dynamics of the retinoid X receptor to reveal receptor function. *Proc. Natl. Acad. Sci. U.S.A.*, 104(44):17323–17328, Oct 2007.
- [465] B. A. Bernard. Adapalene, a new chemical entity with retinoid activity. *Skin Pharmacol.*, 6 Suppl 1:61–69, 1993.
- [466] Q. Le, M. I. Dawson, D. R. Soprano, and K. J. Soprano. Modulation of retinoic acid receptor function alters the growth inhibitory response of oral SCC cells to retinoids. *Oncogene*, 19(11):1457–1465, Mar 2000.
- [467] M. Necula, R. Kayed, S. Milton, and C. G. Glabe. Small molecule inhibitors of aggregation indicate that amyloid beta oligomerization and fibrillization pathways are independent and distinct. *J. Biol. Chem.*, 282(14):10311–10324, Apr 2007.
- [468] M. Wigglesworth and T. wood, eds. *In Management of Chemical and Biological samples for Screening Applications*. Wiley, 2012.
- [469] W. P. Janzen and I. G. Popa-Burke. Advances in improving the quality and flexibility of compound management. *J Biomol Screen*, 14(5):444–451, Jun 2009.
- [470] P. Hortschansky, V. Schroeckh, T. Christopeit, G. Zandomenighi, and M. Fandrich. The aggregation kinetics of Alzheimer’s beta-amyloid peptide is controlled by stochastic nucleation. *Protein Sci.*, 14(7):1753–1759, Jul 2005.

- [471] K. Andrich and J. Bieschke. The Effect of (-)-Epigallo-catechin-(3)-gallate on Amyloidogenic Proteins Suggests a Common Mechanism. *Adv. Exp. Med. Biol.*, 863:139–161, 2015.
- [472] S. Wang, P. Wen, and S. Wood. Effect of LXR/RXR agonism on brain and CSF A40 levels in rats. *F1000Res*, 5:138, 2016.
- [473] D. Eliezer. Biophysical characterization of intrinsically disordered proteins. *Curr. Opin. Struct. Biol.*, 19(1):23–30, Feb 2009.
- [474] B. Brutscher, I. C. Felli, S. Gil-Caballero, T. Hošek, R. Kummerle, A. Piai, R. Pierattelli, and Z. Solyom. NMR Methods for the Study of Intrinsically Disordered Proteins Structure, Dynamics, and Interactions: General Overview and Practical Guidelines. *Adv. Exp. Med. Biol.*, 870:49–122, 2015.
- [475] A. Prestel, K. Bugge, L. Staby, R. Hendus-Altenburger, and B. B. Kragelund. Characterization of Dynamic IDP Complexes by NMR Spectroscopy. *Meth. Enzymol.*, 611:193–226, 2018.
- [476] D. Kurzbach, G. Kontaxis, N. Coudevylle, and R. Konrat. NMR Spectroscopic Studies of the Conformational Ensembles of Intrinsically Disordered Proteins. *Adv. Exp. Med. Biol.*, 870:149–185, 2015.
- [477] K. V. Balakin, N. P. Savchuk, and I. V. Tetko. In silico approaches to prediction of aqueous and DMSO solubility of drug-like compounds: trends, problems and solutions. *Curr. Med. Chem.*, 13(2):223–241, 2006.
- [478] N. Goradia, C. Wiedemann, C. Herbst, M. Gorlach, S. H. Heinemann, O. Ohlen-schlager, and R. Ramachandran. An approach to NMR assignment of intrinsically disordered proteins. *Chemphyschem*, 16(4):739–746, Mar 2015.
- [479] D. P. Frueh. Practical aspects of NMR signal assignment in larger and challenging proteins. *Prog Nucl Magn Reson Spectrosc*, 78:47–75, Apr 2014.
- [480] J. Roche, Y. Shen, J. H. Lee, J. Ying, and A. Bax. Monomeric A(1-40) and A(1-42) Peptides in Solution Adopt Very Similar Ramachandran Map Distributions That Closely Resemble Random Coil. *Biochemistry*, 55(5):762–775, Feb 2016.
- [481] M. Ultsch, B. Li, T. Maurer, M. Mathieu, O. Adolfsson, A. Muhs, A. Pfeifer, M. Pihlgren, T. W. Bainbridge, M. Reichelt, J. A. Ernst, C. Eigenbrot, G. Fuh,

- J. K. Atwal, R. J. Watts, and W. Wang. Structure of Crenezumab Complex with A Shows Loss of -Hairpin. *Sci Rep*, 6:39374, 12 2016.
- [482] C. Dammers, L. Gremer, P. Neudecker, H. U. Demuth, M. Schwarten, and D. Willbold. Purification and Characterization of Recombinant N-Terminally Pyroglutamate-Modified Amyloid- Variants and Structural Analysis by Solution NMR Spectroscopy. *PLoS ONE*, 10(10):e0139710, 2015.
- [483] J. Kragelj, V. Ozenne, M. Blackledge, and M. R. Jensen. Conformational propensities of intrinsically disordered proteins from NMR chemical shifts. *Chemphyschem*, 14(13):3034–3045, Sep 2013.
- [484] J. A. Marsh, V. K. Singh, Z. Jia, and J. D. Forman-Kay. Sensitivity of secondary structure propensities to sequence differences between alpha- and gamma-synuclein: implications for fibrillation. *Protein Sci.*, 15(12):2795–2804, Dec 2006.
- [485] C. Camilloni, A. De Simone, W. F. Vranken, and M. Vendruscolo. Determination of secondary structure populations in disordered states of proteins using nuclear magnetic resonance chemical shifts. *Biochemistry*, 51(11):2224–2231, Mar 2012.
- [486] K. Tamiola and F. A. Mulder. Using NMR chemical shifts to calculate the propensity for structural order and disorder in proteins. *Biochem. Soc. Trans.*, 40(5):1014–1020, Oct 2012.
- [487] G. Bouvignies, P. Vallurupalli, M. H. Cordes, D. F. Hansen, and L. E. Kay. Measuring 1HN temperature coefficients in invisible protein states by relaxation dispersion NMR spectroscopy. *J. Biomol. NMR*, 50(1):13–18, May 2011.
- [488] T. Cierpicki and J. Otlewski. Amide proton temperature coefficients as hydrogen bond indicators in proteins. *J. Biomol. NMR*, 21(3):249–261, Nov 2001.
- [489] T. Cierpicki, I. Zhukov, R. A. Byrd, and J. Otlewski. Hydrogen bonds in human ubiquitin reflected in temperature coefficients of amide protons. *J. Magn. Reson.*, 157(2):178–180, Aug 2002.
- [490] F. Cordier and S. Grzesiek. Temperature-dependence of protein hydrogen bond properties as studied by high-resolution NMR. *J. Mol. Biol.*, 317(5):739–752, Apr 2002.

- [491] G. Nodet, L. Salmon, V. Ozenne, S. Meier, M. R. Jensen, and M. Blackledge. Quantitative description of backbone conformational sampling of unfolded proteins at amino acid resolution from NMR residual dipolar couplings. *J. Am. Chem. Soc.*, 131(49):17908–17918, Dec 2009.
- [492] J. R. Huang, V. Ozenne, M. R. Jensen, and M. Blackledge. Direct prediction of NMR residual dipolar couplings from the primary sequence of unfolded proteins. *Angew. Chem. Int. Ed. Engl.*, 52(2):687–690, Jan 2013.
- [493] J. R. Huang and S. Grzesiek. Ensemble calculations of unstructured proteins constrained by RDC and PRE data: a case study of urea-denatured ubiquitin. *J. Am. Chem. Soc.*, 132(2):694–705, Jan 2010.
- [494] M. D. Mukrasch, P. Markwick, J. Biernat, M. v. Bergen, P. Bernado, C. Griesinger, E. Mandelkow, M. Zweckstetter, and M. Blackledge. Highly populated turn conformations in natively unfolded tau protein identified from residual dipolar couplings and molecular simulation. *J. Am. Chem. Soc.*, 129(16):5235–5243, Apr 2007.
- [495] K. Chen and N. Tjandra. The use of residual dipolar coupling in studying proteins by NMR. *Top Curr Chem*, 326:47–67, 2012.
- [496] A. Bax and A. Grishaev. Weak alignment NMR: a hawk-eyed view of biomolecular structure. *Curr. Opin. Struct. Biol.*, 15(5):563–570, Oct 2005.
- [497] T. Klabunde, S. Sharma, A. Telenti, W. R. Jacobs, and J. C. Sacchettini. Crystal structure of GyrA intein from *Mycobacterium xenopi* reveals structural basis of protein splicing. *Nat. Struct. Biol.*, 5(1):31–36, Jan 1998.
- [498] R. Mohana-Borges, N. K. Goto, G. J. Kroon, H. J. Dyson, and P. E. Wright. Structural characterization of unfolded states of apomyoglobin using residual dipolar couplings. *J. Mol. Biol.*, 340(5):1131–1142, Jul 2004.
- [499] M. Ottiger, F. Delaglio, and A. Bax. Measurement of J and dipolar couplings from simplified two-dimensional NMR spectra. *J. Magn. Reson.*, 131(2):373–378, Apr 1998.
- [500] M. S. Ackerman and D. Shortle. Robustness of the long-range structure in denatured staphylococcal nuclease to changes in amino acid sequence. *Biochemistry*, 41(46):13791–13797, Nov 2002.

- [501] P. Bernado, L. Blanchard, P. Timmins, D. Marion, R. W. Ruigrok, and M. Blackledge. A structural model for unfolded proteins from residual dipolar couplings and small-angle x-ray scattering. *Proc. Natl. Acad. Sci. U.S.A.*, 102(47):17002–17007, Nov 2005.
- [502] P. E. Wright and H. J. Dyson. Linking folding and binding. *Curr. Opin. Struct. Biol.*, 19(1):31–38, Feb 2009.
- [503] T. Mittag, L. E. Kay, and J. D. Forman-Kay. Protein dynamics and conformational disorder in molecular recognition. *J. Mol. Recognit.*, 23(2):105–116, 2010.
- [504] K. A. Ball, A. H. Phillips, P. S. Nerenberg, N. L. Fawzi, D. E. Wemmer, and T. Head-Gordon. Homogeneous and heterogeneous tertiary structure ensembles of amyloid- peptides. *Biochemistry*, 50(35):7612–7628, Sep 2011.
- [505] Y. Yan and C. Wang. Abeta42 is more rigid than Abeta40 at the C terminus: implications for Abeta aggregation and toxicity. *J. Mol. Biol.*, 364(5):853–862, Dec 2006.
- [506] J. L. Jimenez, E. J. Nettleton, M. Bouchard, C. V. Robinson, C. M. Dobson, and H. R. Saibil. The protofilament structure of insulin amyloid fibrils. *Proc. Natl. Acad. Sci. U.S.A.*, 99(14):9196–9201, Jul 2002.
- [507] M. Zeeb and J. Balbach. Millisecond protein folding studied by NMR spectroscopy. *Protein Pept. Lett.*, 12(2):139–146, Feb 2005.
- [508] K. Klenin, B. Strodel, D. J. Wales, and W. Wenzel. Modelling proteins: conformational sampling and reconstruction of folding kinetics. *Biochim. Biophys. Acta*, 1814(8):977–1000, Aug 2011.
- [509] J. A. Raskatov and D. B. Teplow. Using chirality to probe the conformational dynamics and assembly of intrinsically disordered amyloid proteins. *Sci Rep*, 7(1):12433, Oct 2017.
- [510] Y. Mo, J. Lei, Y. Sun, Q. Zhang, and G. Wei. Conformational Ensemble of hIAPP Dimer: Insight into the Molecular Mechanism by which a Green Tea Extract inhibits hIAPP Aggregation. *Sci Rep*, 6:33076, 09 2016.
- [511] J. Zhang, X. Zhou, Q. Yu, L. Yang, D. Sun, Y. Zhou, and J. Liu. Epigallocatechin-3-gallate (EGCG)-stabilized selenium nanoparticles coated with Tet-1 peptide to

- reduce amyloid- aggregation and cytotoxicity. *ACS Appl Mater Interfaces*, 6(11): 8475–8487, Jun 2014.
- [512] C. Nitsche and G. Otting. NMR studies of ligand binding. *Curr. Opin. Struct. Biol.*, 48:16–22, 02 2018.